

**APPENDIX I**

**INER**

**INSTITUTE OF NUCLEAR ENERGY RESEARCH  
CHINA**

Appendix A, Composite Plots, comprises test data compiled and plotted from all organizations that participated in the Prestressed Concrete Containment Vessel (PCCV) Round Robin Pretest Analysis. To avoid duplicating the composite information, individual sets of data and/or plots have been omitted from participants' reports. In some cases this action resulted in disconnects between callouts and content and in the numbering of figures, tables, and pagination in some reports.

In Appendix I, "TNER, Institute of Nuclear Energy Research, China," discontinuity arises from omitting the following material:

Attachment 1, standard output location list

Attachment 2, standard output location plots

## Table of Contents

	Page
1. Finite element modeling of PCCV .....	6
2. Material properties .....	7
2.1 Concrete .....	7
2.2 Tendon .....	8
2.3 Rebar .....	8
2.4 Liner .....	9
3. Tendon preload .....	9
4. Boundary conditions .....	9
5. Loadings .....	10
6. Results and Discussions .....	10
7. Recommendation .....	11
8. References .....	12
Tables .....	13
Figures .....	15

**Table of Contents (Continued)**

	Page
Attachment 1 .....	24
Attachment 2 .....	26

## List of Tables

	Page
Table 1 Stress-Strain Data for High Strength Concrete .....	13
Table 2 Stress-Strain Data for Normal Concrete .....	13
Table 3 Stress-Strain Data for Tendon .....	14
Table 4 Stress-Strain Data for Rebar .....	14

## List of Figures

	Page
Fig. 1 Finite Element Model of PCCV .....	15
Fig. 2 Stress-Strain Curve for High Strength Concrete .....	15
Fig. 3 Stress-Strain Curve for Normal Concrete .....	16
Fig. 4 Stress-Strain Curve for Tendon .....	16
Fig. 5 Typical Stress-Strain Curve for Rebar .....	17
Fig. 6 Simplified Stress-Strain Curve for Liner .....	17
Fig. 7 Deformed Shape of PCCV as Tendon Pre-load Applied ...	18
Fig. 8 Vertical Displacement of Dome Top as Inner Pressure of PCCV Increased .....	18
Fig. 9 Deformed Shape of PCCV as Inner Pressure = 0.6942 Mpa .....	19
Fig. 10 Hoop Stress Distribution for Inner Side of PCCV as Inner Pressure = 0.6942 Mpa .....	19
Fig. 11 Meridian Stress Distribution for Inner Side of PCCV as Inner Pressure = 0.6942 Mpa .....	20

## List of Figures (Continued)

	Page
Fig. 12 Hoop Stress Distribution for Outer Side of PCCV as Inner Pressure = 0.6942 Mpa .....	20
Fig. 13 Meridian Stress Distribution for Outer Side of PCCV as Inner Pressure = 0.6942 Mpa .....	21
Fig. 14 Deformed Shape of PCCV as Inner Pressure = 0.8124 Mpa .....	21
Fig. 15 Hoop Stress Distribution for Inner Side of PCCV as Inner Pressure = 0.8124 Mpa .....	22
Fig. 16 Meridian Stress Distribution for Inner Side of PCCV as Inner Pressure = 0.8124 Mpa .....	22
Fig. 17 Hoop Stress Distribution for Outer Side of PCCV as Inner Pressure = 0.8124 Mpa .....	23
Fig. 18 Meridian Stress Distribution for Outer Side of PCCV as Inner Pressure = 0.8124 Mpa .....	23



## 1. Finite Element Modeling of PCCV

Referring to the outline sketch of the PCCV model shown in Design Package [1,2] Fig. 1, the PCCV is modeled as an axisymmetric structure with the penetrations on the cylinder, the wall thickness variation around these penetrations and the extruding of the buttress be neglected in this work. Using a general purpose computer program of stress analysis, ABAQUS [3], a 2-D axisymmetric shell element was first considered in the finite element modeling of PCCV for simplification. However, the use of this model implies that the tendons on top of the dome are arranged radially, which differs considerably from the actual arrangement shown in Design Drawing No. PCCV-QCON-11 Dome Prestressing Tendon Arrangement. The radiant tendon arrangement on top of the dome is too dense for the case. Consequently, convergence for the model calculation could not be reached due to the unsustainably large pre-loads on the dome top element when tendon pre-loading was imposed to this finite element model. The 2-D axisymmetric shell element model was later discarded accordingly. Considering the arrangement of the vertical tendons shown in Design Drawing No. PCCV-QCON-11, it is clear that the structure is symmetric to cross-section lines of angles  $0^\circ$ ,  $45^\circ$ ,  $90^\circ$ , and  $135^\circ$ . Therefore, finite element modeling on  $1/8$  of the circle is adequate for the case and the portion from  $135^\circ$  to  $180^\circ$  in the figure is selected for modeling. Cartesian coordinates are used with the origin set at the center of the top surface of the basemat. Positive X is in the direction of  $270^\circ$  whereas positive Y lies on the line of  $180^\circ$ . In addition, upward direction is set for positive Z. The dome and the cylinder are both modeled using ABAQUS 3-D shell element, S8R. Each element has 8 nodes with 6 degrees of freedom at each node and 4 integration points.

The basemat is modeled with ABAQUS 3-D solid element, C3D20. Each element has 20 nodes with 3 degrees of freedom at each node and 27 integration points. The finite element mesh of PCCV considered is as shown in Fig. 1. In addition, the interface elements on the bottom of the basemat, which allow the basemat to deform upwards freely when imposed by internal pressure or pre-loads are also used in the current model. These interface elements can also prevent the PCCV from digging into ground by its own weight as well as taking into account the effect of the weight of basemat. Thus, the result in our preliminary study on this PCCV problem regarding to the unreasonable deformation of basemat occurred can be removed.

## 2. Material Properties

### 2.1 Concrete

Concrete can be classified by its compression strength into high strength concrete and normal concrete for use in the PCCV model. Referring to Design Package Table 5, high strength concrete is selected with compression strength  $f_c' = 44.13$  MPa (6860 psi) and elastic limit  $f_y = 0.3 f_c' = 14.19$  MPa. In addition, according to a formula suggested by ACI Committee 318 (ACI, 1989), the initial modulus of elasticity of concrete  $E_c = 5700\sqrt{f_c'} = 4721000$  (psi) = 32552 (MPa), and Poisson's ratio ( $\nu$ ) is equal to 0.2. The maximum tensile strength ( $f_t'$ ) is calculated using  $f_t' = 4\sqrt{f_c'} = 331.3$ (psi) = 2.284 (MPa) as suggested by ASCE. The Stress-Strain correlation of plastic region applied is from Saenz (1964), which is

$$\sigma = \frac{E_c \varepsilon}{[1 + (R + R_E - 2)\left(\frac{\varepsilon}{\varepsilon_c}\right) - (2R - 1)\left(\frac{\varepsilon}{\varepsilon_c}\right)^2 + R\left(\frac{\varepsilon}{\varepsilon_c}\right)^3]}$$

Table 1 shows the corresponding stress for  $\varepsilon$  equals to 0.0007, 0.001, 0.015, 0.002, 0.0025, and 0.003.

The maximum compression strength ( $f_c$ ) for normal concrete is given in Design Package Table 5 to be 39.16 MPa (5680 psi). The other related material properties can be calculated using the formulas described previously. They are  $f_y = 0.3 f_c = 11.75$  MPa,  $E_c = 29619$  MPa and  $f'_t = 2.078$  MPa. Poisson's ratio ( $\nu$ ) is also equal to 0.2 for normal concrete. The stress-strain data for normal concrete is listed in Table 2. Figures 2 and 3 show the stress-strain curves for these two types of concrete.

## 2.2 Tendon

The stress-strain data for the tendon, which is derived for PCCV Design Package, is listed in Table 3. Figure 4 shows a curve plotted using the data in the table. The yielding stress of tendon is set to be 1482.5 Mpa with the average stress at 0.7% of strain. Dividing the yielding stress by 0.7% gives the Young's modulus,  $E = 211784$  MPa.

## 2.3 Rebar

The rebars used to construct PCCV model can be categorized into 11 different types by the material and the size. The typical stress-strain curve of these rebars is shown in Figure 5 by use of the data compiled from the Design Package. Table 4 shows the

values of these data point on the idealized stress-strain curves for these rebars.

## 2.4 Liner

From the data provided in the Design Package, the yielding stress can be set to be 375 MPa for liners, and the corresponding Young's modulus is 22800 MPa while a yielding strain of 0.164% is taken into account. Since the thickness of the liner (1.6 mm) is much smaller than that of the concrete (32.5 cm), the effect of the liner on the PCCV strength is insignificant. Therefore, it is assumed that the stress of the liner remains constant beyond the yielding point. The simplified stress-stain curve is shown in Figure 6.

## 3. Tendon Pre-loads

For simplification, the friction effect is neglected and the tendon pre-load is set to be a constant, being the average pre-load of the tendon between the loading point and the fixed point. For vertical and hoop tendons, the pre-loads are 109.45 kips and 90.3 kips, respectively. The prestress can be calculated by dividing the pre-load by the cross section area of the tendon ( $0.525451 \text{ in}^2 = 339 \text{ mm}^2$ ), which yields 208300 psi (1436 MPa) for the vertical tendon and 171850 psi (1185 MPa) for the hoop tendon.

## 4. Boundary Conditions

Assuming that all the nodes in the center line of the basemat are fixed in place, the nodes on the boundary of both sides can only move in radial and Z directions due to symmetry. There is no movement in the hoop direction.

## 5. Loadings

PCCV loadings include: a. tendon pre-loads as described in the previous section; b. weight of PCCV, only the concrete weight of the dome and the cylinder is considered, neglecting the weight of tendons and rebars embedded in the concrete. In addition, the weight of the basemat and liners is also neglected; c. internal pressure of PCCV, the pressure imposed on the inner walls of the cylinder and the dome, and the top surface of the basemat. According to Riks method which is an approach of proportional loading increment employed for nonlinear analysis in ABAQUS, during the internal pressure buildup process, ABAQUS can adjust the pressure increment correspondingly to the deformation of the structure. As the pressure increment approaches 0, no more stress can be added to the structure and the PCCV will reach its limitation of compression.

## 6. Results and Discussions

As shown in Figure 7, the deformation of the PCCV under pre-loads, the model contracts downwards as well as inwards. With internal pressure imposed, the Z displacement of the node (584) on top of the dome is plotted against the internal pressure as shown in Figure 8. Owing to the weight of the dome and the cylinder as well as the pre-loads of tendons, the dome top node is displaced 3.46 mm downwards initially. As the internal pressure increases, the dome top node is gradually lifted and so is the basemat. As the internal pressure reaches 0.6942 MPa (101.5 psi), 1.78 times the design pressure of 0.39 MPa (57 psi) for PCCV prototype, cracks start to

develop at and near the junction of the cylinder and the basemat. The deformation of the PCCV at this internal pressure is shown in Figure 9 and the corresponding stress distributions in the hoop and the meridian directions for inner and outer sides of the PCCV are shown in Figure 10 - 13. As the internal pressure reaches 0.8124 MPa (118.7 psi), 2.08 times the design pressure for PCCV prototype, the PCCV has reached its limitation of compression. The deformation of the PCCV at this internal pressure is shown in Figure 14 and the corresponding stress distributions in the hoop and the meridian directions for inner and outer sides of the PCCV are shown in Figure 15 - 18.

Originally, the result with the basemat deflected downwards slightly which maybe due to the weight of the dome and the cylinder had been obtained in our preliminary study. However, this will disagree the real practice. In current model, the finite element model with interface elements on the bottom of the basemat has been employed. Basemat will thus to be allowed to deform upwards freely when it is imposed by internal pressure or pre-loads. These interface elements can also prevent the PCCV from digging into ground by its own weight as well as taking into account the effect of the basemat weight. With the modification, the model becomes closer to reality and hopefully more accurate analysis can be obtained.

## 7. Recommendation

As the above mention in this report, the axisymmetric model with 1/8 azimuth circle of the overall PCCV has been developed using the ABAQUS finite element analysis program. The plastic instability of the PCCV is thus analyzed and the limitation of the internal pressure which PCCV can sustain has also been obtained successfully.

But it is worth to note that the current result is for the global structural behaviors of PCCV subjected to the internal pressure, the local responses near the penetration, airlock and equipment hatch are still not obtained yet. For the results near those areas, more detailed models with substructure modeling or a full 3-D modeling need to be used in the future.

## 8. References

- [1] PCCV Round Robin Analysis – Release of Design Package, SO-97-047, received from Dr. Vincent K. Luk of Sandia National Laboratories.
- [2] PCCV Round Robin Analysis – Release of Design Package updated, SO-98-052, received from Dr. Vincent K. Luk of Sandia National Laboratories.
- [3] ABAQUS/Standard User's Manual, Version 5.6, Hibbitt, Karlsson & Sorensen, Inc.

Table 1. Stress - Strain Data for High Strength Concrete

Strain	Stress
0.0007	2925.5472 (psi) = 20.17 Mpa
0.001	3942.2311 (psi) = 27.18 Mpa
0.0015	5296.3478 (psi) = 36.52 Mpa
0.002	6212.0682 (psi) = 42.83 Mpa
0.0025	6712.1024 (psi) = 46.28 Mpa
0.003	6860.0435 (psi) = 47.30 Mpa

Table 2. Stress - Strain Data for Normal Concrete

Strain	Stress
0.0007	2533.9563 (psi) = 17.47 Mpa
0.001	3367.0129 (psi) = 23.22 Mpa
0.0015	4450.4913 (psi) = 30.69 Mpa
0.002	5171.4007 (psi) = 35.66 Mpa
0.0025	5563.2655 (psi) = 38.36 Mpa
0.003	5679.4779 (psi) = 39.16 Mpa

Table 3. Stress - Strain Data for Tendon

Strain (%)	Stress (Mpa)				
	Spe. 1	Spe. 2	Spe. 3	Spe. 6	Avg.
0.0	0	0	0	0	0
0.7	1468.4	1487.0	1484.6	1490.0	1482.5
0.8	1611.1	1613.4	1618.0	1620.4	1615.7
0.9	1701.8	1692.6	1701.3	1701.1	1699.2
1.0	1752.8	1736.2	1746.8	1744.6	1745.1
1.2	1785.0	1763.1	1773.9	1770.9	1773.2
1.5	1811.4	1789.5	1800.0	1803.9	1801.2
2.0	1848.0	1826.9	1859.1	1844.3	1844.6
2.5	1883.4	1863.5	1890.6	1898.7	1884.0

Table 4. Stress - Strain Data for Rebar

TYPE	E (Mpa)	$\sigma_y$ (Mpa)	$\epsilon_y$ (%)	$\epsilon_{st}$ (%)	$\sigma_u$ (Mpa)	$\epsilon_u$ (%)
SD345-D6	1.69 E5	369.4	0.219	1.6	450	7
SD345-D10	1.82 E5	371.0	0.204	1.4	500	8
SD390-D10	1.83 E5	472.9	0.258	1.5	600	8
SD490-D10	1.87 E5	491.1	0.263	1.6	620	7
SD390-D13	1.83 E5	432.3	0.236	1.2	570	7
SD490-D13	1.84 E5	548.3	0.298	1.2	720	7
SD390-D16	1.83 E5	457.5	0.250	1.5	580	7
SD490-D16	1.85 E5	547.0	0.296	1.2	640	7
SD390-D19	1.84 E5	473.1	0.257	1.5	610	7
SD490-D19	1.86 E5	512.2	0.275	1.5	660	7
SD390-D22	1.91 E5	459.0	0.240	1.0	650	7

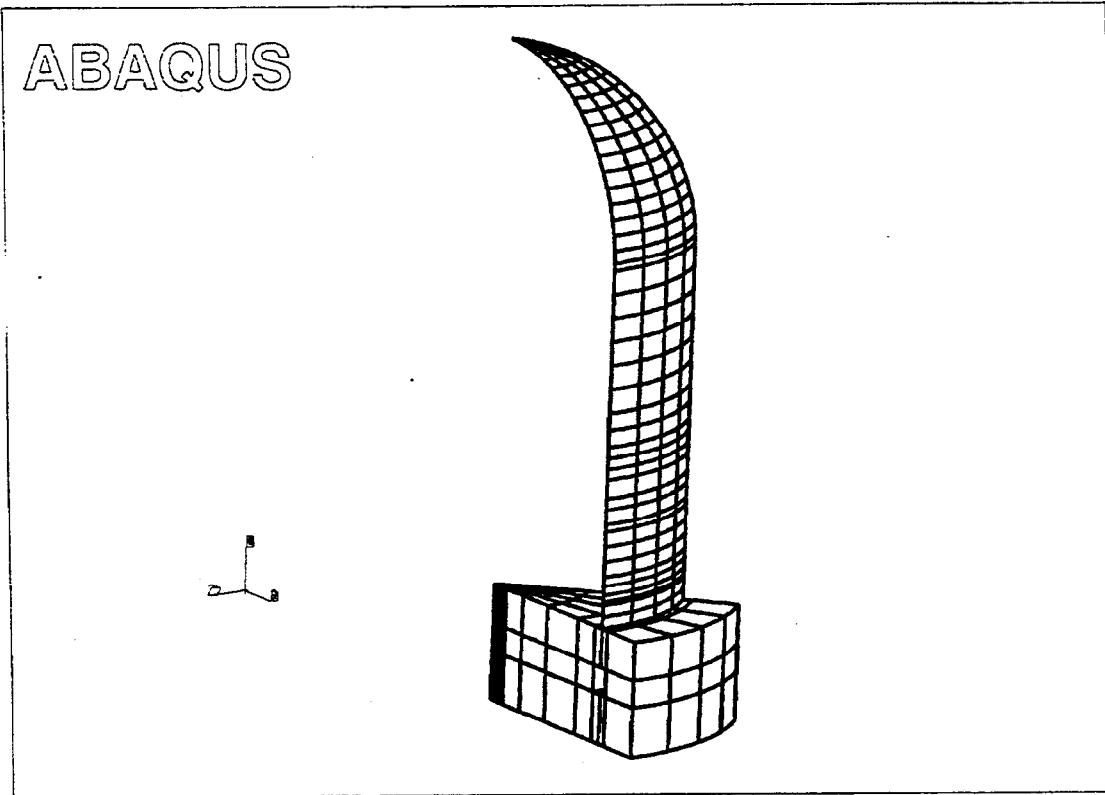


Fig. 1. Finite Element Model of PCCV

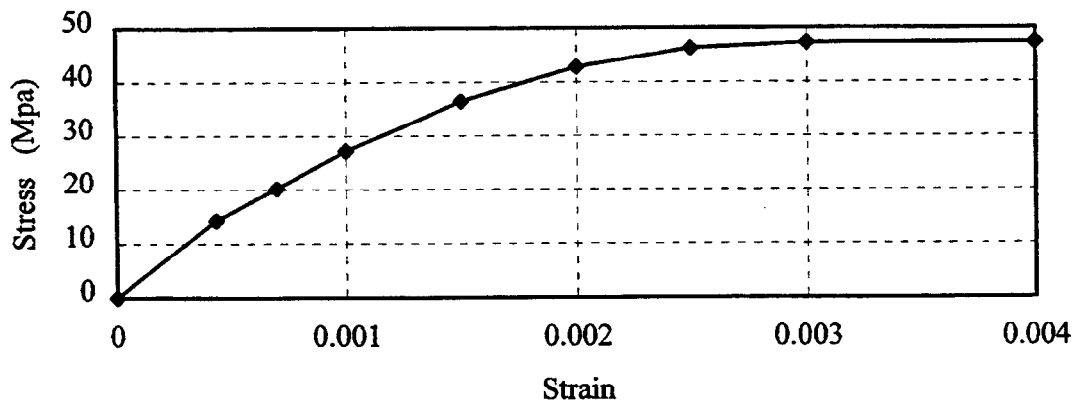


Fig. 2. Stress - Strain Curve for High Strength Concrete

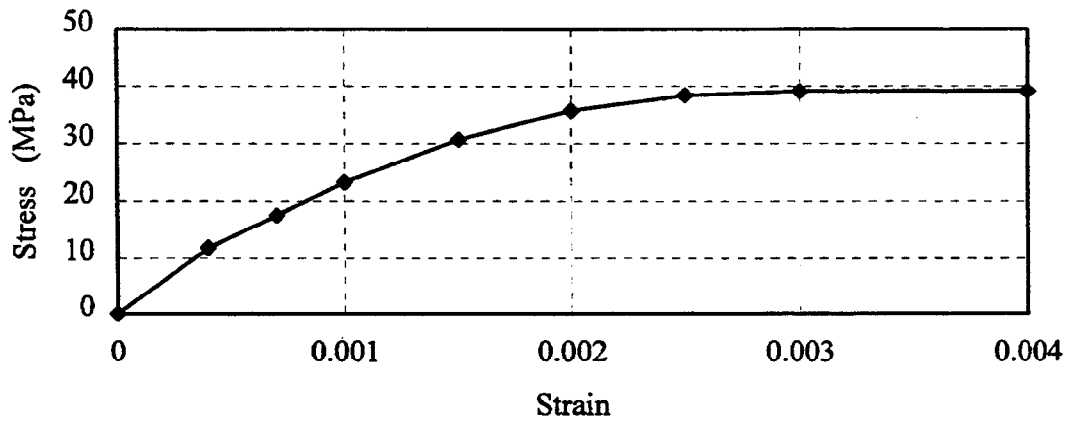


Fig. 3. Stress - Strain Curve for Normal Concrete

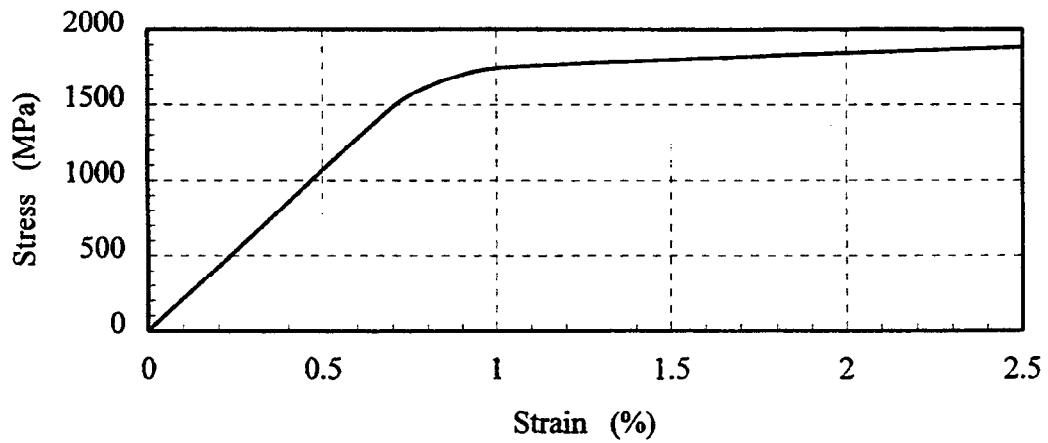


Fig. 4. Stress - Strain Curve for Tendon

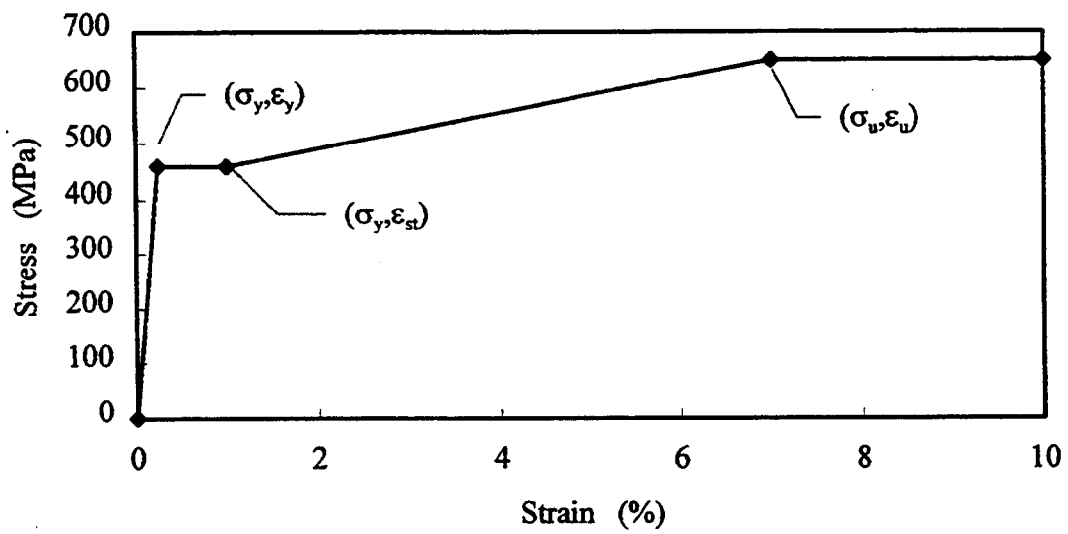


Fig. 5. Typical Stress - Strain Curve for Rebar

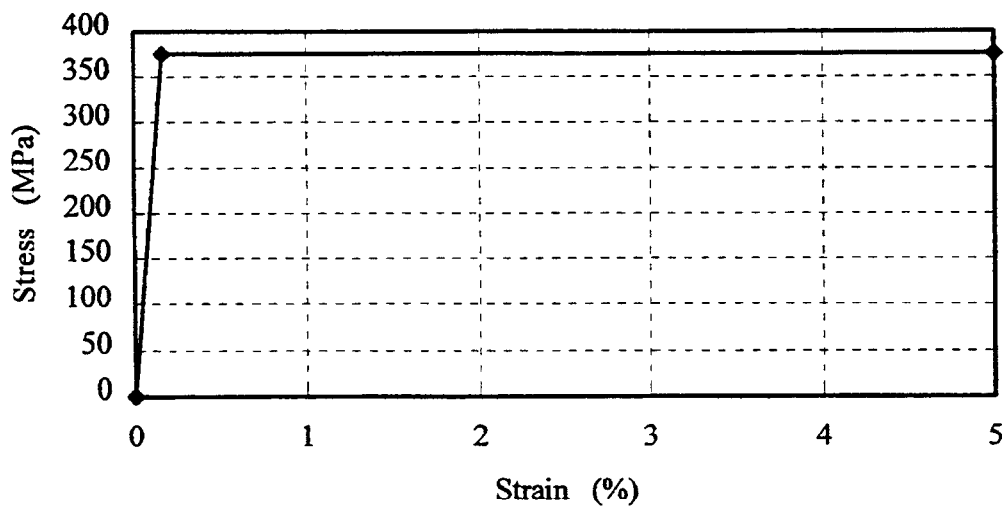


Fig. 6. Simplified Stress - Strain Curve for Liner

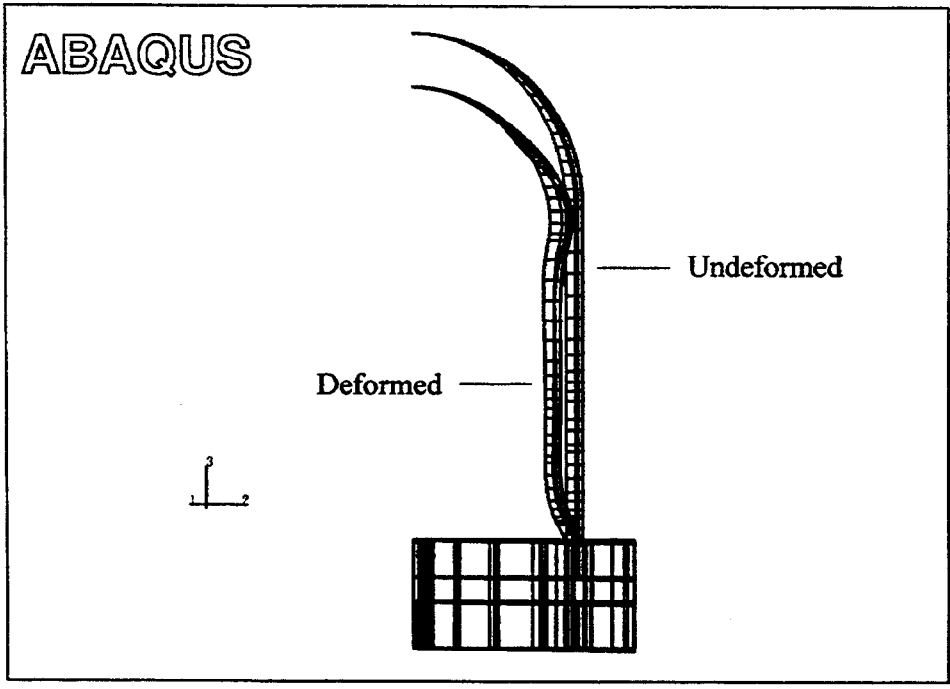


Fig 7. Deformed Shape of PCCV as Tendon Pre-load applied

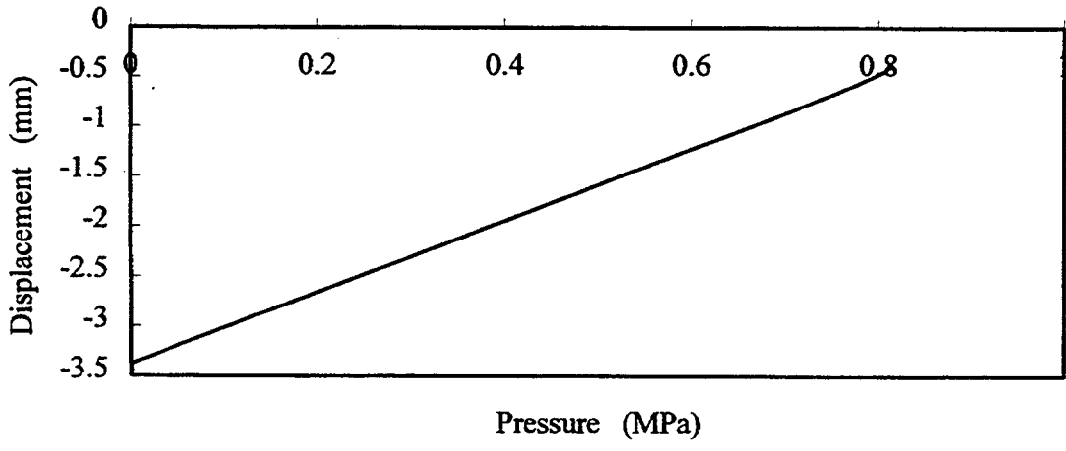


Fig. 8. Vertical Displacement of Dome Top as Inner Pressure of PCCV Increased

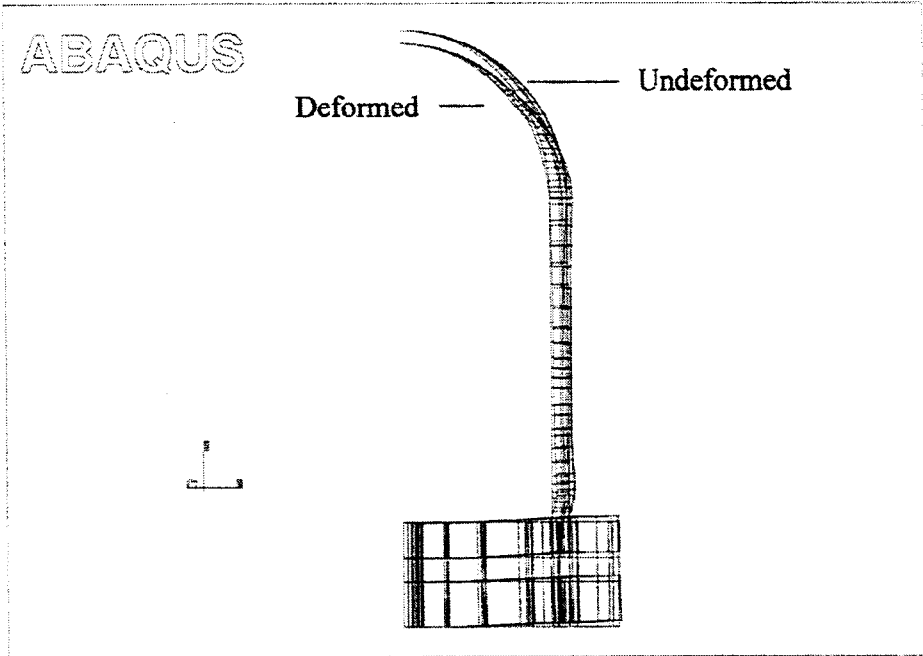


Fig 9. Deformed shape of PCCV as Inner Pressure = 0.6942 Mpa

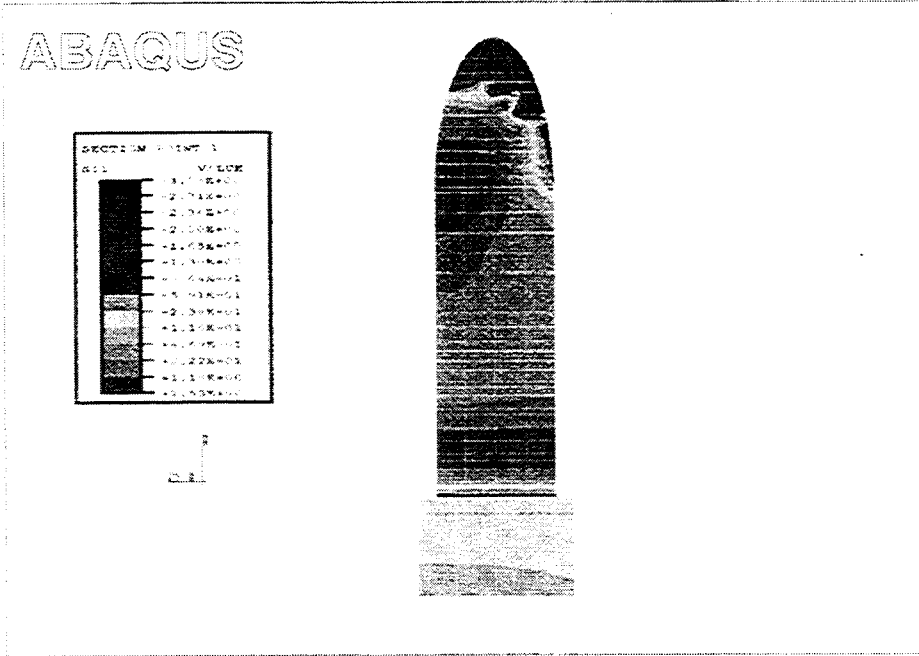


Fig. 10. Hoop Stress Distribution for Inner Side of PCCV as Inner Pressure = 0.6942 Mpa

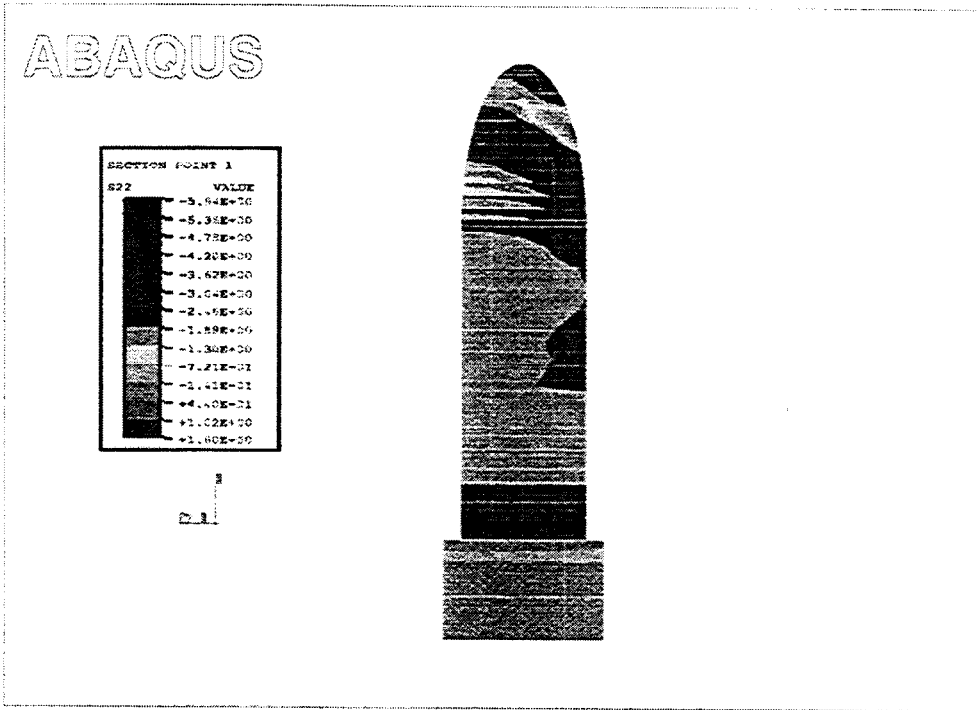


Fig. 11. Meridian Stress Distribution for Inner Side of PCCV as  
Inner Pressure = 0.6942 Mpa

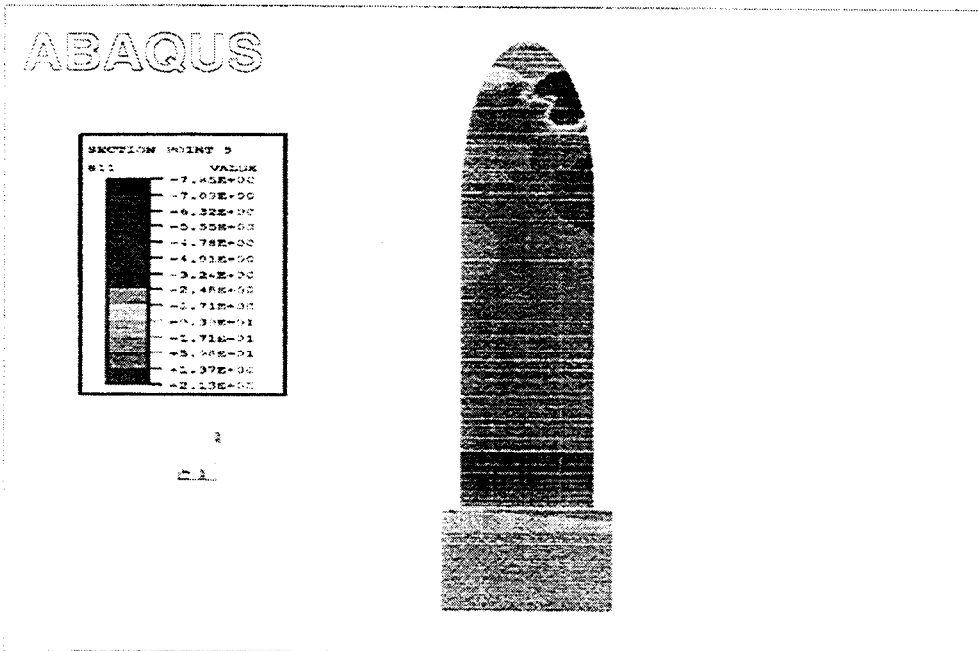


Fig. 12. Hoop Stress Distribution for Outer Side of PCCV as  
Inner Pressure = 0.6942 Mpa

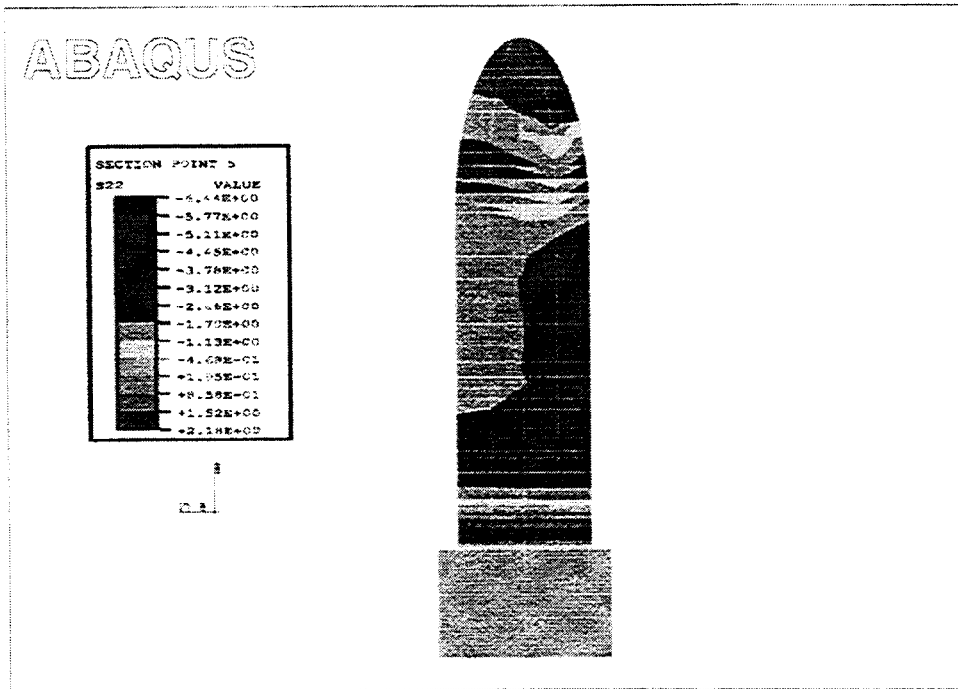


Fig. 13. Meridian Stress Distribution for Outer Side of PCCV as Inner Pressure = 0.6942 Mpa

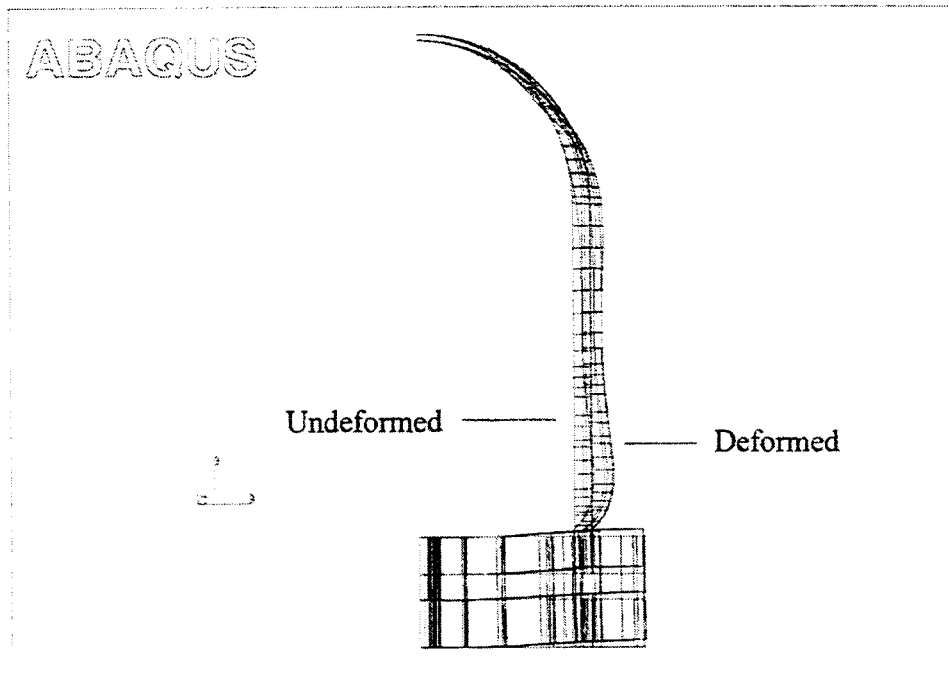


Fig 14 Deformed Shape of PCCV as Inner Pressure = 0.8124 Mpa

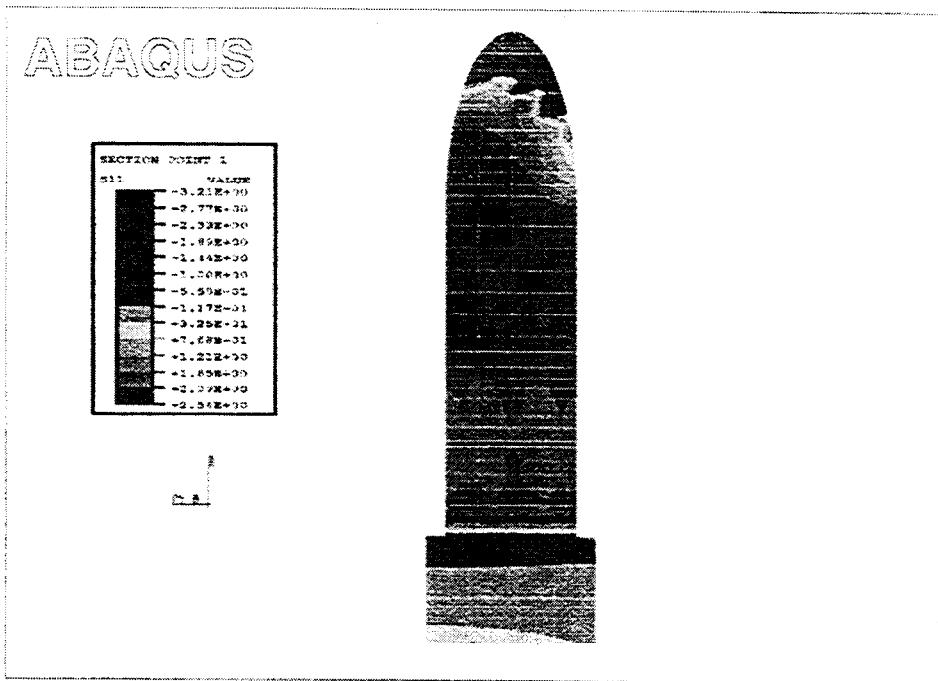


Fig. 15. Hoop Stress Distribution for Inner Side of PCCV as Inner Pressure = 0.8124 Mpa

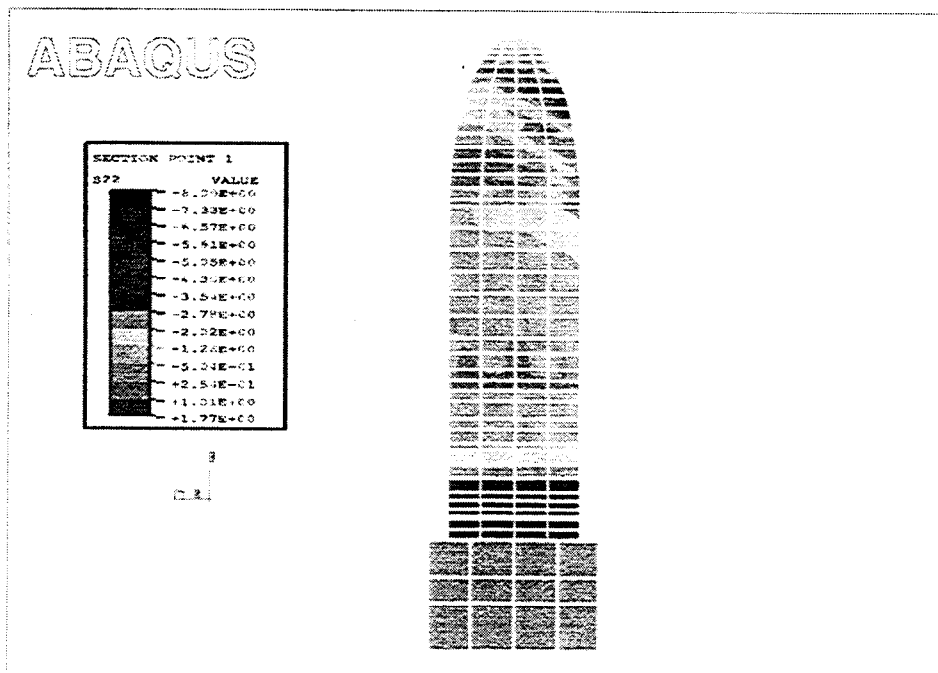


Fig. 16. Meridian Stress Distribution for Inner Side of PCCV as Inner Pressure = 0.8124 Mpa

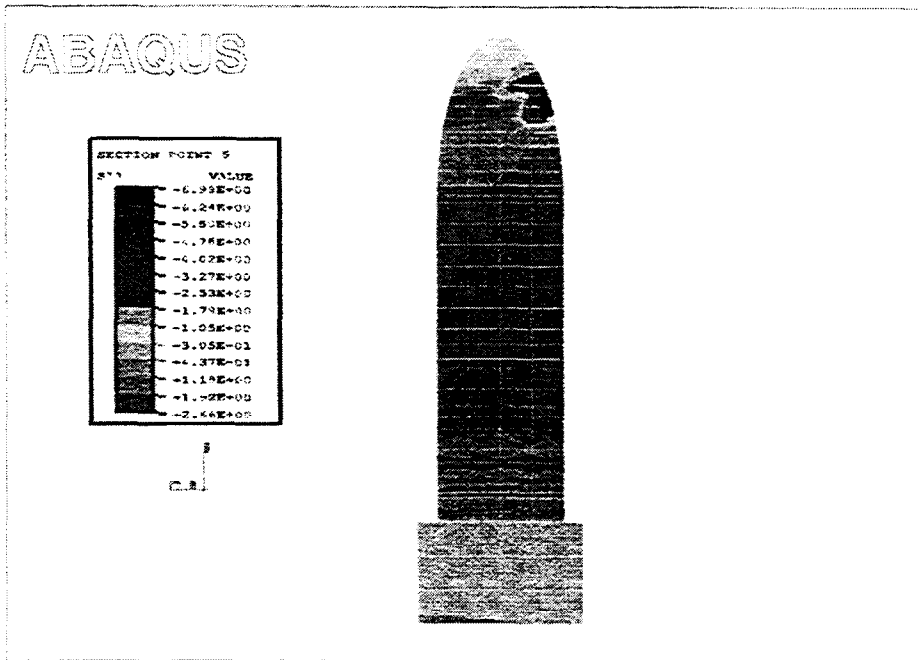


Fig. 17. Hoop Stress Distribution for Outer Side of PCCV as  
Inner Pressure = 0.8124 Mpa

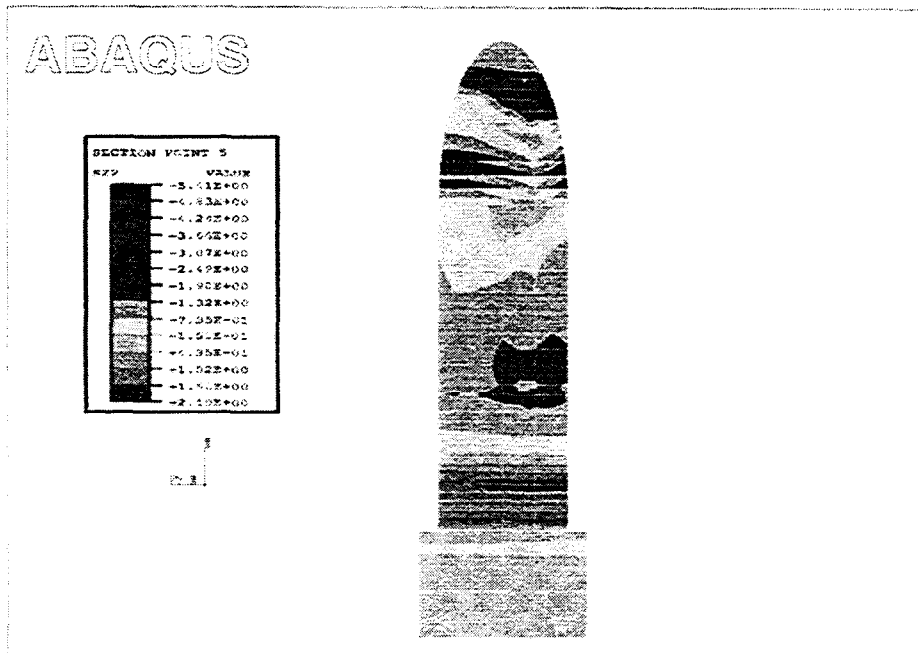


Fig. 18. Meridian Stress Distribution for Outer Side of PCCV as  
Inner Pressure = 0.8124 Mpa

# **APPENDIX J**

**IPSN**

**INSTITUT DE PROTECTION ET DE  
SÛRETÉ NUCLÉAIRE  
FRANCE**

Appendix A, Composite Plots, comprises test data compiled and plotted from all organizations that participated in the Prestressed Concrete Containment Vessel (PCCV) Round Robin Pretest Analysis. To avoid duplicating the composite information, individual sets of data and/or plots have been omitted from participants' reports. In some cases this action resulted in disconnects between callouts and content and in the numbering of figures, tables, and pagination in some reports.

In Appendix J, "IPSN, Institut de Protection et de Sécurité Nucléaire, France," discontinuity arises from omitting the following material:

# **I - Choice of finite element model :**

## **1) Axisymmetric model :**

- Difficulties of axisymmetric modelisation to make equivalent to :  
    **Structural : sections of rebars and tendons.**  
    **Materiel : concrete behaviour in OTTOSEN model.**
- Limitation of results

## **2) Tridimensionnel (3D) model :**

- Difficulties caused by the big number of data to be introduced
- Need of performant computer system with much time for calculations

### **3) Tridimensionnel axisymmetric model (slice model) :**

- Intermediate solution**
- Better representation of rebars**
- Better representation of the concrete model**
- Reasonable time of calculations**
- Disadvantage :**

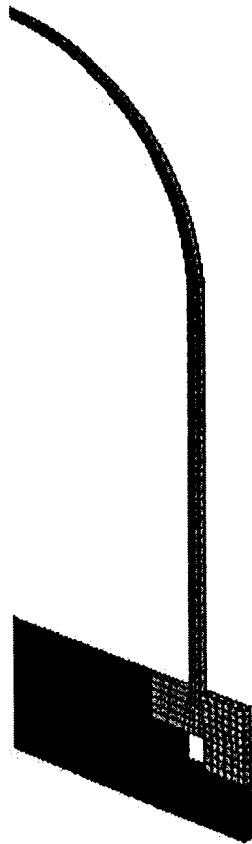
**limitation of results in standard section**

**Difficulties caused by introduction of prestressing load**

## **II - Slice model :**

### **1) Mesh :**

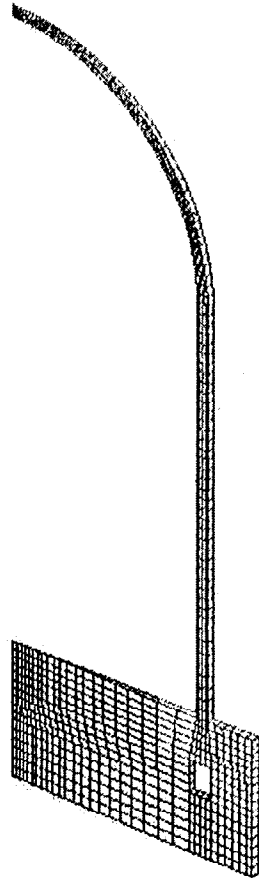
- Represents a thin slice (2° degrees) in a standard section (azimuth 135) around tendon.**
- The concrete is represented by 828 solid elements**
- The liner is represented by 208 shell elements**
- The rebars are represented by 1477 truss elements**



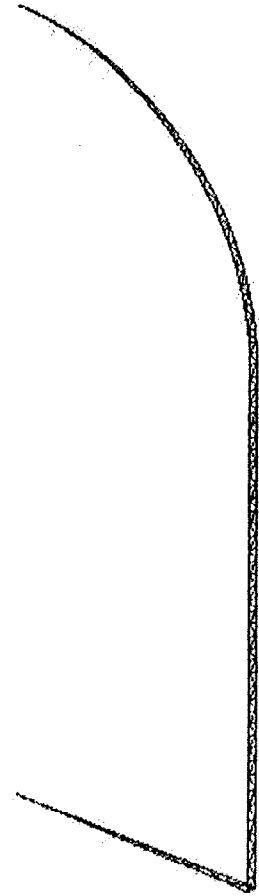
SLICE MODEL



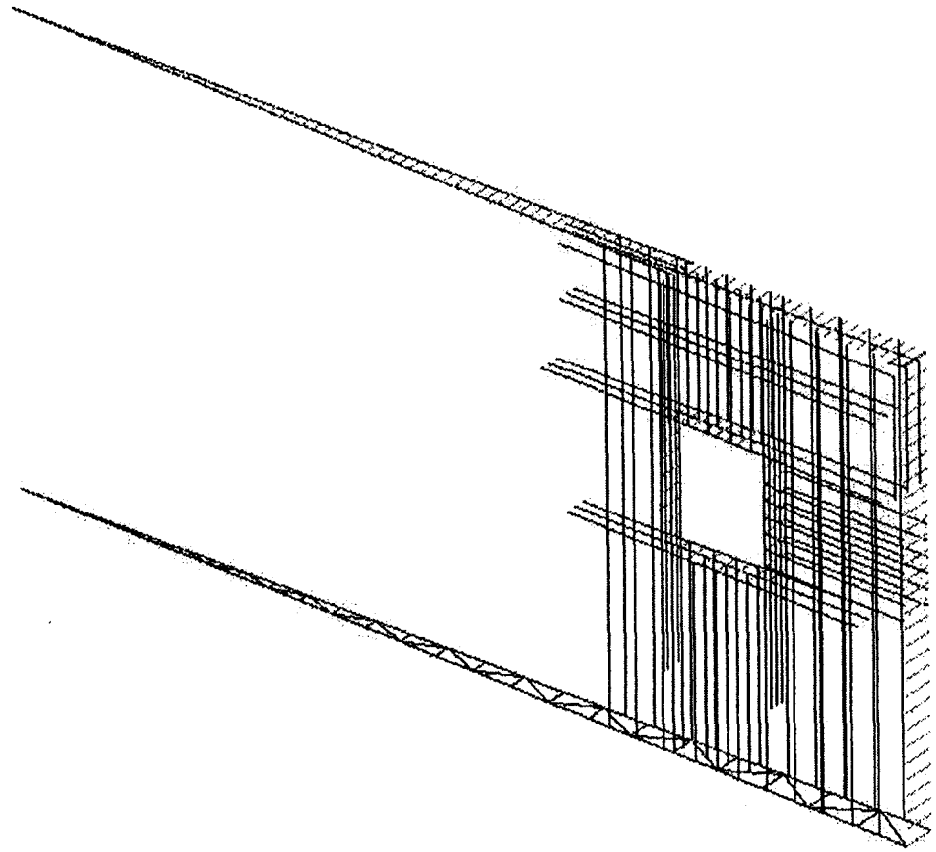
SLICE MODEL



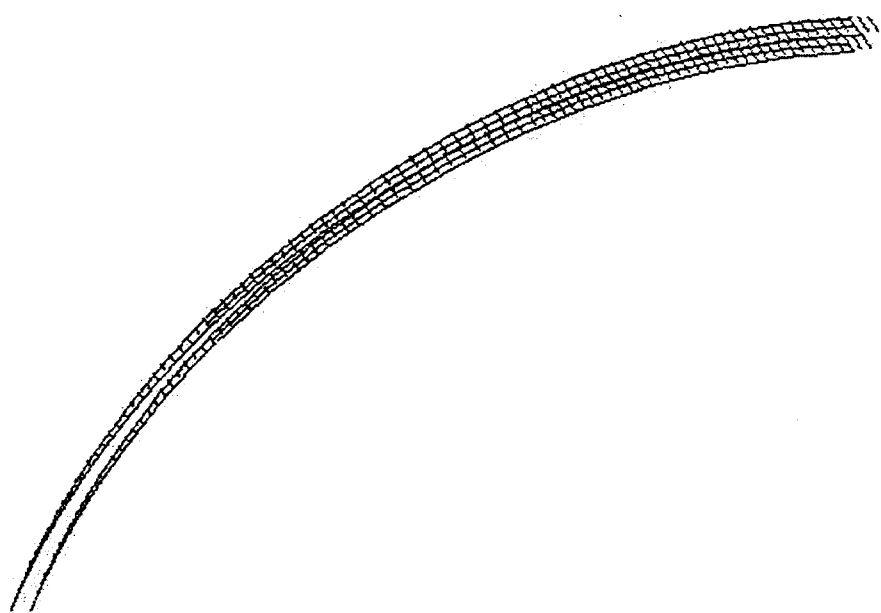
SLICE MODEL



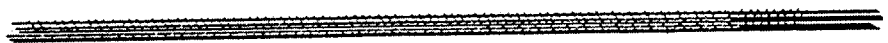
SLICE MODEL



RADIER



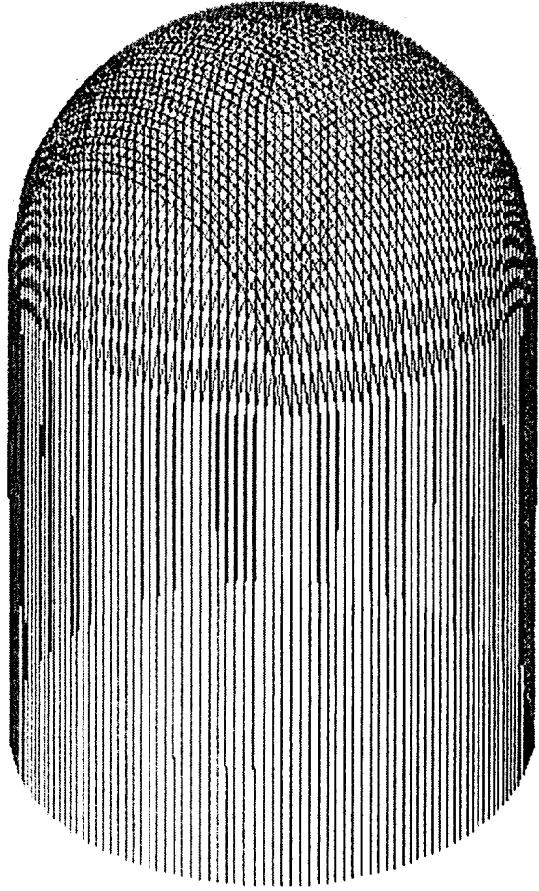
DOMI



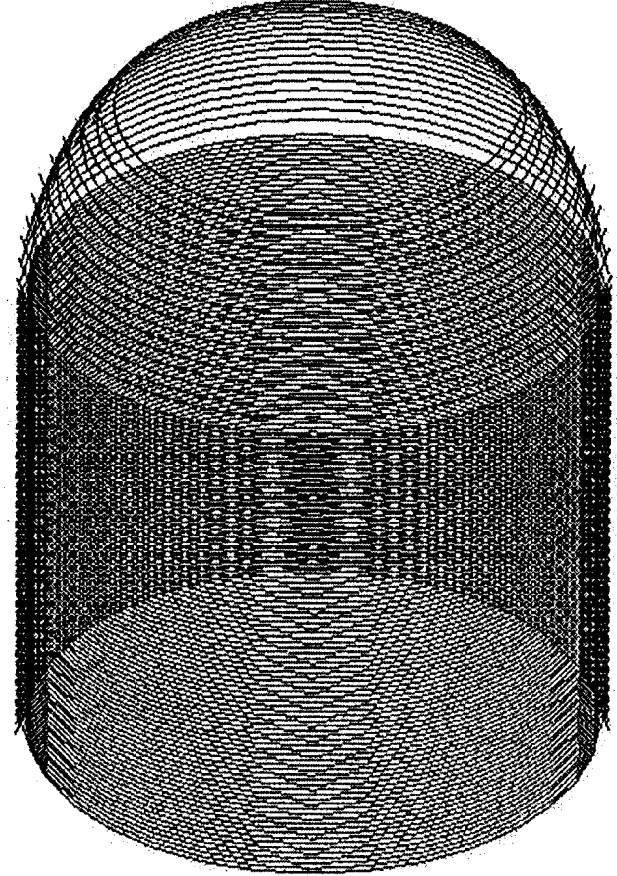
FUI

## **2) Introduction of prestressing load :**

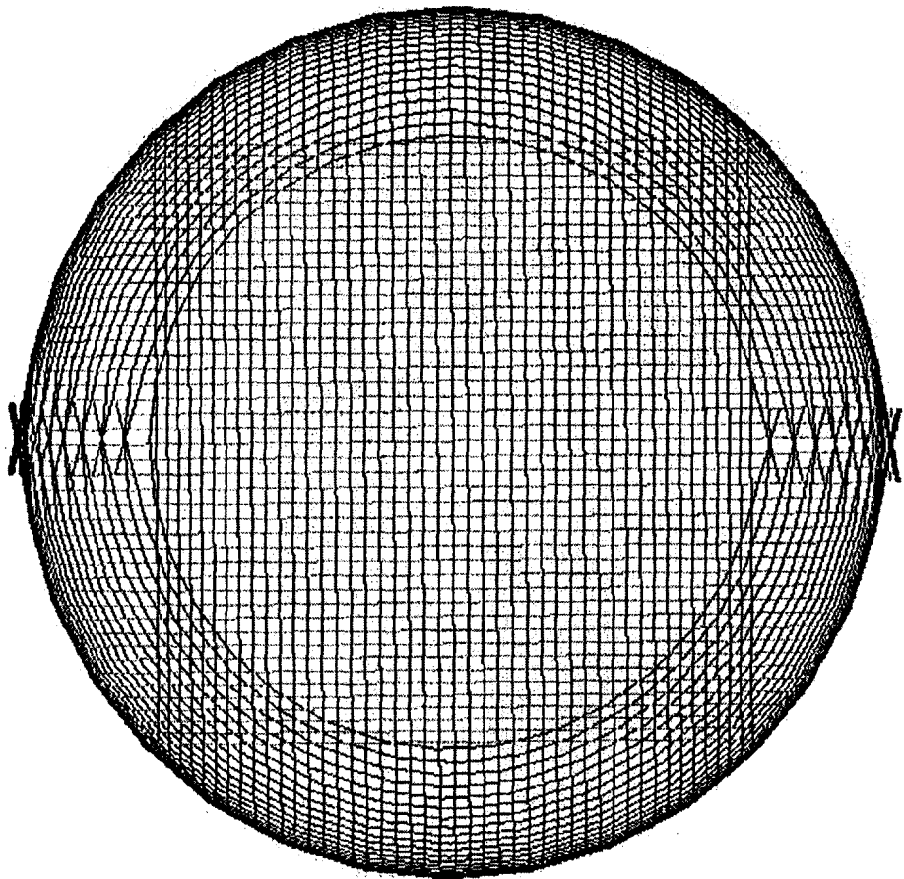
- 3 D model mesh with solid elements**
- The concrete is represented by 5792 solid elements**
- The liner is represented by 868 shell elements**
- The tendons are represented by 6576 truss elements**
- Application of prestressing load on 3 D model**  
**(for each tendon  $F_V = 303.1$  KN,  $F_H = 453.3$  KN)**



VERTICAL PRESTRESSING TENDONS

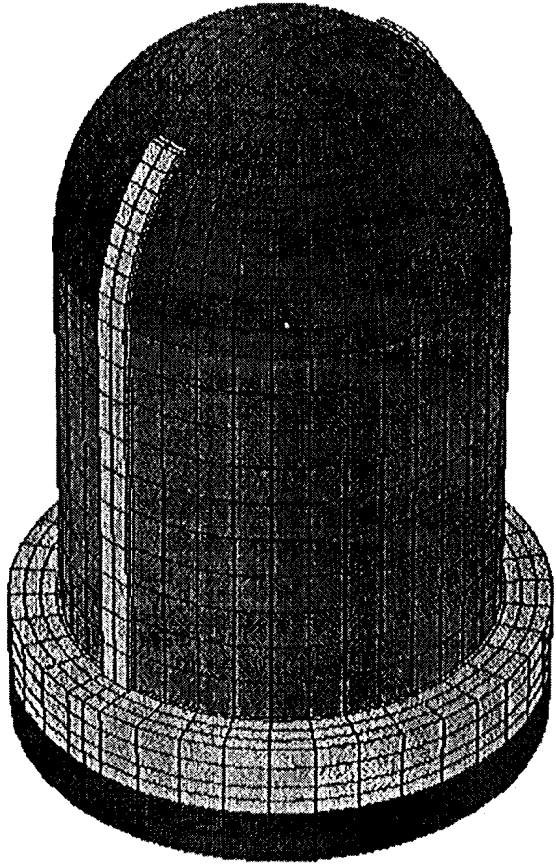


HORIZONTAL PRESTRESSING TENDONS

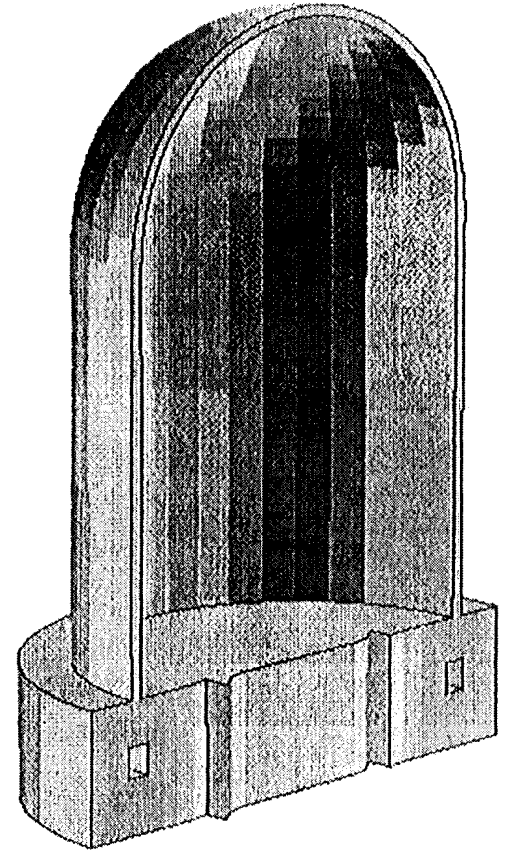


FRSINSSING TIDONS

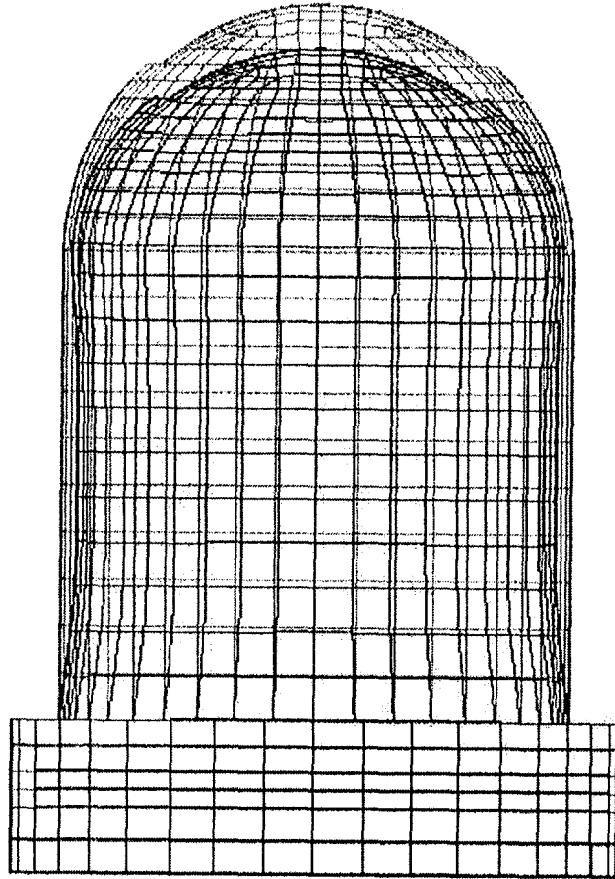
- **Calculation of displacements caused by the prestressing load**
- **Projection of displacements on the slice model**
- **Calculation of forces in the slice model caused by imposed displacements**
- **Introduction of traction force in the tendons**



MAQUETTE FCCV - ENSEMBLE



MAQUETTE FCCV - MOITIE

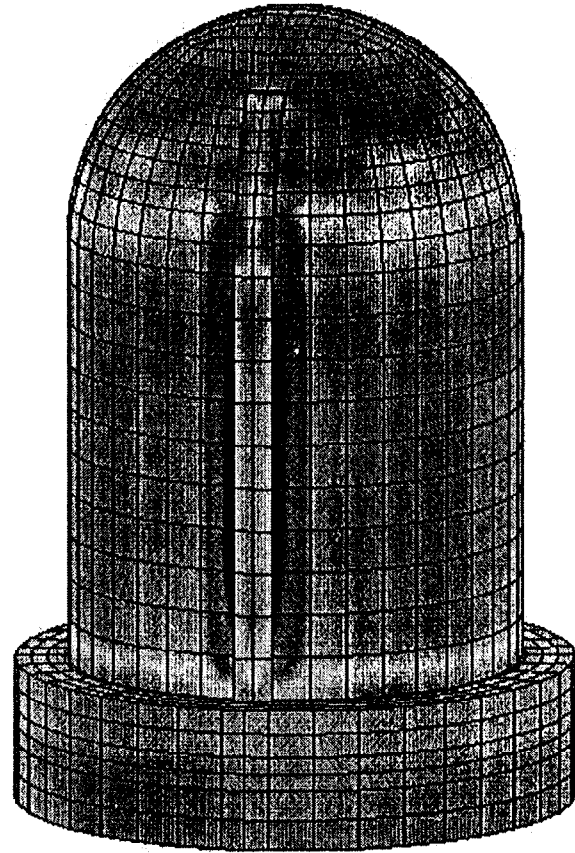


DEFORMED STRUCTURE UNDER PRESTRESSING LOAD 300 AMPL

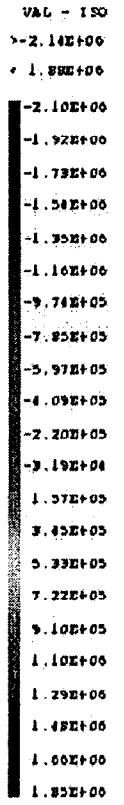
AMPLITUDE

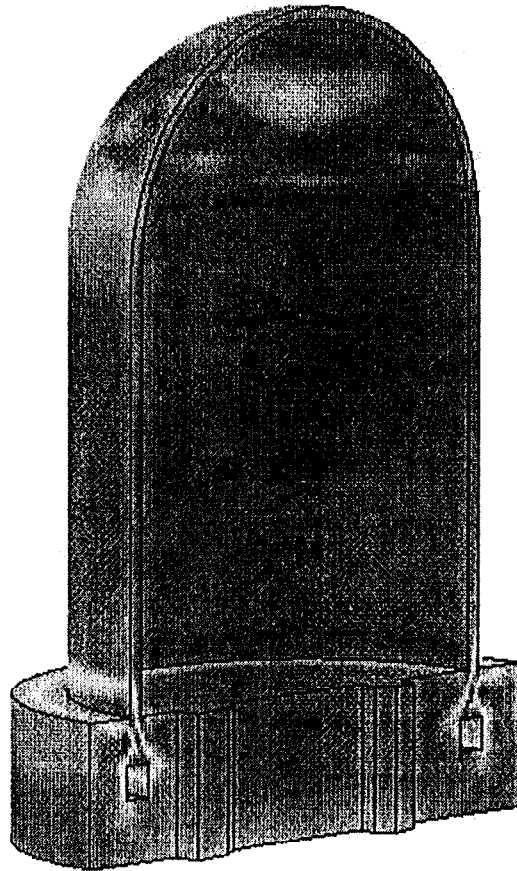
0.00E+00

2.00E+02

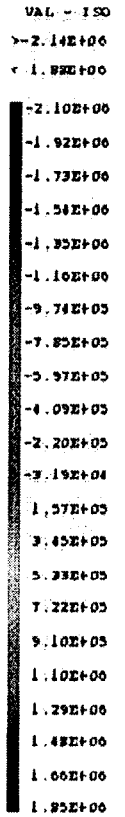


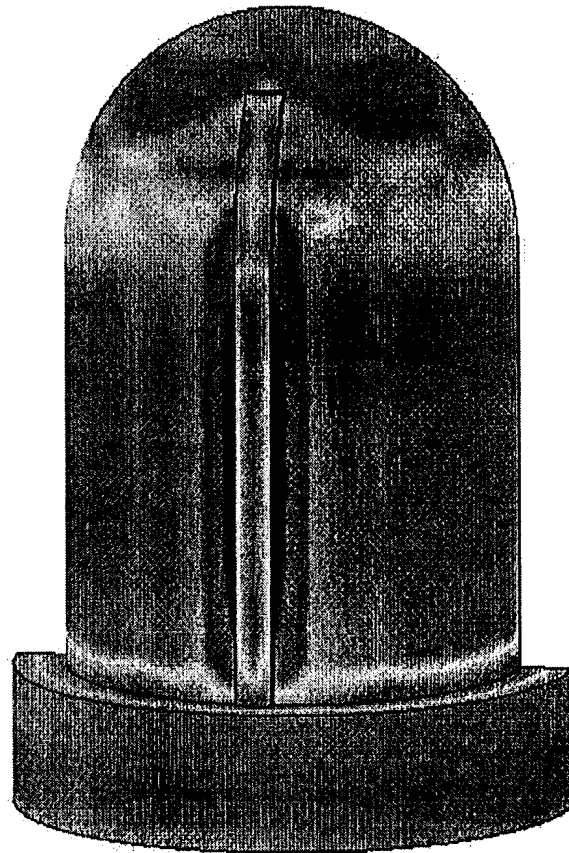
UNDER PRESTRESSING LOAD: PRINCIPAL STRESS MAXI 2.356190+00 MPa



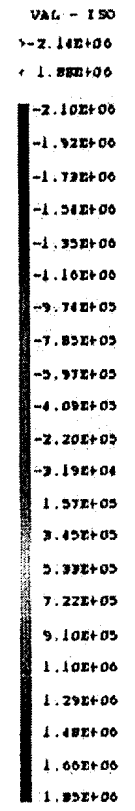


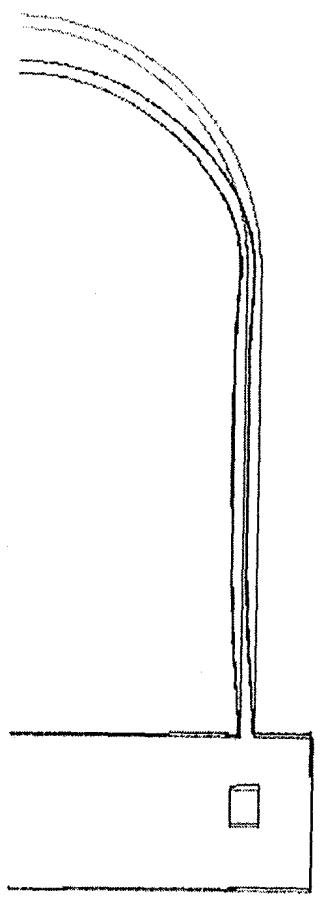
UNDER PRESTRESSING LOAD: PRINCIPAL STRESS MAXI 2.35619E+06 MPa





UNDER PRESTRESSING LOAD: PRINCIPAL STRESS MAXI 2.35619E+06 MPa



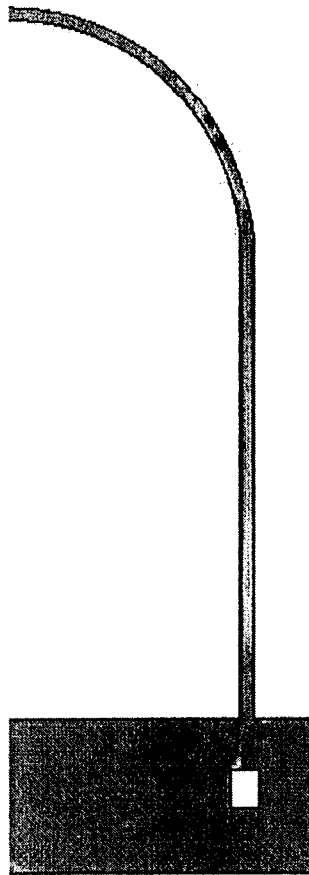


DEFORMED STRUCTURE UNDER PRESTRESSING LOAD 300 AMPL

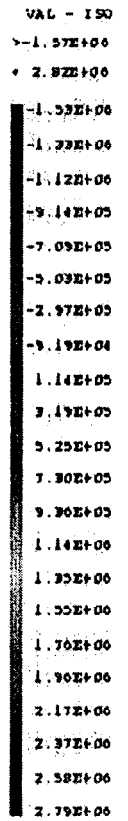
AMPLITUDE

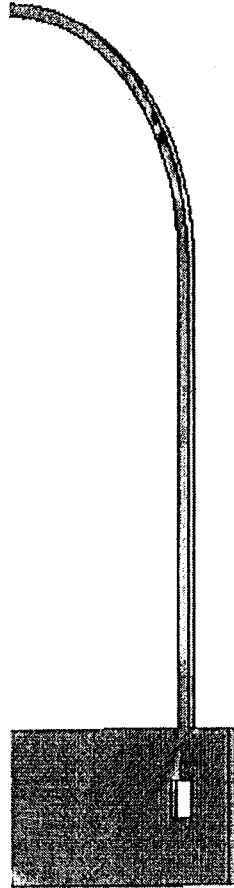
0.00E+00

3.00E+02

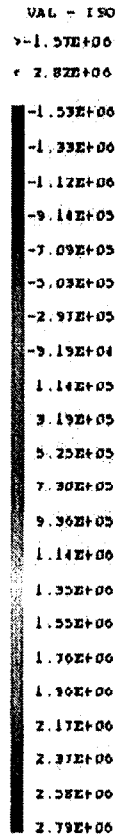


UNDER PRESTRESSING LOAD: PRINCIPAL STRESS MAXI 2.53801E+06 MPa





UNDER PRESTRESSING LOAD: PRINCIPAL STRESS MAXI 2.53861E+06 MPa



### **III - RESULTS :**

#### **1) Actual state :**

- Use of CASTEM 2000 software for computations**
- Difficulties due to the arriving of the computer system**
- The slice model in progress**

#### **2) Next step :**

- realisation of the 3 D model**

**APPENDIX K**

**JAERI**

**JAPAN ATOMIC ENERGY RESEARCH INSTITUTE  
JAPAN**

Appendix A, Composite Plots, comprises test data compiled and plotted from all organizations that participated in the Prestressed Concrete Containment Vessel (PCCV) Round Robin Pretest Analysis. To avoid duplicating the composite information, individual sets of data and/or plots have been omitted from participants' reports. In some cases this action resulted in disconnects between callouts and content and in the numbering of figures, tables, and pagination in some reports.

In Appendix K, "JAERI, Japan Atomic Energy Research Institute, Japan," discontinuity arises from omitting the following material:

figures 12 through 24, standard output location plots

## **Contents**

<b>1. Introductions</b>	<b>1</b>
<b>2. Analytical Models</b>	<b>2</b>
<b>3. Calculated Results</b>	<b>4</b>
<b>4. Discussions</b>	<b>6</b>
<b>5. Conclusions</b>	<b>8</b>
<b>References</b>	<b>45</b>



## 1. Introduction

Containment Model Tests to investigate a failure of the containment vessel have been initiated as a joint research program among Nuclear Power Engineering Corporation (NUPEC), U.S. Nuclear Regulatory Commission (NRC) and Sandia National Laboratories (SNL). For the effective pre and posttest analysis of these tests, the Round Robin analytical activities have been organized.

JAERI has performed the post-test analysis of SNL's 1/6 scale RCCV test [1][2], and the pre and posttest analysis of this Steel Containment Vessel (SCV) test[3] with ABAQUS code. The present paper describes the results of the pre-test analysis for PCCV test.

## 2. Analytical Models

The FEM code for nonlinear analysis, ABAQUS[4] was used to analyze the 1/4 scale PCCV model. In this report, two different FEM models were created. A quarter symmetric three-dimensional model with shell elements was used to analyze behavior at standard output locations. The other model was an axisymmetric shell model, and used to discuss possible failure modes.

### (1) 3D shell model

Concrete and liners on the basemat, the cylinder and the dome were modeled with 4-nodes shell elements(S4R). Reinforcement bars in concrete were modeled with REBAR defined in shell elements. For both hoop and hairpin tendons, BAR elements were used. An area between 90 and 180 degrees in the global coordinate system was modeled to analyze free-field behavior in the azimuth of 135 degrees. The buttress in 90 degree was modeled in the FEM mesh, although the equipment hatch and any other penetrations were not included. The FEM mesh of the 3D shell model is presented in Fig. 1. Figure 2 shows mesh of hoop and hairpin tendons modeled with BAR elements. As shown in Fig. 2, the layout of tendons in dome were different from actual model, because the complex arrangement of rebars and tendons in the dome was hardly modeled as they were constructed. In this portion, section areas of tendons and rebars were set to represent actual values. The center of basemat was fixed and symmetric conditions were given as node constraints to the nodes on symmetric surfaces. The preloads for tendons were applied with thermal expansion, and internal pressure was loaded to shell elements of liners.

### (2) Axisymmetric shell model

In this axisymmetric shell model, only the portions of the cylinder and the dome were included in the FEM mesh. Concrete and liners were modeled with axisymmetric shell elements (SAX2) and defined as composite shell. Rebars and hairpin tendons were modeled with REBAR, while narrow axisymmetric shell elements were used for hoop tendons. The node at the bottom of the model on the basemat was fixed and symmetric condition was applied to the node at the apex of the dome. The FEM mesh of axisymmetric model is presented in Fig. 3. This model was used for parametric study to discuss potential failure modes. Models with various values of the material properties were analyzed.

### **(3) Material properties**

Material properties were measured from test samples. For liner, rebars and tendons, the material test results were averaged to create elastic and plastic property data for the FEM models. The stress-strain relations used in the analysis are shown in Figs. 4 through 8. Material tests for the concrete were performed using two series of trial mix concrete. Results of series B were used as a basic material model. Results of series A test were used for parametric study with the axisymmetric model. The material data of the concrete are shown in Table 1.

### **(4) Loading**

For both 3D shell and axisymmetric shell model, prestress for tendons were loaded as thermal deformations in the first step. The hoop and hairpin tendons were cooled to apply tensile loads for the tendons. It is noted that actual tendons will have tensile strains in preloaded state, while in this model have compressive strains. In the second step of the analysis, internal pressure was loaded to the level of design pressure 0.39MPa. In the last step, internal pressure was increased until the analysis stopped.

### 3. Calculated results

Results of the tow models are presented in this section.

Results at some standard output locations were calculated with the 3D shell model. Because some features like equipment hatches were not included in the model, results only at the free field and at the buttress were presented.

The axisymmetric shell models were subjected to the parametric study of the material properties to discuss failure modes of the test model. So final results in a last time step were mainly presented in this report.

#### (1) 3D shell model

The analysis stopped at internal pressure of 1.24MPa.

Deformed sections in azimuth of 90, 135 and 180 degrees at various pressure levels are shown in Figs. 9 through 11.

Results at standard output locations included in the model are shown in Figs. 12 through 24. In these standard output results, radial displacements and hoop strains in the cylinder show nonlinear behavior over pressure level of 0.87 MPa, because most of the concrete of the cylinder cracked by hoop stresses at the pressure level. At around the pressure of 0.94 MPa, vertical displacement at the apex of the dome began to decrease. Meridional strains in the dome increased quickly at this pressure level. The concrete around the top of the cylinder cracked at the pressure level. Finally just below the pressure of 1.24 MPa, standard output results at the dome in azimuth of 135 degrees and 45 degrees in dome angle jumped up. They were displacements at location #9 and #10, strains at locations #27, #28 and #29. At this location, structural failure seemed to occur.

#### (2) Axisymmetric shell model

Material properties used for parametric studies are shown in Table 2. A base model had same material properties as the 3D shell model. For the models #1 and #2, tensile strength of the concrete changed at 10% more and less than base model, respectively. Model #3 had completely different concrete material property.

Calculated results are summarized in Table 3. Deformations of the base model and models #1, #2 and #3, at the maximum pressure level in each analysis are shown in Figs. 25 through 28. These are final deformed shapes just before the model failed.

Though the final pressure levels were slightly different between these models, final deformations were very similar to each other.

Vertical distribution of hoop strain of the base model is presented in Fig. 29. It exceeds cracking strain at most part of the cylinder. And for the base model and model #1, meridional strains at most part of the cylinder are very close to the cracking strain. Vertical distributions of meridional strains in the concrete of the cylinder and the dome are shown in Figs. 30 through 33. In these figures, values at the inside, middle and outside sections are presented. Large bending deformations are observed at almost same locations, but the distributions are different between the models. The locations of the cracks due to meridional stress were very sensitive to the material properties of the concrete.

#### 4. Discussions

In this section, following two discussions are described.

##### (1) Possible failure modes

The pressurization test of the 1/4 scale PCCV model will be terminated by structural failure like rapture in the dome or the cylinder, or local tear around some penetrations. Because only basemat, cylinder, dome and buttress are included in this model, possibility of structural failure is discussed here. The PCCV model will maintain the pressure until the liner will be broken.

A possible failure mode is rapture of cylinder by hoop stress. Though most of concrete in the cylinder cracked by hoop stress, rebars, tendons and liners did not yield at the final pressure level. This failure mode could occur at higher pressure levels. An other failure mode is buckling or local fracture by bending deformations. Meridional bending deformations in the axisymmetric model and large deformation of the dome in 3D shell model could drive very local large deformations to local fracture. It could happen in lower pressure level if some penetrations or imperfections exist.

##### (2) Pressure levels of the events

###### ● First cracking of concrete in cylinder

The first crack due to meridional stress was observed at pressure of 0.741 MPa, at the bottom of the cylinder and just above the basemat. That due to hoop stress was found at 0.792 MPa around azimuth of 135 degrees and elevation of 8.36m. Cracks due to hoop stress expanded to most part of the cylinder, while the crack of the bottom of the cylinder did not. Histories of strains of the two elements are shown in Fig. 34.

###### ● First cracking of concrete in dome

Elements of the first cracking in dome above and below 45 are presented in Fig. 35. Above 45 degrees, it occurred at pressure of 0.604 MPa, and below 45 degrees it did at pressure of 0.792 MPa. For both elements, meridional stress was dominant.

###### ● Minimum pressure reachable with 90% confidence level

Vertical displacement at the apex of the dome began to decrease at around 0.95 MPa. It means that local deformation happened suddenly at the pressure level, though the sudden deformation was possibly due to arrangement of rebars and tendons in the dome different from actual model. It might be the first chance of structural failure. Minimum pressure reachable is detected 0.95

MPa, which equals to 2.44Pd.

- Maximum pressure reachable with 90% confidence level

Failure mode detected to occur at maximum pressure level is rupture of the cylinder due to hoop stress. With extrapolating result of standard output location #50, strain of the hoop tendon expected to reach to yield strain 0.9% at pressure of 2.4 MPa. It will be more complex in real tests, but the pressure will not exceed that pressure level. Maximum pressure reachable is 2.4MPa, which is 6.2 Pd.

## 5. Conclusions

In this report, 1/4 scale PCCV test model was analyzed with nonlinear FEM code ABAQUS. Two models with 3D shells and axisymmetric shells were created. Preload of tendons and internal pressure were applied to the models, and final pressure levels and deformation mode were evaluated to discuss failure mode of the test model. Results are summarized as followings.

- Cylinder became nonlinear over pressure of 0.84 MPa by hoop strain.
- Large bending deformation occurred at pressure of 0.94 MPa around the spring line of dome and cylinder.
- Possible failure modes are buckling in the dome at around 1.24 MPa and local fracture by bending in the cylinder at around 1.27MPa.
- Minimum pressure reachable in 90% confidence level is 0.95 MPa. Local fracture by bending could occur at the pressure level.
- Maximum pressure reachable in 90% confidence is 2.9 MPa. By extrapolating strain results, hoop tendons detected not to maintain the internal pressure more than 2.9 MPa.

Table 1. Material data for the series of concrete

TYPE	Young's Modulus	Poison's Ratio	Compressive Strength	Tensile Strength	Note
fc[MPa]	[MPa]	---	[MPa]	[MPa]	
44.13	21700.	0.22	63.1	3.91	Series B
29.42	26970.	0.18	48.84	3.45	Series B

Table 2. Material data of concrete used in Parametric Study

Model	Young's Modulus	Poison's Ratio	Compressive Strength	Tensile Strength	Note
	[MPa]	---	[MPa]	[MPa]	
Base	21700.	0.22	63.1	3.91	same as 3D model
#1	21700.	0.22	63.1	4.30	+10% Tensile Strength
#2	21700.	0.22	63.1	3.52	-10% Tensile Strength
#3	26970.	0.18	48.84	3.45	Series A

Table 3 Summary of Axisymmetric Model Tests

Model	Final Pressure	First Cracking	Its Location
	[MPa]	[MPa]	
base	1.27	0.84	cylinder/hoop
#1	1.32	0.90	cylinder/hoop
#2	1.32	0.84	cylinder/hoop
#3	1.24	0.90	cylinder/hoop
3D Shell	1.24	0.60	dome

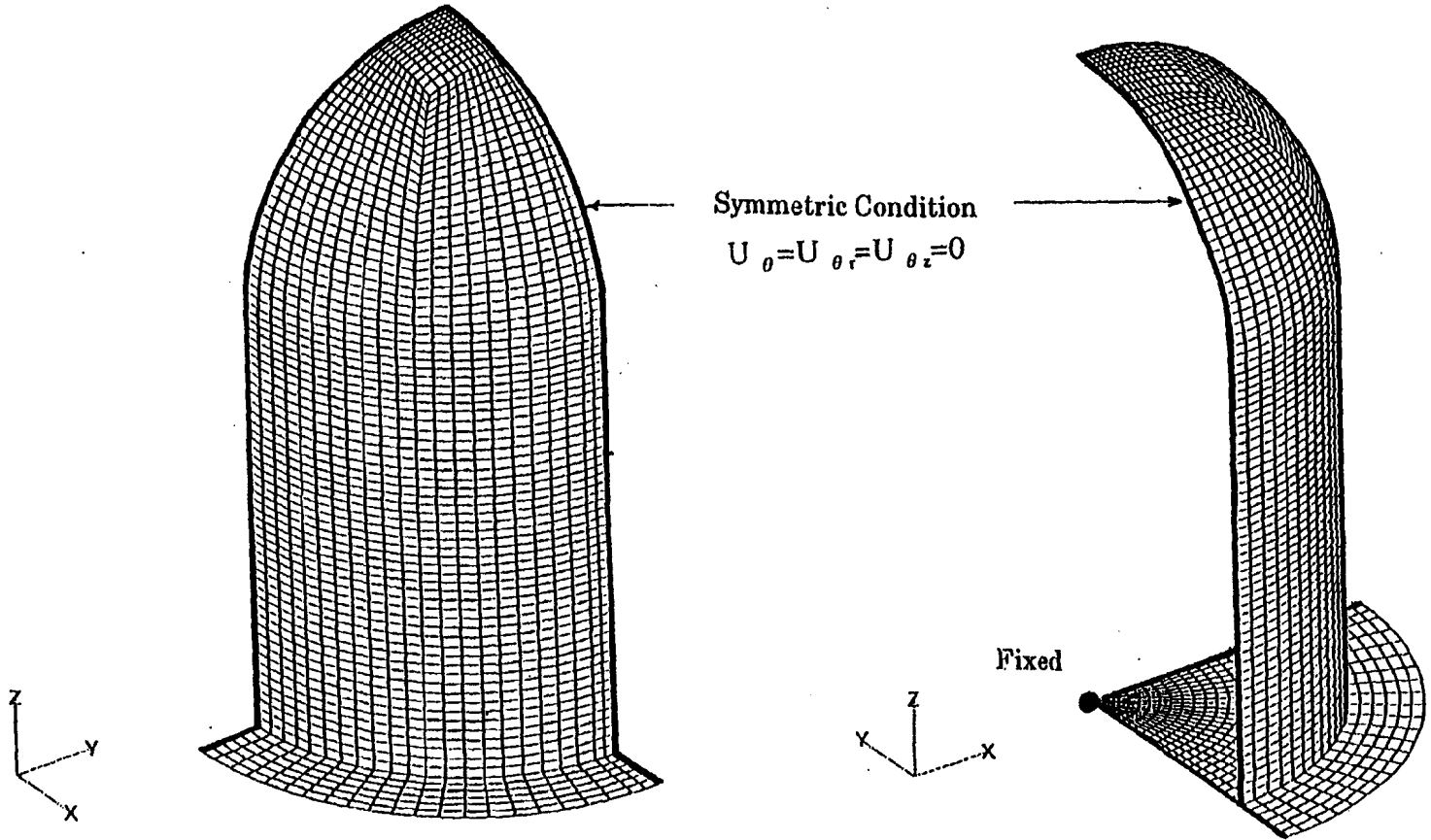


Fig.1 FEM mesh of 3D Shell Model ; Whole Model

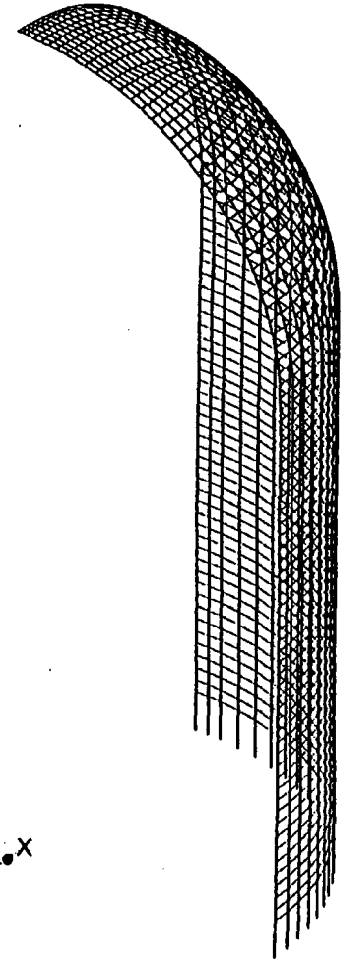
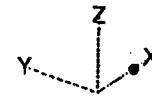
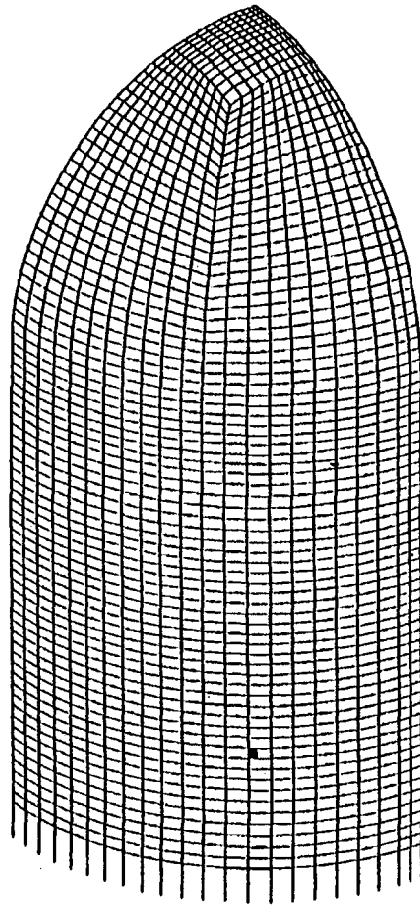
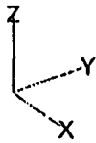


Fig.2 FEM mesh of 3D Shell Model ; Tendon

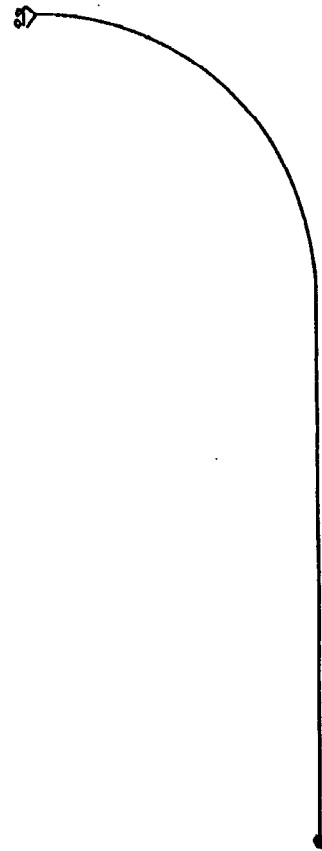
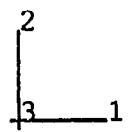


Fig.3 FEM mesh of Axisymmetric Model

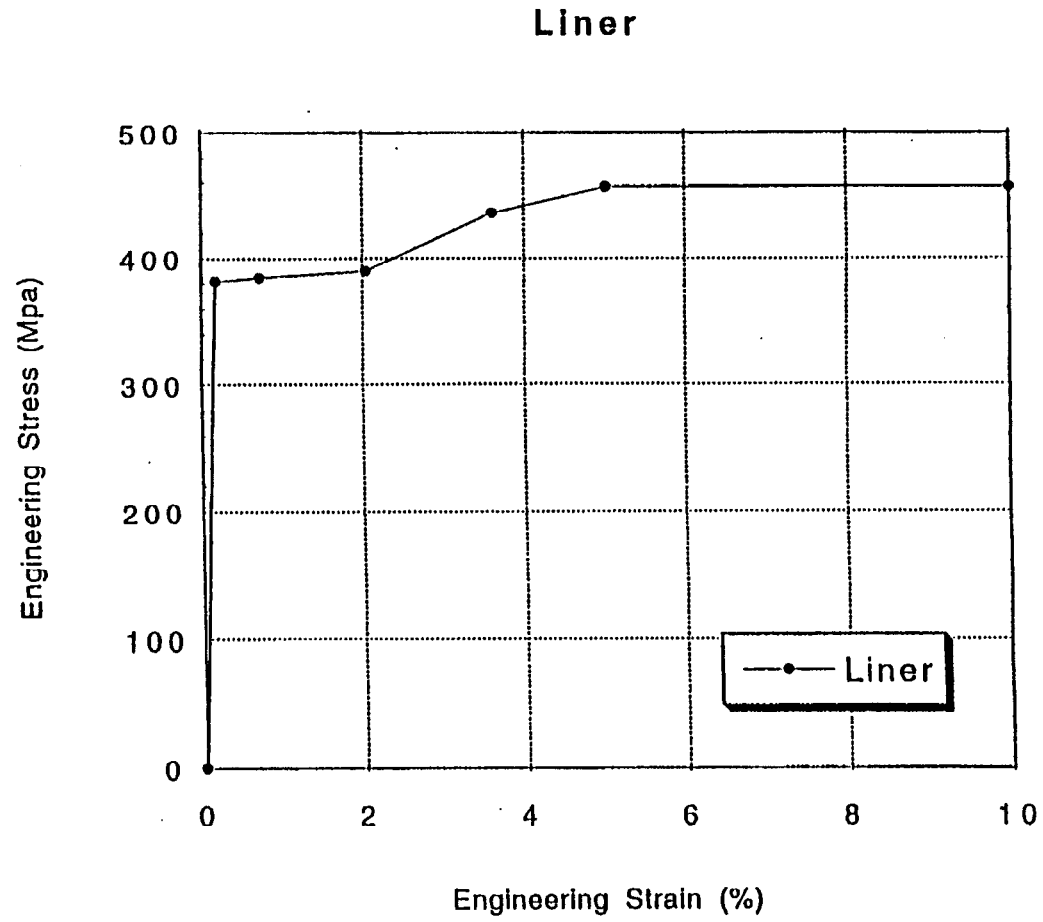


Fig.4 Material Property Data ; Liner

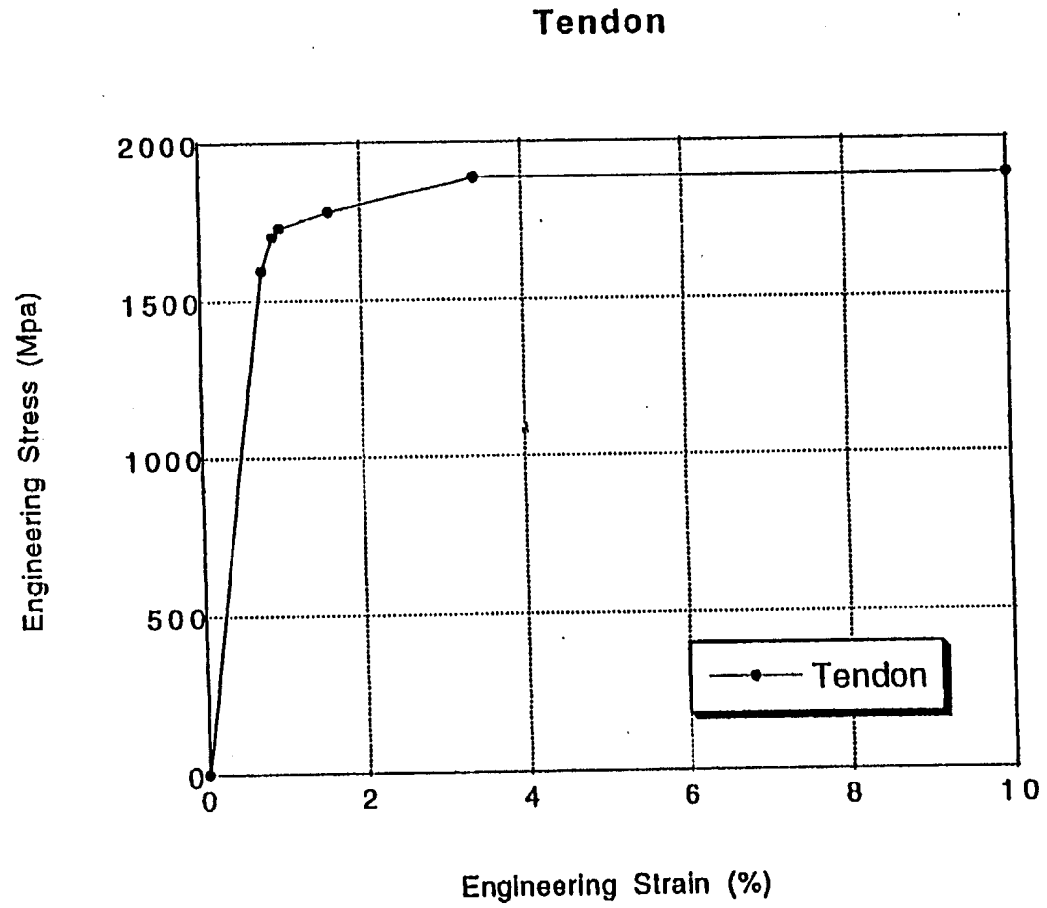


Fig.5 Material Property Data ; Tendon

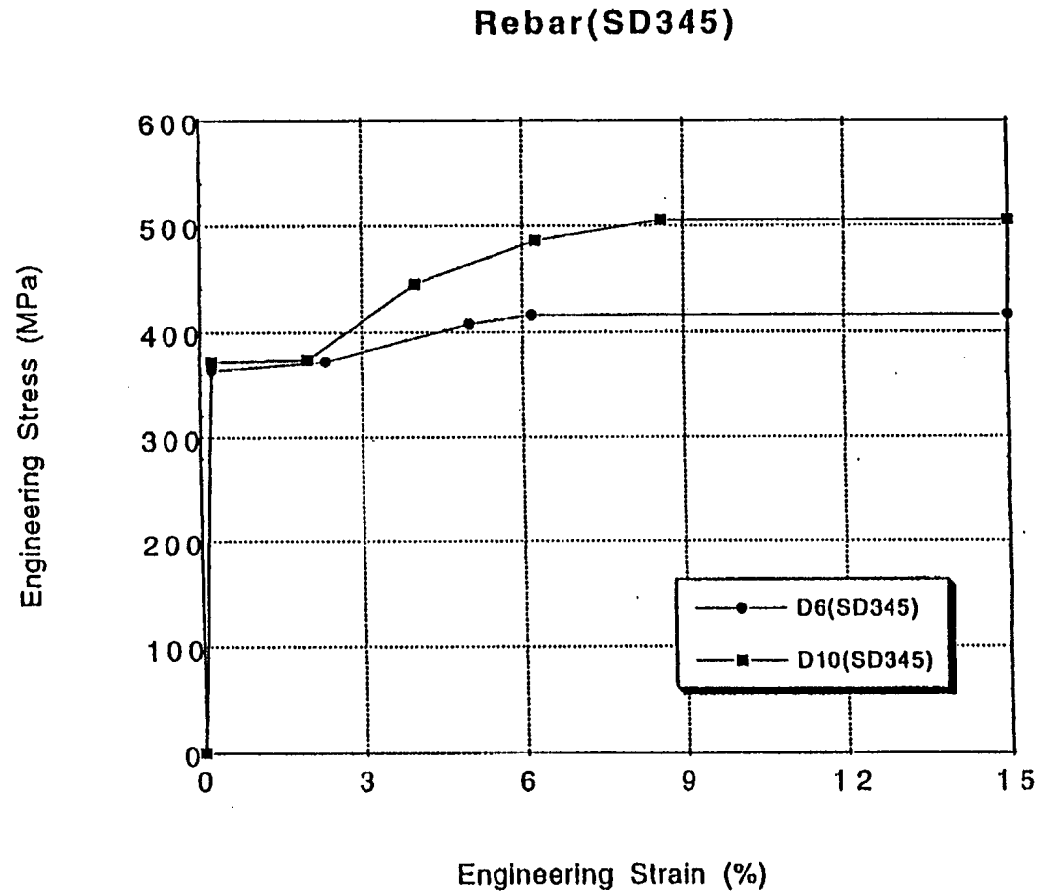


Fig.6 Material Property Data ; Rebar(SD345)

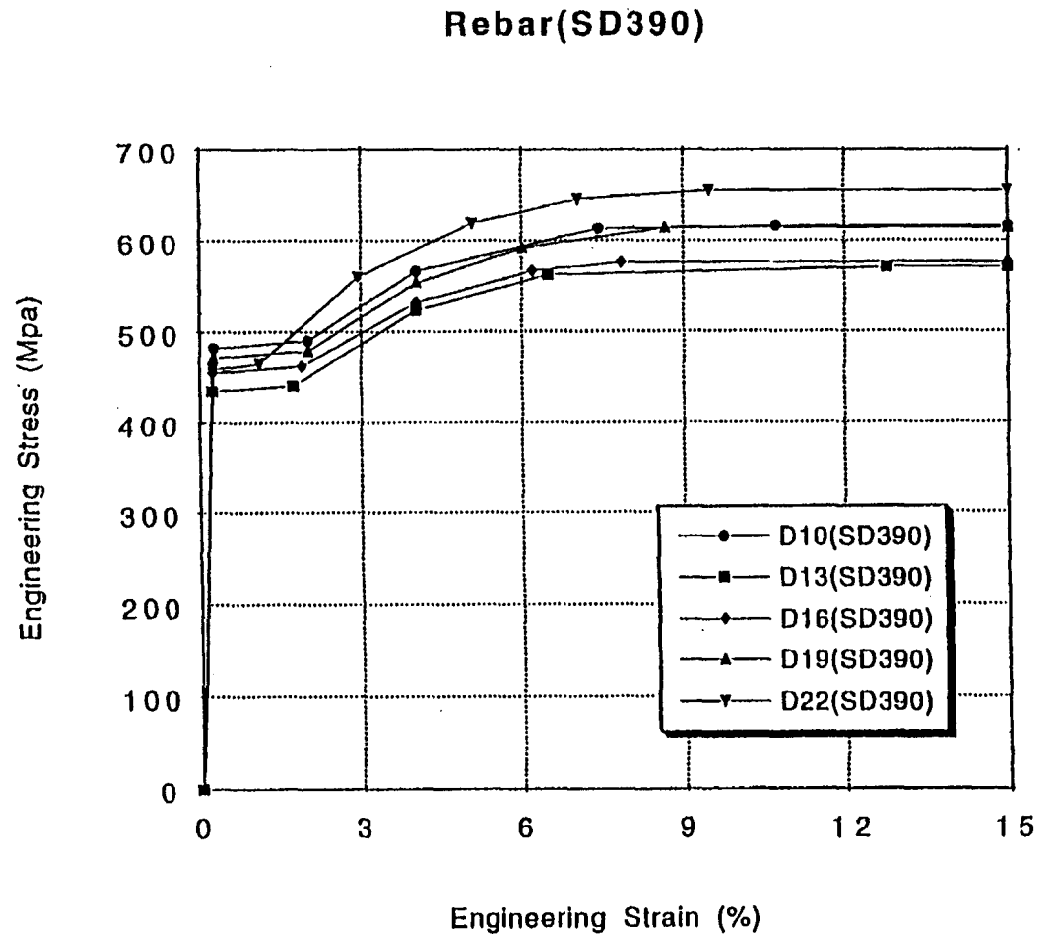


Fig.7 Material Property Data ; Rebar(SD390)

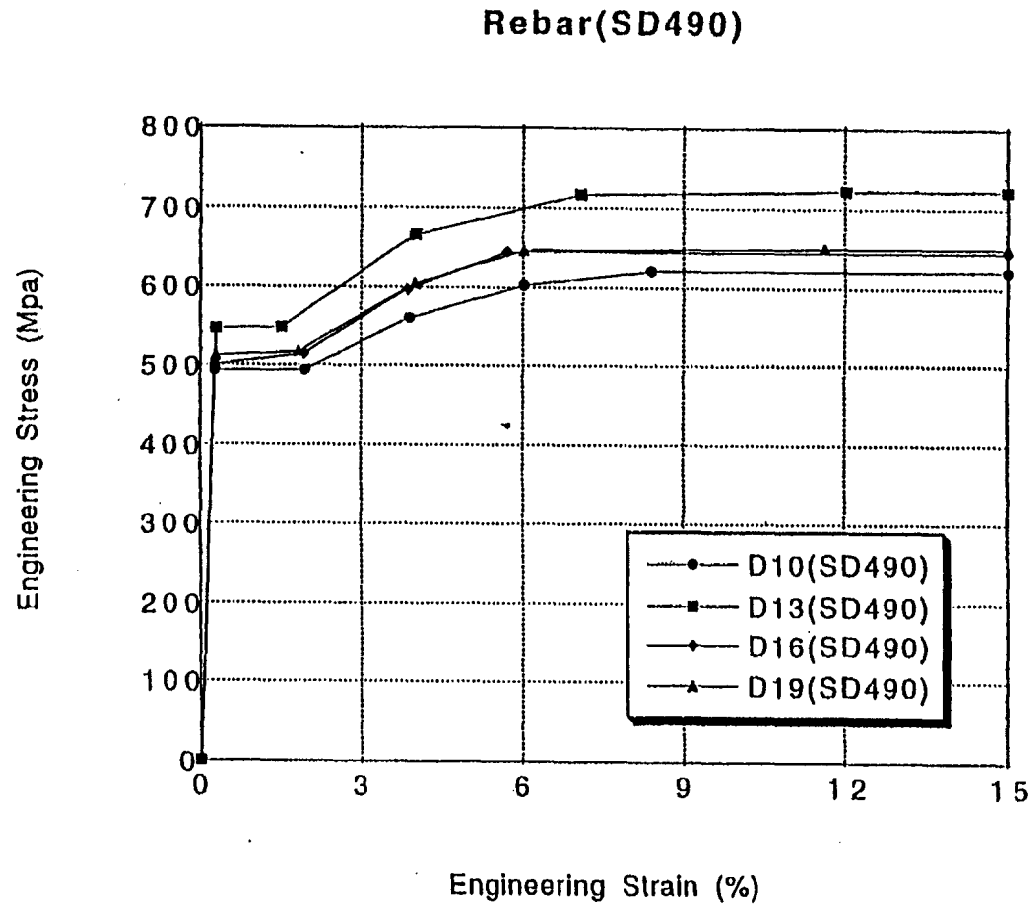
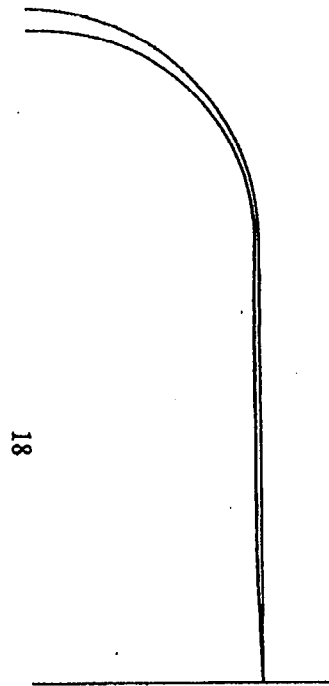
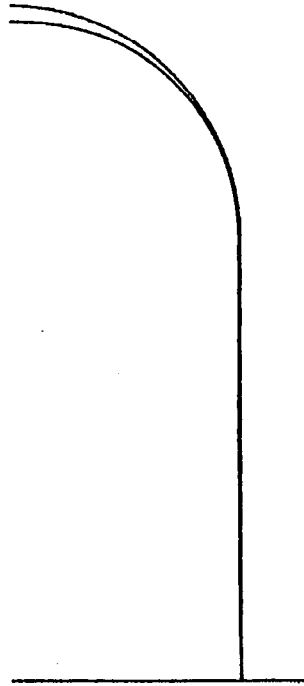


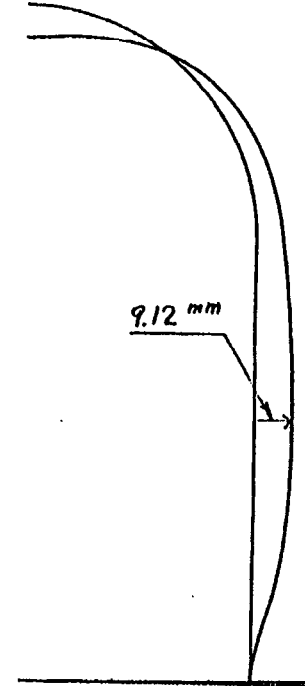
Fig.8 Material Property Data ; Rebar(SD490)



(1) PreStress



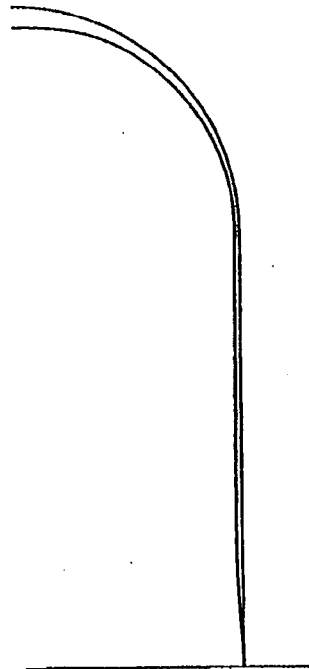
(2) P=0.39 (MPa)  
(Design Pressure)



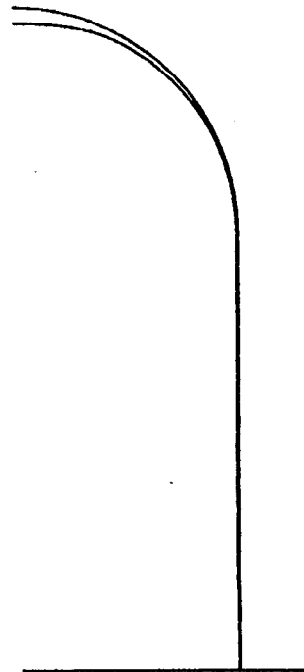
(3) P=1.24 (MPa)

Deformed Scaled × 100

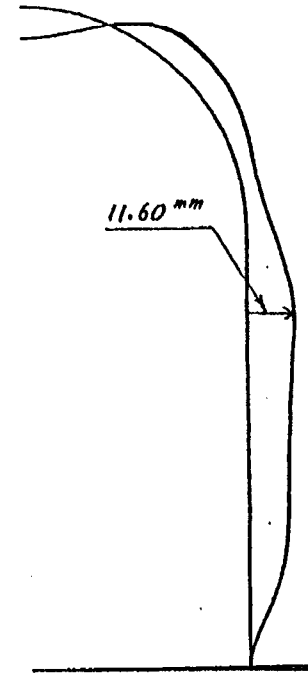
Fig.9 Deformed Shape of 3D Shell Model in 90 degrees



(1) PreStress



(2) P=0.39 (MPa)  
(Design Pressure)

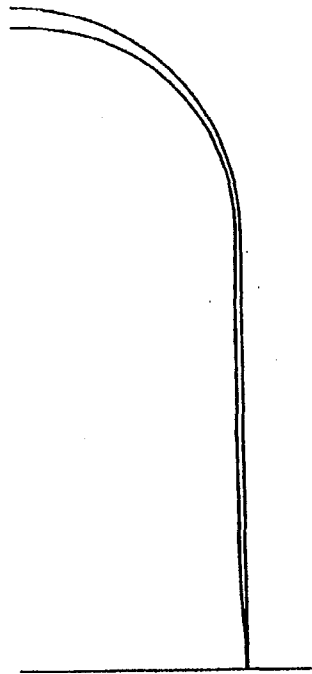


(3) P=1.24 (MPa)

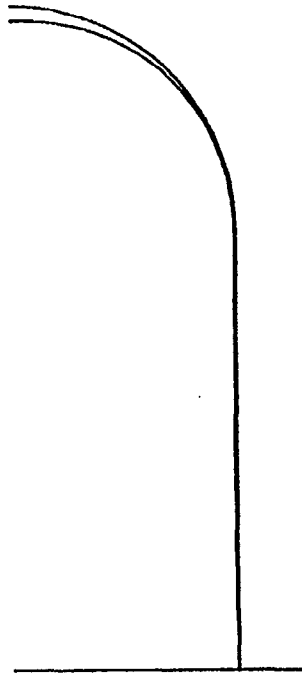
Deformed Scaled  $\times 100$

Fig.10 Deformed Shape of 3D Shell Model in 135 degrees

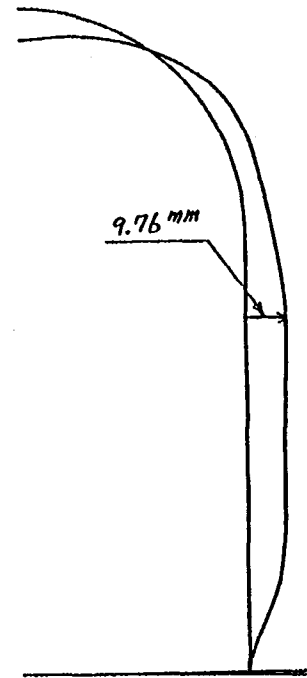
20



(1) PreStress



(2) P=0.39 (MPa)  
(Design Pressure)



(3) P=1.24 (MPa)

Deformed Scaled  $\times 100$

Fig.11 Deformed Shape of 3D Shell Model in 180 degrees

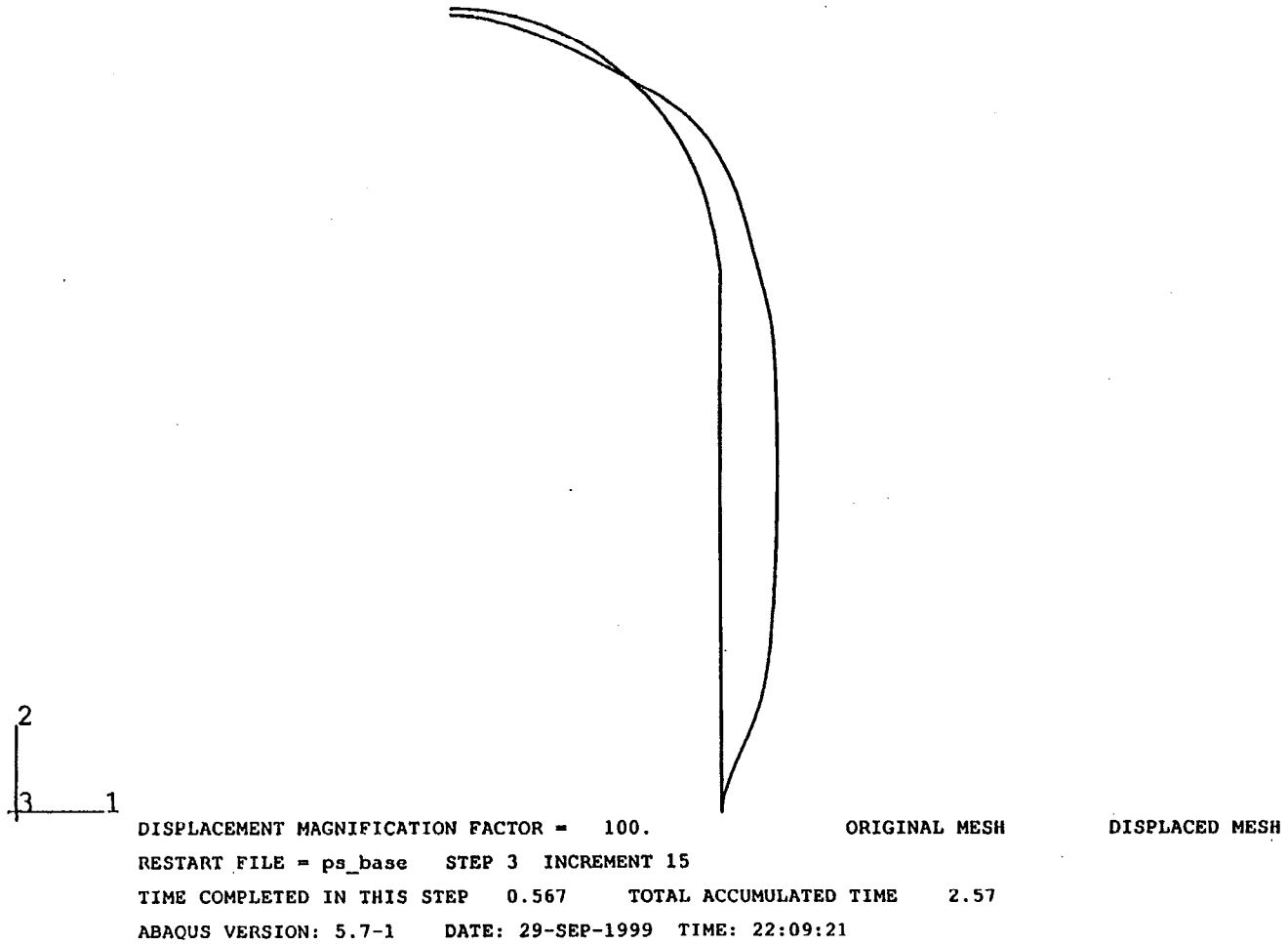


Fig.25 Deformed Shape of Axisymmetric Model ; Base Model

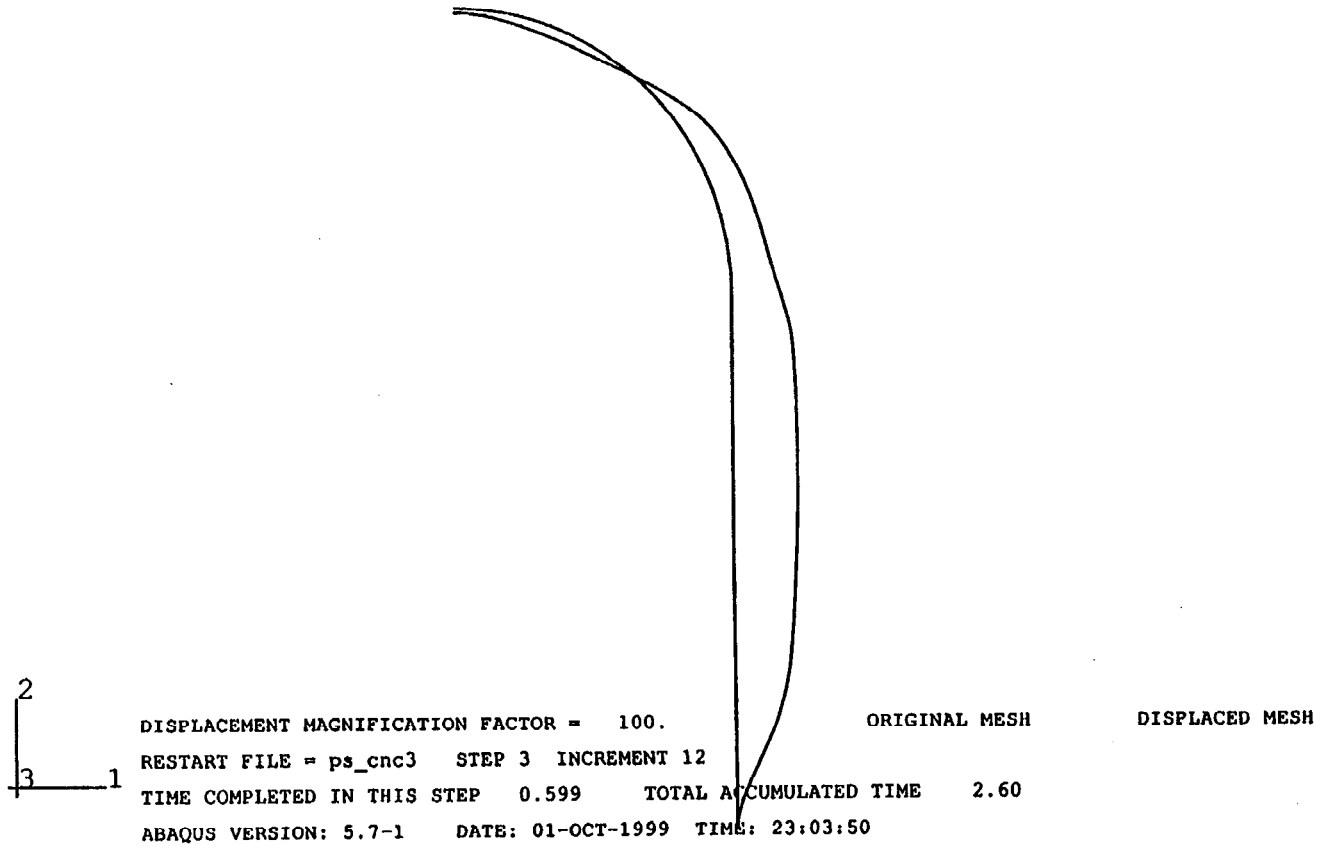


Fig.26 Deformed Shape of Axisymmetric Model ; Model #1

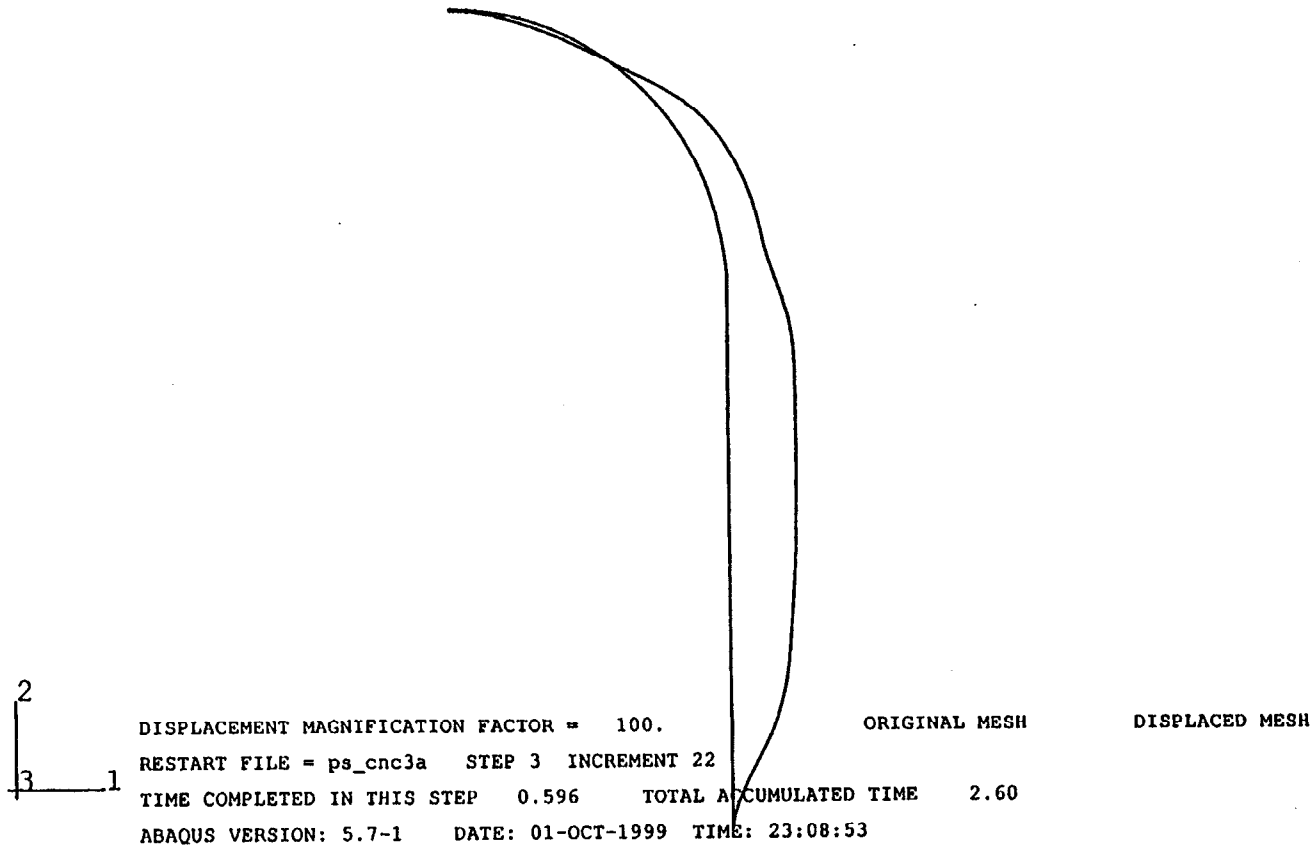


Fig.27 Deformed Shape of Axisymmetric Model ; Model #2

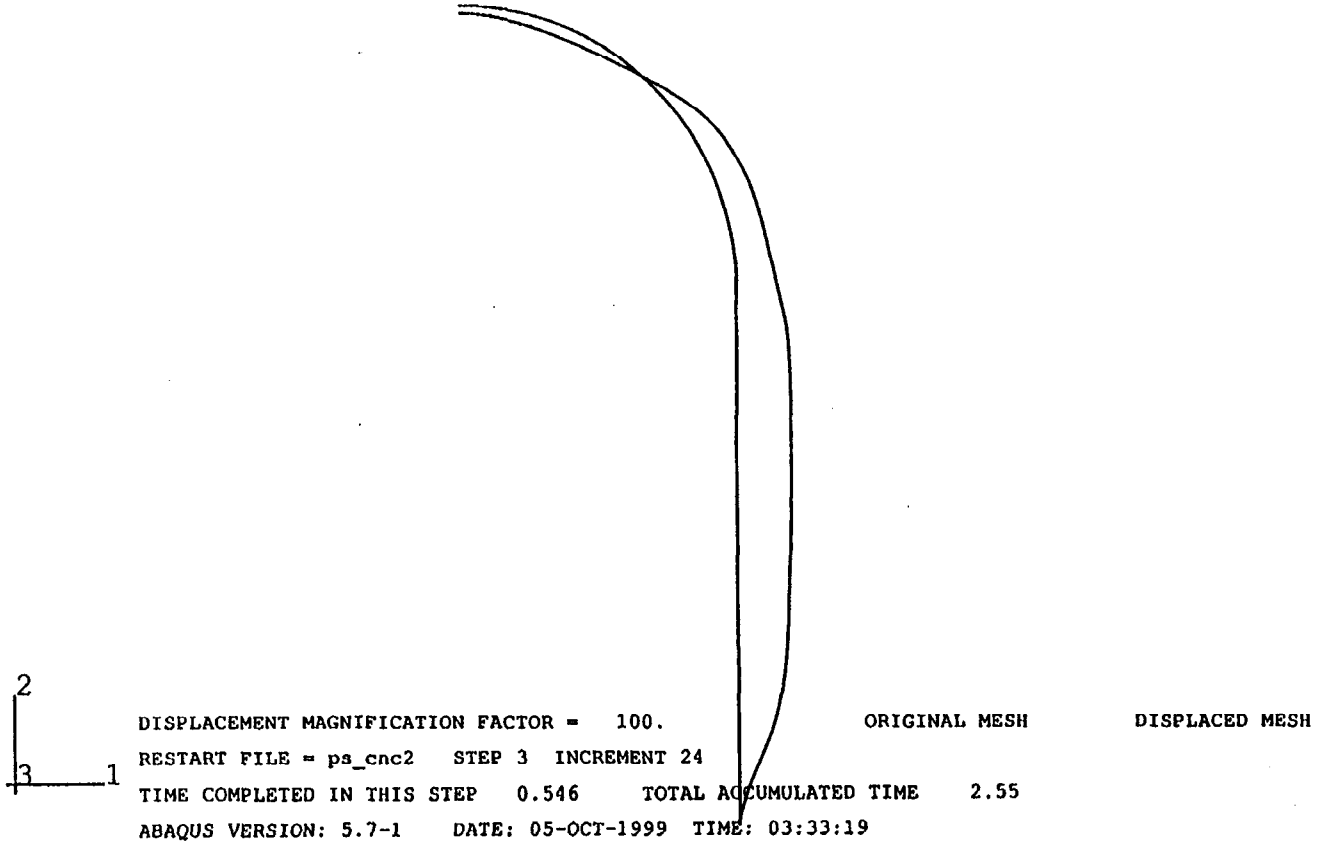


Fig.28 Deformed Shape of Axisymmetric Model ; Model #3

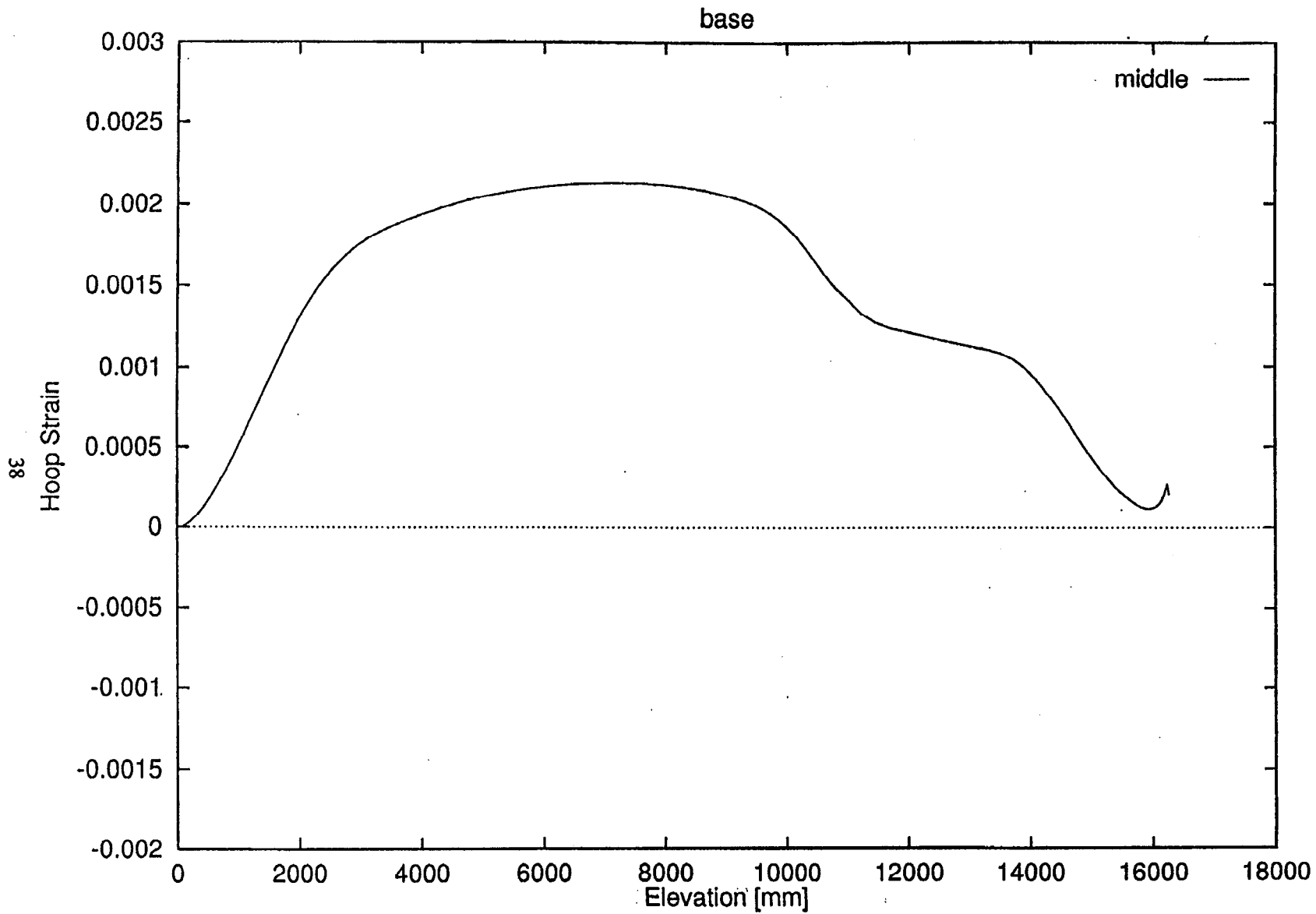


Fig.29 Distribution of Hoop Strain of Axisymmetric Shell Model ; Base Model

K-30

39

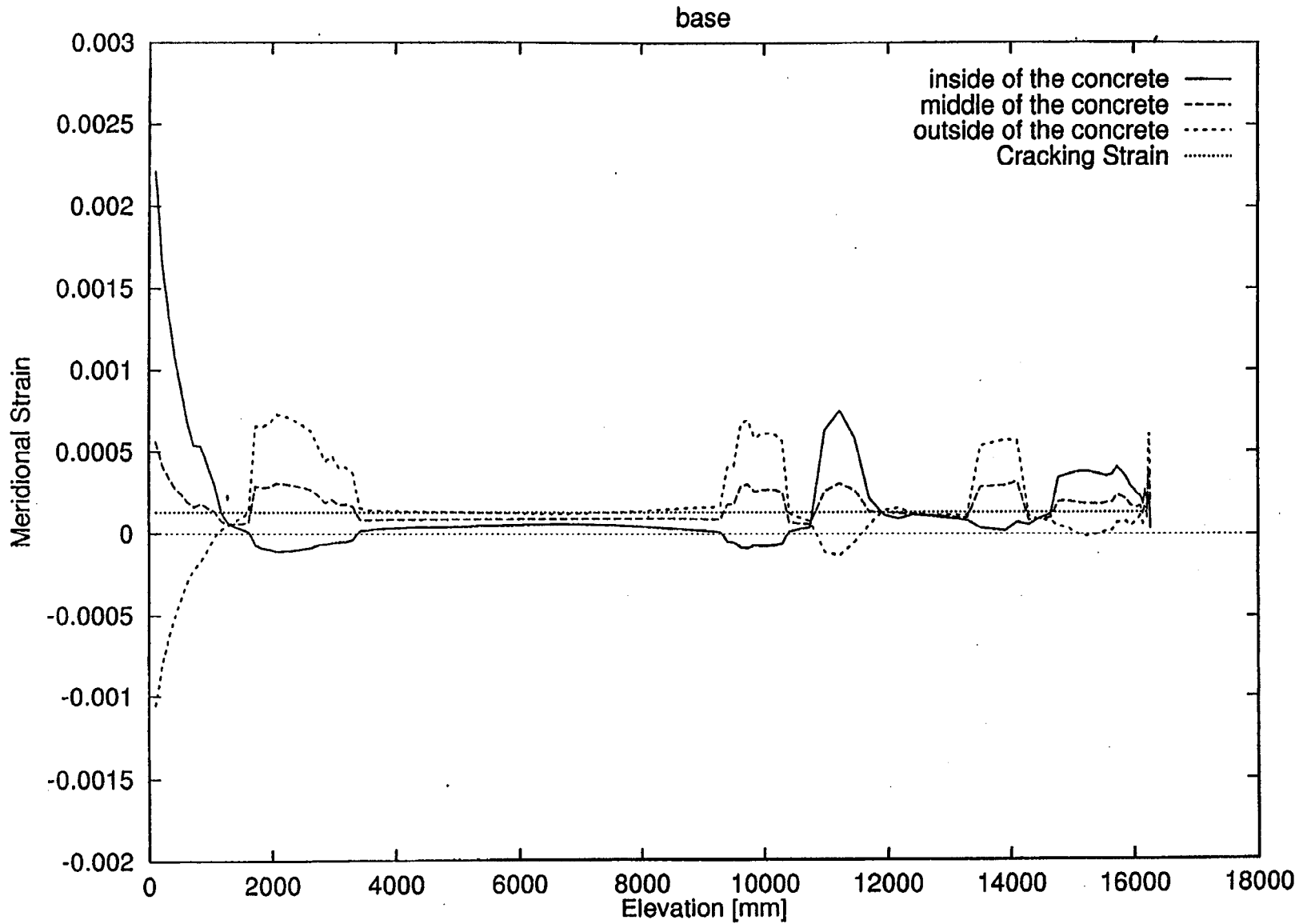


Fig.30 Distribution of Meridional Strain of Axisymmetric Shell Model ; Base Model

K-31

40

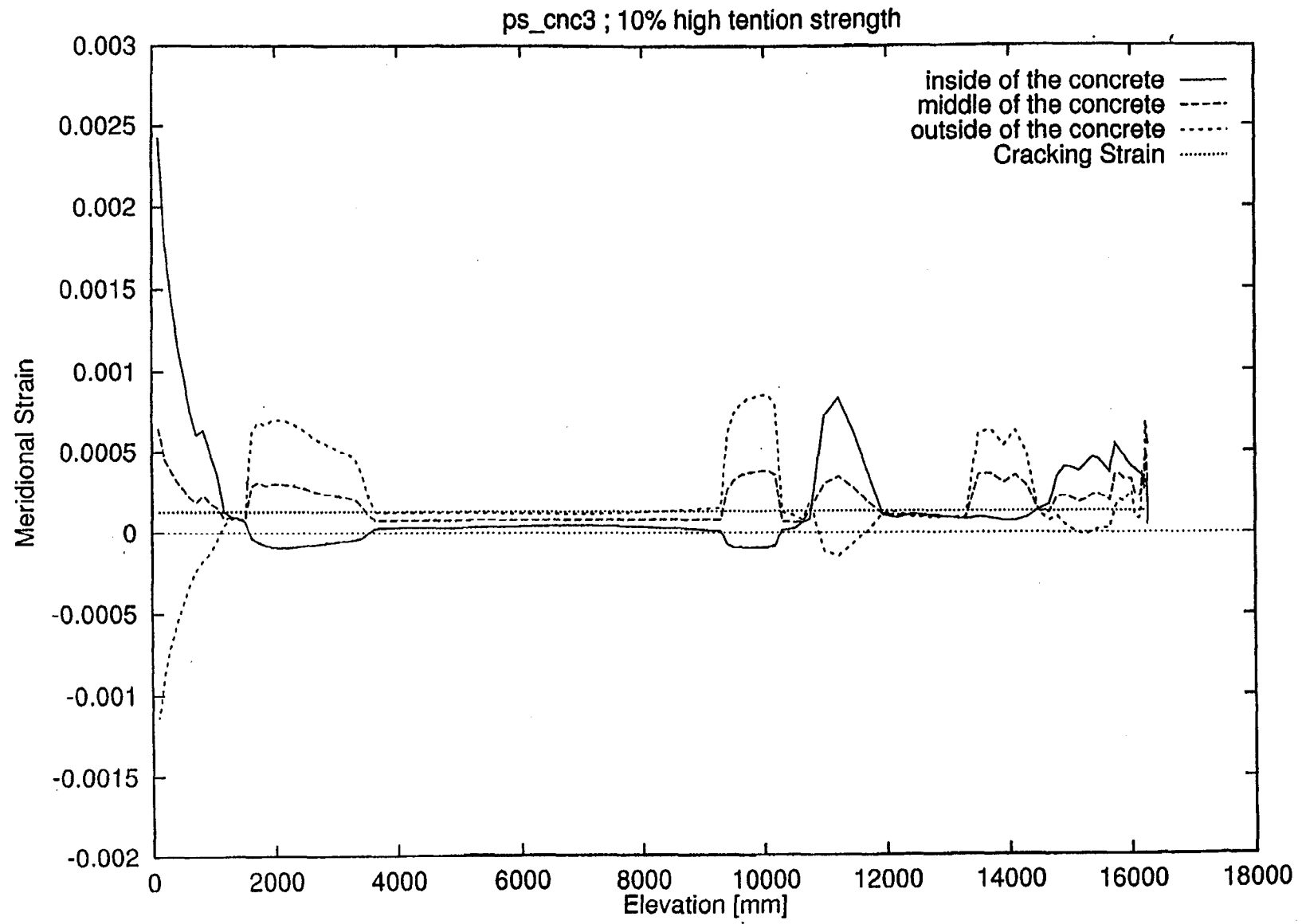


Fig.31 Distribution of Meridional Strain of Axisymmetric Shell Model ; Model #1

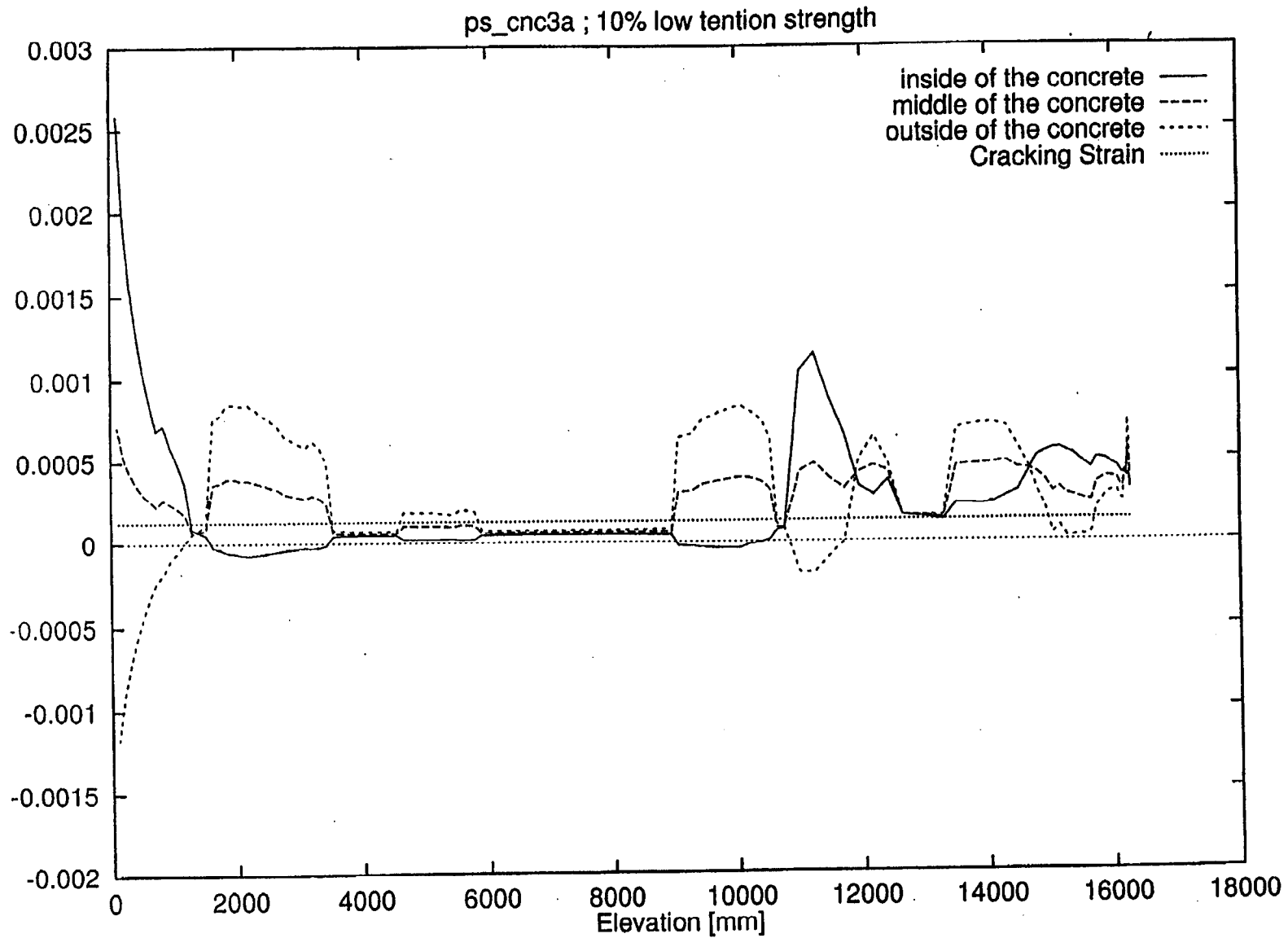


Fig.32 Distribution of Meridional Strain of Axisymmetric Shell Model ; Model #2

K-33

42

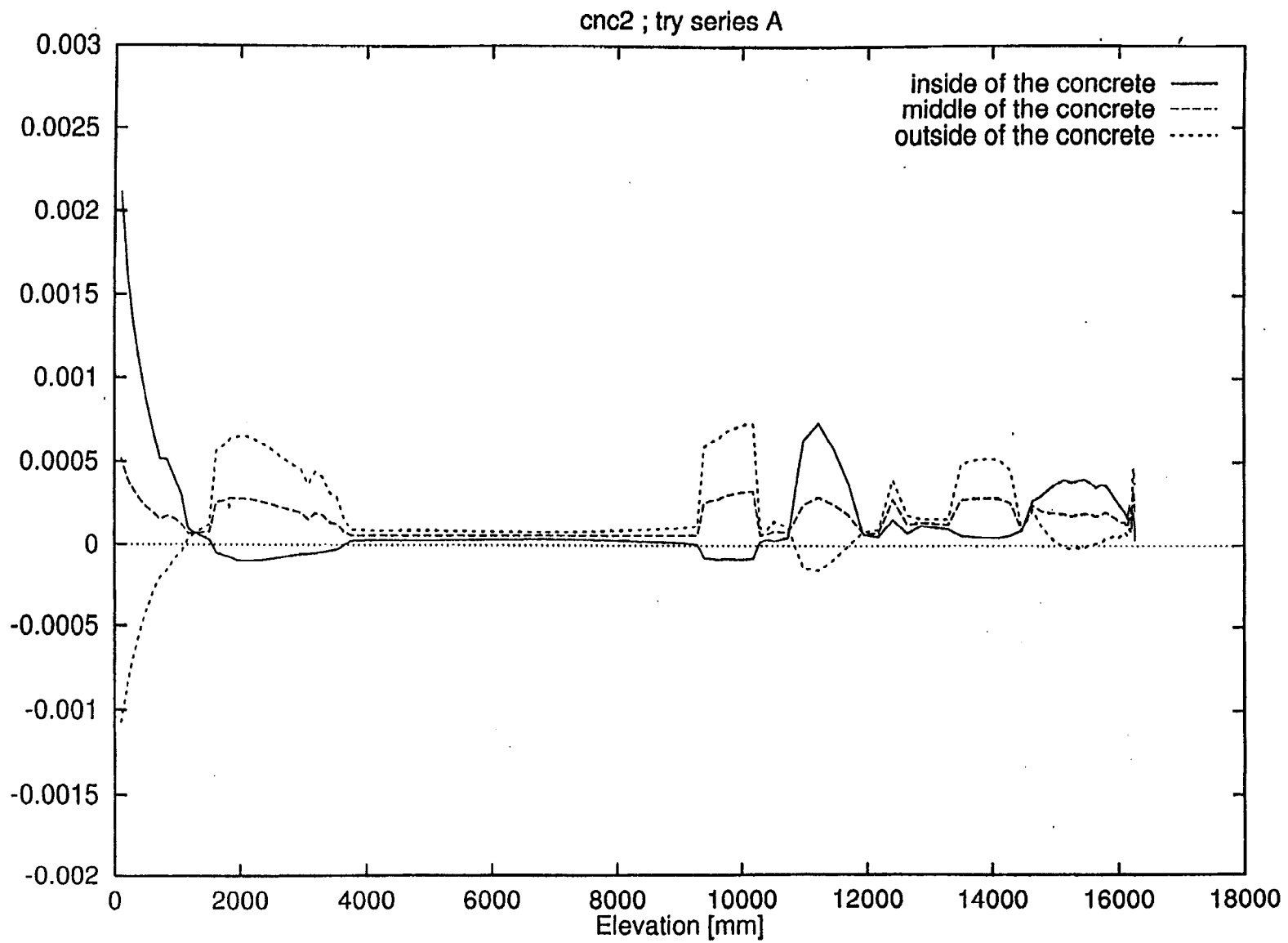


Fig.33 Distribution of Meridional Strain of Axisymmetric Shell Model ; Model #3

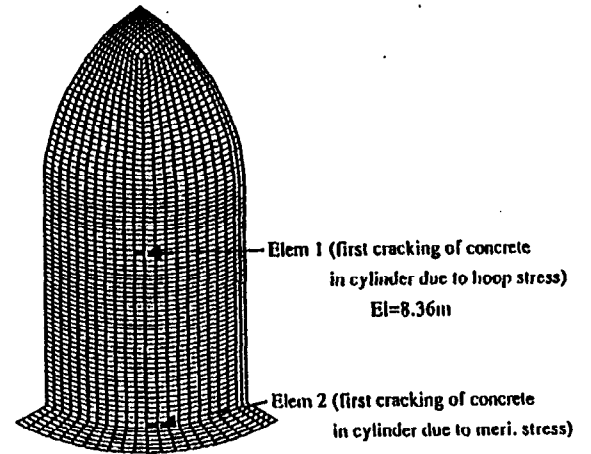
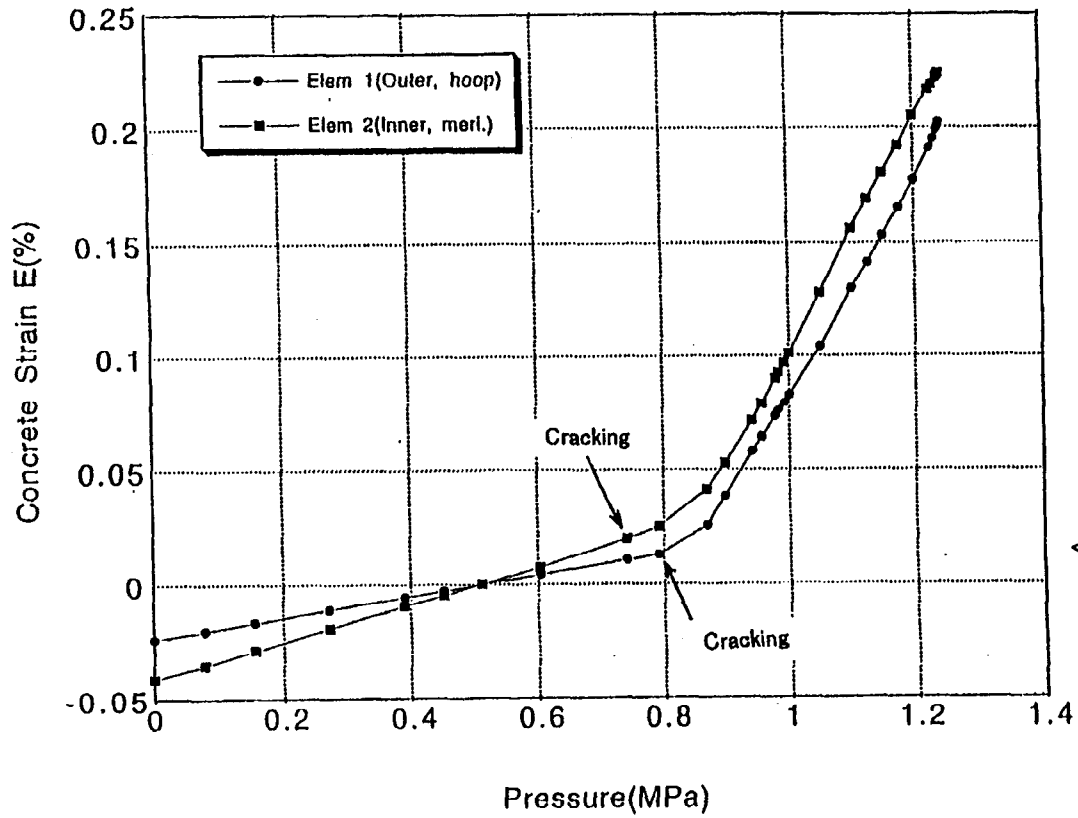


Fig.34 Histories of Strain in First Cracking Elements in the Cylinder

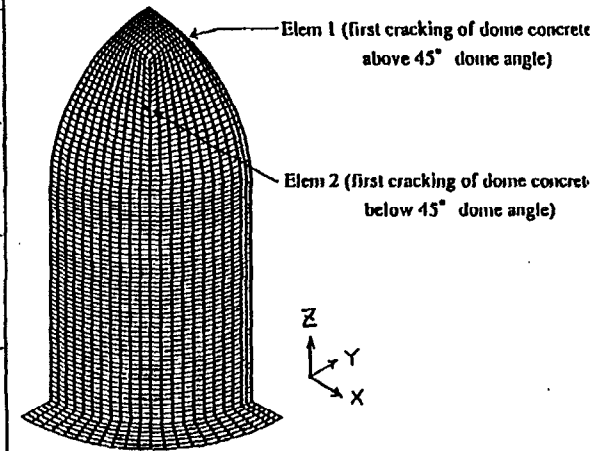
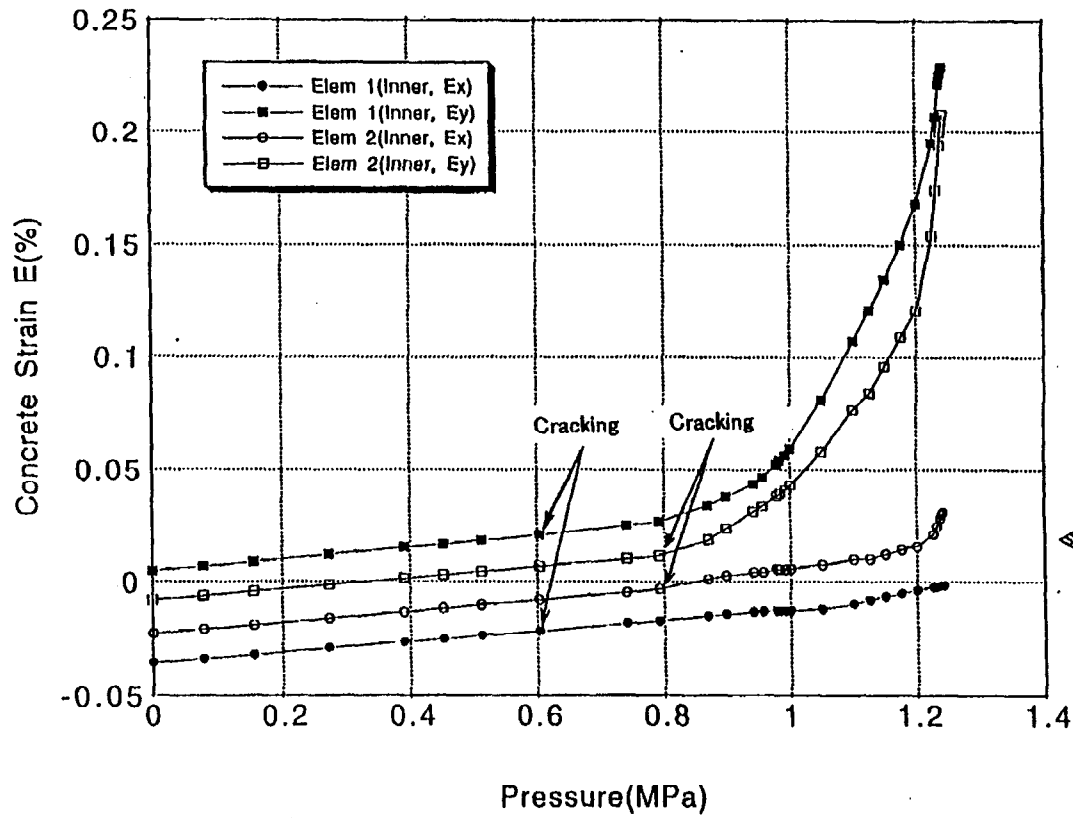


Fig.35 Histories of Strain in First Cracking Elements in the Dome

## References

- [1] K. Soda and H. Kimura, "Structural Analysis of the Reinforced Concrete Containment under Extreme Static and Dynamic Pressure Loading," Second Int. Conf. Containment Design and Operation, Toronto, Canada,(1990).
- [2] J. R. Weatherby, "Posttest Analysis of a 1:6-Scale Reinforced Concrete Reactor Containment Building," NUREG/CR-5476, USNRC,(1990).
- [3] V. K. Luk and E. W. Klamerus, "Round Robin Pretest Analysis of a Steel Containment Vessel Model and Cnstact Structure Assembly Subjected to Static Internal Pressurization," NUREG/CR-6517,USNRC,(1996).
- [4] H. D. Hibbitt, "ABAQUS User's Manual," Hibbitt, Karlsson Sorensen,Inc.,(1995).

**APPENDIX L**

**JAPC**

**THE JAPAN ATOMIC POWER COMPANY  
JAPAN**

Appendix A. Composite Plots, comprises test data compiled and plotted from all organizations that participated in the Prestressed Concrete Containment Vessel (PCCV) Round Robin Pretest Analysis. To avoid duplicating the composite information, individual sets of data and/or plots have been omitted from participants' reports. In some cases this action resulted in disconnects between callouts and content and in the numbering of figures, tables, and pagination in some reports.

However Appendix L, "JAPC, The Japan Atomic Power Company, Japan," contains none of these discontinuities.

## CONTENTS

1	General Remarks .....	L-5
1.1	Outline of this research .....	L-5
1.2	Organization .....	L-6
1.3	Numerical methods for the analyses .....	L-8
2	Stress-strain Relationships of the Materials and their Critical Strains .....	L-9
2.1	Concrete .....	L-9
2.2	Rebars .....	L-10
2.3	Tendons .....	L-11
2.4	Liner .....	L-12
3	Establishment of Tendon Friction Element .....	L-13
3.1	Overview of the friction element .....	L-13
3.2	Verification of friction element .....	L-13
3.3	Summary .....	L-14
4	Establishment of Liner Anchor Element .....	L-16
4.1	Modification of liner anchor .....	L-16
4.2	Verification of analytical models for pull-out tests on liner anchor .....	L-16
4.3	Analytical evaluation of liner anchor model .....	L-17
4.4	Summary .....	L-18
5	Global Analyses of 1/4 PCCV .....	L-19
5.1	Global Analysis by axisymmetric model .....	L-19
5.2	Global Analysis by 3D 90° shell model .....	L-21
5.3	Global Analysis by 3D 180° shell model .....	L-25
6	Local Analyses for 1/4 PCCV .....	L-30
6.1	Local analysis by 3D solid model near cylinder wall-base juncture .....	L-30
6.2	Local analysis by 3D solid model near buttress .....	L-33
6.3	Local analysis by 3D solid model near E/H, A/L openings .....	L-37
6.4	Local analysis by 3D solid model near M/S penetrations .....	L-42
7	Local Liner Analysis by Shell Model near M/S Penetrations .....	L-46
7.1	Study on modeling of the liner analysis .....	L-46
7.2	Analytical results .....	L-46
8	Interference of Possible Failure Modes and Associated Pressures in 1/4 PCCV .....	L-51
9	Conclusions of Pretest Analysis Phase .....	L-56



## Chapter 1. GENERAL REMARKS

### 1.1 OUTLINE OF THIS RESEARCH

In the year 2000, static high pressure tests will be performed on a 1/4 scale prestressed concrete containment vessel (PCCV) model. The Round Robin pretest analysis meeting will be held from Oct.12 to 14 '99 in Albuquerque, USA.

The Japan PCCV research group, who decided to participate in the pretest analysis, has conducted a research program to establish the analysis methodology to predict the nonlinear behaviors and failure modes of PCCVs subjected to increasing internal pressure.

The analysis results obtained from this research program are discussed in this issue.

PCCVs are extremely complicated structures due to their geometrical configurations comprising many types of structural materials, and the variety of their quantitative placements. Therefore, many difficulties must be overcome in analyzing the nonlinear behavior of this kind of structures up to the ultimate state. These include, avoidance of numerical instabilities, improvement of the constitutive laws of concrete and steel materials, and appropriate modifications of structural components into numerical elements.

Moreover, two types of PCCV ultimate states need to be investigated in the analyses : the structural failure mode due to crushing or shear cracking of concrete, tendon rupture or rebar rupture, and the leakage failure mode due to liner tearing.

The tasks in this analysis research program, taking account of these aspects, are as follows :

#### 1) Preliminary Research Works :

- ① Verification analyses for 1/6 scale RCCV test model (SAND89-0349)
- ② Establishment and verification of a tendon friction element.
- ③ Establishment of a liner anchor model verifying its applicability by use of one way pulling test results of a 1/4 scale cut-T type anchor.
- ④ Definition of stress-strain relationships of materials ( concrete, tendons, rebars and liner ) and their critical strains.

#### 2) Round Robin Analysis Works ;

- ① Analyses for the structural failure mode : Appearance of cracking and crushing in concrete, tendon rupture and rebar rupture, and their locations are checked. Failure modes and their associated pressures were also examined.

#### • Global analyses

- Axisymmetric model at the 135° azimuth
- 3D90° shell model including M/S penetrations
- 3D180° shell model including E/H and A/L openings and buttresses

- Local analyses
  - Axisymmetric model of lower cylindrical wall-base junction
  - 3D shell model near M/S penetrations
  - 3D solid model near E/H and A/L openings
  - 3D solid model near buttress and cylindrical wall
- ② Analyses for the leakage failure mode due to liner tearing : Liner tearing modes and the regions in which they occurred were examined by checking the local strain concentrations and liner anchor restraint.
  - Local liner model around M/S penetrations
  - Local liner model near cylinder wall-base junction

### 3) Inferences of Possible Failure Modes and Associated Pressures of 1/4 PCCV

Failure modes and their associated ultimate pressure capacities will be estimated by considering all the analytical results and comparing them with the critical strains of the materials specified.

The comprehensive structure of this research program is shown in Fig. 1.1-1, which clearly shows analytical model images and the interrelation of global and local analyses.

## 1.2 ORGANIZATION

This research has been conducted through the co-operation of six companies (Japan PCCV research group) : Japan Atomic Power Company, Kansai Electric Power Company, Kyushu Electric Power Company, Obayashi Corporation, Taisei Corporation, and Mitsubishi Heavy Industries.

The driving forces behind this research included :

- Y. Watanabe, A. Kato (JAPCO),
- M. Ozaki, H. Matsumoto(Kansai),
- K. Kiyohara, Y. Sono (Kyushu),
- K. Imoto, K. Naganuma, K. Yonezawa, K. Shirahama, T. Ogata, H. Maeno (Obayashi),
- Y. Murazumi, H. Ono, S. Takezaki (Taisei),
- H. Sekimoto, K. Sato, T. Kitani, M. Kondo, H. Matsuoka (Mitsubishi).

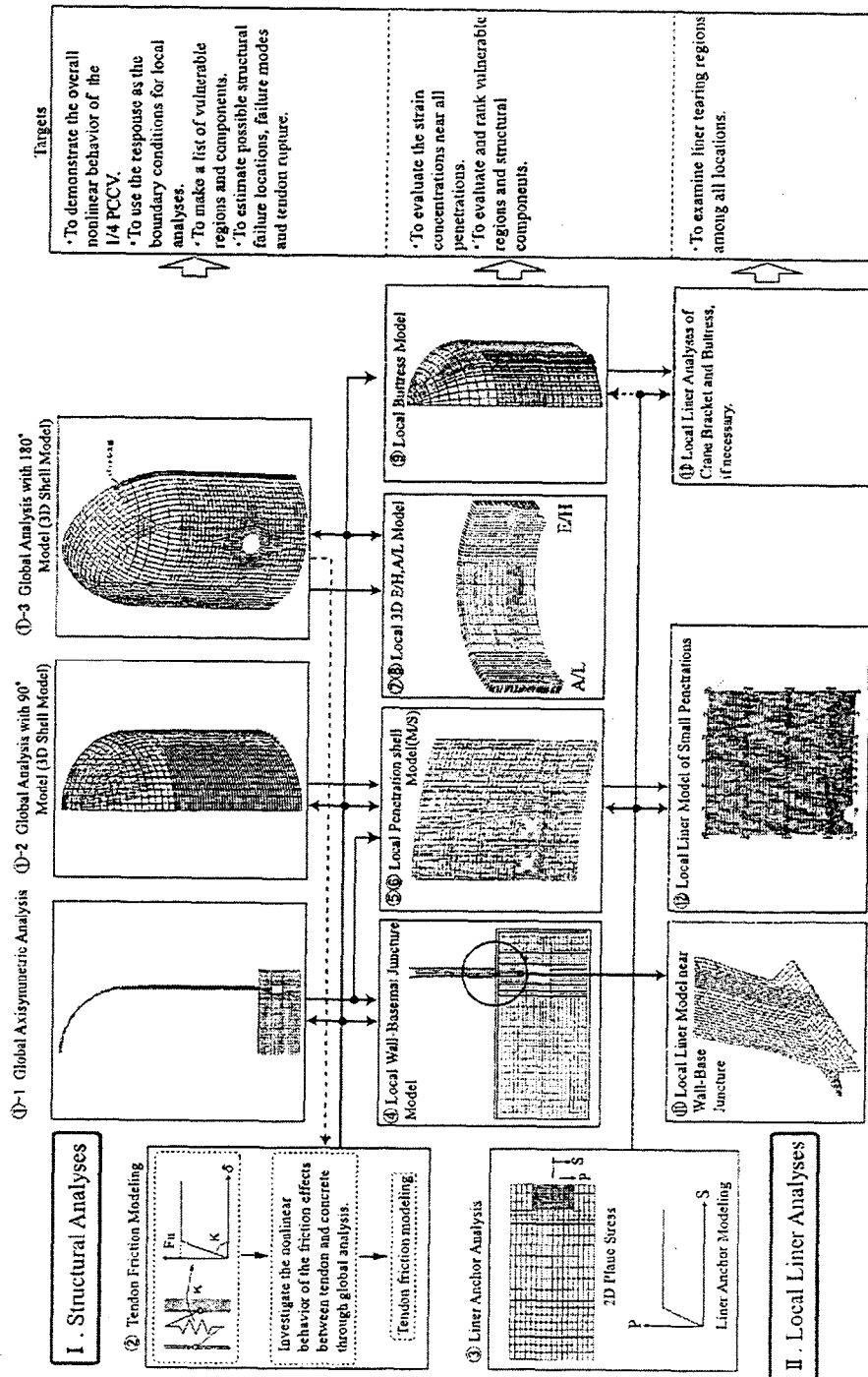


Fig. 1.1-1 Structure of This Research Program

### 1.3 NUMERICAL METHODS FOR THE ANALYSES

In this research, all of the numerical analysis tasks were performed using the finite element method (FEM), taking material nonlinearity into account. Computer codes applied in the analyses are listed in Table 1.3-1. The code "FINAL", developed by Obayashi Corporation, and the DIANA ver.6.2 general purpose code were used for the global and local analyses. The MARC general purpose code was used for the liner analyses. All of the analyses were performed by two- and/or three-dimensional FEM, where a tangential incremental loading method and the Newton method for convergence criteria were adopted.

The concrete was modeled using 4-node quadrilateral multi-layered shell elements, or 8-node solid elements. The rebars were represented by truss elements or orthogonal layers in a shell element. The tendons were replaced by truss elements, and tendon friction elements which take into account the friction effects between concrete and tendons were adopted. The development of these friction elements is described in detail in Chapter 3. The bond characteristics between the concrete and the rebars were assumed to be perfect. The liner was replaced by 4-node shell elements, and a perfect bond between the concrete and liner was assumed in the global and local analyses. The prestressing forces of the tendons were considered in the analyses as an initial stress state.

The material constitutive models are as follows :

For the concrete, the equivalent uniaxial stress-strain model proposed by Darwin et al. was adopted, and the smeared crack model was used. Kupter's failure criteria for a biaxial stress state, and a five parameter model by Willam et al. for a triaxial stress state, were used. The five parameters obtained from the experiments by Ohnuma et al. were also adopted.

For the steel materials such as liner, rebars and tendons, the elasto-plastic theory based on the von Mises yield criterion were used. The uniaxial stress-strain relationships of the steel materials were assumed to be multi-linear models. These models are specified in Chapter 2.

Table 1.3-1 Applications of the computer codes

Name of code	Applications
FINAL	Establishments of tendon friction model and liner anchor model. Global analyses (Axisymmstric, 3D90°shell and 3D180°shell models). Local analyses near E/H, A/L, M/S and wall-basemat juncture.
DIANA	Local analysis near the buttress.
MARC	Local liner analysis near M/S.

Chapter 2. STRESS -STRAIN RELATIONSHIPS OF THE MATERIALS  
AND THEIR CRITICAL STRAINS

In this chapter, the material models and critical strain of each materials (concrete, rebar, tendon, and liner) are set up based on the design package.

2.1 CONCRETE

For the concrete model, the authors adopted the equivalent uniaxial strain model proposed by Darwin et al. and developed for three-dimensional analysis by Murray. A smeared crack model is assumed for the modification of cracks.

○Basic Uniaxial Stress -Strain Relationship

The modified Ahmad model shown in Fig.2.1-1 is used in the compression zone. Elastic behavior is assumed until cracking occurs in the tensile zone. After cracking, tension cut-off or tension stiffening (c=0.8 at Izumo model) is assumed.

○Failure Surface

The five-parameter model developed by Willam et al. in the 3D model, and Kupfer's model in a shell or 2D models are used to model a failure surface. The five - parameters obtained from the experiments by Ohnuma et al. are adopted.

○Shear Retention Model in Cracked Plane.

The Al-Mahaidi equation shown in Fig.2.1-2 is used to model shear retention in a cracked plane.

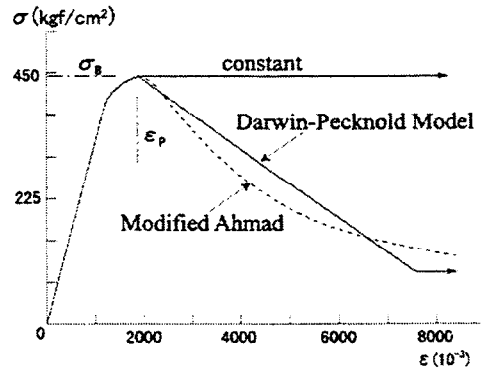


Fig.2.1-1 Uniaxial Stress -Strain Relationship (compression)

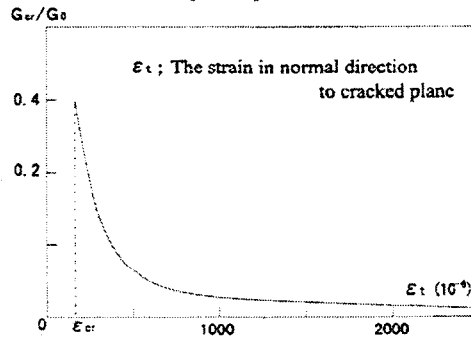


Fig.2.1-2 Shear Retention Model in Cracked Plane.

The compressive strength of the concrete used in the analyses is the same as the design strength recommended by SNL. Young's modulus ( $E_0$ ), tensile strength ( $f_t$ ), and strain ( $\epsilon_p$ ) at maximum strength, used in the analyses, are obtained from the following equations.

$$\epsilon_p = (1.37\sigma_B + 1690)/10^6 ; \sigma_B = 44.13\text{MPa} , \epsilon_p = 0.0023 \quad \text{---Eq.(2.1-1)}$$

$$E_0 = (1.14\sqrt{\sigma_B} + 5.82) \times 10^4 \text{ (kgf/cm}^2\text{)} ; E_0 = 2.94 \times 10^4 \text{ MPa} \quad \text{---Eq.(2.1-2)}$$

$$f_t = 1.07 \cdot \sigma_B^{0.566} \text{ (kgf/cm}^2\text{)} ; f_t = 3.33\text{MPa} \quad \text{---Eq.(2.1-3)}$$

## 2.2 REBARS

### 2.2.1 MODELLING METHOD

The rebar stress-strain relationship obtained from the material test results are approximated as polygonal lines where the following parameters are used:

- Yield point, strain hardening point, 4% strain point, 6% strain point and critical point.

Next, using the stress-strain relationship from the polygonal line approximation, the stress-strain relationship of the rebars is determined according to the following:

- Determine 3 types of stress-strain relationships by averaging the test results for the 5 points stated above for each reinforcement material (SD345, SD390 and SD490).
- Test results for dumbbell-type specimens are not to be used.

### 2.2.2 STRESS-STRAIN RELATIONSHIP

Figure 2.2 shows the stress-strain relationships approximated as the polygonal lines. The stress-strain relationship for the SD390 rebar to be used in the analyses is shown in the thick line. SD390 is the main reinforcement used in the cylindrical portion of the 1/4 PCCV specimen. The critical strain is 21.3%, and is equal to the mean rupture strain of the SD390 rebars.

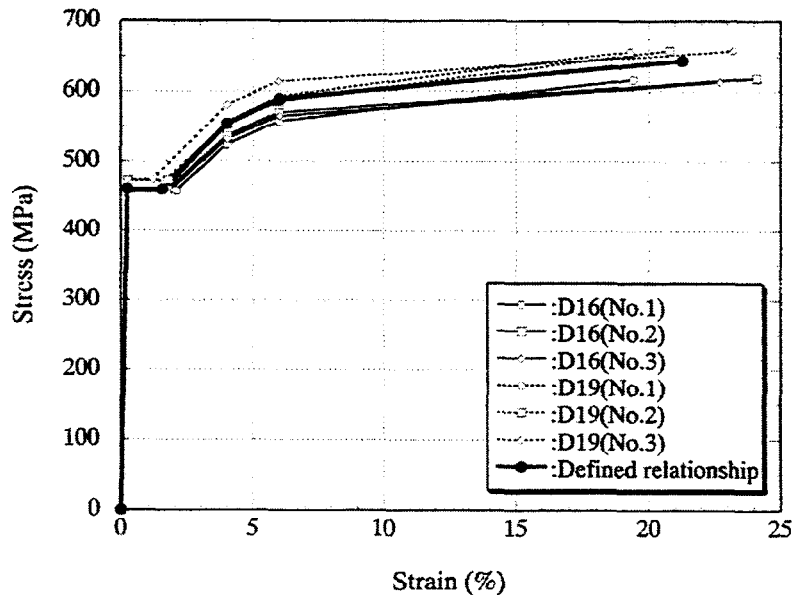


Figure 2.2 Stress-strain relationship for the SD390 rebar

### 2.3 TENDON

The stress - strain relationship of the tendons of the analyses is modeled referring to the results of the PCCV tendon system tensile test and the PCCV tendon strand static tensile test.

Detailed modeling procedure is as follows;

(1) The stress - strain relationship below the critical strain level in the tendon system tensile test is modeled referring to the results of the test.

(2) The relation beyond the critical strain level in the tendon system tensile test is modeled referring to the results of the tendon strand static tensile test.

The modeled stress -strain relationship for the analyses is shown in Fig.2.3-1 with the stress - strain curves by the both tests. The stress - strain relationship is modeled as a tri-linear up to the critical strain of 3.7% in the system test. The stress increase was hardly observed beyond 3.7% in the strand static tensile test, therefore the stress is assumed to be constant beyond the strain level.

The critical strain in straight part near the anchorage is assumed to the critical strain of 3.7% in the system tensile test in which the influence of the wedge anchor was taken into account. The reason is that the tendons is supposed to be ruptured at a lower strain level by the influence of the wedge anchor.

The critical strain in curved part in the cylinder wall is assumed to be 8.0% referring to the tendon strand static tensile test. The critical strain is summarized in Table 2.3-1

Table 2.3-1 Critical strain of the tendons

	Straight part	Curved part
critical strain (%)	3.7	8.0

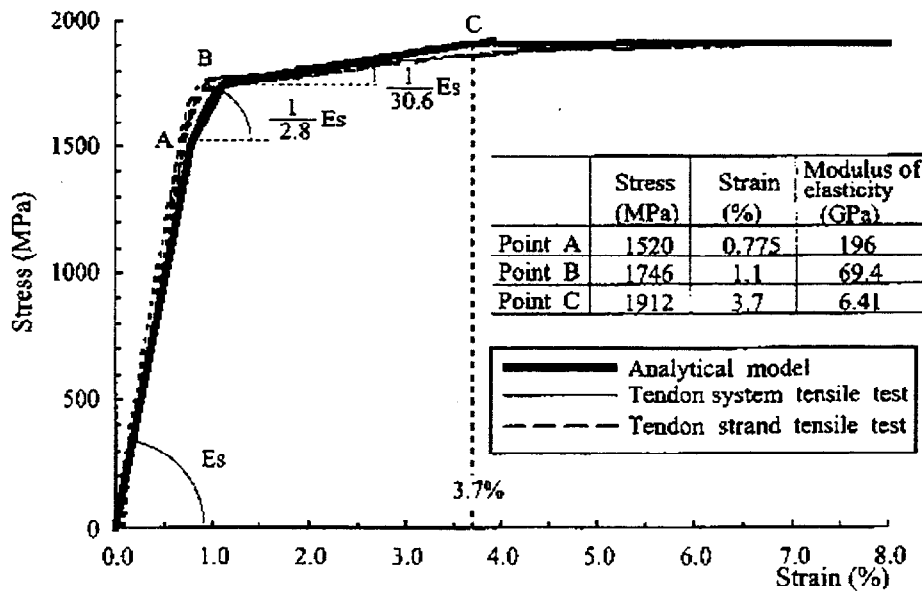


Fig.2.3-1 Stress-strain relationship

## 2.4 LINER

The analysis employs the material properties specified in the PCCV Design Package issued on Nov. 17, 1997. The material tests of the liner material, SGV410, were carried out with several test pieces obtained along with the rolling direction of the plates. The test results demonstrate that the liner materials have 20MPa variations in the yielding points and the variations of other values such as young's modulus and Poisson ratio are within the allowable range. Accordingly the material properties are defined as an average behavior as follows;

The stress-strain relationship was constructed for the analysis as shown in Figure 2.4-1. From Figure 2.4-1, the critical strain of liners is obtained as 33%.

Stress $\sigma$ [MPa]	Total strain $\epsilon$ [%]	$\sigma/E$	Plastic strain $\epsilon_p$ [%]
0	0.000	—	—
382	0.177	0.177	0.000
382	2.000	0.177	1.823
408	2.440	0.189	2.251
436	3.600	0.202	3.398
457	5.000	0.212	4.788
500	33.000	0.232	32.768

Material properties

- Young's modulus  $E = 2.16 \times 10^5$  MPa
- Poisson's ratio  $\nu = 0.3$
- Yield stress  $\sigma_y = 382$  MPa
- Critical strain  $\epsilon_\sigma = 33\%$

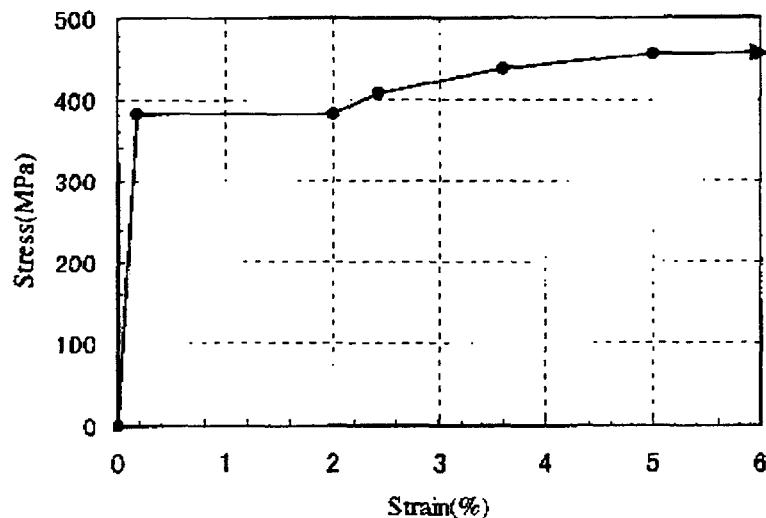


Fig. 2.4-1 : Analytical material property (liner : SGV410)

## Chapter 3. ESTABLISHMENT OF TENDON FRICTION ELEMENT

This chapter outlines the tendon friction element proposed in [1] and examines its application to modeling for PCCV through a few numerical experiments on simple models.

### 3.1 OVERVIEW OF THE FRICTION ELEMENT

Figure 3-1 is a schematic diagram of the sliding surface between the friction element, which transmits frictional force between the tendon and the reinforced concrete, and the tendon. The friction element, which connects the tendon to the reinforced concrete, consists of 3 axial springs which transmit frictional force as well as normal stress. The two axial springs are oriented perpendicular to the tendon's sliding direction and the remaining one is placed parallel to that direction. The tendon's sliding surface is defined as a plane given by the nodal points  $X_2$ ,  $X_1$  and  $X_3$ .  $X_2$  slides along this plane in direction  $\vec{i}$ . The frictional force used in this element is based on Coulomb's Law of Friction. Figures 3-2 and 3-3 show the stress-displacement relationship of the element. The friction characteristics in the sliding direction are indicated as the characteristics of a spring with perfect elasto-plasticity, whose initial stiffness is extremely high. Normal stress is transmitted by the two elastic springs with the same initial stiffness.

### 3.2 VERIFICATION OF FRICTION ELEMENT

To determine the validity of the friction element, we examine the consistency between the theoretical solution of the tensile force in the tendon with the friction and the results of an analysis using the non-linear finite element method. We also examine the distribution of tendon strain using a realistic analysis model that more closely resembles the PCCV. To do this, an internal pressure load is applied to examine tendon strain distribution and confirm that the determined friction model can be used to estimate the 1/4 PCCV's ultimate capacity under internal pressure without numerical instability.

#### 3.2.1 ANALYTICAL CONDITIONS

Figures 3-4 and 3-5 show the study models. The former consists of the tendon and reinforced concrete with the friction elements connecting the two (Model I). In the latter model, the rebars of the reinforced concrete are arranged in a non-uniform manner (Model II). In both models, four tendons are placed in the direction of thickness of the concrete. The boundary conditions for these models specify that the left side is fixed and the right side is roller supported. The friction coefficient between the tendons and the concrete is set at 0.21.

#### 3.2.2 ANALYTICAL RESULTS

Figure 3-6 compares the tendons' tensile force distribution according to the theory of elasticity with the results of the Model I analysis. The theoretical solution of the tendon tensile force is given by:  $P = P_0 \exp(-\mu\theta)$  (where  $P_0$ : tensile force,  $\mu$ : friction coefficient, and  $\theta$ : azimuth). From the figure, we were able to ascertain that the analysis results of the tendon tensile force decrease

exponentially and coincide closely with the theoretical solutions within the elastic range. However, the difference between these results gradually become larger as azimuth  $\theta$  increases. This numerical error may result from the fact that a polygon was used to approximate an arc.

Figure 3-7 shows the slip between the hoop tendon and the reinforced concrete in Model I. In this figure, the slip decreases as the azimuth  $\theta$  increases and when the tensile force reaches 735 kN, slip variation in the plastic state is larger than that in the elastic region.

Figure 3-8 shows the tendon's strain distribution according to analysis results of Models I and II. In Model I, the part to which the tensile force of 735kN is applied becomes plastic between azimuth  $0^\circ$  and  $40^\circ$  and strain concentration is observed there. In Model II, the strain is a minimum at azimuth  $90^\circ$ , and the value increases gradually between azimuths  $60^\circ$  and  $120^\circ$ , in which the cut-off section for the reinforcement ratio exists. This may be caused by the effects of variations in stiffness in the hoop direction.

### 3.3 SUMMARY

- Through verification analyses, the tendon friction element described here is confirmed to avoid the occurrence of any numerical instability up to the ultimate capacity, and to be effective for practical use.

### REFERENCES

1. Yonezawa K., Akimoto M., Imoto K., Watanabe Y.,; Ultimate Capacity Analysis of 1/4 PCCV Model subjected to Increasing Internal Pressure, SMiRT-15 in Seoul, Aug.,1999.

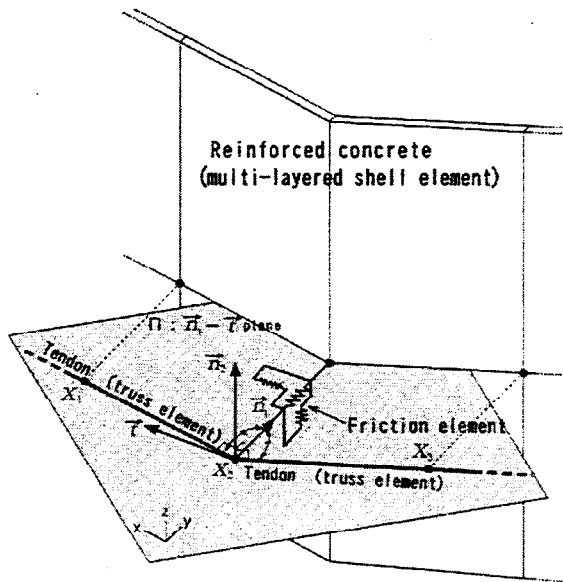


Fig.3-1. Tendon friction element

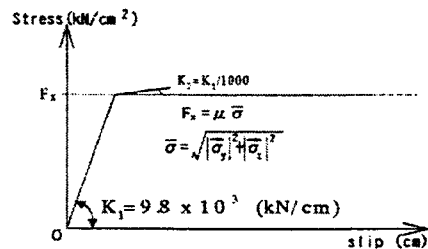


Fig.3-2. Relationship between slip and frictional force (x direction)

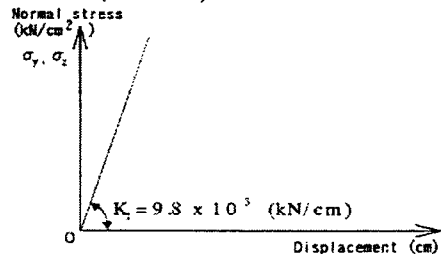


Fig.3-3. Relationship between displacement and normal stress (y,z direction)

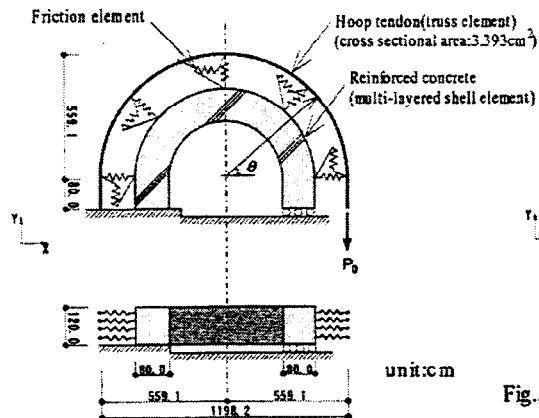


Fig. 3-4. Verification model for tendon friction element (MODEL I)

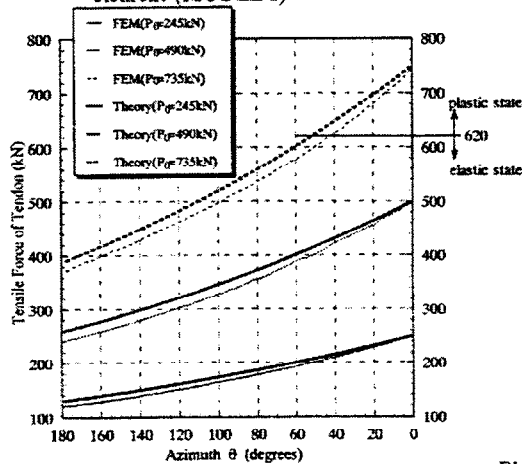


Fig. 3-6. Tensile force distribution of hoop tendon (MODEL I)

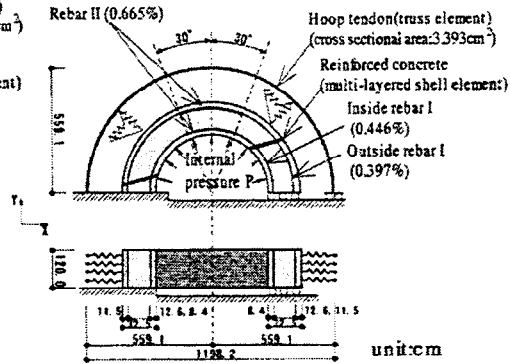


Fig. 3-5. Verification model for tendon friction element (MODEL II) (non-uniformly distributed rebar)

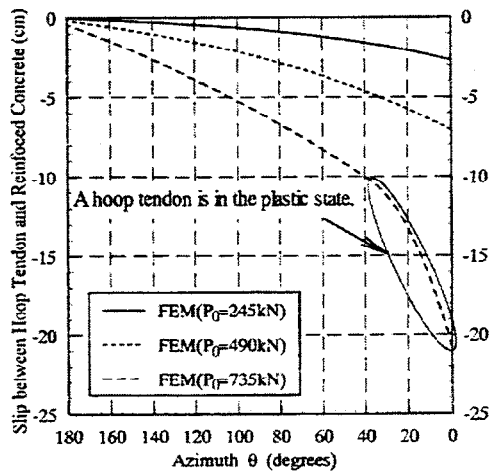


Fig. 3-7. Distribution of slip between hoop tendon and reinforced concrete (MODEL I)

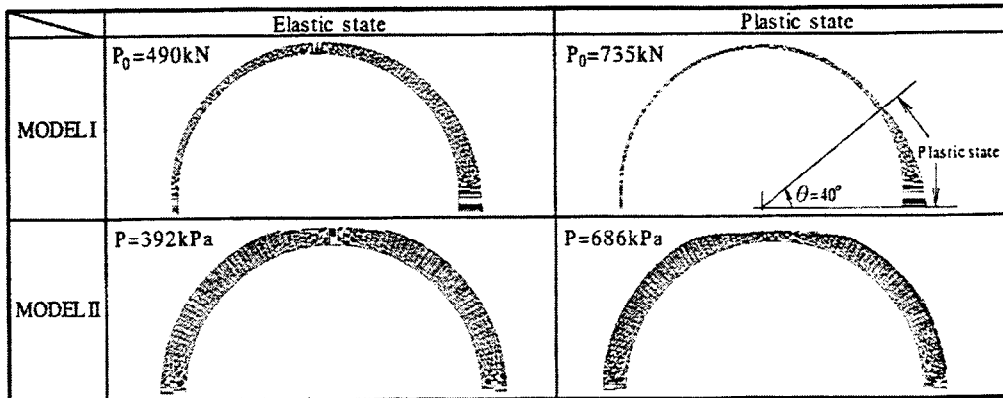


Fig. 3-8. Distribution of tendon strain

## Chapter 4. ESTABLISHMENT OF LINER ANCHOR ELEMENT

This chapter investigates the modeling method of the liner anchor used in the liner analyses according to the following procedure, to determine the failure mode due to liner tearing.

- 1) Modeling of the T-anchor taking into account a three-dimensional directions.
- 2) Verification analysis for the pull - out liner anchor test indicated in the design package is performed to investigate the applicability of this model.
- 3) Numerical experiments considering the nonlinear behavior of the general portion of the cylinder are carried out to determine the characteristics of the liner anchor model.

### 4.1 MODIFICATION OF LINER ANCHOR

This model is represented by linkage elements composed of three springs normal to each other as shown in Fig.4-1, considering the characteristics of the T-anchor.

The directional components of the stiffness (N, S, V) fixed in the liner anchor direction are determined as follows.

- 1) For stiffness (N) in the axial direction of the T-anchor :  $K_N=0$ . If located at the I-anchor(horizontal anchor),  $K_N=\infty$
- 2) For stiffness (V) in the vertical direction of the liner :  $K_V=T_2*L*E/B$  (for tensile force),  $K_V=\infty$  (for compressive force)
- 3) For the equivalent shear stiffness (S) transverse to the T-anchor :  $K_S=L*$  (determined from FEM results).

The parameters used in the above equations are defined as follows.

where L is the length of the meshing element, B is length of the T-anchor web in the vertical direction, T<sub>2</sub> is the thickness of the T-anchor web, and E is the elastic or plastic stiffness of the material. The equivalent shear stiffness (S) transverse to the T-anchor is obtained through 2D-FEM analyses in the following section.

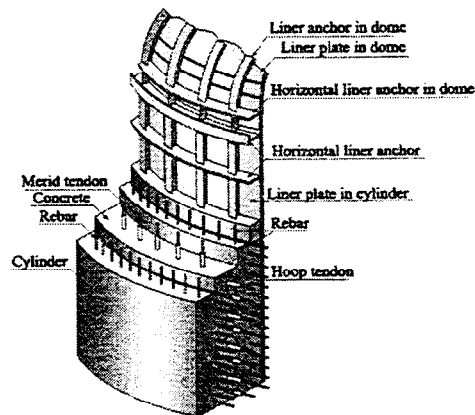


Fig.4-1 Schematic view of PCCV

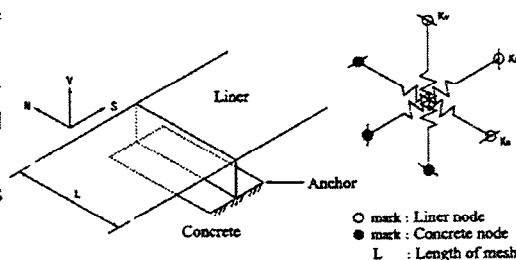


Fig.4.2 Modification of the anchor model

### 4.2 VERIFICATION OF ANALYTICAL MODELS FOR PULL-OUT TESTS ON LINER ANCHOR

- ① The tests are outlined in the design package: In the tests, the T-anchor is subjected to shear force through the liner plate. Five tests have been performed with variables scale, interval, and the T-anchor shape.
- ② Analytical model

Analytical model is shown in Fig.4-3. Perfect bonding is assumed at contact surface between concrete and anchor flange. And no bonding is assumed at the contact surface of liner and anchor web.

③ Analytical results

The force – displacement relationships obtained from the analytical and experimental results are compared in Fig.4-4. Three specimens were used to demonstrate one case in the tests. Displacement at the loading point was used to signify the displacement of the analytical results in Fig.4-4. The analytical results are summarized in Table.4.1. It is seen that the T-anchor behavior can be evaluated by the analytical model used in this study.

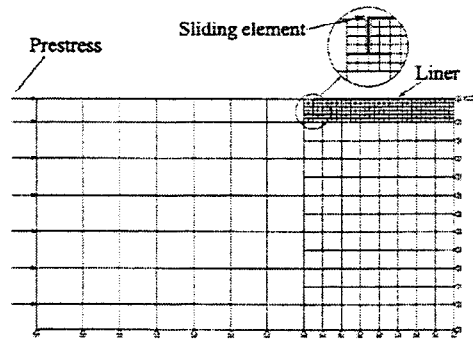


Fig.4-3 Computational grids

Table 4-1 Analytical results

Specimen No.		1	2	3	Ave	
Q-1-1	Exp.	Initial stiffness	25900	14500	17500	15000
		Max.capacity	280	264	269	271
Ana.		Initial stiffness	17600			
		Max.capacity	252			
Q-3-1	Exp.	Initial stiffness	18000	22500	18750	19700
		Max.capacity	473	490	500	484
Ana.		Initial stiffness	17780			
		Max.capacity	384			

Unit ; Initial stiffness : kgf/cm<sup>2</sup>, Max. capacity : kgf/cm

4.3 ANALYTICAL EVALUATION OF LINER ANCHOR MODEL

The equivalent shear stiffness (S) transverse to the T-anchor is obtained by analytical evaluation of the liner anchor behavior on the PCCV subjected to internal pressure.

① Outline of Analysis

The analytical model is shown in Fig.4-5. The model plane represents a wedge section of the cylinder whose angle (1.6°) indicates the spacing of the vertical liner anchor. The symmetrical boundary condition is applied on both sides of this model. The use of sliding elements accounts for the sliding and opening moment between the concrete and the liner.

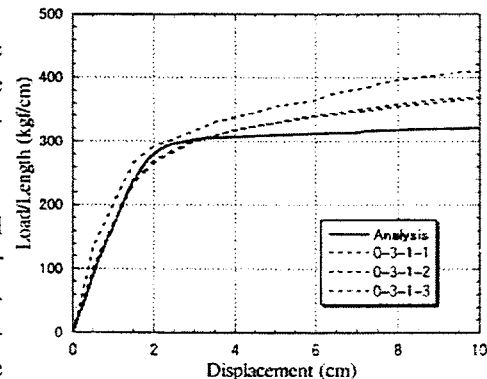


Fig.4-4 Load-displacement relationship

One end of the liner is assumed to be the free end. The rebar area on the right end is twice that of the general portion. Thus, the displacement is concentrated around the liner anchor. For the analytical parameters, four bond characteristics between the concrete and the liner are applied here, as shown in Table.4-2.

② Analytical Result

The load-displacement relationships obtained from CASES1 ~ 3 are shown in Fig.4-6. The vertical axis indicates the shear force acting at the liner anchor, and the horizontal axis indicates the displacement (S) at the juncture of the liner anchor and the liner as shown in Fig.4-6. The dis-

placement at the maximum capacity for CASE3 is found to be comparatively large. However other differences between the three cases are less remarkable. The analytical results are shown in Table.4-3. The results of the pull-out tests are also shown in Table.4-3 for comparison. The maximum capacity obtained from these analyses is about 35% of the test results. This is because the effects under cracking by internal pressure are considered in these analyses, but not in the tests. Therefore, it is found that the maximum capacity depends on whether cracking occurs due to internal pressure.

#### 4.4 SUMMARY

First, 2D-FEM analyses of pull-out tests were performed to investigate the applicability of the analytical model. Next, numerical experiments were performed to idealize the non-linear behavior of the liner anchor of the PCCV subjected to internal pressure. The analytical results of these numerical experiments are almost the same. Therefore, the equivalent shear characteristic transverse to the T-anchor is assumed to be tri-linear as shown in Fig.4-6.

First point :  $S_1=0.01$  cm ,  $\tau_1=90$ kgf/cm  
 Second point :  $S_2=0.035$  cm ,  $\tau_2=130$ kgf/cm

$\tau = 130$ kgf/cm remains constant after the second point.  
 This anchor model is applied to the liner analyses.

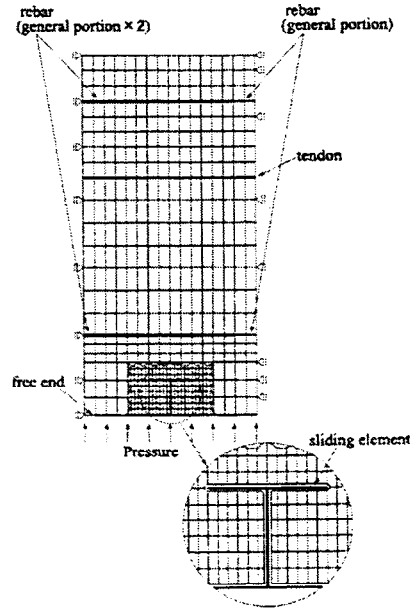


Fig.4-5 Computational grids

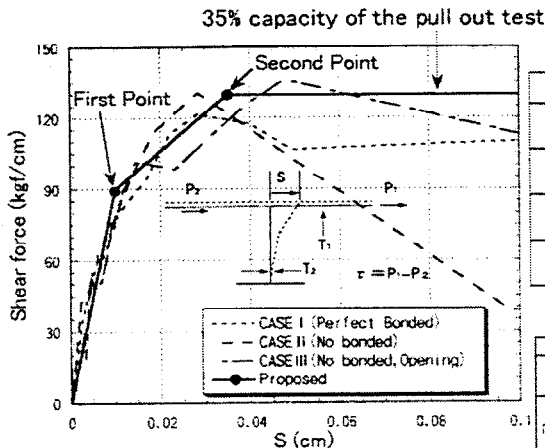


Fig.4-6 Shear force-displacement relationship

Table 4-2 Cases of analyses

	Location	characteristics in parallel direction	Opening in radial direction
I	Between liner and concrete	No bonded	No
	Between anchor and concrete	(flange) perfect bonded (Web) perfect bonded	
II	Between liner and concrete	No bonded	No
	Between anchor and concrete	(flange) perfect bonded (Web) perfect bonded	
III	Between liner and concrete	No bonded	No
	Between anchor and concrete	(flange) perfect bonded (Web) perfect bonded	Yes
IV	Between liner and concrete	No bonded	No
	Between anchor and concrete	(flange) perfect bonded (Web) perfect bonded	Yes

Table 4-3 Analytical results

		CASE1	CASE2	CASE3	Ave.
Analysis	Initial stiffness	14700	19100	11900	15233
	Max capacity	136	131	136	134
pull-out test (Q-3-1)	Initial stiffness	Exp. 18900	22520	18760	19709
	Max. capacity	Exp. 473	480	500	484
		Ana. ---	---	---	384
		---	---	---	---

## Chapter 5. GLOBAL ANALYSES FOR 1/4 PCCV MODEL

This chapter describes global analyses performed to determine the global non-linear behavior of the 1/4PCCV model, and to obtain the boundary conditions of the local analyses.

- 1) Axi-symmetrical analysis
- 2) Global analysis by the 3D-90° shell model idealized for the M/S and F/W side.
- 3) Global analysis by the 3D-180° shell model idealized for the E/H and A/L side.

### 5.1 GLOBAL ANALYSIS BY AXI-SYMMETRIC MODEL

This section describes an axi-symmetrical analysis carried out to determine the base non-linear behaviors and the boundary conditions for local analyses.

#### 5.1.1 ANALYTICAL MODELING

In the analytical model shown in Fig.5.1-1, a 3D FEM for the narrow wedge of the vertical section (2°) is used instead of the normal axisymmetric FEM. This model plane is chosen at the 135° azimuth, which is reasonably far from the penetrations.

The concrete is modeled as an 8-nodes solid element. The meridional tendons are represented by truss elements and attached to the concrete by sliding elements. The bond characteristics between concrete and the meridional tendons are assumed to be unbonded. Rebars are represented by truss elements and shell layers which are given an area equivalent to the rebar area, and a Poisson's Ratio of zero to avoid any in-plane/out of plane stress - strain interactions. The liner is constructed of quadratic shell elements and the liner anchors are represented by shell layers which are given an area equivalent to the liner anchor area. Perfect bonding is assumed between the rebars and the concrete.

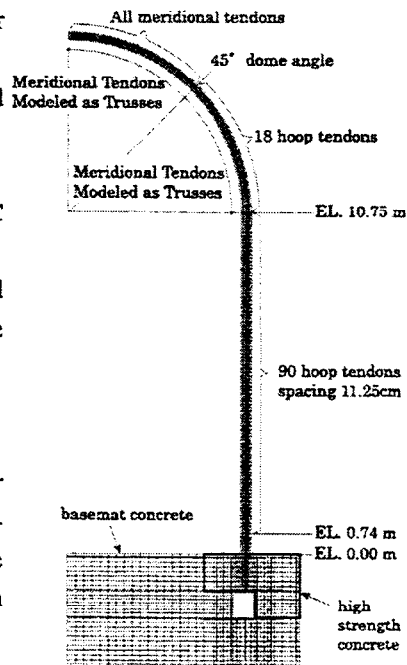


Fig.5.1-1 Computational grids

#### 5.1.2 ANALYTICAL RESULTS

Deformation modes corresponding to each pressure levels are shown in Fig.5.1-2. It is found that the radial displacement at the mid-height of the cylinder is the largest, and the vertical displacement at the apex of the dome is fairly small. The maximum displacement is found at EL. 7.15m at the mid-height of the cylinder.

The pressure-radial displacement at the maximum point is shown in Fig.5.1-3, and the pressure-

vertical displacement at the apex of the dome is shown in Fig.5.1-4.

These plots show a rapid increase of displacement after material yielding (1.35MPa). The apex of the dome begins to move downward at a pressure larger than 1.5MPa, as shown in Fig.5.1-4. However, the amount is fairly small in comparison with the radial displacement at the mid-height of the cylinder.

### 5.1.3 SUMMARY

- (1) The meridional strains are generally fairly small in comparison with the hoop strains.
- (2) The radial displacement at the mid-height of the cylinder is the largest, reaching 247mm at El.7.15m. This is equivalent to 4.6% of the free field strain.

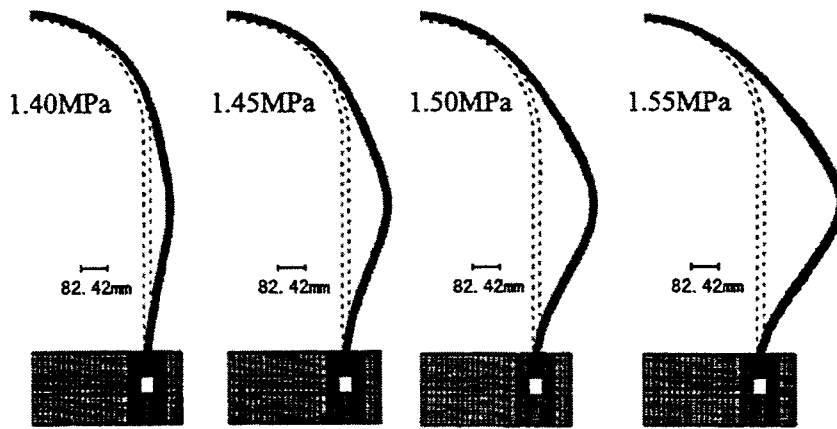


Fig.5.1-2 Deformation mode

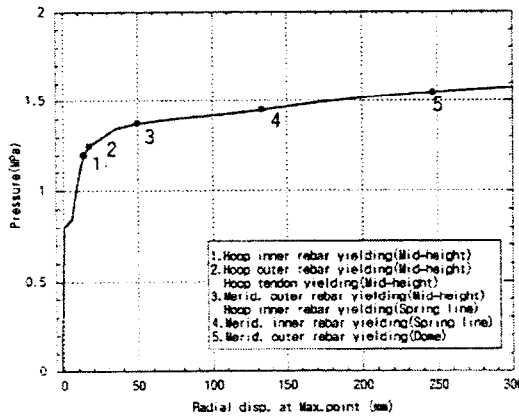


Fig.5.1-3 Pressure-radial displacement relationship at maximum displacement point

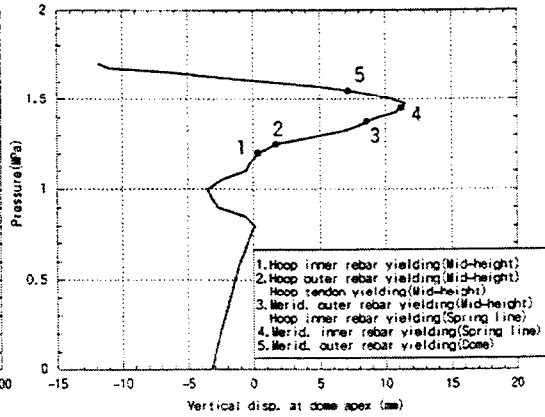


Fig.5.1-4 Pressure-vertical displacement relationship at apex of the dome

## 5.2 GLOBAL ANALYSIS BY 3D90° SHELL MODEL

Here, a global analysis with 3D-shell 90° model is performed to quantitatively determine the global nonlinear behaviors, and to obtain boundary conditions for local analyses. For the model plane, the region from 180° to 270° azimuth, including main steam (M/S) and feed water(F/W) penetrations is chosen.

### 5.2.1 ANALYTICAL MODELING

The 3D-shell 90° model shown in Fig.5.2-1, which idealized a one quarter section of a 1/4 scale PCCV model, takes into account the non-symmetric tendon layout of the dome, buttresses, and the local congestion of the rebar arrangements around these penetrations. The layout of the meridional tendons is idealized as accurately as possible in this model. For the modeling of the basemat, displacements obtained from the axisymmetric model are applied to nodes at the bottom of the cylinder for the boundary conditions. The reinforced concrete wall is modeled using quadratic multi-layered shell elements. The meridional and hoop tendons are represented through truss elements and attached to the concrete with sliding elements. The friction model (friction factor :  $\mu = 0.21$ ) discussed above is used to model the friction characteristics between concrete and tendons. The liner consists of quadratic shell elements.

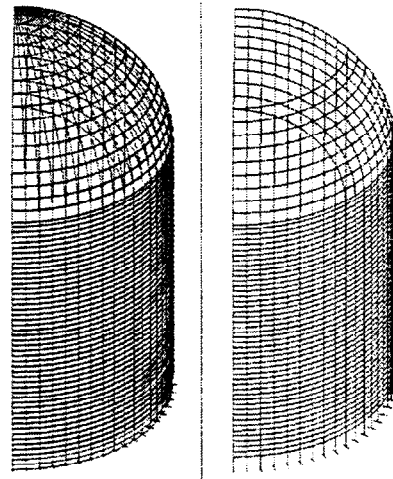


Fig.5.2-1 Computational grids

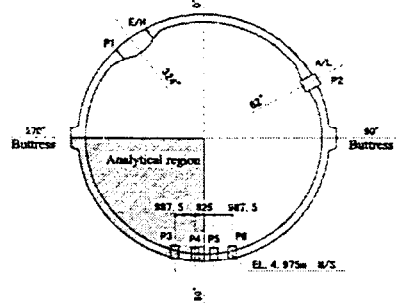


Fig.5.2-2 Analytical region

### 5.2.2 ANALYTICAL RESULTS

The pressure - radial and vertical displacement relationships obtained by analysis are shown in Fig.5.2-3 and Fig.5.2-4, respectively.

The height of the maximum radial displacement obtained by analysis is at about mid-height (EL.7.0) of the cylinder. The apex of the dome begins to move downward at a pressure larger than 1.5MPa as shown in Fig. 5.2-4. However this is fairly small compared to the radial displacement at the mid-height of the cylinder. This behavior is the same as that of the axi-symmetric analysis.

The hoop tendon strain distribution and the slip distributions between the hoop tendon and the RC wall at each elevation level (EL5.2m and EL7.2m) are shown in Fig.5.2-5 and Fig.5.2-6, respectively.

The maximum slip at level 1 is found at the rebar cut-off section around the M/S.

The slip at level 2 is fairly small compared to that of level 1, because there is no rebar cut-off section where stiffness changes at level 2.

The tendon strain around the M/S at level 1 is comparatively small. The tendon strain in the general portion at level 2 appears to be the largest in terms of uniformity.

A deformation mode and contour obtained from the analysis at 1.55MPa is shown in Fig.5.2-7. The location of the maximum displacement is found at the general portion around the 120° or 240° azimuths between the buttress and the M/S.

The contour of the von Mises total strain in the liner at 1.55MPa is shown in Fig.5.2-8. The strain concentrations in the liner occur at the rebar cut-off section around the M/S and the buttress, as shown in Fig. 5.2-8.

The contours of the hoop strain in the inner and outer rebars at 1.55MPa are shown in Fig.5.2-9 and Fig.5.2-10, respectively. The locations of strain concentration in the inner rebars and liner are almost the same. In the outer rebars, strain concentration appears at the general portion around mid-height and the rebar cut-off section around M/S. The hoop strains in the outer rebars appear to be bigger than those in the inner rebars.

### 5.2.3 LOCATIONS OF STRAIN CONCENTRATION

The locations and amounts of the maximum strain in the materials (rebars, liner, and tendons) are summarized corresponding to pressure levels in Table5.2-.1 and Fig.5.2-11. The thick lines and hatches in Fig. 5.2-11 indicate the boundary lines of rebar cut-off sections where the hoop rebar ratios change.

In Fig.5.2-11, it is seen that strain concentration occurs at several portions, such as the hoop rebar cut-off sections around the penetrations and buttress in this analytical region.

The maximum tendon strain is found to be in the hoop tendon at EL7.0m, reaching the critical strain (8.0%) at 1.55MPa. However, there is a margin of safety in the liner and rebar strains.

It is concluded from this analysis that the hoop tendon strain at EL.7.0m is the first to exceed the critical strain at an internal pressure of about 1.55MPa.

### 5.2.4 SUMMARY

- 1) The strain concentrations in materials occur at the portions where the stiffness changes, such as rebar cut-off sections and the buttresses.
- 2) In this analytical region from 180° to 270° azimuths of the 1/4PCCV model, the hoop tendon strain at EL.7.0m is the first to exceed the critical strain (8%) at an internal pressure of about 1.55MPa.

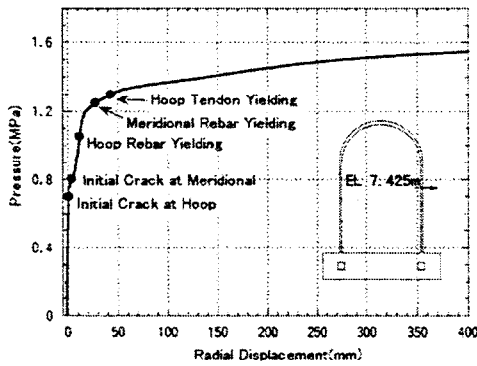


Fig.5.2-3 Pressure-radial disp. relationships at maximum disp. Points

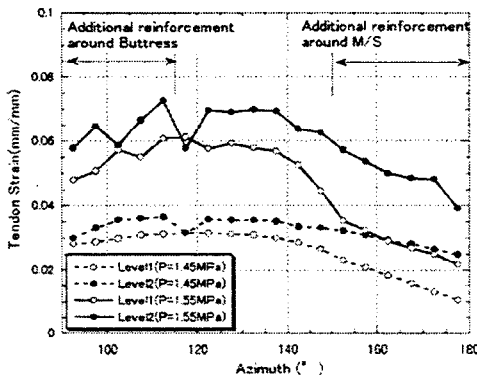


Fig.5.2-5 Distributions of tendon strain

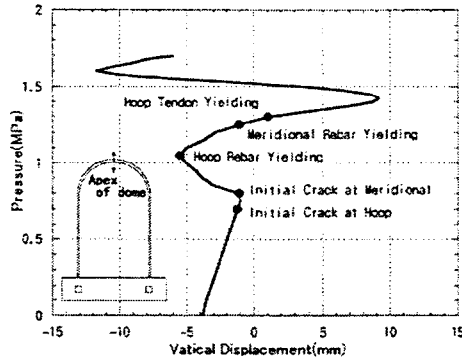


Fig.5.2-4 Pressure-vertival disp. relationships at apex of the dome

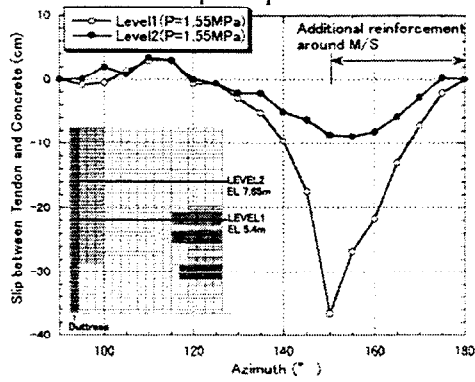


Fig.5.2-6 Distributions of slip between tendon and concrete

Table 5.2-1 Maximum strains versus pressure

	1.45MPa	
	Strain(%)	Location
Tendon	3.65	EL.6.97m (FT1) General Portion
Rebar	4.27	Rebar Cut-off Section around M/S (FR1)
Liner	4.37	Rebar Cut-off Section around M/S (FL1)
	1.55MPa	
	Strain(%)	Location
Tendon	7.27	EL.7.65m (FT2) General Portion
Rebar	8.22	Rebar Cut-off Section around Buttress (FR2)
Liner	7.77	Buttress (FL2)

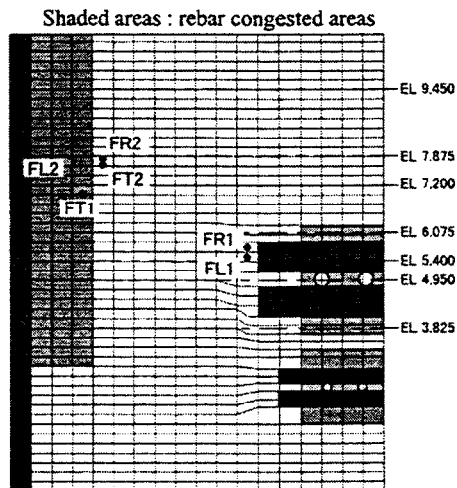
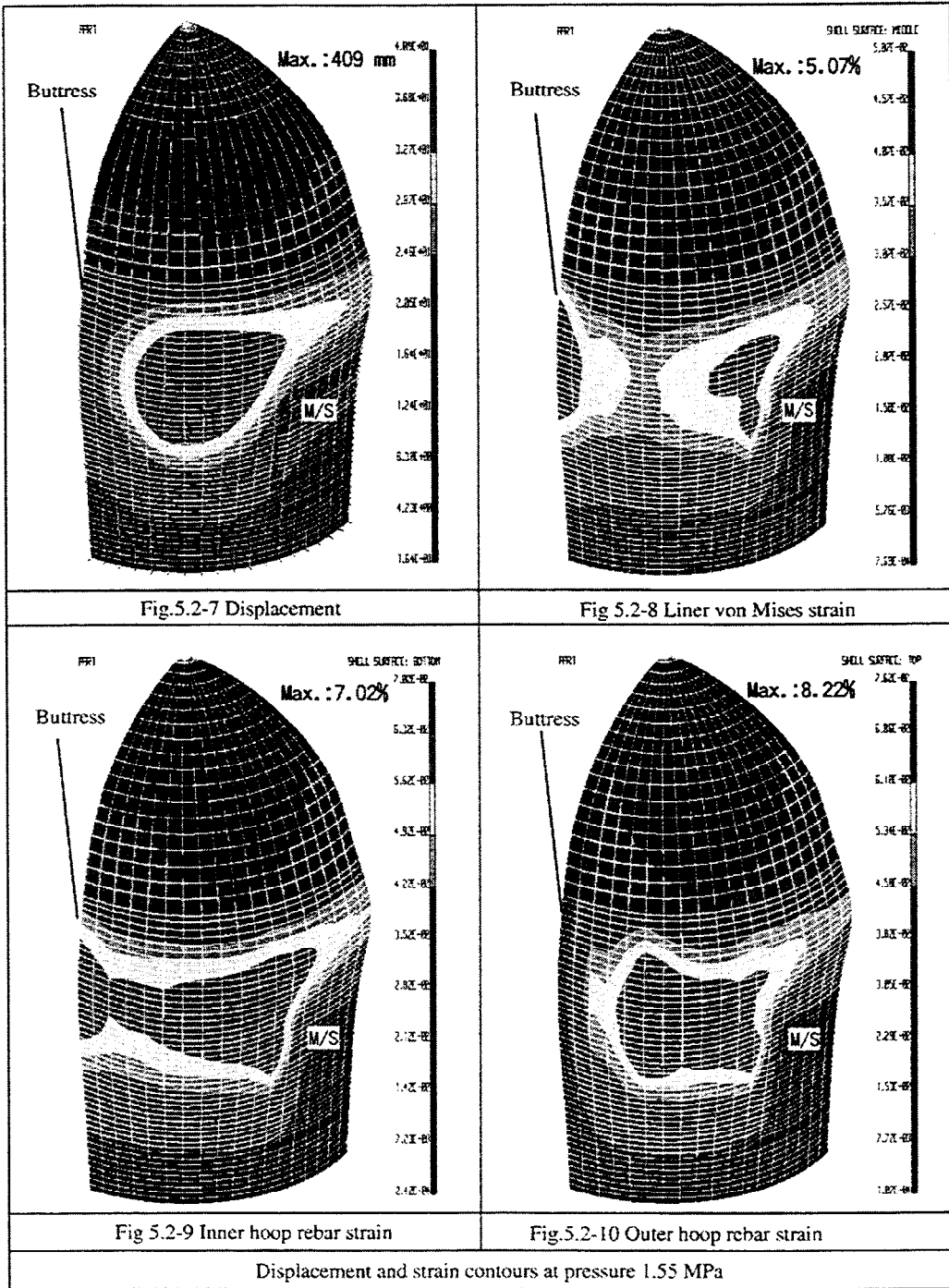


Fig.5.2-11 Locations of the maximum strains of materials



### 5.3 GLOBAL ANALYSIS BY 3D180° SHELL MODEL

The analyses are conducted for the sections between azimuths 0° -90° and 270° - 360° which include the large openings (A/L, E/H) of the 1/4 PCCV specimen. These analyses are used to determine the overall behavior of these sections taking into account the effects of the large openings and the buttress, as well as the distribution characteristics of tendon strain and the determination of the boundary conditions to be used in detailed local analyses.

#### 5.3.1 ANALYTICAL MODELS

Figure 5.3-1 shows the analytical models. These models incorporate the buttress, as well as reinforcement around openings A/L and E/H, and use a multi-layered shell element for the entire reinforced concrete. Tendons are modeled as truss elements - two meridional tendons and three hoop tendons each considered to be one tendon - and the tendon arrangements around the dome and opening areas are faithful reproductions of those found in the specimen. The bottom of the cylindrical wall is fixed. The friction coefficient between the tendon and concrete is defined to be 0.21.

#### 5.3.2 ANALYTICAL RESULTS

Figure 5.3-2 shows the relative displacement of the hoop tendon and the concrete. It shows the displacement between the hoop tendon nodal point and the concrete nodal point at the two levels under internal pressures of 1.45 and 1.55MPa. Tendon-A is at the level of the A/L and E/H openings. The maximum strain in the hoop tendon under an internal pressure of 1.55MPa occurred at the level of Tendon-B. It can be seen that the azimuths at which the relative displacement becomes "0" are the sections where maximum displacements occur at the center of the large opening and the general areas. On the other hand, the areas with maximum relative displacements are at the cut-off sections of the rebars. The tendency of variance of tendon-B is similar to that of tendon-A, but smaller in degree.

Figure 5.3-3 shows the circumferential distribution of the hoop tendon strain at the two levels under internal pressures of 1.45 and 1.55MPa. The levels of evaluation are the same as those used in Figure 5.3-2. For tendon-A, the strain in the reinforcing portion is the smallest at the azimuth at the center of the opening and increases as it goes from the opening, peaking at the 30° azimuth area of the general portion. Variation tendencies of tendon-B are similar to those of tendon-A.

Figures 5.3-4 and 5.3-5 show contours of deformation and liner strain both under an internal pressure of 1.55MPa. Here, deformation refers to the absolute values of the displacement vectors of the nodal points. The maximum value of 39.2cm is registered in the general area between A/L and E/H (near EL. 7.5m). Increases in liner strain are found

at the reinforcement cut-off section on the E/H side of A/L, reinforcement cut-off section on the A/L side of E/H and the buttress.

Figures 5.3-6 and 5.3-7 show strain contours of the inner and outer horizontal reinforcement under an internal pressure of 1.55MPa. The general area between A/L and E/H shows the most strain increase of the inner and outer horizontal reinforcement. Strain concentration is particularly pronounced at the reinforcement cut-off section around the large opening.

### 5.3.3 MAXIMUM STRAIN OF STEEL MATERIALS

Table 5.3-1 lists the maximum strain values. Here we discuss the maximum steel material strain under an internal pressure of 1.55MPa. The maximum horizontal reinforcement strain occurs at the outer reinforcement cut-off section on the A/L side of E/H at a maximum strain of 9.28%. Maximum strain for the hoop tendons occurs at the EL.6.70m level with a maximum strain of 7.33%. The maximum liner strain occurs at the reinforcement cut-off section on the E/H side of A/L at a maximum strain of 8.36%.

### 5.3.4 SUMMARY

While the maximum reinforcement and liner strain under an internal pressure of 1.55MPa is smaller than the critical strain by a sufficient margin, the maximum hoop tendon strain is very near the rupture strain (8% in the general areas). As indicated in the 3D90° shell model analysis, the current analysis similarly shows that the hoop tendons near EL.7.0m will be the first to reach the critical strain.

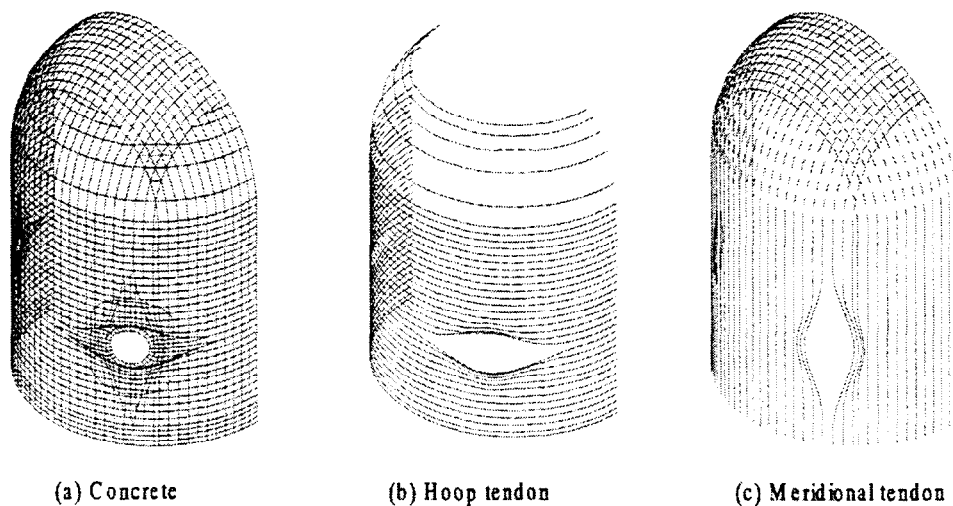


Fig.5.3-1. Analytical model

Table.5.3-1. Maximum strain values

Pressure (MPa)	Material	Maximum strain(%)	Location
1.45	Tendon	3.51	EL.7.7m(FT1)
	Reinforcement	5.37	Rebar cut-offsection around A/L(FR1)
	Liner	4.53	Rebar cut-offsection around A/L(FL1)
1.55	Tendon	7.33	EL.6.7m(FT2)
	Reinforcement	9.28	Rebar cut-offsection around E/H(FR2)
	Liner	8.36	Rebar cut-offsection around A/L(FL2)

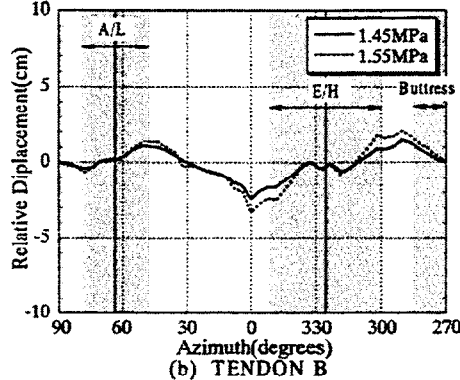
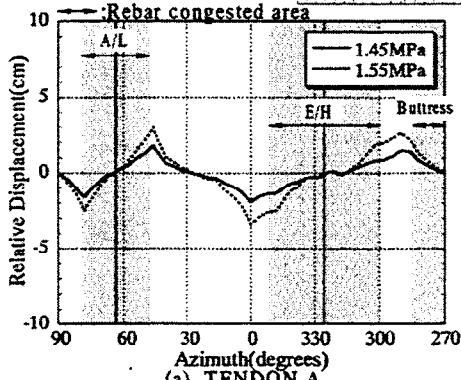
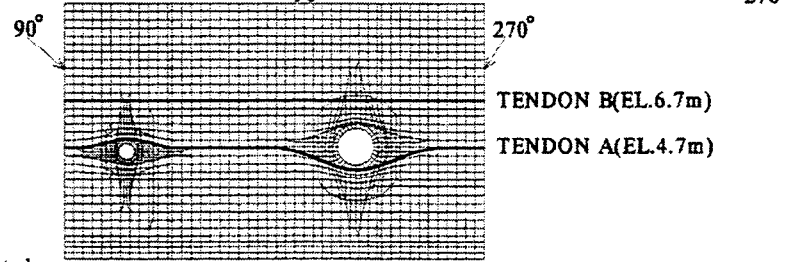
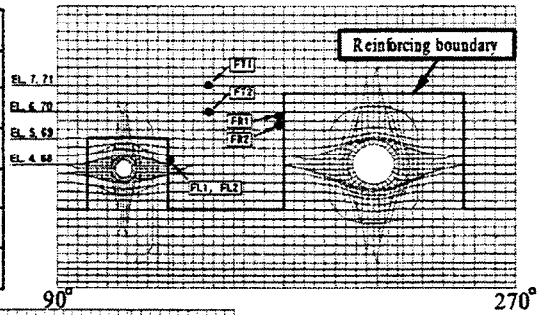


Fig.5.3-2. Relative Displacements between hoop tendon and concrete

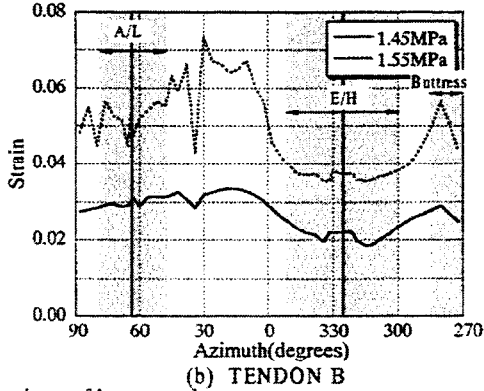
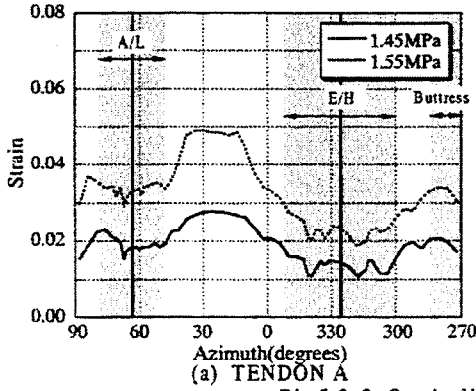


Fig.5.3-3. Strain distributions of hoop tendon

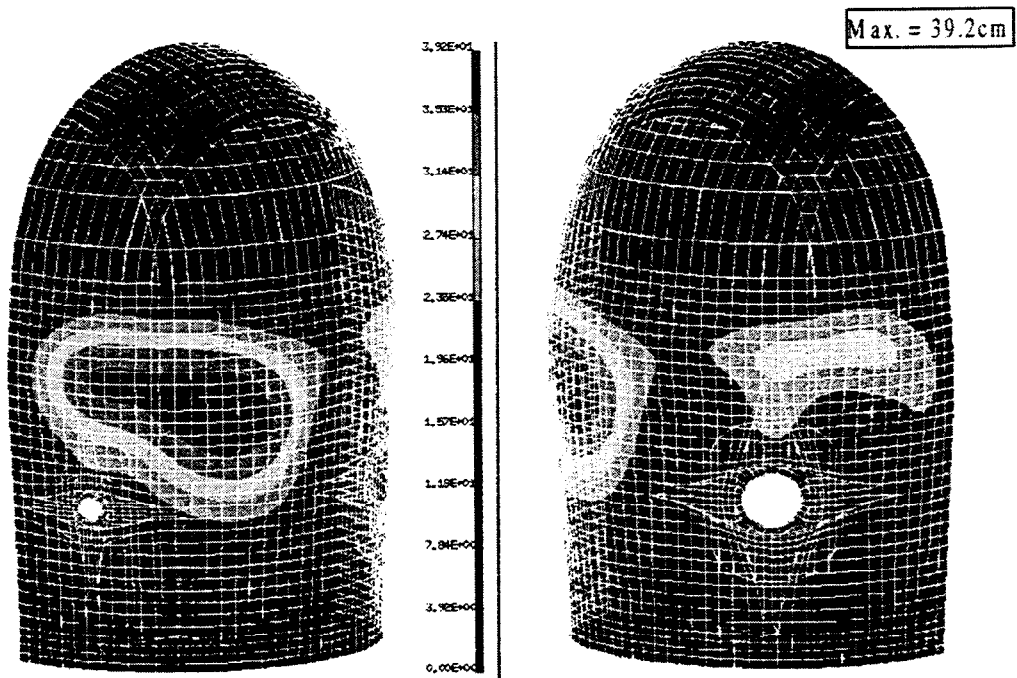


Fig.5.3-4 Deformation contour at 1.55MPa

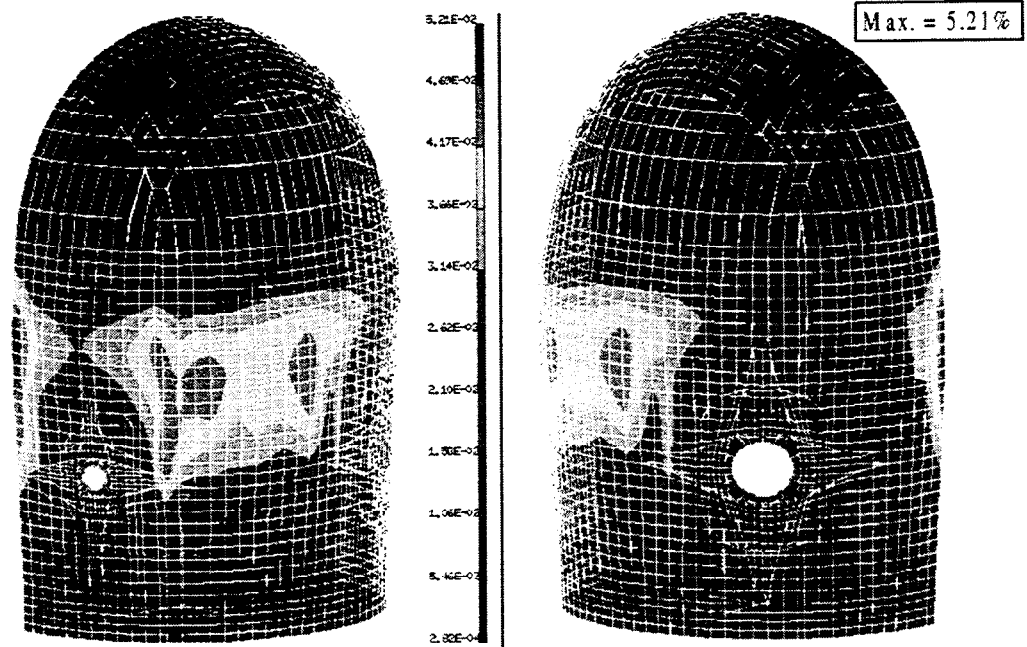


Fig.5.3-5 von Mises strain contour of liner at 1.55MPa

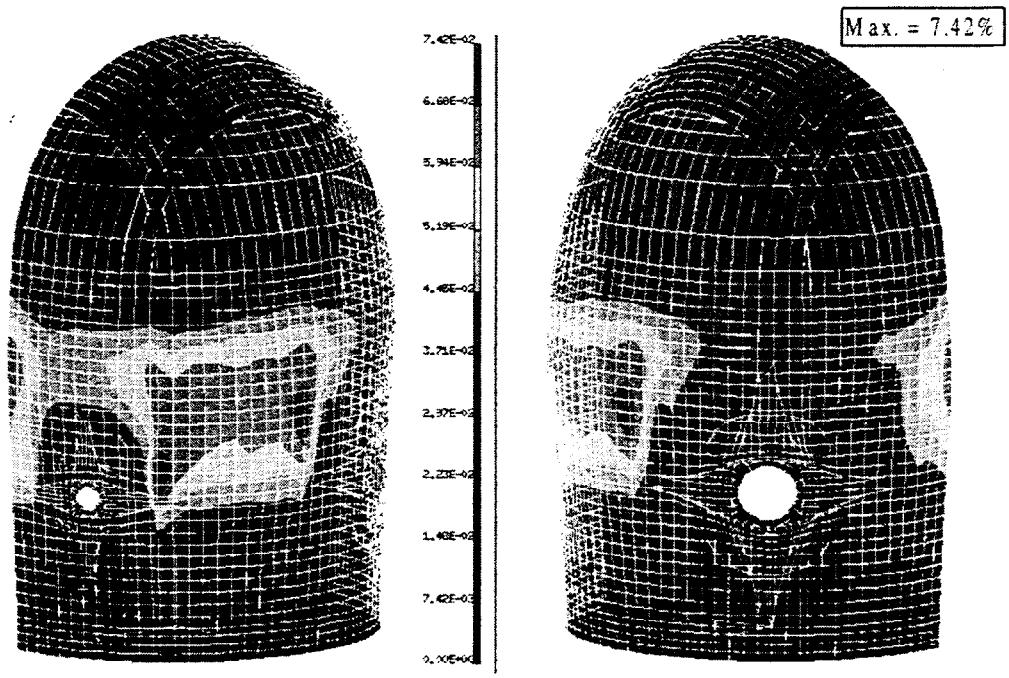


Fig.5.3-6 Strain contour of inner horizontal reinforcement at 1.55MPa

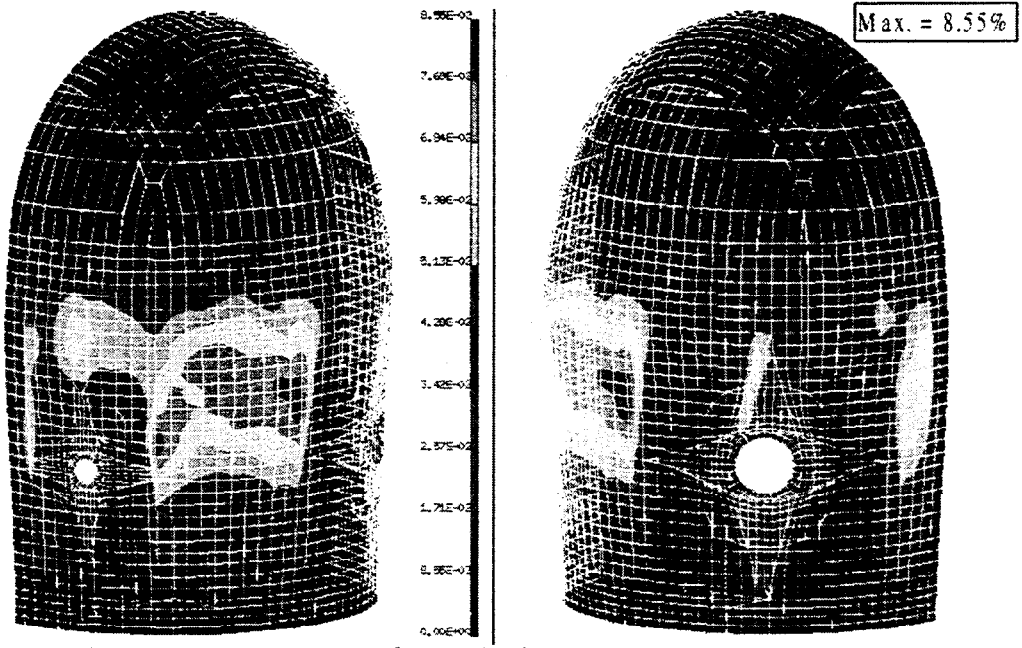


Fig.5.3-7 Strain contour of outer horizontal reinforcement at 1.55MPa

## Chapter 6. LOCAL ANALYSES OF 1/4PCCV MODEL

Potential failure portions have been approximated by considering the results of the global analyses discussed above. Local analyses for these portions are performed in this chapter. The following local analyses take into account the global analysis results.

- 1) The wall-basemat juncture
- 2) Buttresses
- 3) The E/H and A/L openings
- 4) The M/S penetrations

### 6.1 LOCAL ANALYSIS BY 3D SOLID MODEL NEAR CYLINDER WALL-BASE JUNCTURE

In this section, local analyses with fine mesh models are performed taking into account the area near the wall - basemat juncture, in order to determine nonlinear behavior and to evaluate local strain concentration on the structural components.

#### 6.1.1 ANALYTICAL MODELING

The analytical model used here is shown in Fig.6.1-2.

A 3-D FEM for a narrow wedge of vertical section ( $1.6^\circ$ ) is used. This wedge has the same pitch as the liner anchor. The model plane is chosen at the  $135^\circ$  azimuth and lower than EL.2.0m. In this model, the shape of the liner anchors and their connections in the wall-base are idealized in more detail by elemental meshing at depth. Furthermore the rebars around the tendon gallery are modeled one-for-one by truss elements.

For the boundary condition, the internal pressure is applied to the interior surfaces, and displacements obtained from axisymmetrical analysis are applied to the top surfaces of this model.

Two analysis cases are carried out here. The analytical variables are the bond characteristics between the concrete and the liner, i.e., perfect bonding in CASE1, and no bonding in CASE2.

#### 6.1.2 ANALYTICAL RESULTS

The pressure - strain relationships of the meridional rebar at the wall - base juncture are shown in Fig.6.1-2. Axi-symmetrical analysis results are also plotted in Fig.6.2-2. The sequences of non-linearity are almost the same in both cases. The inner rebar yields at a pressure of 1.45MPa, and the outer rebar strain shift from tension to compression due to the crushing of the outer cover concrete at 1.5MPa.

The contour of the minimum principal concrete stress, and the contour of the von Mises strain of the liner at 1.55MPa are shown in Fig.6.1-4 and Fig.6.1-5.

There were no substantial differences between the minimum principal concrete stresses for the two cases.

The maximum compressive stress is found at the outer surface of the wall – base juncture because of flexural deformation. Concrete crushing occurs at the outer surface of this region at 1.5MPa, but the principal stresses elsewhere do not exceed the uniaxial maximum concrete strength. Shear ties in the wall – base juncture remain elastic up to 1.6MPa. It is thus determined that shear failure does not occur in this region.

In the surrounding tendon gallery, the concrete stresses do not exceed the uniaxial maximum strength and the rebars remain elastic up to 1.6MPa. It is thus determined that shear failure does not occur in the surrounding tendon gallery.

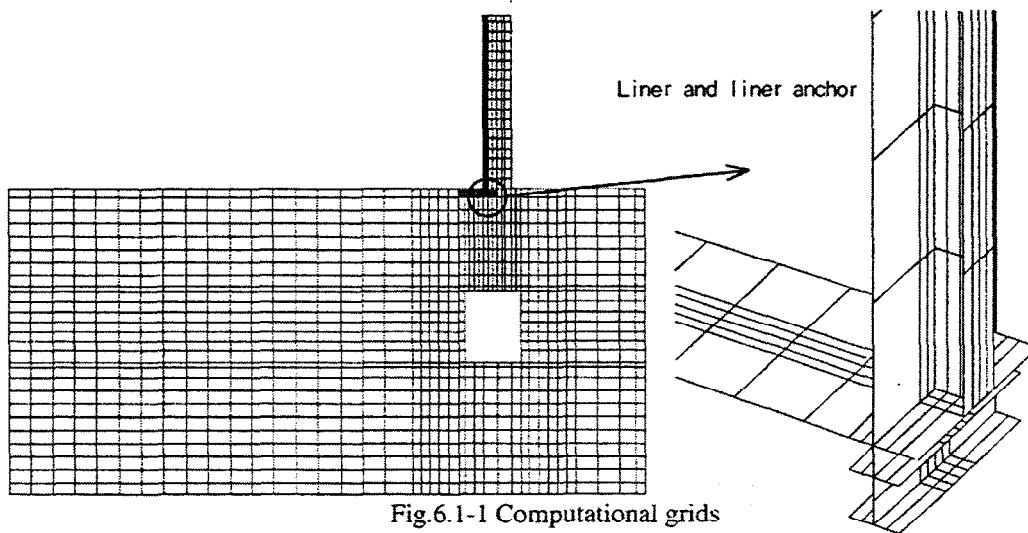
The maximum liner strain occurs at the wall – base juncture. The evaluation of the liner strain in which CASE2 assumed no bonding for the bond characteristic between the concrete and the liner was fairly small in comparison with that in CASE1.

The locations and amounts of maximum strain in the materials obtained from CASE1 are summarized corresponding to pressure levels in Table.6.1-1. The maximum strain is found at the connection of the liner anchor (Point 1), reaching 2.73% at 1.6MPa. There is a margin of safety in the liner for its critical strain.

### 6.1.3 SUMMARY

The maximum liner and rebar strains at the wall – base juncture are fairly small compared to those at mid-height of the cylinder based on global analyses.

Therefore, it is concluded from this study that tendon and rebar ruptures and liner tearing at mid-height of the cylinder wall may still precede structural failure and liner tearing at the wall-base.



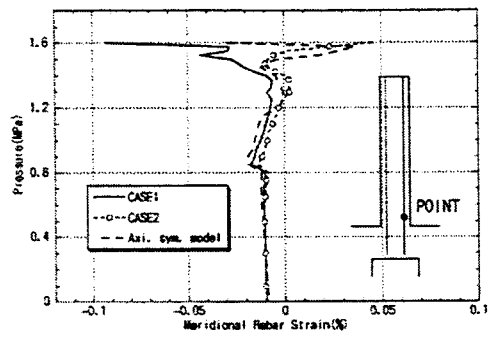
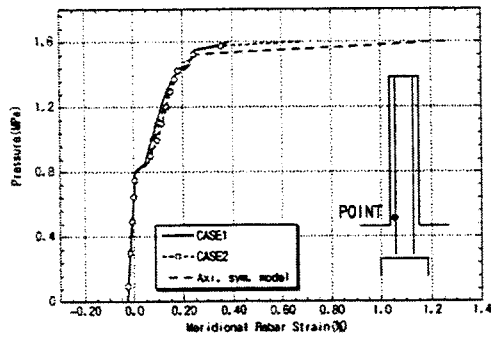


Fig.6.1-2 Pressure - meridional rebar strain relationships

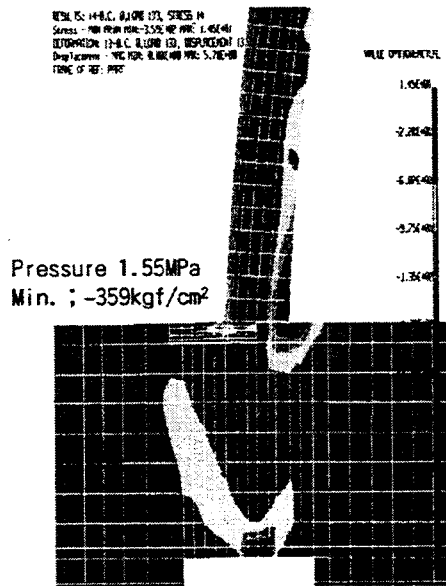


Fig 6.1-3 Min. principal stress contour of concrete

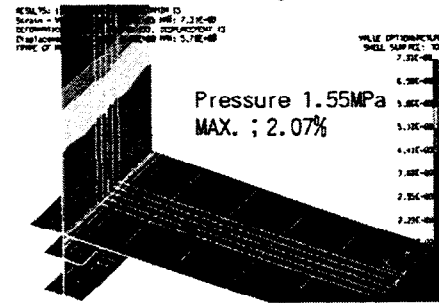
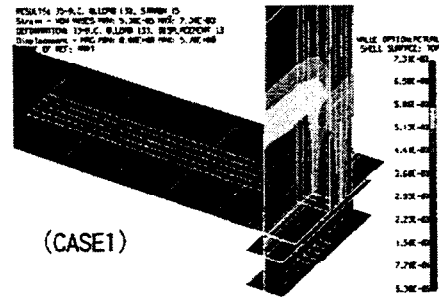


Fig 6.1-4 Max. principal strain contour of liner

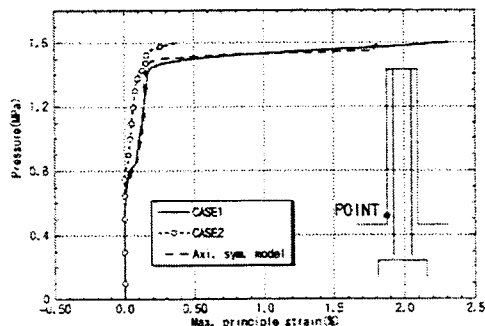
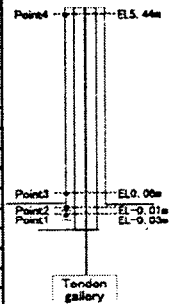


Fig.6.1-5 Pressure - liner max. principal strain relationships

Table 6.1-1 Max. strains versus pressure(%)

		Point1	Point2	Point3	Point4
Liner	1.45MPa	0.97	0.20	0.16	0.23
	1.50MPa	1.43	0.45	0.26	0.35
	1.55MPa	2.07	1.30	0.39	0.47
	1.60MPa	2.73	2.31	0.57	0.59
Inner rebar	1.45MPa	0.25	0.23	0.13	0.12
	1.50MPa	0.36	0.32	0.19	0.17
	1.55MPa	1.62	0.89	0.24	0.20
	1.60MPa	2.03	1.72	0.37	0.23
Outer rebar	1.45MPa	0.04	0.00	-0.03	-0.01
	1.50MPa	0.08	0.01	-0.06	-0.01
	1.55MPa	0.09	0.02	-0.06	-0.01
	1.60MPa	-0.11	-0.15	-0.05	-0.01
Tendon	1.45MPa	0.81	0.81	0.81	0.81
	1.50MPa	0.85	0.85	0.85	0.85
	1.55MPa	0.89	0.89	0.89	0.89
	1.60MPa	0.94	0.94	0.94	0.94



## 6.2 LOCAL ANALYSIS BY 3D SOLID MODEL NEAR BUTTRESS

### 6.2.1 OBJECTIVES

The purpose of this analysis is to investigate the deformation and the strain of cylinder wall near the buttress in detail by a fine meshed model of the buttress part.

The analytical model is a three-dimensional model in which three-dimensional constraint and the normal stress in vertical direction can be taken into accounts. Solid elements, which can express stress concentration, are used for the buttress and its vicinity, and shell elements are used for the rest of the cylindrical wall.

### 6.2.2 OUTLINE OF THE ANALYSIS

#### (1) Analytical method

The model mesh in X-Y-Z coordinates is shown in Fig.6.2-1. The mesh of cylinder part in X-Y coordinates is shown in Fig.6.2-2.

The concrete in the buttress and the vicinity in which the anchored tendons are laid out straight is modeled by eight-node solid elements. The concrete in the rest of the cylinder part is modeled by eight-node curved shell elements. The liner is modeled by eight-node curved shell elements, and the shell elements and solid elements are connected by rigid beams. The hoop tendons and vertical tendons in cylinder part are modeled by truss elements, and the dome tendons and the rebars are modeled by embedded reinforcement elements.

The boundary conditions of lower end of this model is fixed, and side edge of this model are free in radial direction and fixed in hoop direction.

The inner pressure was applied gradually after applying design prestress force to each tendon.

#### (2) Prestress force distribution at initial condition

The prestress force distribution of the hoop tendons in cylinder part was calculated using the friction coefficient ( $\mu = 0.21$  1/rad,  $\lambda = 0.001$  1/m) and set value ( $\Delta L = 0.47$  mm) that were shown in the design package.

The prestress force of hoop tendons in the dome part and vertical tendons are assumed to be constant.

#### (3) Interface elements

The hoop tendon elements and concrete elements are connected by interface elements to represent the friction effect. The interface elements are consist of sliding and vertical direction springs. Coulomb friction model is used for the sliding springs, and the friction coefficient ( $\mu$ ) is assumed to be 0.21. The passing tendons and anchored tendons are modeled separately.

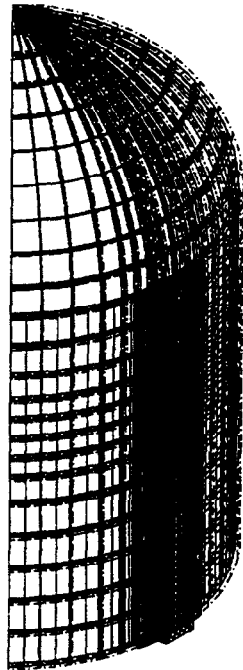


Fig.6.2-1 The model mesh in X-Y-Z coordinates

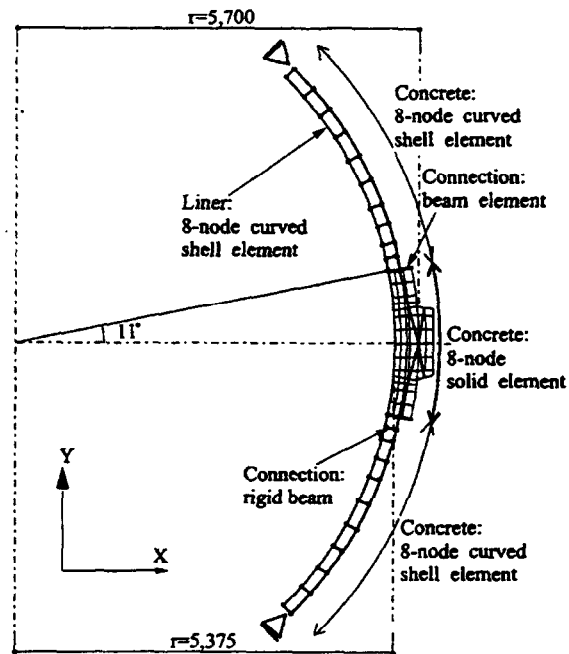


Fig.6.2-2 The model mesh of cylinder part in X-Y coordinates

### 6.2.3 ANALYTICAL RESULTS

#### (1) Deformation

The deformation mode in horizontal section at EL.7600 and the deformation mode in vertical direction at 45 deg. position are shown in Fig.6.2-3(a) and (b).

Fig. 6.2-3(a) shows that the displacement in radial direction at the buttress part is smaller than that of the rest of the cylinder parts, therefore deflection angle become larger at the vicinity of the buttress.

Fig. 6.2-3(b) shows the displacement in radial direction is the largest at EL.7500 to 8000 level in vertical direction.

#### (2) Tendon strain distribution

Fig.6.2-4 shows the strain distribution of the anchored tendon at EL.7600. The strain of the straight part of the anchored tendon is lower than the elongation at rupture strength by the system tensile test (3.7%), and the strain of the curved tendon is lower than the elongation by the strand static tensile test (8.0%).

(3) Liner strain distribution

Fig.6.2-5 shows the liner strain distribution at EL.7600 level. Though the liner strain concentrates at the vicinity of the buttress, the strain level is below critical strain level (33%) at a pressure of 1.55 MPa.

(4) Rebar strain distribution

Fig.6.2-6 shows the strain distribution of inner and outer hoop rebars at EL.7600 level. The inner rebar strains concentrate at the vicinity of the buttress, and reaches the rupture strain level (21.3%) at a pressure of 1.55 MPa.

The outer rebar strains at  $X=2000\text{mm}$  ( $X$ :distance from 0 dig.) where reinforcing ratio changes are larger than the strain in the rest of part, but lower than the critical strain.

The maximum strain of the steel materials are summarized in Table 6.2-1.

6.2.4 THE CRITICAL STRAINS OF THE REBARS EMBEDDED IN CONCRETE

The critical strain of the rebars embedded in concrete is supposed to be smaller than that of bare bars. To investigate the influence of this behavior on the limit pressure, the critical strains of mid height level reinforcement was calculated.

The critical strains depends on crack spacing of reinforced concrete members. The calculated critical strain is 6% to 14.5% for this model condition.

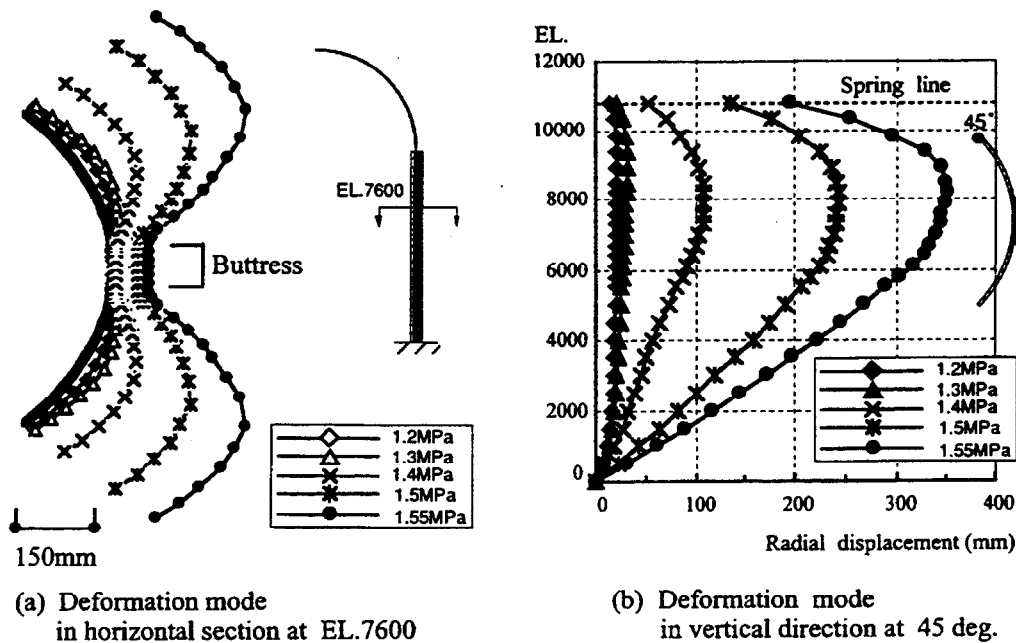


Fig.6.2-3 Deformation mode

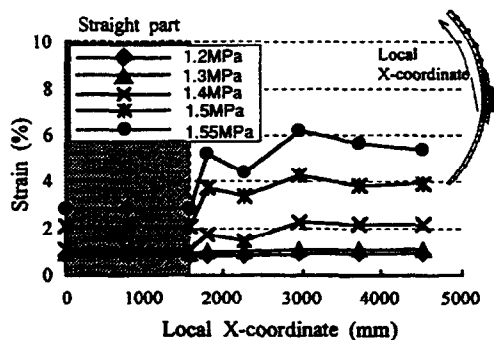


Fig.6.2-4 Strain distribution of anchored tendon at EL.7600

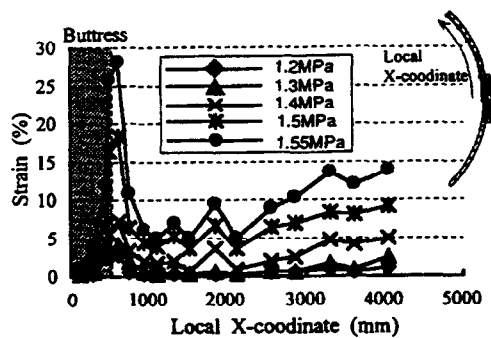
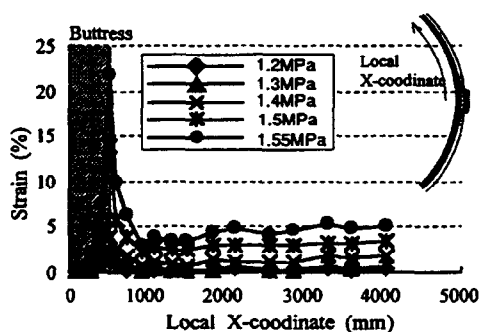
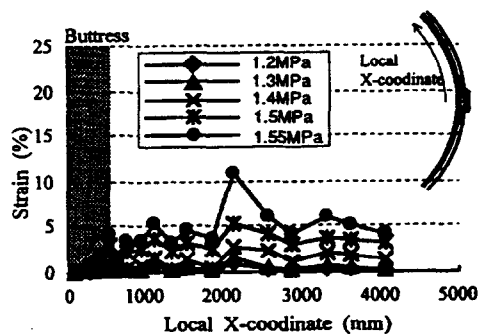


Fig.6.2-5 Strain distribution of liner at EL.7600



(a) Inner hoop rebar



(b) Outer hoop rebar

Fig.6.2-6 Strain distribution of hoop rebar at EL.7600

Table 6.2-1 Maximum strains

	Tendon	Liner	Inner hoop rebar	Outer hoop rebar
1.4 MPa	2.36 % (EL.7300)	7.27 % (EL.8200)	4.05 % (EL.7300)	2.71 % (EL.7000)
1.45 MPa	3.22 % (EL.7000)	11.76 % (EL.8200)	6.86 % (EL.7300)	3.84 % (EL.8200)
1.5 MPa	4.43 % (EL.8200)	19.17 % (EL.7600)	13.93 % (EL.7600)	5.74 % (EL.8200)
1.55 MPa	6.20 % (EL.7600)	30.05 % (EL.8200)	21.72 % (EL.7600)	10.85 % (EL.7600)

### 6.3 LOCAL ANALYSIS BY 3D-SOLID MODEL NEAR E/H, A/L OPENINGS

This section describes local analyses for the areas near E/H and A/L with the fine mesh models performed to obtain the nonlinear behaviors and to evaluate material strain concentrations.

#### 6.3.1 ANALYTICAL MODELS

The two analytical models used here are described as follows :

- 1) EH-AL model : The region between the  $62^\circ$  azimuth and the  $324^\circ$  azimuth, from EL4.675m, to EL6.675m with one quarter of the E/H and the A/L openings is idealized.
- 2) AL model : The region surrounding the A/L with the entire A/L opening is idealized.

These analytical models are shown in Fig.6.3-1 and Fig.6.3-2, respectively.

In the EH-AL model, the A/L center line elevation changed from EL4.52m up to the E/H centerline elevation (EL4.67m) due to simplification of the analytical model.

Concrete is idealized as the 8-node solid elements. Elemental meshing of these models is based on the locations of the liner anchors, and it is divided into six parts in the direction of the wall thickness.

The tendons are represented through truss elements, and attached to the concrete by sliding elements taking into account friction effects. Reinforcement bars are represented by shell layers, which are given an area equivalent to the rebar area, and a Poisson's ratio of zero to avoid any in-plane/out of plane stress - strain interactions. The liner is constructed of quadratic shell elements.

For the boundary condition, internal pressure is applied on the interior surfaces, and displacements from the global analysis with the 3D- $180^\circ$  model are applied on the top, bottom, and both side surfaces. Rigid beams are used on the boundary surfaces for transmitting rotation components, as shown in Fig.6.3-1.

#### 6.3.2 ANALYTICAL RESULTS

For both models, the contours of deformation mode, the von Mises liner strain, and inner and outer rebar hoop strains at 1.55MPa are shown in Fig.6.3-3 and Fig.6.3-4, respectively. Liner and inner rebar strain concentrations occur at the rebar cut-off sections around the E/H and the A/L. In the outer rebar, strain concentration is found at the general portion in addition to the rebar cut-off sections.

Vertical tendon and meridional rebar strains are fairly small in comparison to hoop strain in both analyses.

The strain concentration locations, and the maximum strain of materials at 1.45MPa and 1.55MPa, are shown in Fig.6.3-5, 6.

In Fig.6.3-5, 6, the thick lines indicate the boundary lines of the rebar cut-off sections where hoop rebar ratios change. The shaded areas indicate portions of strain concentration.

It is seen in Fig.6.3-5, 6 that the strain concentration of the materials appears in sections where

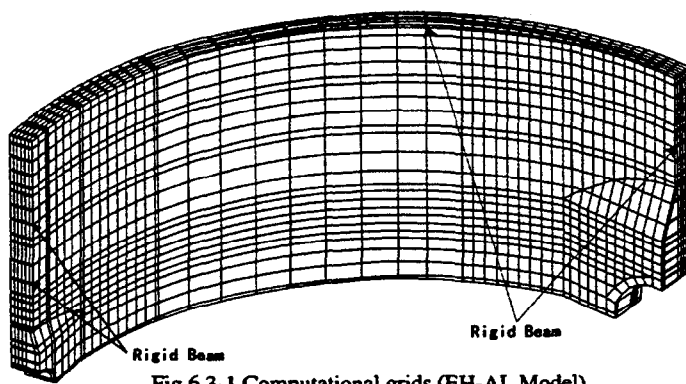


Fig.6.3-1 Computational grids (EH-AL Model)

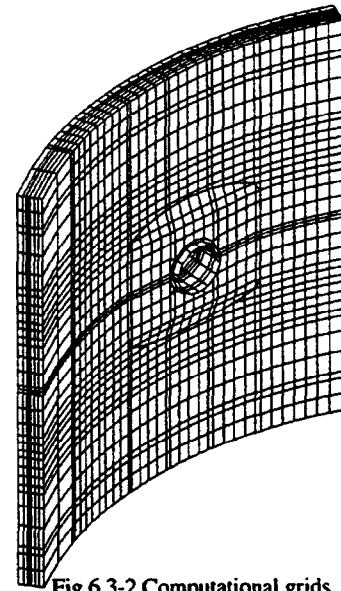


Fig.6.3-2 Computational grids (AL Model)

stiffness changes, such as in the rebar cut-off section. The maximum liner strain is found at the rebar cut-off section around the A/L. The maximum strains of the materials are shown in Table.6.3-1. Maximum strains of the AL model are bigger than those of the EH-AL model, because the boundary displacements are applied where strain concentration occurs.

The hoop tendon strain distributions at each elevation level (refer to Fig.6.3-7) are shown in Fig.6.3-8. The curved hoop tendon strains around the openings are fairly small in comparison to those of other areas. The maximum hoop tendon strain is found in the general portion.

The hoop tendon strain exceeded its critical strain at 1.55MPa according to global analyses. In these local analyses, the maximum liner and rebar strains at 1.55MPa reach 9.68% and 10.1%, respectively. Therefore there is still a margin of safety in the liner and rebar strain in comparison with the critical strains of each material.

### 6.3.3 SUMMARY

The liner and hoop rebar strain concentrations occur at the rebar cut-off sections around E/H and A/L. The maximum tendon strain is found in the hoop tendon between EL7.0m and EL.8.0m.

It should be noted from these analyses that the tendon strains exceed the critical strain at 1.55MPa, before the liner and the rebar strains reach their critical strains. Therefore, liner tearing and rebar ruptures may not occur up to a pressure of 1.55MPa. It is also found that shear failure around E/H and A/L may not occur up to the pressure of 1.55MPa.

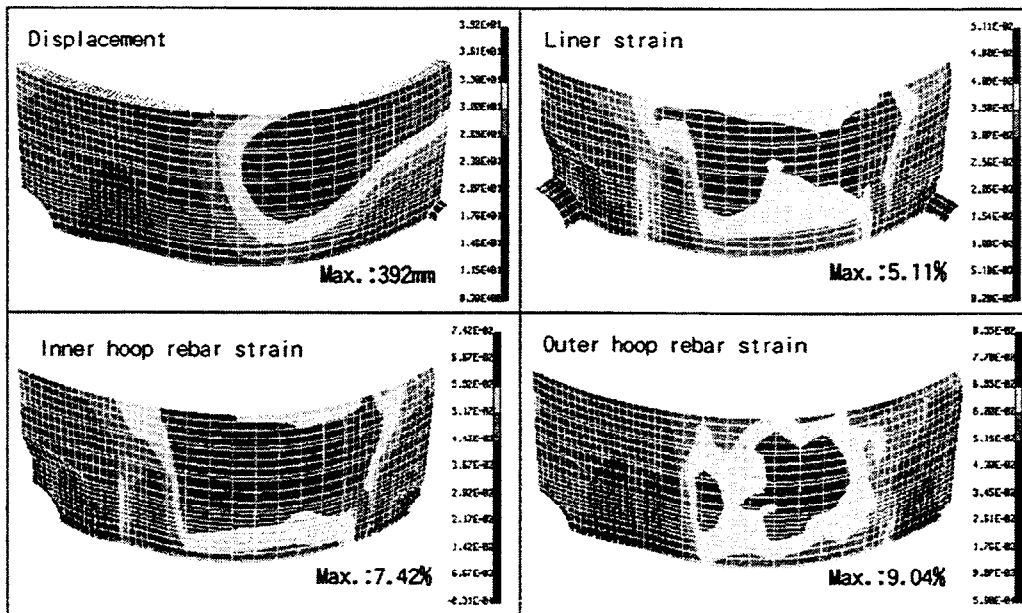


Fig.6.3-3 Displacement and strain contour at 1.55MPa (EH-AL Model )

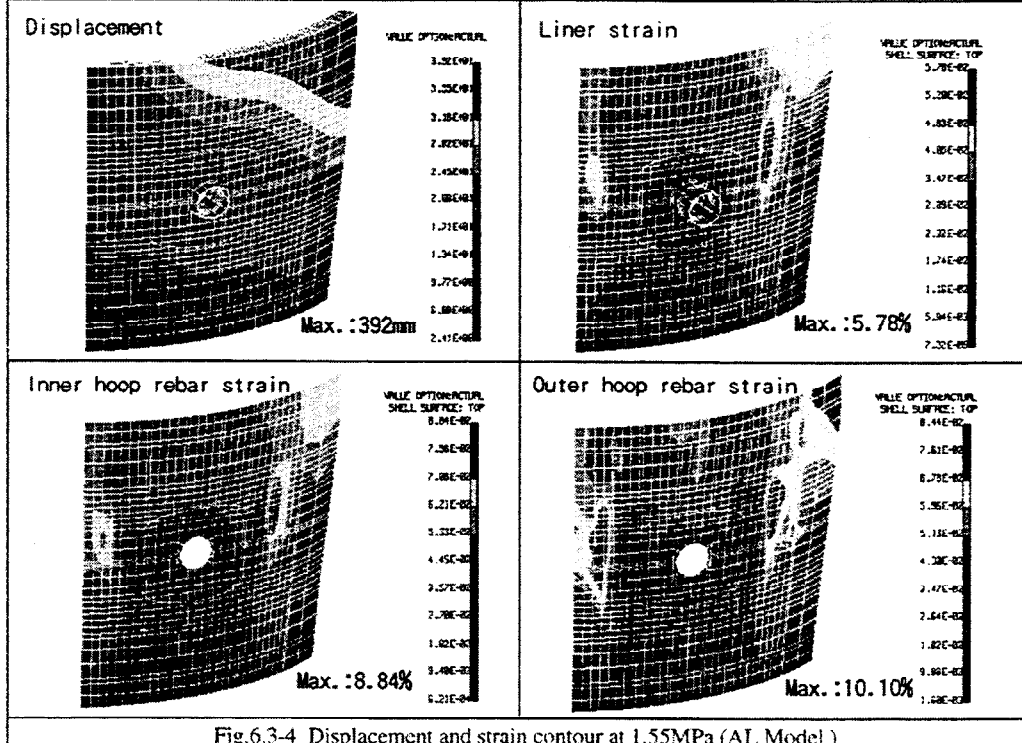


Fig.6.3-4 Displacement and strain contour at 1.55MPa (AL Model )

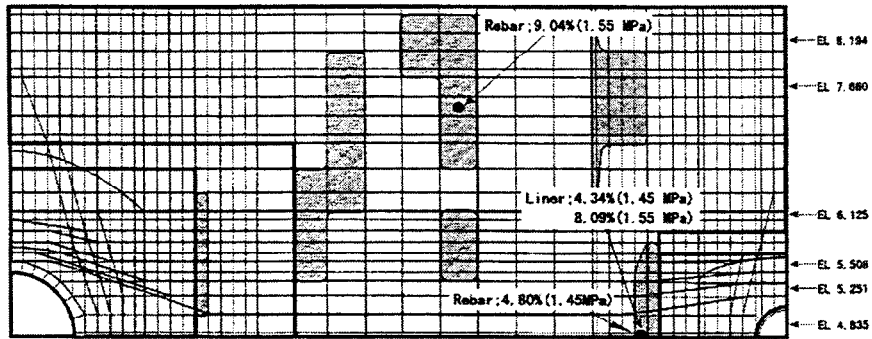


Fig. 6.3-5 Strain concentration of materials at 1.45 and 1.55 MPa (EH-AL Model)

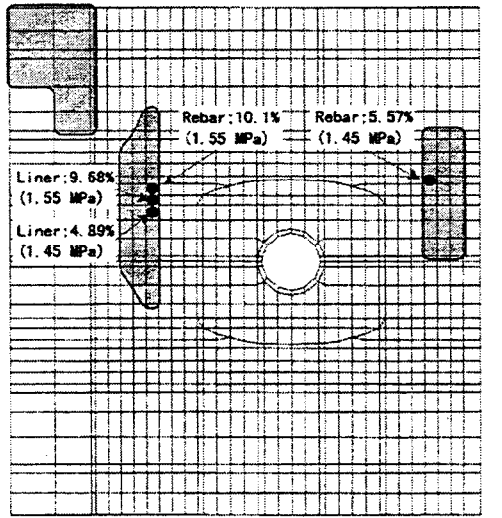


Fig. 6.3-6 Strain concentration of materials at 1.45 and 1.55 MPa (AL Model)

Table 6.3-1 Maximum strains versus pressure

	EH-AL Model		
	Liner	Rebar	Tendon
1.45MPa	4.34%	4.80%	3.66% EL8.19m
1.55MPa	8.09	9.04	7.69 EL8.19m
	AL Model		
	Liner	Rebar	Tendon
1.45MPa	4.89%	5.57%	3.67% EL7.37m
1.55MPa	9.68%	10.10%	7.17% EL6.53m

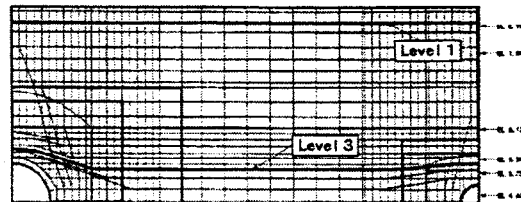


Fig. 6.3-7 Location of tendons in Fig. 6.3-8

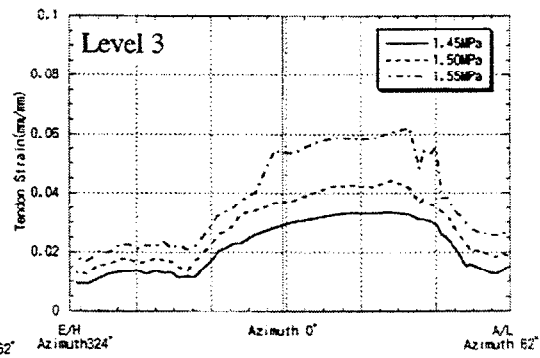
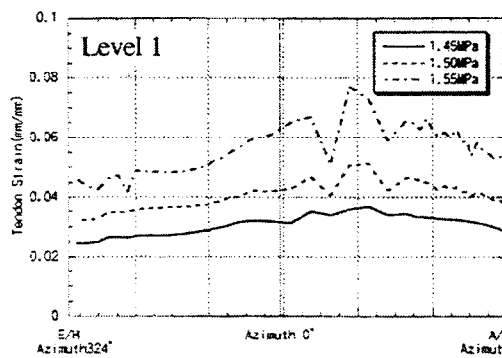


Fig. 6.3-8 Tendon strain distributions

## 6.4 LOCAL ANALYSIS BY 3D SHELL MODEL NEAR M/S PENETRATIONS

This section describes a detailed analysis focusing on the region near M/S penetrations using the boundary conditions obtained from the global analysis by the 3D90° shell model described in section 5.2.

### 6.4.1 PURPOSE OF THIS ANALYSIS

From the 3D90° shell model analysis, it was found that the location of a strain concentration is the rebar cut-off areas near the M/S. The purpose of this analysis is to quantitatively evaluate the boundary behavior of this region using an analytical model which is even more detailed than the 3D90° shell model.

### 6.4.2 ANALYTICAL CONDITIONS

#### (1) ANALYTICAL MODEL

Figure 6.4-1 shows the region for analysis. Circumferentially, this region is between azimuths 180° and 225° and includes the M/S penetrations. Vertically, the upper boundary is the lowest level at which the hoop tendon arrangement becomes the same as in the general region. The lower boundary lies midway between the M/S and F/W, but excludes the latter. This is because it was found from the 3D90° shell model analysis that the maximum strain at the ultimate pressure of the materials near F/W was smaller than that of the materials near the M/S.

Figures 6.4-2 (a)-(d) show the finite element meshes used in this analysis. The model is based on the tendon arrangement and modeled to be a faithful reproduction of the structural members. The reinforced concrete and liner are modeled as a multi-layered shell element and the tendons as truss elements. The rebar stiffness is incorporated as the reinforced concrete's multi-layered shell element. In addition, an interface element between the liner and the reinforced concrete is used to transmit the inner pressure load. The liner anchor is also modeled as an interface element to incorporate its effects.

The friction characteristics between the reinforced concrete and the tendon are used as parameters and presented here are the results for cases where friction is considered.

#### (2) LOAD CONDITIONS

Both internal pressure on the liner and forced displacement load on the boundary are considered. The latter is obtained by interpolating the nodal displacement calculated in the 3D90° shell model, taking into account the symmetrical condition at azimuth 180°. Tendon prestressing is also considered.

### 6.4.3 ANALYTICAL RESULTS

Figures 6.4-3 and 6.4-4 show the distribution of slips between the hoop tendon and the concrete under an internal pressure of 1.55MPa and evaluation locations of the hoop tendons. At the level nearest the M/S (Level 1), the maximum slip occurs in the region where there is no curvature variation caused by by-passing of the M/S and the cut-off section of the horizontal reinforcement. This may be caused by the non-uniform stretching of the hoop tendons due to the large variations in stiffness of the rebar cut-off section between the M/S penetration reinforcement and the general region. However, the slips and their variations are smaller in the general region (Level 2) than in level 1.

Figure 6.4-5 shows a contour of an analytical result under an internal pressure of 1.55MPa. In this figure, both the displacement and the strains are evaluated at nodal points. Concrete displacement is greater the further the measurements are taken from the M/S penetration's reinforced region. This tendency is confirmed in the 3D90° shell model analysis. As in the model, the liner's von Mises strain is concentrated at the horizontal rebar cut-off section near the M/S, but it can be seen that this is approximately half due to the effect of the penetration reinforcement. The strain contours of the inner and outer horizontal rebars show that the strain is concentrated at approximately the same locations as in the liner.

### 6.4.4 MAXIMUM STRAIN IN EACH MATERIAL

Figure 6.4-6 and Table 6.4-7 show the maximum strain in each of the materials, which is evaluated at integration points of finite elements, and their locations under an internal pressure of 1.55MPa. The table primarily indicates material strains in the hoop direction, but we have examined the strains in the vertical direction and confirmed that these are smaller than that in the hoop direction.

Using 6.4-7, we were able to ascertain that the maximum strain in each material under the ultimate internal pressure was smaller than its critical strain.

### 6.4.5 SUMMARY

- 1) We have ascertained that the maximum strains in the various sections under the ultimate internal pressure of 1.55MPa were smaller than their critical strains due to the effect of the penetration reinforcement near the M/S, and therefore, that the region near the M/S will not fracture.
- 2) It has been found that the strain in the liner and the horizontal rebars concentrates near the rebar cut-off sections.

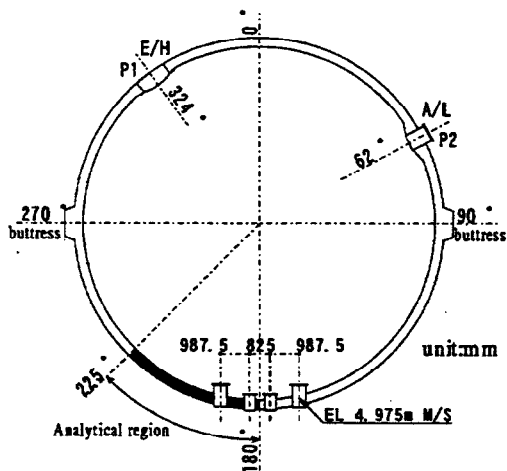
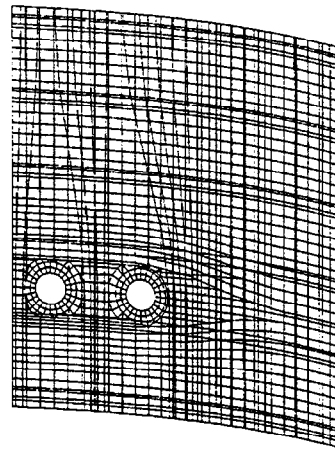
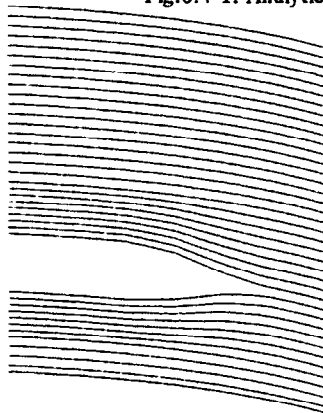


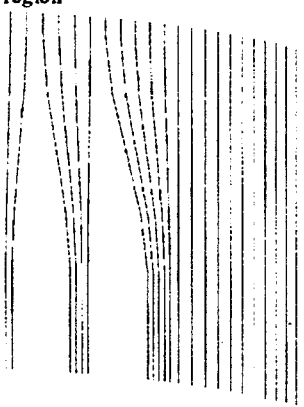
Fig.6.4-1. Analytical region



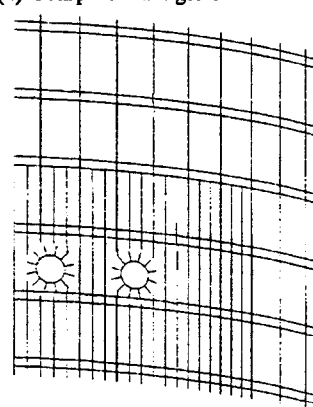
(a) Computational grids



(b) Hoop tendon



(c) Meridional tendon



(d) Liner anchor

Fig.6.4-2. Finite element mesh of analytical model

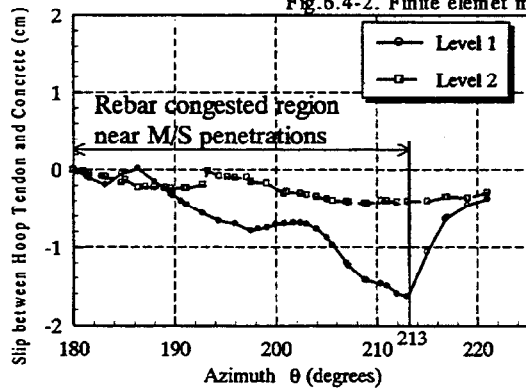


Fig.6.4-3. Distribution of slip between hoop tendon and concrete at 1.55MPa

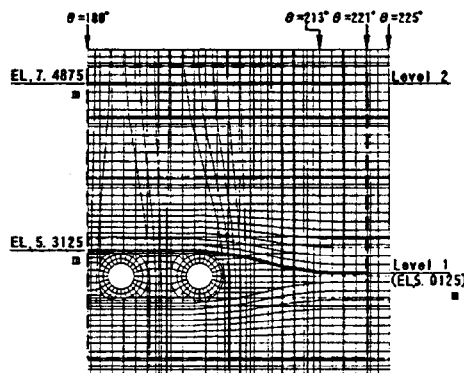


Fig.6.4-4. Locations of tendons referred in Fig.6.4-3

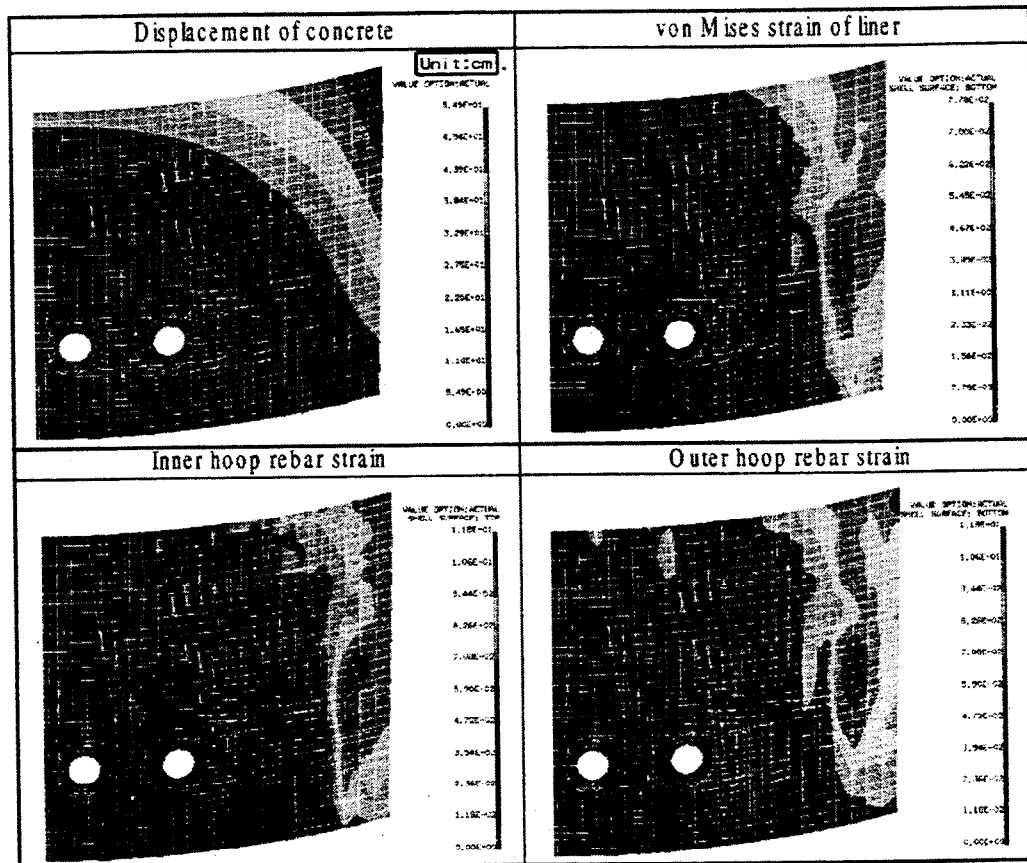


Fig.6.4-5. Displacement and strain contour at 1.55MPa

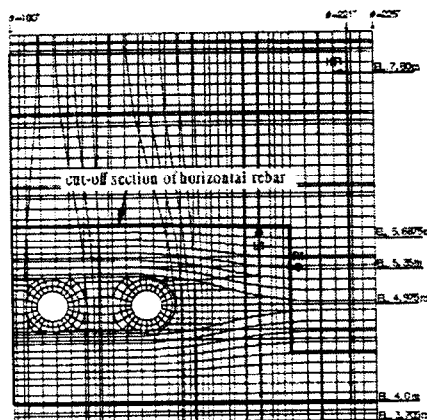


Fig.6.4-6. Locations of the maximum strains of materials

Table 6.4-7. Maximum strains versus pressure

	Internal pressure (MPa)
	1.55
Maximum strain of hoop tendons	7.12 %
Location and its level	(HT1, EL. 7.60m)
Maximum strain of liner	9.40 %
Location and its level	(L1, EL. 5.6875m)
Maximum strain of rebars	8.53 %
Location and its level	(R1, Inner, EL. 5.35m)

## Chapter 7. LOCAL LINER ANALYSIS BY SHELL MODEL NEAR M/S PENETRATIONS

### 7.1 THE STUDY ON MODELING OF THE LINER ANALYSIS

Since the linear analysis with three-dimensional shell elements may underestimate the strain values, the increasing effect, at where the thickness is changed, is evaluated employing the solid elements. Figure 7.1-1 shows the outline of the analytical model and Figure 7.1-2 indicates the strain increasing effects that should be considered in the analysis with shell elements.

### 7.2 ANALYTICAL RESULTS

In this section, the results of the liner analysis near M/S penetrations are presented. The analysis was carried out based on the results of local analysis by 3D shell model.

#### 7.2.1 ANALYTICAL MODEL

The three-dimensional shell elements are employed for the liner plates. (Refer to Fig. 7.2-1 for analytical model) The spring elements are used to represent the stiffness of the liner anchors and the surrounding concrete. The spring stiffness is defined at the anchor location as follows. The rocking springs are not considered because the study, which is mentioned above, demonstrated that the effects of the rocking are very small.

- Stiffness in the axial direction (N) of T-anchor :  $K_N = 0$
- Stiffness in the vertical direction (V) of liner :  $K_V = \infty$
- Equivalent shear stiffness transverse to the T-anchor(S) :  $K_S = 883 \text{ MPa}$

#### 7.2.2 LOAD CONDITION (BOUNDARY CONDITION)

The stiffness of liner anchor is represented by the spring element. The displacements, computed by the "Local Analysis by 3D Shell Model Near M/S Penetrations" described in Section 6.4, are imposed on the fix-end nodes of the spring elements. The displacements of anchor points, which are not presented in Section 6.4, are computed by the linear compensation using the displacements of the surrounding anchor points. The displacements obtained from the local analysis by 3D shell model are imposed on the exterior circumferential of the analytical model. Internal pressure up to 1.7 MPa is applied.

#### 7.2.3 MATERIAL PROPERTIES AND YIELD CONDITION

Constitutive laws of the liner materials are mentioned below.

- Stress-strain relationship formula : Refer to the section 2.4
- Yield condition : Von Mises
- Flow rule : Prandtl – Reuss

#### 7.2.4 ANALYTICAL METHOD

The MARC, general-purpose FEM code, is used for the analysis. The elasto-plastic deformation analysis is carried out. The forced displacements, imposed on the locations of the anchorage, are

increased gradually

### 7.2.5 ANALYTICAL RESULTS

Figure 7.2-2 shows the displacement pattern of the liner plate. It demonstrates that the displacements are small at the reinforced portion for the M/S penetrations and the displacement are large at the rebar cut-off portion. Figure 7.2-3 shows the distribution of the equivalent plastic strain on the surface of the liner. The maximum strain is observed in the direction of  $221^\circ$  at EL7.75m. The maximum equivalent plastic strain is 12.1% when the internal pressure is 1.7Mpa at the final step of the analysis. Near M/S penetration, there exist large strains caused by the difference of the liner plates' stiffness. Although the maximum equivalent plastic strain is 11.1% when the internal pressure is 1.7Mpa, it needs adjustments as described in Section 7.1. Figure 7.1-2 shows the equivalent plastic strain after the adjustment and it demonstrates that the maximum strain is 29.6% when the internal pressure is 1.7Mpa. It is less than the critical strain of 33% of liners. Figure 7.2-4 shows the analysis results at typical calculation steps.

### 7.2.6 SUMMARY

The analysis reveals that the maximum strain is 29.6% near M/S penetrations when the internal pressure is 1.7MPa. It is less than the critical strain of 33% of liners.

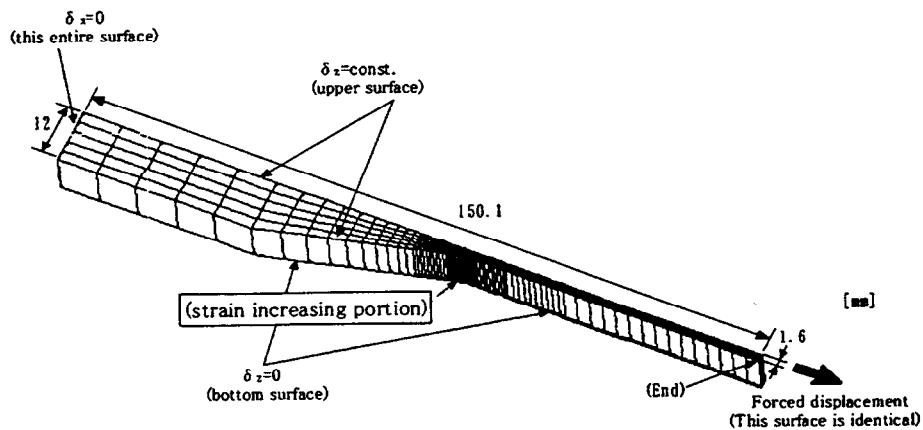


Fig. 7.1-1 : Analytical model of 3D solid

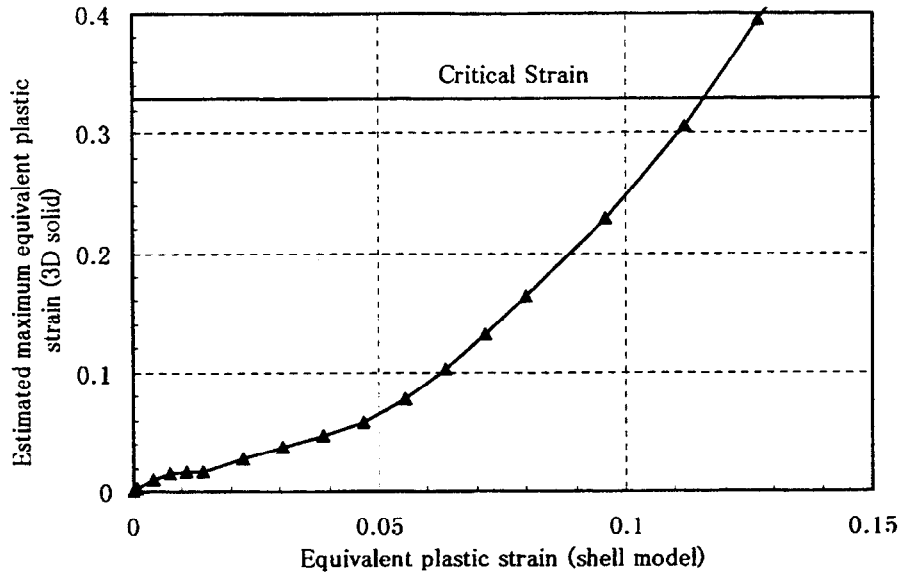


Fig. 7.1-2 : Strain increasing effect to be considered for shell model analysis

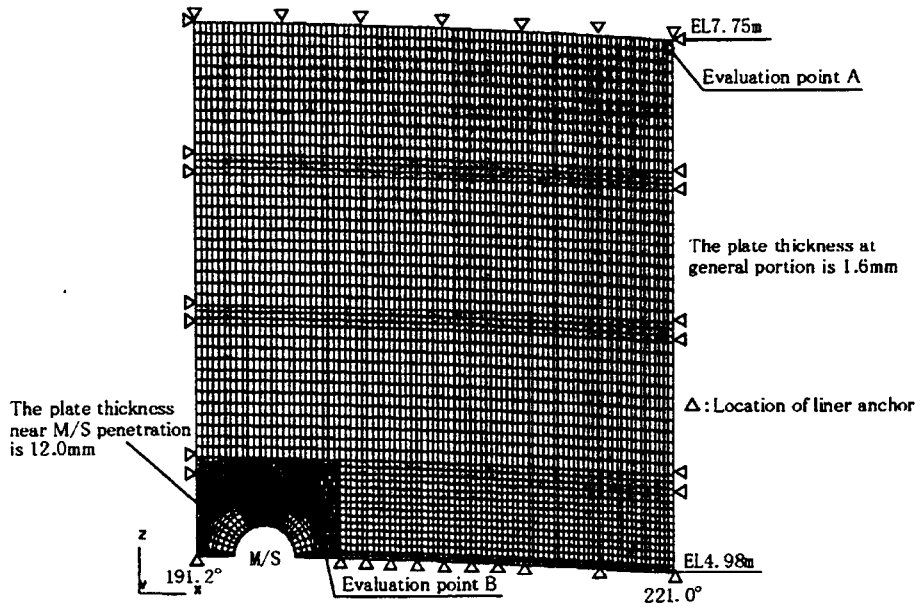


Fig. 7.2-1 : Liner analysis model (shell model)

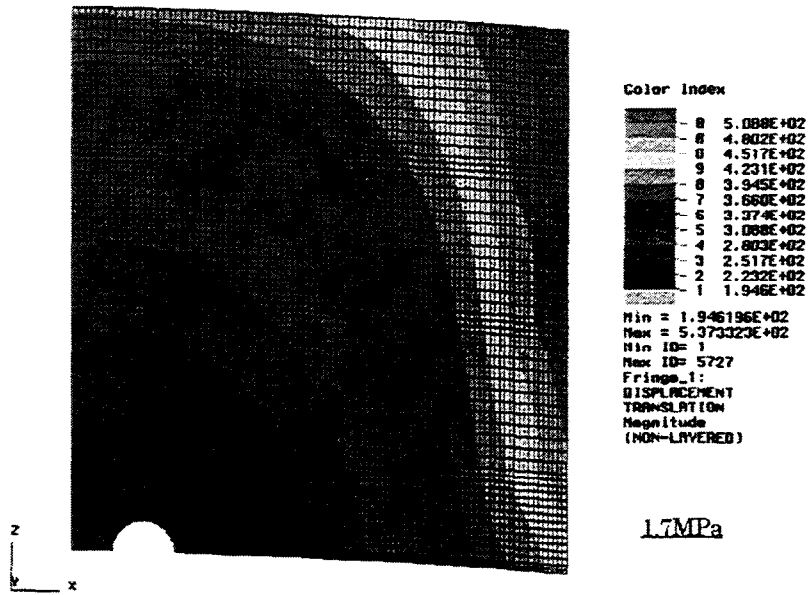


Fig. 7.2-2 : Displacement distribution

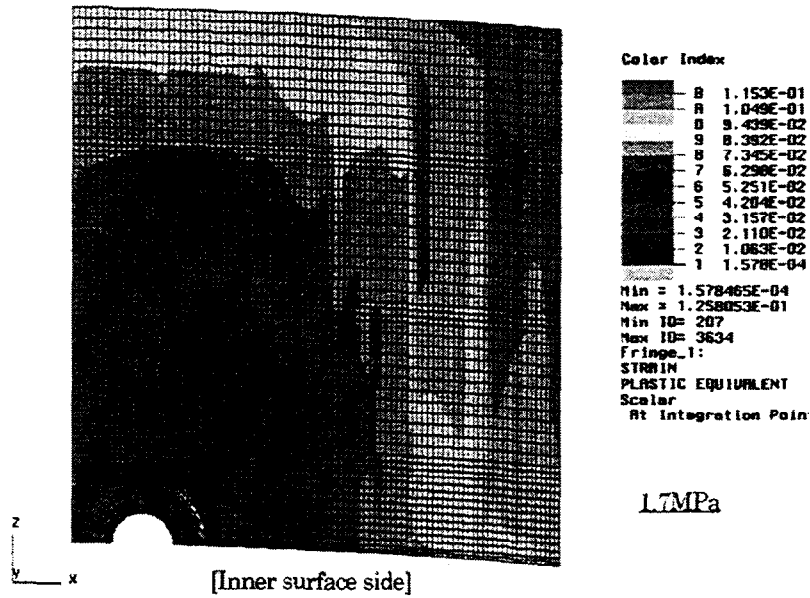


Fig. 7.2-3 : Equivalent plastic strain distribution

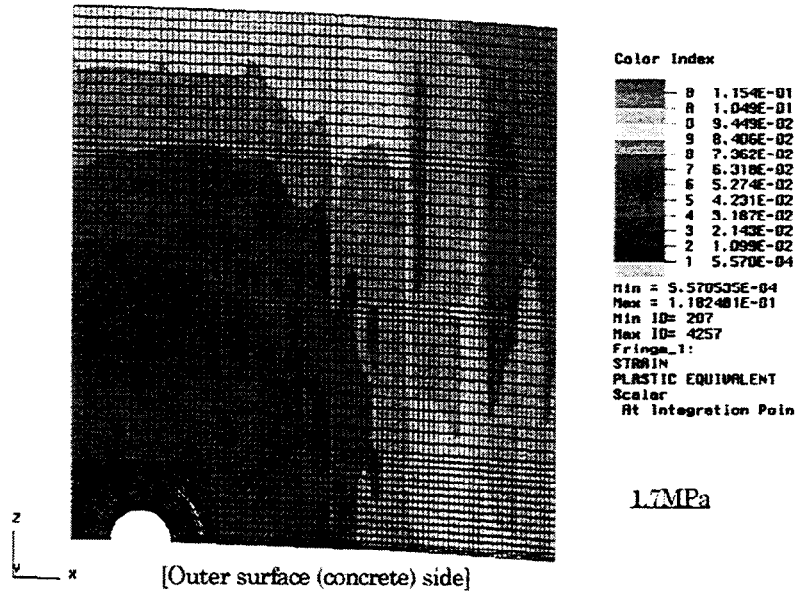


Fig. 7.2-3 : Equivalent plastic strain distribution

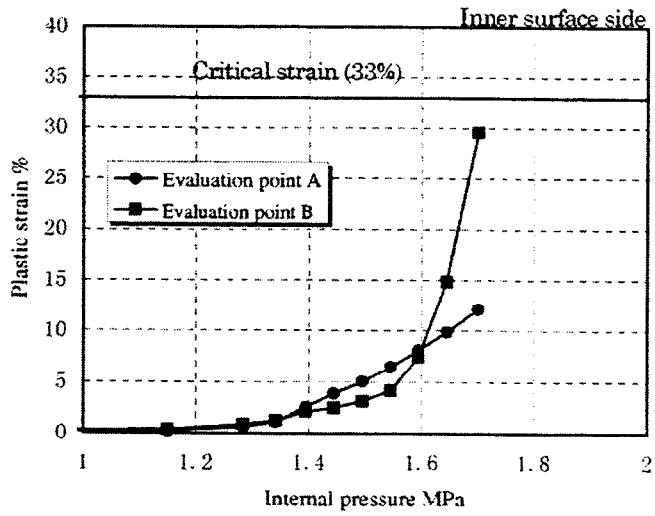


Fig. 7.2-4 Analytical result of the liner near M/S penetration

## Chapter 8. INFERENCE OF POSSIBLE FAILURE MODES AND ASSOCIATED PRESSURES IN 1/4 PCCV

This chapter discusses when, where and what kinds of structural materials of the 1/4 PCCV may cause ruptures, through careful consideration of the global and local analysis results.

The strain contours of the hoop tendons obtained from global analyses of the 3D90° and the 3D180° shell models at a pressure of  $P=1.575\text{MPa}$  are shown in Fig.8-1. Areas of strain concentration in the hoop rebars and the liner obtained by global and local analyses, are shown in Figs. 8-2 and 3, respectively. In these figures, the maximum strains in each areas at pressures of 1.45 and 1.55MPa are also indicated.

Estimation of failure modes of the 1/4 PCCV model can be summarized as follows ;

### (1) Global Deformation Mode

Fig.8-4 compares the deformation modes of the horizontal section at the height (EL7.4m) where maximum displacement appears. Fig.8-5 compares the deformation modes of the meridional sections at the azimuth where maximum displacement appears.

As can be easily seen from this figure, most of the axisymmetric model displacement appear to be small in comparison with those of the 3D90° model and the 3D180° model. This is because all the structure non-symmetries are modeled in detail in the 3D90° and the 3D180° models, but not in the axisymmetric model. In the horizontal section, the location of the maximum displacement is found to be in a general portion around 120° or 240° azimuth between the M/S and the buttresses. Secondly, the displacement becomes large in the general portion at about 30° azimuth between E/H and A/L. In the meridional sections, the maximum displacements for all global analyses appear to occur at about EL7.0m. The vertical displacement of the dome's apex is fairly small in comparison with the radial displacement of the cylinder.

### (2) Tendon Rupture

#### ○ Free field locations

It can be seen from the strain contours of the hoop tendons in Fig. 8-1 that areas of large strain appeared at two free field locations around the midheight of EL.7.0m of the cylinder wall, and that the maximum strain reached the critical strain (8%) at  $P=1.55\text{MPa}$ .

Thus, there is the possibility of the hoop tendon rupturing first in these areas at  $P=1.55\text{MPa}$ .

#### ○ Vicinity of openings (E/H, A/L)

As can be easily seen in Fig. 8-1, there is no possibility of hoop tendon rupture in the vicinity of openings, because strains in these areas are relatively small compared with those in the free field locations.

#### ○ Crushing or concrete shear cone failure at the anchorage portions of the hoop and the vertical tendons.

There is no possibility of concrete rupture in these areas, based on the results of local analyses of the local buttress model and local wall-basemat juncture model.

### (3) Rebar Rupture

As shown in Fig. 8-2, the local rebar strain concentration can be primarily seen at the areas of the rebar cut-off sections around E/H, A/L and F/W and the buttresses, and free field areas at the midheight of the wall at about EL. 7.0m. Those strain concentrations tend to occur in the hoop direction where the stiffness is discontinuous. The maximum rebar strain reaches about 10% at a pressure of  $P=1.55\text{MPa}$ , and does not exceed the critical strain of 21%. However considering the effects of large concrete crack width and the change in bond characteristics, rebar ruptures may occur at locations of local strain concentration.

### (4) Bending/Shear Failure of Concrete

#### ○ Lower wall-basemat juncture and basemat

Crushing of cover concrete at the outer surface of the lower wall occurred in the local wall-basemat juncture analysis. However, concrete stresses in the remaining portion did not reach the compressive strength ( $450\text{kgf/cm}^2$ ) when subjected to a pressure of  $P=1.55\text{MPa}$ , and rebar stresses remained elastic. Thus, there is no possibility of bending/shear failure of the concrete at the wall-basemat juncture.

#### ○ Springline

The global analysis results indicate that hoop strains in the outer and inner rebars and the liner at the location of the springline are much smaller than those in the free field of about EL. 7.0m. Bending/shear failure will not occur at this area.

#### ○ Vicinity of openings (E/H,A/L)

According to the local analysis results for penetrations and openings, local rebar strain concentrations occurred in all the rebar cut-off sections. However the membrane strain state is predominant in these areas, because the outer and inner rebar strains were almost the same. Thus, bending/shear failure will not occur in these areas.

### (5) Liner Tearing

#### ○ Free field locations and vicinity of openings and penetrations

Liner strain concentrations occur at the areas of the rebar cut-off sections and the vicinity of the buttresses, as well as those of the rebars. In Particular, according to the local buttress analysis results, liner strain concentration due to the out-of-plane bending moment are occur in the vicinity of the buttresses. In addition, the concrete crack width, which grows extremely large due to bending, may result in liner tearing in this area. Therefore, liner tearing may occur in the vicinity of the buttresses at the midheight level between EL. 6.0m and 9.0m.

#### ○ Lower wall-basemat juncture

The local analysis results indicate that liner strains close to the H-type anchor, embedded in the concrete at the wall-base juncture, has a maximum value. However, this remains only within the strain level of 2.1%, and there is no possibility of liner tearing in this area.

### (6) Assessment of Lower and Upper Limits of Ultimate Pressure

#### ○ Minimum pressure reachable with 90% confidence level

The lower limit of the ultimate pressure is defined as the lowest of the limit pressures due to

all the failure modes investigated by the analyses. In fact, the minimum rupture strains of the structural materials can be assumed. This way, the critical tendon strain is 3.7%, as given by the system verification tests (Design Package), and that of the rebars embedded in the concrete is 6%, as discussed in the section 6.2. The maximum tendon strain is 3.65% at 1.45MPa at EL.7.0m in the 3D90° model, and 3.51% at 1.46MPa in the 3D180° model. The rebar strain first reached 6% at 1.46MPa in the buttress model. Therefore, the minimum reachable pressure may be P=1.45MPa.

○ Maximum pressure reachable with 90% confidence level

The upper limit of the ultimate pressure is defined as the pressure at which one of the structural materials first reaches its critical strain as specified in chapter 2. The tendon strains first reached 8% at 1.55MPa in the 3D90° model and the 3D180° models. Therefore, the maximum reachable pressure may be P=1.55MPa.

As a result, the prediction of event milestones required by the SNL can be summarized as shown in Table 8-1.

Table 8-1 Prediction of event milestones

Event milestones	Pressure	Location	Analytical Model
First cracking of concrete in cylinder primarily in the hoop direction *1	0.60MPa	Around E/H and A/L	3D180° Shell
First cracking of concrete in cylinder primarily in the meridional hoop direction *1	0.65MPa	Around E/H	3D180° Shell
First yielding of hoop rebar in cylinder	0.95MPa	EL 5.72m 318° azimuth	3D180° Shell
First yielding of hoop rebar in wall-basemat juncture	1.42MPa		3D90° Shell
First cracking of dome concrete above 45°dome angle *1	0.80MPa		3D180° Shell
First cracking of dome concrete below 45°dome angle *1	0.70MPa	Spring line 270° azimuth	3D180° Shell
First hoop tendon in cylinder reaching 1% strain	1.25MPa	EL.7.65m	3D90° Shell
First hoop tendon in cylinder reaching 2% strain	1.37MPa	EL.7.65m	3D90° Shell
First hoop tendon in cylinder reaching 3% strain	1.42MPa	EL.6.75m	3D90° Shell
Minimum Pressure reachable with 90% confidence level	1.45MPa		
Maximum Pressure reachable with 90% confidence level	1.55MPa		

Note \*1 : There is a great possibility of existence of initial cracking of the 1/4 PCCV test model which has experienced severe climate.

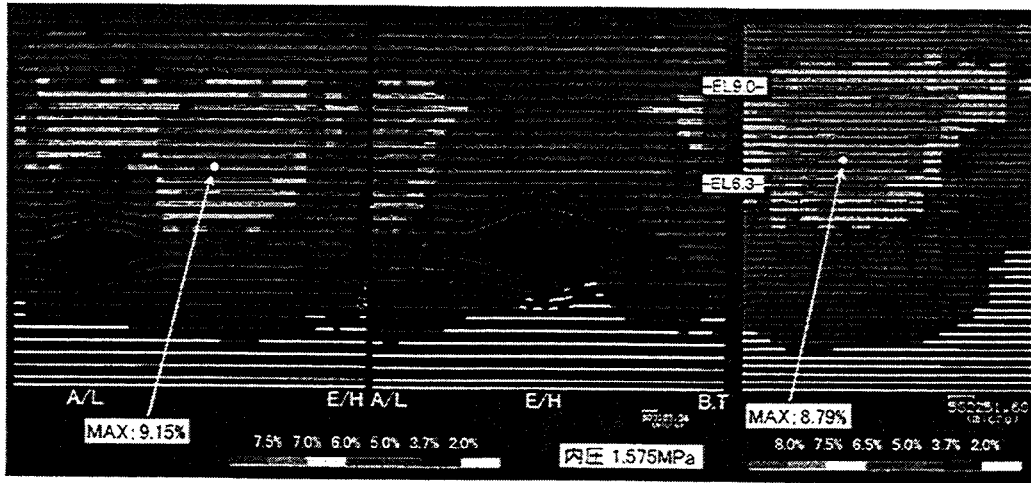


Fig.8-1 Contour of hoop tendon strains

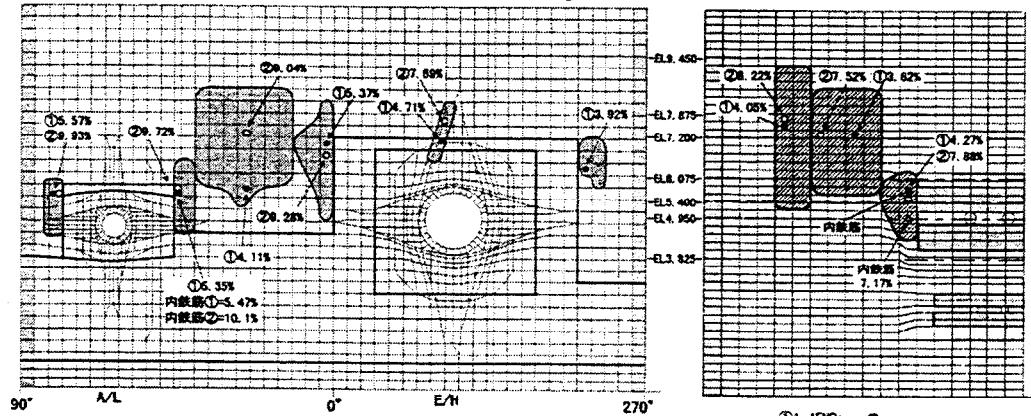


Fig.8-2 Location of strain concentration of hoop rebar

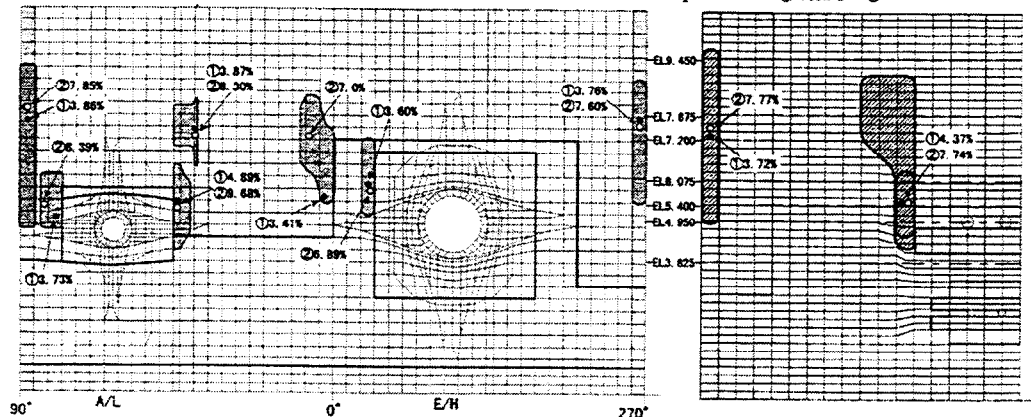


Fig.8-3 Location of strain concentration of liner

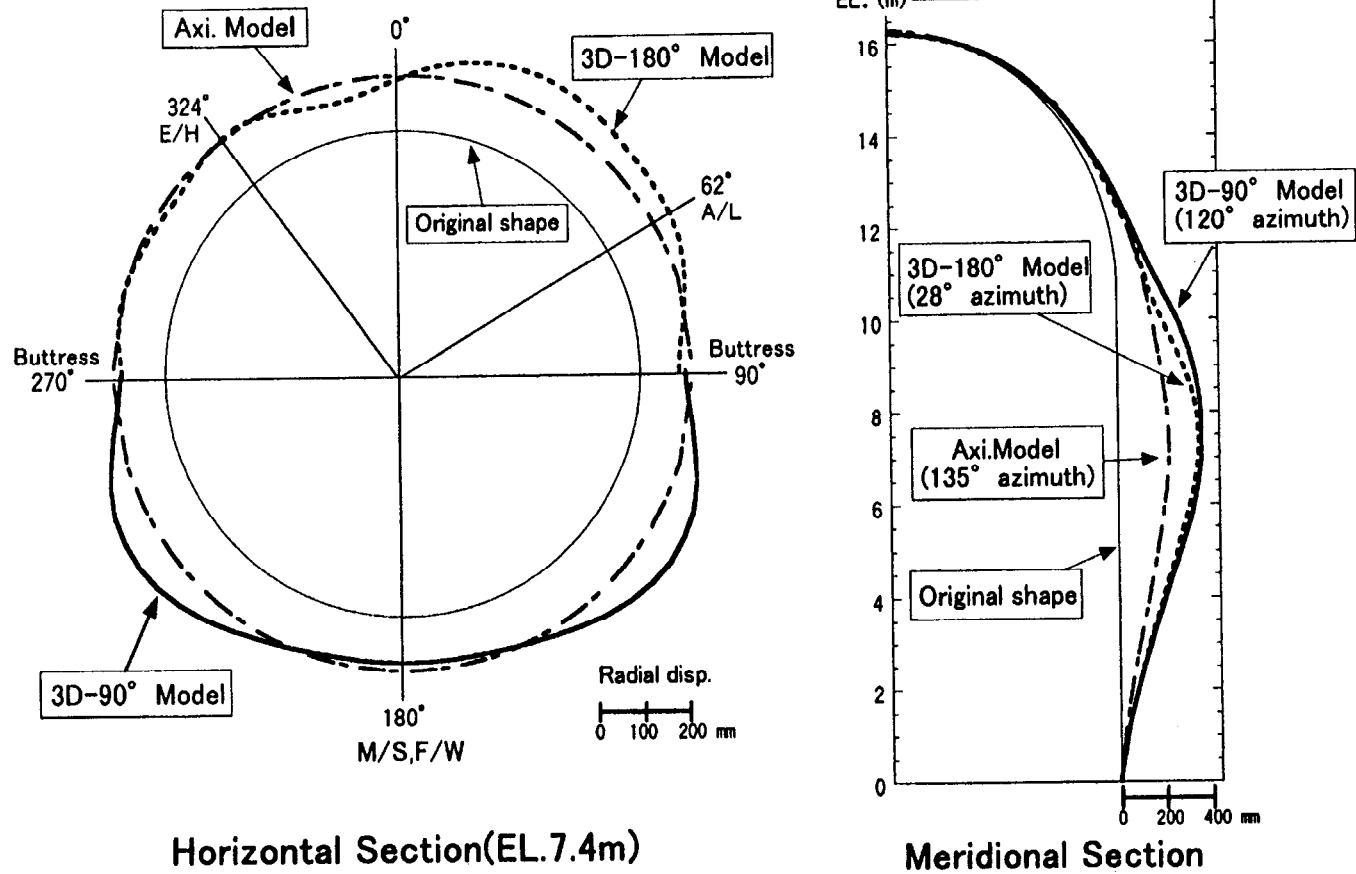


Fig. 8-4 Comparisons of the deformation modes of the results by the global analyses (Axi., 3D90° and 3D180° models) at the pressure of P=1.55MPa.

## Chapter 9. CONCLUSIONS OF PRETEST ANALYSIS PHASE

As a result of this analysis research, failure modes and their associated pressures of the 1/4 PCCV model under increasing internal pressure can be inferred as follows :

- 1) The results obtained from our pretest analyses for 1/4 PCCV are almost the same as those from the pressure tests of 1/6 RCCV (SAND89-0349). That is, the ultimate pressure was reached due to local ruptures of structural components at the midheight of the cylinder wall, where the maximum radial displacements were obtained or observed. The primary difference between 1/6 RCCV and 1/4 PCCV is their geometrical configurations. That is, most penetrations and openings of 1/6 RCCV were located around the circumference at midheight (EL.3.96m) of the cylinder wall. But, those of the 1/4 PCCV were located in lower sections. Thus, radial displacements in the vicinity of E/H, A/L, and M/S of the PCCV were determined to be relatively small compared to the maximum, resulting in no main rupture around these areas. Therefore, it can be said that the ultimate state of concrete containment structures like PCCVs and RCCVs could be induced by local ruptures of structural components due to the local strain or stress concentrations at the midheight of the cylinder wall, where the maximum radial displacements appear.
- 2) During the high pressure stage near the ultimate state, strains of the tendons and rebars which bear approximately 91% of the structural capacity are very close to their critical states. Thus, if one of them initially ruptures, catastrophic failure of the PCCV may occur and it will be very difficult to find out which one failed first. However, if liner tearing occurs first, a slow depressurization of the PCCV will occur.

If the test model was constructed accurately, and if any initial imperfections of the materials and structural components are also negligible at the time of the tests, the ultimate state of 1/4 PCCV can be estimated as follows :

Ultimate pressure : 1.5 MPa

Failure mode : Rupture of structural elements (tendon, rebar or liner) placed in the hoop direction at the cylinder wall height of about EL.7m.

We all hope for the timeliness of the test performances, and that it will be a great success!

The End

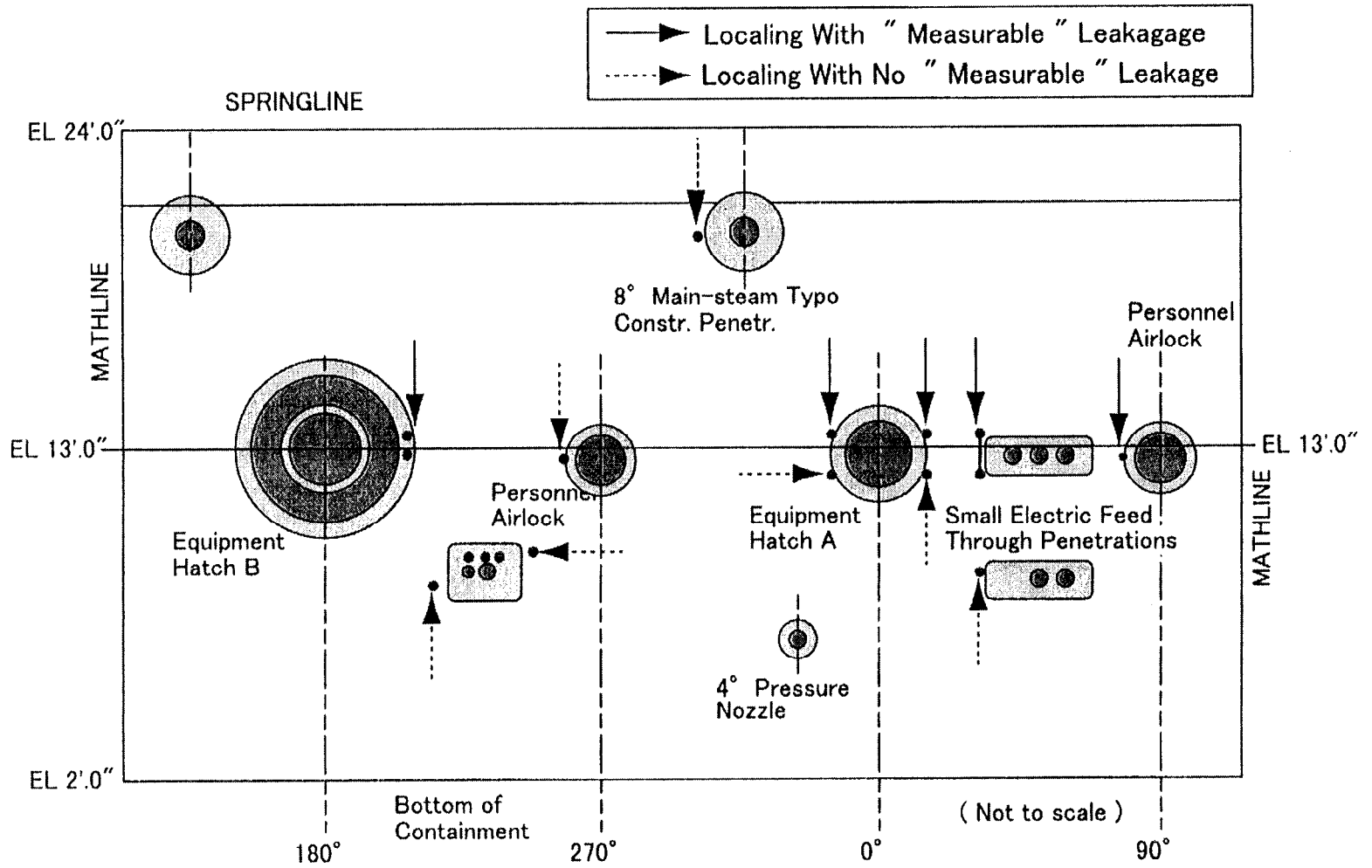


Fig.9-1 Observed failure region of the 1/6 RCCV test model

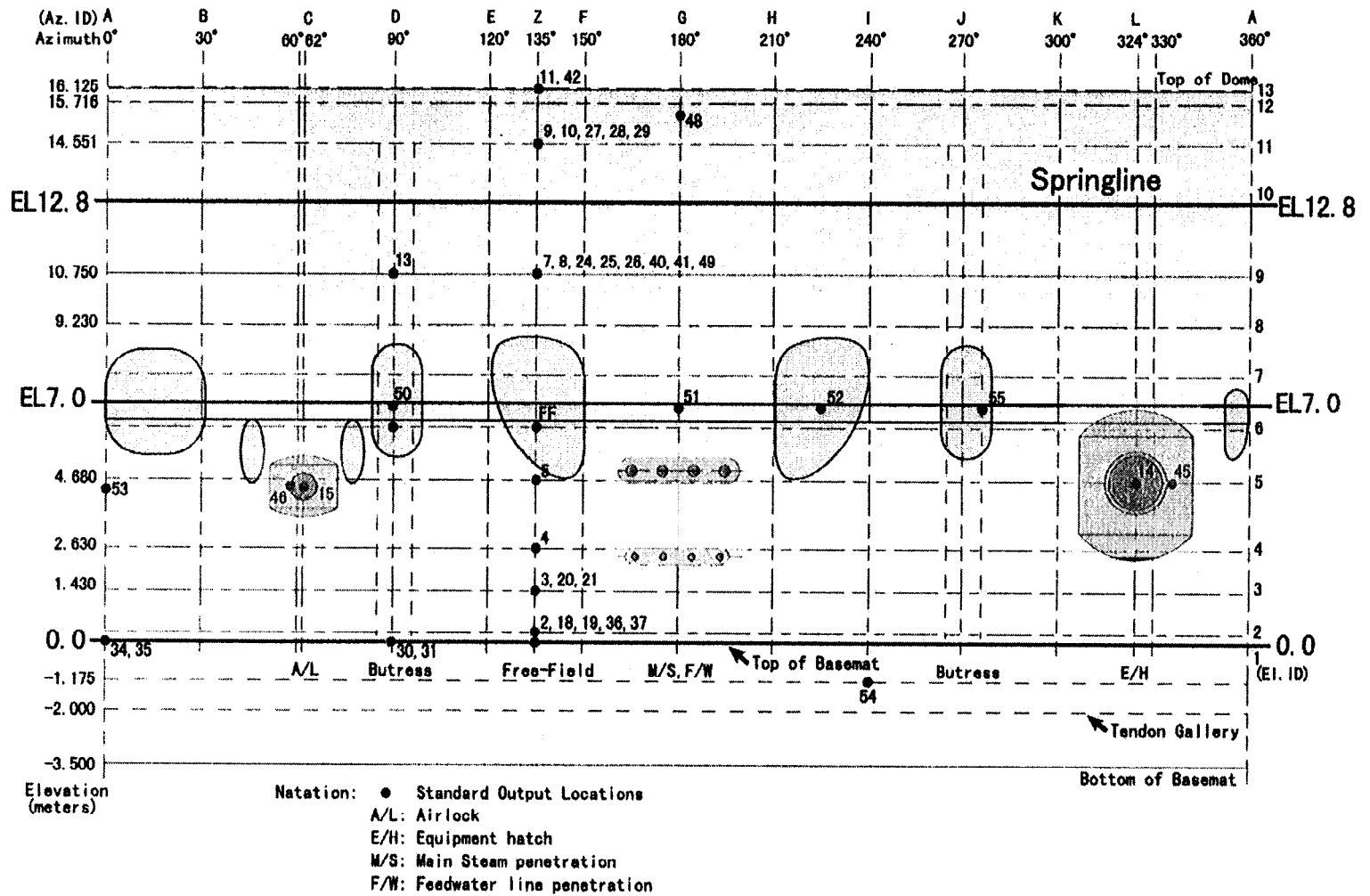


Fig.9-2 Possible failure regions of the 1/4 PCCV model



**APPENDIX M**

**KINS**

**KOREA INSTITUTE OF NUCLEAR SAFETY  
KOREA**

Appendix A, Composite Plots, comprises test data compiled and plotted from all organizations that participated in the Prestressed Concrete Containment Vessel (PCCV) Round Robin Pretest Analysis. To avoid duplicating the composite information, individual sets of data and/or plots have been omitted from participants' reports. In some cases this action resulted in disconnects between callouts and content and in the numbering of figures, tables, and pagination in some reports.

However, Appendix M, "KINS, Korea Institute of Nuclear Safety, Korea," contains none of these discontinuities.

## Summary:

A pre-test analysis results of 1:4-scale prestressed concrete containment model is presented. Based upon configuration of test model and material properties of concrete, liner steel, rebar and tendon provided by SNL, numerical analysis was performed using axi-symmetric and 3 dimensional full model. In this report the result of 3-D model is stated.

## Table Summary

Analytical Method	Load increment non-linear finite element analysis. Newton regular iteration method. Energy based solution convergence criterion.
Constitutive Model	Multi-linear elasto-plastic (rebar and liner) Bi-linear elasto-plastic (tendon) Non-linear Plastic model and smeared cracking model (concrete)
Failure Criteria	Drucker-Prager yield criteria and tension cut off model for concrete Von Mises and work hardening plastic model for steel
Model Geometry	layered shell elements for wall and dome iso-parametric solid element(basemat and buttress concrete) Embedded reinforcement grid (rebar in basemat and buttress)Embedded reinforcement bar (tendon)
Computer Code	DIANA (Release 7.1)
Failure pressure	3.55 P <sub>d</sub> (1.38MPa)

## 1. A description of the mathematical model

### Introduction

The object of the analysis is to predict overall and local behavior of 1/4 prestressed concrete containment model subjected to an increasing internal pressure load until failure. This study has been carried out by joint effort of Korea Institute of Nuclear Safety(KINS) and Concrete Material and Mechanics Laboratory of Yonsei University.

In general, the pressure retaining structure is shaped and designed to resist the pressure by membrane tension, and thus, the transition areas such as juncture and openings are thickened and reinforced compared to general area.

In this study, considering that the failure locations of the previous model tests results performed for RCCV and CANDU-6 containment were general section rather than transition area, the investigation of cylinder wall part was rather focused on in the analysis.

### Computer Code Used

The computer program used in this analysis was the DIANA(Release 7.1). This program was chosen due to its easy modeling capacity for rebar and tendon using embedded bar and grid reinforcement option.

### Modeling - general

Cylinder wall and dome were modeled using the 8-node quadrilateral isoparametric layered shell element and the apex area of the dome( $82^{\circ}$ - $90^{\circ}$ ) was modeled using 6 node triangular isoparametric curved shell elements.(fig. 1) The layered shell element is composed of 8 layers which consist of liner, concrete, inner meridional rebar, inner hoop rebar, concrete, outer meridional rebar, outer hoop rebar, and concrete layer in order.(fig. 5)

The basemat and the buttress were modeled using the iso-parametric solid element.(fig. 3) In order to prevent overlap of stiffness in buttress due to the connection between solid element of buttress and shell element of wall cylinder, the stiffness of overlapped portion in layered shell element was given to zero, and then rebars in this were modeled as grid reinforcement. The solid and the shell element are connected using the tying option.

The rebar in wall and dome is modeled as layer in layered shell element whose thickness is equivalent to rebar amount, and the stiffness of rebar is given to placement direction only, for meridional and hoop, respectively.(fig. 5)

### Modeling – Embedded reinforcement

Rebars in basemat and tendons were modeled as embedded reinforcement grids and bars.(fig. 2) Embedded reinforcements add stiffness to the finite element model. Their main characteristics are:

- Reinforcements are embedded in structural elements, the so-called mother elements
- Reinforcements do not have degrees of freedom of their own
- Reinforcement strains are computed from the displacement field of the mother element. This implies perfect bond between the reinforcement and the surrounding material. Therefore there is limitation to consider the unbonded tendon in the model.

The technique of embedding allows the lines of the reinforcement to deviate from the lines of the mesh. This permits to generate the finite element mesh without having to anticipate on the location of reinforcements

### Modeling – Opening Area

For the openings in containment wall, equipment hatch and airlock are considered in the 3-D model and other penetrations are ignored.(fig. 1) The curved tendons around openings are so modeled as to follow their placing configuration and location.(fig. 2) The pressure acting on the opening area, that is subjected to opening door, is modeled as that the pressure acting on opening area is distributed on the nodes in boundary of opening.

### Modeling - Summary

- 1060 layered shell elements for wall and dome
- 596 iso-parametric solid element for basemat and buttress concrete
- embedded reinforcement grid for rebar in basemat and buttress
- embedded reinforcement bar for all tendons  
(hoop 108, meridional 90)

### Numerical procedure

Physical nonlinearity based on small displacement theory is considered in the analysis. Load increment was chosen as analysis increment: step 1 is dead load, step 2 is prestressing, after then 2steps of  $0.5P_d$ , 20steps of  $0.1 P_d$ , 10steps of  $0.05 P_d$ , and then steps of  $0.025 P_d$  until no further calculation due to divergence.

Newton regular iteration was used for iteration method.

Solution convergence is checked by energy based criterion. This criterion prevent the force residual, induced due to stress discontinuity in cracked concrete, which makes error in using force based criterion.

The 30 times iteration in each step is given, and if the result of 30th iteration still does not meet the convergence value, and then let the analysis proceed to next step.

The analysis is stopped when the energy variation between previous and next iteration is rapidly increase and finally diverged. That means the strain of tendon is exceeded the rupture strain in this analysis.

## 2. A description of how the material data were used in the analysis

### 2.1 concrete property

The parameters to be used to define the uni-axial stress strain curve of concrete are listed hereunder. Since the test model is prestressed and tested at long time after placing, material data of 13 weeks are chosen. With consideration of in-situ curing condition, the in-situ properties are assumed as average value of standard curing and field curing

	Basemat	Shell & Dome
Compressive Strength (MPa)	46.54	54.53
Tensile Strength (MPa)	3.65	3.83
Young's modulus ( $\times 10^3$ MPa)	28.49	29.47
Poisson's ratio	0.19	0.19
Density (ton/m <sup>3</sup> )	2.23	2.23

The behavior of concrete under uni-axial compression is modeled by the idealized stress-strain curve proposed by Hognestad.(fig. 6) For the uni-axial tension, it was assumed that tension is linearly increase up to tensile strength and then linearly decrease and reach to zero at strain of rebar yielding considering tension stiffening of reinforced concrete.(fig. 8-10)

### 2.2 rebar

The stress-strain behavior is assumed as multi-linear elasto-plastic composed of 4 lines.(fig 11-15) Young's Modulus is taken as 210000MPa.

	Yield	2 <sup>nd</sup>	3 <sup>rd</sup>	Ultimate
D10 Strain(%)	0.287	1.314	5.080	8.066
Stress(MPa)	482.0	465.9	589.5	613.6
D13 Strain(%)	0.302	0.941	5.045	8.999
Stress(MPa)	490.1	475.6	616.0	640.4
D16 Strain(%)	0.283	1.092	4.934	7.726
Stress(MPa)	476.6	465.0	588.7	606.2
D19 Strain(%)	0.344	1.474	5.069	9.434
Stress(MPa)	491.9	488.1	609.1	630.4
D22 Strain(%)	0.337	0.704	5.038	9.118
Stress(MPa)	459.0	455.7	618.5	653.2

### 2.3 liner

The stress-strain behavior is assumed as multi-linear elasto-plastic composed of 3 lines. Young's

Modulus is taken as 210000MPa, and Poisson's ratio as 0.3. (fig. 16)

	Yield	2 <sup>nd</sup>	Ultimate
Strain(%)	0.18	5.08	33.2
Stress(MPa)	382.6	465.9	589.5

#### 2.4 tendon

The stress-strain behavior is assumed as bi-linear elasto-plastic. (fig 17)

The curvature and the friction loss of prestress were considered. The setting loss due to slip of wedge was considered as well.(fig. 18-20)

### 3. Description of the failure model used in the analysis

#### 3.1 Concrete model

For concrete material modeling, the plastic model of compression and the smeared cracking model of tension based on Drucker-Prager failure criterion are used. The behavior of concrete under uniaxial compression is modeled by the idealized stress-strain curve proposed by Hognestad.

In the smeared cracking model, it is assumed that an initial crack occurs when the principal tension stress of an integration point on principal stress space reach to tension strength. The second crack at the same integration point occurs when the angle of principal stress direction to the direction of the first crack exceeds  $60^\circ$  and the principal stress reaches to tension strength of concrete.

Tension stiffening due to bond effect between rebar and concrete is so modeled that concrete strength linearly decreases with increase of strain after cracking and reaches to zero at the strain ( $\epsilon_u=0.00233$ ) of rebar yielding.(Fig. 6) For considering the shear strength reduction effect in crack surface due to aggregate interlock, the shear retention factor( $\beta$ ) of 0.02 is used.

#### 3.2 steel

Since rebar, tendon and liner show the same behavior in compression and tension, the von-Mises yield criterion and work hardening assumption are applied to the plastic modeling, and the multi-linear stress-strain relations are used in material modeling.

### 4. Analysis Results and Discussion

(Plots of pressure history for strain, displacement, of force at every standard output location)

#### 4.1 Overall Behavior

The section view of overall deformation at typical load steps is presented in fig.21 – fig.24. In the dome, after introducing prestress, more vertical displacement is occurred as closer to the dome apex. The inward displacement is recovered as increase of pressure, and then expand to outward.

The plan view for elevation of 8.73m at typical loads is presented in fig.25 – fig.28. The deformed shapes are coincident to the section view, and the distortion of circular shape of cylinder wall is taken place due to the effect of openings, buttress, and non-linear behavior and crack of materials.

#### 4.2 Displacement (Standard Output Location #1-#15)

The fig.29 shows vertical displacement of standard output locations(SOL). In the dome, as the pressure build up, vertical displacement(#10 & #11) increases up to around 0.9Mpa, and then going down. The displacement at spring line(#8) goes up gradually, and then follows abrupt increase when the pressure exceeds 1.2 MPa. This pressure is around yielding pressure for tendons in critical section.

The fig.30 shows radial displacement of SOL(#2-#7, #9) in azimuth  $135^\circ$ . The higher the location is, the larger the displacement is. The displacements are rapidly increase when the pressure is beyond 1.2 MPa. The fig.31 shows radial displacement of SOL other then those of azimuth  $135^\circ$ , and the trend of displacement is very similar to COL of fig.30.

#### 4.3 Rebar (Standard Output Location #16-#33)

The fig.32 shows meridional inner rebar strain of SOL. Most of rebar strains are tension and have two transition points. Those are rebar yielding and tendon yielding points. The fig.34 for hoop rebar stain shows same trend but higher value compared to fig.32.

#### 4.4 Liner (standard Output Location #34-#47)

The fig.35 and 36 show Liner strain of SOL. The strains are increase as pressure build up except #38. The deforming trends are similar to rebar.

#### 4.5 Tendon (standard output Location #48-#55)

The fig.37 shows tendon strain of SOL. The large stain is found in #51 and #52.

## 5. Pressure Level at Event Milestones

(Description of pressure levels corresponding to the following event milestones and an explanation of how they were derived)

The pressure level corresponding to each event and the location of event has been determined by searching the computer output step by step.

For the 90% confidence level, it was not easy to be formulated, so that it was proposed by engineering judgement.

- first cracking of concrete in cylinder due to hoop stresses  
Pressure level(MPa/Ratio to Pd) : 0.39/1.0  
Location : between 270° buttress and E/H, EL 392-515cm, outer face
- first cracking of concrete in cylinder due to meridional stresses  
Pressure level(MPa/Ratio to Pd) : 0.62/1.6  
Location : 0° & 180°, El 0-10cm
- first yield of hoop rebar in cylinder  
Pressure level(MPa/Ratio to Pd) : 0.86/2.2  
Location : between 270° buttress and E/H, EL 392-515cm, outer hoop
- first yield of meridional rebar in wall-basemat juncture  
Pressure level(MPa/Ratio to Pd) : 1.27/3.25  
Location : 0° & 180°
- first cracking in dome concrete above 45° dome angle  
Pressure level(MPa/Ratio to Pd) : 0.43/1.1  
Location : 0° & 180°, dome 77°-82°
- first cracking in dome concrete below 45° dome angle  
Pressure level(MPa/Ratio to Pd) : 0.47/1.2  
Location : 97.6°-109.2°, dome 31°-45°
- hoop tendons in cylinder reaching 1% strain  
Pressure level(MPa/Ratio to Pd) : 1.25/3.2  
Location : 180° mid-height(6.58m)
- hoop tendons in cylinder reaching 2% strain  
Pressure level(MPa/Ratio to Pd) : 1.33/3.4  
Location : 180° mid-height(6.58m)
- hoop tendons in cylinder reaching 3% strain  
Pressure level(MPa/Ratio to Pd) : 1.37/3.53  
Location : 180° mid-height(6.58m)
- best estimate of static failure pressure  
Pressure level(MPa/Ratio to Pd) : 1.38/3.55  
(Hoop tendon reaching rupture strain)
- minimum pressure reachable with 90% confidence level  
Pressure level(MPa/Ratio to Pd) : 1.25/3.2  
(Hoop tendon reaching 1% strain)
- maximum pressure reachable with 90% confidence level  
Pressure level(MPa/Ratio to Pd) : 1.44/3.7  
(hoop tendon reaching 4% strain, considering the strain absorbing of adjacent tendon in

unbonded type tendon system and modeling error)

## 6. Conclusion

A pre-test analysis results of 1:4-scale prestressed concrete containment model is presented. By checking the overall deformed section and plan views and deformation-pressure history plot, the results are considered to be reasonable.

After the pre-analysis, the analysis model has been reexamined. The items which the modification and further studies to be required are as follows:

- modeling technique of unbonded tendon
- finer mesh for transition area
- enhancing the connection technique for shell and solid element in juncture

The analysis modeling technique for PCCV, assumption of failure criteria, and etc. will be modified and enhanced with consideration of test results.

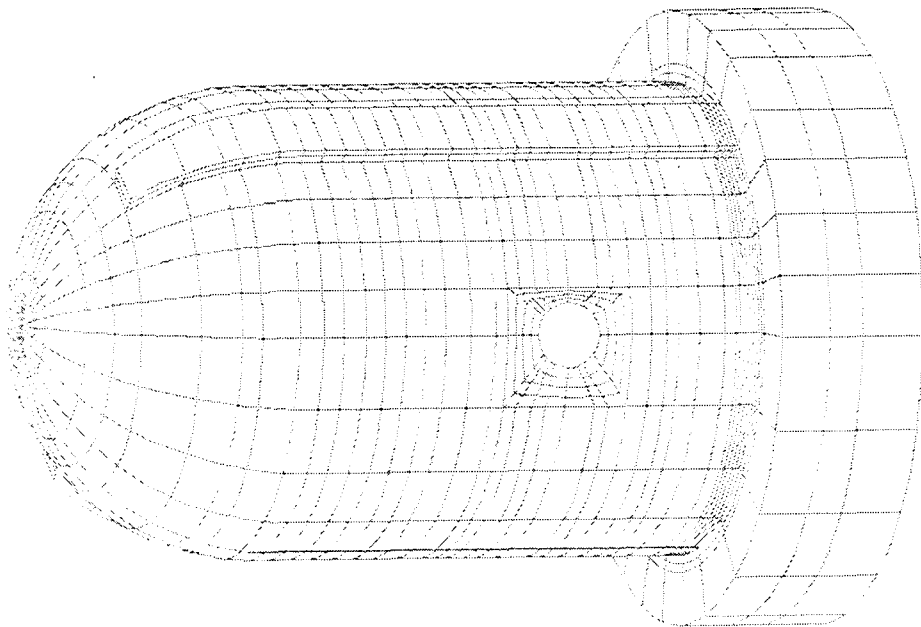


Fig.1 full model

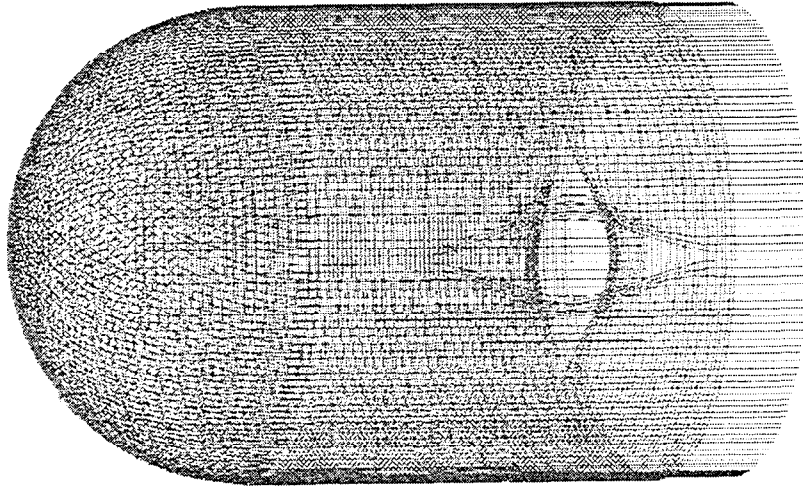


Fig.2 tendon modeling

M-11

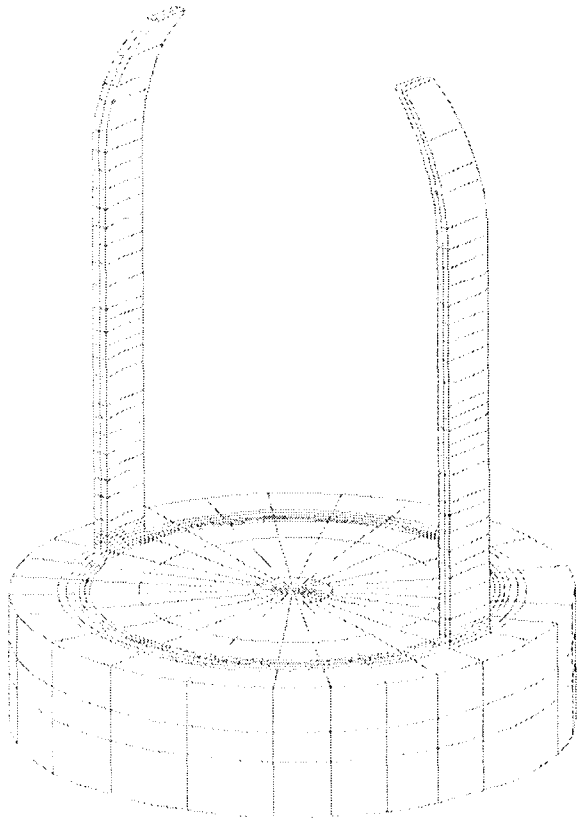


Fig.3 buttress & basemat modeling

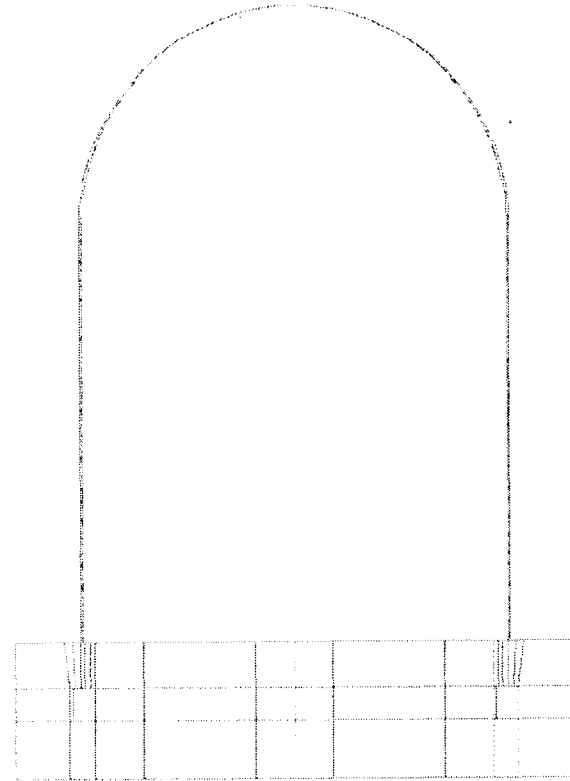


Fig.4 general center section

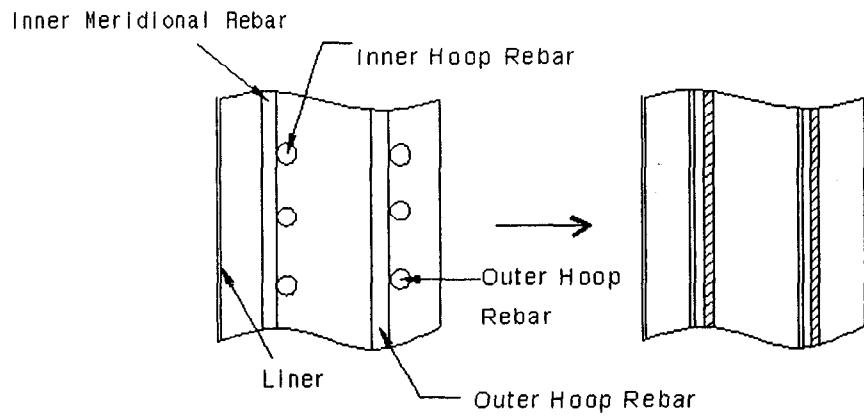


Fig.5 layered shell of wall & dome

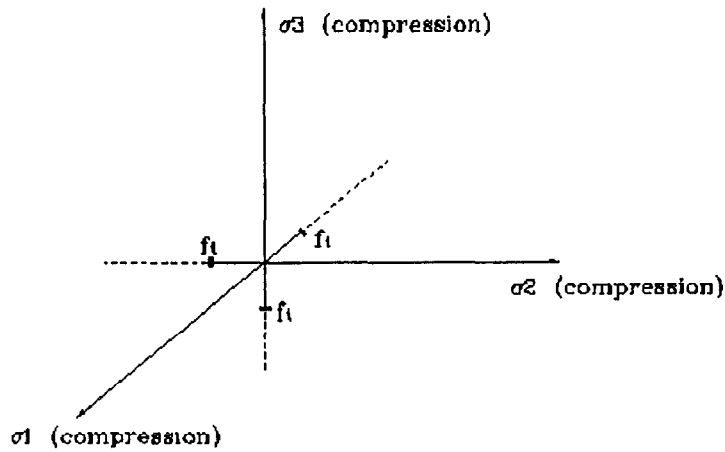


Fig.7 constant tension cut-off model of concrete

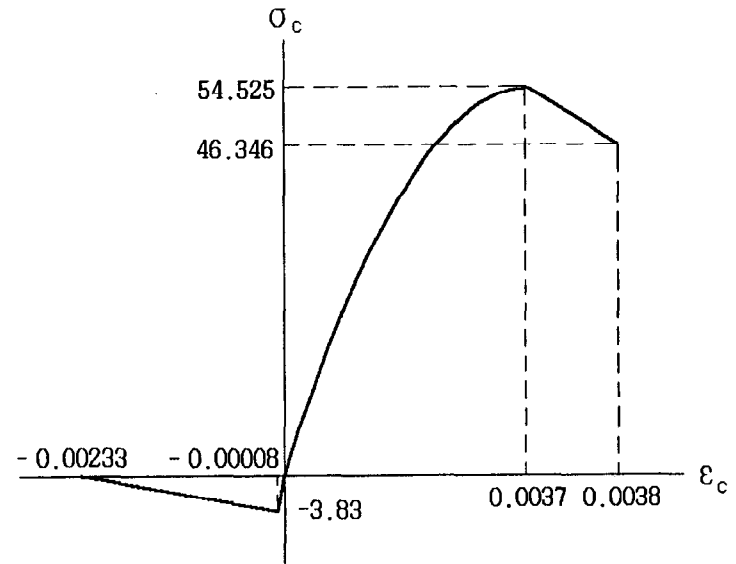


Fig.6 concrete material modeling by Hognested

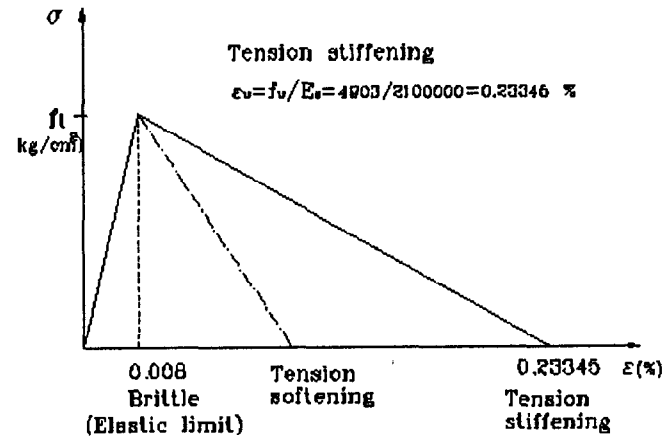


Fig.8 tension stiffening model of concrete

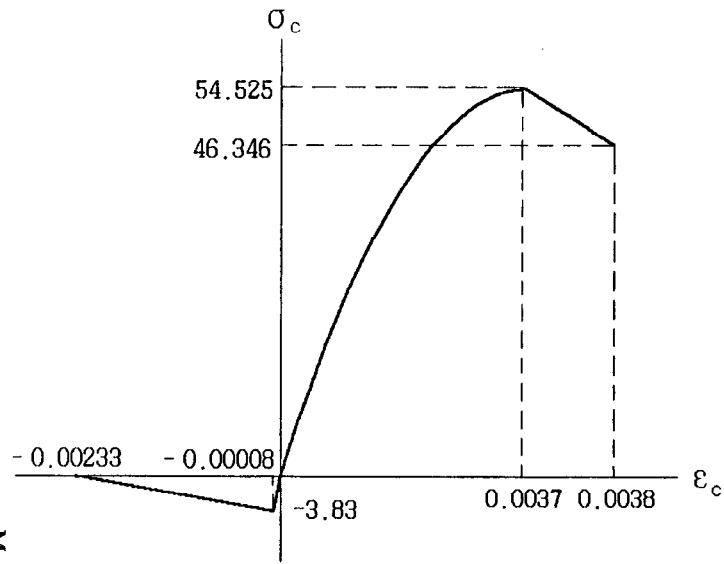


Fig.9 concrete modeling of wall & dome

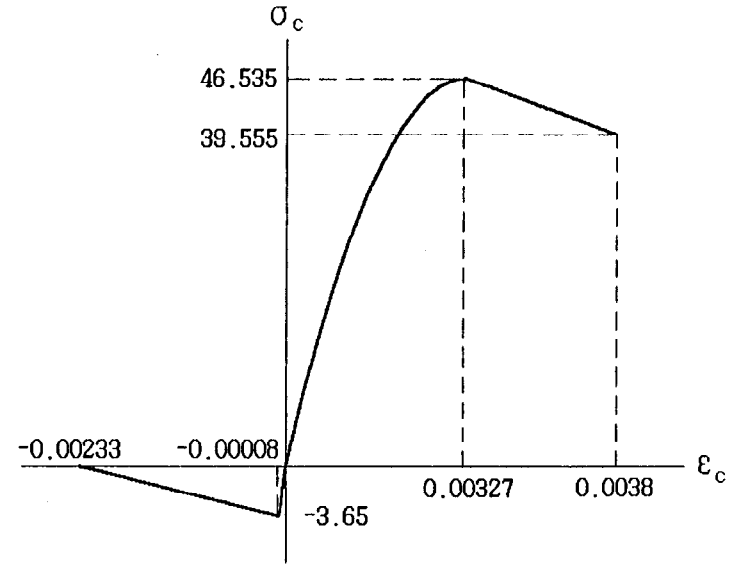


Fig.10 concrete modeling of basemat

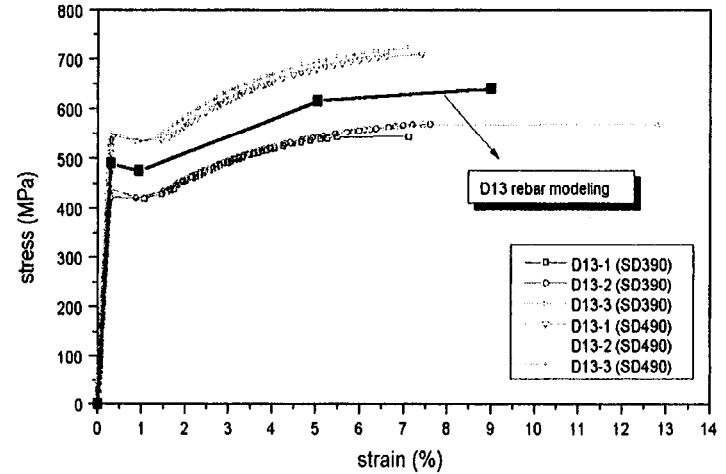
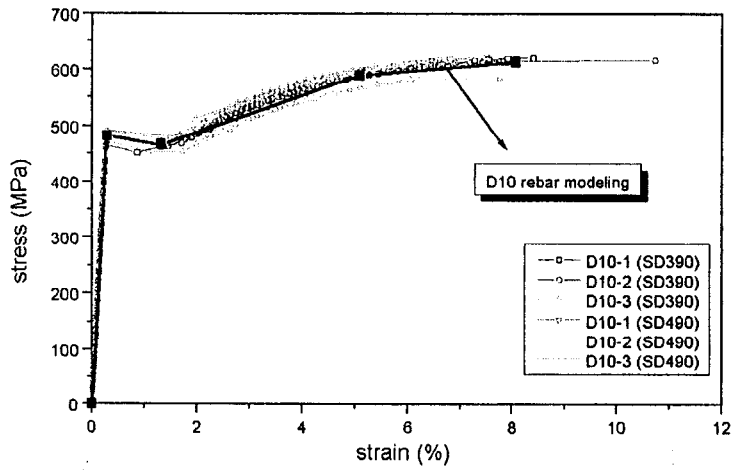


Fig.11 material modeling of D10 rebar

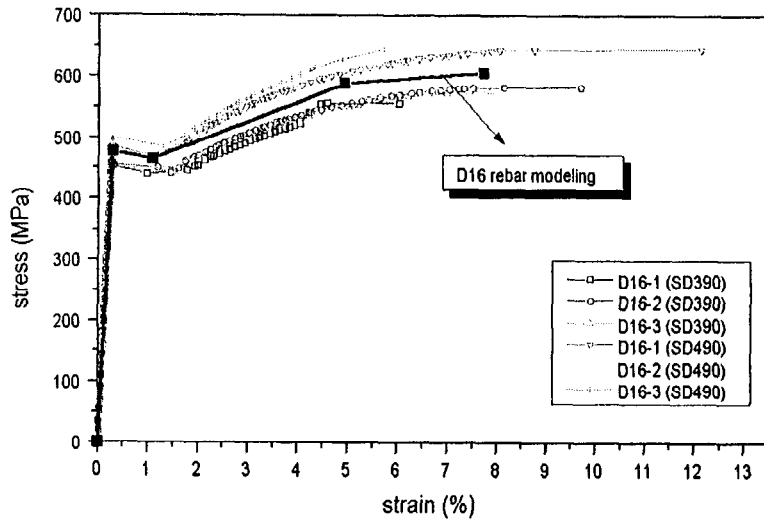


Fig.12 material modeling of D13 rebar

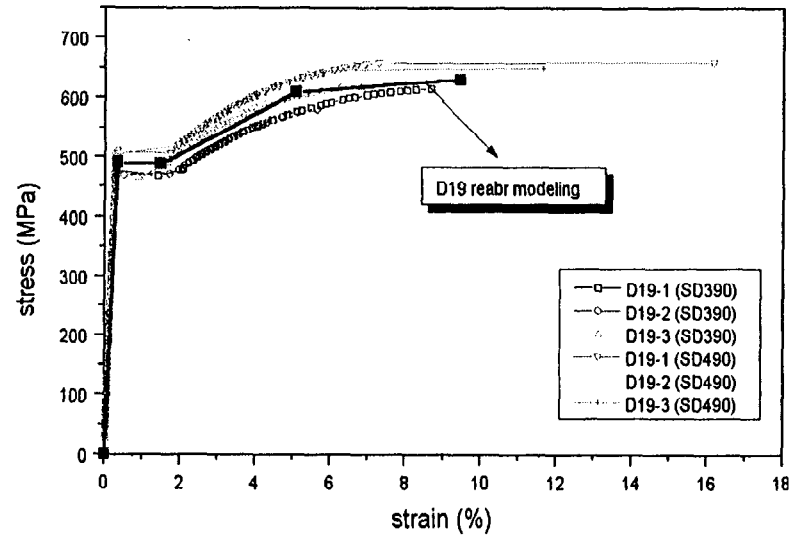


Fig.13 material modeling of D16 rebar

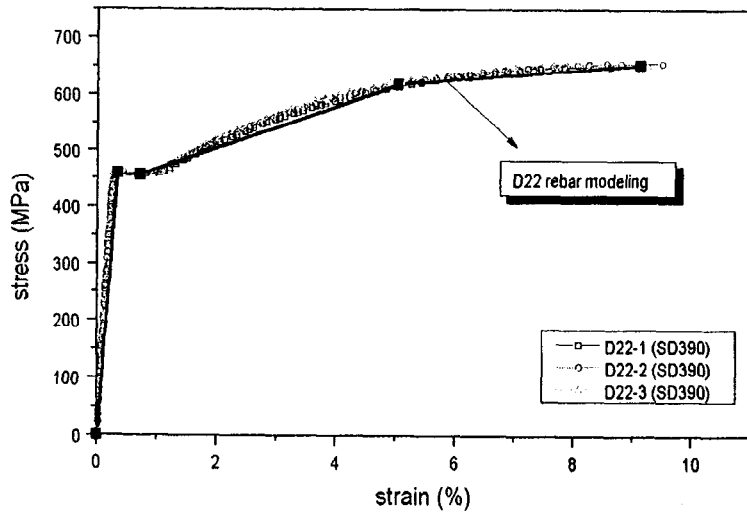


Fig.14 material modeling of D19 rebar

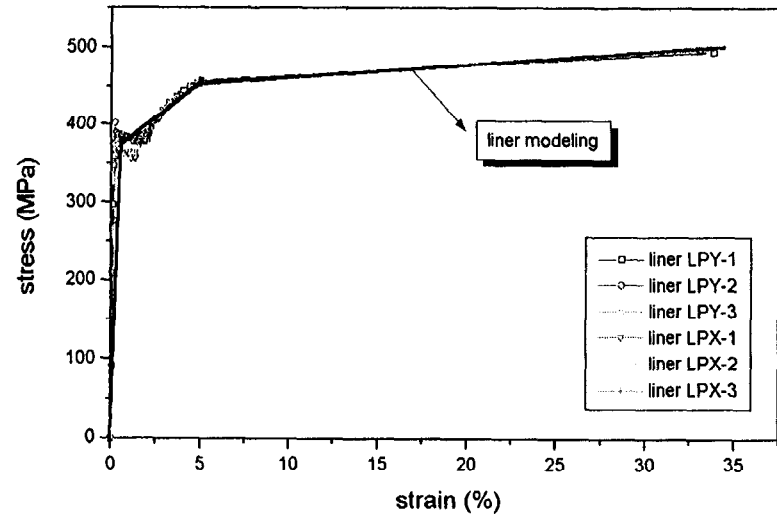


Fig.15 material modeling of D22 rebar

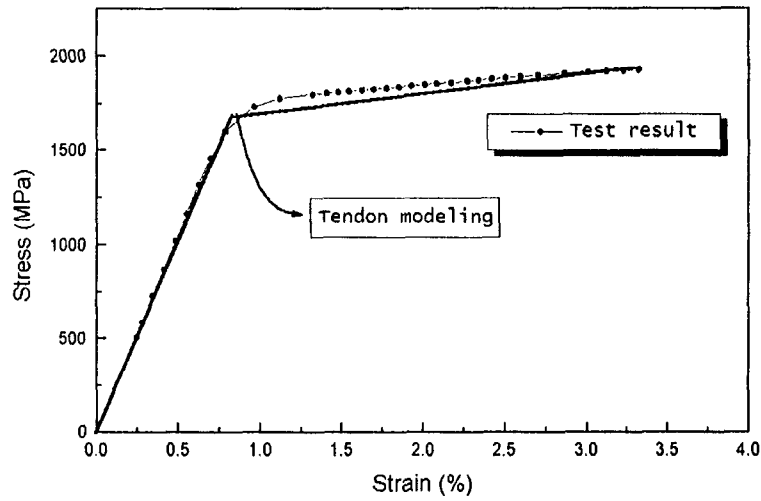


Fig.16 material modeling of liner

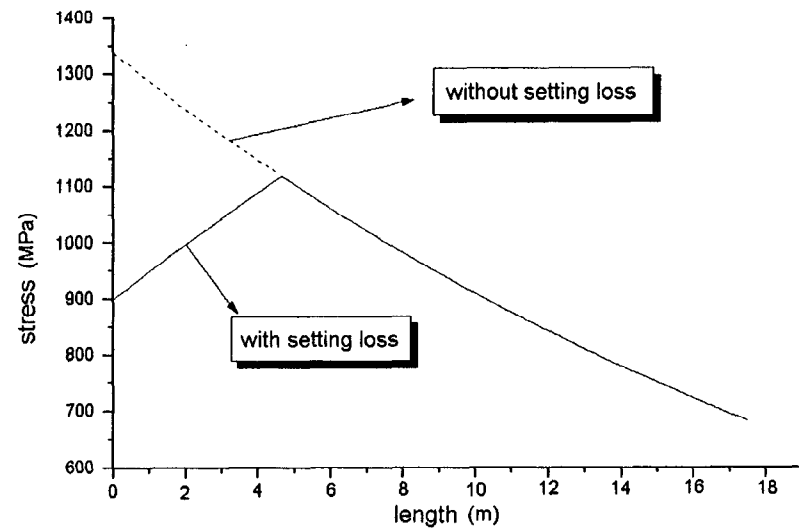


Fig.17 material modeling of tendon

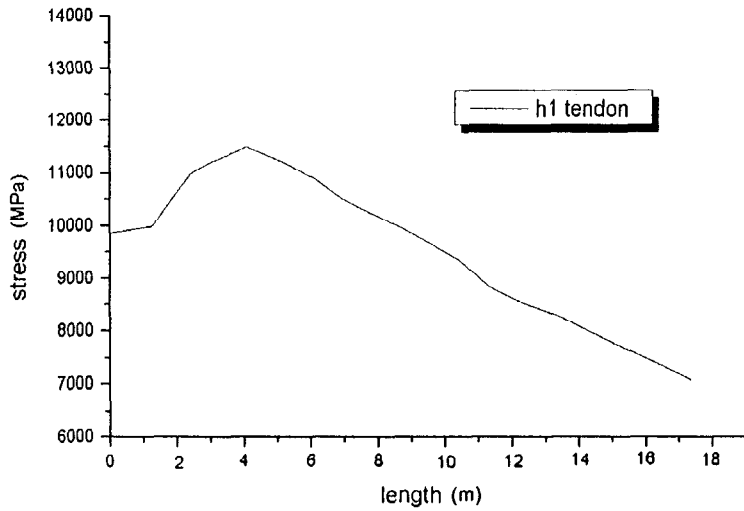


Fig.18 prestress loss of hoop tendon

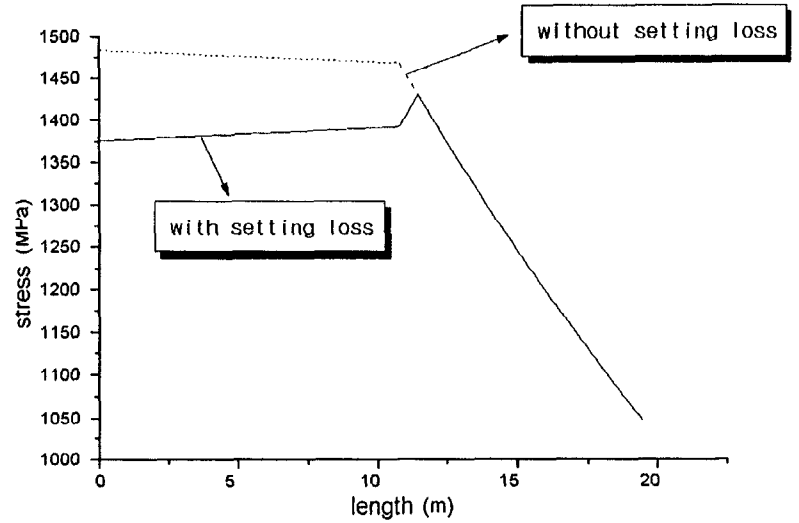


Fig.19 analytical prestress loss of h1 tendon

Fig.20 prestress loss of vertical tendon

M-16

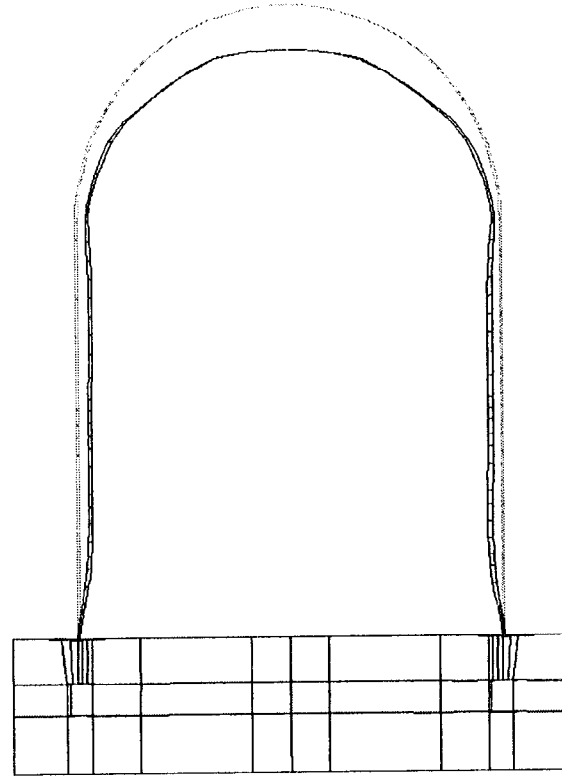
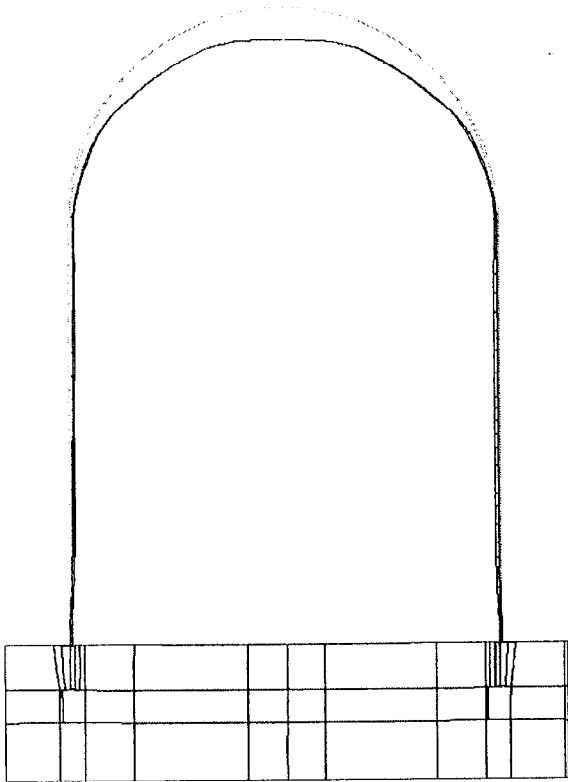


Fig.21 deformation at prestress (300-scale)

Fig.22 deformation at 1.0 Pd (300-scale)

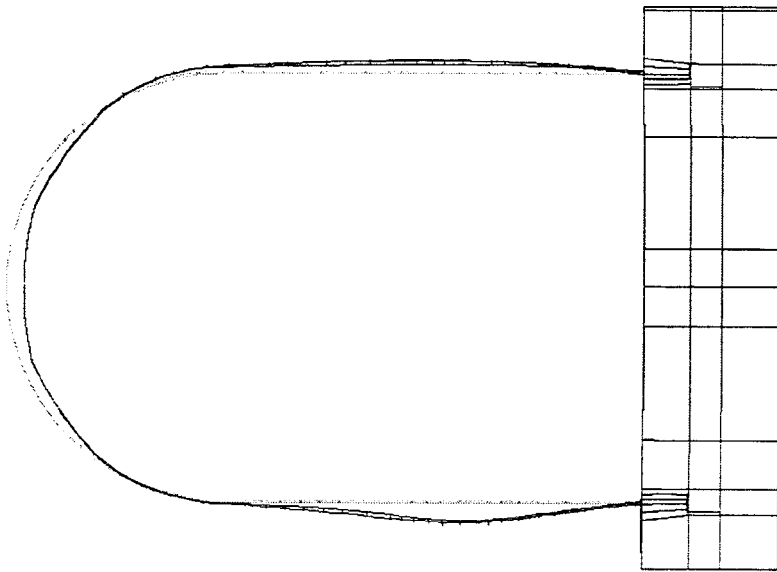


Fig.23 deformation at 2.0 Pd (300-scale)

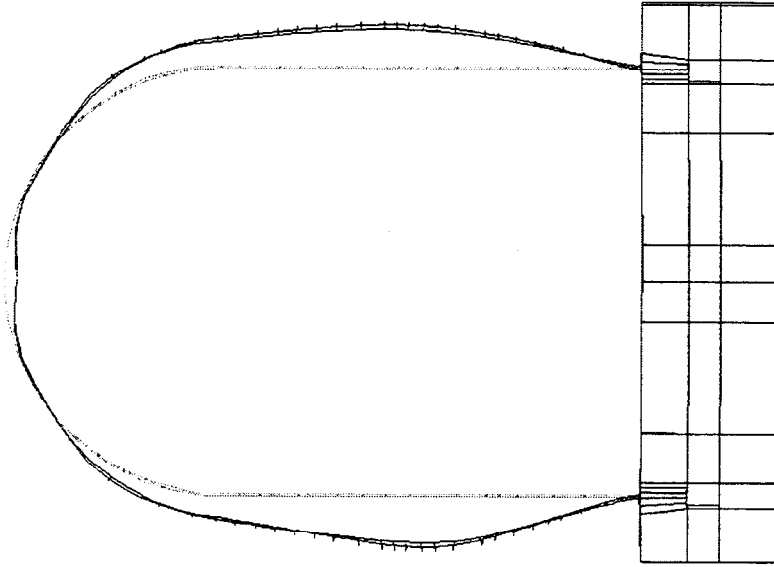


Fig.24 deformation at 3.0 Pd (100-scale)

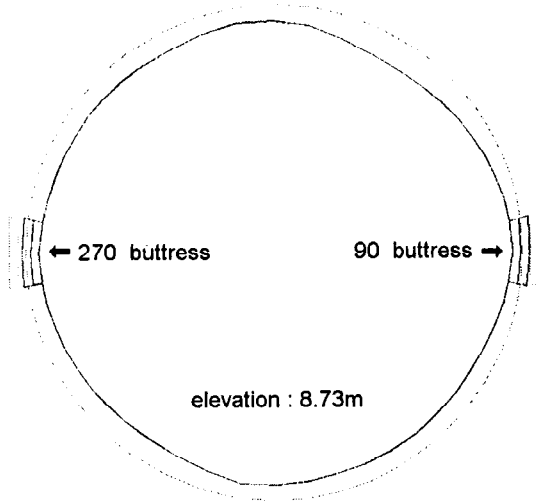


Fig.25 deformation at prestress (300-scale)

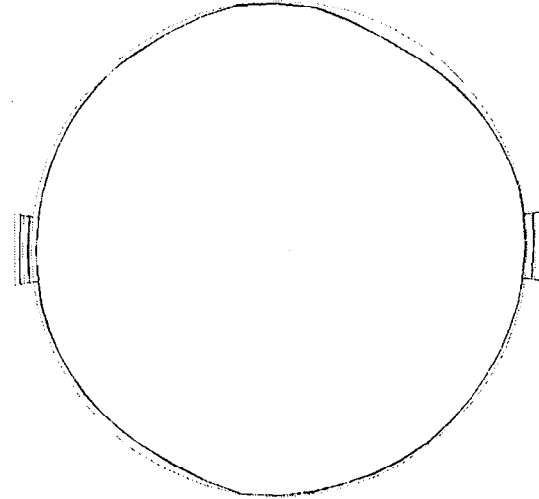


Fig.26 deformation at 1.0 Pd (300-scale)

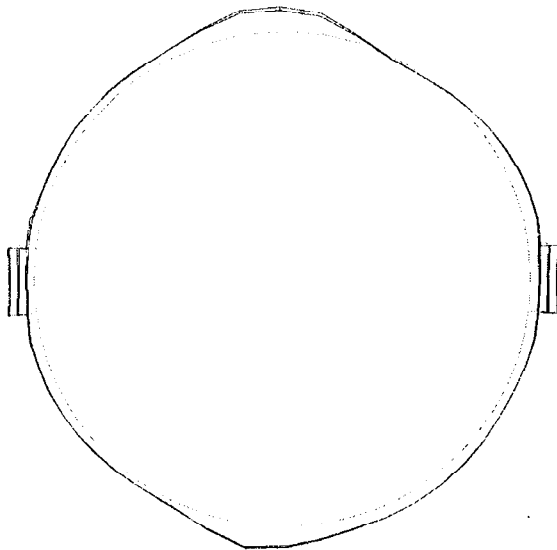


Fig.27 deformation at 2.0 Pd (300-scale)

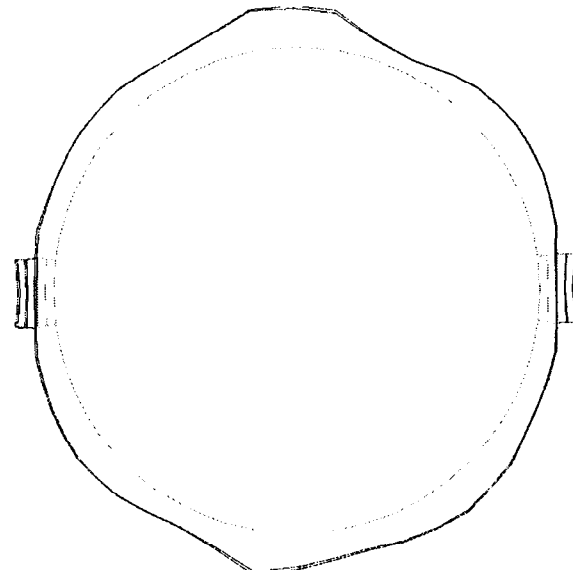


Fig.28 deformation at 3.0 Pd (50-scale)

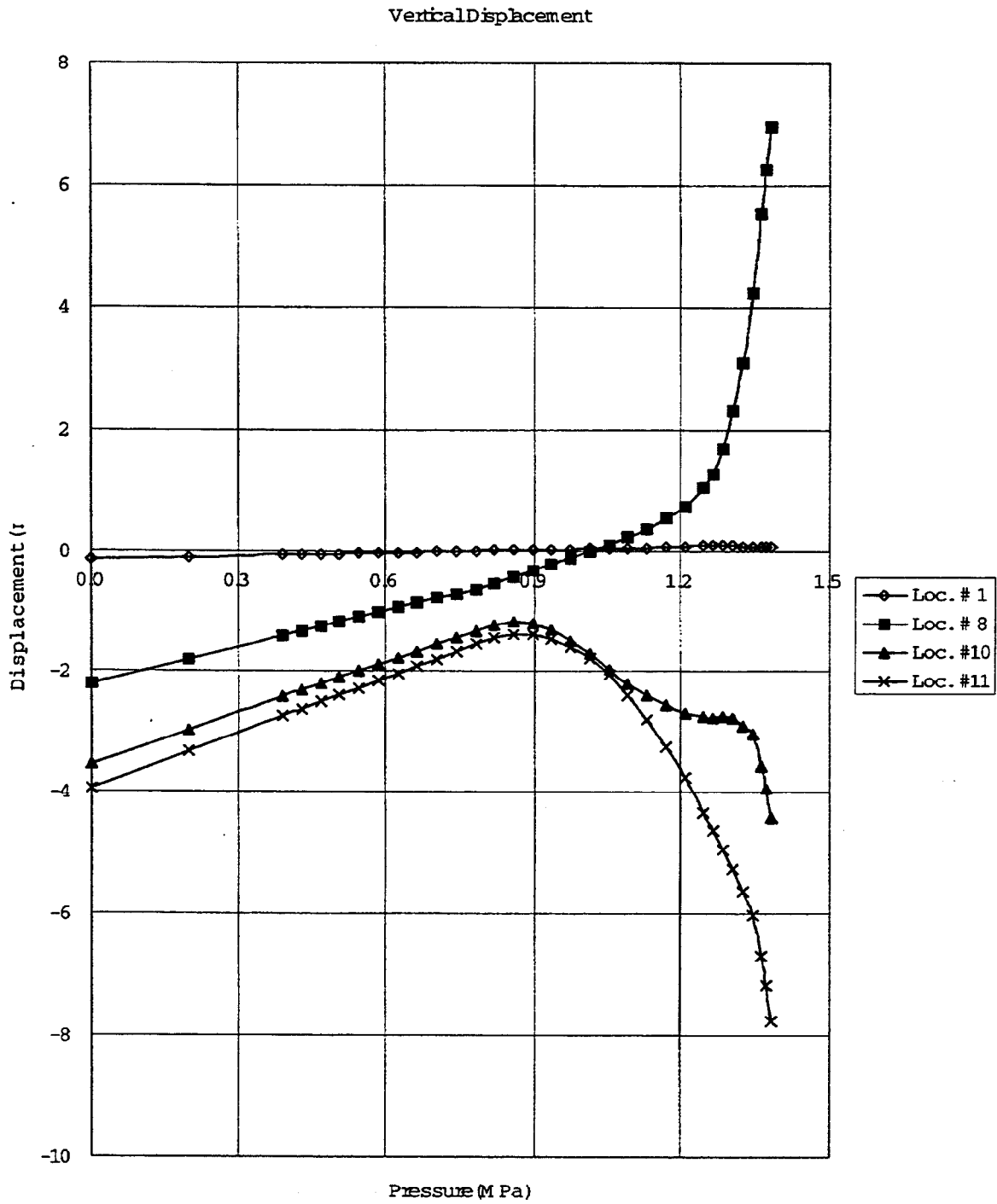


Fig. 29 Vertical Displacement

RadialDisplacement(Az135)

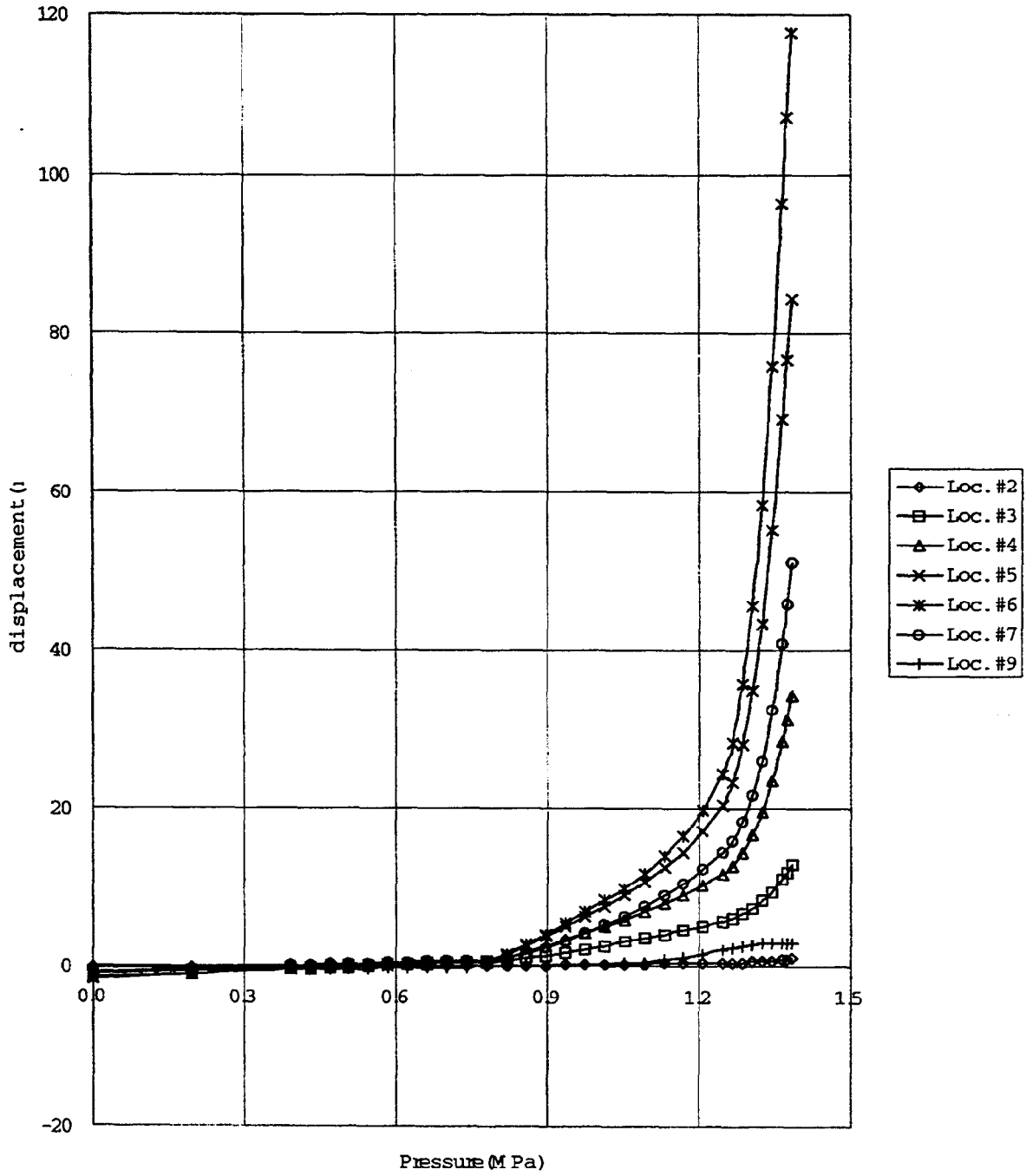


Fig. 30 Radial Displacement I

Radial Displacement

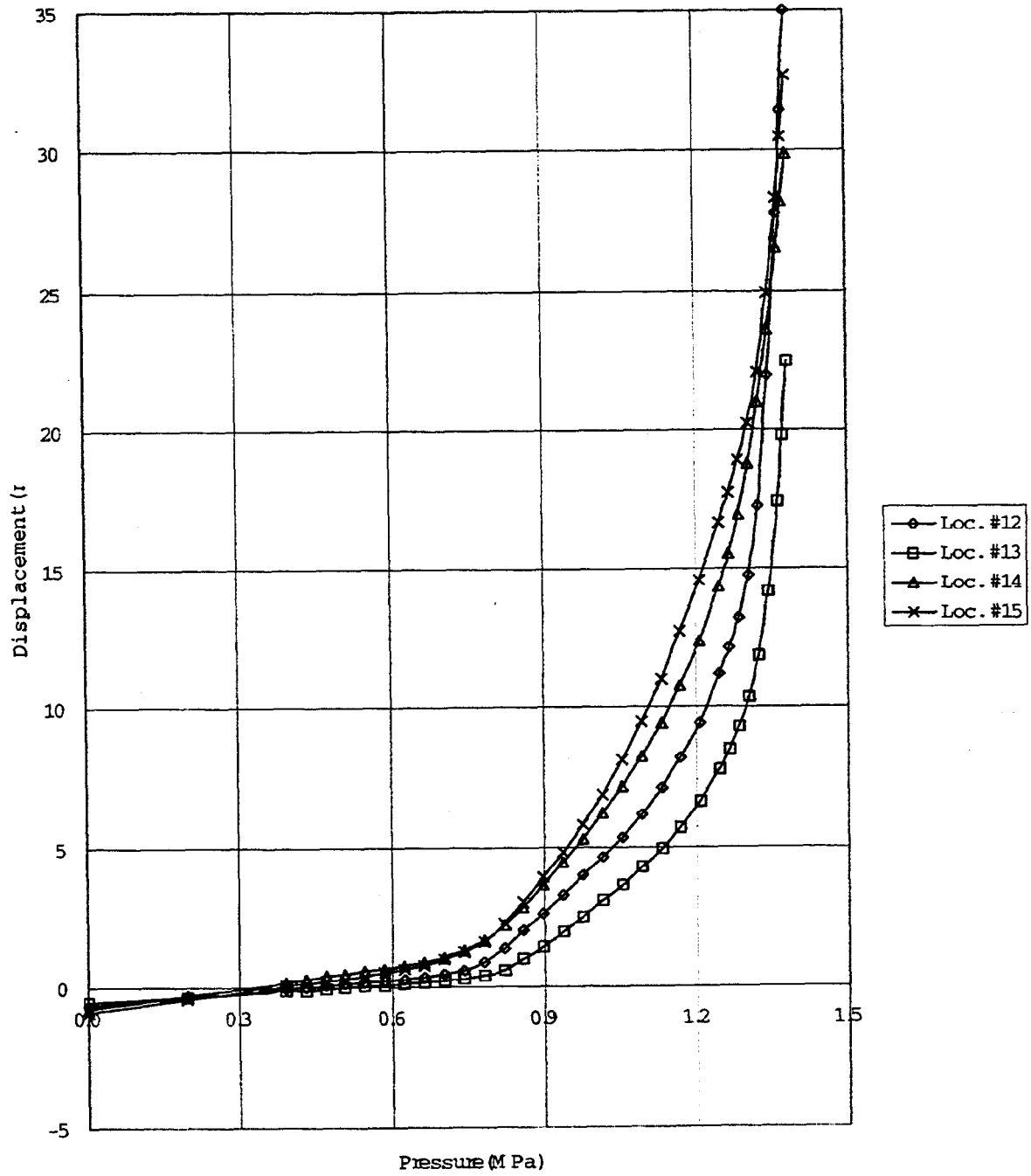


Fig. 31 Radial Displacement II

Meridional Rebar Strain (Inner Layer)

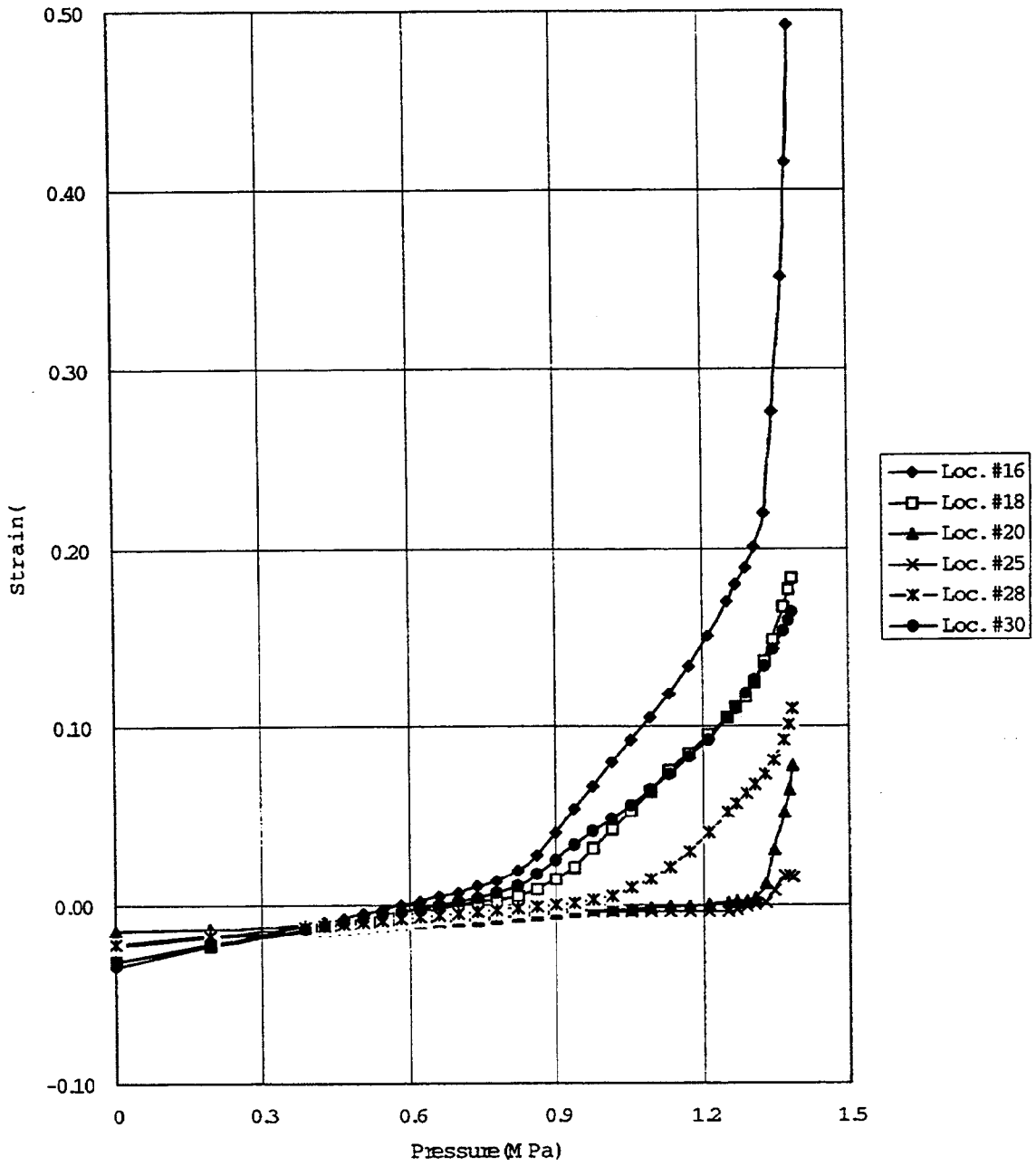


Fig. 32 Meridional Rebar Strain (Inner Layer)

Meridional Rebar Strain (Outer Layer)

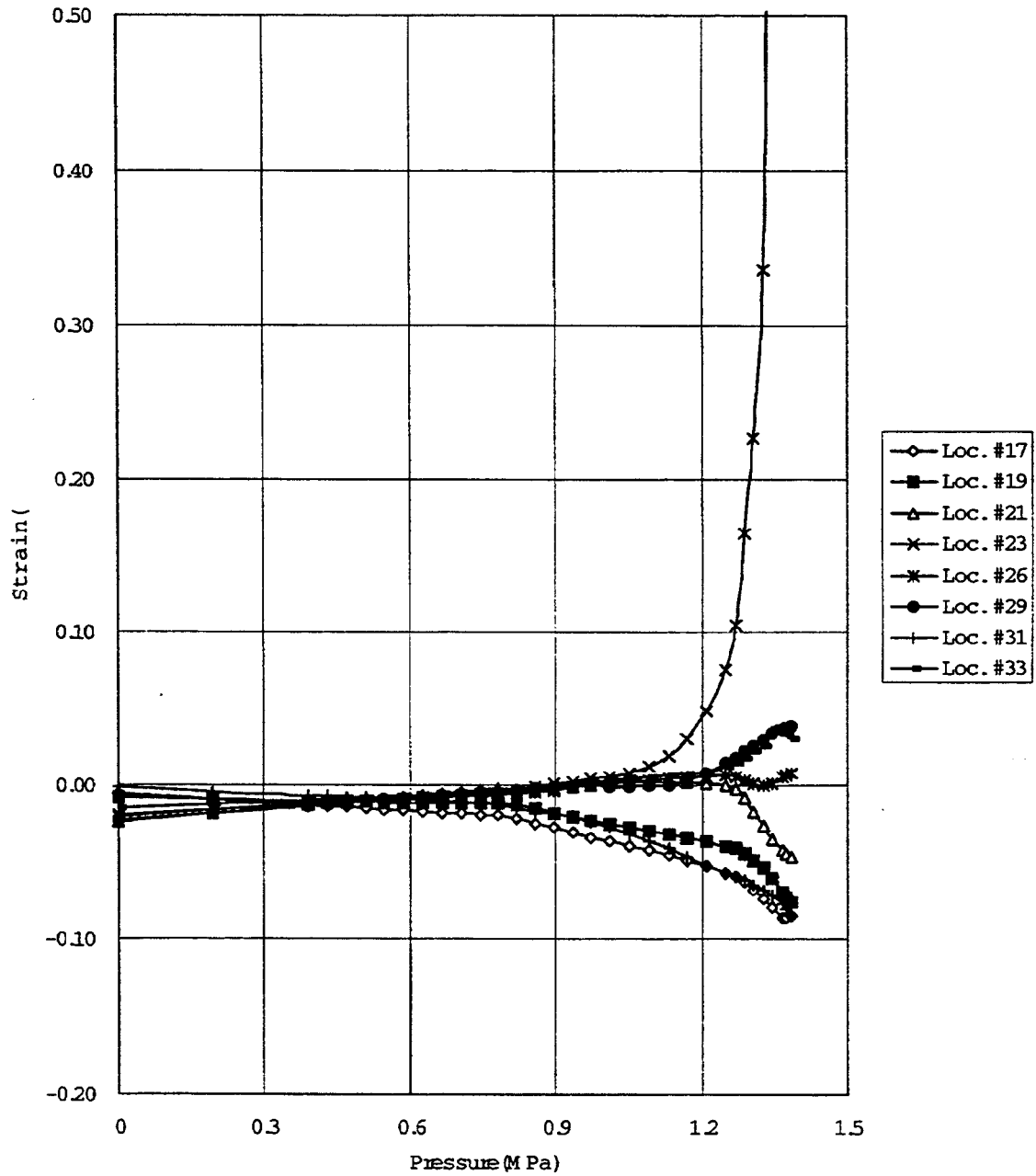


Fig. 33 Meridional Rebar Strain(Outer Layer)

### Hoop Rebar Strain

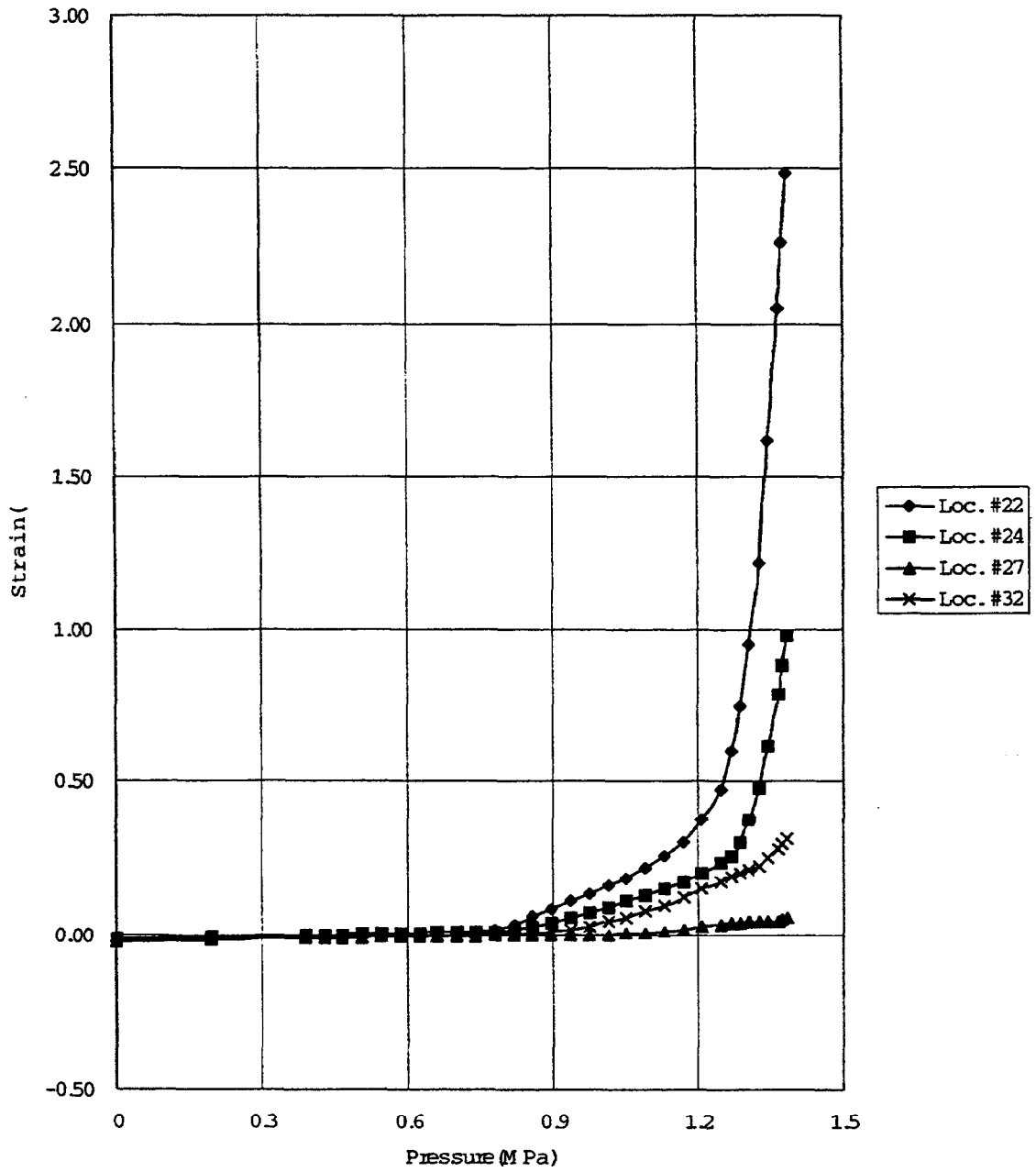


Fig. 34 Hoop Rebar Strain

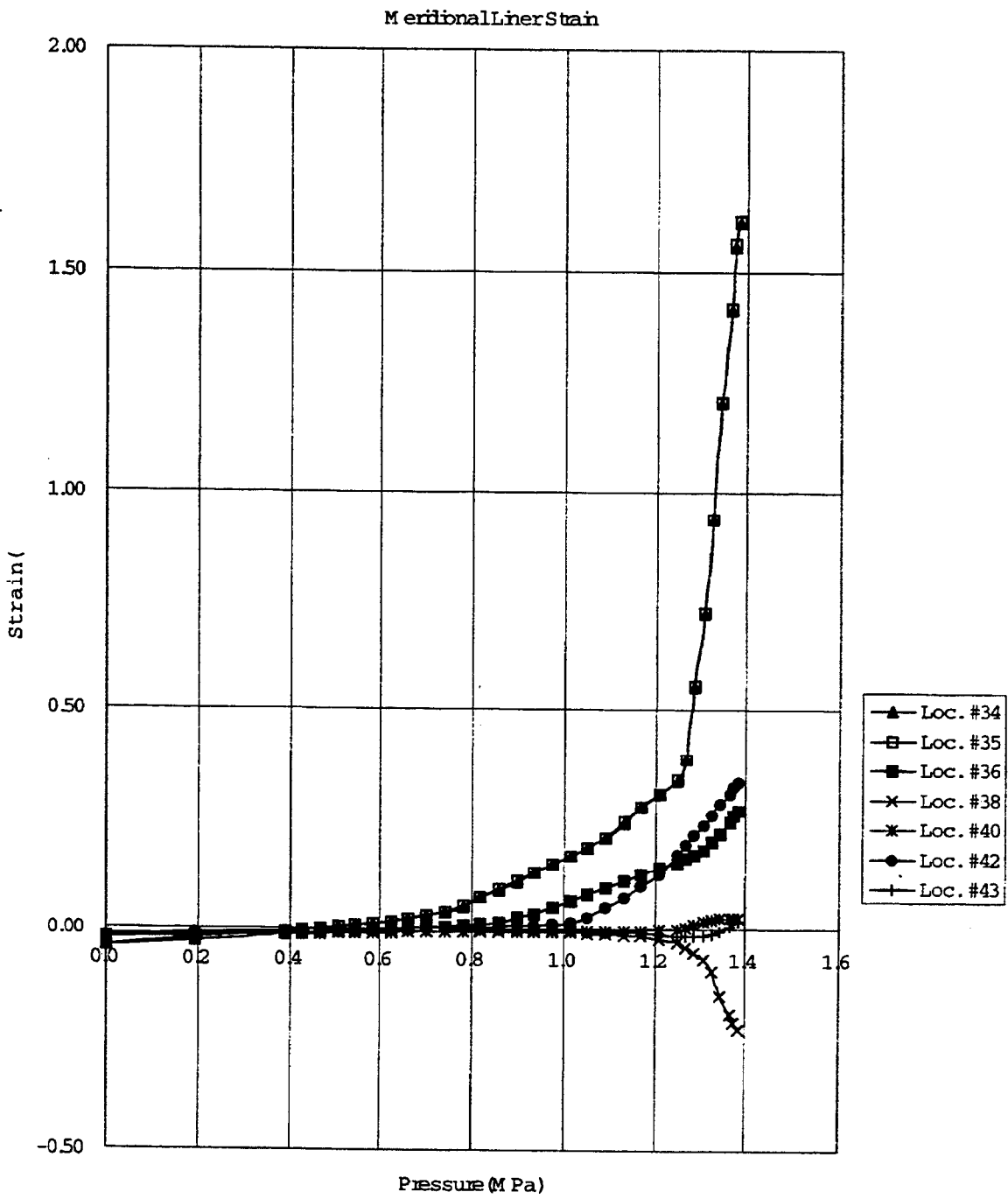


Fig. 35 Meridional Liner Strain

### Hoop Liner Strain

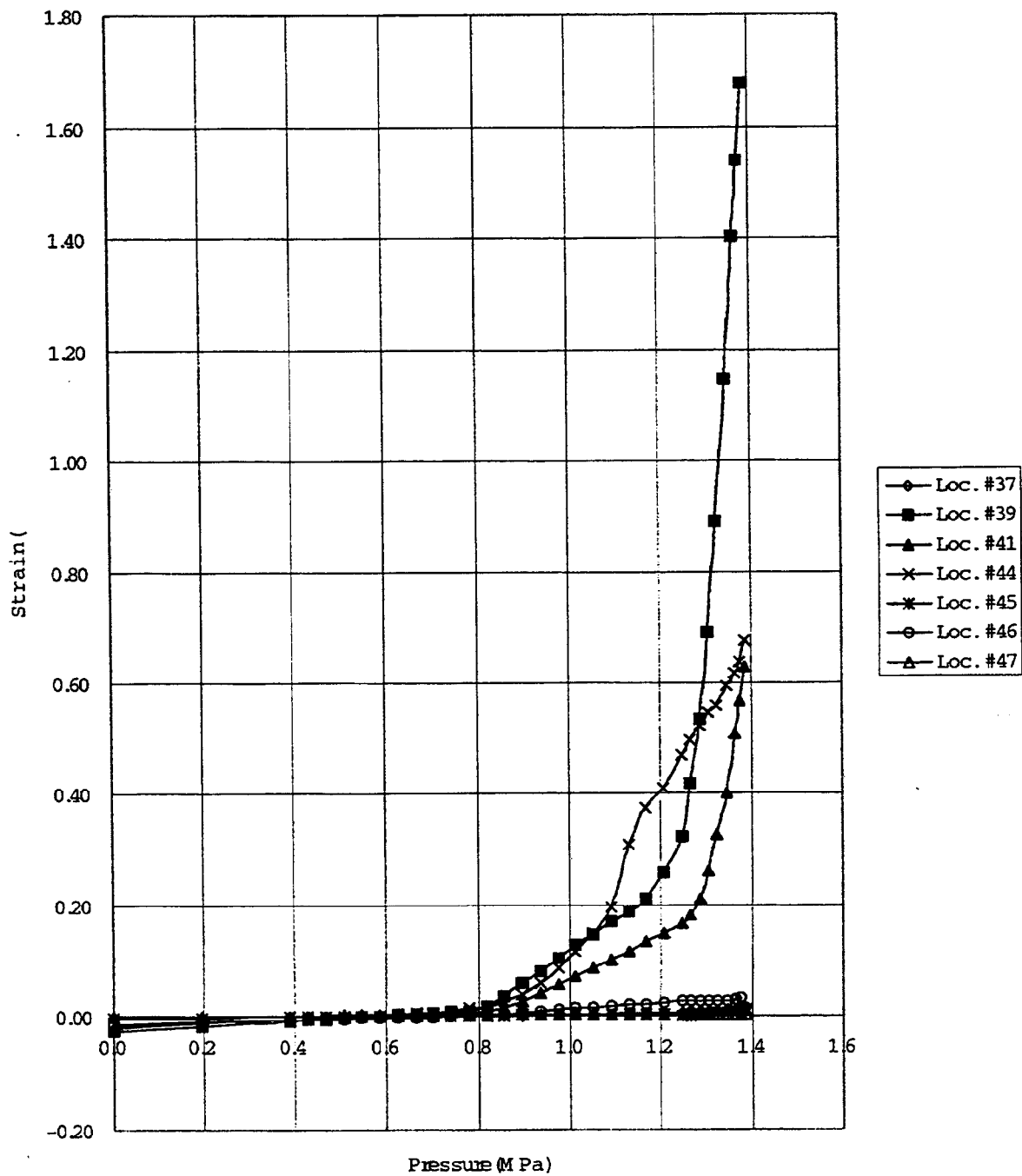


Fig. 36 Hoop Liner Strain

Tendon Strain

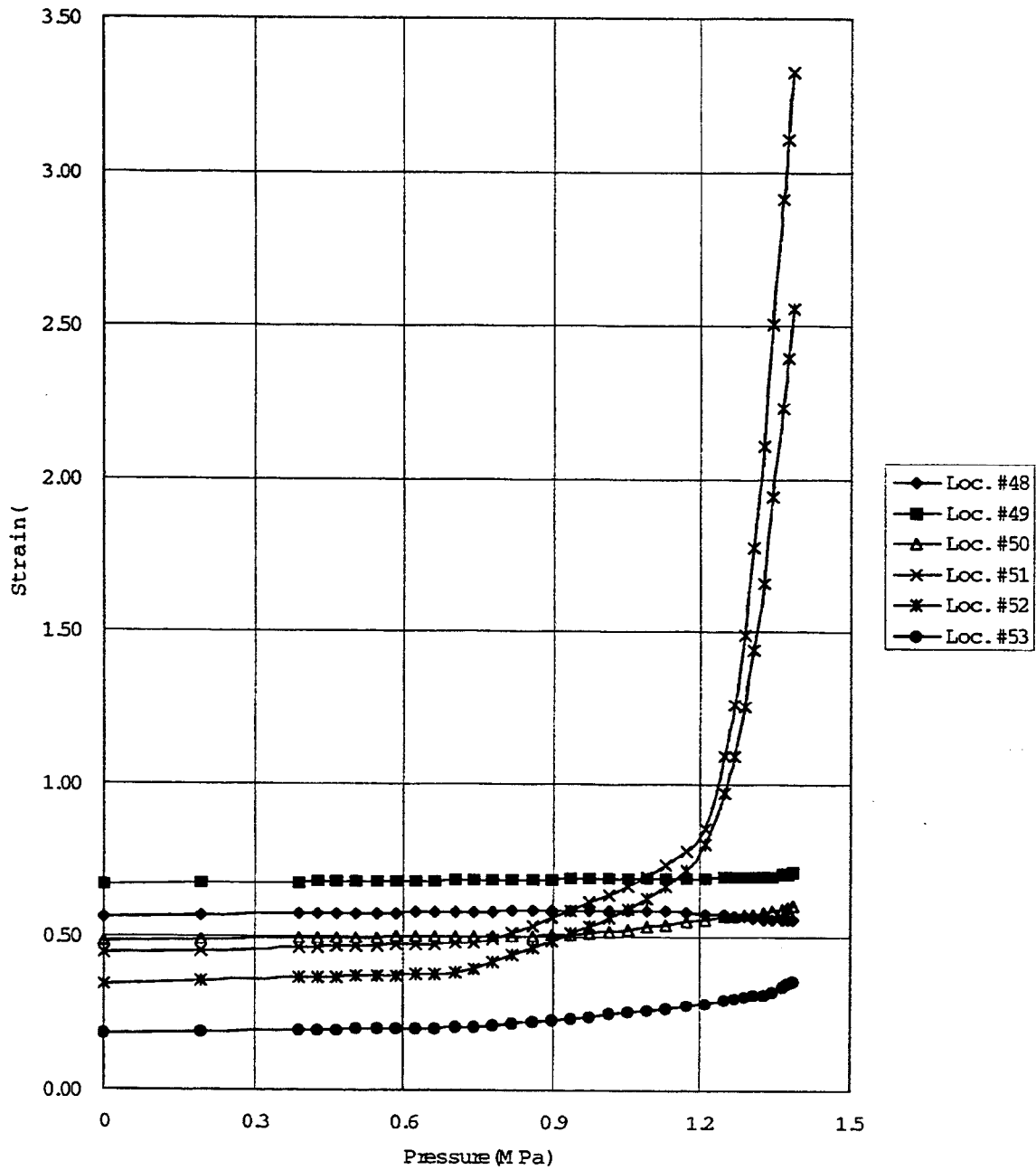


Fig. 37 Tendon Strain

Tendon Force

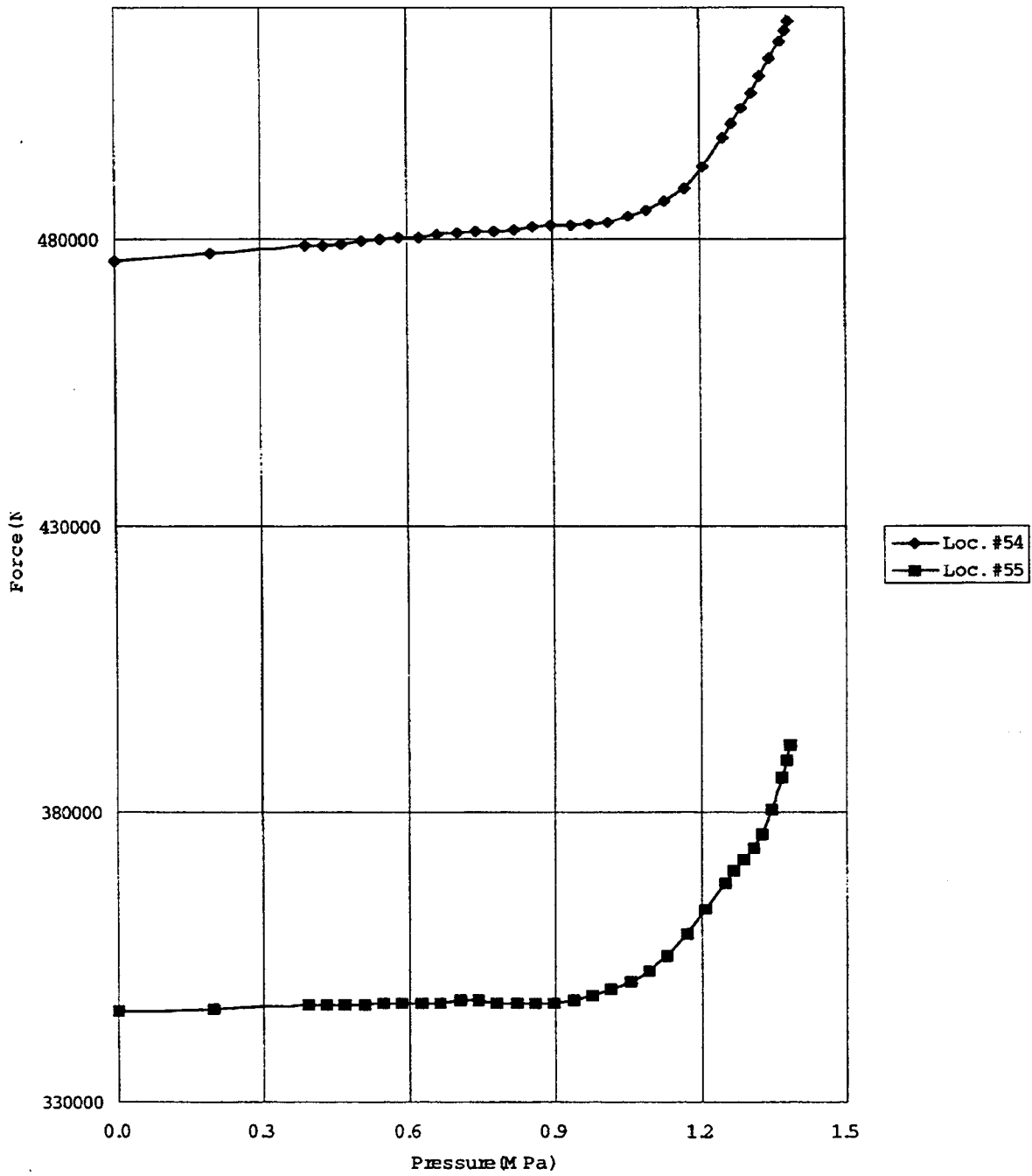


Fig. 38 Tendon Force

**APPENDIX N**

**KOPEC**

**KOREA POWER ENGINEERING COMPANY**

**KOREA**

Appendix A, Composite Plots, comprises test data compiled and plotted from all organizations that participated in the Prestressed Concrete Containment Vessel (PCCV) Round Robin Pretest Analysis. To avoid duplicating the composite information, individual sets of data and/or plots have been omitted from participants' reports. In some cases this action resulted in disconnects between callouts and content and in the numbering of figures, tables, and pagination in some reports.

In Appendix N, "KOPEC, Korea Power Engineering Company, Korea," discontinuity arises from omitting the following material:

Appendix A, "55 Standard Output for PCCV Round Robin Analysis"

# Table of Contents

I. Introduction	1
II. Constitutive Equations and Mathematical Model	3
1. Concrete	3
1.1 Menetrey-Willam's Failure Criterion for Axisymmetric Model	3
1.2 Modified Drucker-Prager's Failure Criterion for Three-dimensional Model	4
2. Stress-Strain Relationship of Reinforced steel (Rebar)	5
3. Stress-Strain Relationship of Tendon	6
4. Stress-Strain Relationship of Liner Steel	7
III. Material Properties	8
1. General	8
2. Concrete	8
3. Reinforcing Steel	8
4. Post-tensioning Steel Tendon	9
5. Liner Plate	9
IV. Finite Element Analysis Model	11
1. Simplified Numerical Analysis	11
2. Axisymmetric Finite Element Model	11
2.1 General	11
2.2 Shell and Dome Model	12
2.3 Base Slab Model	12
3. Three-dimensional Finite Element Model	13
3.1 General	13
3.2 Shell and Dome Model	13
3.3 Base slab Model	15
3.4 Prestressing Tendon Model	15

3.5 Self-weight and Internal Pressure	18
4. Probabilistic Pressure Capacity	18
V. Analysis results and Discussions	20
1. Standard Outputs for PCCV Round Robin Analysis	20
2. Results and Discussions	20
2.1 General	20
2.2 Axisymmetric Model	21
2.3 Three-dimensional Model	22
References	29
Appendix-A : 55 Standard Output for PCCV Round Robin Analysis Submitted to Sandia National Lab.	
Appendix-B : Output for PCCV Round Robin Analysis for Comparison with the Results from Three-dimensional Model	

## **I. Introduction**

The purpose of the work contained herein is to summarize the pretest analysis results performed by Korea Power Engineering Company to determine the ultimate pressure capacity of pre-stressed concrete containment (1:4 scale PCCV) designed by OBAYASI and MISUBISHI [1].

For the nonlinear finite element analysis, the Sandia National Laboratories 1:4-scale prestressed concrete containment structure is idealized as an axi-symmetric model and a three dimensional global model. In order to simulate the real behavior of the PCCV, both numerical models are refined by the comparison of the results or the existing research results. Also, more recently developed material models for concrete are introduced to the finite elements models: One is Menetrey-Willam's concrete failure criterion which is used for the axisymmetric model, and the other is the Modified Drucker-Prager's model which is used for the three dimensional global model.

Prior to performing the nonlinear finite element analysis, the internal pressure capacity of the containment shell sections in which only membrane forces are predominant, such as the midheight cylindrical portion is first predicted by a simple numerical analysis. The actual pressure capacity and the mode, location, and size of failure were determined based upon nonlinear finite element analysis for increasing pressure magnitudes including pressure levels corresponding to the requested events milestones

The computer program ABAQUS [2] was used to analyze an axisymmetric finite element model and a three dimensional model of the containment using nonlinear material properties of concrete, liner plate, reinforcing steel, and prestressing tendon by increasing the internal pressure to failure. The final results include the failure mode and the corresponding internal pressure level.

Nonlinear analysis results showed that the hoop membrane section near mid-height of the cylinder wall is the critical section in both models. Based on the analysis results, the ultimate internal pressure capacity is determined to be 1.514MPa and 1.491MPa, respectively, for the axisymmetric model and the three dimensional global model. The ultimate pressure capacities obtained from both finite element analysis models are larger than the ultimate pressure capacity obtained by simple numerical analysis using Mathcad calculations.

Details of the analysis are provided in the body of this report. The response plots at 55 standard output locations are derived from both models, axisymmetric and three-dimensional model. However, the results from the three-dimensional analysis model are officially submitted to Sandia National Laboratories and those from the axisymmetric model are provided for a reference. The response plots from both are included in Appendix-A and B, respectively. Also, in order to obtain better understanding of the

numerical modeling, a comparisons addressing the consistency or inconsistency of both results from the two finite element modeling is performed for the PCCV.

## II. Constitutive Equations and Mathematical Model

### 1. Concrete

Concrete is characterized by nonlinear material deformation behavior. The material non-linearity is assumed to occur due to cracking of concrete in tension and plasticity of concrete in compression. However, the material non-linearity due to the latter, that is the compressive failure of the concrete, is relatively less important than that due to the former in this study since the failure mode of the containment structure under internal pressure governs the tensile cracking mode. Therefore, the Menetrey-Willam's and the Modified Drucker-Prager's failure model to represent the tensile concrete cracking are respectively introduced for the axisymmetric and the three-dimensional finite element analysis

#### 1.1 Menetrey-Willam's Failure Criterion for Axisymmetric Model

The concrete non-linearity has been reproduced by using the Menetrey-Willam's Model with non-associated plastic flow potential which is able to reproduce a pressure dependent yield criterion where tensile and compressive strength are different.

The concrete failure criteria in this model depend on a set of three independent scalar invariants. For geometric interpolation, the Haigh-Westergaard coordinates are used in the following equation.

$$\zeta = \frac{1}{\sqrt{3}} I_1 \quad (1)$$

$$\rho = \sqrt{2J_2} \quad (2)$$

$$\cos 3\theta = \frac{3\sqrt{3}}{2} \frac{J_3}{\sqrt{J_2^3}} \quad (3)$$

Where  $\zeta$  is the hydrostatic stress invariant,  $\rho$  is the deviatoric stress invariant, and  $\theta$  is the deviatoric polar angle. The circular trace of the deviatoric polar radius  $\rho(\theta)$  is transformed into a triple symmetric ellipse through the elliptic function  $r(\theta, e)$  as follows, which was developed by Klisinski based on the five-parameter model by Willam-Warnke [3].

$$r(\theta, e) = \frac{4(1-e^2)\cos^2\theta + (2e-1)^2}{2(1-e^2)\cos\theta + (2e-1)\sqrt{4(1-e^2)\cos^2\theta + 5e^2 - 4e}} \quad (4)$$

The polar radius  $r(\theta, e)$  extends to all polar directions  $0 \leq \theta \leq 2\pi$  using the three-fold symmetric. Convexity and smoothness of the elliptic function require that  $0.5 \leq e \leq 1.0$ .

This model is characterized by hyperbolic yield surface in the meridian plane  $p - R_{mw}q$ , where  $p$  is a pressure and  $R_{mw}q$  is a Menetrey-Willam equivalent stress.

From the relationships between the Willam-Warnke model, the Mohr-Coulomb model, and the Menetrey-Willam model, equation (4) can be translated into equation (5) [3].

$$R_{mw}(\theta, e) = \frac{4(1-e^2)\cos^2\theta + (2e-1)^2}{2(1-e^2)\cos\theta + (2e-1)\sqrt{4(1-e^2)\cos^2\theta + 5e^2 - 4e}} R_{mc}\left(\frac{\pi}{3}, \phi\right) \quad (5)$$

Where  $R_{mc}\left(\frac{\pi}{3}, \phi\right) = \frac{(3 - \sin\phi)}{6 \cos\phi}$  is a polar radius of the  $\phi$ -plane in the Mohr-Coulomb model. When the eccentricity value is taken as  $e = 0.52$ , the resulting failure trace of this model provides close agreement with the experimental data by Kupfer, Hilsdorf, and Rush[4]. When the eccentricity value is 0.52, the friction angle and the dilation angle, which can be induced from the relationships between the Mohr-Coulomb model, the Drucker-Prager model, and the Menetrey-Willam model, are 71.56 degrees and 56.97 degrees, respectively. Also, based on Smith's experimental study the non-associated plastic flow potential is adopted for this model[5]. Therefore, an unsymmetric system of equations is created and the UNSYMM=YES parameter on the \*STEP option is used in ABAQUS.

## 1.2 Modified Drucker-Prager's Failure Criterion for 3D Model

A Modified Drucker-Prager's failure criterion is used to represent the tensile concrete cracking for the three-dimensional analysis model as aforementioned. In this failure model, the yield surface and flow potential parameters for elastic-plastic material are defined by setting of the model parameters such as the  $K$ -factor, the friction angle  $\beta$ , and the dilation angle  $\psi$ [2]. The non-associated flow potential and the strain hardening are considered. This failure model provides approximate global solutions since the orthotropic nature of the post-cracking is not captured.

The Drucker-Prager yield function is written as equation (6)[2, 6].

$$F = t - p \tan \beta - d = 0 \quad (6)$$

Where  $t = (q/2)[1 + (1/K) - (1 - 1/K)(r/q)^3]$ , with the stress invariants,  $p$ ,  $q$ ,  $r$ , defined in stress and strain measurements. The shear strength of the material,  $d$ , is related to the uniaxial tension or compression yield stress. In the case of tension yield stress, the shear strength of the material is defined by equation (7).

$$d = \left(\frac{1}{K} + \frac{1}{3} \tan \beta\right) \sigma, \quad (7)$$

The material parameter  $K(\theta, f_\alpha)$  controls the shape of the yield surface in the deviatoric plane. To ensure convexity of the yield surface,  $K(\theta, f_\alpha)$  must use between 0.778 and 1.0. The friction angle  $\beta$  is the angle between the yield surface and the pressure stress axis in the meridian plane.

The plastic flow potential for this model is written as equation (8),

$$G = t - p \tan \psi \quad (8)$$

where the dilation angle  $\psi$  is the angle between the flow potential and the  $p$ -axis in the meridian plane. When the material parameter is taken as  $K = 0.778$ , the resulting failure trace of this model provides good agreement with the failure trace of the Menetrey-Willam model at  $e = 0.52$ . The friction angle and the dilation angle, which can be induced from the relationships between the Mohr-Coulomb model, the Drucker-Prager model, and the Menetrey-Willam model, are 71.56 degrees and 56.97 degrees, respectively. The non-associated plastic flow potential is adopted for this model and thus the UNSYMM=YES parameter on the \*STEP option is used in ABAQUS.

## 2. Reinforcing Steel (Rebar)

Rebar materials are generally incompressible when they deform plastically and yielding is independent of the pressure stress. The von Mises failure criterion is therefore used for this steel material.

According to Hsu's study result [7], the stress-strain curves of a bare steel bar and of a steel bar embedded in concrete are quite different. The stress-strain relationship of rebars embedded in concrete are introduced in the analysis instead of those for bare rebars. The shape of the stress-strain curve of the rebar resembles two straight lines with the slope of  $E_s$  before yielding and the slope of  $E_p'$  after yielding as shown in the Figure 1. The stress level at which the two straight lines intersect is designated as  $f_y'$ .

$$f_s = E_s \varepsilon_s \quad \text{for } f_s \leq f_y', \quad (10)$$

$$f_s = f_o' + E_p' \varepsilon_s \quad \text{for } f_s > f_y', \quad (11)$$

where,  $f_o'$  is the vertical intercept of the post-yield straight line. The intersection stress level  $f_y'$  and the plastic modulus  $E_p'$  depend mainly on the level of the apparent yield stress  $f_y^*$ . Assuming that  $f_y'$  and  $E_p'$  are linear functions of  $f_y^*$ ,

$$\frac{f_y'}{f_y} = 0.43 + 0.5 \frac{f_y^*}{f_y} \quad (12)$$

$$\frac{E_p'}{E_p} = 3.3 - 2.5 \frac{f_y^*}{f_y} \quad (13)$$

The plastic modulus,  $E_p$ , is the slope for the strain-hardened bare rebar. All rebars in the prestressed containment structure are modeled by using the rebar sub-element provided by ABAQUS.

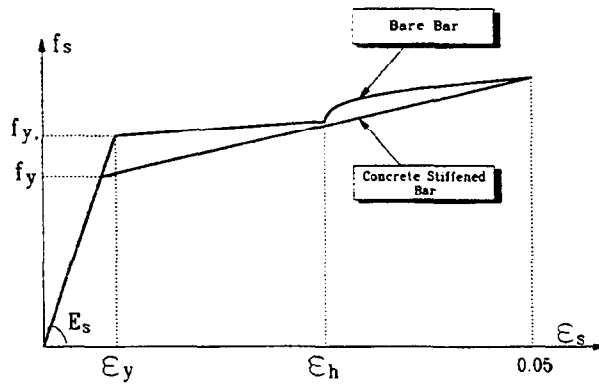


Figure 1 Stress-strain relationship of rebar using bilinear model

### 3. Prestressing Tendon

The stress-strain curve of tendon consists of two straight lines jointed by a curve knee shown in Figure 2. The first part is a straight-line up to  $0.7f_{pu}$ , where  $f_{pu}$  is the ultimate strength of the tendon. The second part is expressed by the Ramberg-Osgood equation that meets the first part at a stress level of

$0.7f_{pu}$ . The Ramberg-Osgood equation (14) is as follows :

$$f_p = \frac{E_{ps}' \varepsilon_p}{\left[ 1 + \left( \frac{E_{ps}' \varepsilon_p}{f_{pu}} \right)^4 \right]^{1/4}} \quad (14)$$

where  $f_p$  is the stress in the tendon,  $E_p'$  is the tangential modulus Ramberg-Osgood curve at zero load, and  $\varepsilon_p$  is the sum of the strain in the tendon.

In the finite element methodology, tendons can be modeled by either the discrete, the embedded or the smeared approach. KOPEC has used the embedded approach available in ABAQUS and thus tendons are modeled by using the rebar sub-element in concrete. Modeling the tendons as rebar sub-elements implies that the tendons are assumed bonded to the concrete. That is, slippage of a tendon within the tendon sheath is not considered due to the limitation of ABAQUS in the study.

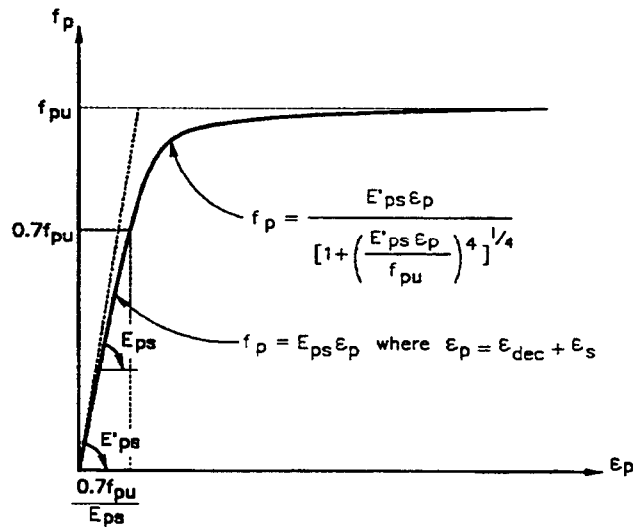


Figure 2 Stress-strain relationship of prestressing tendon

#### 4. Liner Steel

The stress-strain behavior of the liner plate steel is modeled by using an elasto-plastic model that is available in ABAQUS. The von Mises failure surface with kinematic hardening is used to represent the nonlinear behavior of the material.

### III. Material Properties

#### 1. General

To obtain a realistic estimate of the capacity of the 1:4-scale prestressed concrete containment structure, the actual properties are used instead of nominal properties for the concrete, reinforcing steel, post-tensioning tendons and liner plate. The actual material properties used in the construction of the 1:4-scale PCCV are established from test data provided by Sandia National Laboratories for materials[1].

#### 2. Concrete

The material data for trial mix concrete based on the field curing are used for the numerical analysis and the compressive strengths of concrete for pours to date, 13 weeks (@91 days) are used instead of the specified strength to simulate more realistic behavior of the 1:4 scale PCCV. The selected material properties based on the above are given in Table 1.

Table 1 Concrete material properties

	Basemat	Shell & Dome
Elastic modulus (MPa)	$2.795 \times 10^4$	$2.697 \times 10^4$
Compressive strength(MPa)	-39.16	-47.30
Tensile strength(MPa)	3.37	3.45
Poisson's ratio	0.18	0.18

#### 3. Reinforcing Steel

The stress-strain behavior of the reinforcing steel is modeled by using the elasto-plastic model in the computer program ABAQUS. The material properties for each rebar type are selected from the test data and the following rebar sizes shown in Table 2 are included in the numerical model. Also, the rebar types are decided per the rebar specification shown in drawing of model-general arrangement [1] as, (1) SD 490 for basemat main bar and around tendon gallery opening, (2) SD390 for the basemat shear bar, main bar and bar around wall opening, and (3) SD345 for the radial tie. However, the shear bar in the basemat and the radial tie in the wall are not included in the three-dimensional finite element model due to limitation

of numerical model.

Table 2 Reinforcing material properties

	D6 (SD345)	D10 (SD390)	D13 (SD390)	D16 (SD390)	D19 (SD390)	D22 (SD390)	D19 (SD490)
Elastic modulus(MPa)	1.69E5	1.83E5	1.83E5	1.83E5	1.84E5	1.91E5	1.86E5
Poisson's ratio	0.3	0.3	0.3	0.3	0.3	0.3	0.3
Yield stress(MPa)	369.4	472.9	432.3	457.5	473.1	459.0	512.2
Ultimate stress(MPa)	489.4	652.8	610.6	616.5	658.3	680.8	709.7
Elongation(%)	30.4	20.5	24.2	22.1	21.1	18.7	17.8

#### 4. Prestressing Tendon

The following material properties are decided based on the tendon system test data from Sandia Laboratories and the stress-strain relationship of tendon aforementioned in section II.4. The smallest ultimate stress of tendon among those for the six specimens tested are used for post-tensioning tendon model. The elastic modulus and elongation are directly from the tendon system test data. Also, the elastic limit stress is defined as 70% of the ultimate stress and the yield stress corresponding to 1% yield strain is calculated by the equation (14).

- Elastic modulus = 1.91E5MPa
- Poisson's ratio = 0.3
- Elastic limit stress = 1.339E3Mpa
- Yield stress = 1.691E3Mpa
- Ultimate stress = 1.912E3MPa
- Elongation = 3.51%

#### 5. Liner Plate

Two sets of liner material samples, LPY in meridional and LPX in hoop, were provided by Sandia national Laboratories [1]. However, for simplified numerical modeling, the following average material

properties for hoop with lower yield stress are considered for both directions in the numerical model. The differences of material properties for both are negligible and thus the effects on the analysis results are judged to be also negligible.

- Elastic modulus = 2.187E5Mpa(2.23E+04 kgf/mm<sup>2</sup>)
- Poisson's ratio = 0.3
- Yield stress = 375.595Mpa(38.3 kgf/mm<sup>2</sup>)
- Ultimate tensile stress = 499.158Mpa(50.9 kgf/mm<sup>2</sup>)
- Elongation = 33.0%

## **IV. Finite Element Analysis Model**

This section describes the finite element analytical model developed for the iterative nonlinear analysis by the ABAQUS computer program [2] to determine the internal pressure capacity of the pre-stressed concrete containment. Two finite element models are developed for the analysis of 1:4 scale PCCV model: One is an axisymmetric finite element model and the other is the three-dimensional global model.

### **1. Simple Numerical Analysis**

A preliminary prediction of internal pressure capacity of the containment concrete section is needed to make a more efficient finite element model. Therefore, the capacity of containment shell section such as the midheight cylindrical portion in which only membrane forces is predominant, is first predicted by using a the simple numerical analysis. Mathcad performs the simple analysis with algorithm considering force equilibrium and strain compatibility [8].

The predicted pressure at concrete cracking from the simple calculation is determining to 0.64MPa. The pressures corresponding to liner yielding and reinforced steel yielding are respectively 1.005MPa and 1.198MPa. The pressures at the elastic limit or at yielding strain of the tendon are predicted as 1.034MPa and 1.323Mpa, respectively. That is, the predicted internal pressure capacity of the 1:4 PCCV model can be judged 1.323MPa. Also, the pressure corresponding to 2% and 3% strain of the tendons are calculated as 1.358MPa and 1.393MPa, respectively.

The simple analysis shows that the concrete cracks are first developed, yielding of the liner and reinforcing bars occurred next and finally the prestressing tendon yield. The radial displacements corresponding to the pressures are shown in the Figure 3 and the above-predicted capacity can be also judged from this figure.

### **2. Axisymmetric Finite Element Model**

#### **2.1 General**

The axisymmetric finite element model which is utilized to predict the overall response of the 1:4 PCCV under internal pressurization is first established as shown in Figure 4. This model consists only of the axisymmetric cylindrical vessel, a spherical dome and the concrete base slab. This model is intended to provide the general global behavior of the PCCV model considering uplift. This model consists of 809 axisymmetric solid elements, nonlinear soil spring elements and 4698 nodal points as shown in Figure 4. Prestressing tendon modeling, pressurization and self-weight are similarly considered as those for three-

dimensional model in the following Section 3.

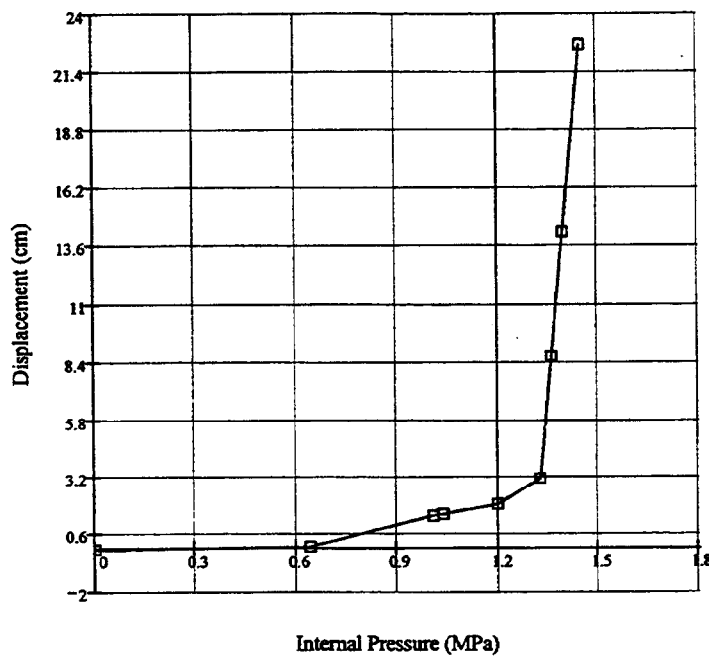


Figure 3 Radial displacement corresponding to the internal pressure

## 2.2 Shell and Dome Model

The dome and cylindrical wall concrete is modeled with eight-node axisymmetric solid elements. The liner steel on the inside surface of the PCCV is made up of three-node shell elements. The liner elements, which are offset from the prestressed concrete elements, are connected to the concrete solid elements by rigid link elements. All rebars and tendons are assumed to remain rigidly bonded to the concrete and thus are modeled by using the rebar sub-element provided by the ABAQUS computer program. Vertical liner anchors are modeled as a beam of rectangular cross-section dimension. The cross-sections of liner anchors are computed based on the area and the bending stiffness of the embedment. Prestressing is induced in the tendons with use of the \*INITIAL CONDITIONS option in ABAQUS.

## 2.3 Base Slab Model

The base slab is included in the finite element model to simulate the possible vertical uplift of the base

during internal pressurization and to estimate the effect of the base slab on the failure mode. The previously described shell and dome model is connected to the base slab model and consists of eight-node solid elements. The tendon gallery is considering in the model.

The floor liner plate is assumed rigidly connected to the eight-node concrete solid elements since the effect of steel and concrete interaction during the flexural deformation of the slab is not significant for the thick base slab of the PCCV. Reinforcement of the slab is estimated from the provided structural drawings and is included in the analysis model. All rebars in the basemat are modeled as those of shell portion by using the rebar subelement of ABAQUS.

The bottom of the slab rests on a soil foundation, which is modeled by nonlinear soil springs with tension cut-off. Since Sandia National Laboratories did not provide the soil properties, the compression stiffness is considered as an empirically large value, which did not, happen the compressive behavior and the tension stiffness was neglected.

### **3. Three-dimensional Finite Element Model**

#### **3.1 General**

The three-dimensional finite element model includes large penetrations, such as equipment hatch and airlock, which will cause deviation from an axisymmetric response and may decrease the capability of the PCCV. In order to simulate more realistic behavior near these regions, a more refined mesh is developed as shown in Figure 5. Also, a rigid interconnection between shell element in the base slab and shell elements in the wall is introduced to properly simulate the shell/slab junction. The model consists of 1720 four-node shell elements, nonlinear soil spring elements and 1425 nodal points.

#### **3.2 Shell and Dome Model**

The dome and cylindrical wall are modeled with composite shell elements consisting of a thin inner layer of steel representing the liner and much thicker outer concrete multi-layers. All reinforcing bars in the dome and cylindrical wall are modeled by using the rebar sub-elements provided by the ABAQUS computer program. The tendons are also modeled as rebar sub-elements. Prestressing described in the following Section 3.4 is induced in the tendons with use of the \*INITIAL CONDITIONS option in ABAQUS. Aforementioned in the axisymmetric model, the tendons are similarly assumed to remain rigidly bonded to the concrete and thus modeled by using the rebar sub-element provided by ABAQUS computer program. Therefore, the slippage of a tendon within the tendon sheath can not be considered in the analysis model.

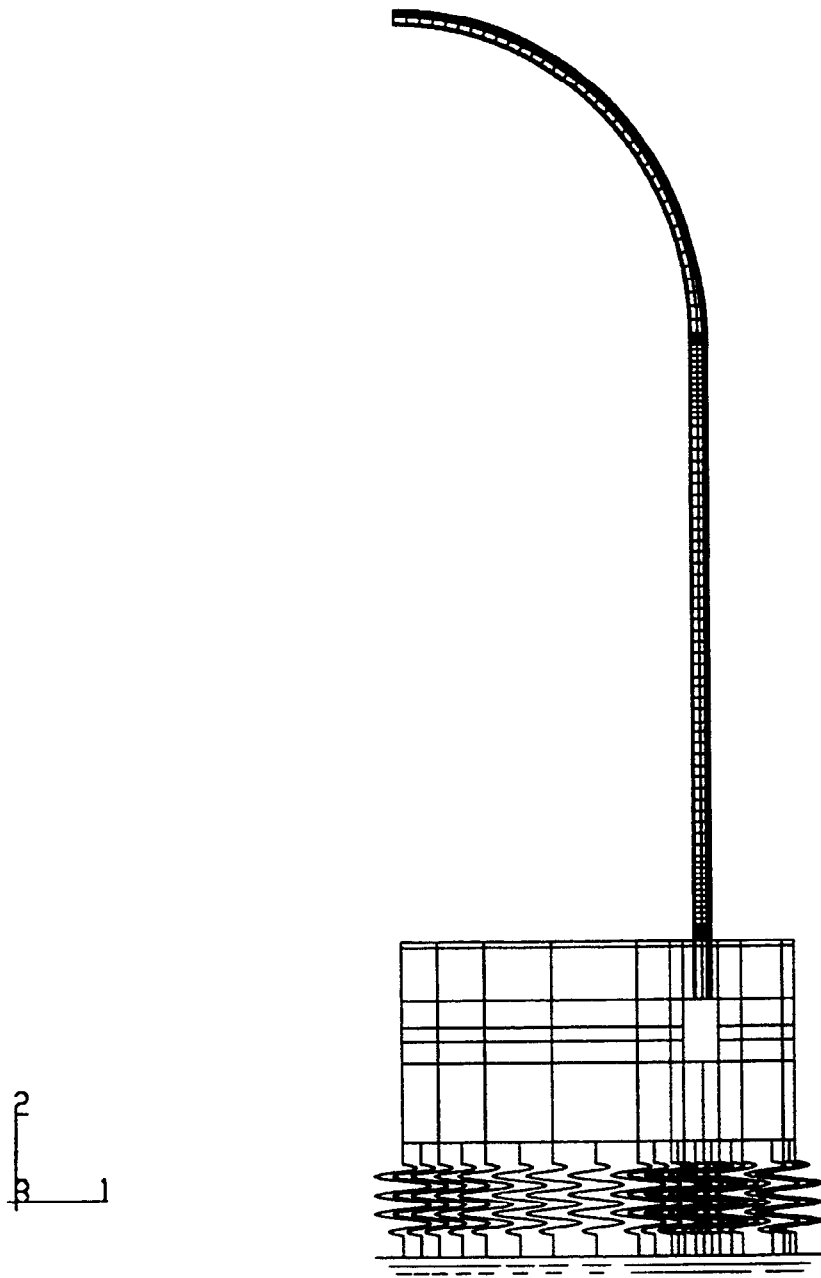


Figure 4 Axisymmetric Finite Element Model

### **3.3 Base Slab Model**

The reinforced concrete base slab is also modeled by four-node composite shell elements consisting of an inner thin layer of steel representing the liner and much thicker outer concrete multi-layers. Since the base slab is modeled by shell elements, the tendon gallery is not included in the three-dimensional model.

The bottom of the slab rests on a soil foundation, which is modeled by the nonlinear soil spring with tension cut-off as those for the previously described axisymmetric model. Since the soil properties were also not provided, an appropriate elastic modulus was introduced only to simulate the uplift by using the nonlinear spring with tension cut-off. That is, the compression stiffness is considered as an empirically large value, which did not happen the compressive behavior and the tension stiffness was neglected. All rebars in the base slab are modeled by using the rebar sub-element of ABAQUS.

### **3.4 Prestressing Tendon Model**

The magnitudes of stress along the length of the meridional and hoop tendon in the concrete are calculated with considering the prestress losses, which result from: (1) the friction between the tendon and the concrete, (2) the elastic shortening of the concrete, (3) the creep and shrinkage of the concrete, and (4) the stress relaxation in the prestressed tendons.

The vertical prestressing forces of 113.1kips before anchoring and 105.8kips after anchoring are introduced from the PCCV Model-General Arrangement provided by Obayashi Cooperation [1]. Based on the prestressing at anchorage, the magnitudes of stress along the length of the vertical tendon shown on Figure 6 are calculated and introduced in the finite element analysis model with consideration of losses shown in Table 3. That is, the tendon stresses after friction loss are considered at three locations of the numerical model, i.e. 1128.0MPa at the anchorage, 1221.0MPa at the springline and 789.988MPa at the apex of dome.

The hoop tendon forces of 101.9kips before anchoring and 78.7kips after anchoring provided by Obayashi Cooperation are also used in the calculation of tendon stress. The magnitudes of stress along the length of the hoop tendon are calculated as those for the vertical tendon and are shown on Figure 7. For the simplified numerical modeling, the averaged stress of 724.915MPa along the length of the hoop tendon is introduced in the finite element analysis model instead of varied tendon profile.

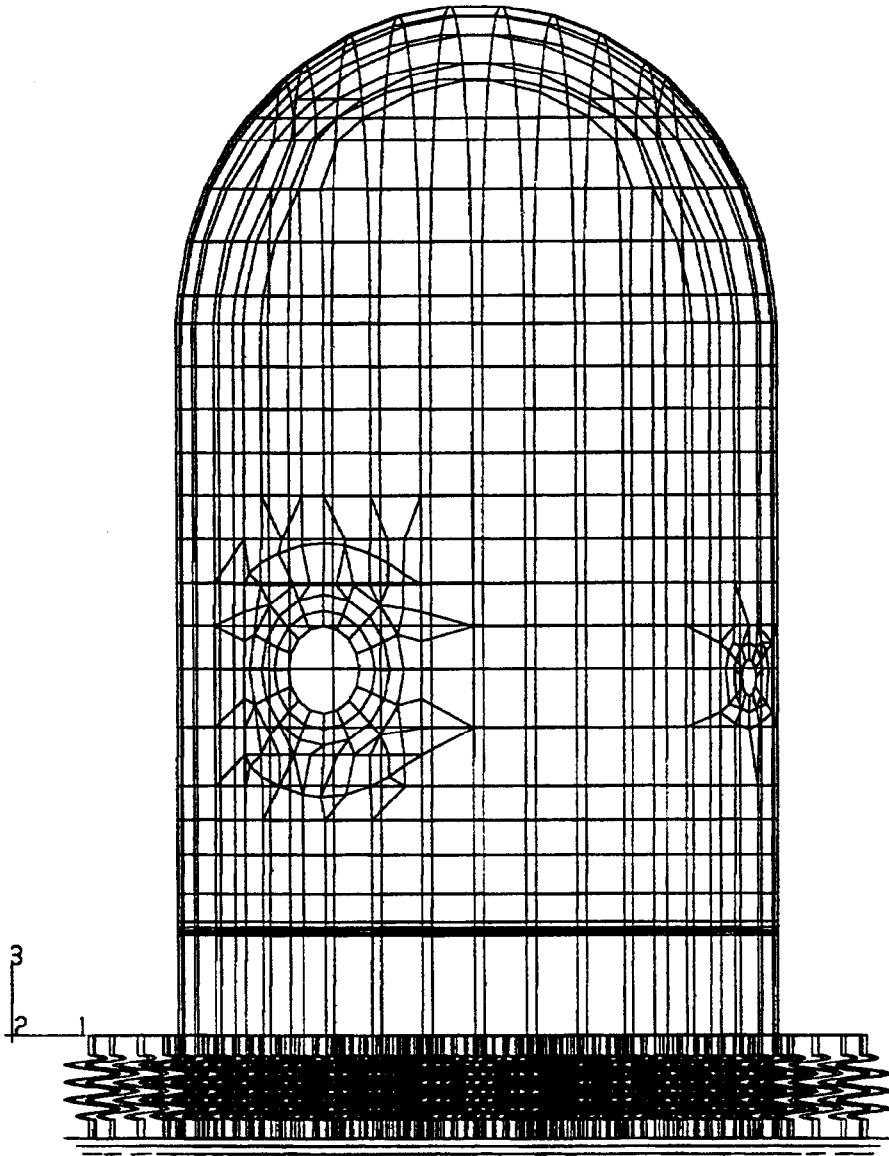
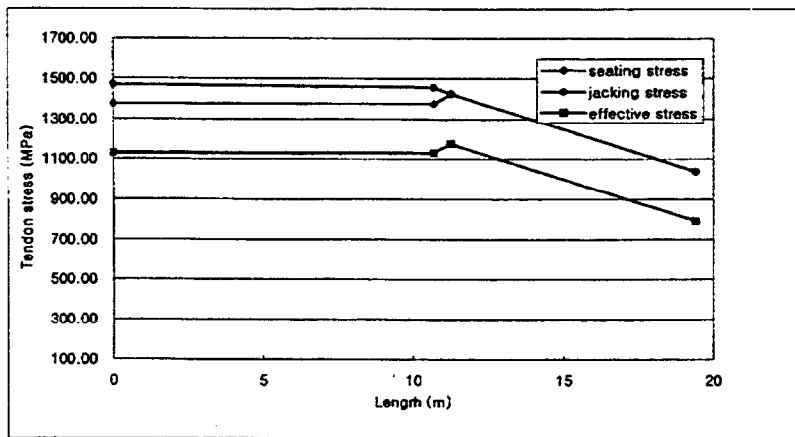


Figure 5 Three-dimensional finite element model

**Table 3 Losses of prestress**

	Vertical Tendon Loss, MPa(ksi)	Hoop Tendon Loss, MPa(ksi)
Elastic shortening of concrete	31.855(4.620)	31.855(4.620)
Creep of concrete	66.999(9.717)	83.829(12.158)
Shrinkage of concrete	129.309(18.754)	129.309(18.754)
Steel relaxation	19.747(2.864)	14.473(2.099)
<b>Total losses</b>	<b>247.910(35.955)</b>	<b>259.473(37.632)</b>



**Figure 6 Vertical Tendon Stress**

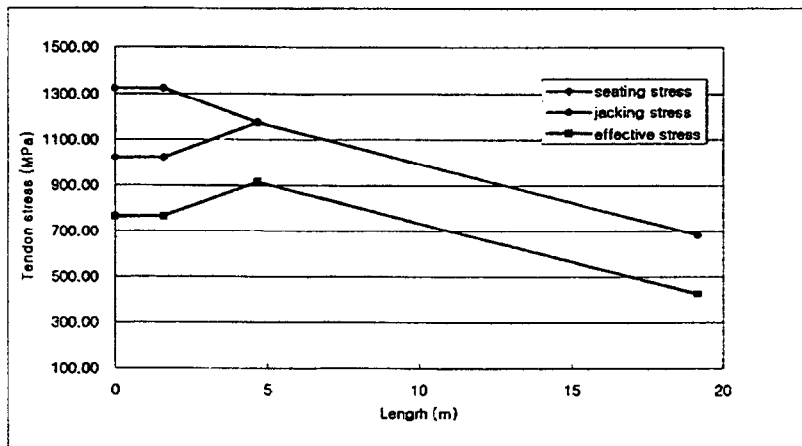


**Figure 7 Hoop Tendon Stress**

### 3.5 Self-weight and Internal Pressure

Because of the elastic support below the bottom slab, the effect of the weight of the structure had to be accounted. This is accomplished by specifying as a mass proportional load for each material included in the 1:4 scale PCCV model prior to initiating the internal pressure. The weights of each material are considered in the numerical model by using the GRAVITY parameter of \*DEAD LOAD option in ABAQUS.

Pressure loads are specified to act as a uniformly distributed force, remained normal to the interior element surface of the containment shell and base slab as it deforms. The magnitude of the internal pressure is applied in increments as shown in Figure 8 up to or beyond the failure pressure as defined by 3% strain in the post-tensioning tendons.

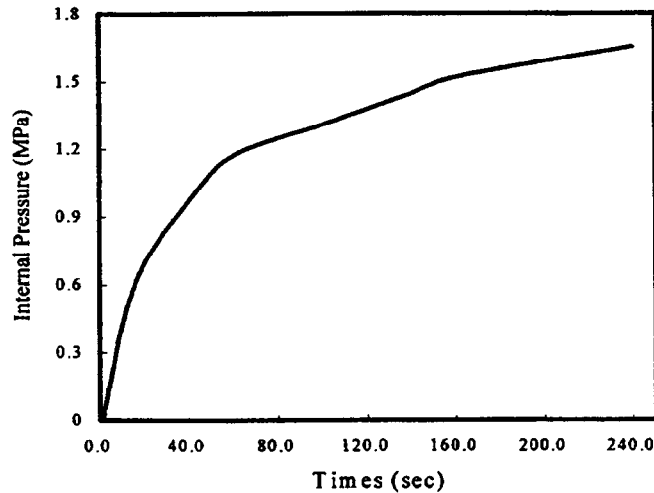


Figure 8 Internal Pressurization

### 4. Probabilistic Pressure Capacity

The internal pressure fragilities of the 1:4 scale PCCV model are determined in a similar procedure in Reference 9. Therefore, this report does not describe the detailed approach and only show how to derive the value for uncertainties. The pressure fragilities for the PCCV can be defined as the conditional probability of failure for a given level of internal pressure and thus is expressed in terms of its ultimate pressure capacity,  $P$ . In most case, the pressure capacity is expressed in the form:

$$P = P_m \beta_U \quad (15)$$

in which  $P_m$  is the median internal pressure capacity at which failure occurs and a logarithmic standard deviation  $\beta_U$  is a random variable that represents uncertainty in the median pressure capacity. The median internal pressure capacity  $P_m$  is the result derived from finite element analyses in the previous section.

The pressure capacity with a low probability of failure is considered to be the pressure at which there is only a 10% probability of exceedance or 90% non-exceedance. This capacity is determined as follows:

$$90\% \text{ Non - exceedance Pressure} = P_m \exp(-1.29 \beta_U) \quad (16)$$

Based on the properties of the lognormal distribution, the lognormal standard deviation associated with the uncertainty is composed of the lognormal standard deviations associated with the structure strength,  $\beta_S$  and the modeling accuracy,  $\beta_M$  as follows:

$$\beta_U = (\beta_S^2 + \beta_M^2)^{1/2} \quad (17)$$

The uncertainties of materials included in the PCCV model is obtained from SAND96-2445 and therefore, uncertainties for each material property is 0.08 for tendons, 0.10 for the reinforced steel, and 0.05 for the steel liner. The model uncertainty was neglected in this study. The uncertainty, therefore, is  $\beta_U = 0.13747727$ .

Based on the above, the maximum pressure capacity reachable with 90% confidence level is calculated to be 1.329MPa and 1.299Mpa, respectively, for the axisymmetric finite element analysis and the three dimension finite element analysis.

## **V. Analysis Results and Discussions**

### **1. Standard Outputs for PCCV Round Robin Analysis**

The pretest analysis results at 55 standard output locations from the three-dimensional model were officially submitted to the Sandia National Laboratories and are shown in the Appendix-A. Also, in order to provide information on the response of the 1:4 PCCV model, several output locations are added by KOPEC and analysis results at 55 standard locations from the axisymmetric model are shown in Appendix-B for comparison.

We considered the yielding of rebar to have occurred when the stresses in the rebars exceeded the nominal yield stresses defined as each rebar type. The computer program ABAQUS indicates the yielding for each rebar included in the finite element model automatically and thus the corresponding pressure level can be captured. The behavior of concrete up to the tensile strength is characterized by the theory of linear elasticity and a crack is initiated at tensile strength. In the ABAQUS, cracking is assumed to occur when the stresses reaches a failure surface, which is called the “crack detection surface”, and the program indicates the cracking automatically. Based on the above, the pressure levels corresponding to the events milestones requested by Sandia National Laboratories are shown in Table 4.

In addition to the events requested by Sandia national Laboratories, it is observed that the hoop rebar in the mid-height cylinder first yields at a pressure of 1.183MPa and the meridional outer rebar in the wall at spring line first yields at a pressure of 1.407MPa. Maximum radial displacement is obtained at the El. 6.20m and the azimuth 135° that is a standard output location and is shown in the plot-6. The analysis result indicates that the maximum strain of hoop tendon happens at mid-height of the cylinder near azimuth 225° and is shown in the plot-52.

### **2. Results and Discussions**

#### **2.1 General**

This section provides information on the response of the PCCV with regard to the deformations along shell and dome, as well as the strain or stress in the liner, the rebars and tendons. The overall deformed configuration of the PCCV at final stage is shown in figure 9 for axisymmetric with magnification 4.0 and in figure 10 for the three-dimensional model with magnification 7.3.

In order to improve the numerical model, the behaviors from both finite element models are also compared for each result. Comparison for the following cases is typically shown in this Section: (1) The

radial displacements at midheight of cylinder for each increments of internal pressure (Figure 11), (2) the vertical displacements at dome apex and wall base (Figure 12 and Figure 13), and the strain in the rebar, the liner and tendon (Figure 14 ~ Figure 17). The modes of failures predicted by both analysis models are similar except for a few cases.

**Table 4** Pressure levels(MPa) corresponding to the events milestones

	Axisym. Model	3-D Model
First cracking of concrete in cylinder due to hoop stresses	0.540	0.537
First cracking of concrete in cylinder due to meridional stresses	0.602	0.606
First yield of hoop rebar in cylinder	1.051	1.083
First yield of meridional rebar in wall-basemat juncture	-	1.469
First cracking of dome concrete above 45° dome angle	0.602	0.606
First cracking of dome concrete below 45° dome angle	0.602	0.606
Hoop tendons in cylinder reaching 1% strain	1.435	1.407
Hoop tendons in cylinder reaching 2% strain	1.474	1.453
Hoop tendons in cylinder reaching 3% strain	1.514	1.491
Best estimate of static failure pressure	-	-
Minimum pressure reachable with 90% confidence level	-	-
Maximum pressure reachable with 90% confidence level	1.329	1.299

## 2.2 Axisymmetric Model

Concrete cracking is initiated at 0.491MPa from the inside surface of the cylinder base and this is judged due to the out-of-plane bending behavior. Then, the hoop and meridional cracking of the cylinder are observed from the outside face of midheight at 0.540Mpa and 0.602Mpa, respectively. The cracks at the dome concrete above 45° dome angle and below 45° dome angle also formed at the same pressure of 0.602MPa. Cracks spreading over PCCV are occurred at the ultimate state.

The liner yielding at midheight of the cylinder is observed to start at a pressure of 0.76MPa, and then reaches the wall base at 0.89MPa. The hoop rebar yielding begins at midheight of the cylinder at 1.051Mpa and the maximum strain of hoop rebar at the final stage is observed as 7.84%. The maximum

strain of rebar is relatively small compared to the ultimate strain (22.1%) given for the PCCV.

The yield of hoop tendons starts at midheight of cylinder at 1.397Mpa, and the maximum strain of hoop tendon becomes 7.84% at final stage and the corresponding pressure is 1.525MPa. This strain is relatively larger than the ultimate strain of the tendon given as minimum 3.51% for the PCCV.

The probabilistic pressure of PCCV is calculated per the simplified method mentioned in the previous Section. The maximum pressure reachable with 90% confidence level is 1.329MPa.

### **2.3 Three-dimensional Model**

The concrete cracking is initiated from inside surface of cylinder base at 0.406Mpa. This is a little bit smaller than the corresponding pressure (0.491Mpa) from axisymmetric model. The hoop and meridional cracking of the cylinder occurs from outside face similarly to those from axisymmetric model at 0.537MPa and 0.606MPa, respectively. The cracks at the inside face of dome concrete above a 45° dome angle and below a 45° dome angle are formed at the same pressure as that for the meridional crack in cylinder, i.e. at 0.606MPa. Cracks are widely spreaded over the PCCV at the ultimate state.

The liner yielding corresponding to the 1% strain begins at midheight of cylinder when the pressure of 0.84MPa is applied and the yielding at the wall base is finally detected at 0.89MPa. The maximum strain of liner at the final stage reaches 3.16%. This is much less than the ultimate strain 33% and thus the failure of liner judged not to occur at final stage.

Similarly to the axisymmetric case, the yielding of hoop rebar begins at midheight of cylinder and the corresponding pressure is 1.083Mpa. The highest strain of hoop rebar observed is near the cylinder midheight in which the strained to 3.16% and the hoop rebar is strained to 3.18%.

The yield of hoop tendon is detected at first near the midheight of cylinder at 1.376MPa. The maximum strain of hoop reaches finally to 3.93% with 1.518Mpa and this strain can be compared to the minimum strain of the tendon, 3.51%.

The probabilistic pressure of PCCV is estimated based on the previously described simplified method. The calculated maximum pressure reachable with 90% confidence level is 1.299Mpa, which is a little less than that from the axisymmetric model. This may come from the missing of shear and radial tie due to the limitation of the three-dimensional finite element model.

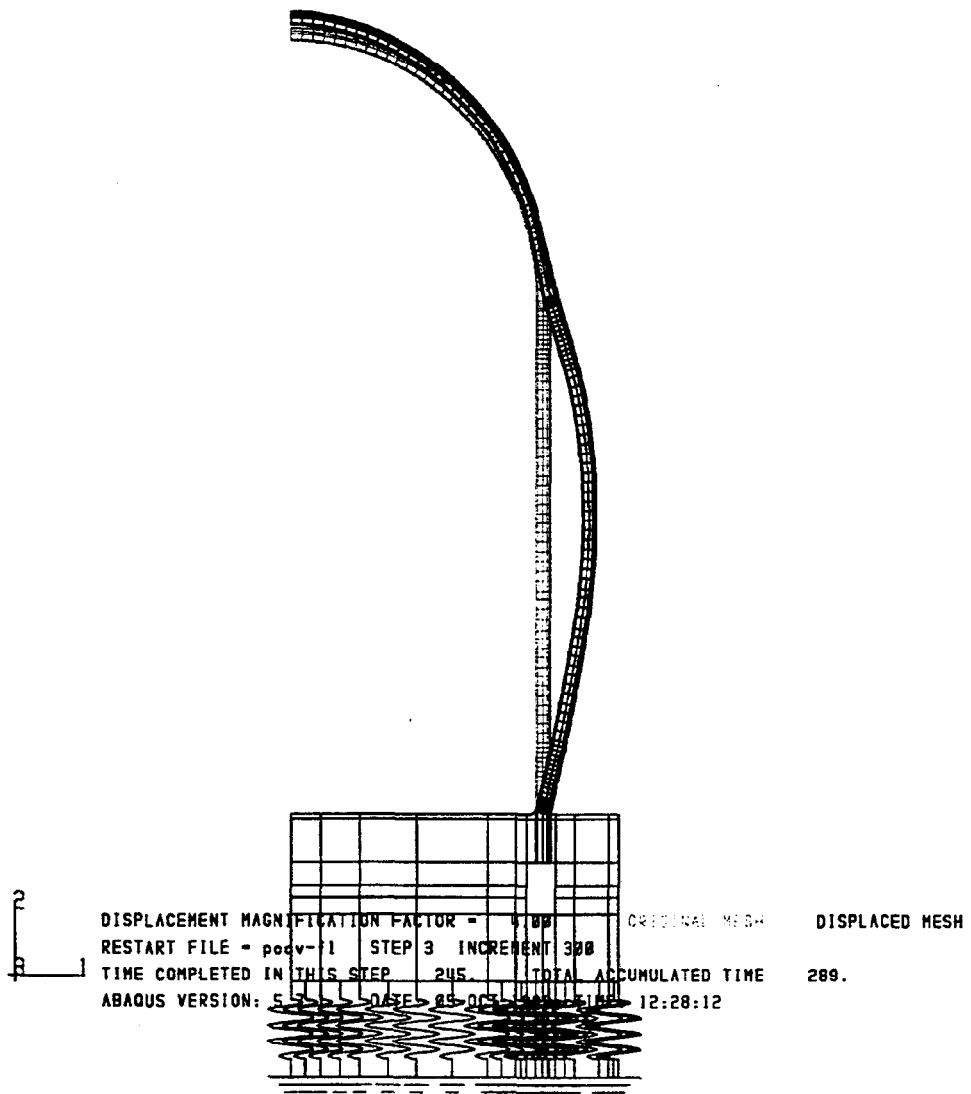


Figure 9 Deformed configuration of axisymmetric finite element model

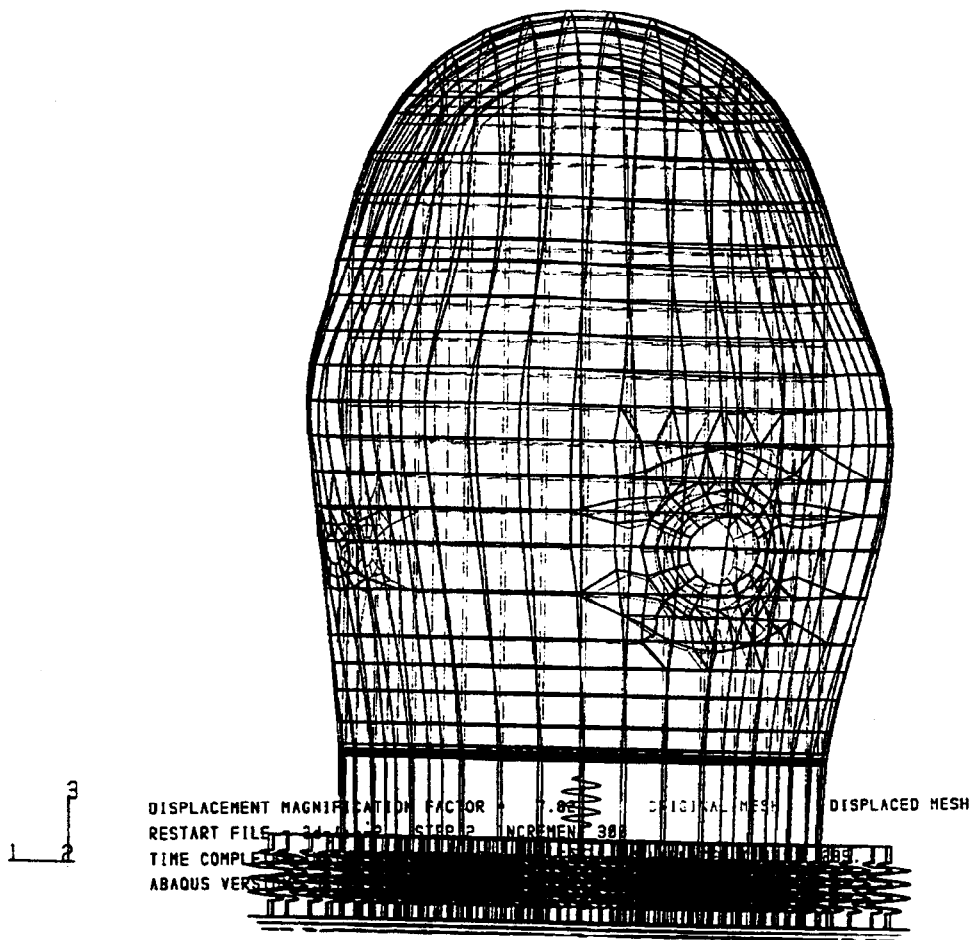


Figure 10 Deformed configuration of three-dimensional finite element model

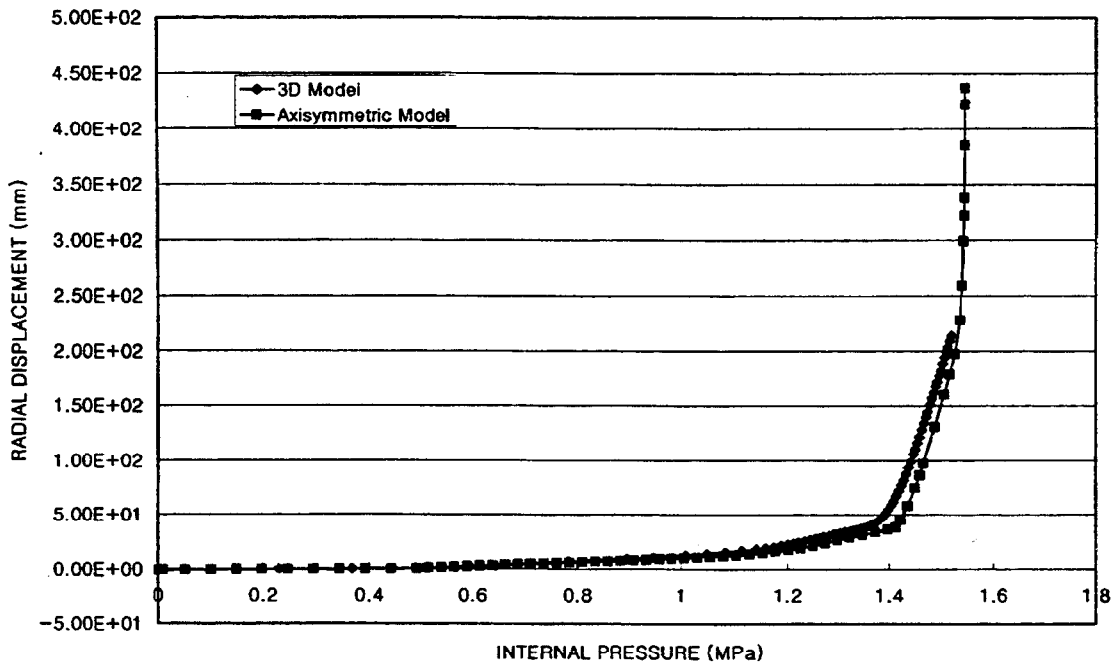


Figure 11 Radial displacement at the midheight of cylinder

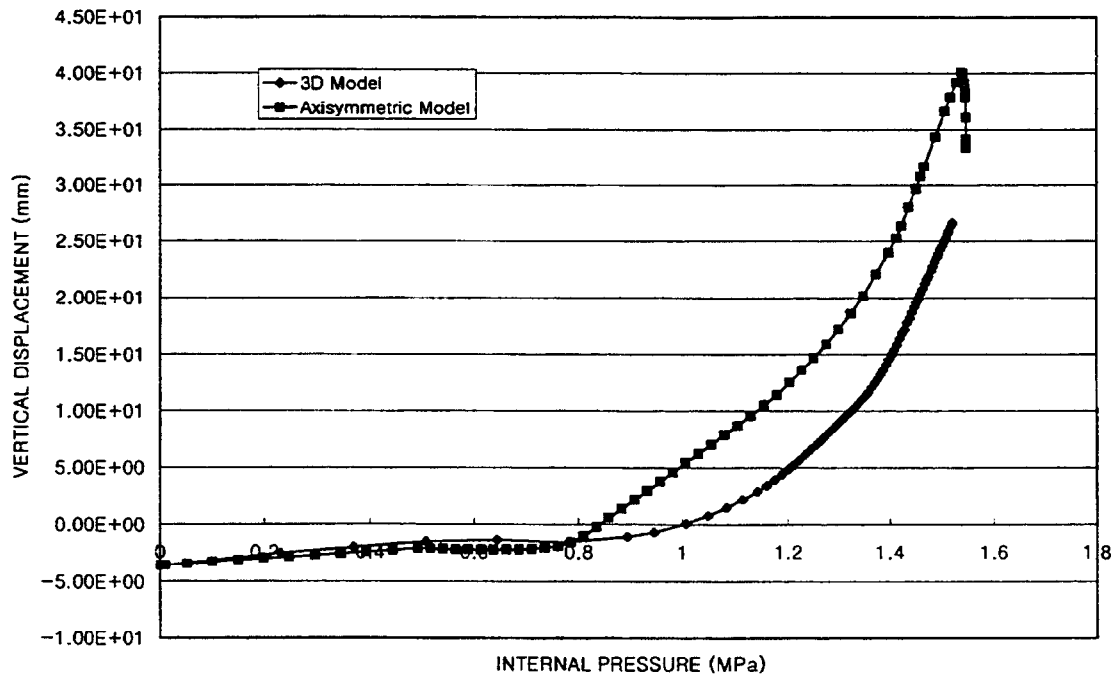


Figure 12 Vertical displacement at dome apex

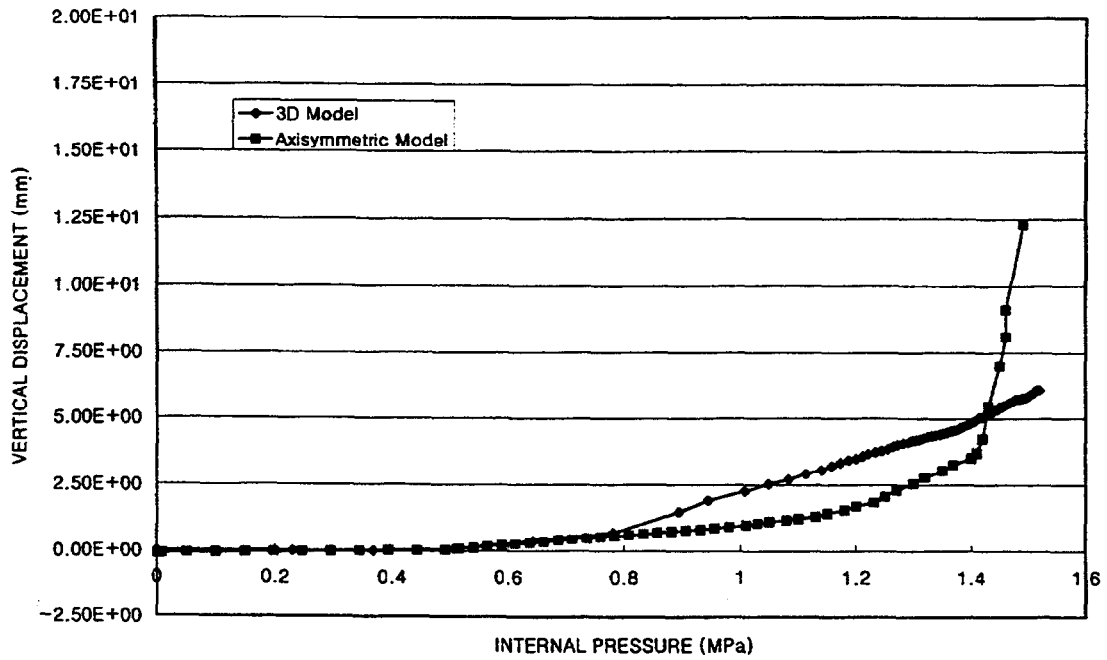


Figure 13 Vertical displacement at base slab

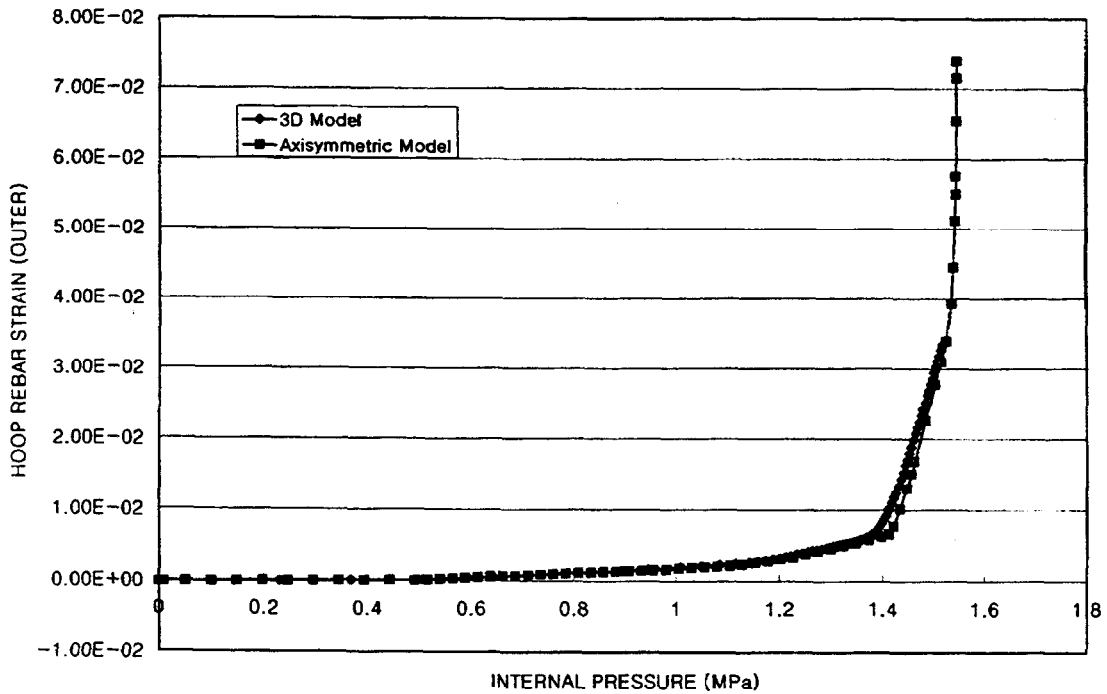


Figure 14 Strain of outer hoop rebar at the midheight of cylinder

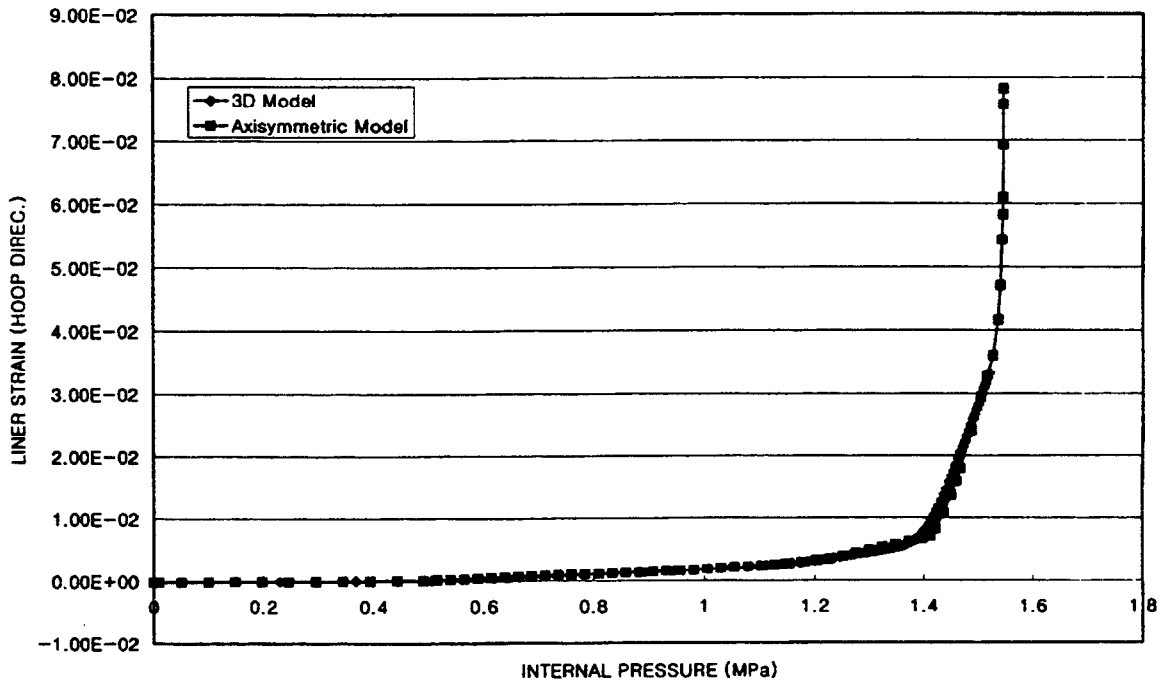


Figure 15 Hoop strain in liner at the midheight of cylinder

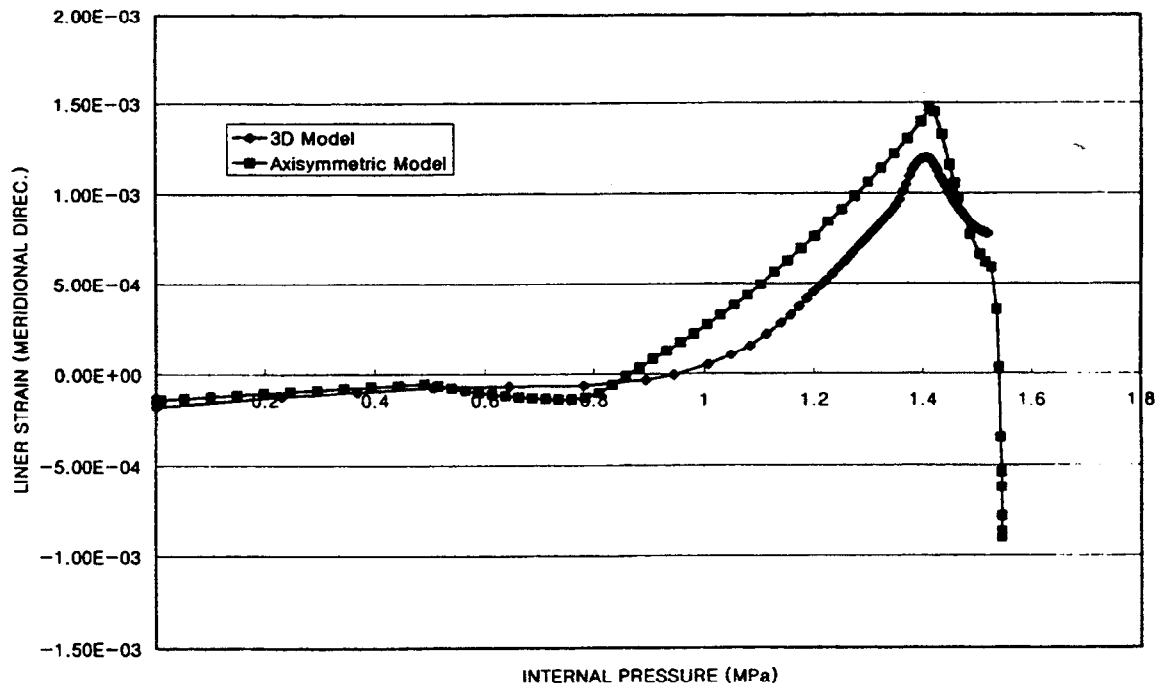


Figure 16 Meridional strain in liner at cylinder base

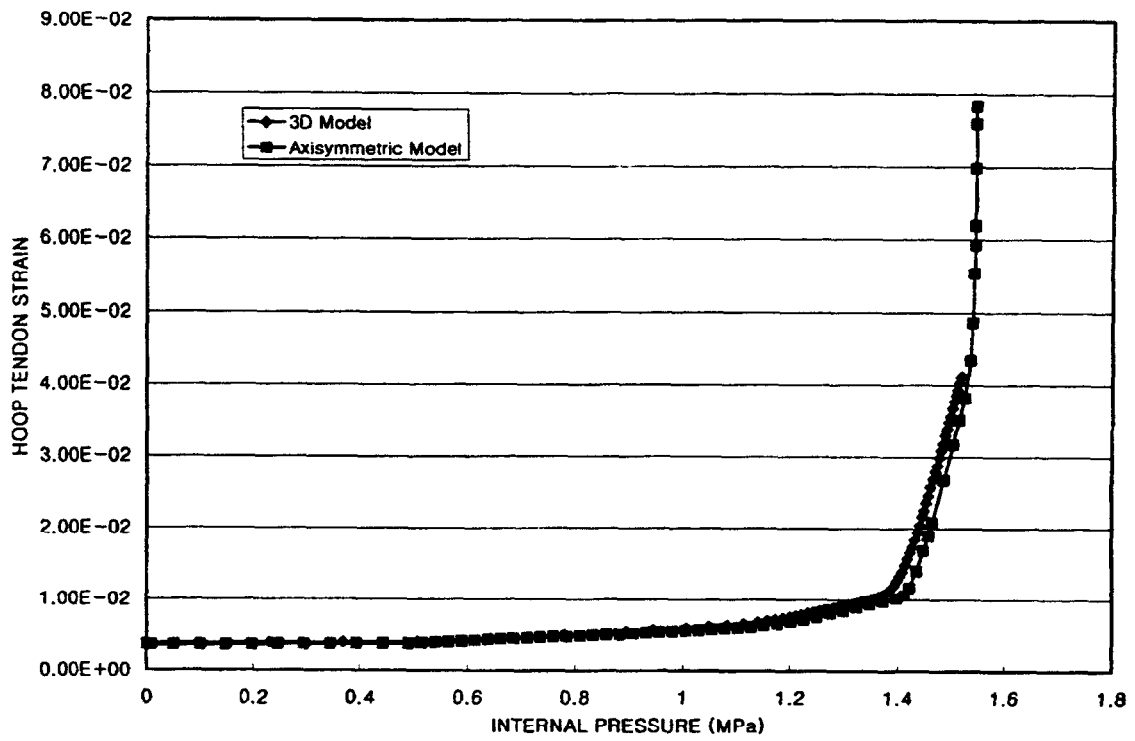


Figure 17 Strain in the hoop tendon at the midheight of cylinder

## References

1. Sandia National Laboratories, PCCV Round Robin Analysis, 1997.
2. Hibbit, H.D., et al., ABAQUS User's Manual, Version 5.7, HKS Inc., 1998
3. Ph Menetrey and K. J. Willam, " Triaxial Failure Criterion for Concrete and Its Generation", ACI Structural journal, Vol. 92, No. 3, May-June 1995, pp. 311-318.
4. Kupfer, H., Hilsdorf, H.K., and Rusch, H., "Behavior of Concrete under Biaxial Stresses", ACI Journal, Proceedings Vol. 66, No. 8, August 1969, pp. 656-666.
5. Smith, S., On Fundamental Aspects of Concrete Behavior, MSc Thesis, University of Colorado, Boulder, Colorado, 1987.
6. Wai-Fah Chen, Constitutive Equations for Engineering Materials, Volume 2 : Plasticity and Modeling , Elsevier, 1994.
7. Tomas T.C. Hsu, Unified Theory of Reinforced Concrete, CRC Press, 1993.
8. Mathcad, User's Guide, Version 8, Mathsoft, Inc., 1998
9. U.S. NRC, Containment Performance of Prototypical Reactor Containments Subjected to Severe Accident Conditions, NUREG CR6433, 1996



**APPENDIX O**

**NUPEC**

**NUCLEAR POWER ENGINEERING CORPORATION  
JAPAN**

Appendix A, Composite Plots, comprises test data compiled and plotted from all organizations that participated in the Prestressed Concrete Containment Vessel (PCCV) Round Robin Pretest Analysis. To avoid duplicating the composite information, individual sets of data and/or plots have been omitted from participants' reports. In some cases this action resulted in disconnects between callouts and content and in the numbering of figures, tables, and pagination in some reports.

However, Appendix O, "NUPEC, Nuclear Power Engineering Corporation, Japan," contains none of these discontinuities.

## CONTENTS

1. INTRODUCTION -----	1
2. GLOBAL ANALYSIS -----	1
2.1 Computational Models -----	1
2.1.1 Material properties -----	1
2.1.2 Material models -----	1
2.1.3 Modeling of 1/4 PCCV test facility -----	2
2.1.4 Analytical modeling -----	3
2.2 Sensitivity Studies for the Determination of Analytical Modelings -----	6
2.2.1 Treatment of dome part meridional tendon-----	6
2.2.2 Consideration of soil spring -----	6
2.2.3 Treatment of gravity -----	7
2.3 Global Analysis -----	10
2.3.1 Structural behavior of 1/4 PCCV model -----	10
2.3.2 Summary of global analysis -----	12
3. LOCAL ANALYSIS -----	20
3.1 Evaluation of Failure Parts and Failure Criteria -----	20
3.1.1 Selection of failure parts -----	20
3.1.2 Failure criteria -----	20
3.2 Wall-base Junction Analysis -----	21
3.2.1 Material properties and models -----	21
3.2.2 Analytical modeling -----	21
3.2.3 Analysis results -----	22
3.3 Free Field Analysis in Vertical Direction -----	30
3.3.1 Analysis condition -----	30
3.3.2 Analytical results -----	31
3.4 Hatch Analysis -----	37
3.4.1 Equipment hatch -----	37
3.4.2 Air lock -----	43
3.4.3 Main steam nozzle -----	44
4. CONCLUSION -----	47
ACKNOWLEDGMENT -----	49
REFERENCES -----	49

## List of Table and Figure

- Fig. 2-1-1 Sensitivity calculation on tension-stiffening model
- Fig. 2-1-2 Axisymmetric global analysis modeling
- Fig. 2-2-1 Effect of meridional tendon modeling on vertical displacements
- Fig. 2-2-2 Effect of meridional tendon modeling on overall deformation behavior under 3.0 Pd
- Fig. 2-2-3 Effect of meridional tendon modeling on hoop crack behavior under 2.4 Pd
- Fig. 2-3-1 Deformation of test vessel for various internal pressures
- Fig. 2-3-2 Radial displacements at various locations
- Fig. 2-3-3 Vertical displacements at various locations
- Fig. 2-3-4 Concrete cracking behavior in both hoop and meridional directions
- Fig. 2-3-5 Hoop liner strains at various locations
- Fig. 2-3-6 Hoop rebar stresses at various locations
- Fig. 2-3-7 Meridional liner strains at various locations
- Fig. 2-3-8 Hoop tendon strains at various locations
- Fig. 2-3-9 Relation of several stresses at various internal pressures
- Table 3-1-1 Failure criteria
- Fig. 3-1-1 Principal compressive stress at 3.8 Pd (Global analysis)
- Fig. 3-2-1 Analysis region of wall-base junction
- Fig. 3-2-2 Duplicate concrete modeling
- Fig. 3-2-3 Location and pressure level of deleted concrete elements
- Fig. 3-2-4 Boundary conditions of wall-base junction analysis
- Fig. 3-2-5 Deformation behaviors of wall-base junction
- Fig. 3-2-6 Concrete cracking behaviors of wall-base junction
- Fig. 3-2-7 Vertical liner strains compared with global analysis
- Fig. 3-2-8 Principal compressive stress under 3.0 Pd
- Fig. 3-2-9 Principal compressive stress under 3.74 Pd
- Fig. 3-3-1 Analysis region of middle cylinder part
- Fig. 3-3-2 Boundary conditions of middle cylinder part
- Fig. 3-3-3 Radial displacements compared with global analysis
- Fig. 3-3-4 Deformation behaviors of middle cylinder part
- Fig. 3-3-5 Tendon tensile force distribution under several pressure conditions
- Fig. 3-3-6 Friction coefficient between tendon and sheath
- Fig. 3-3-7 Contact force between tendon and sheath under prestressing condition
- Fig. 3-3-8 Tendon tensile force distribution with contact friction case

- Fig. 3-3-9 Friction force between tendon and sheath
- Fig. 3-3-10 Tendon strain distribution
- Fig. 3-4-1-1 Analysis region of equipment hatch
- Fig. 3-4-1-2 Alternate tendon modeling
- Fig. 3-4-1-3 Boundary conditions of equipment hatch
- Fig. 3-4-1-4 Radial displacements various pressures compared with global analysis
- Fig. 3-4-1-5 Concrete cracking behavior in hoop direction under two pressures
- Fig. 3-4-1-6 Liner yielding region under several pressures
- Fig. 3-4-1-7 Principal tensile strain under several pressures
- Fig. 3-4-2-1 Analysis region of air lock
- Fig. 3-4-2-2 Analytical modeling of air lock
- Fig. 3-4-2-3 Principal tensile strain under 2.2 Pd compared with E/H analysis
- Fig. 3-4-3-1 Analysis region of main steam nozzles
- Fig. 3-4-3-2 Analytical modeling of main steam nozzles
- Fig. 3-4-3-3 Principal tensile strain under 2.2 Pd compared with E/H analysis



## **1. INTRODUCTION**

Many techniques of treating post-cracking concrete behavior have been proposed for concrete structure analysis and the analysis modeling itself sometimes depends on the experiences. Although many seismic tests and analyses on reactor containment vessels have been conducted, few tests and analyses, focused on static internal pressure loading beyond design basis condition, have been conducted. As for reactor concrete containment Sizewell B in U.K.<sup>(1)</sup> and 1/6 scale reinforced concrete containment vessel (RCCV) test in U.S.<sup>(2)</sup> were only available. Sizewell B was internal pressure loading test using 1/10 scale prestressed concrete containment vessel (PCCV) model, which was interrupted because of basemat uplift and could not reach ultimate structural condition. 1/6 RCCV test was conducted up to liner tearing and provided valuable data. However, it did not include the effect of prestressing of tendon.

Considering the above situation, NUPEC has been planning the ultimate strength test of 1/4 uniform scale PCCV imaging severe accident. The pre-test analysis will be compared with measured data and the post-test analysis using this test data will improve analysis model.

This paper deals with pre-test analysis results of axisymmetric global analysis and local analysis of wall-base junction, free field analysis of middle cylinder part and several hatches analysis.

## **2. GLOBAL ANALYSIS**

### **2.1 Computational Models**

#### **2.1.1 Material properties**

The measured average data of concrete Young's modulus, Poisson's ratio, compressive strength, and tensile strength were used based on the trial mix concrete tests after field curing. As for rebars, the average stress-strain curves of each rebar material test were used except dumbbells. The average stress-strain curves obtained from the liner material tests were also used, assuming isotropy of the material. Two-dimensionality of liner material was considered by Mises yield function. The measured stress-strain curve of a tendon material test was used.

#### **2.1.2 Material models**

A finite element program ABAQUS/Standard Ver. 5.8 was used to predict the global behavior of 1/4 PCCV test. The stress-strain curve of post-cracking concrete was determined through the following sensitivity study, referring to the displacement data at the cylinder mid

point of the 1/6 RCCV test results conducted at SNL.<sup>(1)</sup> That is, various tension-stiffening curves were adopted under full shear retention model. The tension-stiffening was assumed to be linearly decreased and was reduced to zero at strain values of 10, 20, 30, 40 and 50 times of the concrete crack strain of  $1.28 \times 10^{-4}$ , considering the simplicity of global analysis. The 10 times model was the best agreement with 1/6 RCCV data, as shown in Fig. 2-1-1. However this 10 times model induced unstable behavior above 3.0 times design pressure (Pd) condition so that 1 % crack stress was retained even after 10 times of the crack strain.

The reduction of the shear modulus after concrete cracking was determined as follows. The full shear retention model was compared with the model in which shear stiffness under cracking condition was reduced linearly to zero at 10 times of crack strain, similar to the above tension stiffening model. Both models were calculated up to 3.4 Pd where concrete cracking in hoop direction extended to the whole region. The analysis results were almost same so that the full shear retention model was adopted because of the better convergence of calculation.

Non-linear behavior in multi-axial stress field was traced by crack detection surface and compressive surface incorporated in ABAQUS code. Except for the measured ratio of the tensile strength to the compressive strength, defaults values of the surface parameters in ABAQUS were used because of no biaxial test data.

### **2.1.3 Modeling of 1/4 PCCV test facility**

The axisymmetric global analysis was conducted as the first step pre-test analysis. The analytical model included general parts of a dome, a cylinder and a basemat, as shown in Fig. 2-1-2. The wall of dome part and cylinder part was divided into 6 elements to evaluate bending behavior. The dome part was divided into 45 elements and the cylinder part was divided into 60 elements. The basemat had 10 vertical elements and 42 radial elements. However, the juncture region between basemat and cylinder had finer elements. The model included the total numbers of 1963 nodes and 1279 elements.

In order to select an element type for the concrete, three solid element types were compared (4-node bilinear (ABAQUS:CAX4), 8-node biquadratic reduced integration (ABAQUS:CAX8R) and 4-node bilinear incompatible mode (ABAQUS:CAX4I)). When 8-node biquadratic reduced integration element and the 4-node bilinear incompatible mode element were used, very high stress occurred in the loading end at about 3.0 Pd and the calculation became divergent. It was supposed that the force directions of some nodes in a element was inconsistent with the direction of element stress in these cases. Since the materials exhibited strong non-linearity and the contact between tendon and concrete was important under high internal

pressure condition, 4-node bilinear element was adopted.

Rebar was defined as reinforcement (ABAQUS:REBAR) in solid element. Liner was modeled by shell element (ABAQUS:SAX1) and the liner node was commonly shared with inside node of concrete.

#### 2.1.4 Analytical modeling

Hoop tendon was modeled by rebar bonded to the concrete. Meridional tendon was modeled by shell element and the hoop direction stiffness was made zero in the cylinder part. The hoop direction stiffness was considered only above 45° dome angle, because the meridional tendons in the dome part are arranged as like mesh. Friction was specified between the concrete and the meridional tendon. The meridional tendon was allowed to slide relative to the concrete. Friction coefficient at dome part was 0.2156 which consisted of  $\mu=0.21$ , average value of the measured friction coefficient, and friction coefficient considering tendon length effect ( $\lambda=0.001$  per unit length). For cylinder part,  $\mu=0$  and  $\lambda=0.001$  were used to stabilize the analysis. Although an empirical friction correlation between tendon and sheath was proposed as a function of loading end load and circumferencial angle,<sup>(3)</sup> it was not used for the present global axisymmetric analysis. Because hoop tendons don't have a tensile force distribution and meridional tendons are arranged as like mesh.

As a boundary condition, a horizontal direction was fixed along axisymmetric axis to realize axisymmetric condition. Non-linear soil springs were placed at the bottom of basemat to simulate the ground reaction force. The actual ground stiffness was used against compression force and it was zero against tension force. However, the soil springs in non-uplift part had stiffness against tension force, because the vertical displacement became too large when all tensile stiffness of soil springs in non-uplift part were zero. The gravity was considered only at the bottom of basemat as a concentrated force. That is, gravitational force at each node was neglected because of quite smaller force compared with tendon tensile force.

In order to simulate a setting loss condition of tendon, meridional tendon was prestressed with the prescribed value of 503 kN and then loosed to the prescribed value of 470 kN. As for hoop tendon initial stress of 991 MPa, corresponding to the average value of hoop tendon stress, was imposed.

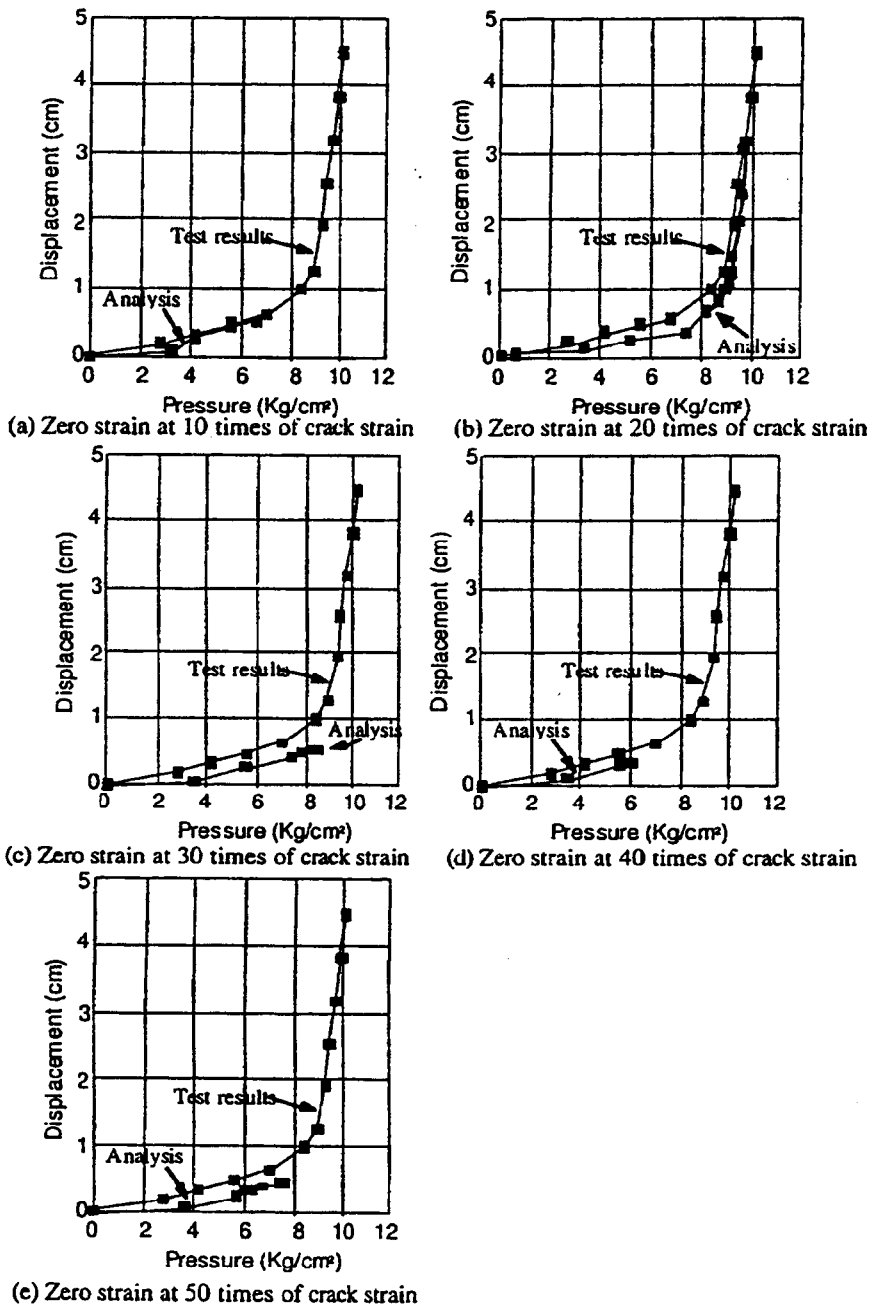


Fig. 2-1-1 Sensitivity calculation on tension-stiffening model

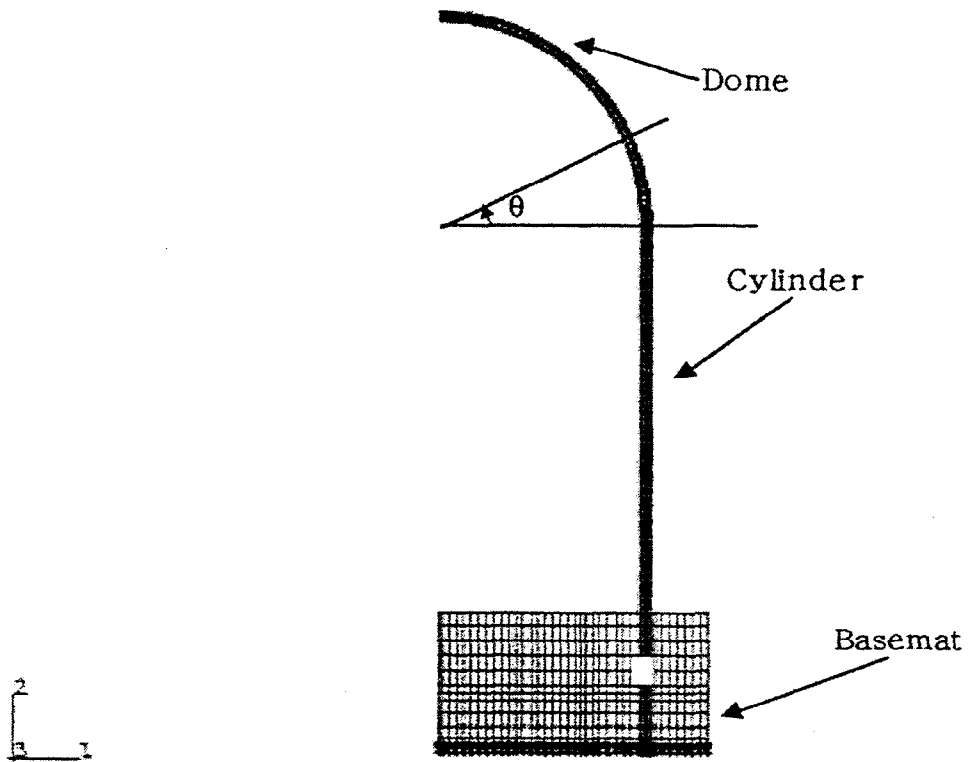


Fig. 2-1-2 Axisymmetric global analysis modeling

## **2.2 Sensitivity Studies for the Determination of Analytical Modelings**

This section describes the analytical techniques to obtain appropriate analysis results. The main techniques are treatments of dome part meridional tendon, consideration of soil spring and treatment of gravity.

### **2.2.1 Treatment of dome part meridional tendon**

Figure 2-2-1 shows the analytical results of vertical displacements of the test model for two modelings of meridional tendon in dome part. The one model simulated hoop stiffness in the meridional tendon above 45° dome angle (model (a)), and the other model simulated hoop stiffness in the meridional tendon above spring line (model (b)). The difference of two models was observed from 2.3 Pd. The apex displacement of model (a) increased in downward direction, while in model (b) it increased in upward direction. This was more clearly demonstrated in Fig. 2-2-2 showing the deformation of test vessel under 3.0 Pd condition.

Model (b) exhibited as if spring line were fixed. Fig. 2-2-3 shows cracking condition in hoop direction at 2.4 Pd where the difference of cracking condition for the two models became remarkable. In model (a) cracking extended to dome part, while in model (b) it occurred in the cylinder part only.

As mentioned above, the vertical displacement depended on tendon modeling in the dome part. However, the test model failure will occur near penetrations in the middle cylinder part and the strain distribution of the cylinder part for both models were same. The model (a) was finally selected in the present analysis because of the better convergence under higher internal pressure.

### **2.2.2 Consideration of soil spring**

Ground stiffness affects the global deformation behavior via ground reaction force under high internal pressure condition. Therefore, the reaction force of the ground was taken into account by placing soil springs at each node of basemat. The uniform soil spring stiffness values of  $1 \times 10^{12}$  N/mm,  $1 \times 10^6$  N/mm,  $1 \times 10^4$  N/mm and  $1 \times 10^2$  N/mm were used for sensitivity analysis. As a result, it was found that soil spring stiffness affected not only deformation behavior but also the convergence under high internal pressure condition. The difference of analysis results under high pressure condition was governed by the uplift condition of the basemat. The stiffness values of  $1 \times 10^6$  N/mm provided the best convergence which was consistent with the ground

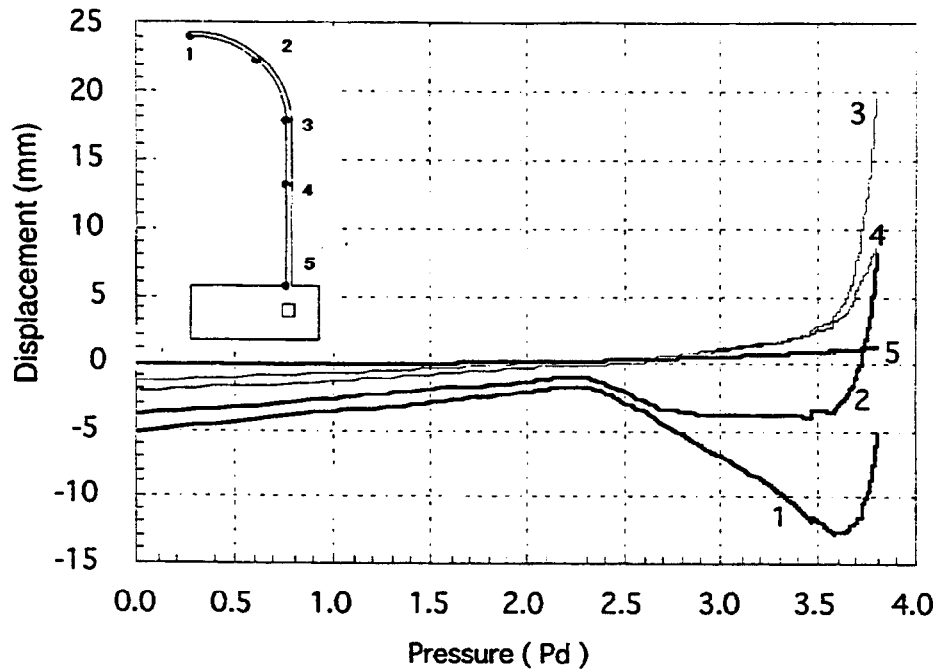
stiffness of actual test site of 30 MPa<sup>(4)</sup>. Therefore, the value of soil spring stiffness was finally distributed in proportion to the node area on the bottom of basemat which provided 30 MPa ground stiffness at each node.

### 2.2.3 Treatment of gravity

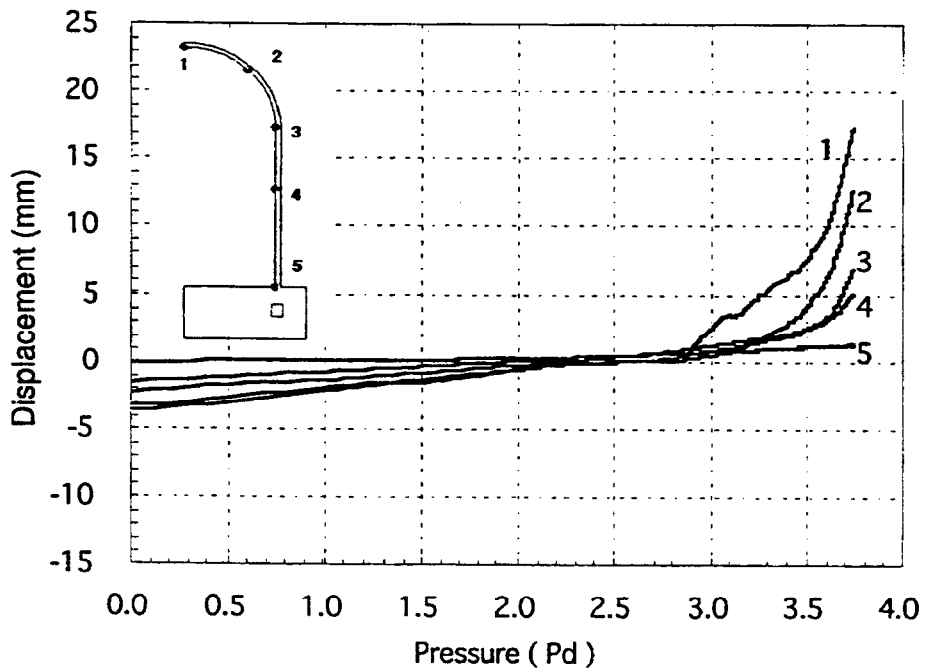
Gravitational force should be considered correctly to evaluate uplift behavior of the model, since actual soil spring of 30 MPa was adopted. Two models were compared. In one case, gravity was considered as concentrated mass at each Gaussian point as usual and in the other case, gravity was considered only at the bottom of the basemat as concentrated force.

Both analysis results were almost same, because vertical force by gravity was negligible compared with tendon tension force. For example, force balance of two elements at the apex of dome was evaluated as follows. Vertical component of the tensile force of meridional tendon was 25 kN. On the other hand, the vertical force by gravity was 0.49 kN, which was only 2 % compared with meridional tendon vertical force. Therefore, the gravity was considered only at the bottom of basemat as concentrated force.

In the ABAQUS model gravity is usually considered as concentrated mass at each Gaussian point and the displacement is calculated by solving equation of motion. Hence, calculation time was longer and the convergence of calculation became worse under large displacement condition.



Model (a)



Model (b)

Fig. 2-2-1 Effect of meridional tendon modeling on vertical displacements

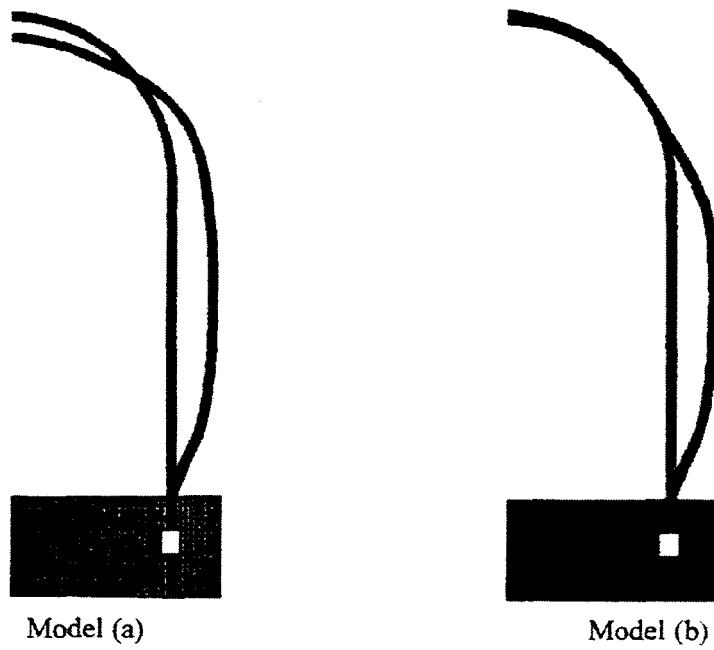


Fig. 2-2-2 Effect of meridional tendon modeling on overall deformation behavior under 3.0 Pd

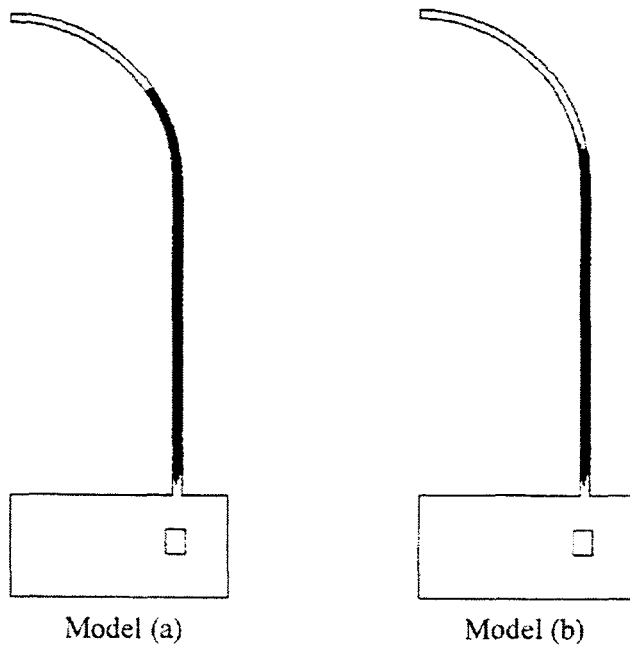


Fig. 2-2-3 Effect of meridional tendon modeling on hoop crack behavior under 2.4 Pd

## **2.3 Global Analysis**

### **2.3.1 Structural behavior of 1/4 PCCV model**

#### **(1) Global deformation behavior**

Figure 2-3-1 shows global deformation behavior for various internal pressures. A slight inward deformation was observed under setting condition due to the influence of prestressing. The cylinder part shape under 1.5 Pd became almost same as that before prestressing. The dome part deformed inward slightly under this pressure. The mid cylinder part began to deform in outward direction at 2.2 Pd, while the dome part was compressive condition. Outward deformation of the mid cylinder part became remarkable at 3.6 Pd so that the dome part deformed downwards.

#### **(2) Local displacement behavior**

Figure 2-3-2 shows radial displacements versus pressure at various locations. The largest displacement was analyzed at slightly upper region (No. 4) from the mid plane of cylinder part. This was because the constraint force at basemat was larger than that at dome part. The region near the basemat (No. 5) and the dome (No. 2) part had small displacement. The displacements in the cylinder part (No. 3), (No. 4) increased linearly until about 2.1 Pd, in which concrete cracking occurred in hoop direction as described below. They increased drastically at about 3.5 Pd due to the concrete cracking in meridional direction.

Figure 2-3-3 shows vertical displacements versus pressure at various locations. The apex (No. 1) had maximum downward deformation at setting condition due to the existence of mesh-like meridional tendon. Downward displacement of the apex decreased linearly up to about 2.4 Pd and it increased from about 2.4 Pd. However, it decreased from 3.6 Pd again, since vertical concrete cracking crack extended to the whole cylinder part. The displacement at 45° point from spring line (No. 2) had also downward deformation. It was smaller than the displacement at the apex. The displacement at mid part of cylinder part (No. 4) and spring line (No. 3) gradually increased until about 3.2 Pd and increased drastically from 3.5 Pd. The displacement near basemat (No. 5) deformation remained small.

#### **(3) Concrete cracking behavior**

Figure 2-3-4 shows concrete cracking behavior in both hoop and meridional directions. Hoop cracking initially occurred at 2.1 Pd (Fig 2-3-4(a)-2). The hoop cracking caused the non-

linear radial displacement as shown in Fig. 2-2-5. The hoop cracking extended above spring line at 2.4 Pd (Fig. 2-3-4(b)-2). Since the dome part constraint force was large, linear vertical deformation of cylinder part was maintained up to about 2.4 Pd as shown in Fig. 2-3-3. The cylinder part deformed outward slightly as shown in Fig. 2-3-1(c). Although outer surface cracking in the meridional direction extended to cylinder part at 3.4 Pd, there was no inner surface cracking as shown in Fig. 2-3-4(c)-1. Both hoop and meridional cracking almost extended to the whole region at 3.6 Pd (Fig. 2-3-4(d)), under which radial displacement increased drastically as shown in Fig. 2-3-2. Concrete stiffness became almost zero in both hoop and meridional directions at 3.6 Pd. Hence, vertical displacement in dome part changed from downward direction to upward direction as shown in Fig. 2-3-3. Bending behavior was observed in the meridional direction so that meridional cracking mainly occurred outside of concrete wall as shown in Fig. 2-3-4(d)-1.

#### **(4) Strain distribution**

Figure 2-3-5 shows hoop liner strains versus pressure at various locations. Hoop liner strain remained negative until about 1.5 Pd due to the tensile force of tendon. Hoop rebar stresses exhibited same behavior as shown in Fig. 2-3-6. The liner strain of mid part (No. 4) of cylinder increased non-linearly from about 2.1 Pd and it increased drastically at about 3.5 Pd. These were closely related to the concrete cracking condition in the hoop direction at 2.1 Pd as shown in Fig. 2-3-4(a)-2 and concrete cracking in meridional direction at 3.6 Pd as shown in Fig. 2-3-4(d)-1. Although similar strain behavior occurred at spring line (No. 3) and dome part (No. 2), the strain level was lower than that in mid part of cylinder. The strain near basemat (No. 5) was almost zero because of the strong constraint force of the basemat. The hoop stiffness of concrete became almost zero at 3.4 Pd and the rebar in cylinder part was almost yielded at this pressure, as shown in Fig. 2-3-6 (yield stress : 459 MPa). That is, the change in liner strain was explained by the changes in concrete and rebar stiffness.

Figure 2-3-7 shows the meridional liner strain versus pressure at various locations. The meridional strain near basemat (No. 5) was increased non-linearly from about 2.0 Pd due to the initiation of ballooning of cylinder part as shown in Fig. 2-3-1(c). On the other hand, the strains of other locations were very small up to 3.4 Pd due to the lack of inner surface concrete cracking in meridional direction as shown in Fig. 2-3-4(c)-1. The strain of spring line (No. 3) increased drastically from 3.4 Pd, because the spring line deformed outwards remarkably as shown in Fig. 2-3-2 and the dome part was tensiled in both hoop and meridional directions. As a result, the strain was concentrated at spring line where structure was discontinuous.

Figure 2-3-8 shows the hoop strains of tendon. It exhibited similar behavior as liner strain if the initial prestressing strain condition was considered.

### 2.3.2 Summary of global analysis

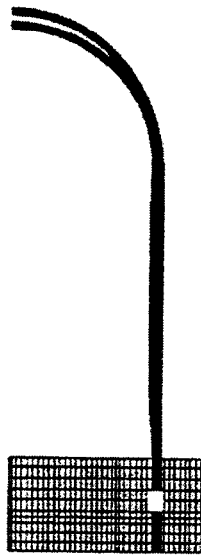
Figure 2-3-9 shows the distribution relationship of hoop stress of outside concrete, hoop stress of outside rebar and hoop stress of tendon, in contrast with the cracked region in hoop direction and the overall deformation for several values of  $P_d$ .

The stress of tendon and outside rebar were almost uniform under 2.0  $P_d$  condition as shown in Fig. 2-3-9(a). Because internal pressure was imposed equally on the inner surface of containment and hoop rebar and hoop tendon were not constrained by the vertical force under low pressure condition. The stress of concrete was nearly uniform in the cylinder part except near basemat and spring line, since the constraint forces of dome part and basemat governed the local displacement. The concrete stress decreased along the top of the dome and increased slightly in the apex region. Since hoop stress was proportional to the radius, the membrane stress should reduce to zero at the apex. However, outside stress increased slightly at the apex region because of the occurrence of bending behavior in the apex region.

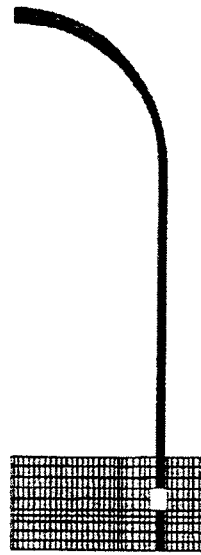
Concrete crack initiated at 2.4  $P_d$ , thereby the stress of concrete in the cylinder part decreased as shown in Fig. 2-3-9(b). As a result, the stress of rebar and tendon increased remarkably. This clearly demonstrated the role of prestressed concrete, in that the decreasing stress of concrete was supplemented by rebars and tendons.

The stress of concrete became almost zero and the stress of rebar became nearly uniform because of the yielding at 3.7  $P_d$  as shown in Fig. 2-3-9(c). The stress of tendon also became nearly uniform in the cylinder part because of the yielding. Hence the displacement increased in the radial direction remarkably.

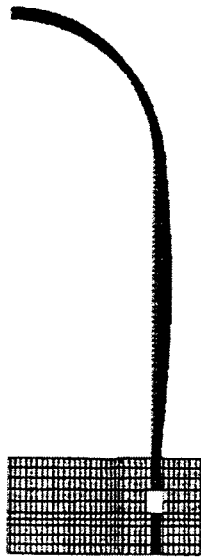
In summary, concrete cracking governed the global behavior of PCCV. That is, the reduction of concrete stress due to cracking caused the changes in stress distribution of rebars and tendons and resultant global deformation behavior.



(a) Setting condition



(b) 1.5 Pd



(c) 2.2 Pd



(d) 3.6 Pd

Fig. 2-3-1 Deformation of test vessel for various internal pressures

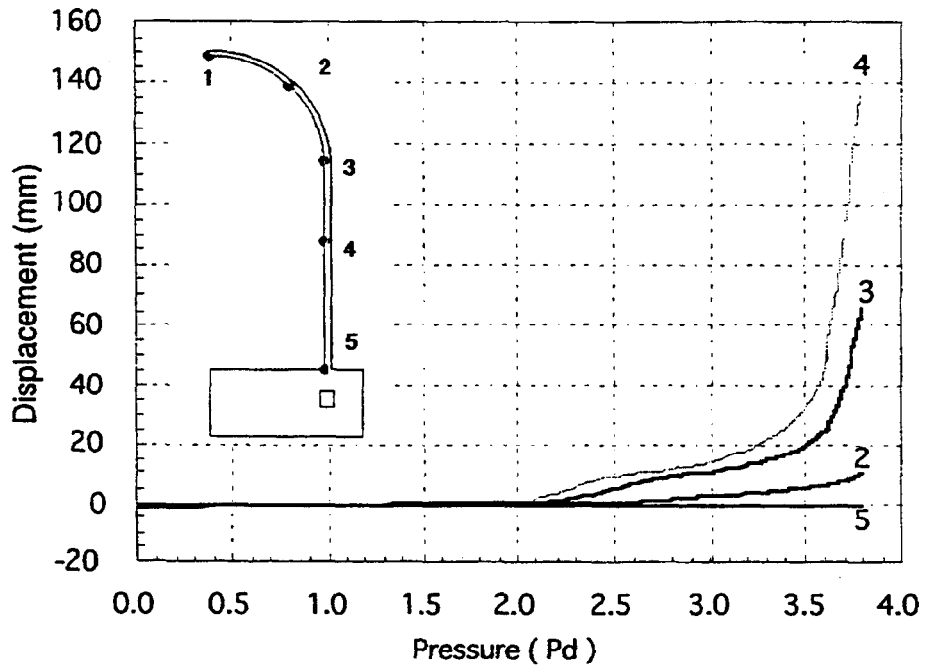


Fig. 2-3-2 Radial displacements at various locations

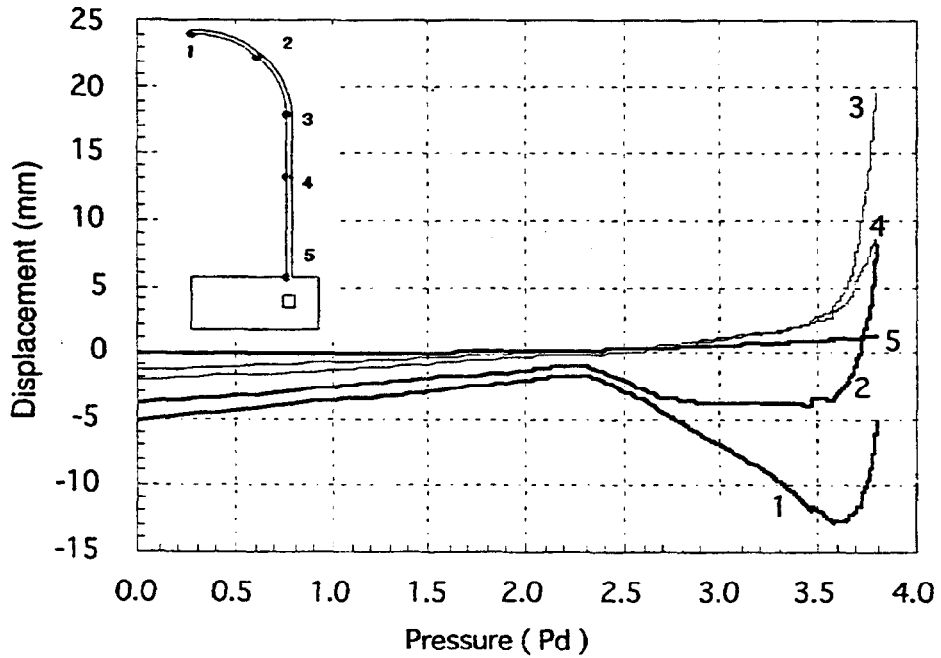


Fig. 2-3-3 Vertical displacements at various locations

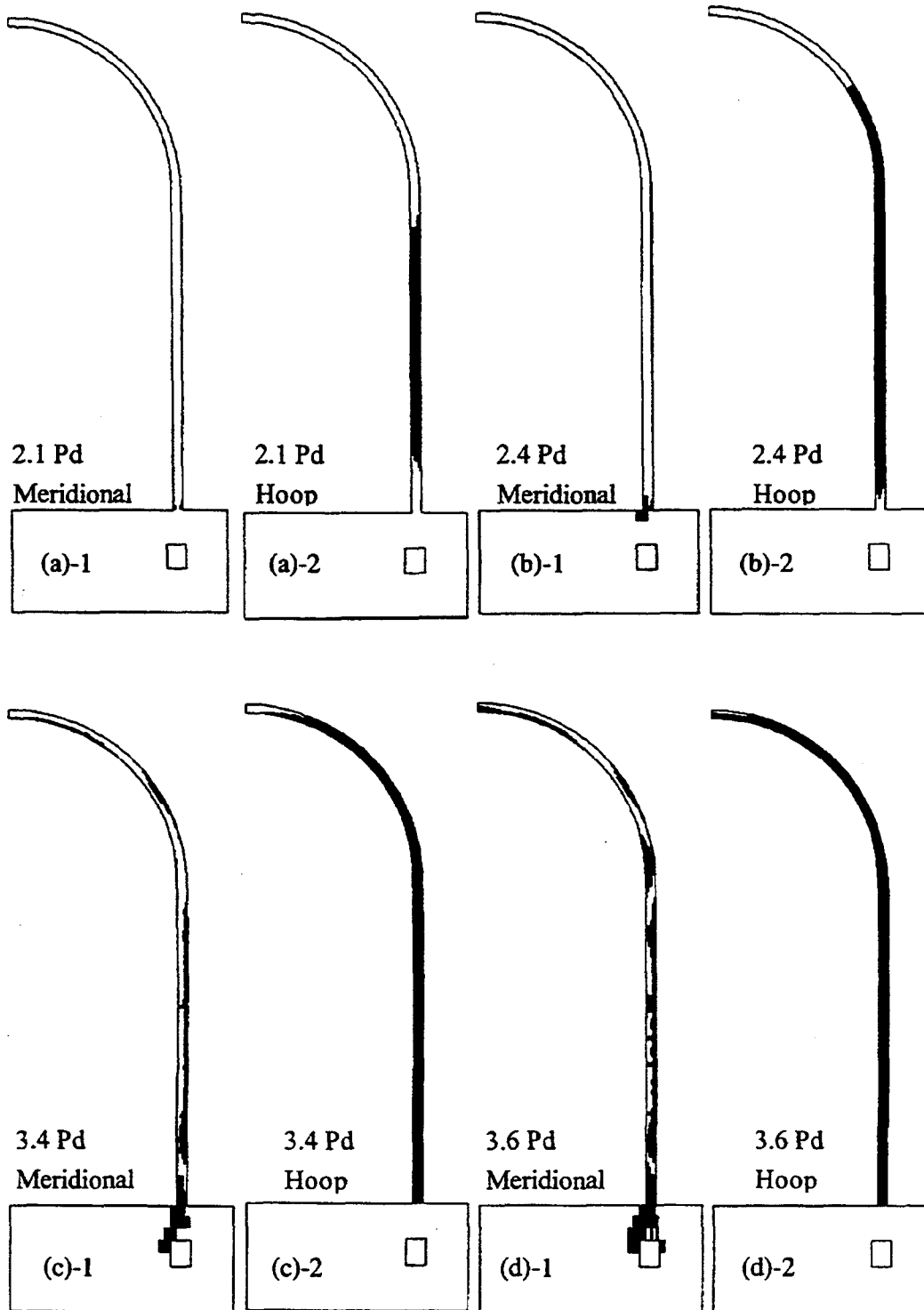


Fig. 2-3-4 Concrete cracking behavior in both hoop and meridional directions

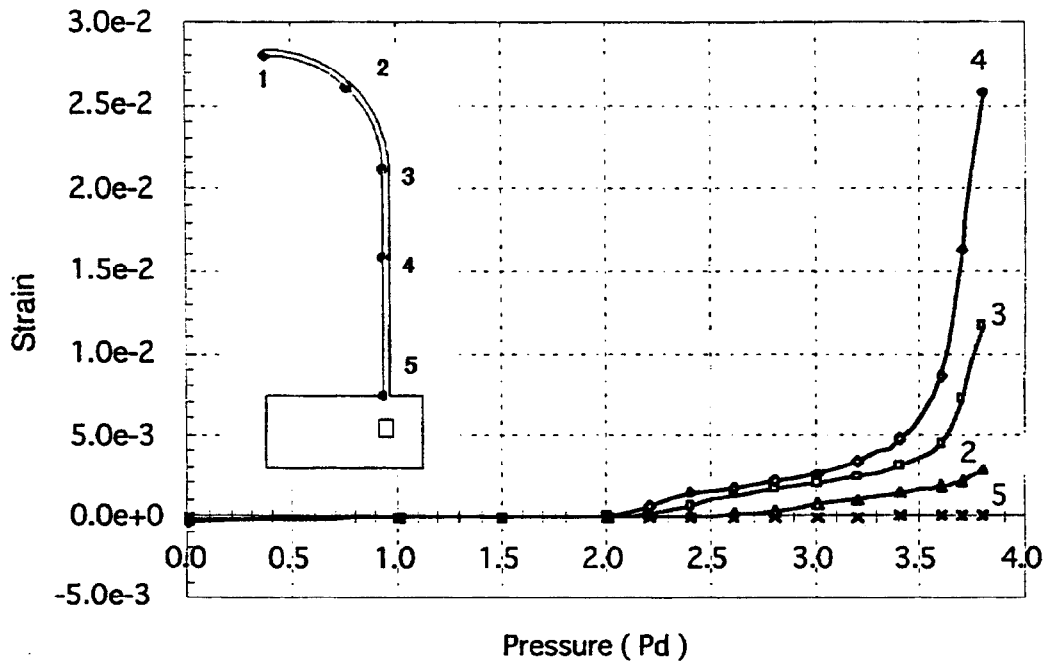


Fig. 2-3-5 Hoop liner strains at various locations

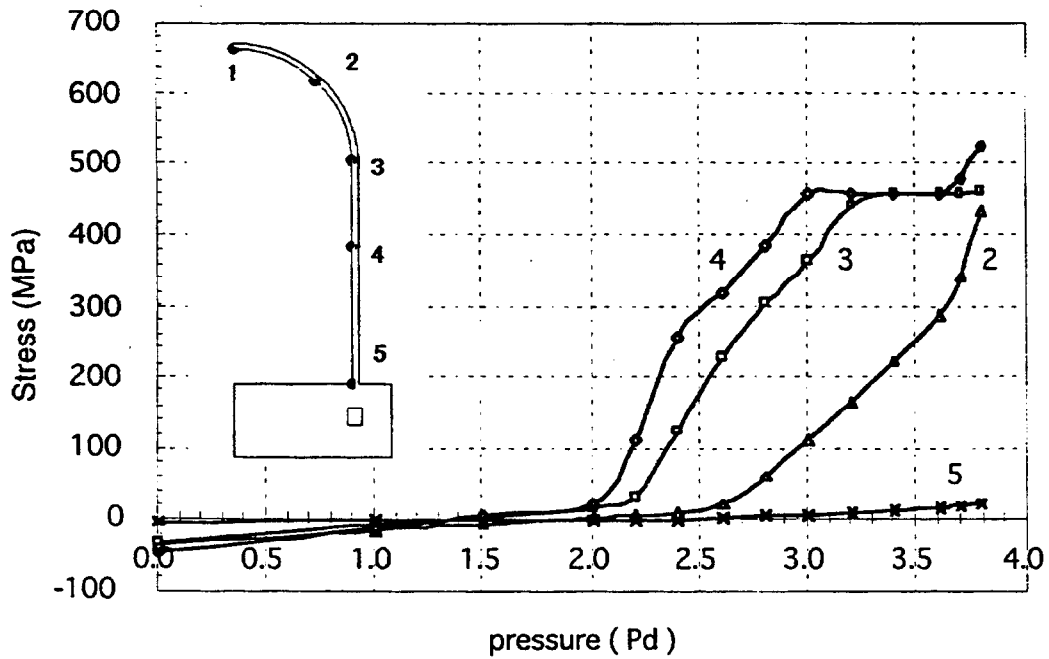


Fig. 2-3-6 Hoop rebar stresses at various locations

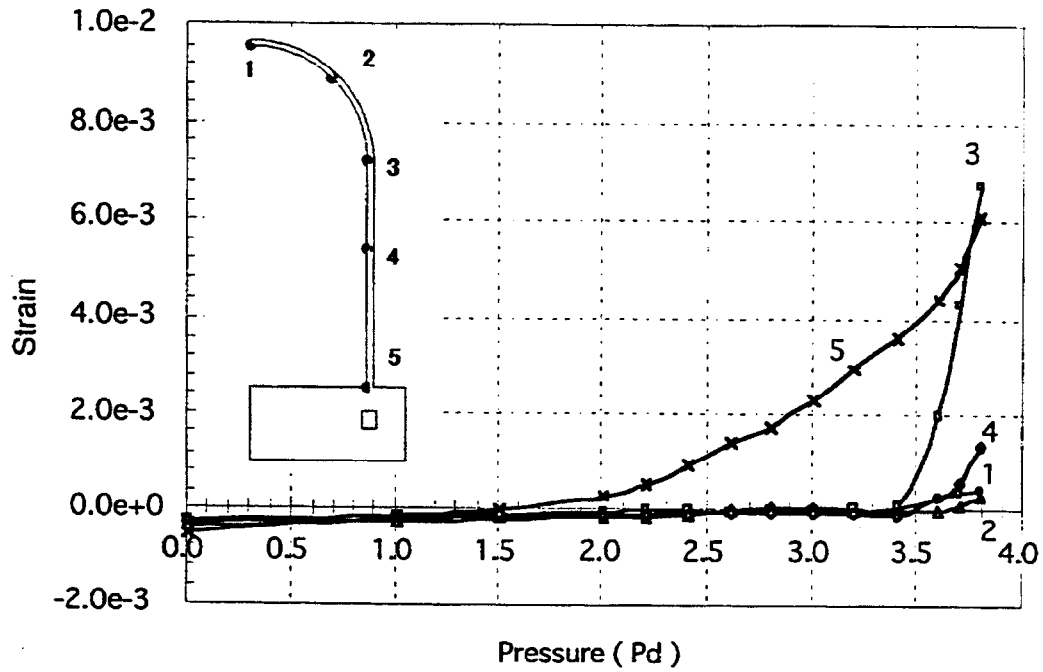


Fig. 2-3-7 Meridional liner strains at various locations

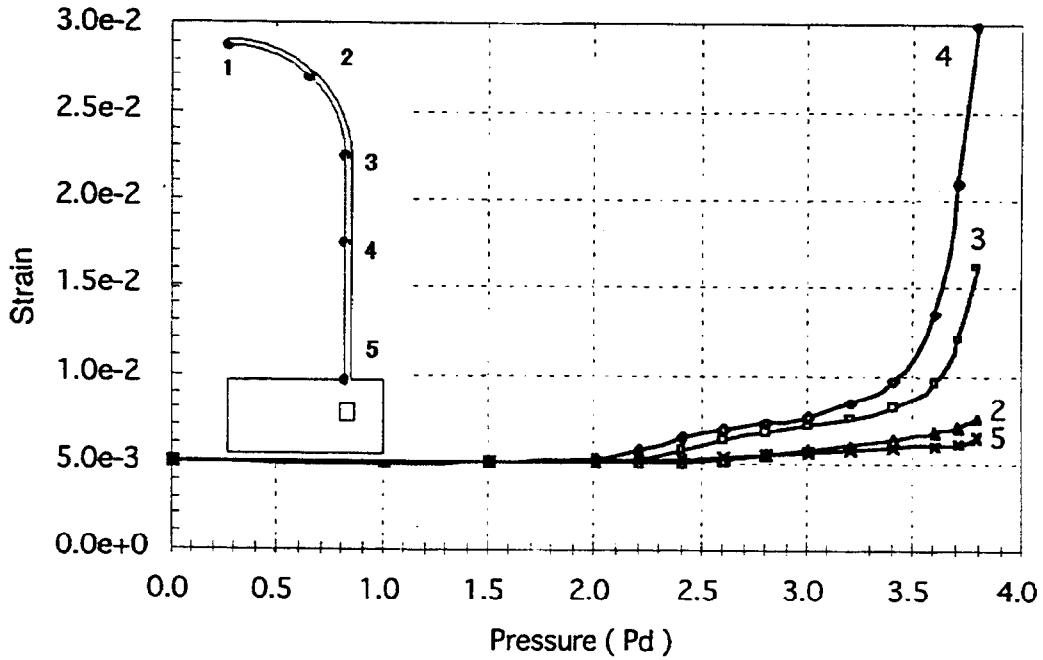
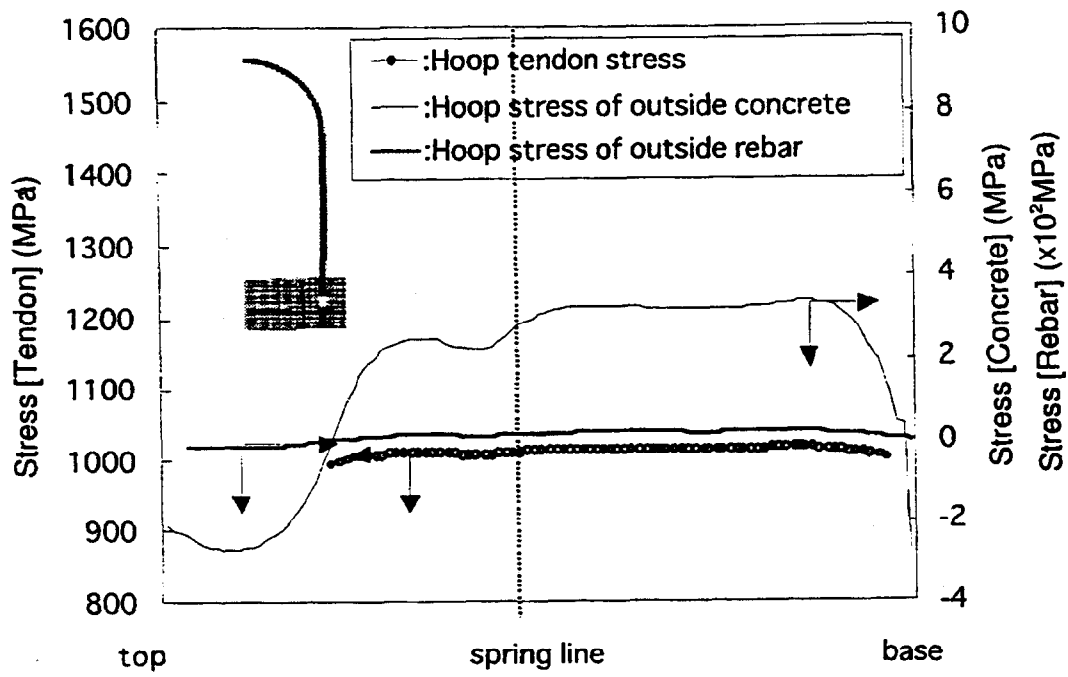
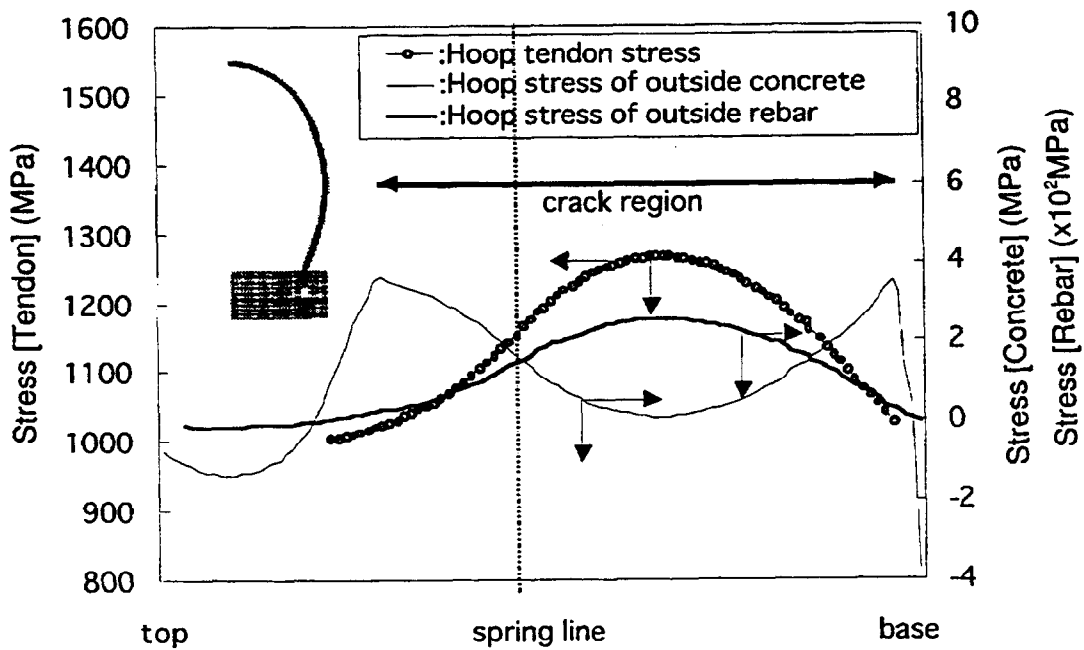


Fig. 2-3-8 Hoop tendon strains at various locations

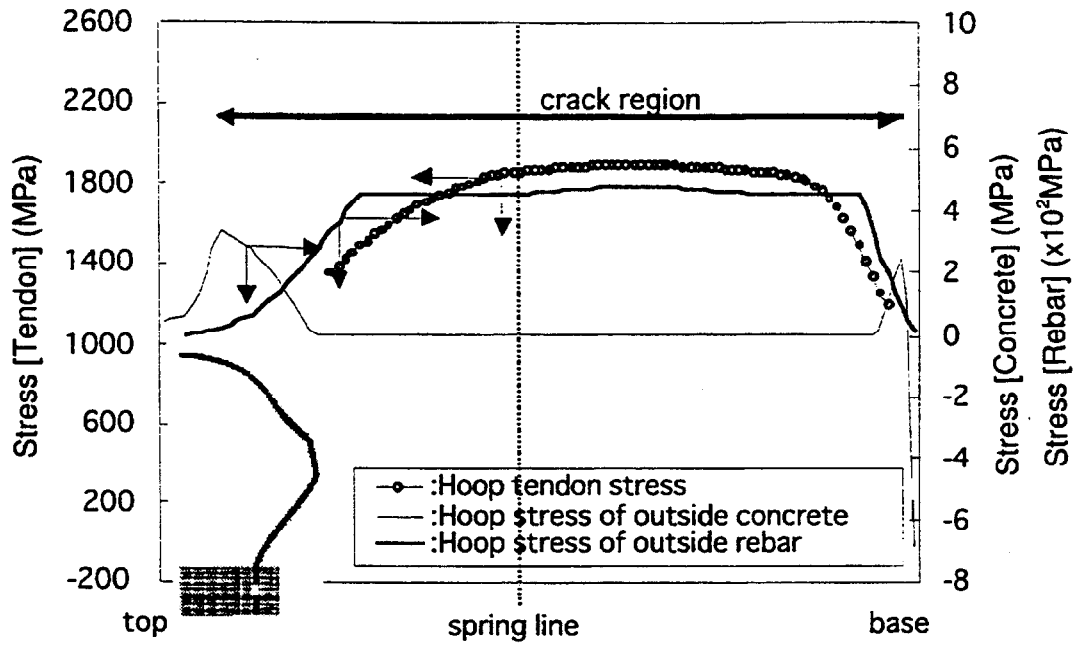


(a) 2.0 Pd



(b) 2.4 Pd

Fig. 2-3-9 Relation of several stresses at various internal pressures



(c) 3.7 Pd

Fig. 2-3-9 Relation of several stresses at various internal pressures (continued)

### **3. LOCAL ANALYSIS**

#### **3.1 Evaluation of Failure Parts and Failure Criteria**

##### **3.1.1 Selection of failure parts**

The failure parts of 1/4 PCCV test model had been investigated during its design stage. According to the investigation, potential failure parts had been crane brackets, hatches, wall-base junction, buttress, spring line and tendon gallery. 1/6 RCCV test demonstrated that liner tearing concentrated on the mid cylinder part<sup>(2)</sup>. NUPEC SCV shell model was failed by liner tearing at the junction of thick plate around a hatch<sup>(5)</sup>. Based on these two tests, the 1/4 PCCV test model might fail by liner tearing around hatches in the mid cylinder part.

The global analysis results, described in chapter 2, predicted that liner strain in the mid part was larger than that in other parts similar to the above studies, and outer concrete compressive stress at the junction between wall and basemat was also quite high, as shown in Fig. 3-1-1. Considering the all above results, several hatches in the mid part and the junction between wall and basemat were considered as potential failure parts, and their analyses were conducted.

##### **3.1.2 Failure criteria**

Determination of failure criteria was indispensable to predict failure part. Failure criteria of concrete was set to be 42 MPa for  $F_c=300$  concrete and 49 MPa for  $F_c=450$  concrete based on the measured average data of concrete trial mix tests after 13 weeks field curing. It is well known that the concrete compressive strength normal to the initial concrete cracking direction is reduced<sup>(6)</sup>. The reduction factor was calculated by compressive field theory using the global analysis results. The average value was about 30 %. However, concrete body is not totally failed by a local failure so that the failure judgement should be decided considering the extent of failure region.

Although rebar tensile test showed larger value of failure strain depending on diameter and material, JIS nominal value was adopted because of the large data scattering. That is, 18 % for SD345, 16 % for SD390 and 12 % for SD490.

While MITI No. 452 specifies nominal value of 2.0 % strain for tendon failure criteria, the measured average data of failure strain was 3.8 % in the tendon system tests. Hence, a failure criterion of tendon was chosen as 3.0 %, considering site setting condition of tendon.

The average measured data of liner tearing strain was 33.5 % in the hoop direction and it was 33.0 % in the meridional direction in the liner tensile test. NUPEC 1/10 SCV model test showed the failure strain of 5.3 % and 8.8 % around  $E/H$ <sup>(5)</sup>. SNL 1/6 RCCV test showed 8.3 %

failure of strain around  $E/H^{(2)}$ . On the other hand, the tearing strain of one axial tensile tests was 26 % for SCV material, different from 1/4 PCCV material, and it was about 20 % for the 1/6 RCCV material, similar to 1/4 PCCV material. NUPEC cylinder failure test model for the SCV material showed 8 ~ 12 % tearing strain<sup>(5)</sup>. That is, biaxial failure strain of test model is smaller than measured failure strain at one axis tensile test. In addition, these exist inevitable strain difference between sensor location and local failure location. Similar situation occurs in the analysis due to element size limitation. Hence, failure criteria of liner was determined as 8 % based on tearing strain of 1/6 RCCV which was similar to the 1/4 PCCV material and structure. Since liner does not constitute structural boundary and concrete has role of leak boundary even after liner tearing, so that the judgment of failure should be decided considering liner failure extent and its relation to other parts. Table 3-1-1 shows summary of failure criteria.

## **3.2 Wall-base Junction Analysis**

### **3.2.1 Material properties and models**

Same material properties were used as those in global analysis. The stress-strain curve of post-concrete cracking was also same. Same material models were adopted as those in global analysis except for shear retention model. The shear stiffness under concrete cracking condition was reduced linearly to zero at 10 times of concrete crack strain, because shear failure was predicted in this region.

### **3.2.2 Analytical modeling**

The analysis region included basemat with tendon gallery and containment wall, as shown in Fig. 3-2-1. The analysis region for basemat was symmetrical around tendon gallery. The modeled region of basemat was from 3825 mm inner radius to its outer surface in the radial direction and from basemat upper surface to el. -3000 mm in the vertical direction. Analysis region for containment wall was modeled from basemat upper surface to el. 1200 mm.

Concrete was modeled by axisymmetric solid element (ABAQUS:CAX4). Rebar, tendon and vertical liner anchor were defined as reinforcement (ABAQUS:REBAR) in solid element. Concrete was simulated by duplicate element of concrete and elastic body having 1/1000 stiffness compared with concrete stiffness, as shown in Fig. 3-2-2. REBAR was defined in the elastic body. The concrete element of the duplicate element was deleted in order to continue the analysis under high pressure condition after substantial zero strain occurred due to concrete cracking. Pressure level and location of the deleted concrete elements, after reaching

quite small meridional stress are shown in Fig 3-2-3 for example. Sheath was not modeled so that tendon was not allowed to slip. Liner and liner anchor were modeled by shell element (ABAQUS:SAX1). The model included the total numbers of 2194 elements and 1159 nodes.

As boundary conditions, the vertical displacement and radial displacement of the global analysis were imposed on boundary surfaces, as shown in Fig 3-2-4. As for meridional tendon, initial stress of 470 kN, corresponding to the prescribed value of setting condition, was imposed. As for hoop tendon, initial stress of 991 MPa, corresponding to average design value of hoop tendon stress, was imposed. After that internal pressure was imposed.

### 3.2.3 Analysis results

Figure 3-2-5 shows the overall deformation behaviors for various internal pressures. A slight inward deformation was observed at setting condition due to the influence of prestressing. The deformed shape under 1.5 Pd became almost same as that before prestressing. It deformed outwards above 1.5 Pd. The deformation trend was similar to that of global analysis.

Figure 3-2-6 shows concrete cracking behaviors for both vertical and hoop directions. Vertical cracking initially occurred at the left side corner of tendon gallery and inner corner of the junction at 1.5 Pd. The former was governed by the shear force in the upper region of tendon gallery which was tensiled upwards. The latter was governed by the shear force in the cylinder part deformed by internal pressure, because cylinder part was deformed more easily than basemat. Hoop cracking initially occurred at 2.2 Pd at upper boundary surface region, similar to global analysis as shown in Fig2-2-7. The cracking region was extended according as pressure increasing. Vertical cracking was extended to tendon gallery and hoop cracking to whole cylinder region at 3.2 Pd.

Figure 3-2-7 shows vertical liner strains versus pressure at two locations compared with global analysis results. The vertical liner strain at el. 250 mm, lower than horizontal liner anchor, was lower than the global analysis result. Because the liner anchor suppressed the strain. On the other hand, the liner strain at el. 1000 mm, close to the boundary condition level, was similar to that of global analysis due to small influence of liner anchor. The strains at all locations of this analysis were less than 0.25 %. Hence, probability of liner tearing up to about 3.8 Pd will be small.

Figure 3-2-8 shows principal compressive stress under 3.0 Pd. This shows maximum compressive stress of 42 MPa at outside of the junction. If the reduction of failure criteria normal to initial concrete cracking direction is assumed to be 30 %, the failure criteria becomes 34 MPa. However, only 2 elements exceeded the 34 MPa and it did not extend beyond rebar layer.

Figure 3-2-9 shows principal compressive stress under 3.74 Pd. This shows maximum compressive stress of 67 MPa at outside of the junction. However, only 4 elements exceeded the 34 MPa and it did not extend beyond rebar layer. Hence, the probability of concrete shear failure at this location up to about 3.8 Pd will be small.

Table 3-1-1 Failure criteria

Material		Failure criteria	Base
Concrete	Fc=300	Compressive stress 42 MPa*	Compressive strength of trial mix concrete test data after 13 weeks curing
	Fc=450	Compressive stress 49 MPa*	
Rebar	SD345	Strain 18 %	Nominal value of JIS
	SD390	Strain 16 %	
	SD490	Strain 12 %	
Tendon		Strain 3 %	Engineering judgement based on the tendon system test data of 3.8 %
Liner		Strain 8 %	Referring to 1/6 RCCV test

\*30 % reduction of these concrete failure criteria in the direction normal to initial concrete cracking direction

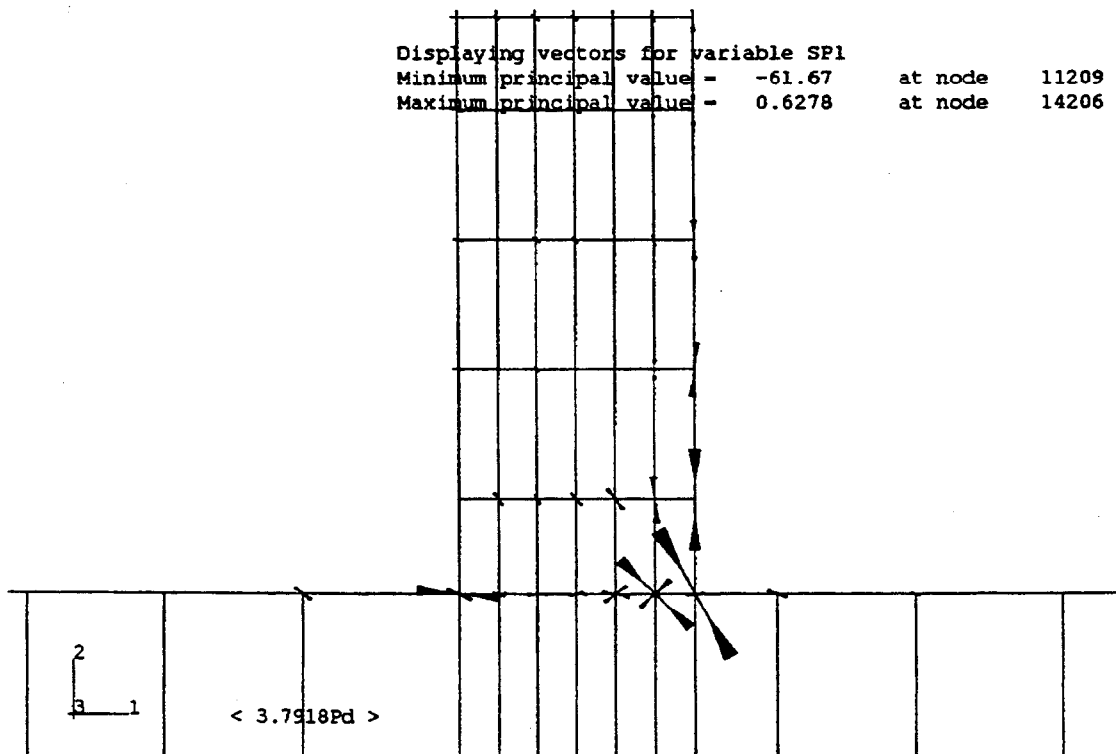


Fig. 3-1-1 Principal compressive stress at 3.8 Pd (global analysis)

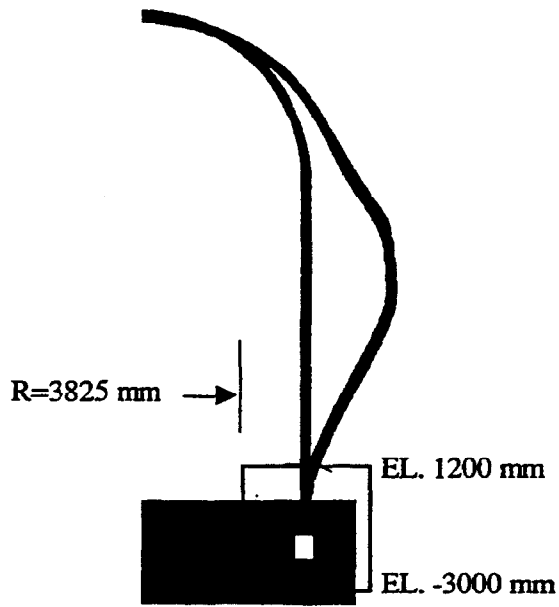


Fig. 3-2-1 Analysis region of wall-base junction

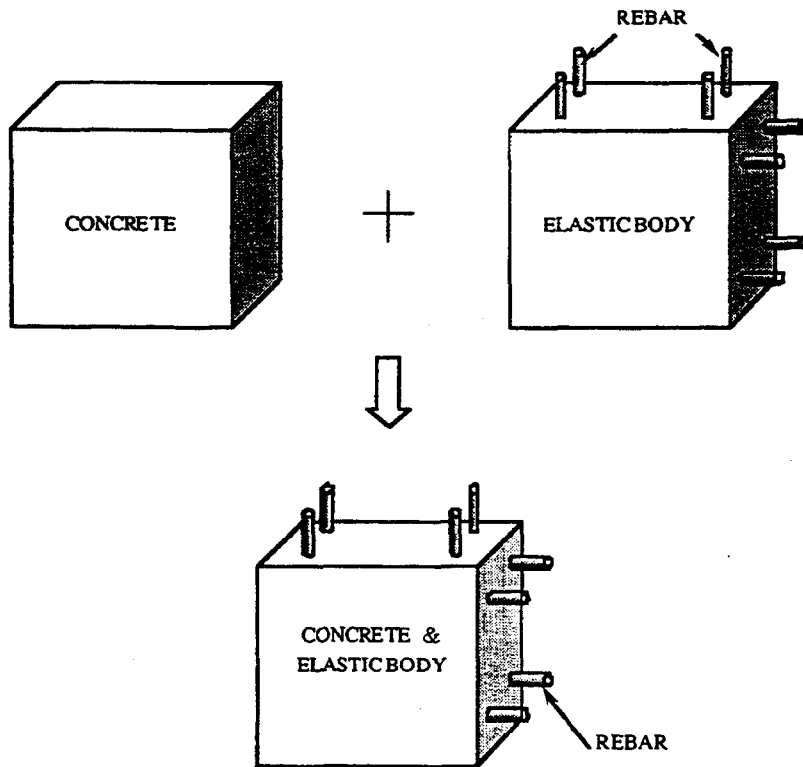


Fig. 3-2-2 Duplicate concrete modeling

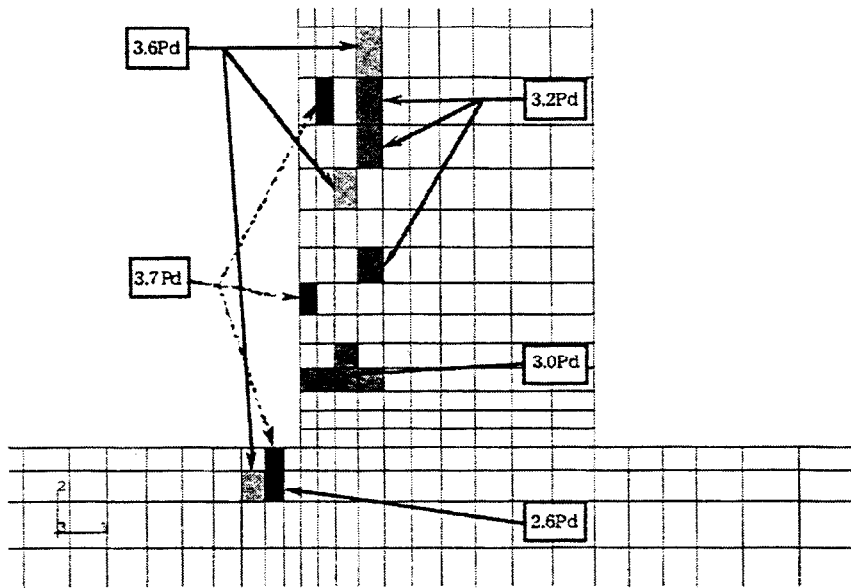


Fig. 3-2-3 Location and pressure level of deleted concrete elements

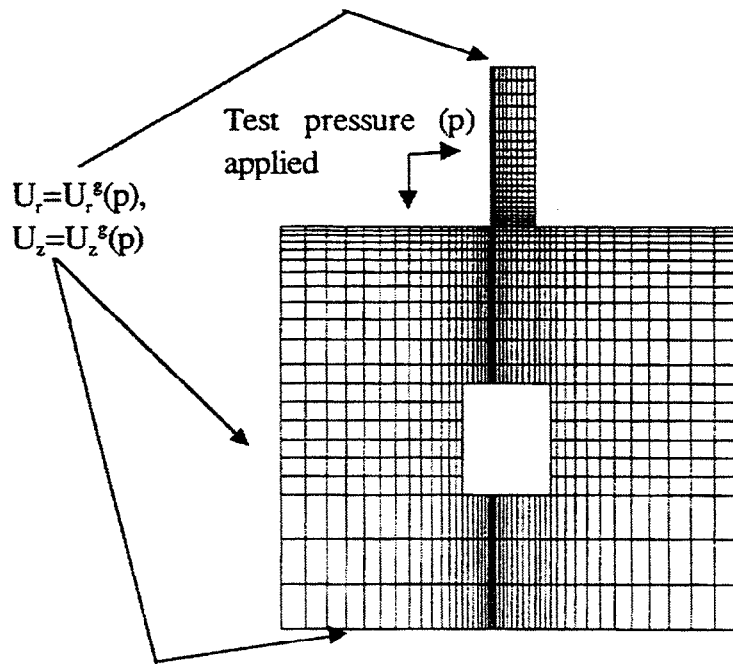


Fig. 3-2-4 Boundary conditions of wall-base junction analysis

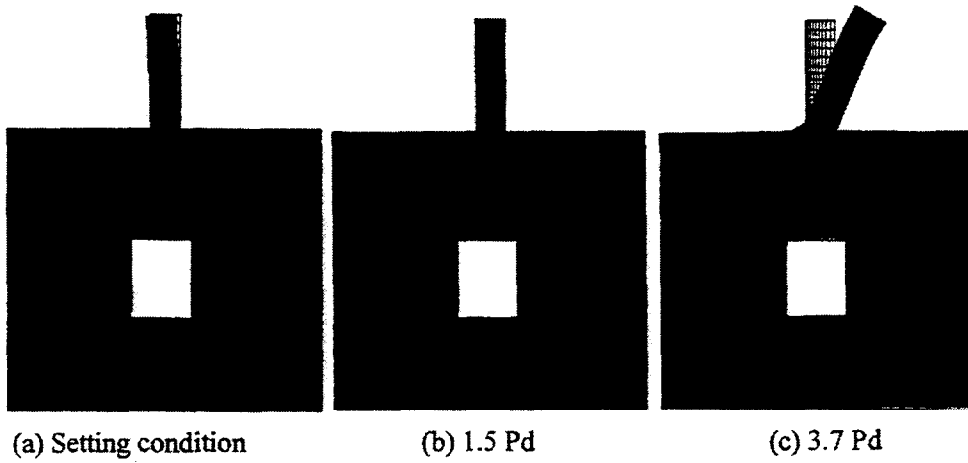


Fig. 3-2-5 Deformation behaviors of wall-base junction

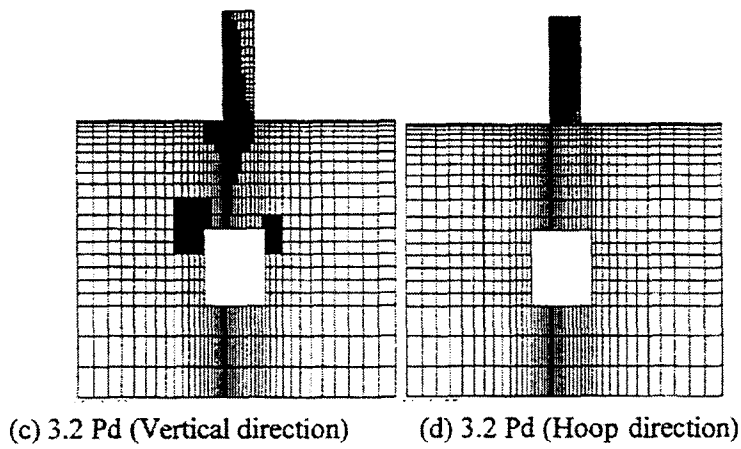
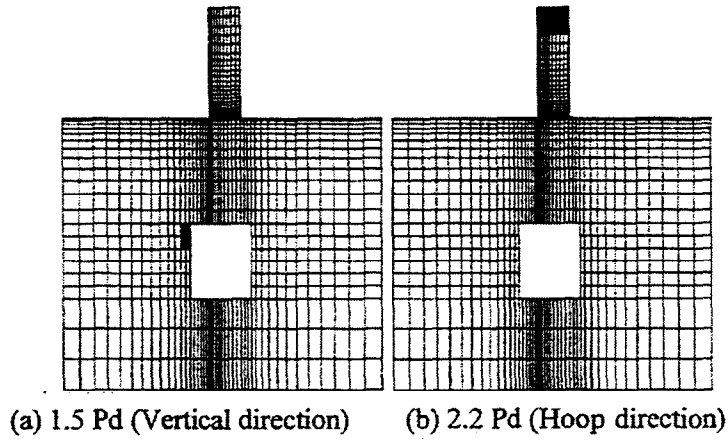


Fig. 3-2-6 Concrete cracking behaviors of wall-base junction

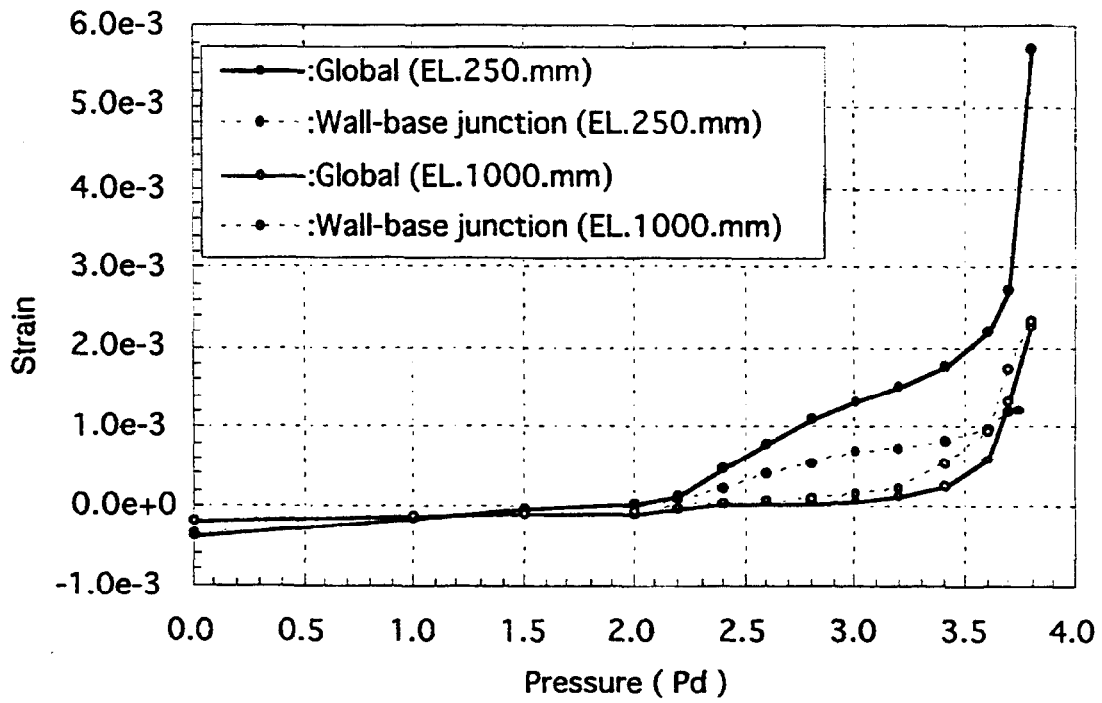


Fig. 3-2-7 Vertical liner strains compared with global analysis

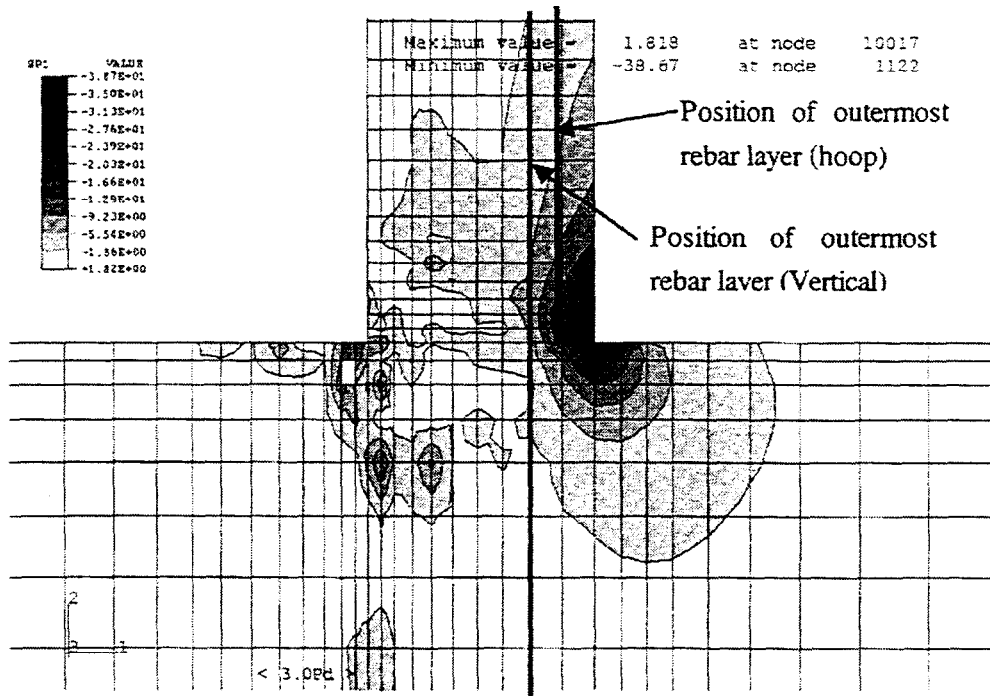


Fig. 3-2-8 Principal compressive stress under 3.0 Pd

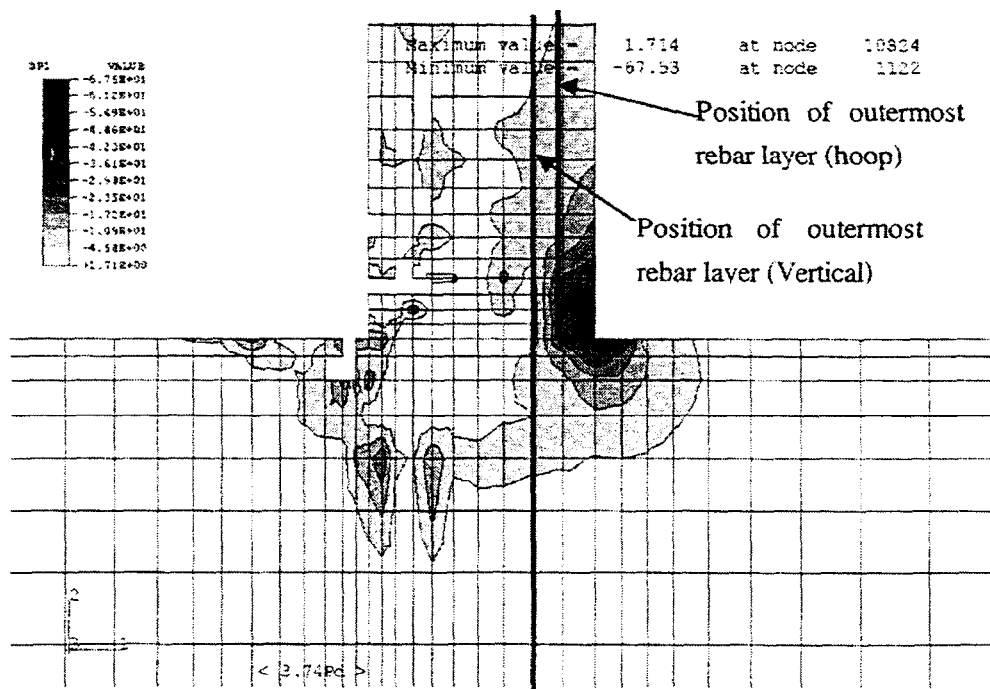


Fig. 3-2-9 Principal compressive stress under 3.74 Pd

### **3.3 Free Field Analysis in Vertical Direction**

#### **3.3.1 Analysis conditions**

In order to investigate hoop tendon tensile force distribution, free field analysis was conducted, including buttress. Same material properties and same material models were used as those in global analysis. The region of the analysis was ranged from el. 7093.75 mm to el. 5968.75 mm in vertical direction and 180 sector in hoop direction with buttress at both ends, as shown in Fig. 3-3-1.

Concrete was modeled by solid element (ABAQUS:C8D8). Rebar and vertical tendon were defined by reinforcement (ABAQUS:REBAR) in solid element. Concrete was simulated by duplicate element of concrete and elastic body with rebars, same as that in the wall-base junction analysis. As for vertical tendon, sheath was not modeled so that slip of vertical tendon was not allowed. Hoop tendon and its sheath were modeled by 2-node beam element (ABAQUS:B31). Contact element (ABAQUS:ITT31) was placed between tendon and sheath so that slip of hoop tendon was considered. Friction coefficient between tendon and sheath was modeled by the correlation depending on loading end load and the angle from loading end<sup>(3),(7)</sup>. That is, friction coefficient was not constant value. The straight part of the tendon inside buttress was not simulated because of simplicity. However, the friction coefficient of the circular part corresponding to the straight part was set at 0.001 1/m. The steel sheath had ordinary stiffness. The thickness of the sheath was made 1 mm thicker than that of model to enable contact analysis. The yielding of sheath was set at 300 MPa smaller than rebar yielding of 459 MPa. Liner was modeled by 4-node shell element (ABAQUS: S4R). Liner anchor was not modeled because of small influence. The model included the total numbers of 15810 elements and 10780 nodes.

As boundary conditions, the vertical displacement of the global analysis was applied to both upper and lower surfaces, and 0 displacement in the hoop direction to both side surfaces, as shown in Fig. 3-3-2.

As for meridional tendon, initial stress of 470 kN, corresponding to the prescribed value of setting condition, was imposed. Hoop tendon was prestressed with the prescribed value of 453 kN and then loosed to the measured value of 394 kN in ancillary tests. All concrete elements were deleted at 3.0 Pd to void unreasonable termination of the analysis, after confirming quite small hoop stress of concrete in preliminary analysis.

### 3.3.2 Analytical results

Figure 3-3-3 shows liner radial displacements compared with that of the global analysis. The displacement of free field was similar to that of global analysis, which confirmed the validity of analytical modeling.

Figure 3-3-4 shows deformation behaviors under several pressure conditions. A slight inward deformation was observed except buttress region at setting condition. The shape of the cylinder part was changed from ellipse at setting condition to circle at 2.0 Pd. The radial displacement in buttress region was smaller than that in other parts due to buttress stiffness below 3.0 Pd. The difference between free field and buttress region was quite small above 3.0 Pd since the buttress was totally cracked at this pressure level. The shape became circle again above 3.0 Pd due to total cracking of buttress.

Figure 3-3-5 shows tendon tensile force distribution. The distribution had its maximum value at about 50 degree up to 3.0 Pd due to friction loss at prestressing condition. Even before concrete cracking at 2.1 Pd, tensile force of loading end region was rather flat because the present friction coefficient correlation provided smaller friction coefficient in this region, as shown in Fig. 3-3-6. That is, tendon in the loading end region behaved like straight part. Fig. 3-3-7 shows contact force distribution compared with constant friction case. Contact force in the vicinity of loading end was fluctuating in constant friction case. The analysis became unstable due to sudden change in friction coefficient at the boundary between straight part and circular part. On the other hand, in friction correlation case, the friction coefficient increased gradually with circumferential angle so that the contact force was not fluctuating in the vicinity of loading end. In constant friction case larger convergence criteria was used than that of friction correlation case. Figure 3-3-8 shows the tendon tensile force distribution up to 4.0 Pd comparing friction correlation case and constant friction case. This shows larger tensile force change in loading end region at prestressing condition in constant friction case. Tensile force in friction correlation case was larger than that in constant case up to 3.0 Pd and the difference became negligible under 4.0 Pd due to larger elongation of rebars associated with its yielding at 3.2 Pd. The tendon tensile distribution shape changed as internal pressure increased. The change of tensile force distribution was governed by the change of friction force, as shown in Fig. 3-3-9. Friction force decreased due to concrete cracking and yielding of liner and rebar, in turn. Figure 3-3-10 shows strain distribution of H53 tendon. The strain of H53 tendon at loading end reached as high as 3 %, corresponding to tendon failure criteria, at 4.0 Pd. Hence, the probability of tendon rupture will be high.

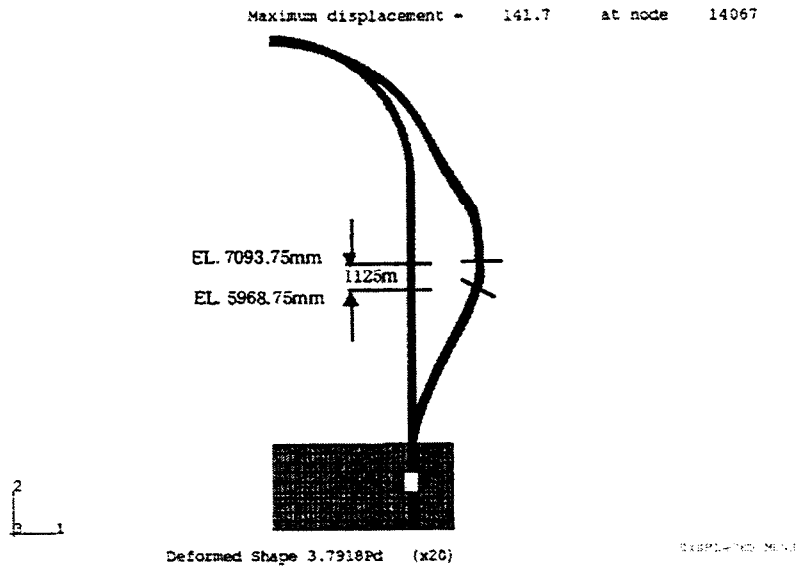


Fig. 3-3-1 Analysis region of middle cylinder part

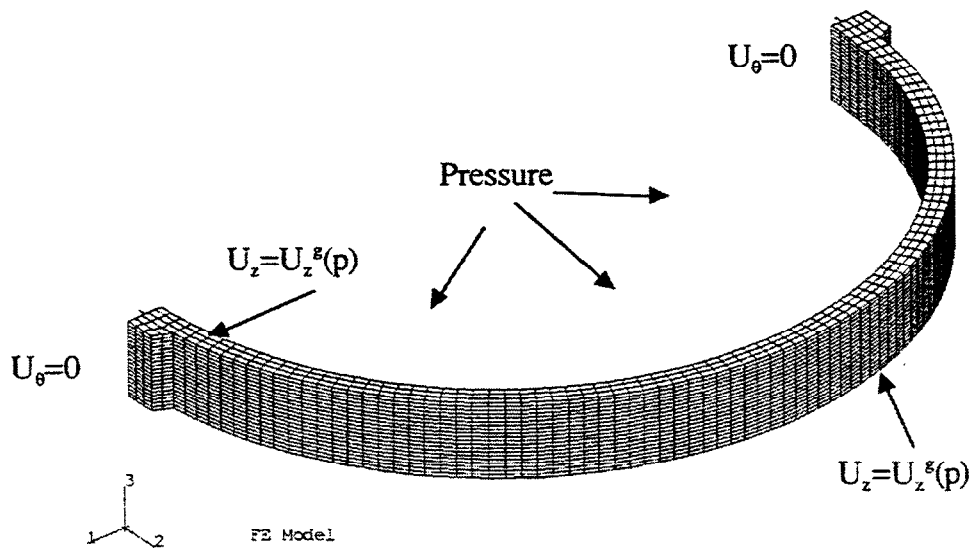


Fig. 3-3-2 Boundary conditions of middle cylinder part

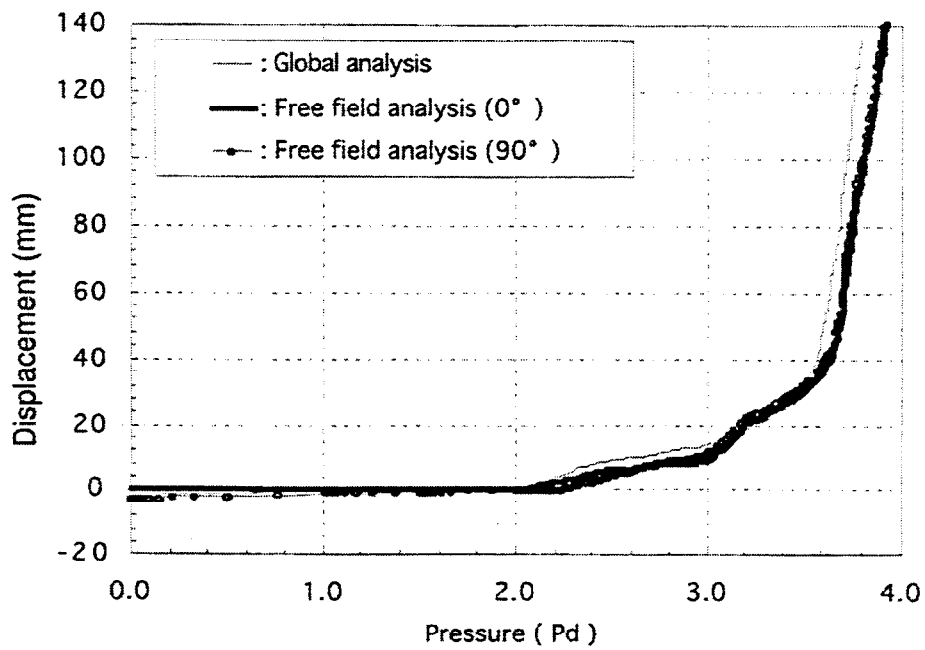


Fig. 3-3-3 Radial displacements compared with global analysis

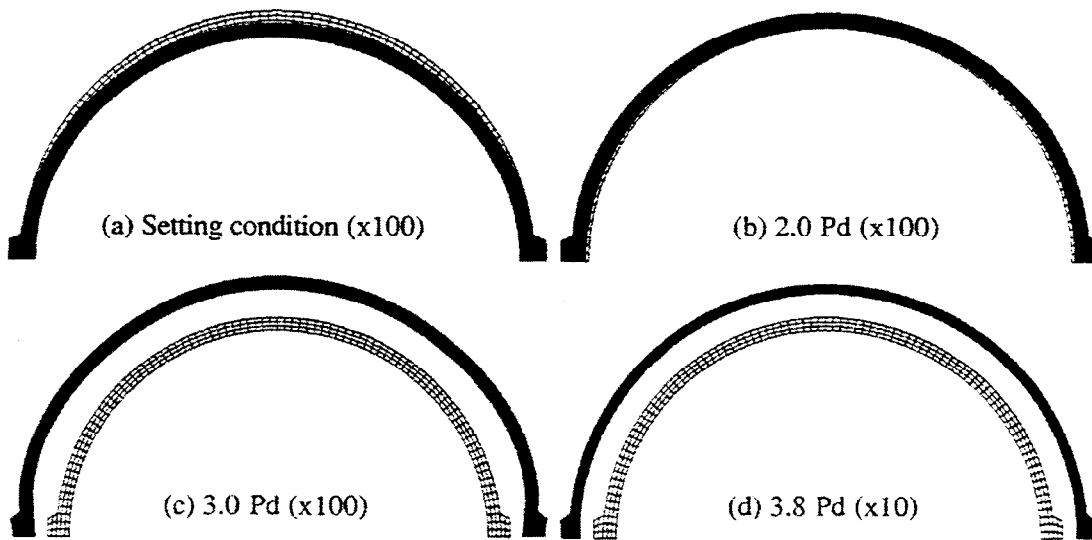


Fig. 3-3-4 Deformation behaviors of middle cylinder part

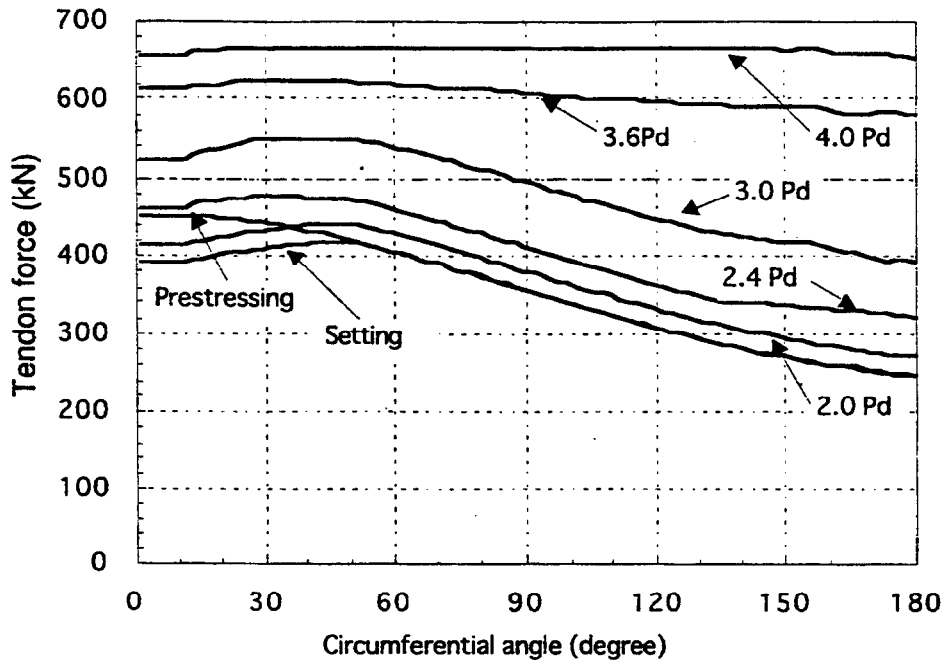


Fig. 3-3-5 Tendon tensile force distribution under several pressure conditions

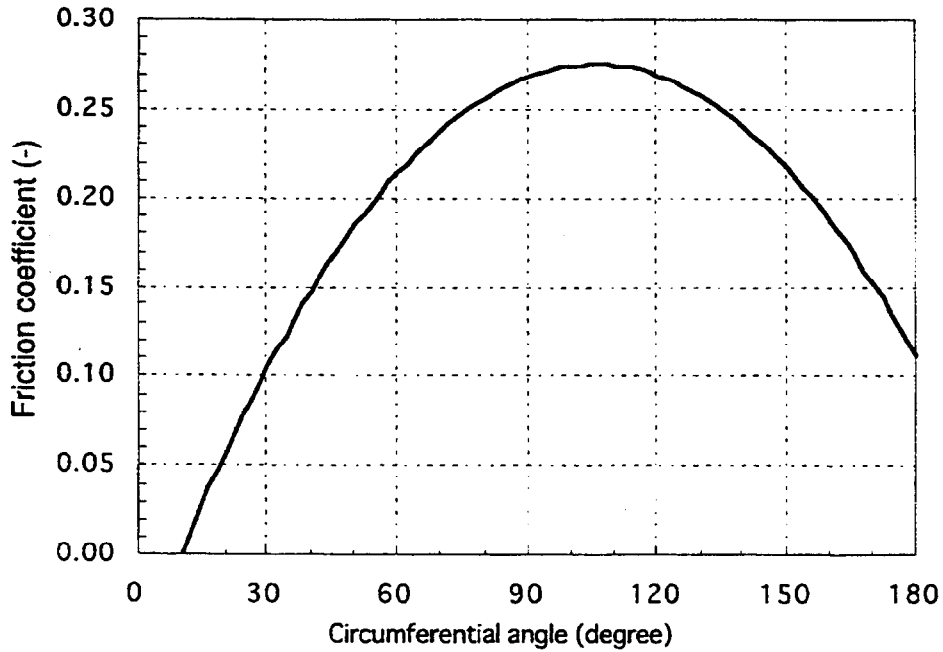


Fig. 3-3-6 Friction coefficient distribution between tendon and sheath

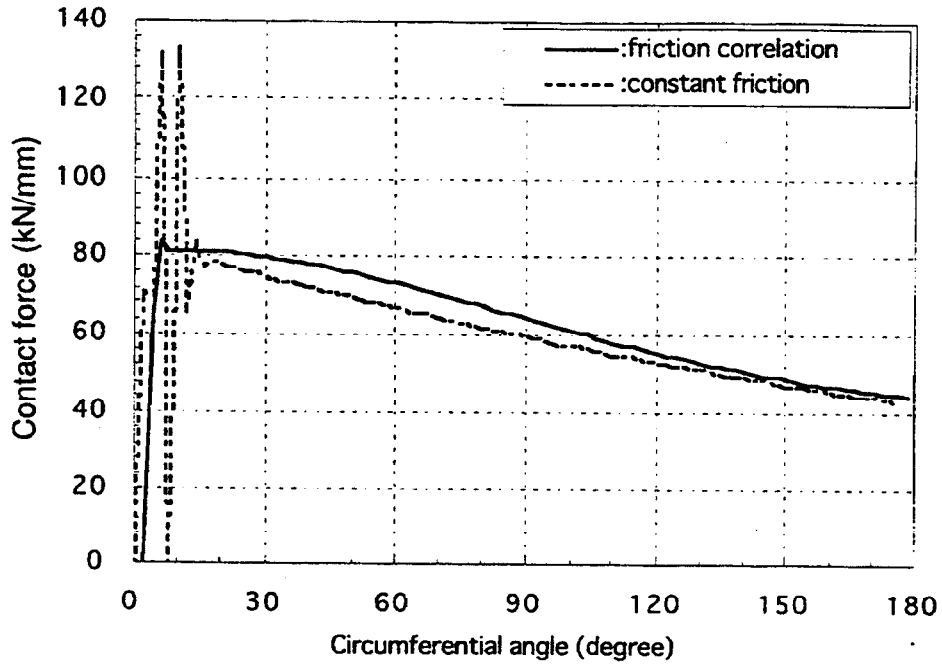


Fig. 3-3-7 Contact force between tendon and sheath under prestressing condition

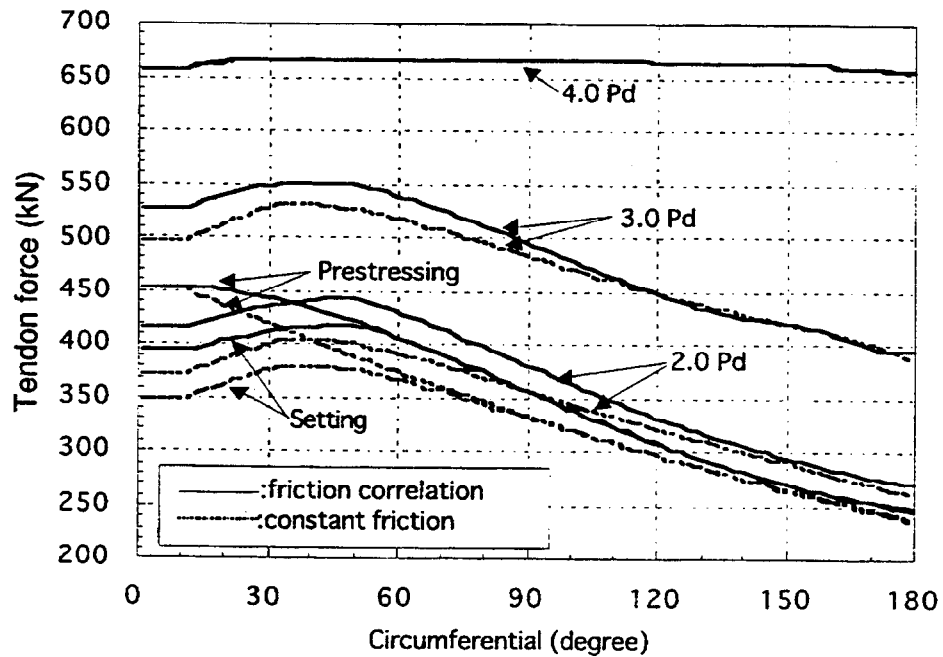


Fig. 3-3-8 Tendon tensile force distribution compared with contact friction case

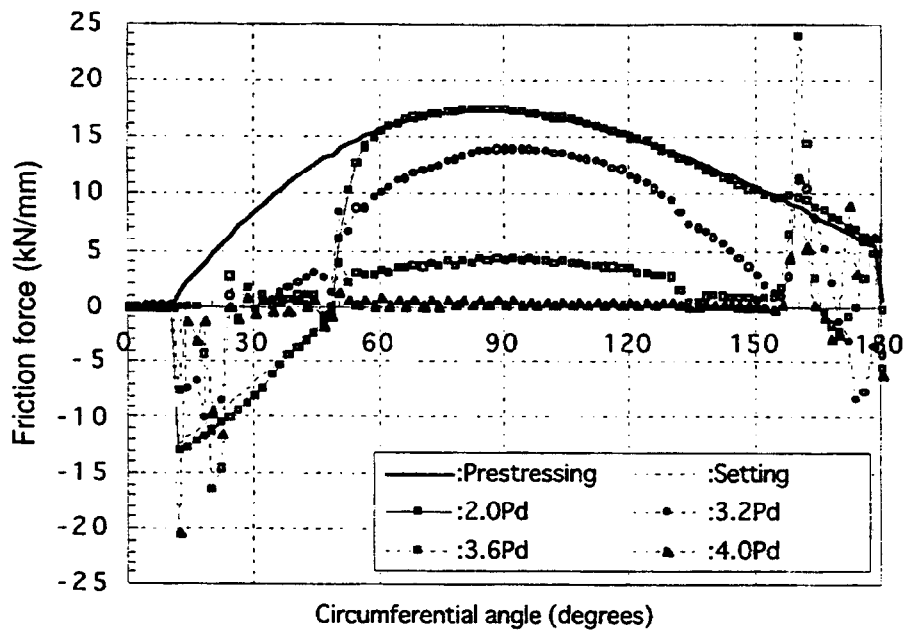


Fig. 3-3-9 Friction force between tendon and sheath

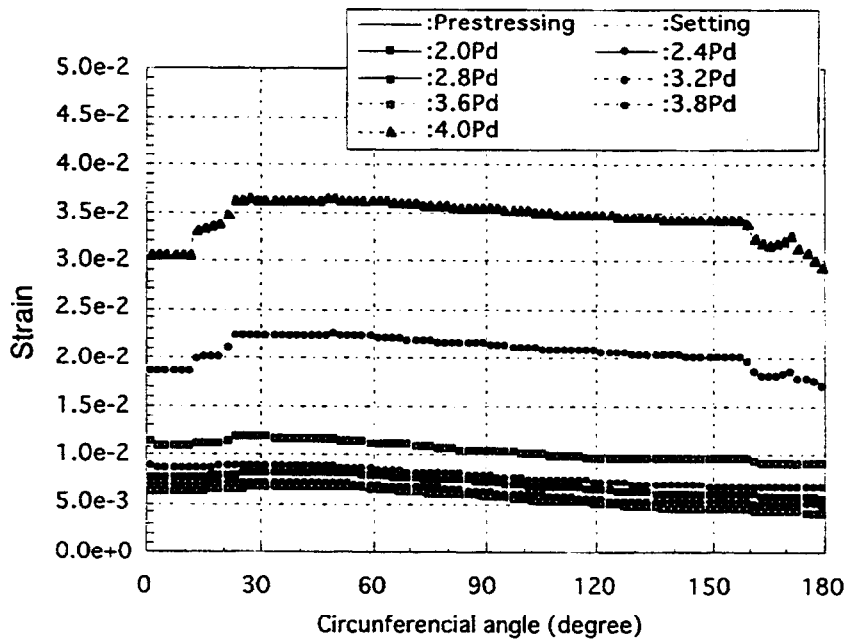


Fig. 3-3-10 Tendon strain distribution

### **3.4 Hatch Analysis**

#### **3.4.1 Equipment hatch**

##### **(1) Analysis conditions**

Same material properties and same material models were used as those in global analysis. The analysis region was ranged from the horizontal central axis plane of equipment hatch (E/H) to the plane at 4500 mm above it in vertical direction and 90 degree sector from buttress center, as shown in Fig. 3-4-1-1

Concrete was modeled in the same manner as that in free field analysis. One hoop tendon of the analytical model included 2 tendons which had same loading end, alternately arranged and 2 times area of actual area as shown in Fig. 3-4-1-2. Friction coefficient between tendon and sheath was modeled, in the same manner as that in free field analysis. Liner, sleeve and hatch cover were modeled by shell element (ABAQUS:S4). Liner anchor was not modeled because of small effect. The model included total numbers of 16567 elements and 9172 nodes.

As boundary conditions, the vertical displacement of the global analysis was applied to both upper and lower surfaces. Zero displacement in the hoop direction was applied to both side surfaces, as shown in Fig. 3-4-1-3. Since two vertical adjacent tendons in the model should be considered as one set, the tensile forces of two adjacent tendons at the symmetrical plane had same value at anti-buttress boundary surface.

As for meridional tendon, initial stress of 470 kN, corresponding to the prescribed value of setting condition, was imposed. Hoop tendon was prestressed with the prescribed value of 453x2 kN and then loosed to the measured value of 350x2 kN in ancillary test. All concrete elements were deleted at 2.8 Pd, after confirming quite small stress in preliminary analysis.

##### **(2) Analytical results**

Figure 3-4-1-4 shows radial displacements versus pressure at two locations compared with global analysis results. The displacement of free field was similar to that of global analysis, which confirmed the validity of modeling of this local analysis. The displacement of center of hatch cover increased drastically after concrete hoop stress reached basically zero.

Figure 3-4-1-5 shows concrete cracking behavior on both inner and outer surfaces in hoop direction under two pressures. Hoop cracking occurred near buttress and around E/H. The cracking near buttress was caused by reduction of tendon tensile force. The cracking around E/H was caused by change in stiffness due to discontinuous change of concrete thickness. The cracking extended as internal pressure increased. Hoop direction cracking extended to the whole

region at 2.8 Pd.

Figure 3-4-1-6 shows liner yielding region under several pressures. Initial liner yielding occurred at buttress and discontinuous position of concrete thickness at 2.6 Pd. The yielding region extended to free field of anti-buttress region at 2.8 Pd. It extended to the whole region except thick concrete place at 3.0 Pd. It extended to the whole region except hatch cover at 4.0 Pd.

Figure 3-4-1-7 shows principal tensile strain of liner under several pressures. Principal strain concentrated on upper region of hatch cover at 1.0 Pd. The principal tensile strain concentrated also on buttress and discontinuous position of concrete thickness at 2.2 Pd because of concrete cracking. The principal strain of discontinuous position became larger than that of buttress at 3.8 Pd. The maximum strain reached 3.5 % at 4.0 Pd, which was much less than 8 % of liner failure strain. That is, liner tearing was not predicted up to 4.0 Pd around E/H. On the other hand, tendon strain reached 3.2 % in the vicinity of loading end at 4.0 Pd, which was larger than 3 % of tendon failure strain. That is, tendon rupture was predicted at 4.0 Pd near equipment hatch. This was different from the failure modes of RCCV<sup>(2)</sup> and SCV<sup>(5)</sup> tests, because local strain concentration around E/H was unlikely to occur due to existence of prestressing of tendon in 1/4 PCCV model.

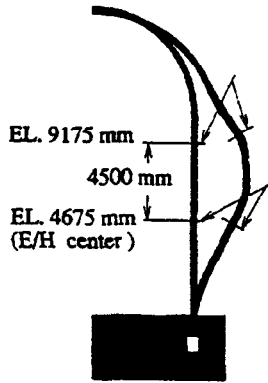


Fig. 3-4-1-1 Analysis region of equipment hatch

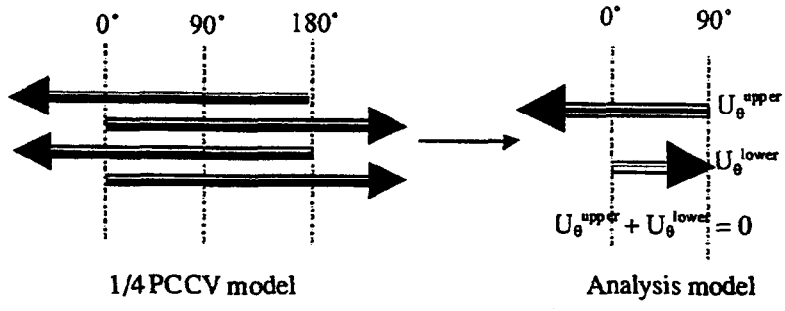


Fig. 3-4-1-2 Alternate tendon modeling

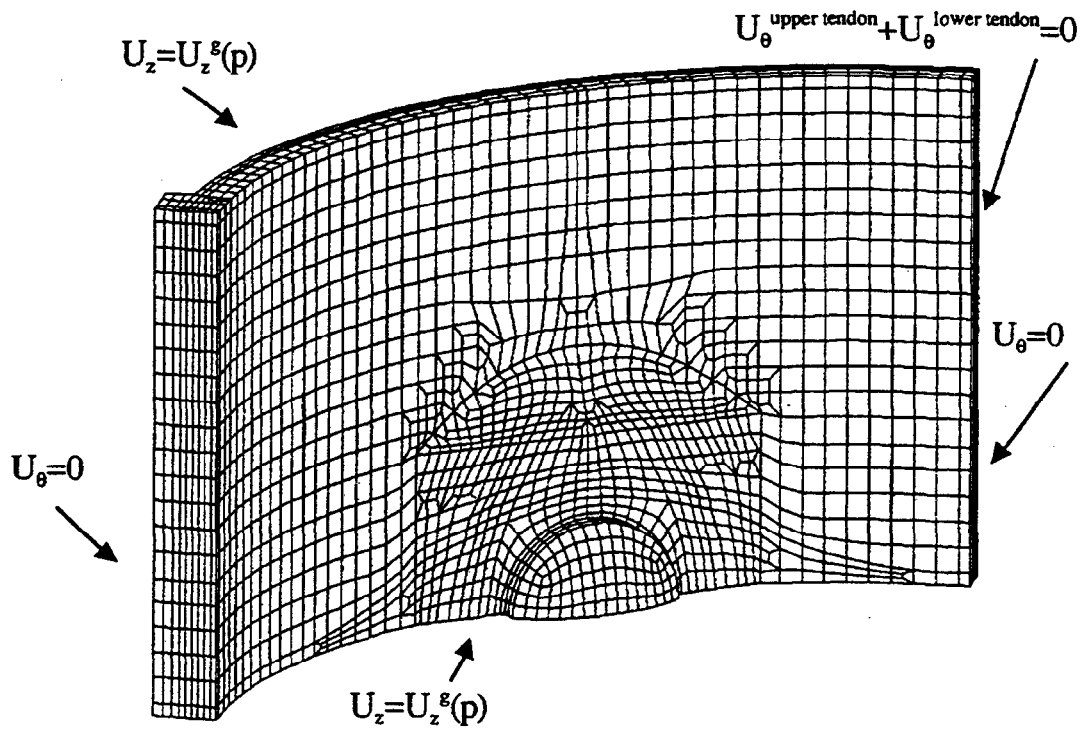


Fig. 3-4-1-3 Boundary conditions of equipment hatch

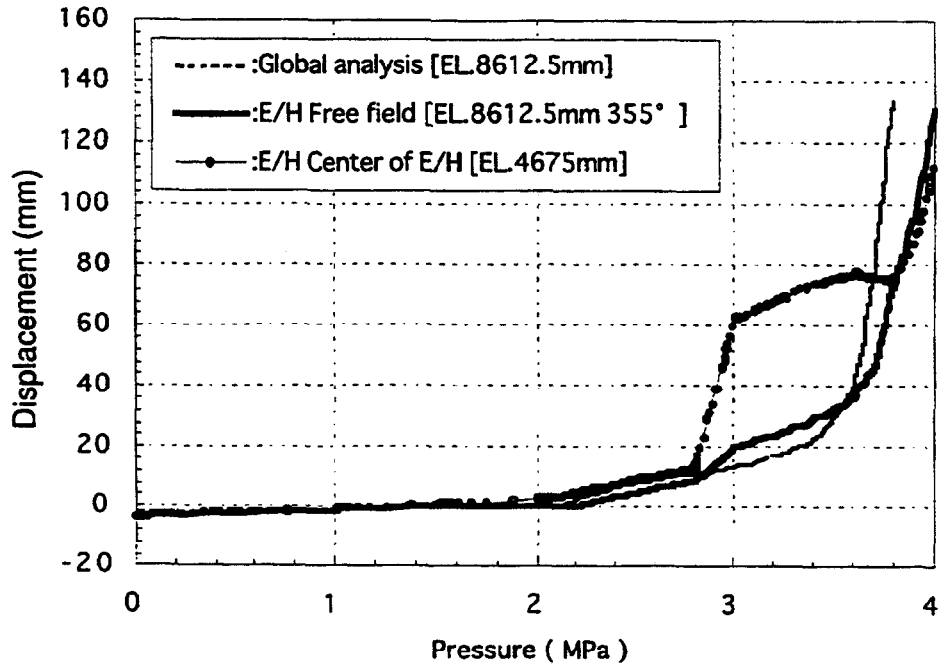


Fig. 3-4-1-4 Radial displacements various pressures compared with global analysis

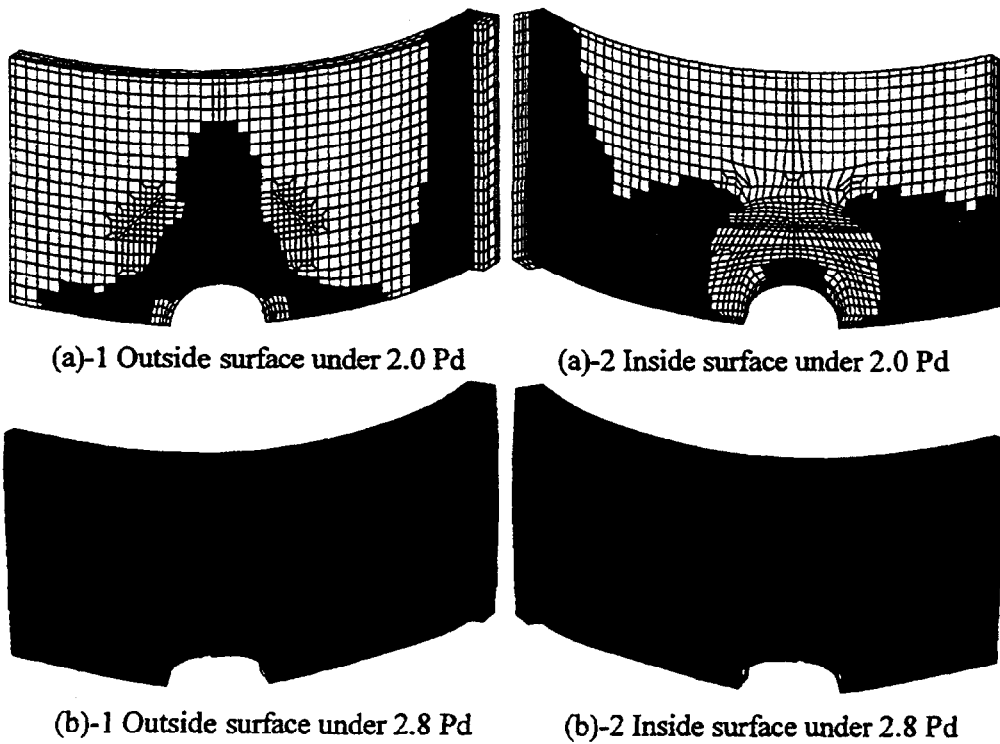


Fig. 3-4-1-5 Concrete cracking behavior in hoop direction under two pressures

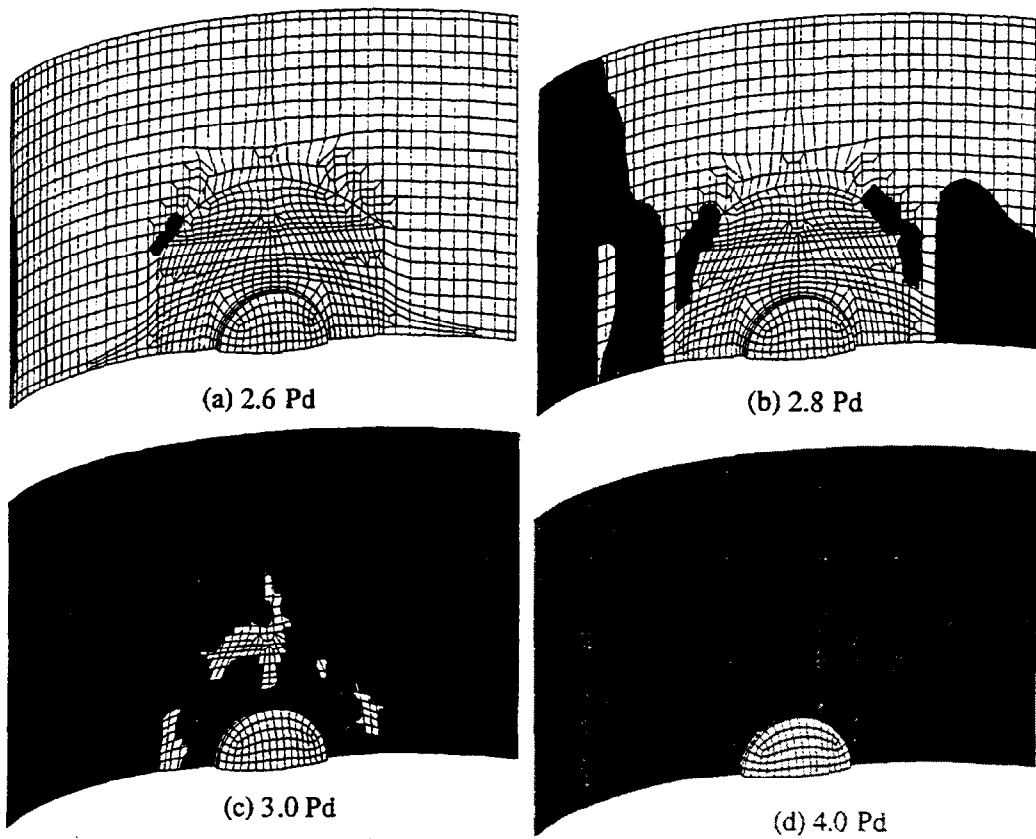


Fig. 3-4-1-6 Liner yielding region under several pressures

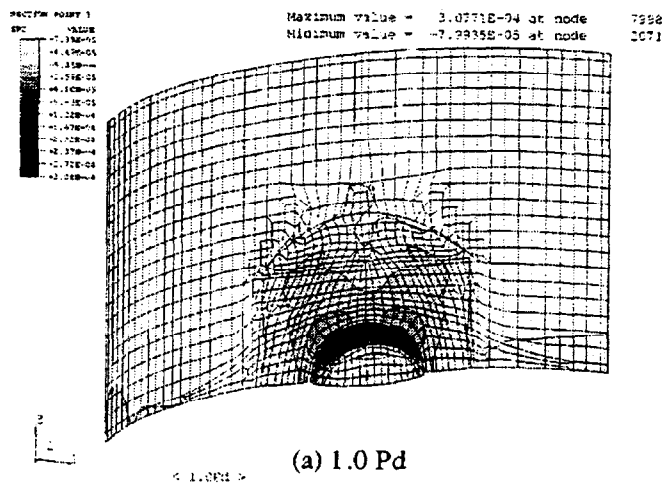
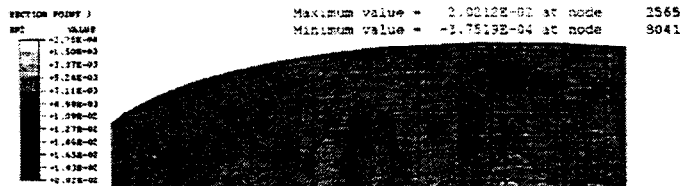


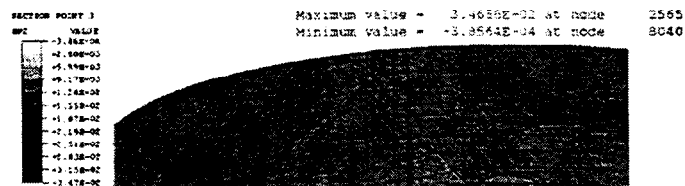
Fig. 3-4-1-7 Principal tensile strain under several pressures



(b) 2.2 Pd



(c) 3.8 Pd



(d) 4.0 Pd

Fig. 3-4-1-7 Principal tensile strain under several pressures (continued)

### **3.4.2 Air lock**

#### **(1) Analysis conditions**

Same material properties and same material models were used as those in global analysis. The analysis region was ranged from the horizontal central axis plane of air lock (A/L) to the plane at 4425 mm above it in vertical direction and 90 degree sector from buttress center, as shown in Fig 3-4-2-1. Analysis modelings were same as those in E/H analysis. The model included total numbers of 16425 elements and 11088 nodes. Boundary conditions were also same as those in E/H analysis. The analytical model is shown in Fig. 3-4-2-2.

#### **(2) Analysis results**

Figure 3-4-2-3 shows principal strain of liner at 2.2 Pd compared with that of E/H analysis. Local analysis of A/L was not successful above 2.2 Pd probably due to the existence of larger curvature of tendon around A/L compared with the curvature around E/H. The strain was concentrated at around buttress, and not around A/L. This was due to earlier concrete cracking near buttress region. The maximum principal strain of 0.10 % was similar to that of E/H analysis (0.11 %), so that liner tearing around A/L will not occur before liner tearing around E/H.

### **3.4.3 Main steam nozzles**

#### **(1) Analysis conditions**

Same material properties and same material models were used as those in global analysis. The analysis region was ranged from the horizontal central axis plane of main steam nozzles (M/S) to the plane at 3975 mm above it in vertical direction and 90 degree sector from buttress center, as shown in Fig 3-4-3-1. Analysis modelings were same as those in E/H analysis. The model included total numbers of 13081 elements and 9208 nodes. Boundary conditions were also same as those in E/H analysis. The analytical model is shown in Fig. 3-4-3-2.

#### **(2) Analysis results**

Figure 3-4-3-3 shows principal strain of liner at 2.2 Pd compared with that of E/H analysis. Local analysis of M/S was not successful above 2.2 Pd probably due to the existence of larger curvature of tendon around M/S compared with the curvature around E/H. The strain was concentrated at around buttress, and not around M/S. This was due to earlier concrete

cracking near buttress region. The maximum principal strain of 0.078 % was smaller than that of E/H analysis (0.11 %), so that liner tearing around M/S will occur after liner tearing around E/H.

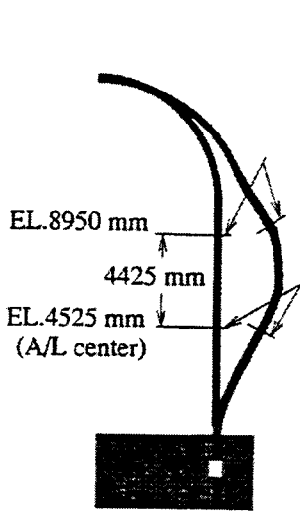


Fig 3-4-2-1 Analysis region of air lock

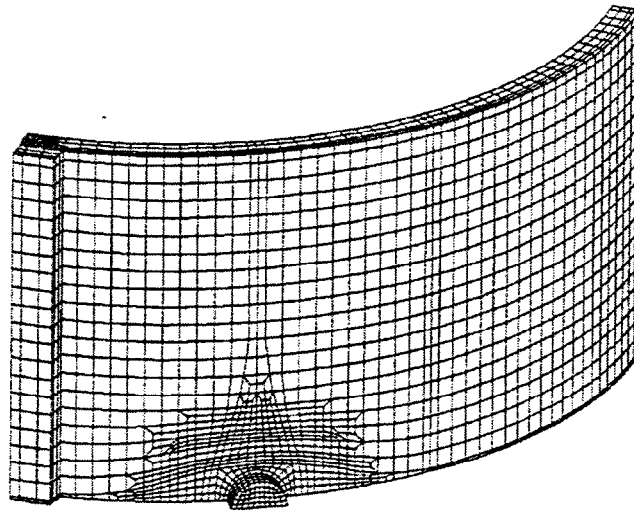
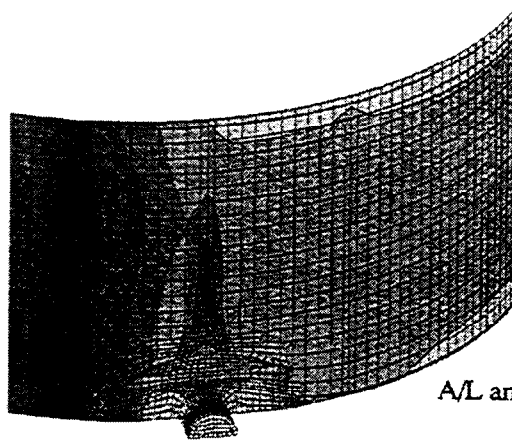


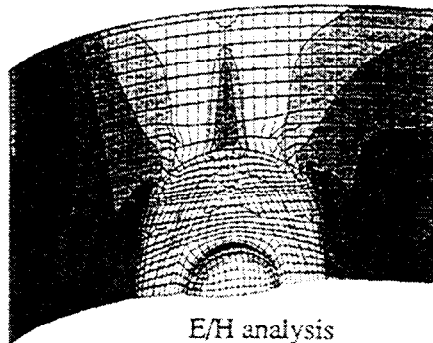
Fig. 3-4-2-2 Analytical modeling of air lock

SECTION POINT 1	VALUE
1	-3.78E-05
2	-6.10E-05
3	+1.00E-04
4	-2.34E-04
5	-4.17E-04
6	-5.37E-04
7	-6.56E-04
8	-7.72E-04
9	-8.92E-04
10	-1.01E-03
11	-1.05E-03

Maximum value = 1.0468E-03 at node 6179  
 Minimum value = -1.7396E-05 at node 159



A/L analysis



E/H analysis

Fig. 3-4-2-3 Principal tensile strain under 2.2 Pd compared with E/H analysis

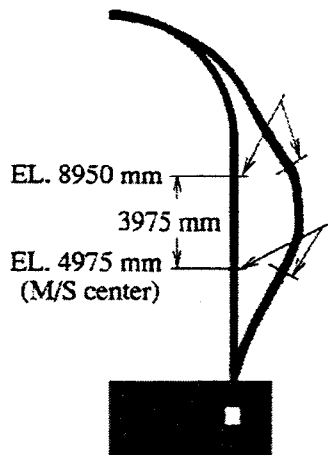


Fig. 3-4-3-1 Analysis region of main steam nozzles

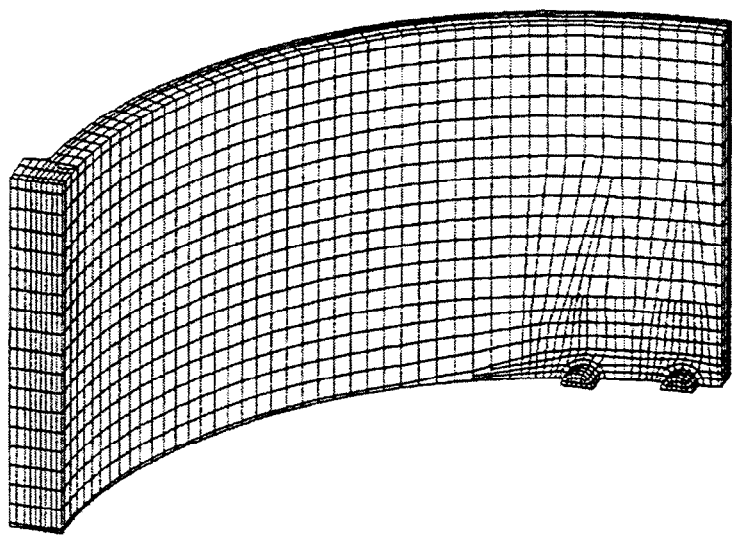
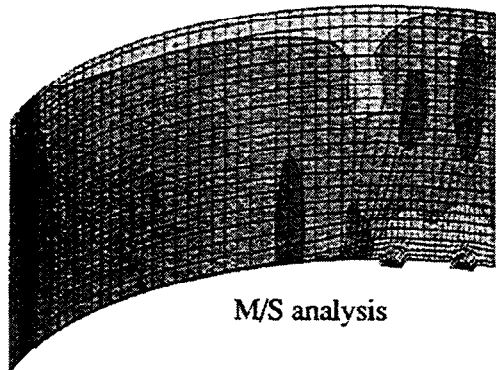


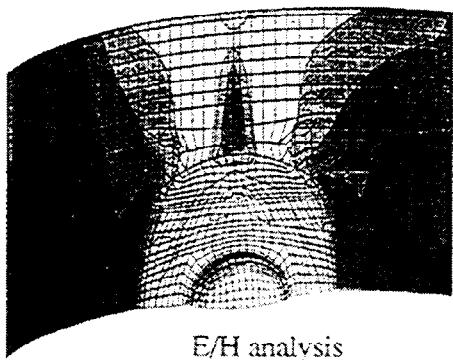
Fig. 3-4-3-2 Analytical modeling of main steam nozzles

SECTION POINT #	VALUE
1	-4.528E-05
2	-4.458E-04
3	-4.748E-04
4	-4.728E-04
5	-4.118E-04
6	-5.228E-04
7	-4.728E-04
8	-4.718E-04
9	-4.718E-04
10	-4.718E-04
11	-4.718E-04
12	-4.718E-04

Maximum value = 7.8551E-04 at node 237  
 Minimum value = -4.8727E-05 at node 5119



M/S analysis



E/H analysis

Fig. 3-4-3-3 Principal tensile strain under 4.0 Pd 2.2 Pd compared with E/H analysis

#### 4. CONCLUSION

As the first step of pre-test analysis, axisymmetric global analysis was conducted. The stress of concrete was nearly uniform in the cylinder part except near basemat and spring line up to about 2.0 Pd so that the stress of tendon and outside rebar were almost uniform in this region.

Concrete crack initiated at about 2.0 Pd, thereby the stress of concrete in the cylinder part decreased. As a result, the stress of rebar and tendon increased remarkably. This clearly demonstrated the role of prestressed concrete, in that the decreasing stress of concrete was supplemented by rebars and tendons.

The stress of concrete became almost zero and the stress of rebar became nearly uniform because of the yielding at 3.7 Pd. The stress of tendon also became nearly uniform in the cylinder part because of its yielding. Hence, the displacement increased in the radial direction remarkably.

In short, concrete cracking governed the global behavior of 1/4 PCCV model. That is, the reduction of concrete stress due to cracking caused the change in stress distributions of rebars and tendons and resultant global deformation behavior.

Free field analysis was conducted to investigate hoop tendon tensile force distribution, using the friction coefficient correlation depending on loading end load and the angle from loading end. The friction correlation provided better convergence compared with constant friction due to the continuous change in friction coefficient at the boundary between straight part and circular part in the vicinity of buttress region. The tendon tensile force distribution shape was changed as internal pressure increased. The change of tensile force distribution was governed by the change of friction force. Friction force decreased due to concrete cracking and yielding of rebar and liner, in turn. The strain of H53 tendon at loading end as high as 3% at 4.0 Pd. Hence, the probability of tendon rupture will be high.

Local analyses were conducted at 4 parts of wall-base junction, equipment hatch, air lock and main stream nozzles where the failure was initially predicted.

The wall-base junction analysis was conducted by axisymmetric analysis. The vertical liner strain at wall-base junction was suppressed by horizontal liner anchor and they were less than 0.25 %. Hence, probability of liner tearing up to about 3.8 Pd will be small. The region, exceeding failure criteria strain, was quite small at about 3.8 Pd. Hence, the probability of concrete shear failure at this location up to about 3.8 Pd will be also small.



- First hoop tendon in cylinder reaching 2% strain 3.8 Pd  
(1.49 MPa)
- First hoop tendon in cylinder reaching 3% strain 4.0 Pd  
(1.57 MPa)
- A qualitative assessment of the lower and upper limits of the PCCV model failure pressure range
  - minimum pressure reachable with 90 % confidence level 3.8 Pd  
(1.49 MPa)
  - maximum pressure reachable with 90 % confidence level 4.0 Pd  
(1.57 MPa)

## ACKNOWLEDGMENT

This work is sponsored under the contract by the Ministry of International Trade and Industry, Japan.

## REFERENCES

- (1) Twidale, D., and Crowder R., 1991, "Sizewell 'B' - a One Tenth Scale Containment Model Test for the UK Programme," Nuclear Engineering and Design 125 85-93
- (2) Horschel, D. S., 1992, "Experimental Results from Pressure Testing A 1:6-Scale Nuclear Power Plant Containment," NUREG/CR-5121, SAND88-0906
- (3) Kashiwase, T., and Nagasaka, H., 1997, " Analysis Study on Change of Tendon Tension Force Distribution during the Pressurization Process of Pre-stressed Concrete Containment Vessel," Proceedings of ICON-5
- (4) Miller, C. M., 1992, "Geotechnical Investigation job No. 1-20904 Containment Technology Test Facility - west Albuquerque, New Mexico," GEO-TEST
- (5) Nuclear Power Engineering Corporation, "Report for Containment Integrity Test in fiscal 1997," 1998
- (6) F. J. Vecchio and M. P. Collins, 1986 "The Modified Compression-Field Theory or Reinforced Concrete Elements Subjected to Shear," ACI Journal March-April 1986
- (7) Kashiwase, T., and Nagasaka, H., 1998, " Extension of Tendon Friction Coefficient within Elastic Region to Plastic Region," Summaries of Technical papers of Annual meeting Architectural Institute of Japan 1998



**APPENDIX P**

**PRINCIPIA**

**PRINCIPIA**

**SPAIN**

Appendix A, Composite Plots, comprises test data compiled and plotted from all organizations that participated in the Prestressed Concrete Containment Vessel (PCCV) Round Robin Pretest Analysis. To avoid duplicating the composite information, individual sets of data and/or plots have been omitted from participants' reports. In some cases this action resulted in disconnects between callouts and content and in the numbering of figures, tables, and pagination in some reports.

In Appendix P, "PRINCIPIA, Spain," discontinuity arises from omitting the following material:

Figure 2-3  
Appendix II, "Plots at standard output locations"

## TABLE OF CONTENTS

	<u>Page.</u>
1. INTRODUCTION .....	1
1.1 Preamble .....	1
1.2 Object .....	1
1.3 Scope .....	1
1.4 Layout of the report .....	2
2. GEOMETRICAL DEFINITION .....	3
3. DESCRIPTION OF THE MODEL .....	7
3.1 Geometrical model .....	7
3.2 Material modelling.....	7
4. RESULTS.....	16
5. CONCLUSIONS.....	25

Appendix I. List of references

Appendix II Plots at standard output locations

## LIST OF FIGURES

	<u>Page.</u>
Figure 2-1 Outline sketch of PCCV model.....	4
Figure 2-2 PCCV model coordinates and measurements locations .....	5
Figure 2-3 Stretched layout of PCCV model .....	6
Figure 3-1 Finite element model .....	9
Figure 3-2 Detail of steel reinforcing .....	10
Figure 3-3 Uniaxial stress-strain data for liner.....	11
Figure 3-4 Uniaxial stress-strain data for SD345.....	12
Figure 3-5 Uniaxial stress-strain data for SD390.....	13
Figure 3-6 Uniaxial stress-strain data for SD490.....	14
Figure 3-7 Uniaxial stress-strain data for tendons .....	15
Figure 4-1 Deformed shape $P/P_d=3.25$ .....	18
Figure 4-2 Deformed shape $P/P_d=3.45$ .....	19
Figure 4-3 Deformed shape $P/P_d=3.62$ .....	20
Figure 4-4 Radial displacement history .....	21
Figure 4-5 Stress history in tendons.....	22
Figure 4-6 Stress history in rebars .....	23
Figure 4-7 Equivalent plastic strain in the liner at $P/P_d=3.62$ .....	24

## LIST OF TABLES

	<u>Page.</u>
Table 3-1 Prestressing force per tendon.....	8
Table 3-2 Properties for steel.....	8
Table 3-3 Properties for concrete.....	8
Table 3-4 Stress-strain softening .....	8
Table 4-1 Sequence of events .....	16



## **1. INTRODUCTION**

### **1.1 Preamble**

Sandia National Laboratories (SNL) is constructing and instrumenting a 1:4 scale Prestressed Concrete Containment Vessel (PCCV) as part of a containment research program co-sponsored by Nuclear Power Engineering Corporation (NUPEC) of Japan and the US Nuclear Regulatory Commission (NRC). The containment will be subject to static internal pressurisation until failure during 2000.

One of the key program objectives is to develop validated methods to predict the structural performance of containment vessels when subjected to beyond design basis loadings. With this aim, SNL is co-ordinating Round Robin analyses to predict the structural response up to failure before the test is performed. Thus participants were required to submit the pre-test predictions at selected standard output locations in order to be compiled for preparing a pre-test analysis report.

Principia is one of the fifteen organisations participating in the present pre-test Round Robin analyses and who have submitted the pre-test analysis results.

### **1.2 Object**

The object of this report is to describe the methodology followed and the modelling approach employed for obtaining the results at the different requested output locations, results which were already submitted to SNL. It also attempts to provide a qualitative assessment of the lower and upper limits of the pressure range within which failure of the PCCV model may be expected.

### **1.3 Scope**

In order to fulfil the above objectives, the following tasks have been conducted:

- a) Gathering all the relevant information for conducting the analyses: geometrical definition, mechanical properties, etc.
- b) Generating of a global 2D axisymmetric model, including the reinforcing bars and prestressing tendons.

- c) Modelling the constitutive response of the different materials from the test data provided.
- d) Conducting the analyses and obtaining the results at the different output locations.
- e) Monitoring and description of the pressure levels at which cracks initiate in the concrete, as well as those causing yielding of the liner, rebars and tendons.
- f) Providing a qualitative assessment of the most likely pressure range within which failure can be expected to occur.

#### **1.4 Layout of the report**

The rest of the present report comprises four additional chapters.

Chapter 2 presents a brief description of the geometrical definition of the containment under consideration.

The geometrical modelling assumptions, as well as the constitutive behaviour adopted for the different materials, are provided in Chapter 3.

The results of the analysis are presented and discussed in Chapter 4. Finally, Chapter 5 gathers the tentative conclusions arising from the work conducted to date.

Two appendixes complete the report. Appendix I provides the list of the references mentioned in the text. The second appendix gathers the plots representing the evolution of the variables at the different output locations as a function of the gradually increasing pressure.

## 2. GEOMETRICAL DEFINITION

The PCCV model is a uniform 1:4-scale model of an existing pressurized water reactor (PWR) prestressed concrete containment vessel in Japan. The model includes a steel liner and a scaled representation of the equipment hatch, the personnel airlock and the main steam and feedwater line penetrations. The design pressure of this prototype containment vessel is 0.39 MPa.

The overall geometry of the model, as shown in Figure 2-1, was provided in the design package information (SNL, 1997). Figure 2-2 shows the standard global coordinate system used to describe the model and Figure 2-3 shows in solid dots the standard output locations where participants were requested to provide the pretest analysis predictions.

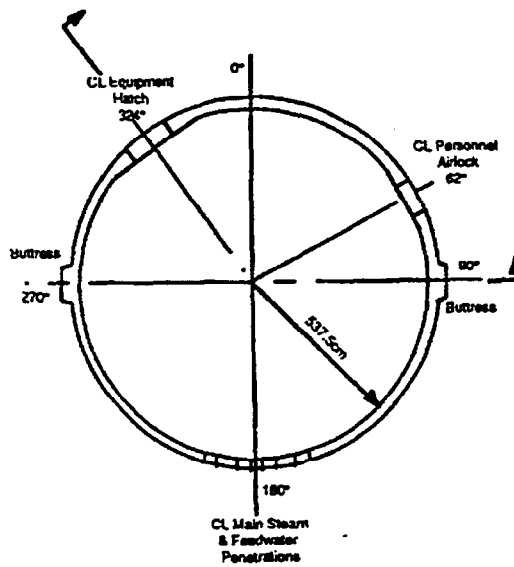
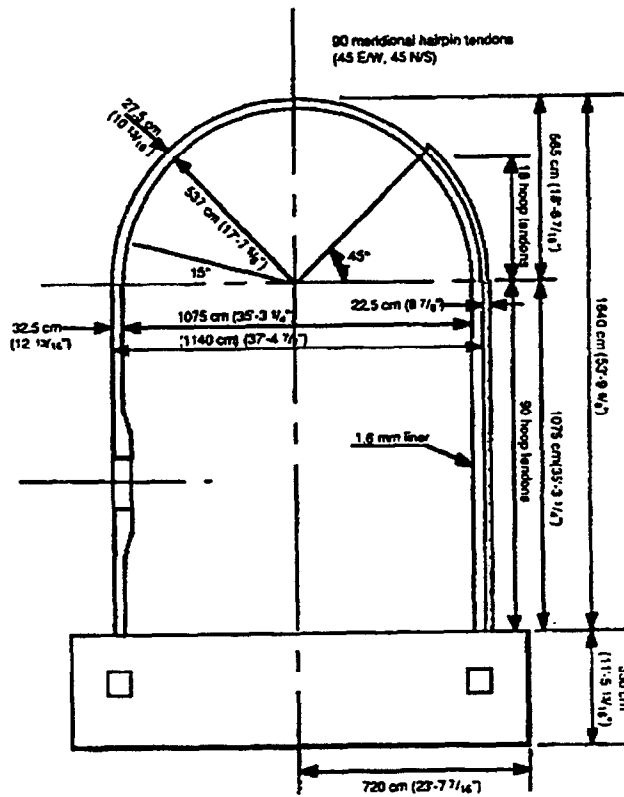


Figure 2-1 Outline sketch of PCCV model.

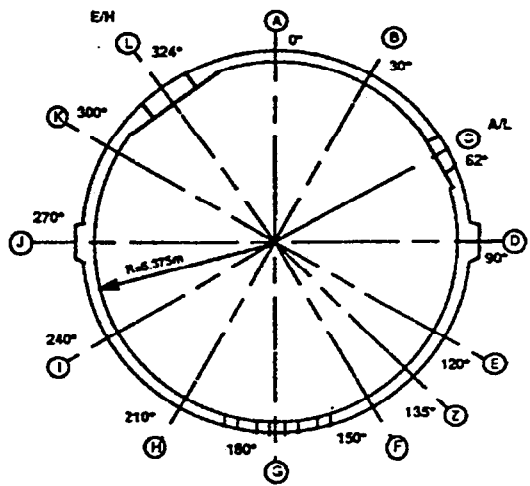
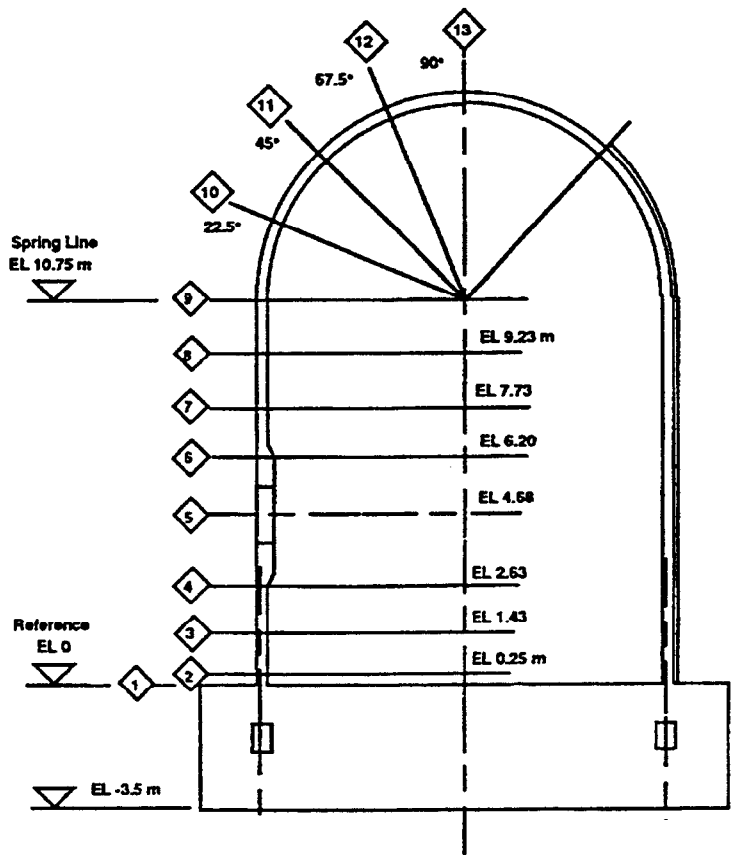


Figure 2-2 PCCV model coordinates and measurements locations

### 3. DESCRIPTION OF THE MODEL

#### **3.1 Geometrical model**

A global 2D axisymmetric model has been generated with the general purpose finite element code ABAQUS/Standard (HKS, 1998). The concrete cylindrical wall, the concrete dome and the basemat are modeled with 8-node quadrilaterals with reduced (2x2) Gaussian integration. Four elements have been used through the thickness of the wall. The liner has been represented with axisymmetric second order shells which share the nodes with the continuum elements.

A general view of the mesh is shown in Figure 3-1. It has a total of 1300 nodes and 510 elements.

Reinforcing steel bars and horizontal tendons have been represented within the continuum elements. As an example Figure 3-2 shows a detail of the rebar layers around the anchorage gallery. In some areas the actual reinforcement is not axisymmetric; thus, a mechanically equivalent axisymmetric reinforcement had to be determined and was introduced in the model.

Vertical tendons are not adherent; hence, they have modelled as independent truss elements which can slide with respect to the concrete with a friction coefficient between the tendons and the sheaths of 0.21. Table 3-1 gathers the final force adopted for the tendons including the different prestressing losses.

#### **3.2 Material modelling**

The steel of the liner, rebars and prestressing tendons has been modelled as an elastic-plastic material with isotropic hardening. The mechanical constants adopted are shown in Table 3-2 and the uniaxial stress-strain curves for the different steels are represented in Figures 3-3 to 3-7.

The properties adopted for the concrete are provided in Table 3-3. The constitutive model is elastic-plastic in compression, but is brittle with strain softening in tension once the tensile strength is reached (HKS, 1998). The postfailure stress-strain relationship in tension is defined by a linear reduction of the stress according to Table 3-4.

Table 3-1 Prestressing force per tendon

	After Anchorage Set (kN)	Shrinkage Loss (kN)	Creep Loss (kN)	Relaxation Loss (kN)	Final (kN)
Hoop	360	17	20	7	316
Vertical	470	17	8	7	437

Table 3-2 Properties for steel

	E (GPa)	$\nu$ (-)	$\sigma_y$ (MPa)	$\sigma_u$ (MPa)	$\epsilon_u$ (-)
Liner	219	0.3	384	498	0.28
SD345	175	0.3	371	662	0.24
SD390	186	0.3	460	782	0.19
SD490	185	0.3	526	832	0.17
Tendons	220	0.3	1742	1892	0.08

Table 3-3 Properties for concrete

	E (GPa)	$\nu$ (-)	$f_c$ (MPa)	$f_{ct}$ (MPa)
C29	27	0.18	44	3.6
C45	28	0.18	55	3.6

Table 3-4 Stress-strain softening

$\epsilon_u (10^{-3})$	$\sigma/f_{ct}$
0.7	0.5
1.3	0.1

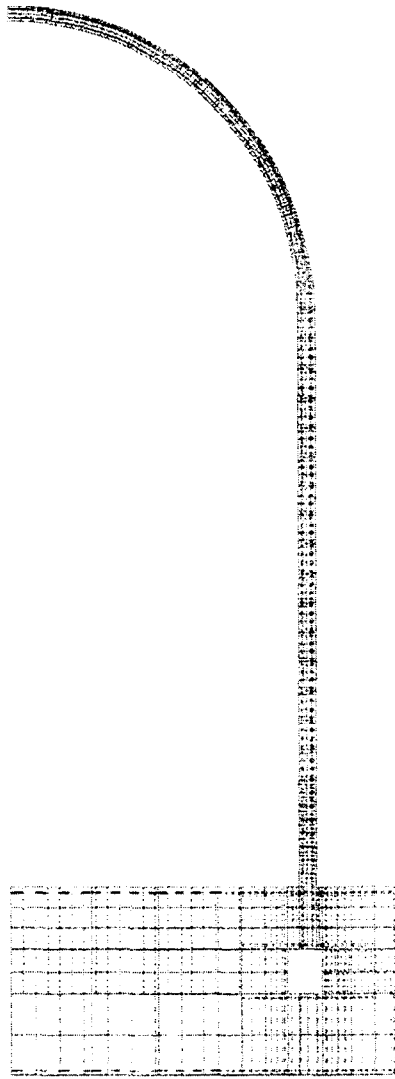


Figure 3-1 Finite element model

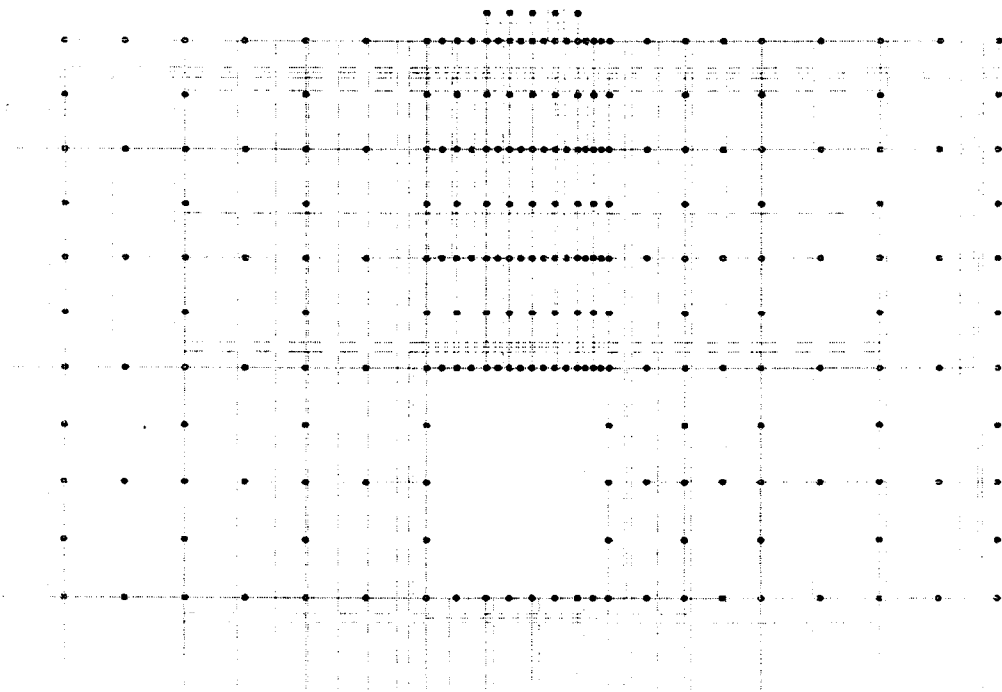


Figure 3-2 Detail of steel reinforcing



### Reinforcing Steel - SD345

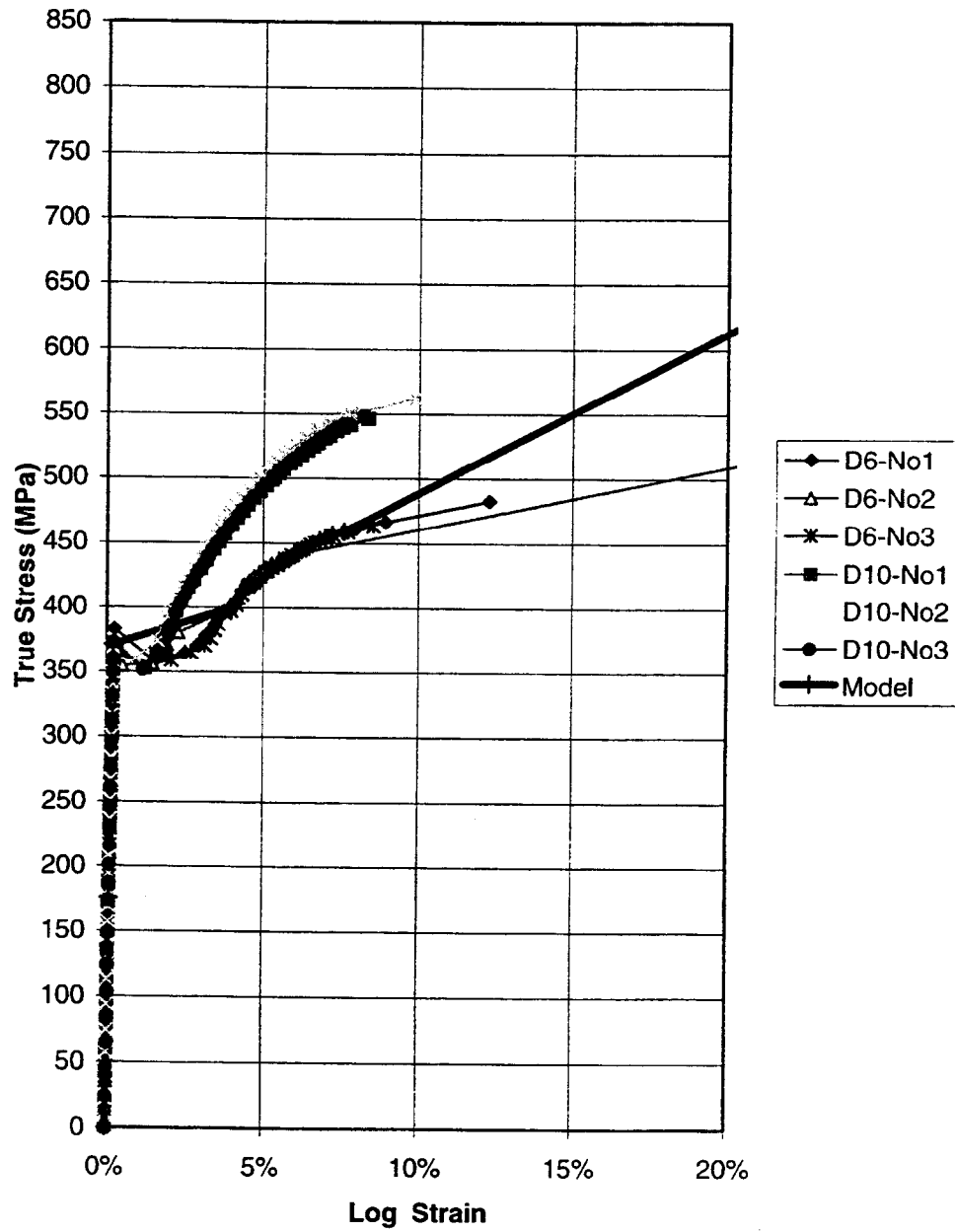


Figure 3-4 Uniaxial stress-strain data for SD345

### Reinforcing Steel - SD390

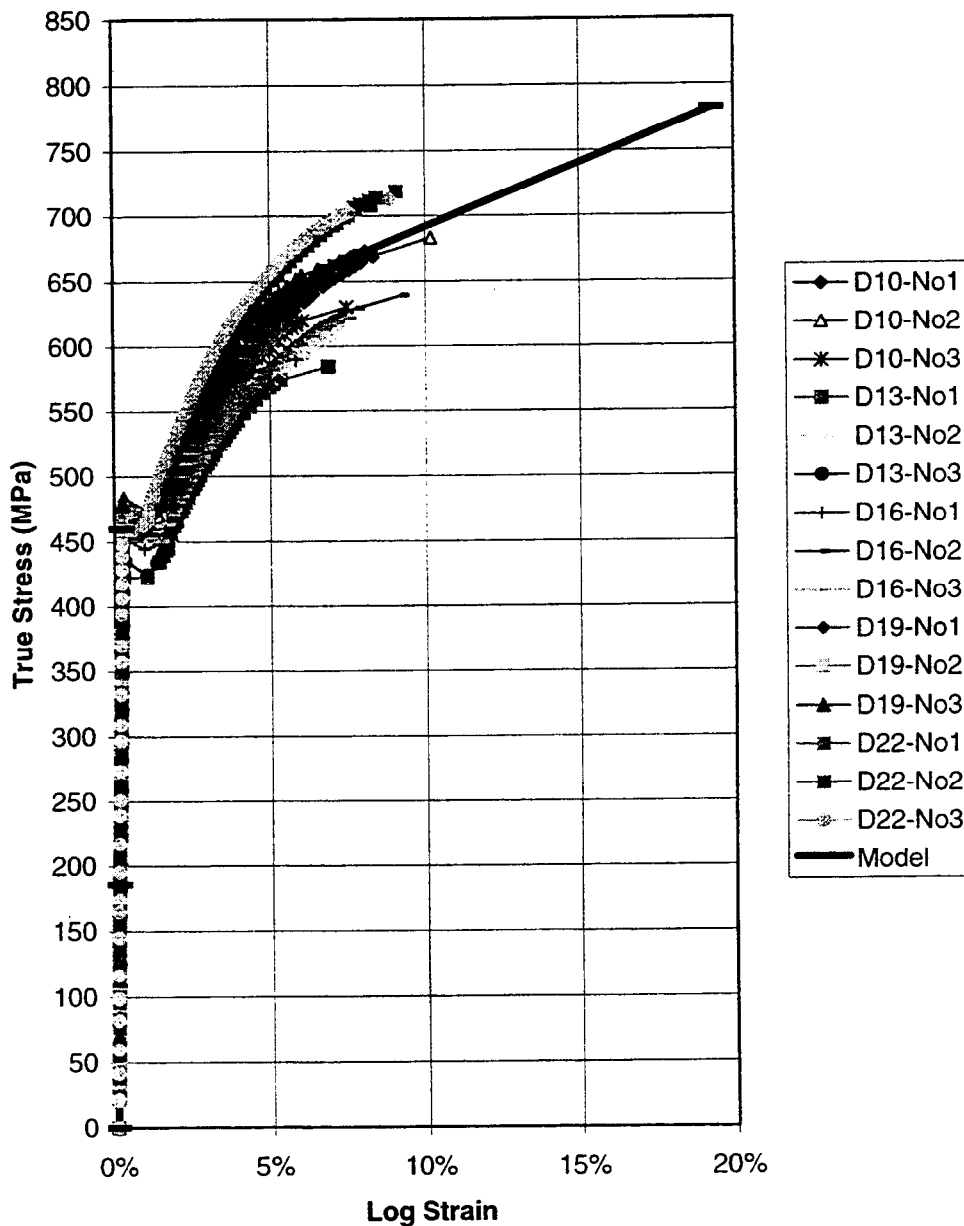


Figure 3-5 Uniaxial stress-strain data for SD390

### Reinforcing Steel - SD490

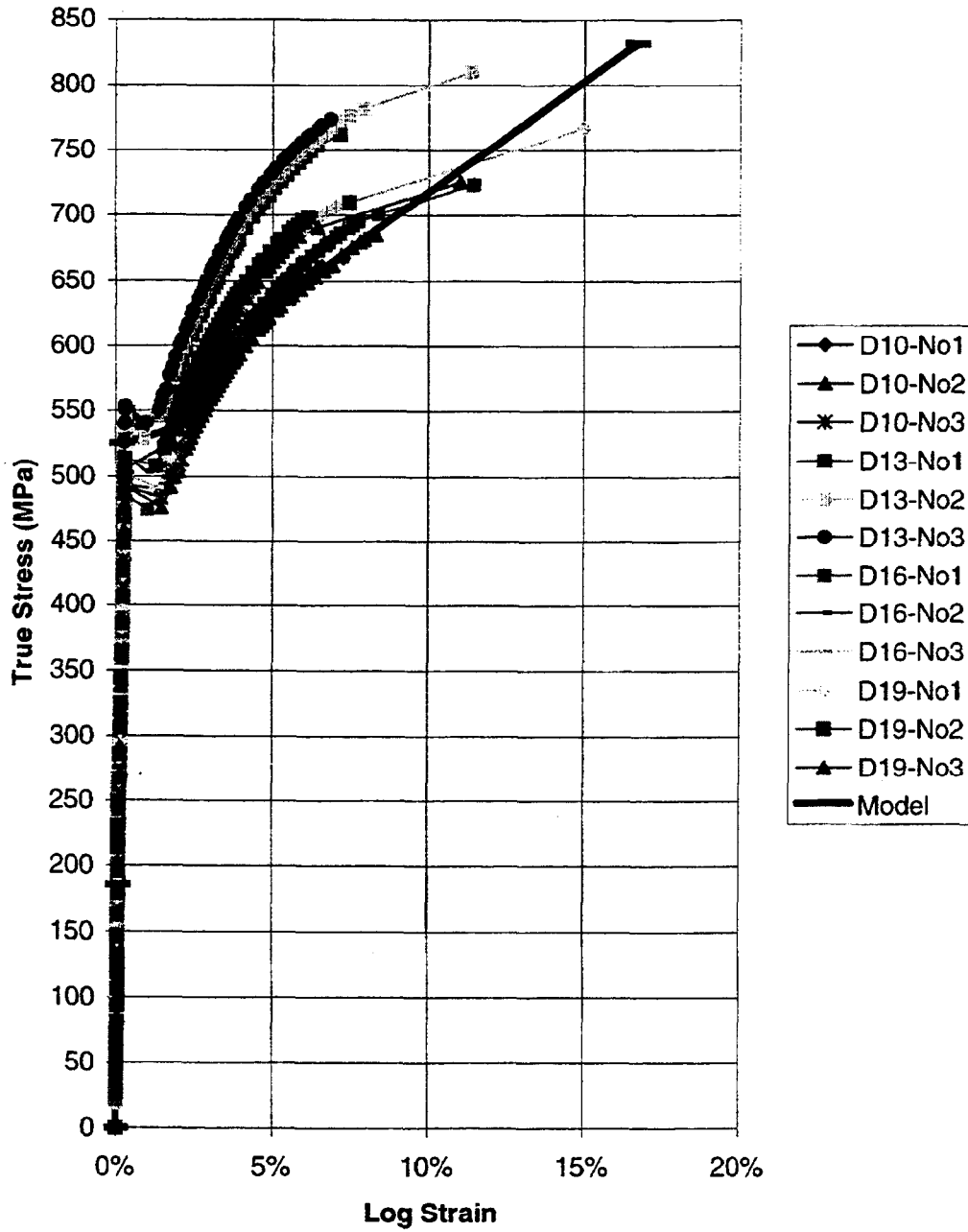


Figure 3-6 Uniaxial stress-strain data for SD490

### Tendons

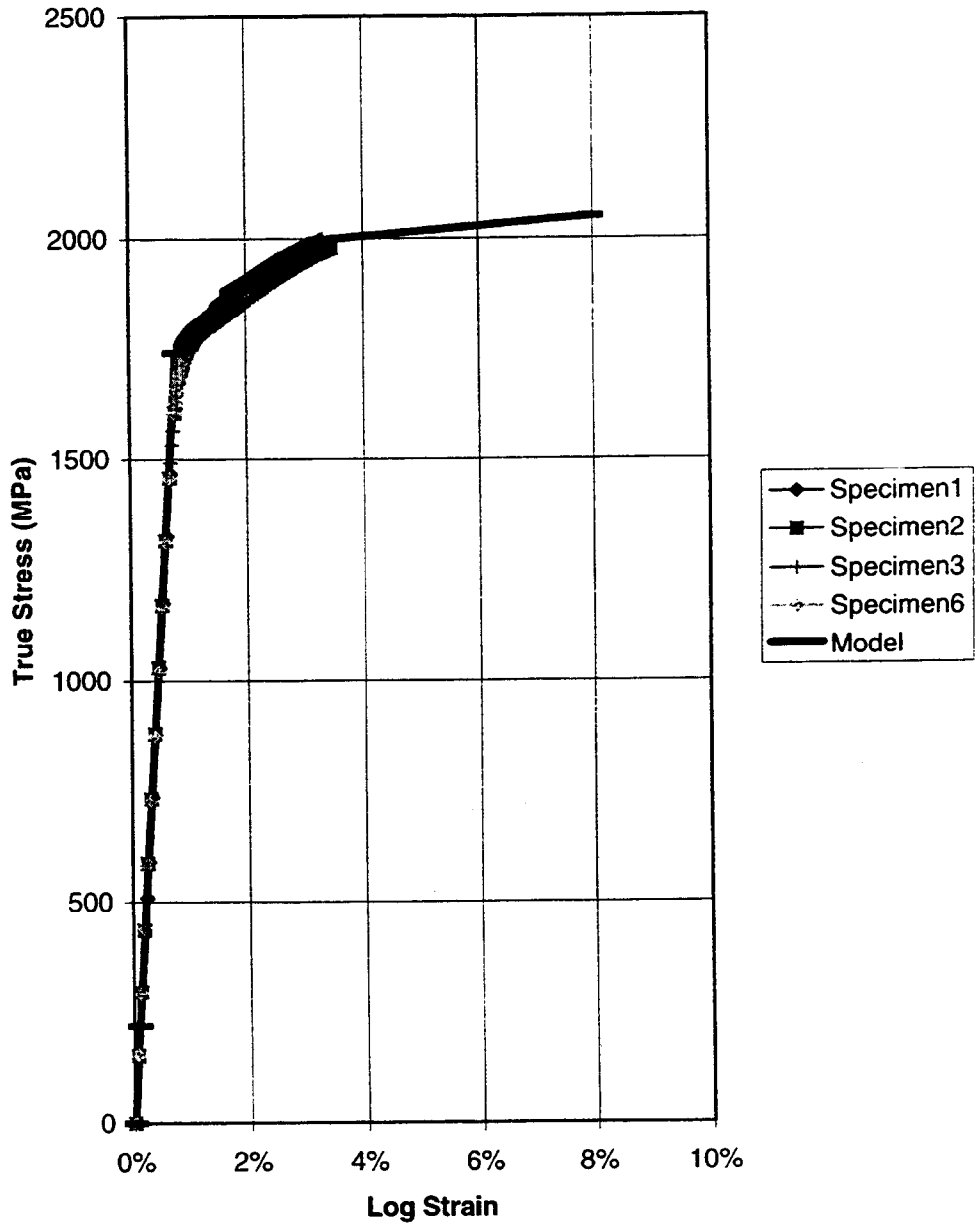


Figure 3-7 Uniaxial stress-strain data for tendons

**This page inadvertently left blank.**

## 4. RESULTS

The results obtained at different output locations are plotted in Appendix II. A summary of the event milestones is presented in Table 4-1.

Table 4-1 Sequence of events

(P/P <sub>design</sub> )	Event
1.7	First cracking in cylinder in hoop direction
2.6	Liner starts yielding
3.0	First cracking in cylinder in meridional direction
2.9	Hoop rebars start yielding
3.0	Vertical rebars start yielding
3.3	Hoop tendons start yielding
3.4	First hoop tendon in cylinder reaching 1% strain
3.5	First hoop tendon in cylinder reaching 2% strain

Figures 4-1 to 4-3 show the deformed shapes of the containment which correspond, respectively, to 3.25, 3.45 and 3.62 times the design pressure.

The global response of the structure may be visualised through the evolution of the radial displacement at the levels of midheight of the cylinder and the springline as shown in Figure 4-4.

Figures 4-5 and 4-6 depicted, respectively, the evolution of stresses in the prestressing tendons and the reinforcement at midheight of the cylinder. Finally, the effective plastic strains in the liner at 3.6 times de design pressure are presented in Figure 4-7.

The results indicate that cracking of the concrete causes a sudden change of the stiffness of the structure at approximately 2.0 times the design pressure. From this point, tendons and rebars have to sustain the pressure. Hoop rebars start yielding at 2.9 times the design pressure and horizontal tendons at 3.33, which provides a limit for the pressure.

The global response of the structure indicates that the most likely pressure range for failure is comprised between 3.33 and 3.50 times the design pressure.

It is difficult to predict the possibility of a local failure mode (arising, for example, as a consequence of strain concentrations near penetrations) without conducting detail analyses. However, the level of global plastic strains in the liner shows that, if a strain concentration factor of 10 is adopted, the tearing of the liner would occur in the same range of pressures mentioned earlier.

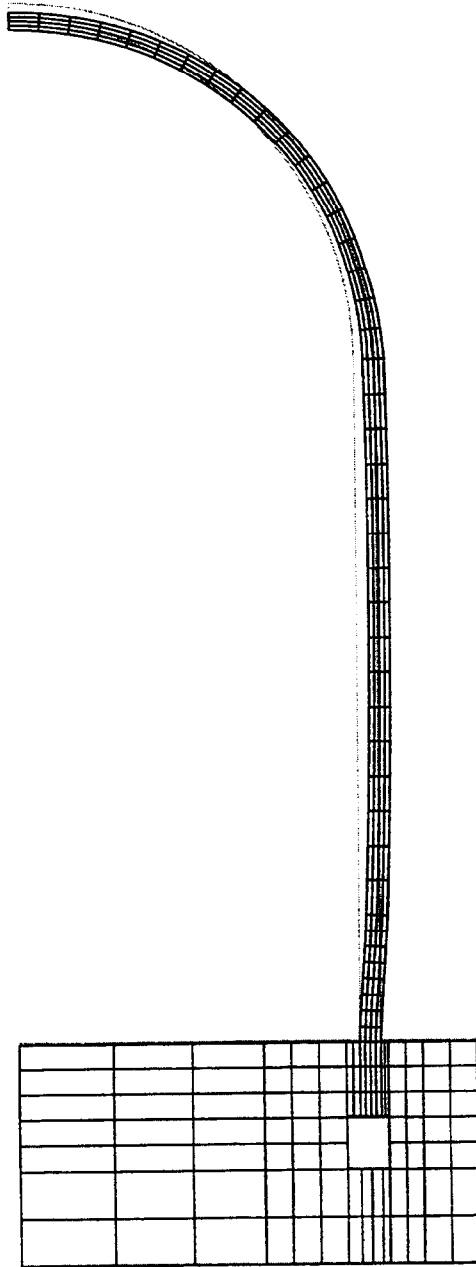


Figure 4-1 Deformed shape  $P/P_d=3.25$

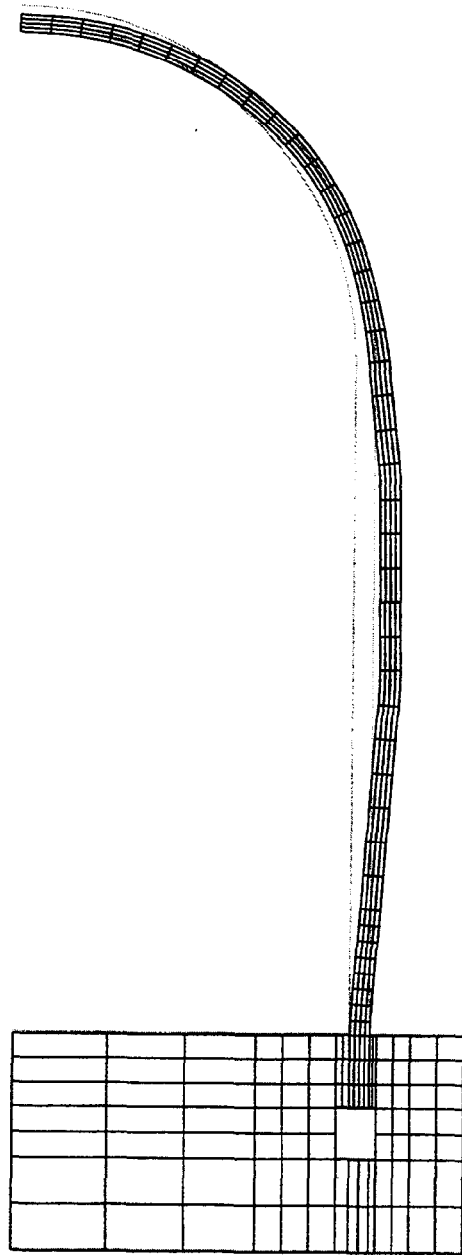


Figure 4-2 Deformed shape  $P/P_d=3.45$

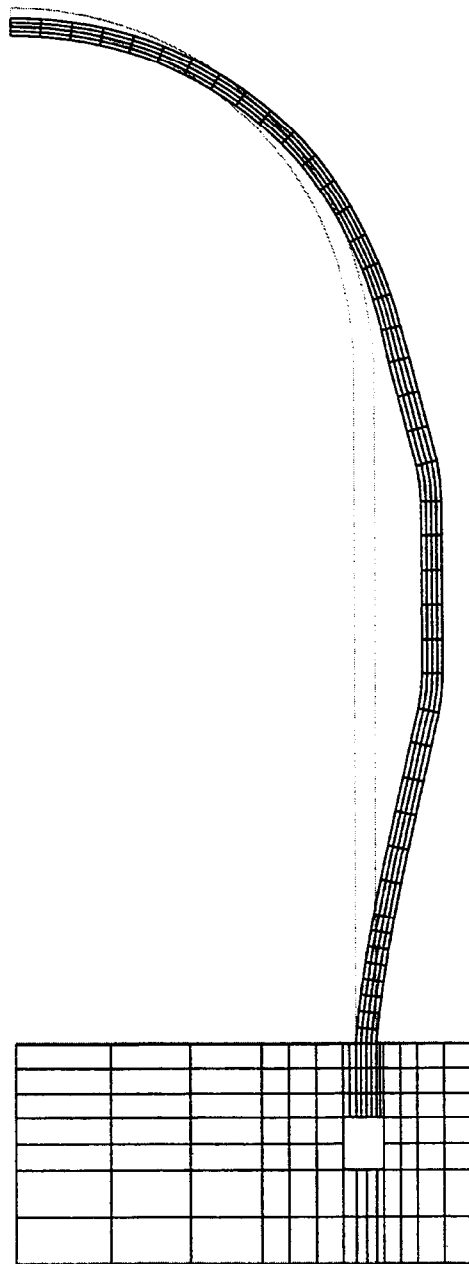


Figure 4-3 Deformed shape  $P/P_d=3.62$

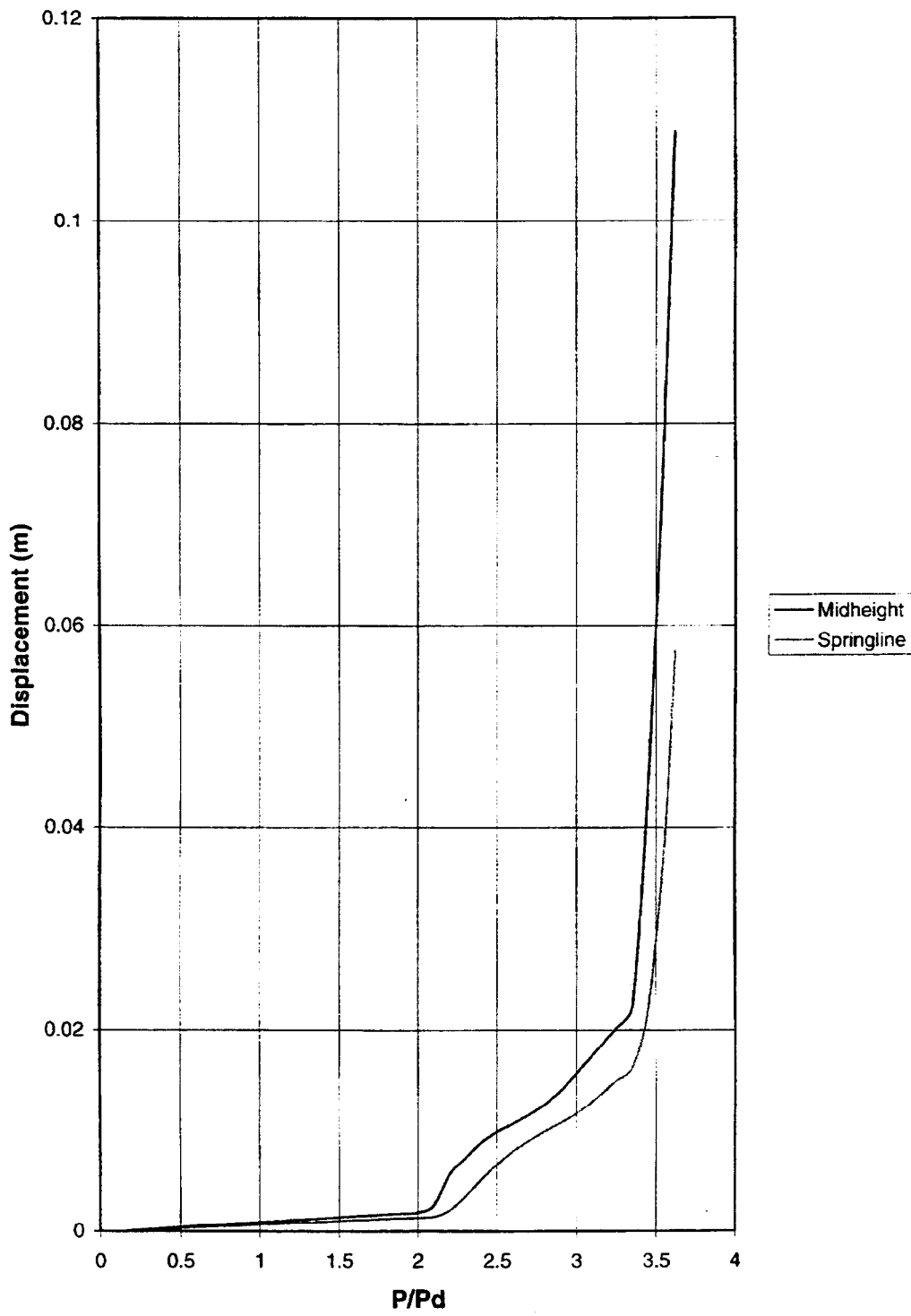


Figure 4-4 Radial displacement history

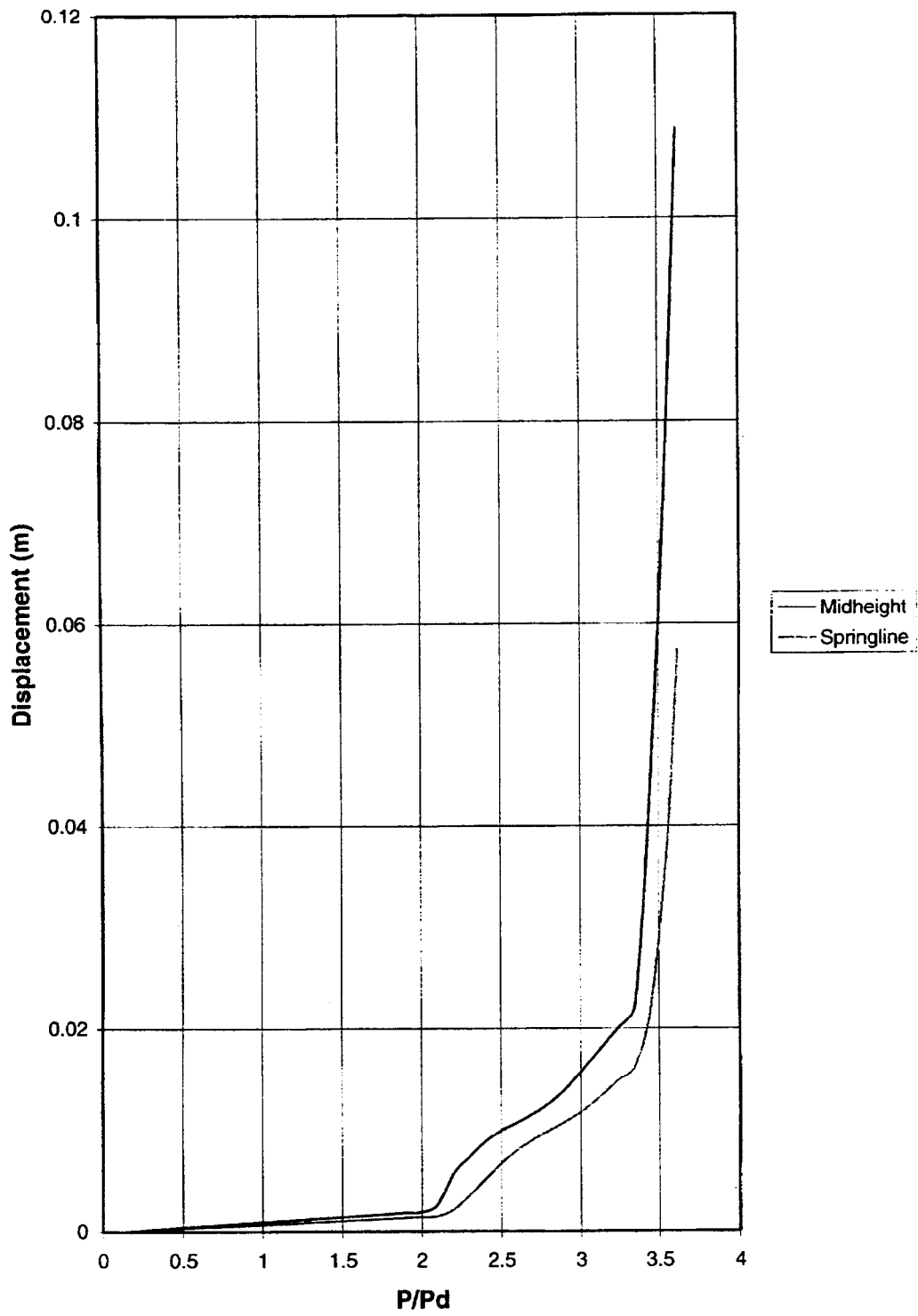


Figure 4-4 Radial displacement history

# Prestressing Tendons

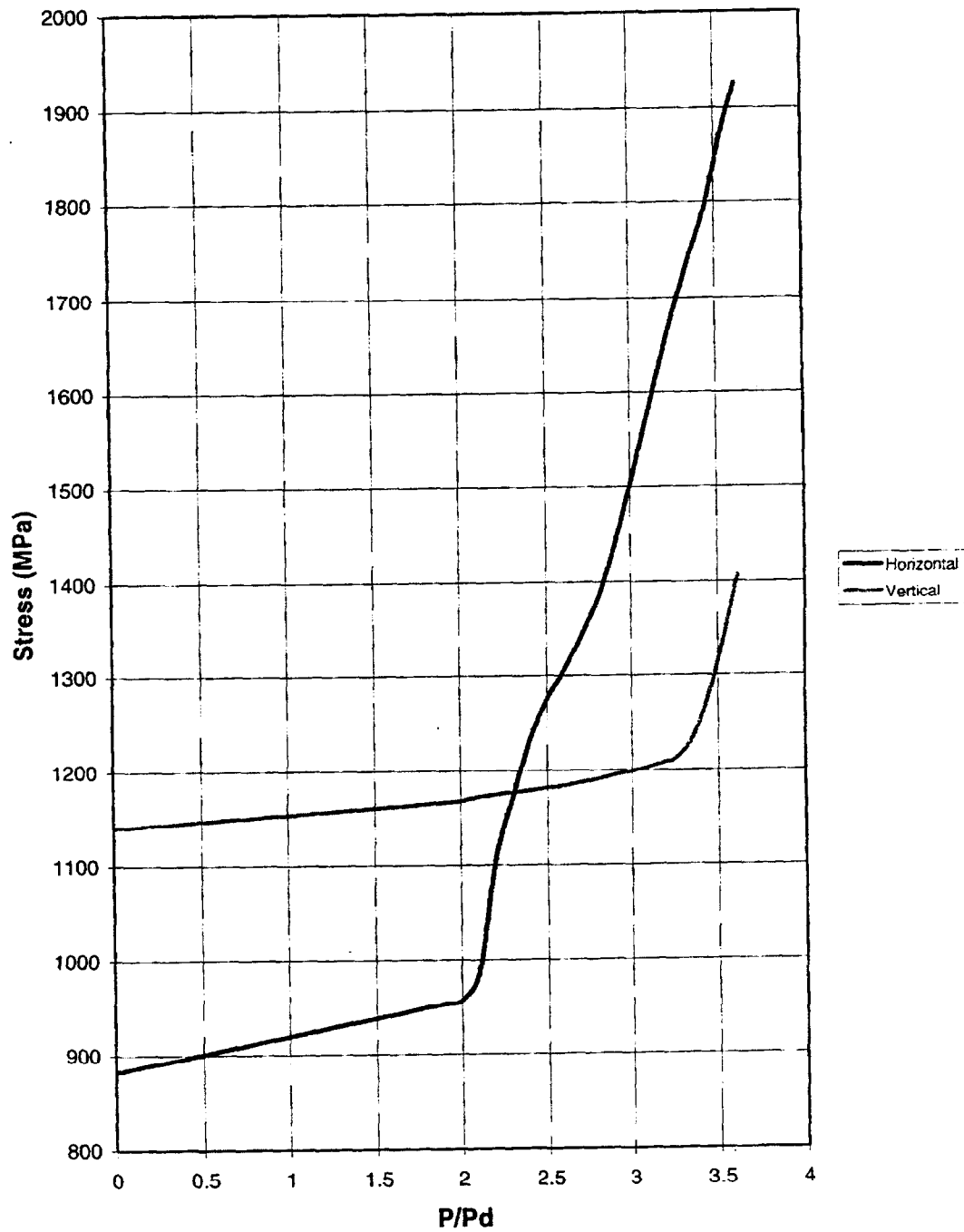


Figure 4-5 Stress history in tendons

PEEQ  
SNEG, (fraction = -1.0)  
(Ave. Crit.: 75%)

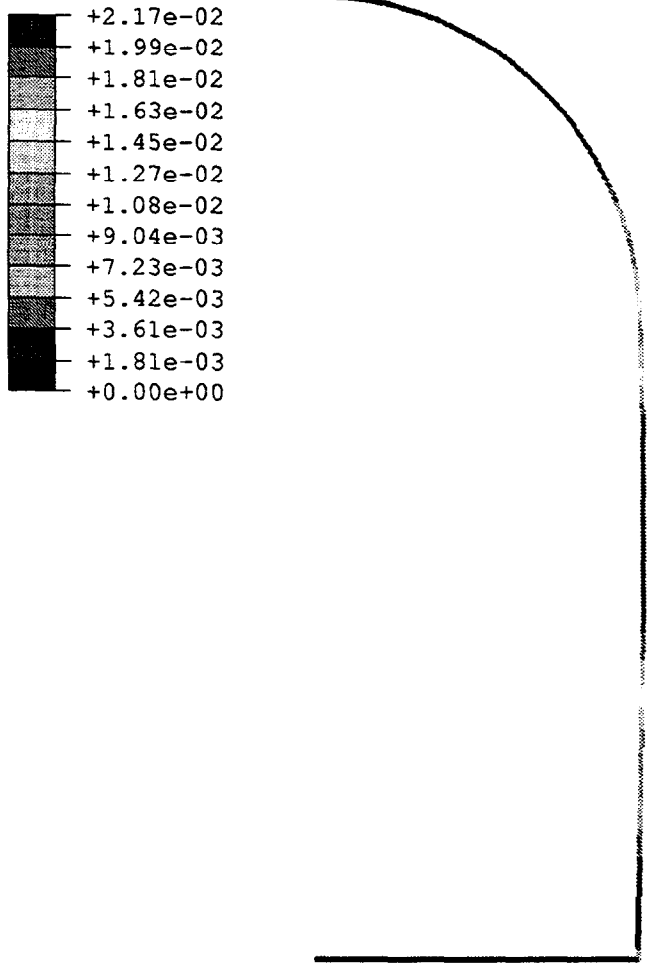


Figure 4-7 Equivalent plastic strain in the liner at  $P/P_d=3.62$

## 5. CONCLUSIONS

A global 2D axisymmetric model has been generated for providing a first insight of the general structural behaviour prior to failure. Several tentative conclusions may be drawn from the calculation performed at this stage:

- a) Linear behaviour of the PCCV is expected up to 2.0 times the design pressure, when concrete wall starts cracking.
- b) The cracking of the concrete causes a sudden change in the stiffness of the structure. Beyond this point tendons and rebars have to sustain the pressure.
- c) Hoop rebars start yielding at 2.9 times the design pressure and vertical rebars yield in the range of 2.9 to 3.3 times the design pressure.
- d) The limit for the pressure is approximately given by the yielding of the horizontal tendons, which occurs at 3.33 times the design pressure.
- e) Global failure would be most likely to occur between 3.33 and 3.50 times the design pressure.
- f) Further detail analyses are required for assessing the possibility of local failure modes developing in the liner near penetrations. However, the level of effective plastic strains observed in the global model suggests that local failures are also most likely to take place within the same pressure range.

## **Appendix I. List of References**

HKS - Hibbitt, Karlsson and Sorensen, Inc. (1998) "ABAQUS /Standard User's Manual, Version 5.8", Pawtucket, Rhode Island.

SNL - Sandia National Laboratories. (1997) "PCCV Round Robin Analysis – Release of Design Package". November.

SNL - Sandia National Laboratories. (1998) "PCCV Round Robin Analysis - Updated Information Package". August.



**APPENDIX Q**

**RINSC**

**RUSSIA INTERNATIONAL NUCLEAR SAFETY CENTER  
RUSSIA**

Appendix A, Composite Plots, comprises test data compiled and plotted from all organizations that participated in the Prestressed Concrete Containment Vessel (PCCV) Round Robin Pretest Analysis. To avoid duplicating the composite information, individual sets of data and/or plots have been omitted from participants' reports. In some cases this action resulted in disconnects between callouts and content and in the numbering of figures, tables, and pagination in some reports.

However, Appendix Q, "RINSC, Russia International Nuclear Safety Center, Russia," contains none of these discontinuities.

## INTRODUCTION

This Report describes ongoing work on the analysis of behavior of PCCV structure model in the containment of water reactor (PWR) manufactured of prestressed reinforced concrete. During Phase 2 the computational scheme was chosen and the behavior of structure subjected to project inner pressure of 0.4MPa.

Here we present computational analysis of structure behavior under inner pressure of interval 0-1.5MPa. As distinct from previous phase of work (phase 2) the mechanical characteristics of concrete and reinforcement elements have been changed in some degree according to the recommendations of specialists from Argon National Laboratory.

This task was performed in frame of work of Russian International Nuclear Safety Centre (RINSC) and American International Nuclear Safety Centre. Main goal of these efforts is verification of program codes for structural analysis of spatial structures and selection of codes adequately describing experimental data.

In this Report we present results of calculation employing DANCO code. Comparison of results of these studies with experimental data will be performed after completion of developing PPCV model and conducting corresponding experiments.

## 1. COMPUTATIONAL SCHEME OF PCCV MODEL.

Fig.1 presents general view of PCCV structure. Descriptions of structure and mechanical properties of materials used are obtained from Sandia National Laboratory.

During fabrication concrete part of PCCV is prestressed with steel tendons. Forces in tendons are 470kN, in hoops - 350kN.

Accounting structure's behavior both in going from common state to prestressed one and during loading by inner pressure, the computational scheme of PCCV structure (Fig.2) with two distinctive symmetry planes was developed. The computational scheme of structure is based on possibilities of DANCO code (see Report, phase 1), which allows to account following:

- concrete - physically nonlinear material with different maximum strength properties under compression and tension; equation of state of concrete accounts its possible destruction;
- reinforcement and tendons are subjected to longitudinal stresses only; elasto-plastical deformation is taking into consideration;
- tendons are considered as thin-wall shell ribbons without flexural rigidity. Simulation of creating prestressed state of concrete using system of tendons in computational scheme is realised by employing the model of contact on non-matching meshes with possible slip. Model of contact provides the transfer of load from tendons to concrete by the normal during tensioning. Boundary conditions allow to conserve mechanical trajectory of every tendon through its tensioning. Friction between concrete and tendons is not accounted. Only those parts of tendons which lay in spherical dome were taken into consideration whereas tendons in cylindrical part of containment do not affect on its stressed-strained state.

According to recommendations obtained from Sandia National Laboratory following values of mechanical properties of materials were used in calculations:

Material	Density, kg/m <sup>3</sup>	Young's modulus, GPa	Yield point, MPa
Reinforcing bars	7800	200	400
Tendons	7800	210	1690
Concrete	2190	26,97	---

In calculations axial tensile strength of concrete was assumed equal to  $3.46 \cdot \dots$ , axial compressive strength (prism strength) -  $48.84 \cdot \dots$ .

In computational scheme longitudinal and circumferential reinforcements were presented as thin-wall layers with equivalent thickness.

Creating prestressed state in concrete and specified character of loading of PCCV structures are slow, static processes. As the DANCO program is intended to solve problems of non-stationary deformation of structure elements, to simulate slow deformation in the DANCO program we employed technique of slow loading of structure and dynamic "stationarization" (dampening) of arising vibrations. Content of this technique is following. Time of increment of applied load is equal to 3-5 natural cycles of structure's vibration (see Fig.3,4). On each computational step general vector of velocities was multiplied by "stationarization" factor. Its value was determined empirically and here it equals 0.99. Calculations were continued until all vibrations of structure died down completely.

The structure's behavior analyses was performed in two stages. Firstly, the prestressed state of the model was created by tensioning of the tendons.

Time when whole structure goes into steady-state conditions (all vibrations are decayed) after tensioning of all tendons is completed, was choose as the starting point of next stage of analyses.

Then to determine the values of pressure which may create crack in concrete and plastic deformation of reinforcement, inner pressure of range from 0.4 up to 1.5 MPa (0.4 MPa, 1.0 MPa, 1.25MPa, 1.4 MPa and 1.5MPa ) was applied to pre-stressed structure. (Again, calculations were stopped when complete decaying of vibrations occurred.)

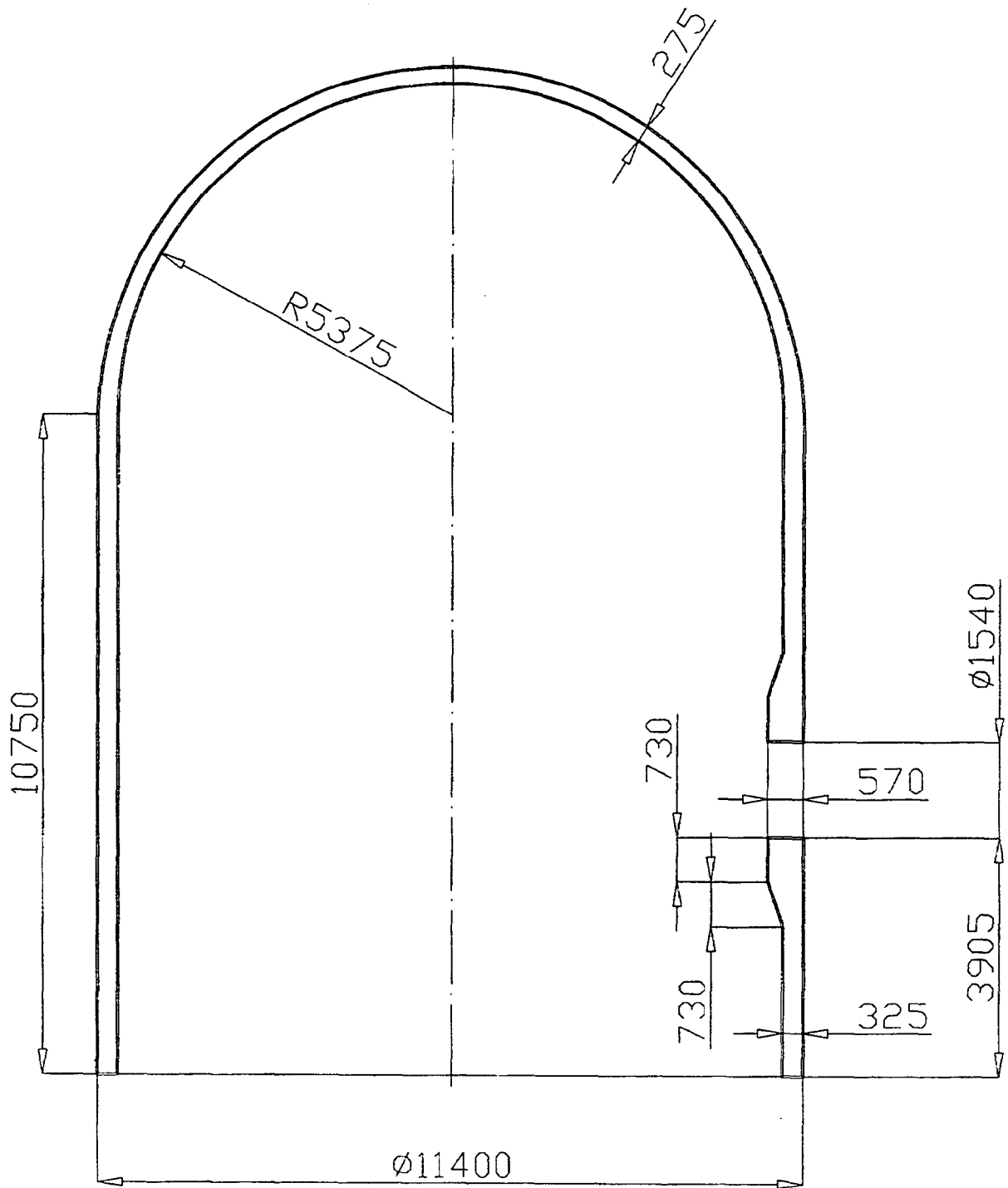


Fig.1.Geometry of the structure

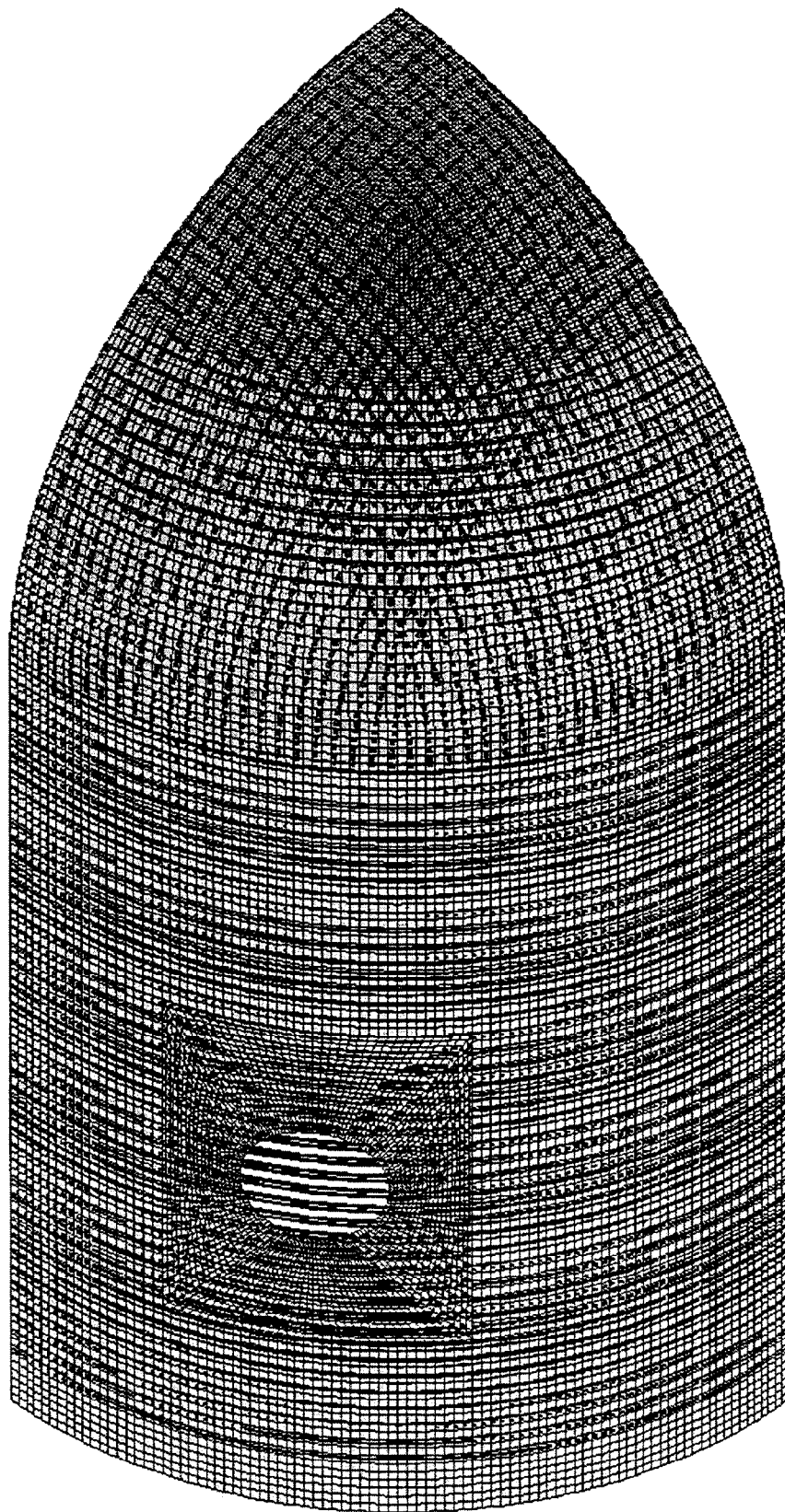


Fig.2a. Computational scheme of the structure ( $1/4^{\text{th}}$  part)

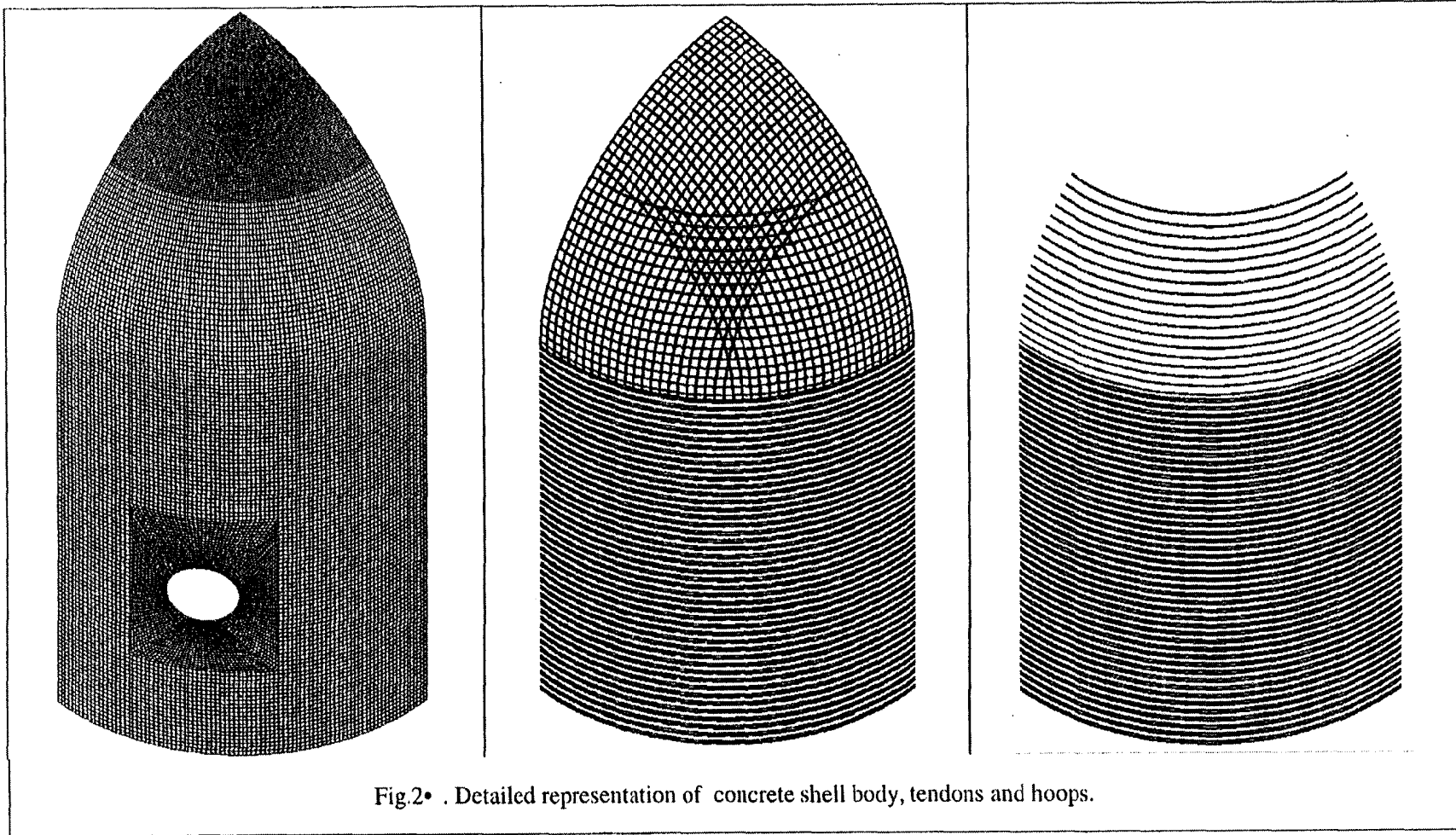


Fig.2• . Detailed representation of concrete shell body, tendons and hoops.

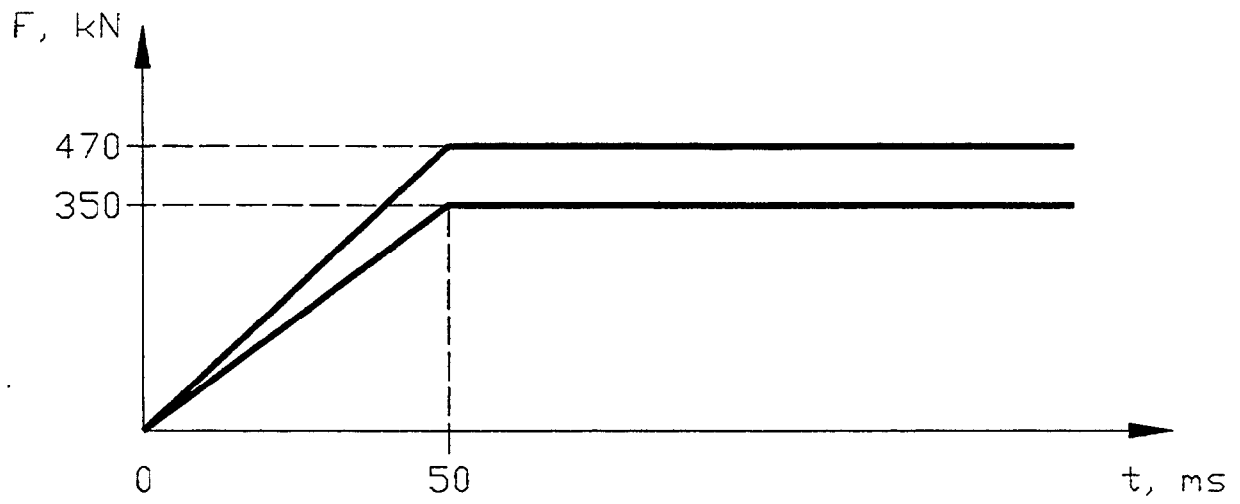


Fig. 3. Time profile of load, applied to tendons and hoops.

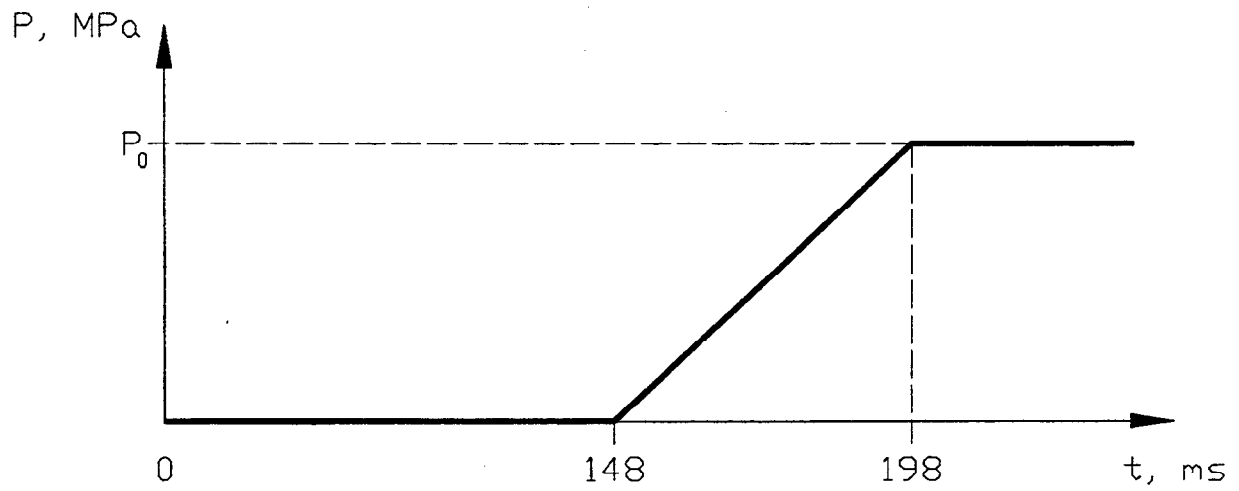


Fig. 4. Time profile of inner pressure.

## 2. RESULTS

Basic results of calculation of stresses-strained state of PCCV structure are presented in Fig.5-25.

Fig.5 - 10 shows radial displacement distribution over the shell body under different inner pressure applied.

Fig.11 - 16 present vertical displacements distribution over the shell body under different inner pressure applied. The displacements take a value from the range  $-6.0...+10.0\text{mm}$ .

Fig.17 - 22 shows distribution of stress intensity in the inner and outer layers of reinforcement. When inner pressure is less than  $1.0\text{MPa}$ , stress intensity is under yield point and reinforcement deforms elastically. When inner pressure equals  $1.5\text{MPa}$ , stress in reinforcement layers adjacent to the hole exceeds the yield strength. It may cause the appearance of penetrating cracks in concrete and the loss of air-tightness.

Fig.23 -25 shows places of possible appearance of non-penetrating face cracks in the concrete shell of PCCV. In these places the transition to plastic deformation of reinforcement begins.

As it may be seen from the figures in circumferential belt of cylindrical shell which includes the hole, the noticeable radial displacement of body (up to  $130\text{mm}$ ) is occurred under inner pressure of  $1.5\text{MPa}$ . In these places strength of concrete degrades under given level of deformation, and effectiveness of hoops is decreased due the hole presence.

Table 1 contains the calculated values of following parameters: displacement, strain and stress - in the standard locations according to input specifications. Graphical dependencies of the parameters versus inner pressure in some of these locations are given in Table 2.

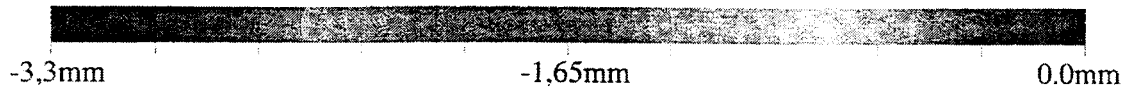
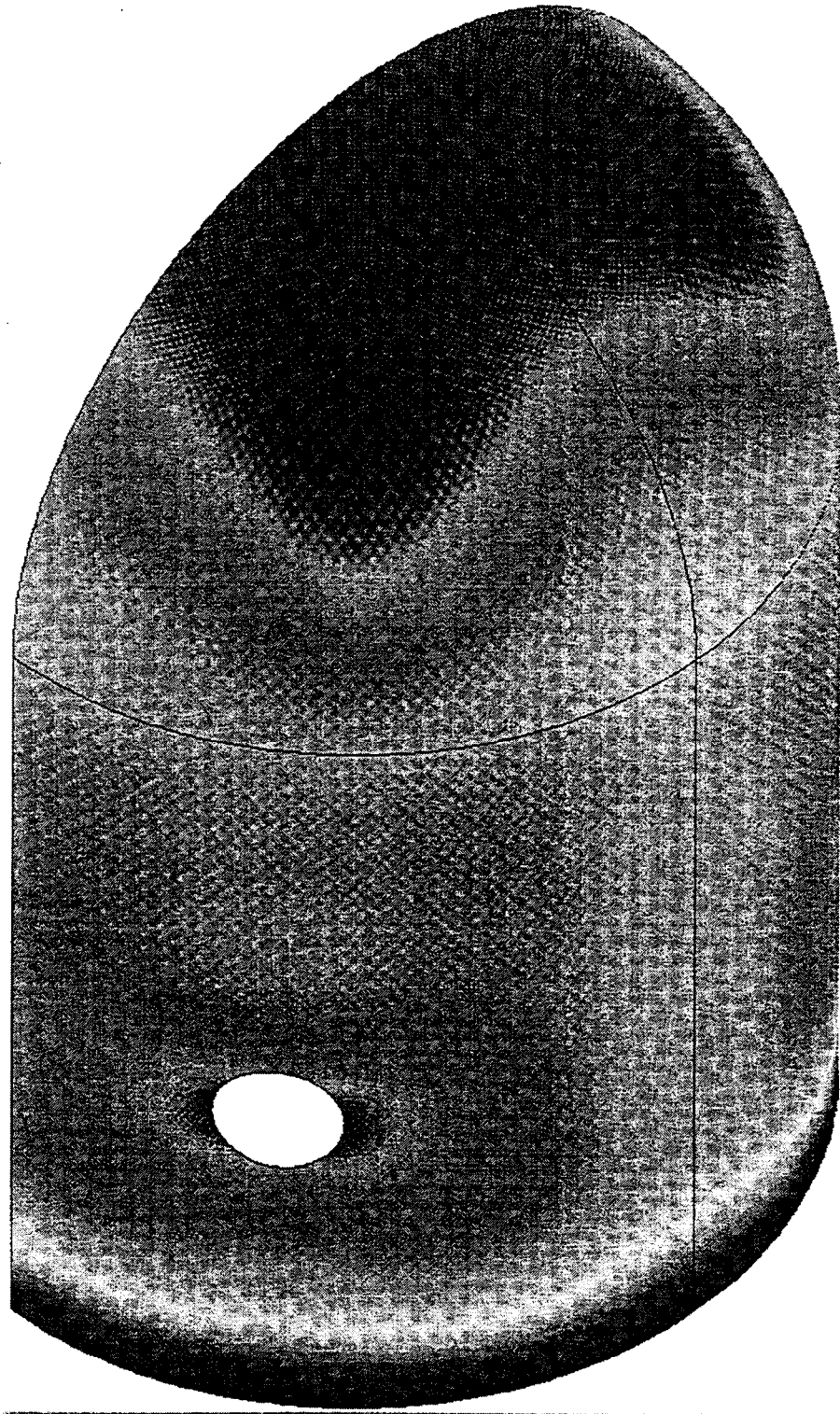


Fig. 5 Distribution of radial displacements of concrete shell of PPCV without inner pressure

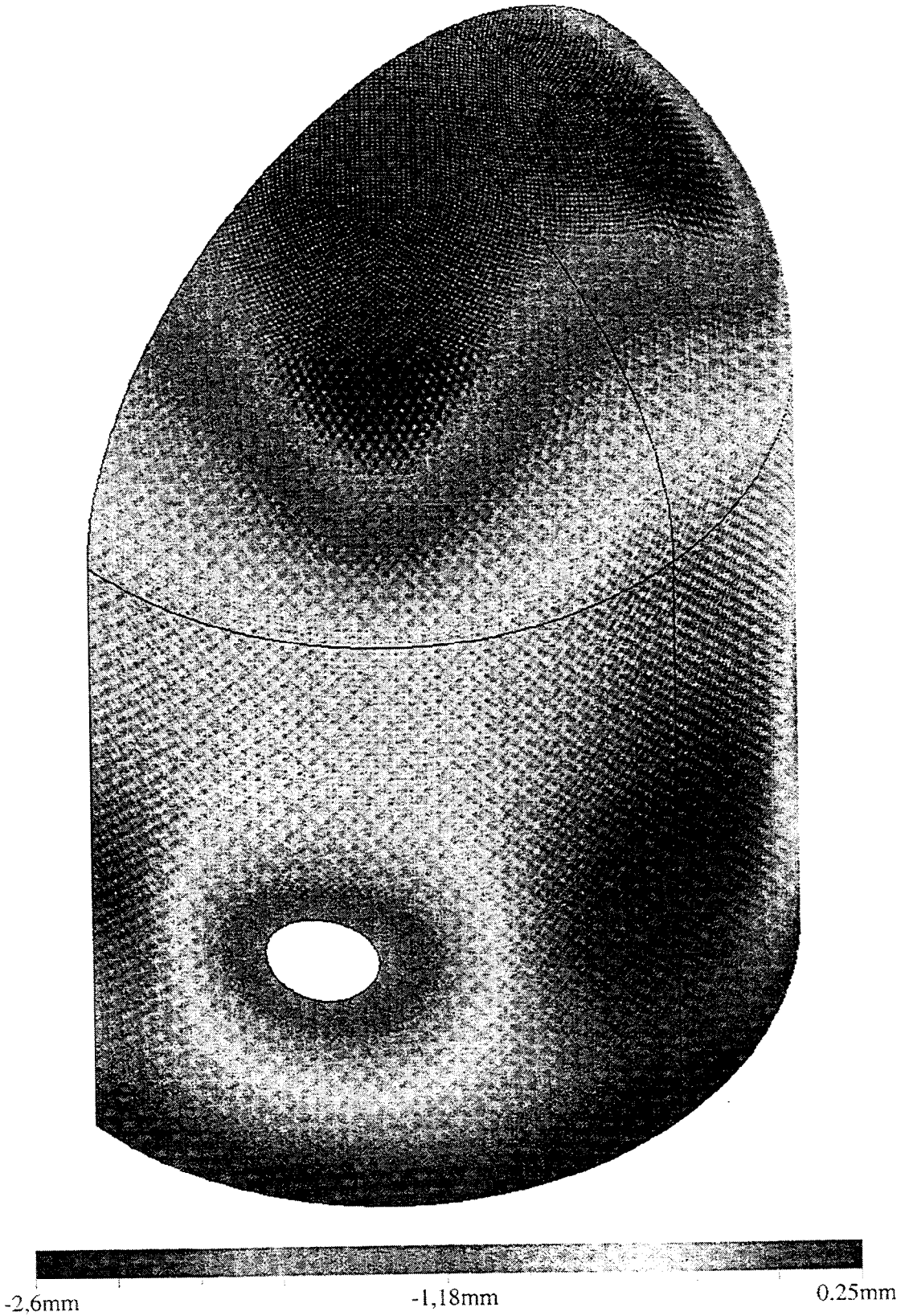
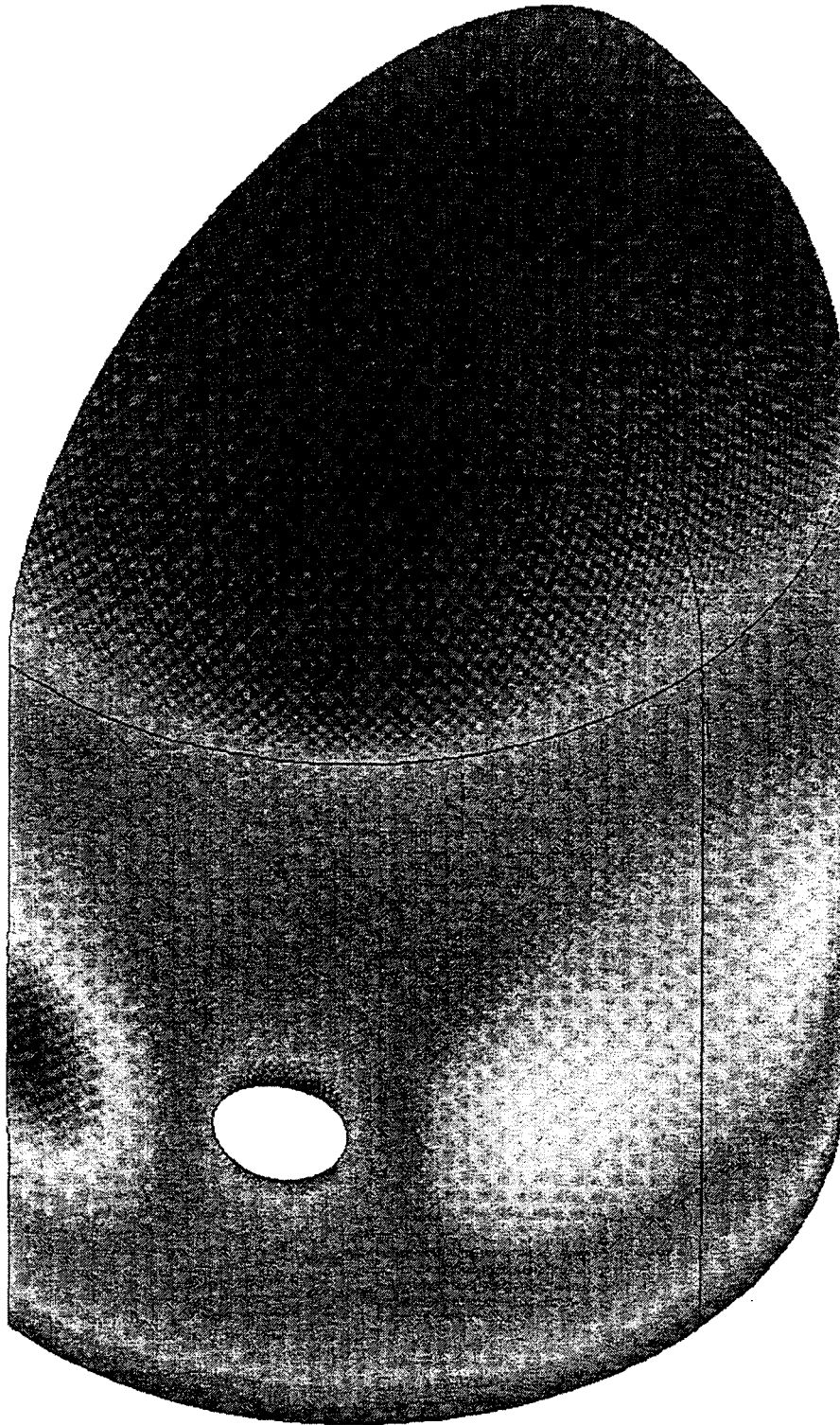


Fig. 6 Distribution of radial displacements of concrete shell of PPCV, inner pressure 0.4MPa



-2,2mm

4,4mm

11.0mm

Fig. 7 Distribution of radial displacements of concrete shell of PPCV, inner pressure 1.0MPa.

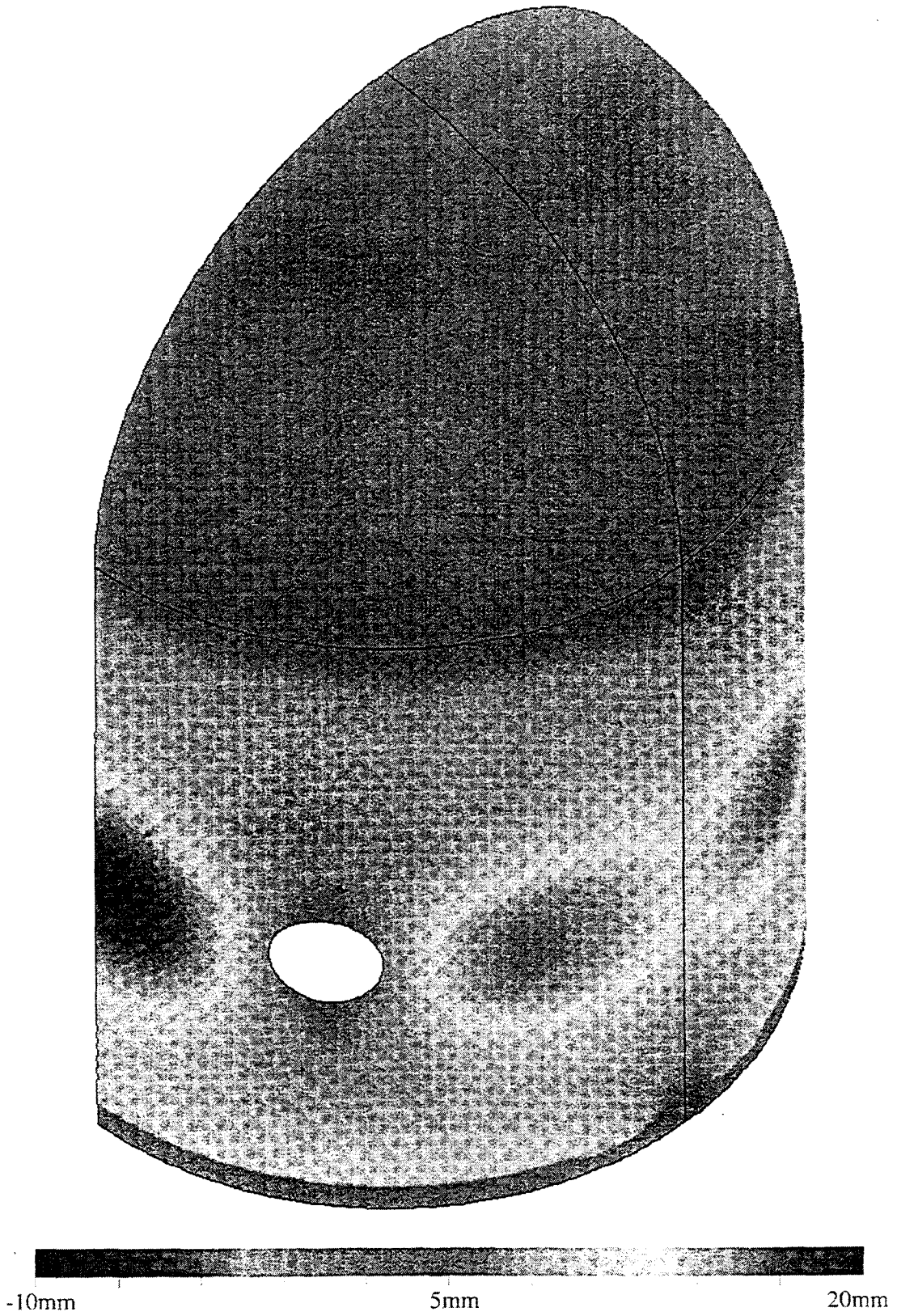


Fig. 8 Distribution of radial displacements of concrete shell of PPCV, inner pressure 1.25MPa.



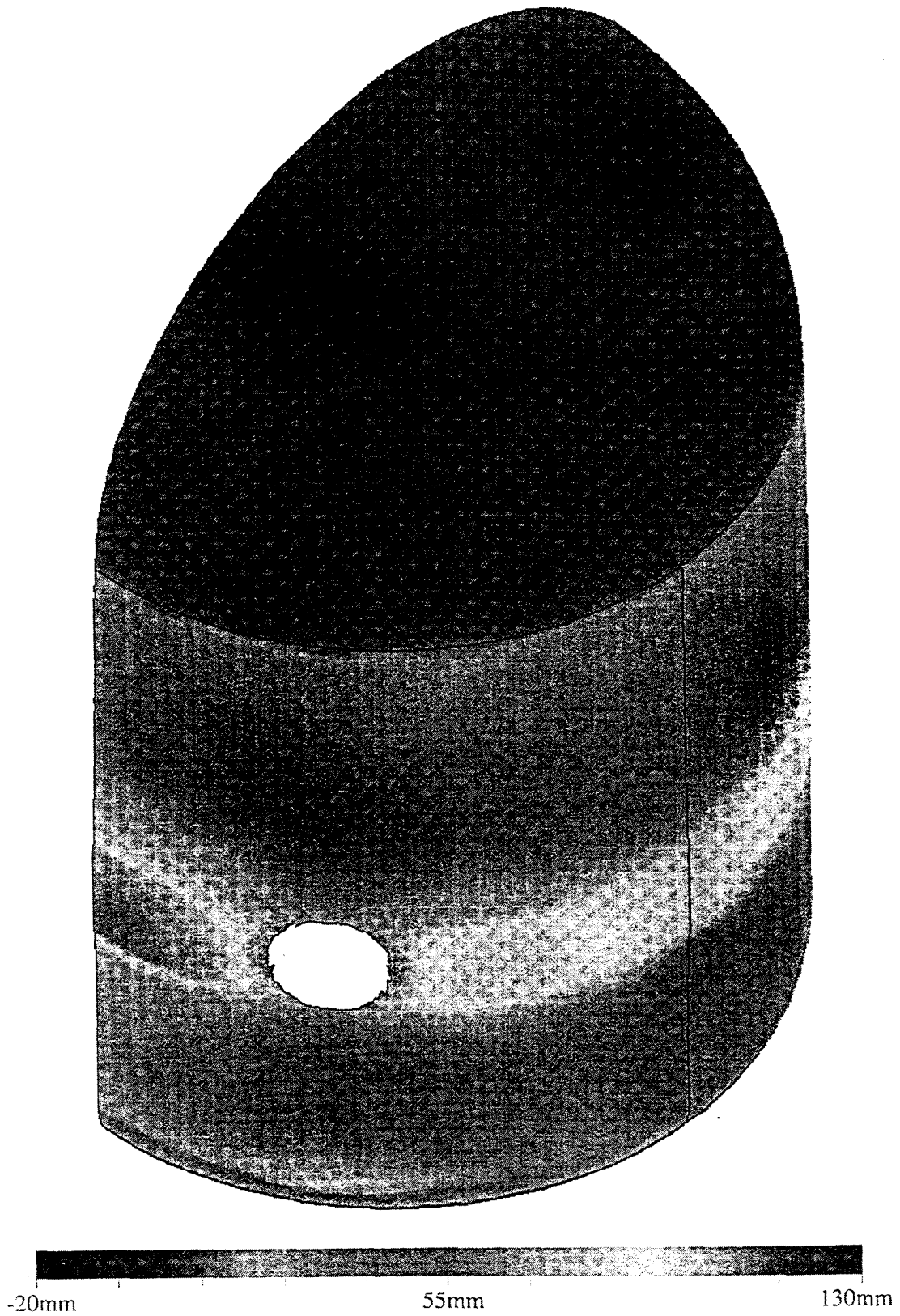


Fig. 10 Distribution of radial displacements of concrete shell of PPCV, inner pressure 1.5MPa. (process not damp)

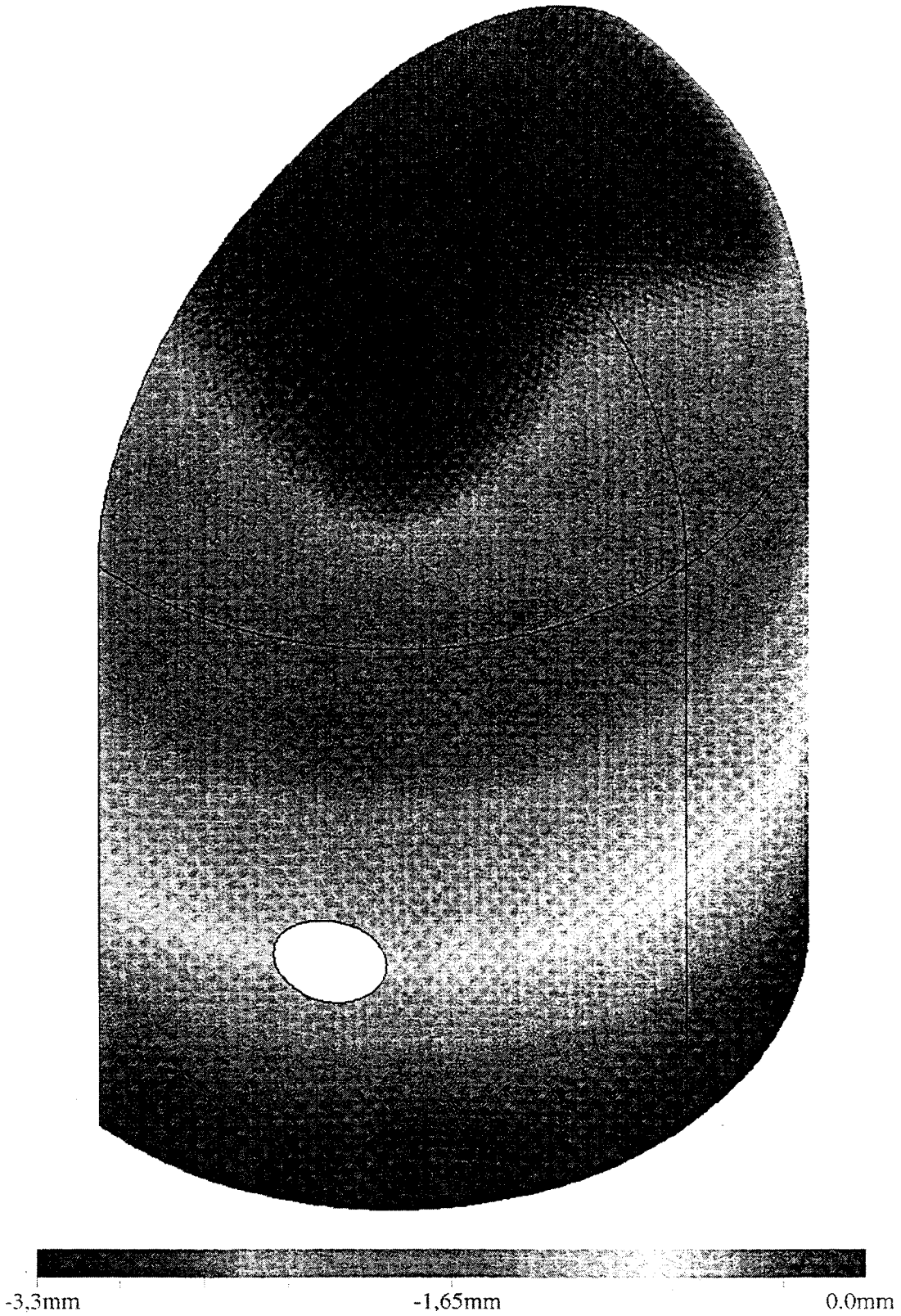


Fig. 11 Distribution of vertical displacements of concrete shell of PPCV, without inner pressure.

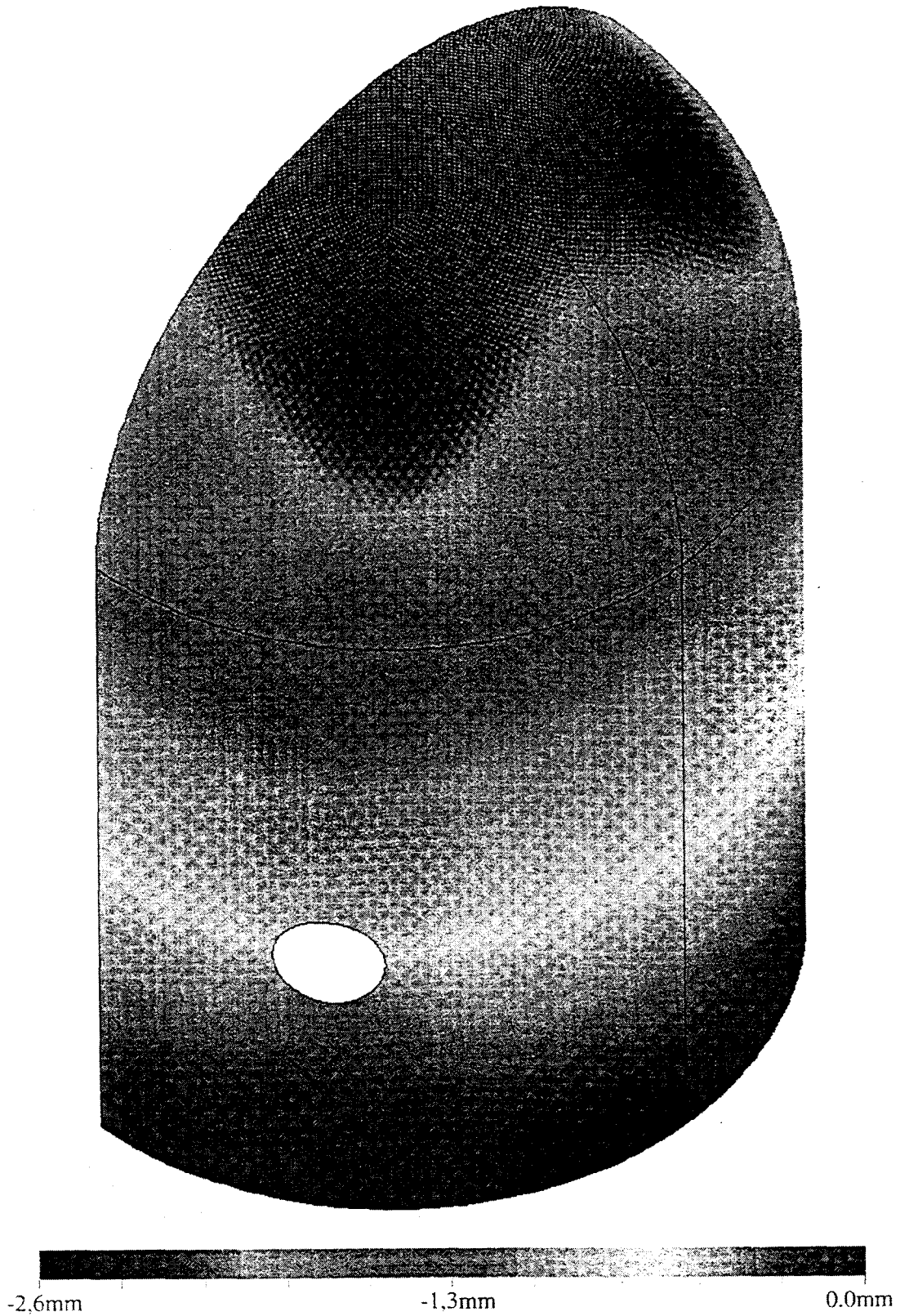
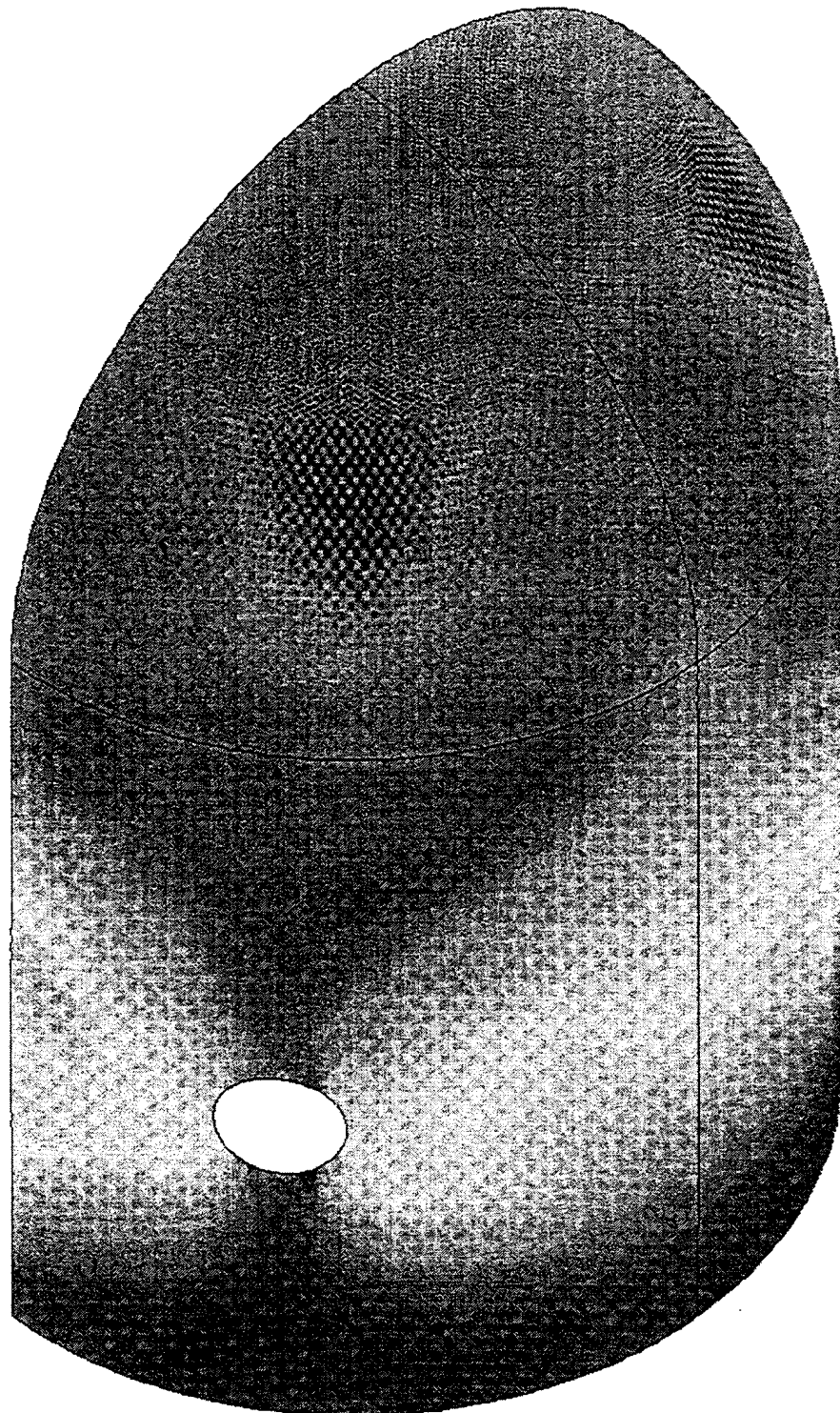


Fig. 12 Distribution of vertical displacements of concrete shell of PPCV, inner pressure 0.4MPa.



-2,3mm

1,0mm

0,3mm

Fig. 13 Distribution of vertical displacements of concrete shell of PPCV, inner pressure 1.0MPa.

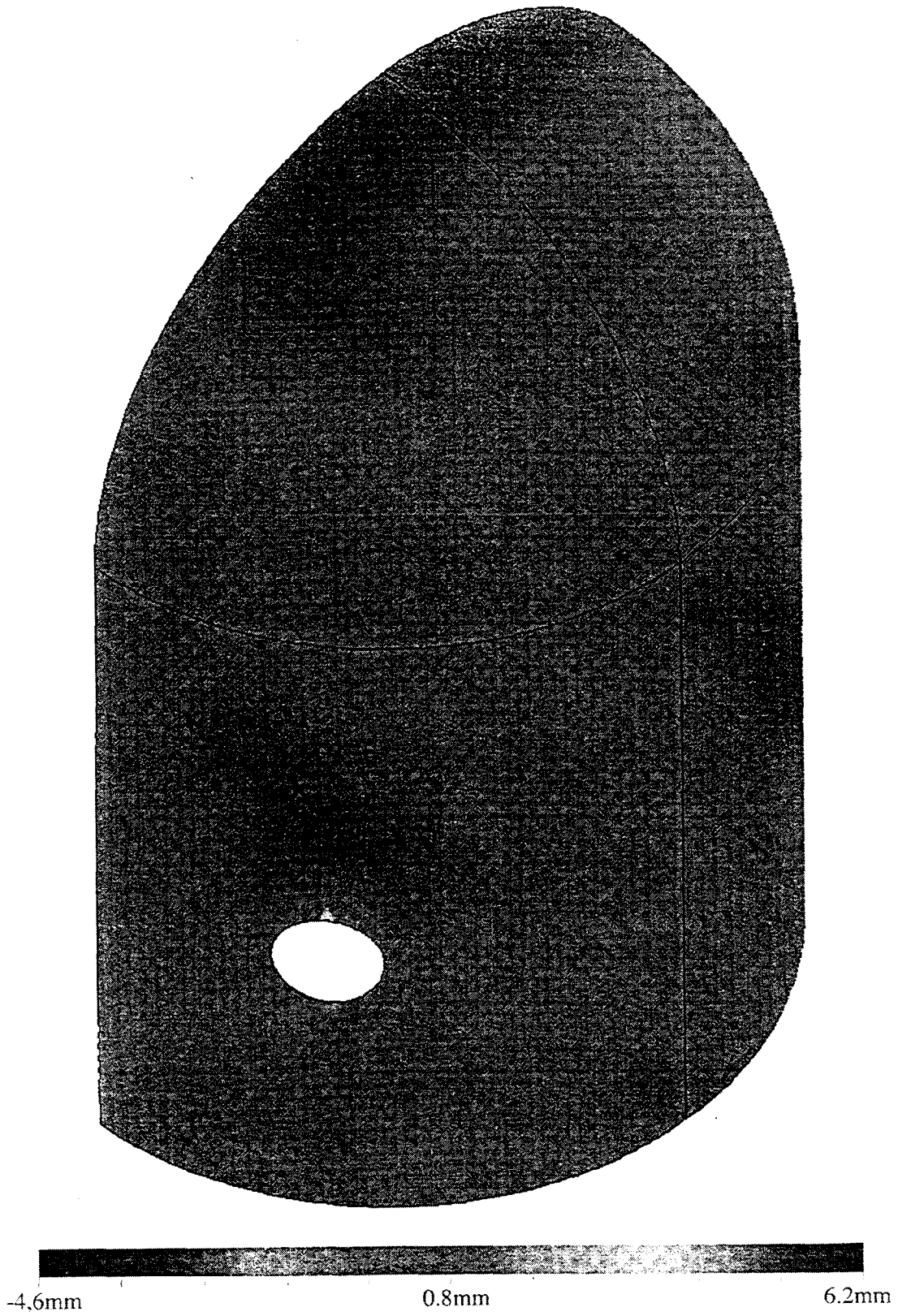


Fig. 14 Distribution of vertical displacements of concrete shell of PPCV, inner pressure 1.25MPa.



-6mm

2mm

10mm

Fig. 15 Distribution of vertical displacements of concrete shell of PPCV, inner pressure 1.4Mpa

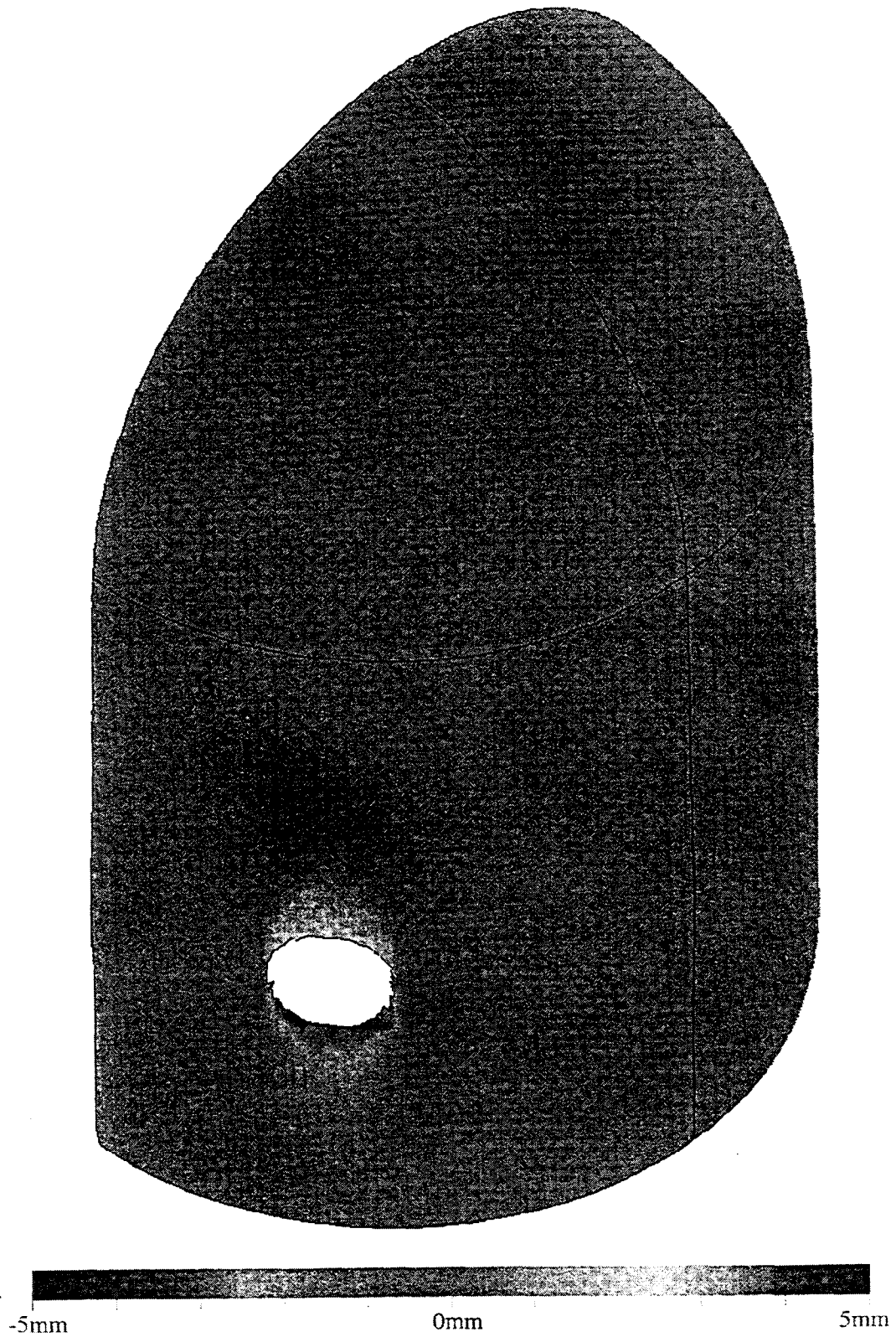


Fig. 16 Distribution of vertical displacements of concrete shell of PPCV, inner pressure 1.5MPa.(process not damp)

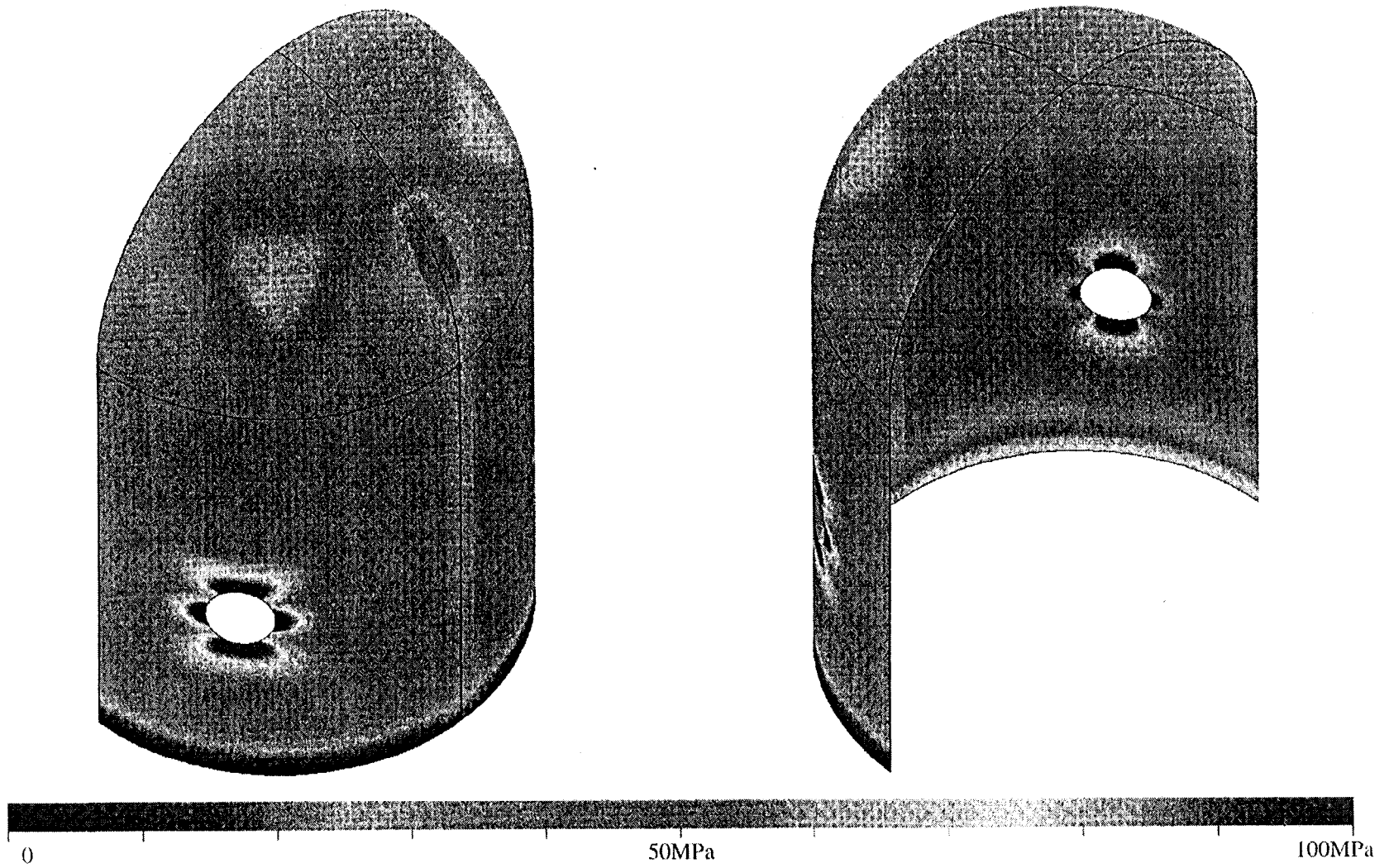


Fig. 17. Distribution of stress intensity on surface of reinforcement of PCCV shell without inner pressure.

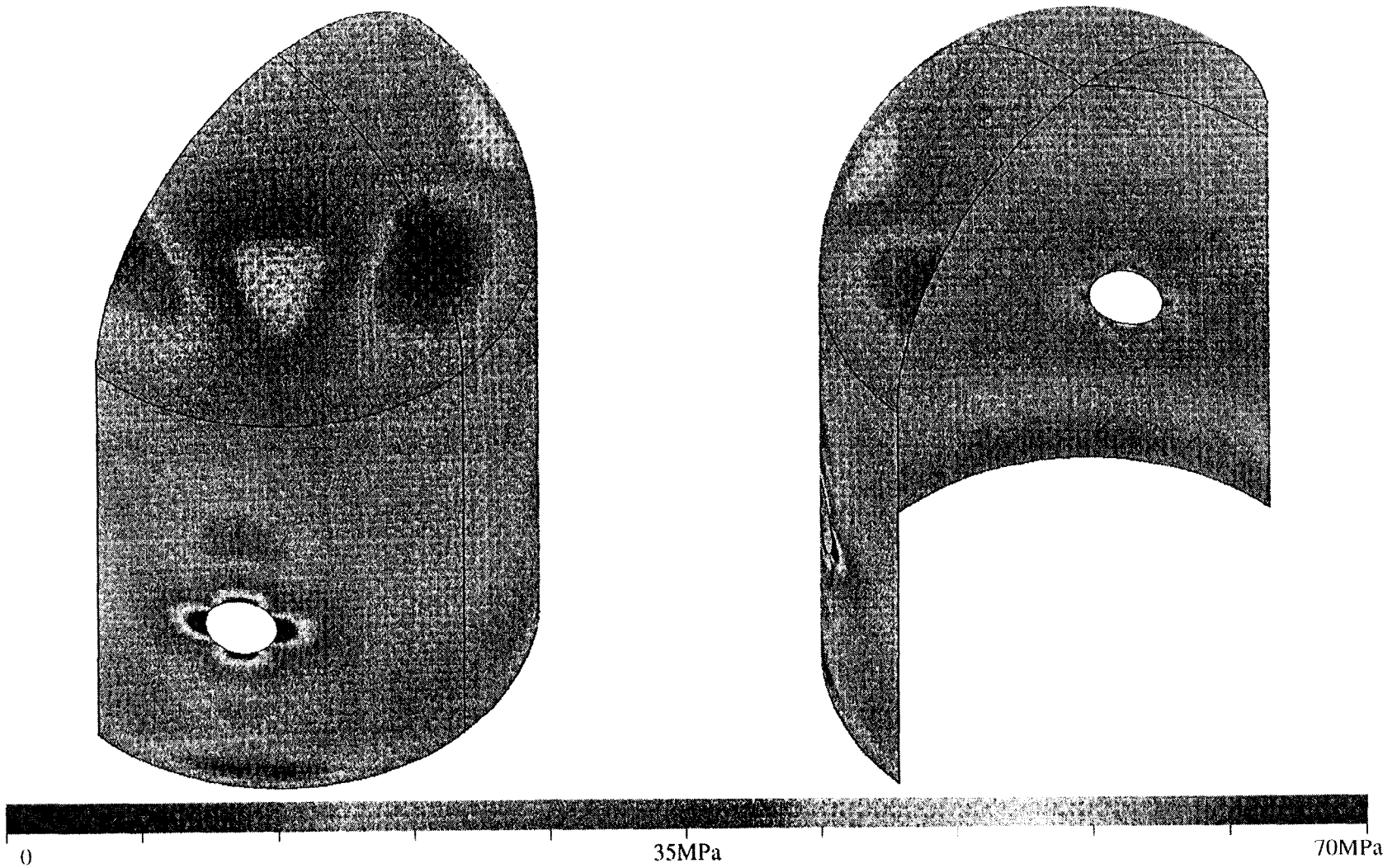


Fig. 18. Distribution of stress intensity on surface of reinforcement of PCCV shell, inner pressure 0.4MPa

Q-25

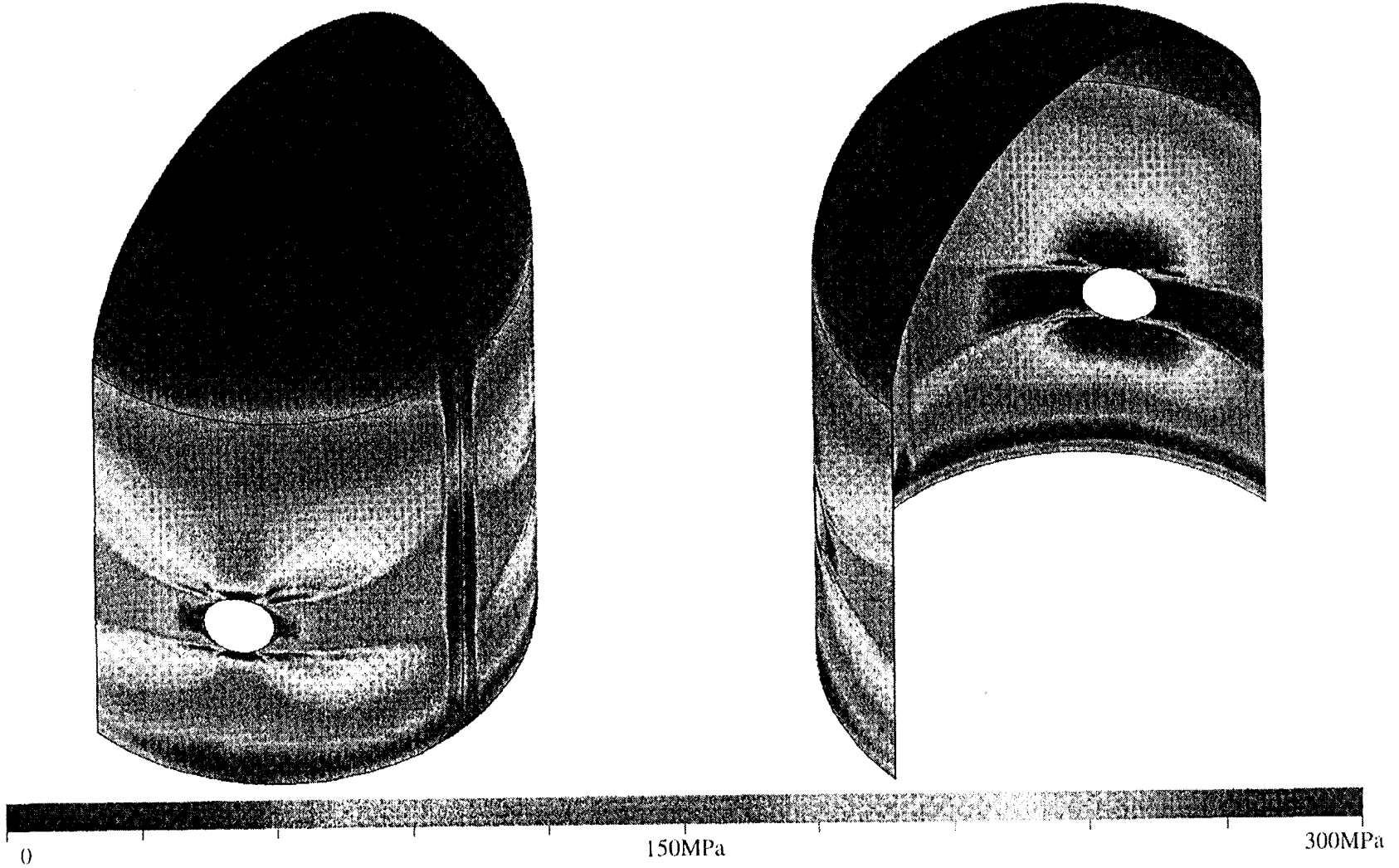


Fig. 19. Distribution of stress intensity on surface of reinforcement of PCCV shell, inner pressure 1.0Mpa

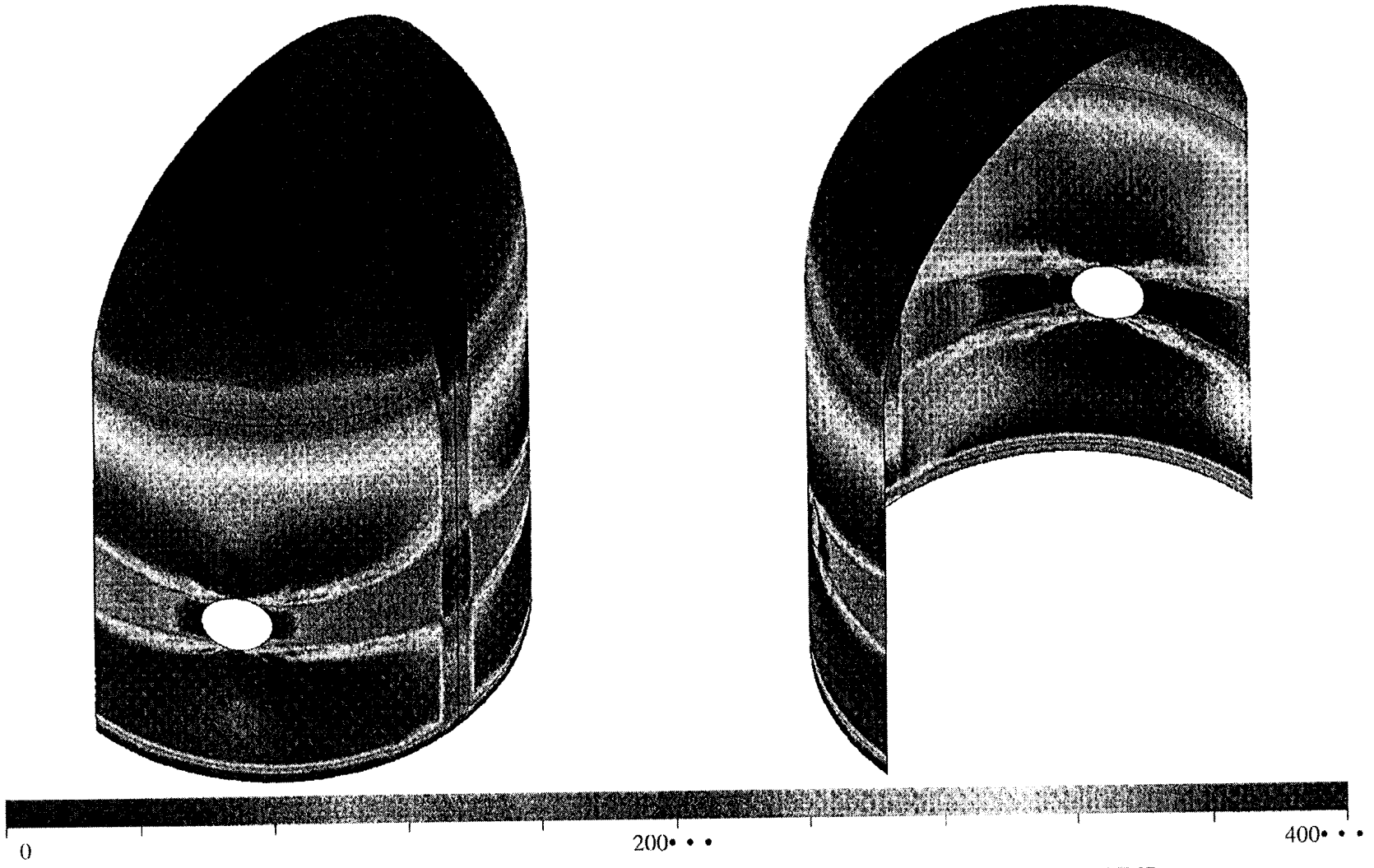


Fig. 20. Distribution of stress intensity on surface of reinforcement of PCCV shell, inner pressure 1.25MPa.

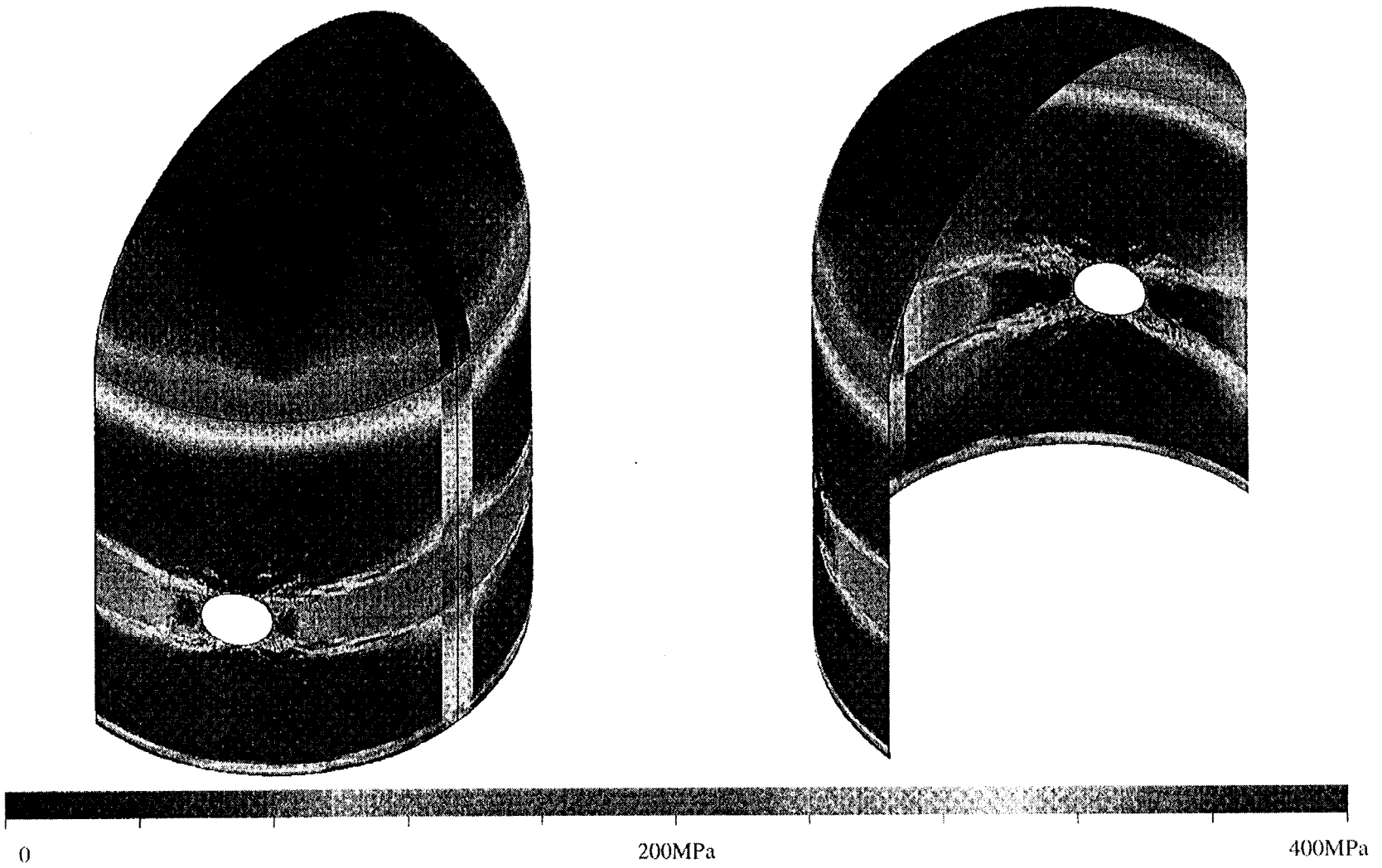


Fig. 21. Distribution of stress intensity on surface of reinforcement of PCCV shell, inner pressure 1.4MPa.

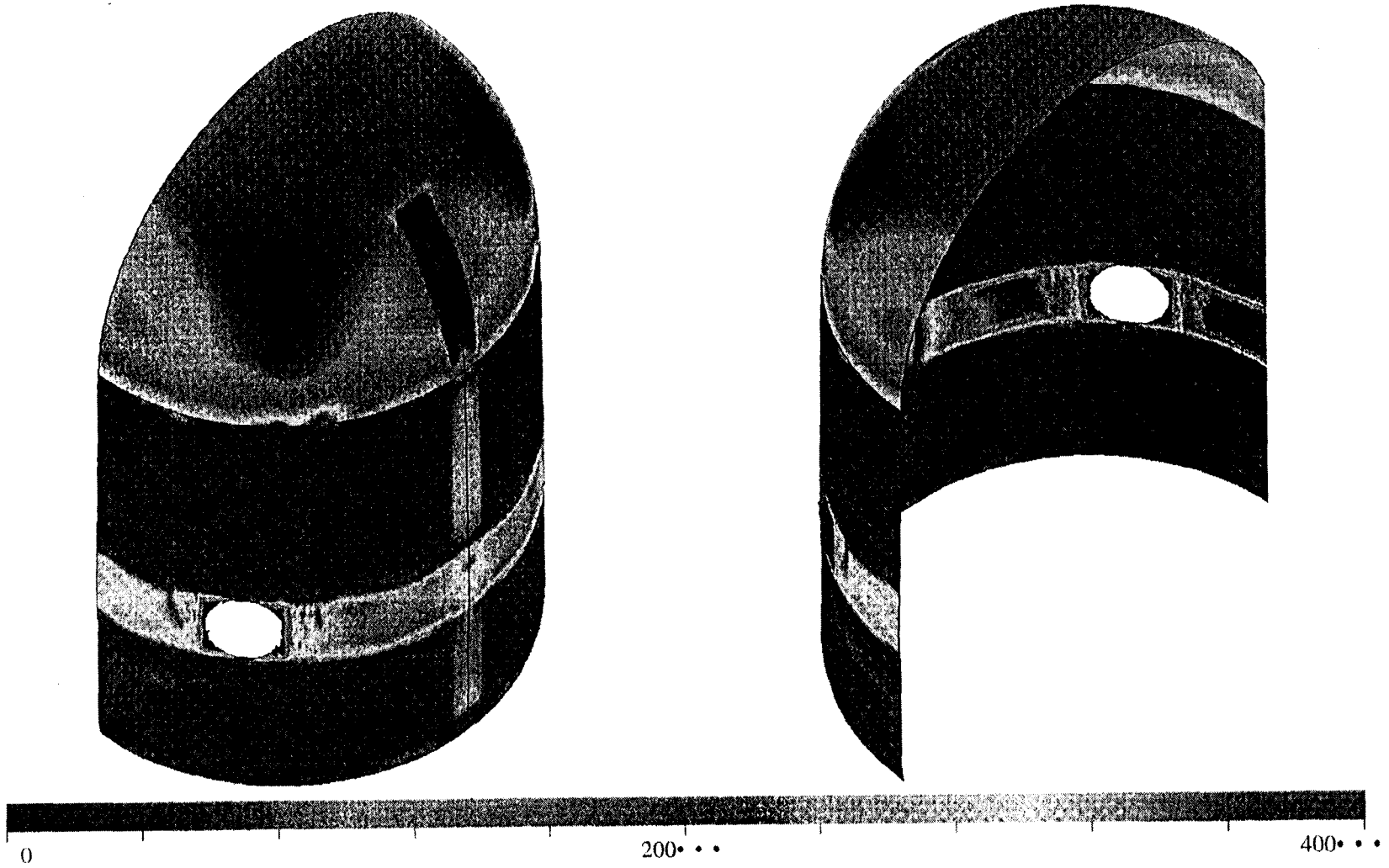


Fig. 22. Distribution of stress intensity on surface of reinforcement of PCCV shell, inner pressure 1.5MPa. (process not damp)

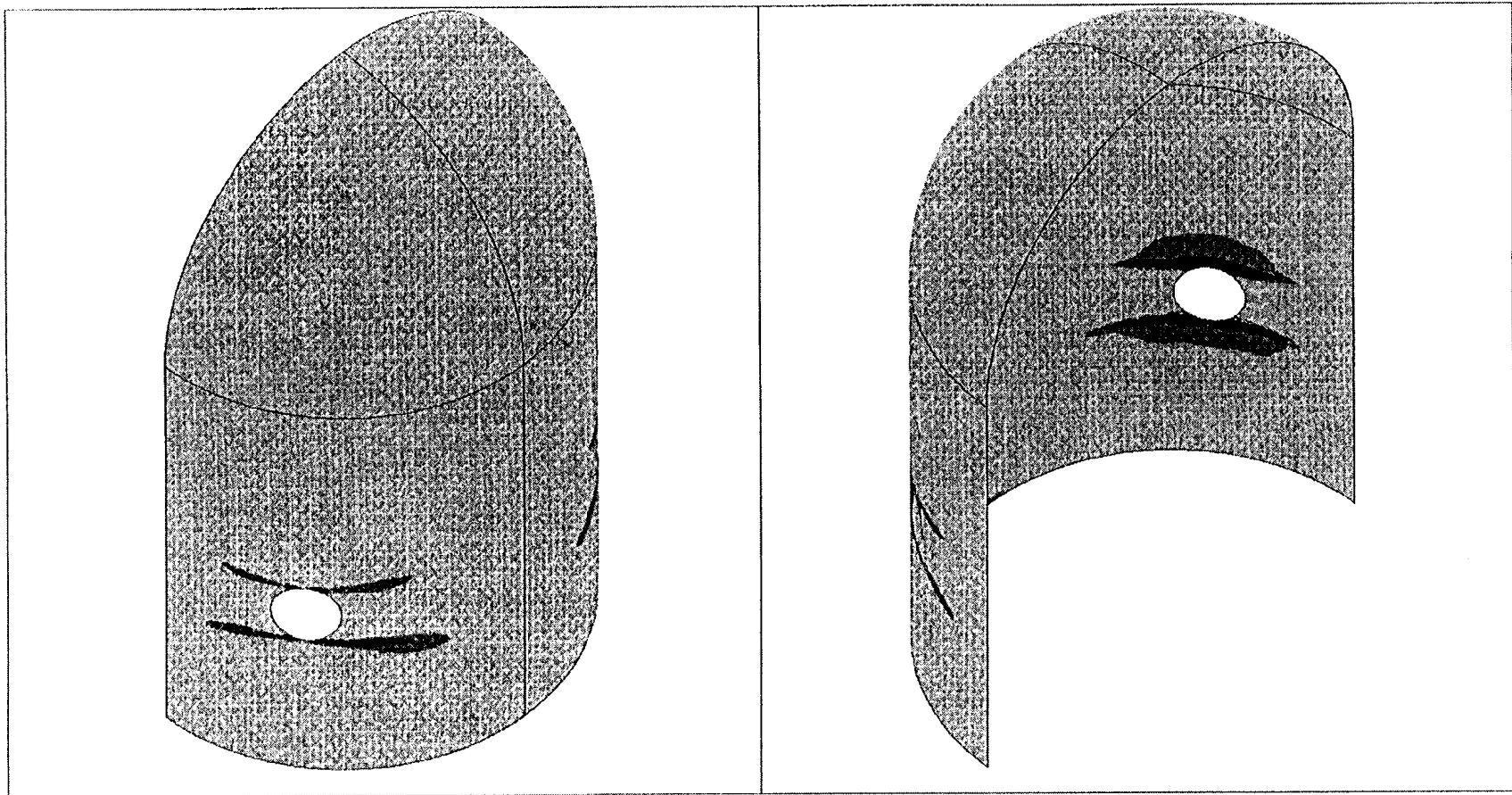


Fig. 23. The place of possible appearance of non-penetrating face cracks in concrete shell of PCCV under inner pressure 1.0MPa (shown more dark)

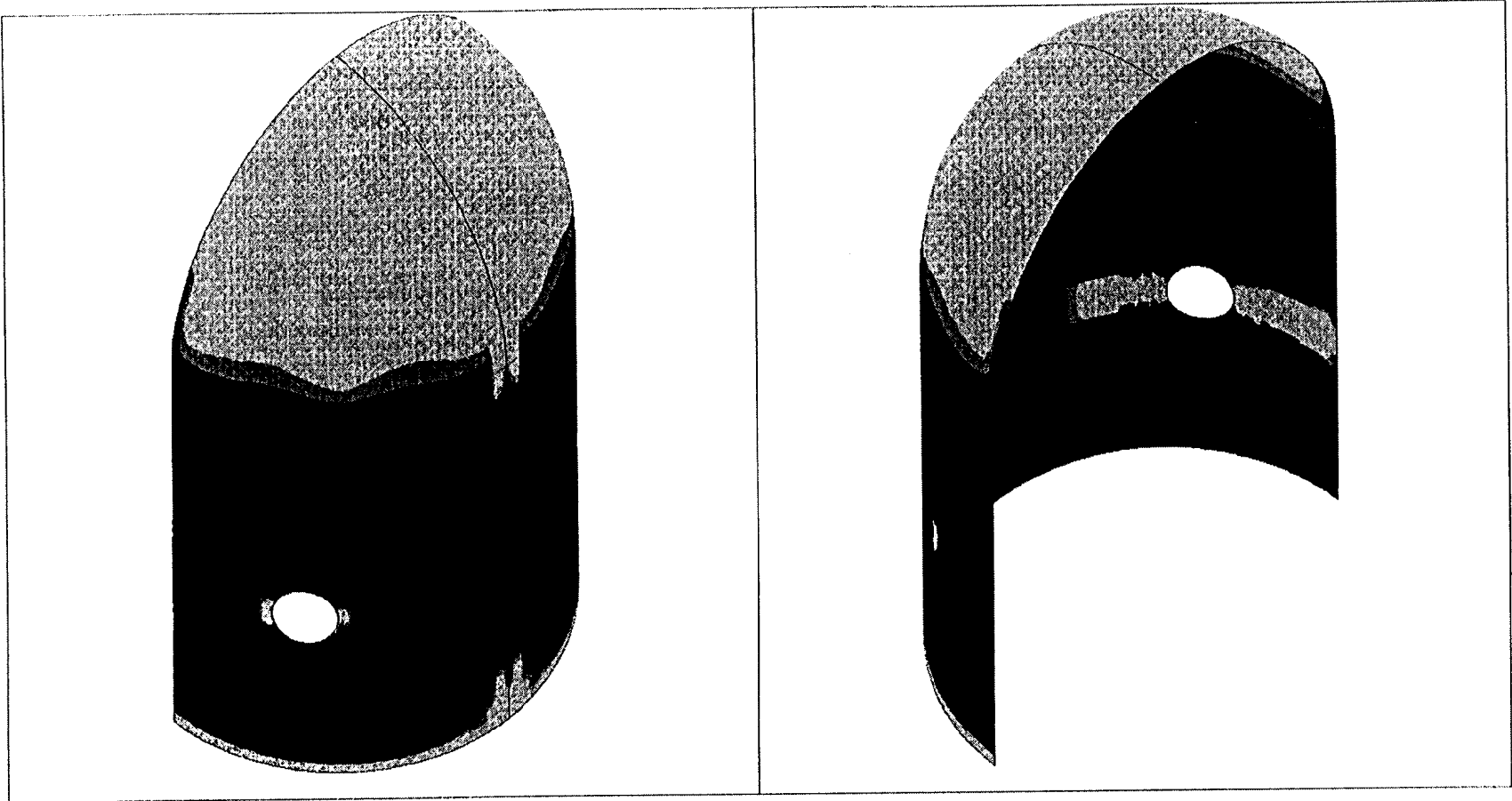


Fig. 24. The place of possible appearance of non-penetrating face cracks in concrete shell of PCCV under inner pressure 1.25 MPa (shown more dark).

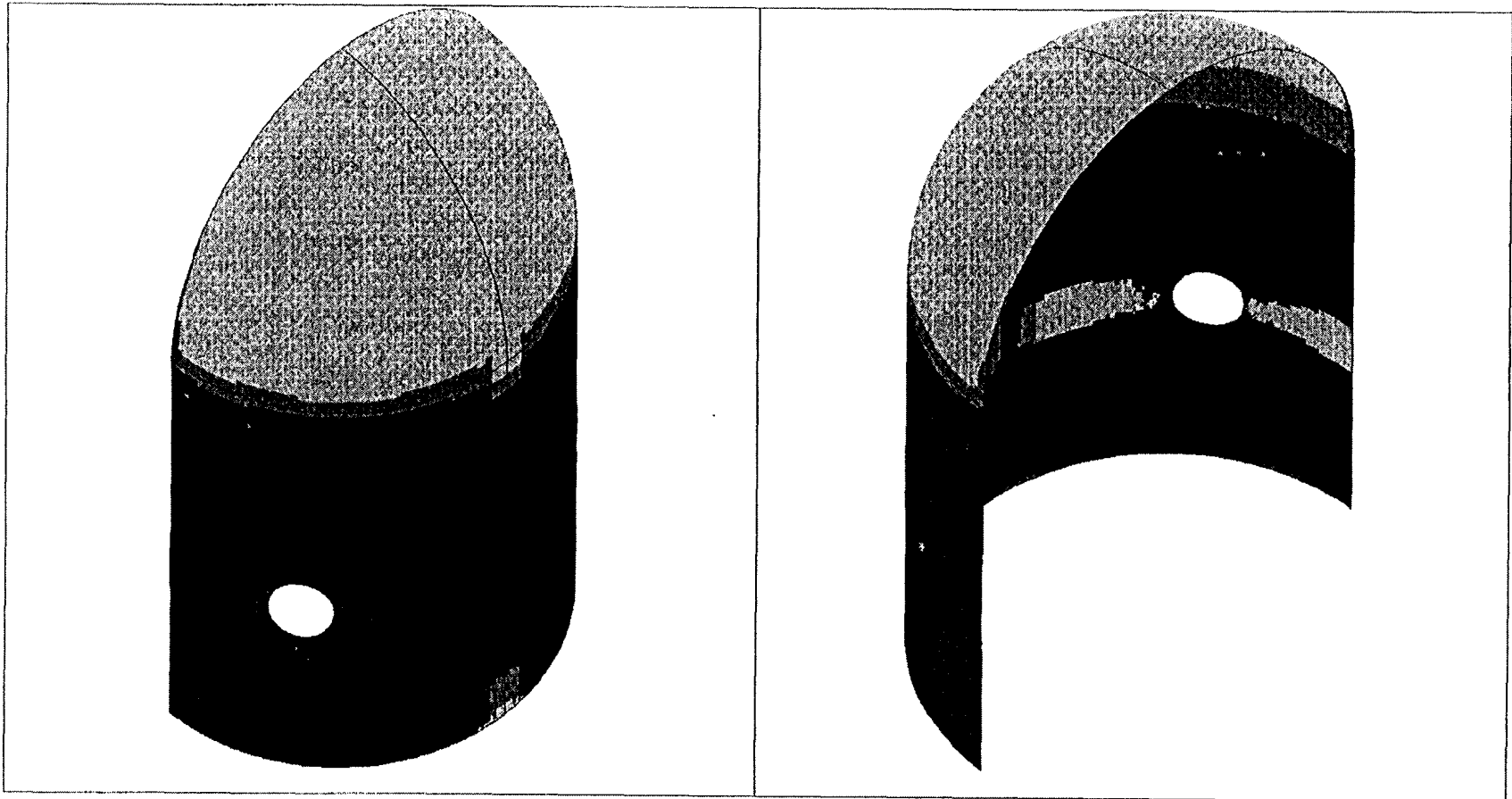


Fig. 25. The place of possible appearance of non-penetrating face cracks in concrete shell of PCCV under inner pressure 1.40MPa (shown more dark)

Table 2.

## PCCV Standard Output Locations

Loc.#	Type	Orientation	Az.(deg)	El.(m)	Results for points					
					P=0	P=0.4	P=1.0	P=1.25	P=1.4	P=1.5 destruction <sup>1</sup>
1	Displacement	Vertical	135	0.00	0 mm	0 mm	0 mm	0mm	0mm	0mm
2	Displacement	Radial	135	0.25	-0.06mm	0.0045mm	0.27mm	1.68mm	15.45mm	>49.12mm
3	Displacement	Radial	135	1.43	-0.96mm	-0.30mm	2.26mm	10.26mm	14.89mm	>62.99mm
4	Displacement	Radial	135	2.63	-1.58mm	-0.74mm	3.30mm	9.17mm	13.89mm	>61.48mm
5	Displacement	Radial	135	4.68						
6	Displacement	Radial	135	6.20	-1.56mm	-0.72mm	3.10mm	9.32mm	15.24mm	>66.41mm
7	Displacement	Radial	135	10.75	-1.44mm	-0.67mm	0.74mm	3.9mm	5.90mm	>9.05mm
8	Displacement	Vertical	135	10.75	-1.91mm	-1.41mm	-1.34mm	0.3mm	1.21mm	>-2.37mm
9	Displacement	Horiz.(Rad)	135	14.55	-3.29mm	-2.58mm	-2.14mm	-1.25mm	-0.72mm	>-3.8mm
10	Displacement	Vertical	135	14.55	-3.28mm	-2.59mm	-2.24mm	-1mm	-0.24mm	>-3.73mm
11	Displacement	Vertical	135	16.13	-3.27mm	-2.52mm	-1.99mm	-0.67mm	0.17mm	>-2.41mm

<sup>1</sup> Process not damp

12	Displacement	Radial	90	6.20	-1.40mm	-0.08mm	6.2mm	11.15mm	15.23mm	>61.17mm
13	Displacement	Radial	90	10.75	-1.17mm	-0.41mm	1.43mm	3.26	4.88mm	7.13mm
14	Displacement	Radial	324	4.675						
15	Displacement	Radial	62	4.525						
16	Rebar Strain	Meridional	135	0.05	-0.00039	-0.00012	0.0011	0.00092	0.00075	0.00086
17	Rebar Strain	Meridional	135	0.05	$-1.20 \cdot 10^{-5}$	-0.0001	-0.00034	0.00012	0.00077	0.00102
18	Rebar Strain	Meridional	135	0.25	-0.00037	-0.00015	0.00041	0.00018	0.00017	-0.00427
19	Rebar Strain	Meridional	135	0.25	$-5.57 \cdot 10^{-5}$	$-7.18 \cdot 10^{-5}$	-0.00018	$9.22 \cdot 10^{-5}$	0.0006	0.00076
20	Rebar Strain	Meridional	135	1.43	-0.00013	-0.00011	-0.00019	$6.35 \cdot 10^{-5}$	-0.00135	0.00077
21	Rebar Strain	Meridional	135	1.43	-0.00022	-0.00011	$4.27 \cdot 10^{-5}$	$7.78 \cdot 10^{-5}$	-0.00153	0.00039
22	Rebar Strain	Hoop	135	6.20	-0.00033	-0.00011	0.00097	0.0022	0.0023	0.00292
23	Rebar Strain	Meridional	135	6.20	$-7.53 \cdot 10^{-5}$	$-7.54 \cdot 10^{-5}$	-0.00025	-0.00014	0.00031	0.00036
24	Rebar Strain	Hoop	135	10.75	-0.00022	$-6.64 \cdot 10^{-5}$	0.00037	0.00092	0.00125	0.00431
25	Rebar Strain	Meridional	135	10.75	-0.00019	-0.00014	$-7.28 \cdot 10^{-5}$	$4.81 \cdot 10^{-6}$	0.00013	0.00153
26	Rebar Strain	Meridional	135	10.75	-0.00020	-0.00013	-0.00014	$-3.61 \cdot 10^{-5}$	0.00015	0.00021
27	Rebar Strain	Hoop	135	14.55	-0.00032	-0.00024	$-8.15 \cdot 10^{-5}$	$-4.26 \cdot 10^{-5}$	$-2.65 \cdot 10^{-5}$	$7.65 \cdot 10^{-5}$
28	Rebar Strain	Meridional	135	14.55	-0.00019	$-9.56 \cdot 10^{-5}$	$4.83 \cdot 10^{-5}$	0.00011	0.00014	0.00034

29	Rebar Strain	Meridional	135	14.55	-0.00028	-0.00019	$-5.54 \cdot 10^{-5}$	$-2.33 \cdot 10^{-5}$	$3.27 \cdot 10^{-6}$	$7.87 \cdot 10^{-5}$
30	Rebar Strain	Meridional	90	0.05	-0.00031	-0.00013	0.0011	0.0018	0.00087	0.00098
31	Rebar Strain	Meridional	90	0.05	$-5.61 \cdot 10^{-5}$	-0.00015	-0.00016	0.00039	0.00019	0.00072
32	Rebar Strain	Hoop	90	6.20	-0.00015	$-3.25 \cdot 10^{-5}$	0.00028	0.00085	0.0023	0.00194
33	Rebar Strain	Meridional	90	6.20	-0.00017	-0.00011	$-1.76 \cdot 10^{-5}$	0.00011	0.00031	0.00066
34	Liner Strain	Meridional	0	0.010	-0.00048	-0.00013	0.0014	0.00104	0.00099	0.00122
35	Liner Strain	Meridional	0	0.010	-0.00048	-0.00013	0.0014	0.00104	0.00099	0.00122
36	Liner Strain	Meridional	135	0.25	-0.00039	-0.00017	0.00054	0.00019	0.0001	-0.00489
37	Liner Strain	Hoop	135	0.25	$-1.65 \cdot 10^{-5}$	$3.79 \cdot 10^{-6}$	$7.92 \cdot 10^{-5}$	0.00033	0.00146	0.0231
38	Liner Strain	Meridional	135	6.20	-0.00023	-0.00017	-0.00022	$-8.34 \cdot 10^{-5}$	0.00025	-0.00045
39	Liner Strain	Hoop	135	6.20	-0.00031	$-4.52 \cdot 10^{-5}$	0.0013	0.00201	0.00258	0.00494
40	Liner Strain	Meridional	135	10.75	-0.00019	-0.00014	$-6.2 \cdot 10^{-5}$	$1.19 \cdot 10^{-5}$	0.00013	0.0019
41	Liner Strain	Hoop	135	10.75	-0.00021	$-4.86 \cdot 10^{-5}$	0.00043	0.00093	0.00125	0.0023
42	Liner Strain	Meridional	135	16.13	-0.00022	-0.00013	$5.55 \cdot 10^{-5}$	$5.97 \cdot 10^{-5}$	$8.6 \cdot 10^{-5}$	0.00032
43	Liner Strain	Meridional	90	6.20	-0.00017	-0.00012	-0.00013	$7.46 \cdot 10^{-6}$	0.00013	0.00047
44	Liner Strain	Hoop	90	6.20	-0.00017	$-4.89 \cdot 10^{-5}$	0.00045	0.0014	0.00191	0.00246
45	Liner Strain	Hoop	332	4.675	-0.00030	-0.00011	0.00027	0.0007	0.00063	0.00045

46	Liner Strain	Hoop	59	4.525	-0.00030	-0.00011	0.00027	0.0007	0.00063	0.00045
47	Base Liner	Radial	135	0.00						
48	Tendon Strain	Hairpin	180	15.60	0.0015	0.0014	0.0014	0.0013	0.0013	0.0013
49	Tendon Strain	Hairpin	135	10.75	0.0028	0.0025	0.0024	0.0023	0.0024	0.0024
50	Tendon Strain	Hoop	90	6.58	0.0022	0.0022	0.0021	0.0021	0.0023	0.0021
51	Tendon Strain	Hoop	180	6.58	0.0023	0.0023	0.0021	0.0021	0.0021	0.0021
52	Tendon Strain	Hoop	280	6.58	0.0022	0.0022	0.0021	0.0021	0.0023	0.0021
53	Tendon Strain	Hoop	0	4.57	0.0023	0.0023	0.0021	0.0021	0.0021	0.0021
54	Tendon Force	Hairpin	241	-1.16	470kN	470kN	470kN	470kN	470kN	470kN
55	Tendon Force	Hoop	275	6.58	350kN	350kN	350kN	350kN	350kN	350kN



**APPENDIX R**

**SNL/ANATECH**

**SANDIA NATIONAL LABORATORIES  
UNITED STATES**

Appendix A, Composite Plots, comprises test data compiled and plotted from all organizations that participated in the Prestressed Concrete Containment Vessel (PCCV) Round Robin Pretest Analysis. To avoid duplicating the composite information, individual sets of data and/or plots have been omitted from participants' reports. In some cases this action resulted in disconnects between callouts and content and in the numbering of figures, tables, and pagination in some reports.

However, Appendix R, "SNL/ANATECH, Sandia National Laboratories, United States," contains none of these discontinuities.

## LIST OF FIGURES

<u>Figure No.</u>		<u>Page</u>
2-1	Cylinder Concrete (Spec. $f'_c = 48.55$ MPa) Stress-Strain Idealization and Sample Measurements	R-13
2-2	Basemat Concrete (Spec. $f'_c = 48.80$ MPa) Stress-Strain Idealization and Sample Measurements	R-13
3-1	Basis for Strain Failure Criteria in Reinforcement	R-19
4-1	Designers' Prestress Force Estimates Including Friction, Anchor Set, and Other Losses	R-27
4-2a	Modeling of Tendon Friction Behavior	R-28
4-2b	Modeling of Prestress Application with Jacking Element	R-28
4-3	Finite Element Model of PCCV	R-29
4-4	Profile Results from Axisymmetric Analysis	R-30
4-5	Deformed Shapes, Displacements Magnified by 50	R-31
4-6	Axisymmetric Model, Maximum Principal Strain Contours (Displacements x 50) at $P = 3.0 P_d$	R-32
4-7	Axisymmetric Model, Maximum Principal Strain Contours (Displacements x 50) at $P = 3.4 P_d$	R-32
4-8	Axisymmetric Model, Minimum Principal Strain Contours (Displacements x 50) at $P = 3.4 P_d$	R-32
4-9a	Crack Pattern of Axisymmetric Model at $3.0 \times P_d$ Pressure	R-33
4-9b	Crack Patterns of Axisymmetric Model at $3.0 \times P_d$ Pressure-Enlarged View	R-33
4-10	Deformed Shape and Crack Pattern of Wall-Base Juncture Region	R-33
4-11	Comparison of PCCV Shear Strength from Modified Compression Field Theory to Shear Demand from the Global Analysis Model	R-34
5-1	Inside "Stretchout" View of Portion of PCCV Modeled in 3DCM Model	R-40
5-2	Isometric View of 3DCM Model and Tendon Modeling	R-41
5-3	3DCM Rebar for $270^\circ - 360^\circ$ (E/H)	R-42
5-4	3DCM Model Vertical Boundary Conditions	R-43
5-5	Changes to Tendon Friction Modeling to Include Setting Losses	R-44
5-6	Other Setting Loss Cases for Parameter Study	R-44

5-7	3DCM Model Deformed Shape at Pressure = 3.5 Pd (mag. factor = 10x)	R-45
5-8	Stress Contours in Tendons after Prestress	R-46
5-9	3DCM Deformed Shapes at Various Pressures	R-47
5-10	3DCM and Axisymmetric Radial Displacement Comparison vs. Pressure at Elevation 4.6752	R-48
5-11	Stress and Strain Contour Plots of Hoop Tendons at P = 3.5 Pd	R-49
5-12	3DCM Liner Hoop Strains at 3.0 Pd (Magnification factor = 35x)	R-50
5-13	Tendon Stress Profile for Instrumented Hoop Tendon #H35	R-51
6-1	Schematic of Liner Anchor Model and Boundary Conditions	R-57
6-2	Strain Contours for Free Edge Case at Far-Field Strain = $8.4E-3 \mu = 0.5$	R-58
6-3	Force vs. Displacement Results for Liner Anchor Studies	R-58
6-4	Idealized Modeling of Anchors and Stiffeners	R-59
6-5	Force-Displacement Results of Liner Anchor Model vs. Idealized Model	R-59
6-6	Detailed Liner Analysis Near E/H (View from Inside PCCV Looking Out Radially)	R-60
6-7	Boundary Conditions and Geometry for 3D Equipment Hatch Model	R-61
6-8	Finite Element Mesh including Tendons, Liner, Anchors, and Stiffeners	R-61
6-9	Deformed Shape of E/H Model at Pressure = 3.25 Pd (Magnification factor = 20x)	R-62
6-10	E/H Hoop Tendon Stress and Strain Contours at Prestress	R-63
6-11	E/H Hoop Tendon Stress and Strain Contours at Pressure = 3.25 Pd	R-63
6-12	Liner Contours Strain Plots at P=3.25 Pd	R-64
6-13	Boundary Conditions and Geometry for 3D Airlock Model	R-65
6-14	Finite Element Mesh including Tendons, Liner, Anchors, and Stiffeners	R-65
6-15	Deformed Shape of A/L Model at Pressure = 3.75 Pd (magnification factor = 2x)	R-66
6-16	A/L Hoop Tendon Stress and Strain Contours at Pressure = 3.75 Pd	R-67
6-17	Liner Contour Strain Plots at P=3.75 Pd	R-68
6-18	M/S Local Model Liner Details	R-69
6-19	Finite Element Mesh including Liner and Anchors	R-69

6-20	Prestress Deformed Shape of M/S Model at Pressure =3.8 Pd (Magnification factor = 2x)	R-70
6-21	Liner Contour Strain Plots at P = 3.8 Pd	R-71
7-1	Driving Strains at Liner Strain Concentration Locations	R-76
7-2	Peak Strains at Liner Strain Concentration Locations	R-77
7-3	Categorization of Liner Strain Concentration Locations	R-78
7-4	Strain Concentration Type 1 Near 90° Buttress and Near A/L	R-79
7-5	Strain Concentration Type 1 Near 270° Buttress and Near E/H	R-79
7-6	Strain Concentration Type 2,3,4 Near A/L	R-80
7-7	Strain Concentration Type 2,3,4 Near E/H	R-80
7-8	Strain Concentration Type 2,4 Near M/S Penetrations	R-81
7-9	Strain Concentration Type 1,2,3,4 Near F/W Penetrations	R-81

### LIST OF TABLES

<u>Table</u>		<u>Page</u>
Table 1-1	List of Potential Failure Modes, Failure Mechanisms and Analysis Methods for the 1:4 Scale PCCV	R-10
Table 4-1	Initial and Final Tendon Stresses After Losses (in MPa) from Design Package	R-21
Table 7-1	1:4 Scale PCCV Pretest Predictions Analysis Table of Response Events and Pressure Milestones	R-72

## EXECUTIVE SUMMARY

This report describes pretest analyses of a 1:4 scale model of a prestressed concrete containment vessel (PCCV) constructed by the Japanese Nuclear Power Engineering Corporation (NUPEC) at Sandia National Laboratories. It documents the analytical predictions of the model behavior performed by ANATECH for Sandia for submittal to an international Round-Robin pretest exercise. The test program is part of a cooperative effort between the United States Nuclear Regulatory Commission and NUPEC.

The first analysis consisted of a 2D axisymmetric global model with discrete representation of concrete, liner, rebar, and tendons, but "smeared" representation of non-axisymmetric features. The typical azimuth chosen for the modeling plane was 135°. The ABAQUS general purpose finite element program with the ANACAP-U concrete and steel constitutive modeling modules were used for the analysis. Tendons and their prestressing were modeled to replicate expected tendon stress-strain behavior and friction effects. Concrete cracking was simulated with the "smeared crack" approach where cracking is introduced at the finite element integration points. A list of possible failure modes and failure locations was developed based on the global axisymmetric analysis and based on experience. A liner failure at the midheight of the cylinder near a penetration and a shear/bending failure at the base of the cylinder wall were both investigated in detail. Local models studied with detailed analysis were the Equipment Hatch region, the Personnel Airlock region, and the Mainsteam Penetration region. A detailed 3d model of the entire cylinder midheight region was also developed for detailed investigation of tendon behavior in the cylinder and three dimensional effects which drive the local strain concentrations near the penetrations.

The local models showed that liner tearing failure near the E/H is likely by  $3.2 P_d$  ( $3.2 \times$  design pressure = 1.27 MPa, or 185 psig). The failure strain, using a strain-based failure criteria that considers the triaxiality of stress and a reduction in ductility in the vicinity of a weld, was 0.162. The high strain locations are at the base of a vertical liner anchor which terminates near the E/H 2 o'clock position, about 20 mm out from the edge of the thickened liner insert plate, and near a hoop stiffener which also terminates nearby. Other local models showed other candidate liner tear locations, several of which are likely to occur during the pressure range  $3.2 P_d$  to  $3.5 P_d$ , if they are not precluded first by the growth of the first tear and subsequent depressurization of the vessel. A significant candidate tear location was also found near the 90 degree buttress where hoop strains are elevated due to bending, and a weld seam and hoop stiffener "rat-hole" are coincidentally located. A study of potential shear failure at the wall-base juncture showed that while wall-base outer surface concrete spalling is predicted to occur by  $3.2 P_d$ , a through-wall shear failure is not likely until at least  $4.0 \times P_d$ , and other failure modes are judged to be more likely to occur prior to reaching this pressure.

The detailed models described herein demonstrate a new tendon modeling approach in which friction losses are explicitly represented by friction truss tie elements. Expected tendon stress distributions at various pressures are provided. Capturing the tendon stress distributions in more detail has helped improve the prediction of displacement response and liner strains, especially near the E/H where the tendon layout and tendon friction is very complex. The 3DCM model with its detailed tendon representation, predicted a rupture of the hoop tendon closest to the E/H at a model pressure of about  $3.5 P_d$ , and if this occurred prior to earlier depressurization associated with liner tearing/leakage, rupture of other tendons and large deformations of the vessel would quickly follow. However, this mode is predicted to be precluded by the liner tearing and leakage failure mode.

## 1.0 INTRODUCTION

This report describes pretest analyses of a one-fourth scale model of a prestressed concrete containment vessel constructed by NUPEC at Sandia National Laboratories. The analysis work was performed for Sandia as part of a cooperative effort between the USNRC and NUPEC. The results of the pretest analysis form the basis for submittal to a Round-Robin pretest prediction analysis exercise.

### 1.1 Background

The testing of the one-fourth scale PCCV model represents a valuable opportunity to examine the ultimate pressure capacity of a steel-lined, prestressed concrete containment model in a manner similar to Sandia's USNRC-sponsored 1:6 scale model of a reinforced concrete containment[1,2]. Pretest predictions and post-test analysis of the 1:6 scale model were carried out by ANATECH as part of the Electric Power Research Institute's (EPRI's) participation in Sandia's round-robin analysis program. In that effort, concrete analysis methodology and liner tearing criteria developed under EPRI's sponsorship were utilized to obtain reasonably close predictions of the failure pressure and obtain a list of the possible liner tearing locations, several of which ultimately occurred in the 1:6 scale model test. The analysis methodology used in the present work is similar to that employed in the analysis of the 1:6 scale model. However, the 1:4 scale PCCV model introduces new analytical aspects due to the prestressed design.

While there is extensive evidence supporting liner tear and leak-before-break as the dominant failure mode of steel lined concrete containments (as occurred in the 1:6 scale model), some containment research[3,4,5] has indicated that prestressed containments may be more prone to a structural failure (rather than leak) than reinforced containments. This is due to the following: (1) there is a generally narrower pressure range that exists in prestressed containments over which most significant deformations occur (and lower ductility due to lower failure strains in tendons versus rebar), and (2) prestressed containments have generally thinner walls and rely more heavily on the concrete as a structural component. The former issue becomes relevant for accident scenarios with high rates of loading (rates that could "leap frog" beyond a liner tearing pressure) and the latter issue suggests the possibility of a shear or other brittle concrete failure mode.

The Sizewell B test of a 1:10 Scale PCCV in England and associated analyses emphasized investigation of structural failure modes, but this was because that test was loaded with a water-filled rubber bladder which precluded leak-before break. The issues stated above make the 1:4 Scale PCCV model test particularly interesting for purposes of addressing competing structural and liner tearing failure modes. In the current work, prediction of ultimate capacities and of gross structural failure modes are, therefore, of at least equal importance to predicting liner tearing failure.

### 1.2 Scope and Objectives of Pretest Analysis

The objectives of the pretest analyses are:

- (1) To obtain a database for the validation of analytical models for predicting the global structural response of a prestressed concrete containment;
- (2) To gain insight, through pretest predictions, into the potential structural failure modes of a prestressed concrete containment; and
- (3) To aid in the design, gage placement, and planning of the test.

In addition to prediction of global response with 2d global models, predictions of possible failures near penetrations in the test structure are provided with a suite of 3d local models that includes the E/H and

P/A models, and a model of the Mainsteam (M/S) Penetration Group. The global axisymmetric model predicts a radial displacement versus pressure at the cylinder midheight that may serve as an average displacement, but the radial displacement around the circumference of the cylinder may be highly variable due to the existence of buttresses or wall embossments. Prediction of this behavior and the development of boundary conditions for local models required prediction of the 3-dimensional response of the mid-height region of the cylinder. A 3-D cylinder midheight (3DCM) model was developed that extends 360 degrees circumferentially, and included both buttresses.

### 1.3 Behavior and Failure Modes Investigated

Prior to starting the analyses, a list of potential failure mechanisms and vulnerable regions and components of the structure were developed. The list was intended to be as comprehensive as possible, regardless of the relative likelihood of the events in the list. Then a detailed plan was developed for systematically eliminating or investigating each of the failure mechanisms and vulnerable components. Table 1-1 lists these items and the method proposed at the outset of the work to evaluate each item.

Many of the items listed in the table are identified as either "free-field" behavior or localized behavior. Free-field refers to a failure mechanism at a reasonable distance away from stiffness discontinuities such as penetrations or the wall-base juncture. Local failure mechanisms are those near stiffness discontinuities caused by local stress or strain concentrations near discontinuities or connection details. In general, global analyses only predict free-field behavior. However, based on experience from prior structural testing, inferences can be made from free-field behavior about local behaviors. This issue is discussed in more detail in the discussion of failure criteria and failure predictions.

Each of the local penetration analyses investigated and ranked the potential for liner tearing failure mode. The potential for liner tearing near penetrations is increased by strain concentrations:

- (1) near the edges or ends of vertical T-anchors;
- (2) near the edges or ends of horizontal stiffeners;
- (3) near liner thickness discontinuities;
- (4) near liner bending points (edges of embossments where a liner angle change occurs);
- (5) near weld seams, i.e., at a corner where a vertical seam meets a horizontal seam.

The local models described herein investigate strain concentrations 1 through 4, but not 5. Strain concentration 5 is addressed through judgment and through evaluation of welded liner test data which is discussed in the development of the liner strain failure criteria.

The analytical models also investigate shear and bending in the containment wall, elevated rebar strain, elevated tendon strain, and the models will predict failure in these modes, if it were to occur. The only significant local deformations and strains that were found other than in the liner are the wall bending near the buttresses and the elevated wall membrane strains at local rebar termination points. These modes were all investigated by the 3DCM model.

### 1.4 Computational Tools

The ANACAP-U material modeling modules are called by ABAQUS through ABAQUS's subroutine UMAT utility. For all of the analyses described herein, ABAQUS Version 5.6 and ANACAP-U Version 2.5 were used.

The ANACAP-U concrete constitutive (material) model is based on the smeared-cracking methodology developed by Rashid[6] and a  $J_2$ -plasticity theory that permits the incorporation of cracking and other significant concrete response characteristics. The theoretical basis for this model is fully described in [7].

Within the concrete constitutive model, cracking and all other forms of material nonlinearity are treated at the finite element integration points. Thus, the cracking and stress/strain state can vary within an element. Cracks are assumed to form perpendicular to the principal strain directions in which the cracking criterion is exceeded. Multiple cracks are allowed to form, but they must be mutually orthogonal. When cracking occurs, the stress normal to the crack direction is reduced to zero which results in redistribution of stresses around the crack. Once a crack forms, the direction of the crack remains fixed, and it can never "heal." However, cracks may close and re-open under load reversals. The shear stiffness also is reduced upon cracking and further decays as the crack opens. This effect is known as "shear retention", and it is attributed to crack roughness and aggregate interlock.

Rebar is modeled as individual sub-elements within the concrete elements. Rebar sub-element stiffness is superimposed on the concrete element stiffness in which the rebar resides[8]. The rebar material behavior is handled with a separate constitutive model that treats the steel plasticity, strain hardening, and bond-slip behavior (if bond slip is expected to be significant). The theoretical basis for the rebar constitutive model are also described in [7]. The concrete and rebar formulations can handle arbitrary strain reversals at any point in the response, whether in tension or compression.

Table 1-1. List of Potential Failure Modes, Failure Mechanisms and Analysis Methods for the 1:4 Scale PCCV

Failure Mode	Failure Mechanism	Evaluation Method
Loss of Prestressing	Tendon rupture in free-field	Global axisymmetric model
	Tendon rupture near a penetration	3DCM Model
	Tendon grip, local concrete crushing, or other anchorage failure	Ancillary tests by tendon supplier and/or NUPEC and Sandia
Failure of Reinforcement	Rebar rupture in free-field	Global axisymmetric and 3DCM Models
	Rupture of rebar around a penetration	Local 3D and 3DCM models
	Rebar bond slip or anchorage failure	Detailed axisymmetric wall-base model
Shear/Bending Failure	Basemat-wall juncture	Global axisymmetric model
	Through-basemat	" "
	Springline	Global axisymmetric analysis
	In wall adjacent to Equipment Hatch/Personnel Airlock	Local 3D models of penetrations
Pressure Loss Due to Liner Tearing	Tear in free-field liner	Global Axisymmetric Model
	Horizontal tear at wall-base juncture	Global Axisymmetric Model and Detailed Liner-only wall-base model
	Horizontal Tear at Springline	Global Axisymmetric Model
	Horizontal Tear Near Penetrations or other Liner Anchor Discontinuity	Global Axisymmetric and Local 3D Penetration Models
	Vertical Tear Near Penetrations	Global Axisymmetric and Local 3D Penetration Models
	Vertical Tear at Edges of Buttress	3DCM and Local 3D Models

## 2.0 PCCV TEST STRUCTURE GEOMETRY AND PROPERTIES

### 2.1 Geometry and Loading

Geometry and material property information for the PCCV model was provided by Sandia[9]. The model consists of a 10.8m diameter cylinder with a wall thickness of 325mm, a 3.5m thick basemat and a hemispherical dome of thickness 275mm. The model rests on a 15cm thick mudmat built over engineered backfill. There is no bond between the basemat and the mudmat, so the model is free to lift up. The basemat reinforcement consists of radial, hoop, and orthogonal rebar patterns. The meridional tendons are a hairpin design laid out orthogonally and anchored in the tendon gallery. The hoop tendons all span 360°, and the anchorages are staggered between the two buttresses located at 90° and 270°.

The cylinder wall contains a scaled version of an equipment hatch (E/H), a personnel airlock (A/L), and several smaller penetrations. The two main openings (e.g. the Hatch and Personnel Airlock) are located at Azimuth 324° and 62°, respectively. Because of the existence of buttresses and penetrations, the azimuth of the model that is believed to be influenced the least by non-axisymmetric features of the structure is at 135°. This azimuth is located no closer than 45° from any perturbation in free-field stiffness. Thus, this azimuth of the model was adopted specifically for measuring and analyzing "global" response.

The test calls for nitrogen pressurization. The design pressure  $P_d$  of the model is 0.393 MPa. The planned loading sequence includes a loading cycle to  $1.125 \times P_d$  (the SIT) prior to ultimate pressurization of the model. This loading sequence was followed in the global axisymmetric analysis, but since the response prediction was nearly identical with and without the initial SIT pressure cycle, this cycle was not included in the local model analyses.

### 2.2 Materials

The material property input to the analyses was prepared based on data provided by Sandia[9]. The idealizations of these data made for analysis reported herein are outlined below.

The concrete properties used in the analysis were based on stress versus strain data of the trial mix concrete and on a few measurements that were available from construction prior to January 1999. In the preliminary analysis, strength of ten percent higher than specified on the drawings was assumed. The 10% increase was added to account for additional strength associated with aging of the material between the time of placement and the time of testing. In the process of selecting a representative concrete material curve, it was noted in Sandia's final information package released to Round Robin Analysts [9] that the actual concrete poured was much weaker than the trial mix tests. Based on this information, the trial mix data was not used directly for the  $f_c' = 44.13$  MPa concrete. The data was used, however, to calibrate the shape of the stress-strain curve and to establish parameters such as  $\epsilon_{crush}$ ,  $\epsilon_{fracture}$ , Young's Modulus, and Poissons Ratio. ( $\epsilon_{crush}$  is the uniaxial strain at maximum compressive strength, and  $\epsilon_{fracture}$  is the cracking strain). For the compressive strength, the specified strength plus 10% for aging was used. The stress strain curve that was assumed and the various data provided by Sandia are plotted in Figure 2-1.

For the  $f_c' = 29.42$  MPa concrete, on the other hand, tests taken at the time of construction showed better correlation to the trial mix data, so these data were used to establish  $f_c'$  and the other material parameters. From past experience with the 1:6 scale and other test models, actual strength corresponds best to field cured specimens. This is because the PCCV model itself is subjected to the same atmospheric elements and temperature variations as the field cured specimens. The stress-strain curve

used in the analysis is shown in Figure 2-2. All of the inputs to the analytical material models are itemized below:

	Spec. $f'_c = 29.42$ MPa	Spec. $f'_c = 44.13$ MPa
Uniaxial Compressive Strength	48.81 MPa (1.1 x Avg. of Series A, Series B at 13 weeks, Field Cured)	48.54 MPa (1.1 x Spec. Value)
Uniaxial Tensile Strength*	2.65 MPa (assumed $\epsilon_{fracture} = 80 \times 10^{-6}$ )	2.64 MPa (assumed $\epsilon_{fracture} = 80 \times 10^{-6}$ )
Initial Young's Modulus*	33,071 MPa (57,000 $\sqrt{f'_c}$ , with $f'_c$ in psi)	32,979 MPa (57,000 $\sqrt{f'_c}$ , with $f'_c$ in psi)
Poisson's Ratio*	0.2	0.2
Density	2.2 ton/m <sup>3</sup>	2.2 ton/m <sup>3</sup>

\* Tensile Strength, Young's Modulus and Poisson's Ratio were based on experience and on formulae built-in to the ANACAP-U constitutive model, but they all compare fairly well to the Trial Mix Data.

Stress-strain data from rebar pull tests were also provided in the Sandia information sent to all Round Robin Analysts [9]. In general three test curves were provided for each bar size and specified strength. For some bar sizes, results of pull tests on dumb-bell shaped specimens fabricated from the standard bars were also provided. It was generally observed that the dumb-bell specimens produced significantly higher yield and ultimate strengths than the unaltered bar specimens. Based on experience, it was deduced that the yield curve for the standard (unaltered) specimens provided the best representation of engineering stress versus engineering strain to use in the analysis, but that the dumb-bell specimens provided the best representation of Young's Modulus. This rule was followed in the generation of the idealized curves for analysis. In each case one data set which appeared to represent the average of three reliable datasets, was selected as the representative stress-strain data. Single "outlier" curves which deviated significantly from the other two curves were ignored. In all cases Young's Modulus was set equal to 200,000 MPa. It should be noted that since the measured stress-strain data is based on a measured force divided by nominal area, it is mathematically appropriate to input nominal areas to the finite element model, regardless of the presence of the "ribs" or irregularities on the deformed bars.

Strand and tendon stress and strain data were obtained from information from Sandia [9] by testing both individual strands and tendon assemblies (including anchor hardware) according to Japanese test standards JISG 3536 and JISZ 2241. Engineering stress was calculated from the applied force and the initial cross-sectional areas. Elongation was determined from the stroke of the testing machine and strain was obtained by averaging the data from strain gages mounted on individual strand wires. It should be noted that the strain gage data was not corrected to account for the pitch of the wires in the strand which could, based on experience, affect the accuracy of the strain readings by as much as 20%, depending on the skill of the installer. Based on these observations, the most appropriate data to use directly in finite element representation of the tendons is the tendon system load versus elongation data provided in the PCCV Material Property Report [R-SN-P-004]. The load cell data was then divided by the nominal area (3.393 cm<sup>2</sup>) to get engineering stress. Young's Modulus was set equal to 195,200 MPa.

Six sets of liner stress-strain measurements were provided by Sandia: three for the hoop direction and three for the vertical direction. Since the differences in the hoop and vertical properties were too small to warrant the added complexities of using an anisotropic plasticity model, the data was averaged.

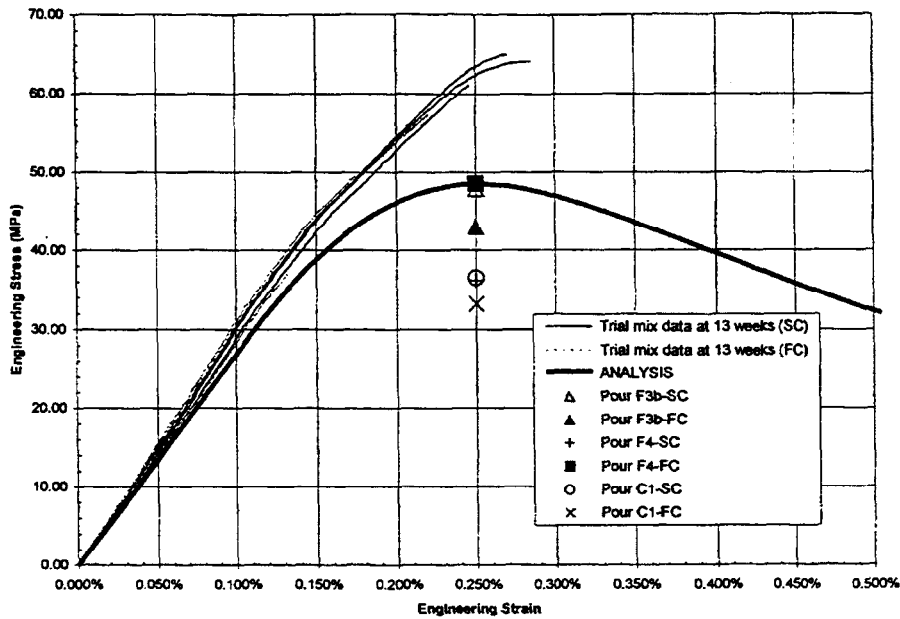


Figure 2-1. Cylinder Concrete (spec.  $f_c' = 48.55$  MPa)  
Stress-Strain Idealization and Sample Measurements

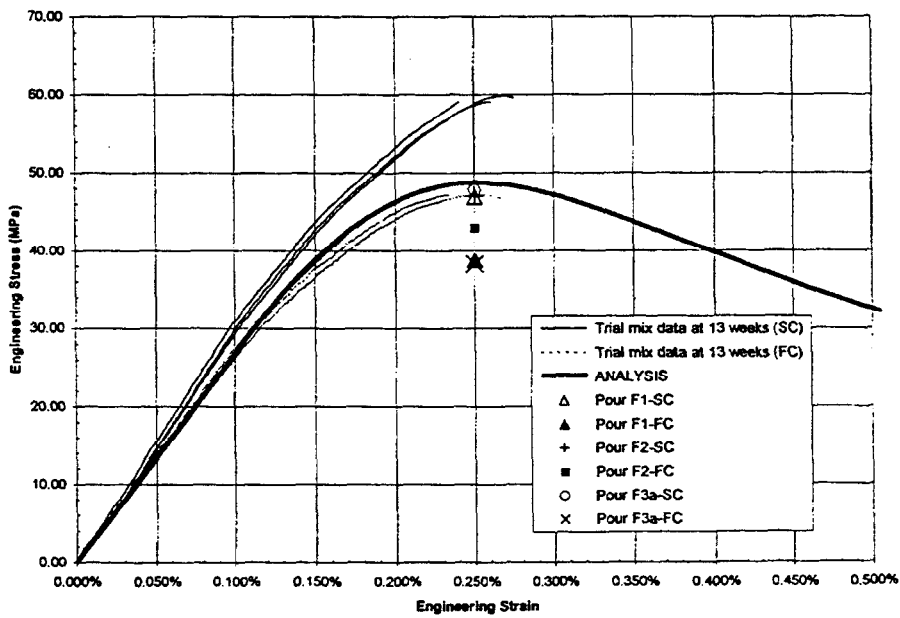


Figure 2-2. Basemat Concrete (spec.  $f_c' = 48.80$  MPa)  
Stress-Strain Idealization and Sample Measurements

### 3.0 FAILURE CRITERIA

#### 3.1 Concrete

For the concrete material the only failure mode that has meaningful consequences if exceeded is shear failure. (Failure in direct tension in the form of cracking is expected and does not lead to structure failure. It simply results in stress redistribution to steel elements). Shear failure criteria found in concrete behavior literature are generally dependent on the geometry of the section being considered (depth of section and amount of shear reinforcement) and on the simultaneous presence of bending moment. Thus shear failure criteria for the PCCV must be very location-specific. The PCCV preliminary analyses showed elevated shear stresses at various locations in the model, but only the shear stresses of the wall-base juncture location are close enough to failure to warrant detailed consideration.

Shear response of concrete has been found to follow three stages of deformation:

- i. The concrete resists the deformation with no assistance from the reinforcement or the aggregate; as soon as cracks begin to develop at some angle (between 0 and 45° depending on location) to the direction of the applied shear force, the structural shear stiffness drops suddenly.
- ii. Frictional resistance increases with further deformations as aggregate interlock begins to mobilize; during this stage the cracks grow wider.
- iii. The structure reaches its maximum resistance and begins to soften in a mixed mode of shear sliding, crushing and rebar yielding under combined tension and dowel action; the latter mechanisms are due to the dilation of the cracks which forces rebars into direct tension and bending beyond their yield limit. When the shear reinforcement fractures a general shear failure occurs.

These deformation states vary considerably over the failure "plane", but tests to measure shear behavior are generally expressed only in terms of average shear stress across a section vs. average shear strain. Experimentalists have developed shear behavior material models from such tests. However, to apply such models in a continuum analysis approach where the models have to be applied locally (at an integration point) requires consideration of fundamental mechanics, and use of damage parameters calibrated to match experimental results. This is the approach used in the ANACAP-U modeling. Explicit shear failure prediction is thus made by using an appropriately detailed analytical model and then observing when large shear distortions of the entire wall base section exceed prescribed criteria for the reinforcement in the section. Thus the concrete failure criteria is not a set expression or strain limit, but rather a complex continuum response prediction model. The prediction is believed to be reasonably good partly due to a recent improvement to ANACAP-U called the shear shedding model. Background and development of the shear shedding model is described below.

In smeared crack formulations such as ANACAP-U, there has always been concern about the buildup of shear stress across an open crack in excess of the actual ability of cracked concrete to resist such stresses. Buildup of shear stresses across open cracks is possible because of the requirement that cracks only form in orthogonal planes. The Shear Shedding Model attempts to address such limitations. The purpose of the model is to reduce the buildup of shear stress across an open crack.

The standard "Shear Retention" Model reduces the incremental shear modulus across on open crack according to the Al-Mahaidi formula:

$$G = 0.4 G_0 g (\varepsilon_{\text{frac}}/\varepsilon), \quad (3-1)$$

Where  $G = G(\varepsilon)$  is the incremental shear modulus across an open crack,  $G_0$  is the uncracked shear modulus,  $\varepsilon_{\text{frac}}$  is the cracking strain ( $\sim 100\mu$ ),  $\varepsilon$  is the normal strain across an open crack, and  $g$  is the shear retention factor. Since cracks form in the principal strain directions in general, there is no shear across a crack when it first opens. However, as the loading continues, even if it is monotonic and "proportional", there is a tendency for shear stress to build up across an open crack. The ANACAP-U constitutive model uses an incremental formulation to update the stress, which for shear takes the form

$$\tau_{n+1} = \tau_n + G(\varepsilon) \Delta\gamma, \quad (3-2)$$

where  $\Delta\gamma$  is the incremental shear strain across an open crack in a load increment from "n" to "n + 1". The shear shedding model reduces this buildup by modifying Eq. (3-2) in the following empirical manner

$$\tau_{n+1} = \tau_n e^{-(\Delta\varepsilon/\varepsilon_{\text{ss}})} + G(\varepsilon)\Delta\gamma, \quad (3-3)$$

where  $\Delta\varepsilon$  is the incremental normal (tensile) strain across an open crack and  $\varepsilon_{\text{ss}}$  is a shear shedding degradation parameter. Note that there is no change in the incremental shear modulus. There is also a second parameter that has been included in the Shear Shedding Model,  $\varepsilon_{\text{beg}}$ , which represents the normal (tensile) strain at which Equation (3-3) will be activated (begins). The shear shedding model, first introduced into test versions of ANACAP-U in 1996, has now been successfully calibrated to several building structure component tests, and so is judged to be a reasonably reliable improvement over the old shear retention model.

While shear failure prediction for the project is based on the continuum response prediction coupled with the rebar strain criteria, it is appropriate to turn to the concrete design/performance literature for a check on the final prediction. On the capacity side, criteria can be based on forces or average stresses within the section. The most promising stress-based criteria the authors have found for the PCCV is the Modified Compression Field Theory developed by Collins & Mitchell [10].

This theory is a refined version of a strut and tie model which provides a rational basis for calculating compression strut angles of less than 45 degrees, and, with the "modified" theory, the local resistance of concrete in tension between cracks and the effect of aggregate interlock is considered. The difficulty with applying force or stress-based theories to the PCCV is that the shear force is indeterminate, i.e., it is a function of the pressure, the relative hoop stiffness of the cylinder to the basemat, and the flexural stiffness of the cylinder wall. Because of these factors, the shear at the section does not necessarily increase monotonically with pressure. The modified compression field theory is invoked herein to check for shear failure in the axisymmetric analysis.

Very little is found in the literature for deformation based criteria which would be useful for FE analysis implementation. For the PCCV failure prediction, the primary criteria has been based on strain in the shear reinforcement. If strain in the shear reinforcement at the wall-base juncture reaches the failure threshold (Section 3.2) this is judged to lead to shear failure of the section. The modified compression field theory is retained as a back-up check to the shear formulations in the constitutive model.

### 3.2 Rebar

The failure criteria used for predicting failure of reinforcement is based on rebar strain, but there are also rebar-concrete interaction issues which influence the strain level.

As described in Chapter 2, the material representation of reinforcement is based on a plastic stress versus strain curve, where the strain is analogous to the "elongation" (engineering strain) measured in a direct tension test of a rebar specimen. Although this does not consider local strain concentrations between the reinforcement "ribs", bar tension test data from the PCCV project using elongations did not deviate substantially from similar tests where strain gages were placed directly on the bars. The other factor to consider in reinforcement, however, is the effect of rebar-concrete interaction. This phenomenon is known to produce a strain pattern in embedded rebar like that shown in Figure 3-1. A good discussion of this phenomena and some measured strain profiles which illustrate it can be found in [10]. Strains are lowest midway between cracks and are highest at the cracks. No simulation of this phenomenon is attempted in the smeared crack representation of the PCCV analysis described herein. The phenomenon can, however, influence the actual strain level at rebar fracture. The shape of the strain profile in Figure 3-1 is dependent on many factors including

- Bar diameter
- Crack spacing
- Bond characteristics (like aggregate size)
- Strain level

With these known trends, but lacking a specific criteria based on tests, a failure criteria for the rebar of approximately  $\epsilon_{\text{failure}} = 0.05$  has been used in the predictive analysis.

### 3.3 Tendons

Since unbonded pre-stressing tendons do not experience bond interaction with concrete as do rebar, the tendon failure criteria is strain, without any applied factors. The material stress-strain curve plotted in Chapter 2 predicts and simulates tendon fracture and post-fracture behavior in the analysis.

It should be noted, of course, that tendons can fail in different ways, including failure of strands far from the anchorage, failure near the anchorage, failure of the anchorage itself, and failure of the concrete surrounding the anchorage. For the pretest predictions it has been assumed that since the stress-strain behavior (Chapter 2) is derived from the Force-elongation response of the tendon system, this is the correct representation of the tendons up to and including all tendon system failure modes.

### 3.4 Liner Failure Criteria

#### *3.4.1 Liner-Away From Welds*

The liner failure criteria is also based on strain, but the strain at failure is influenced by the multi-axiality of the stress state and by possible reductions in ductility in the vicinity of welds. If the strain due to the strain concentration near a penetration or other stiffness discontinuity exceeds the strain criteria of the liner, the liner will tear and leakage will occur. A literature survey conducted by ANATECH in the early stages of the 1:6 scale model work [1] resulted in adoption of a liner strain-based failure criteria that takes into account the triaxiality of stress when computing the failure strain. This criteria, based on the work of Manjoine [11] and others, has subsequently been used also by Sandia for predicting the ductility capacity of liner and other steel plate material subjected to multi-axial stress. The criteria development is as follows. The ductility ratio  $\mu$  is defined as

$$\mu = \frac{\varepsilon_{\text{eff}}}{\varepsilon_{\text{uf}}}$$

$$\mu = 2 \sqrt{\text{TF}}$$

where TF is the Davis triaxiality factor.

$$\text{TF} = \frac{\sqrt{2}(\sigma_1 + \sigma_2 + \sigma_3)}{[(\sigma_1 - \sigma_2)^2 + (\sigma_2 - \sigma_3)^2 + (\sigma_3 - \sigma_1)^2]^{1/2}} \quad (3-5)$$

$\varepsilon_{\text{eff}}$  is the effective plastic strain predicted from analysis including any concentration factors that may be appropriate.  $\varepsilon_{\text{uf}}$  is used to denote uniaxial failure strain, which is the standard uniaxial elongation limit that is obtained from a coupon test. In the case of the PCCV, this average value is 0.34 for liner material uninterrupted by welds. The ductility relationship, Eq. (3-5), has been found to be a reliable formulation, particularly for triaxiality factors which occur in containment liners. While Manjoine proposed Eq. (3-5) for the range  $0 < \text{TF} < 5$ , containment analysts need only be concerned with the range of approximately  $1 < \text{TF} < 2$ . To make this statement it has been assumed that at stress states of interest, no membrane compressive stress exists in the liner and out-of-plane stresses ( $\sigma_3$ ) are small and so have a negligible effect on TF. This makes Eq. (3-5) reduce to.

$$\text{TF} = \frac{(\sigma_1 + \sigma_2)}{(\sigma_1^2 - \sigma_1\sigma_2 + \sigma_2^2)^{1/2}} \quad (3-6)$$

With this formula it is straightforward to calculate ductility ratios at various liner stress states. For example, for uniaxial tension,  $\sigma_2 = 0$ ,  $\text{TF} = 1$ , and ductility ratio = 1. For  $\sigma_1 = \sigma_2$  (for example the approximate stress condition in the containment dome),  $\text{TF} = 2$ , ductility ratio = 0.5, which means that the liner will tear at an effective plastic strain of only half the uniaxial failure strain.

### 3.4.2 Liner Near Welds

Based on NUPEC testing of dog-bone shaped specimens with and without welds [9] and based on qualitative observations from other welded steel plate tests, there is evidence to support a reduction in ductility of liner plate material near welds. The testing in [9] was done to verify that the repairs of welds in the PCCV model that were not meeting radiography specifications would reach strengths equivalent to the virgin material. Fortunately, these tests also provide some information on how, and at what elongation, the liner may fail near a weld.

Based on test standard JIS-Z-2201, which was used for defining liner plate test specimens (Test Piece No. 5 13a, or 13b), the Gauge Length, L, over which the elongation is measured is 50 mm. Based on the supplementary liner welding test documentation (Document #MH-K9-41), the coupon specimens for the liner weld tests were identical to those for the virgin material. The tests also recorded where the fractures occurred. In 2/3 of the cases, the fractures were in the virgin parent metal; in the rest of the cases it occurred partly in the heat affected zone (HAZ) and partly in the parent metal.

Based on the liner reweld test data the following conclusions were drawn and actions taken:

- (1) There is a small (10% or less) reduction in the apparent yield strength of a welded specimen versus a virgin specimen. This is probably due to a reduction in yield strength of the material in the heat affected zone (HAZ). Because liner failure is

strain-controlled not strength-controlled and because of the complexities of incorporating this into a finite element model, it was decided to ignore this effect in the pretest prediction analysis.

- (2) There is very little effect on the ultimate strength of welded specimens versus virgin specimens.
- (3) There is no consistent trend in the elongation or strength measurements that delineates the as-welded versus repaired specimens; nor is there any consistent trend differentiating the behavior of specimens with or without backing bars.
- (4) The measured elongations are consistently, significantly lower for welded specimens than for unwelded specimens.

Part of observation #4 is probably due to gage length effects, since the weld material undergoes little or no plastic deformation. While this gage length effect is difficult to quantify, it is approximately addressed in the failure criteria as follows. A ductility reduction is incorporated into the liner failure criteria at locations where a weld is located by a general reduction in elongation at fracture, with a small correction factor for gage length effects of the welded specimens as follows:

$$\varepsilon_{\text{eff}_w}^{\text{failure}} = K_w \varepsilon_{\text{eff}}^{\text{failure}} \quad (3-7)$$

where  $\varepsilon_{\text{eff}_w}^{\text{failure}}$  is the effective plastic strain assumed sufficient to cause a fracture where a seam weld of the liner is located. Welds of stiffeners or anchors onto the liner are assumed to have lesser effect on liner ductility than the full penetration seam welds and so will be ignored.

$$K_w = \left[ \frac{(L)}{(L - w)} (\text{Elong. of welded specimens}) / (\text{Avg. Elong. of unwelded specimens}) \right]$$

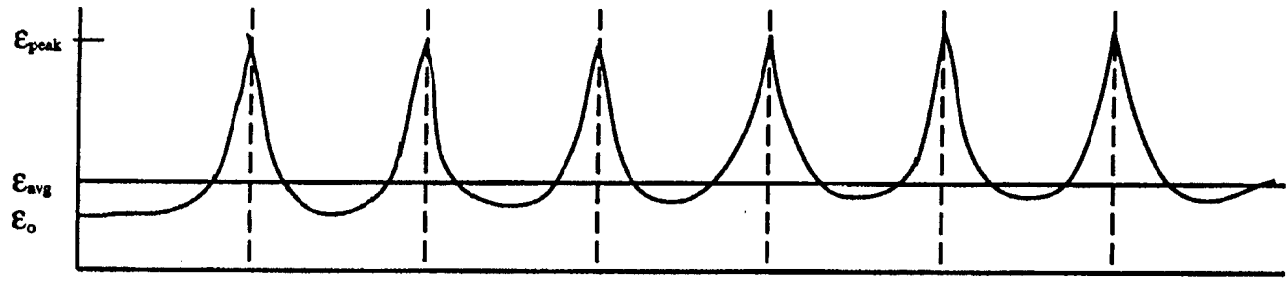
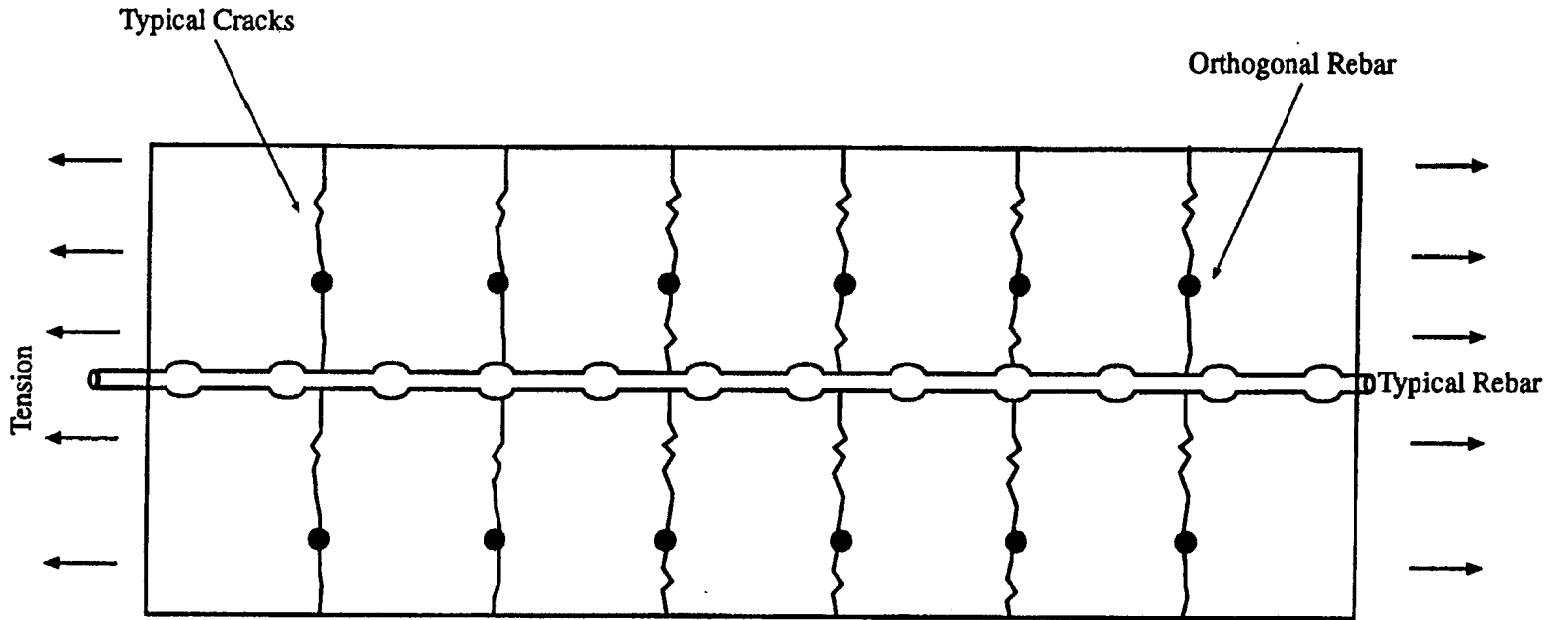
where L = liner test specimen gage length (50 mm)

w = root gap of weld

Averaging the data from the re-weld specimens and using 0.34 as the unwelded specimen average elongation gives:

$$K_w = 0.60$$

Therefore, a 40% reduction in failure strain is applied in the failure prediction where high strain concentrations occur at a location coincident with a seam weld.



Strain Distribution in the Bat

Figure 3-1. Basis for Strain Failure Criteria in Reinforcement

## 4.0 GLOBAL AXISYMMETRIC ANALYSIS

### 4.1 Hand Calculations

The first step in the analytical predictions was to compute the approximate response behavior in order to establish the load stepping strategy for nonlinear finite element analysis. A summary of the major milestones predicted by hand calculation are listed below. These calculations are based on an infinite cylinder with concrete, reinforcement, and prestressing geometry and properties of the PCCV model.

Pressure at which the cylinder stress overcomes prestress,  $P_o = 0.422$  MPa (61.2 psig)

Cylinder hoop cracking pressure,  $P_{hc} = 0.598$  MPa (86.7 psig)

Pressure at rebar yield,  $P_{ry} = 1.05$  MPa (152 psig)

Ultimate cylinder failure based on 5% uniform hoop strain,  $P_{ult} = 1.58$  MPa or  $4.0 P_d$  (229 psig)

### 4.2 Prestressing Loss Assumptions

Prestressing losses must be estimated to accurately represent the actual stresses that will exist in the model at the time of testing. In general, the philosophy used in applying initial tendon stress was as follows: 1) calculate best estimate "test-time" values based on the nominal values targeted by the designers and modified for creep or any other in situ conditions that may not have been anticipated by the designers; 2) apply tendon stresses according to best estimate values, and allow the model to equilibrate to final tendon stresses that are reasonably close to these best estimate values, including anchor slip. In the axisymmetric analysis, there is no opportunity to model friction along the tendon path in the hoop tendons, but there is the opportunity to model this in the meridional tendons.

A consideration of losses was conducted prior to setting up the analysis. Standard prestressing losses, from Reference [10], along with a brief explanation of the basis for their consideration are listed below:

- (1) Elastic Shortening - Considered in the finite element analysis.
- (2) Creep of Steel - Considered by designers calculating the "nominal target" values.
- (3) Shrinkage of Concrete - Considered only in combination with creep.
- (4) Creep of Concrete - A small value of creep was included by designers; a larger value was observed in ancillary test measurements, so this was used in the analysis.
- (5) Anchor Slip - Considered explicitly in local analysis; Not relevant for axisymmetric.
- (6) Angular Friction - Considered explicitly in local analysis hoop tendons, and in global axisymmetric analysis meridional tendons in dome.
- (7) Temperature - Not considered.

Therefore, the three types of losses given specific modeling consideration are elastic shortening, anchorage slip, and angular friction. These modeling considerations are described below.

**Elastic Shortening.** In post-tensioning, the amount and distribution of elastic shortening depends upon the order of post-tensioning. From the post-tensioning schedules, it has been assumed that the tendons are jacked in a sequence appropriate to reacting the total desired lock-off force. In the ABAQUS analyses, an option called "PRESTRESS HOLD" allows an initial post-tensioning equilibrium step that holds the tendon stresses at a preset value while the structure iterates to equilibrium and thus maintains a constant stress regardless of elastic shortening. By using the "PRESTRESS HOLD" option, elastic shortening losses are only addressed in the analysis to the extent that they were considered in the design calculations. This procedure was used for the hoop tendons, with the prestress hold value corresponding to the designer's target values listed in Table 4-1.

Anchorage loss (lock-off slip). The assumption for these losses comes from hand calculations and from the specifications that the coefficient of tendon friction is equal to 0.21. Anchorage loss calculations by the designers are summarized in Figure 4-1.

Angular Friction. From standard prestressed concrete texts [16], the angular friction was included in the curved tendon portions with the formula: (Wobble friction and friction in straight portions of meridional tendons in the barrel below the springline was neglected).

$$T_2 = T_1 e^{-(\mu\alpha)}$$

where  $\alpha$  is the angle between  $T_1$  and  $T_2$ , and  $\mu$  is the coefficient of static angular friction.  $T_1$  is the tendon force next to a jack before friction losses, and  $T_2$  is the tendon force at some angle  $\alpha$  away. A summary of these calculations and input to the preliminary analytical models is given in Table 4-1.

Table 4-1. Initial and Final Tendon Stresses After Losses (in MPa) from Design Package

	Group 1	Hoop Tendons Group 2	Meridional Tendons
Target prestress force from drawings*	453 kN (101.9k)	453kN (101.9k)	503 kN (113.1k)
Initial prestress without loss after anchoring (MPa)	1,337MPa (193.9 ksi)	1337MPa (193.9 ksi)	1483 MPa (215.0 ksi)
After additional loss assumed due to creep	1268 MPa (183.9 ksi)	1268 MPa (183.9 ksi)	1414 MPa (205.0 ksi)
Prestress with friction loss (MPa) at 135° azimuth	797 MPa (115.6 ksi)	1109 MPa(160.8 ksi)	location dependent see below
Stress at anchor after anchor set	1122 MPa (162.7 ksi)**	1122 MPa (162.7 ksi)**	1318 MPa (191.1 ksi)
Target stress at anchor for F.E. models	"	"	1341 MPa (194.5 ksi)

\* Includes designer's calculations of relaxation and concrete shrinkage

\*\* Not needed for axisymmetric analysis

#### Meridional Tendon Stresses and Losses

Dome angle (deg) measured from springline	0°	15°	30°	45°	90°
Target prestress after all losses (MPa)	1,334	1,365	1,236	1,170	977
Stress in analytical model after prestress (MPa)	1,342	1,269	1,220	1,139	962

### 4.3 New Tendon Friction Modeling Approach

#### 4.3.1 Tendon Friction Loss Representation

Because of the importance of the tendon stress levels, a methodology was devised to more accurately represent the tendon sliding friction behavior. Since rebar representation of the prestressing tendons does not account for sliding between the tendon and the concrete, the meridional tendons of the axisymmetric analysis were modeled as truss elements (as were all tendons of the local models described in later chapters). Initial attempts to model the sliding friction explicitly as a contact surface in ABAQUS gave unsatisfactory numerical stability. Therefore, the following approach was adopted.

A two-node tendon truss element was included for each row of concrete elements along the tendon path. The resulting grid has a 1:1 ratio of concrete nodes to tendon nodes along the tendon. The concrete nodes were placed at the inside face of the tendon duct. The analogous tendon nodes were placed at the

center of the tendon duct. To account for the tendon friction along curved surfaces, tendon nodes were offset from concrete nodes along the tendon path so that the angle between each concrete node and tendon node was equal to the angle of friction. A graphical representation of this modeling technique is shown in Figure 4-2. The representation in the local models was similar. As shown in the figure, the friction coefficient used was  $\mu = 0.21$ . The friction force accumulates in the truss elements between the concrete and the tendon. The calculations performed using this modeling technique use small displacement theory so that the friction angle remains constant throughout the analysis. Tendon friction is assumed to be negligible over straight surfaces, so the friction angle is set to zero along straight sections.

#### 4.3.2 Tendon Prestress Application at Boundaries

Prestress could not be applied as an initial condition when using this modeling approach because the preset friction angle assumes the force comes from the jacking direction. Therefore, a method was devised to pull the end of the tendon at the jacking location and cause the reaction force to be imparted into the concrete at the tie down. This makes the analytical application of prestress completely analogous to the physical application. The prestress was applied using an extra, elastic, two-node truss element at the jacking location. One end of this “jacking” element was connected to the end of the tendon, and the other was mathematically constrained to the concrete nodes in the tie down region. In the first analysis step, the jacking element was loaded with a prestress that produced enough strain to stretch the entire tendon to the target level of prestress. The approximate relationship between the prestress in the jacking element and the prestress in the tendon is given as:

$$\sigma_j = \sigma_t * (l_t/l_j) + \text{jacking and anchoring losses}$$

$\sigma_j$  = Prestress applied to jacking element

$\sigma_t$  = Prestress transmitted to tendon

$l_t$  = effective tendon length

$l_j$  = length of jacking element

Since the effective tendon length over a curved surface is difficult to calculate, the appropriate jacking prestress was arrived at through iteration. Jacking elements were modeled 31mm long so the ratio  $l_t/l_j$  was large. To accommodate the large stress and strain, the jacking elements were modeled with elastic material properties. The prestress and strain in the jacking elements are large and are not meant to represent physical values. All that is important is that after reaching equilibrium in the prestress load step, the end of the tendon is loaded with the appropriate design stress, after losses.

The ends of the tendons opposite the direction of force are mathematically connected to the concrete nodes through the wall thickness. As a result, the tendon force is transmitted as an appropriate stress at the boundary locations, which simulates the tendon anchor plate reacting against the concrete.

## 4.4 Computational Grid

### 4.4.1 Element Layout

The axisymmetric model is illustrated in Figure 4-3. The grid has 12 elements through the wall near the basemat, and 10 elements through the wall elsewhere. The concrete and liner were represented with 8-node quadrilaterals (ABAQUS CAX8R) and 3-node axisymmetric shells, respectively.

The reinforcement in the structure was represented with ABAQUS rebar subelements as shown in Figure 4-3. These subelement stiffnesses are overlaid onto their parent concrete elements in which they reside, but they do not have separate degrees of freedom, and so have strain compatibility with the concrete. The rebar stress-strain behavior is evaluated separately from the concrete, however. Also

added as rebar subelements is the steel associated with the "tendon sheath support frame". This frame adds the equivalent of the following to the structure:

- 7 hoops of areas  $2.79 \text{ cm}^2$  to cylinder
- 35 verticals of areas  $4.61 \text{ cm}^2$  to cylinder
- extra  $\rho=0.0018$  to dome (reinf. ratio)

The bottom of the model is supported by nonlinear contact springs. These springs have "zero" resistance to uplift and have compression stiffness based on the elastic stiffness of the concrete mudmat. The stiffness of the subgrade was not considered in the analysis.

The total number of elements used in the revised model is 2009. The vertical tendon is modeled with 144 two-node truss elements and 36 two-node axisymmetric shell elements. Axisymmetric shells were used to represent the tendons in the dome above a dome angle of  $45^\circ$  to accommodate the "smeared" hoop and vertical components of the hairpin tendons in the dome. This modeling approach is reasonable because above  $45^\circ$ , the tendons are all vertical (no hoop) and at the  $135^\circ$  azimuth they all intersect the model plane at  $\pm 45^\circ$ . This avoided the difficulties of terminating the truss elements at the dome apex with finite cross-section area but zero radius.

The liner is constructed of quadratic shell elements and 3 node quadratic beam elements for the liner anchors. The thickness of the liner elements is 1.6 mm (0.063") as specified in the structural drawings. The cross-section of the T-shaped liner anchor beams is computed in such a way that the thickness of the web and the width of the flange are scaled by the total number of T-anchors in the circumferential direction, namely by 225 from elevation -25 mm (0.98") to elevation 712.4 mm (28.05") and by 75 for the rest of the T-anchor beams.

The concrete in the PCCV is made of two different materials as shown in Figure 4-3. One is the high strength concrete that is used for the dome, the cylinder, and part of the basemat around the tendon gallery. The other is the concrete in the remainder of the basemat, part of which is poured after prestressing.

#### 4.5 Global Axisymmetric Analysis Results

Pressure load was applied to interior model surfaces over 161 increments. As is normally the case for concrete containment analysis, the ABAQUS feature "DIRECT=NOSTOP" was used with five iterations per load step. The five iterations insure that materials in the plastic range stay on a yield surface, but the "NOSTOP" parameter allows advancement of the solution before achieving full force convergence, which is difficult to achieve after extensive cracking occurs. Instead of achieving force convergence, displacement convergence is used to ensure the quality of the solution.

Results of the axisymmetric analysis are plotted in Figures 4-4 through 4-8. The first figures show shear and moment diagrams at the wall-base at various pressures. The deformed shapes for four different pressure loads are shown in Figure 4-5. Standard displacement and strain versus pressure history plots are not included here due to space limitations (they are included in the standard output plots).

Observations on strain behavior are described below. Hoop liner strains are maximum at the wall-midheight. Meridional liner strains are maximum at the wall-base. Strain response in the dome is consistently lower than the cylinder, thus indicating very minimal damage to the dome during the test. The most important observation to make is that wall-midheight hoop liner strain reaches 2% (a threshold to be discussed later) at nearly the same pressure (3.7 versus  $3.9 P_d$ ) as wall-base meridional liner strain.

This suggests the existence of two closely competing failure mechanisms, which require close evaluation to determine which will occur first. Strain distributions plotted onto the deformed model shape are shown in Figures 4-6 through 4-8. The strain contours are maximum and minimum principal strains, which show the general locations and levels of damage predicted to occur. It should also be noted that since the liner and rebar have strain compatibility with the concrete mesh, the strain contour plots are also indicative of rebar strains.

#### 4.6 Potential Failure Modes Evidenced From Global Axisymmetric Analysis

The axisymmetric analysis described in this chapter provides a set of predictions which can eventually be compared to strain and displacement gage readings that will be measured in the test, thereby evaluating the adequacy of the analytical method. The focus of the axisymmetric analysis, however, was also to gain insight into potential failure mechanisms listed in Table 2-1, and to add failure scenarios to that list. The various failure scenarios are discussed below vis-a-vis the global analysis model results and experience from other containment pressure tests.

(1) Tendon Rupture: The straining of the hoop tendons (and rebar) at the mid-height of the barrel to their ductility limits was the final limit state in the global axisymmetric analyses. General tendon rupture is predicted at approximately  $4 \times P_d$ .

(2) Other Loss-of-Prestress Failures: The chance of tendon slippage or other anchorage failure is presumed minimized by design and by verification from NUPEC's ancillary tests. Local damage under the tendon bearing plates is possible, however. A significant path of shear cracking develops in the basemat passing inward and upward from the meridional tendon anchorage, but strains are not predicted to be severe enough to lead to failure in the basemat. Bursting of the anchorage zones in the buttress have not been thoroughly investigated.

(3) Simultaneous Shear Failure and Rupture of Reinforcement at Shear Cracks: Failure of reinforcement crossing major shear cracks is the trigger for shear failure. The possibility of local rebar failure exists wherever large rebar strains in excess of the failure criteria are predicted in the analysis. Shear reinforcement do exhibit relatively large strains at the wall-basemat juncture. This is evaluated in more detail in the next subchapter.

(4) Loss of Pressure Due to Liner Tearing and Leakage: This is considered to be the most likely failure mode. Based on observations from other tests, reaching global liner strains in the PCCV model beyond approximately 2% is judged to be very unlikely. Strain concentrations at local discontinuities include liner thickness changes, stiffener terminations, and bending points near penetrations. The liner's vulnerability is further amplified by the fact that it experiences highly biaxial stress. Under such conditions, its ductility (or observed engineering strain at fracture) can be reduced by a factor of 2 or more. Based on this qualitative evidence, failure of the test model is predicted to occur due to liner tearing and leakage at global (far-field) strains of no larger than 2%. Without examining local model results, this places the failure pressure at no larger than  $3.7 \times P_d$ . The more detailed analyses of the local models refine this estimate and predict more precisely where the most likely failure location will be.

#### 4.7 Wall-Base Juncture Shear Failure Conclusions

Zones of potential shear problems in a concrete structure are generally indicated by cracks, especially cracks inclined to the direction of flexure or primary tension. Figure 4-9 shows cracking patterns at pressure of 3.0 times design pressure. The crack symbols occur at each integration point that is cracked and they show the crack orientation. Lines are drawn in the crack zones to demonstrate the estimation of

actual cracks that can be made based on the crack symbols and on the assumption that crack spacing will coincide generally with rebar spacing.

In preliminary axisymmetric analyses a wall-base shear modeling study was conducted as follows:

- (1) A refined mesh in the wall-base region was developed.
- (2) The strain field and failure potential near the wall-base was evaluated with different constitutive modeling approaches to modeling shear:
  - with the "standard" shear retention concrete model;
  - with a more recently developed concrete model with "shear shedding."
- (3) Differences in failure mode at this location versus other locations were considered:
  - perhaps shear failure of the concrete section increases the local liner strain and causes a small tear and leakage;
  - perhaps a brief crack pressurization causes a more energetic failure.
- (4) A brief mesh-size sensitivity was conducted.

In the preliminary analysis crack pressurization was an additional consideration, believed possible where a crack might exist but a leak path through the containment wall might not exist. In this event, it was postulated that crack pressurization could cause a rapid failure that could lead to a rupture that is much larger than that observed in other concrete test models.

Plotted results of the wall-basemat shear study are not included herein because there was little discernable difference between the failure behavior of the standard and "shear shedding" concrete models in the PCCV wall-basemat analyses. Secondly, the parameter studies did not show any acceleration of failure due to crack pressurization. To address questions of mesh-size sensitivity preliminary analyses used a local axisymmetric model with different element mesh sizes in the wall-basemat region. The mesh size study showed little difference in the computed response of the wall or in the liner strains, but some noticeable differences in the crushing strains at the outer wall surface were observed, so the grid with additional refinement was incorporated into the final global axisymmetric model. The final global axisymmetric model with twelve elements through the wall thickness in the region near the basemat was used to examine the potential shear failure mode near the bottom of the wall.

In the actual structure a large crack is predicted to form at the wall-base juncture re-entrant corner as sketched in Figure 4-10. This crack will allow the bottom edge of the vertical liner anchor to rotate with the wall concrete while the "I" shape that the vertical liner is anchored to 25 mm below the juncture will essentially move with the basemat. Shear damage is associated with large shear distortions of the entire wall-base section and large strains in the reinforcement crossing the shear plane. Shear failure of the wall-section was not predicted to occur, based on the strains observed in the wall-base juncture region and on the rebar failure criteria.

In order to further quantify the shear conditions in the wall-base juncture region and double-check the finite element prediction of "non-failure" a comparison to the Modified Compression Field Theory [16] was conducted. The Modified Compression Field Theory evaluation provides a "capacity" check. A hand analysis was conducted for a two-degree segment of the PCCV at a given principal tensile strain. Going through the 15 step procedure outlined in [10] produced a shear force of 77.2 kips (343 kN) at a diagonal shear crack angle of 30° and an axial force of N-258 kips (1148 kN).

This is close to the modified section axial load of 232 kips (an equivalent axial load which has the same tensile strain at mid-depth as found from the combined flexure and tension, as suggested in [10]), indicating that the assumed crack angle of 30 degrees is slightly off. At this point an iteration to the above process is conducted by changing the assumed crack angle in Step 2 and checking the modified section axial load, until the desired convergence is reached. In a computer analysis of the section using the 15 step procedure the shear capacity and diagonal crack angle, at this principal tensile strain, were found to be 78.3 kips and 29.9 degrees compared to 77.2 kips and 30 degrees found by hand. For the full 360 degree PCCV these results are multiplied by 360/2, which gives shear capacities of 13896 kips (6.18E4 kN) and 14094 kips (6.27E4 kN) for the hand and computer analyses.

This process was conducted at increasing principal tensile strains, with a constant axial load (modified to account for the flexure at the section) until the ultimate shear capacity was found. For each pressure step, the tension load was found and the corresponding moment was determined using Figure 4-4 at the point of maximum shear demand just above the base of the wall. A comparison between the ultimate shear capacity from the Modified Compression Field Theory and the demand from the global axisymmetric model is presented in Figure 4-11, indicating that the PCCV has reserve shear strength within the range of pressure loads applied.

Later chapters will show that a liner tear near a penetration has a high probability of occurring between  $3.2 P_d$  and  $3.5 P_d$ . Based on this and the results in this section, a liner tear at the wall-base juncture can be postulated, but it is judged to have a very low probability of occurrence because it would occur at much higher pressure than at other locations.

The axisymmetric analyses showed extensive spalling on the outer, lower edge of the containment wall and extensive cracking associated with shear and flexure. The analysis did not predict a shear failure at less than  $4.0 P_d$ , but it did predict large flexure and shear deformations in the inner half of the wall and local strains of up to 3% across part of the section. A general decrease in total shear force through the wall-base was observed at pressures larger than  $2.5 P_d$ . This shows that the concrete becomes heavily damaged at this pressure and that the concrete contribution to the total shear is declining at pressures beyond the  $2.5 P_d$  pressure. The shear reinforcement is still predicted to have reserve capacity so a liner tear at a penetration is judged to precede a shear failure or liner tear at the wall-base juncture.

PS Load Estimation Results

Unit Translation :  $1 \text{ MPa} = 1019.7 \text{ kg/mm}^2$

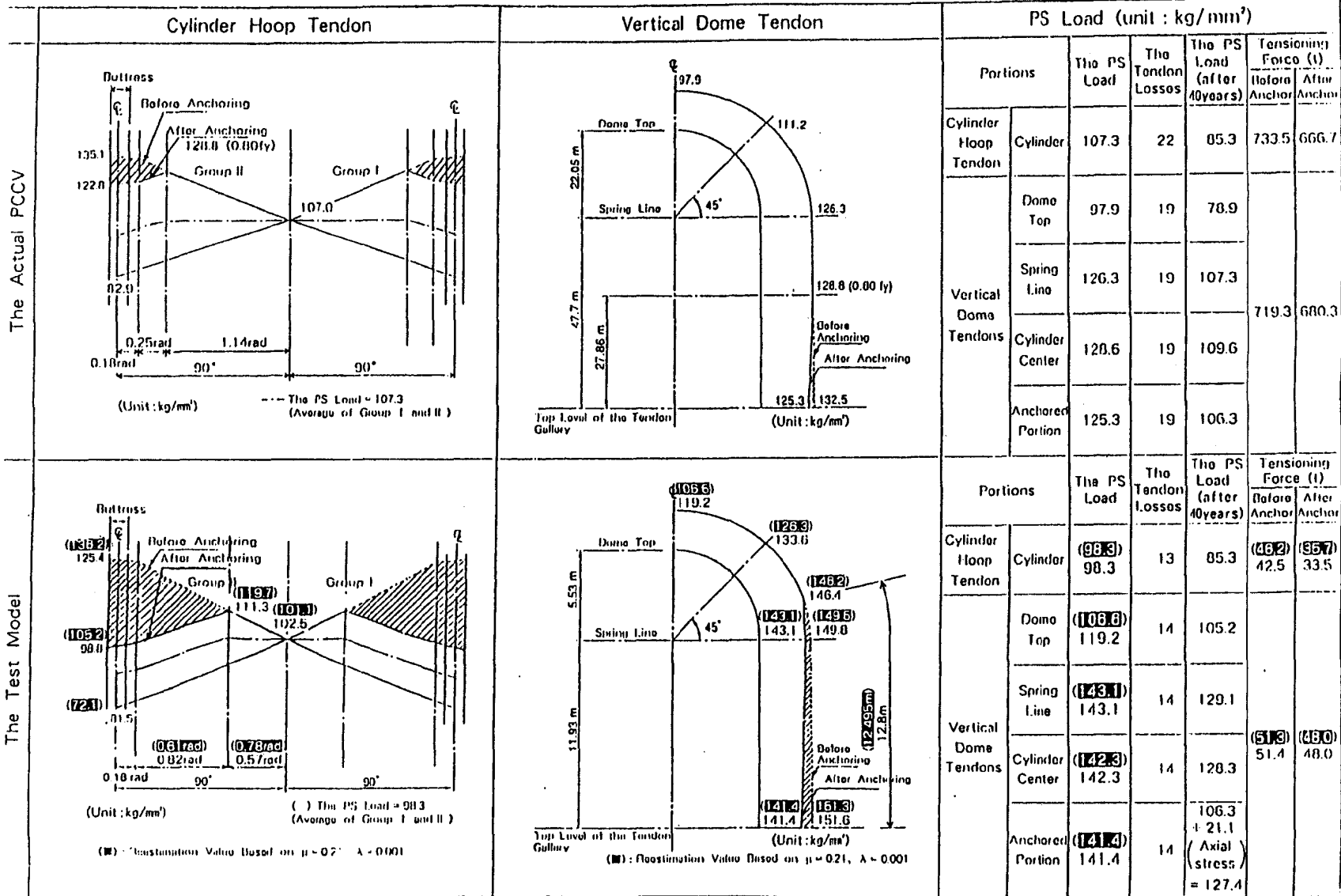
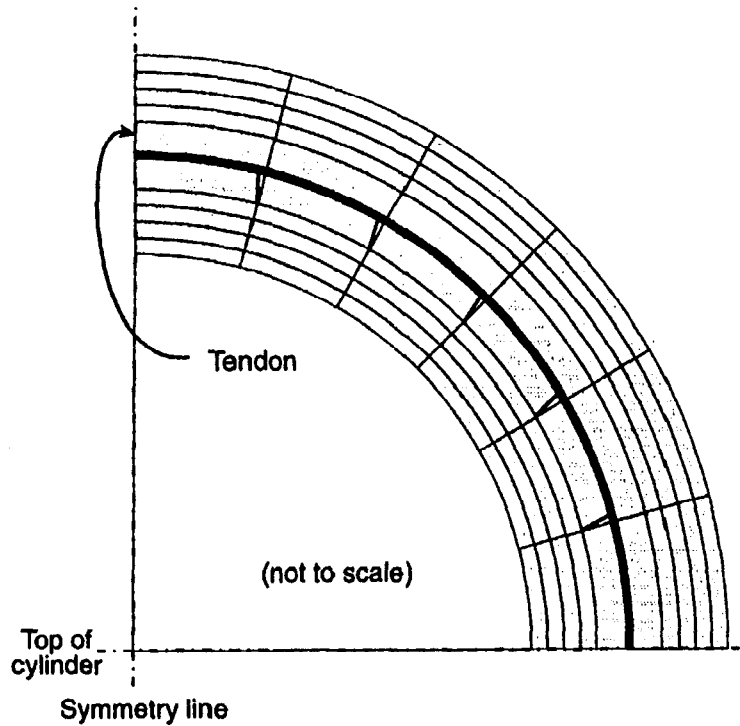


Figure 4-1. Designers' Prestress Force Estimates Including Friction, Anchor Set, and Other Losses

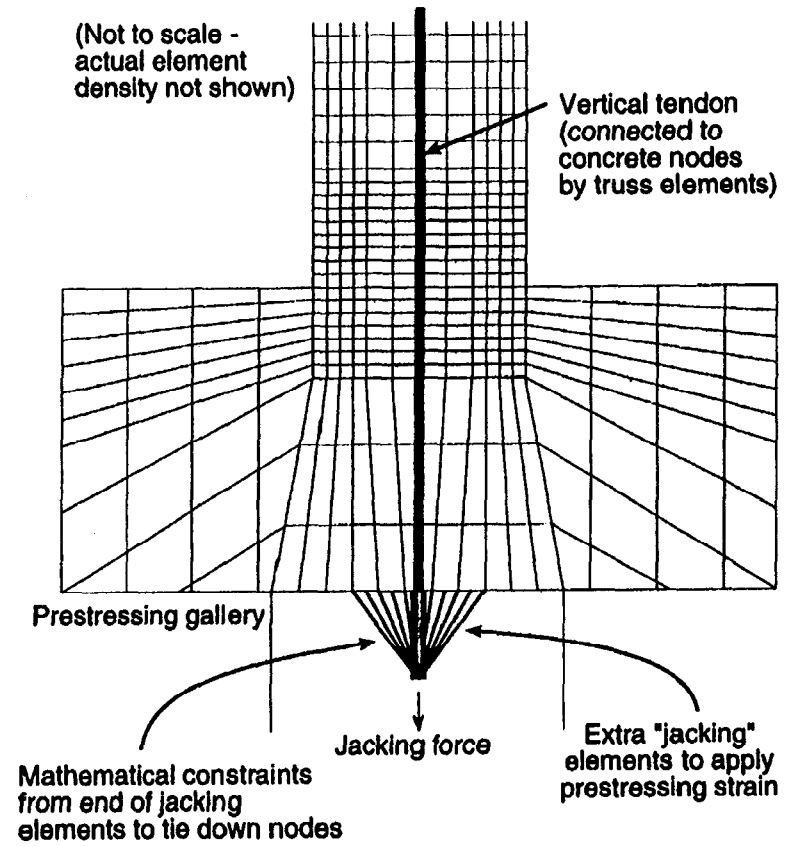


Friction trusses at all nodes between vertical dome tendon and concrete

Friction angle,  $\alpha = \text{Arctan}(\mu)$   
 (angle from radial projection to truss)  
 where  $\mu = 0.21$

Schematic of Axisymmetric Model meridional tendons

Figure 4-2a. Modeling of Tendon Friction Behavior



Jacking force is applied as an initial stress in the jacking element

Figure 4-2b. Modeling of Prestress Application with Jacking Element

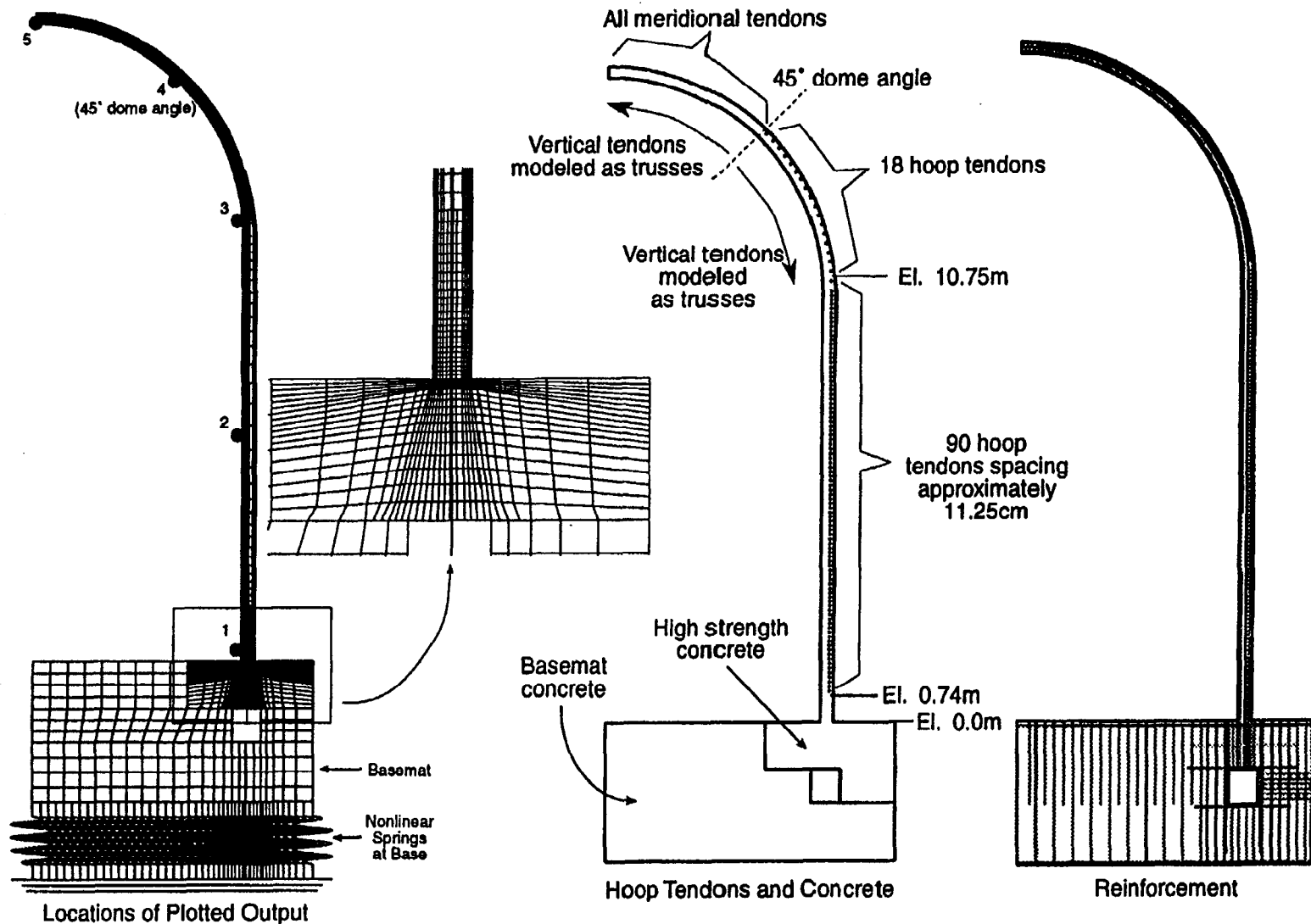


Figure 4-3. Finite Element Model of PCCV

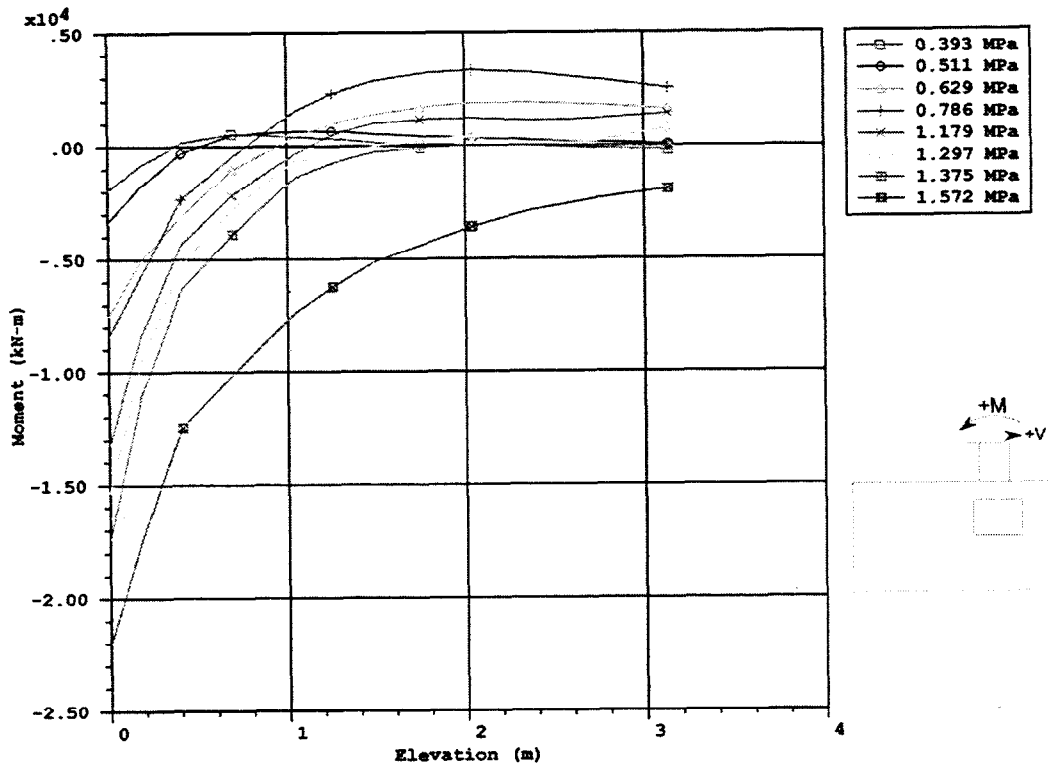
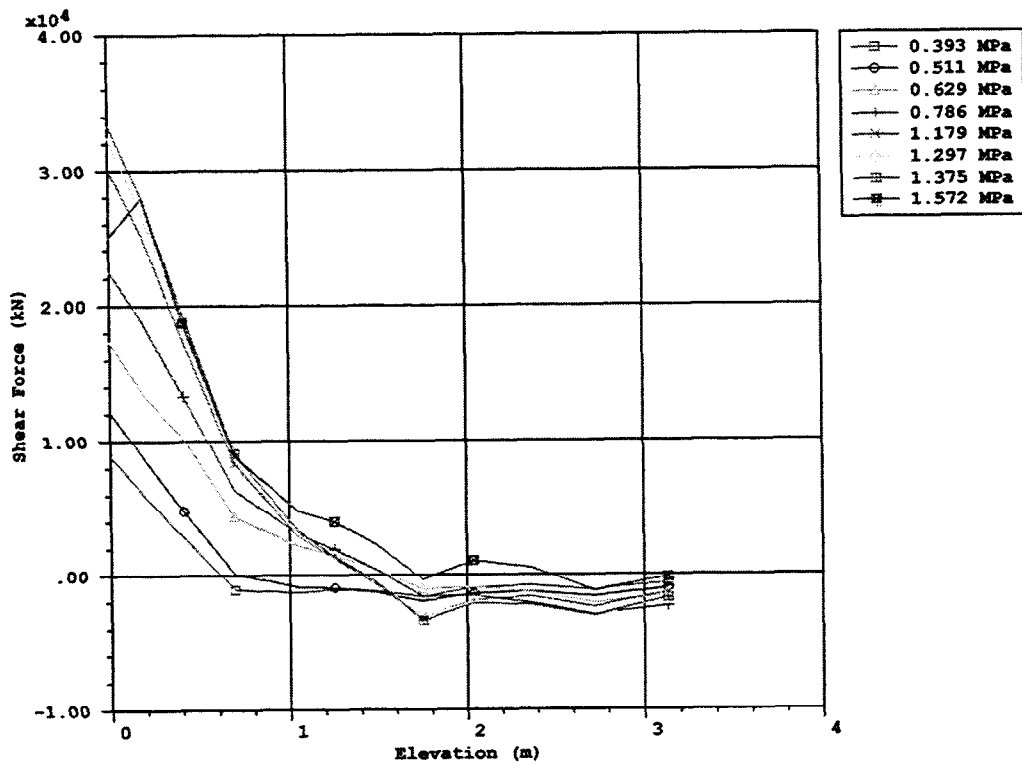
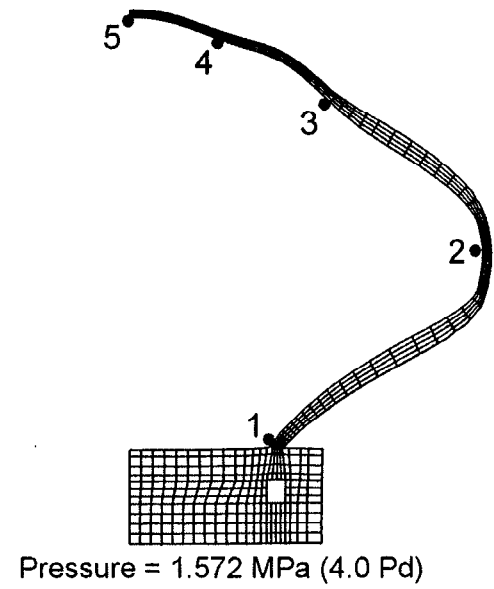
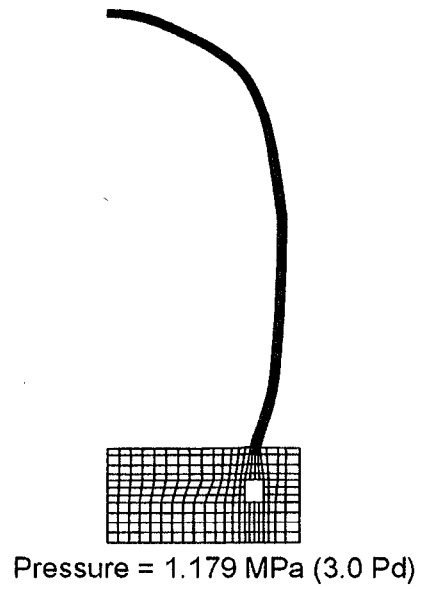
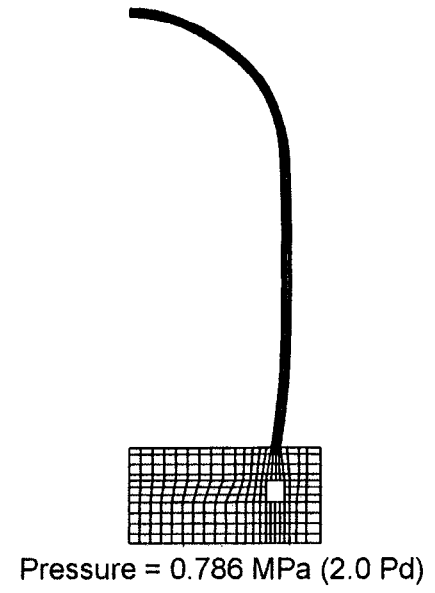
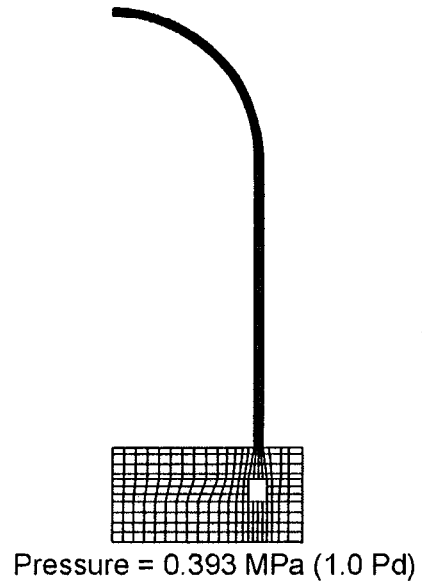


Figure 4-4. Profile Results from Axisymmetric Analysis

modell4.inp



model14.inp

Figure 4-5. Deformed Shapes, Displacements Magnified by 50

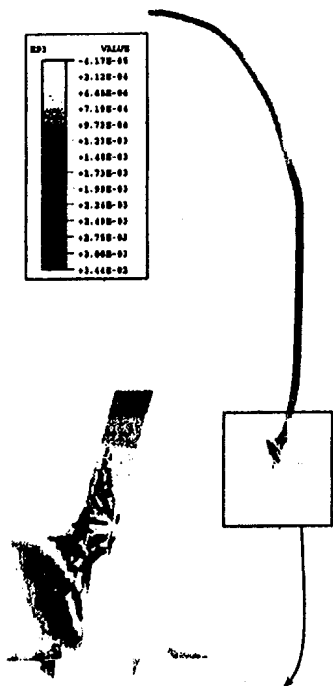


Figure 4-6. Axisymmetric Model, Maximum Principal Strain Contours (Displacements x 50) at P = 3.0 Pd

model14.inp

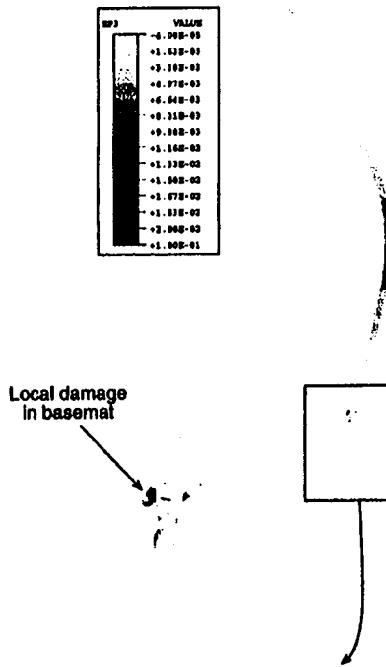


Figure 4-7. Axisymmetric Model, Maximum Principal Strain Contours (Displacements x 50) at P = 3.4 Pd

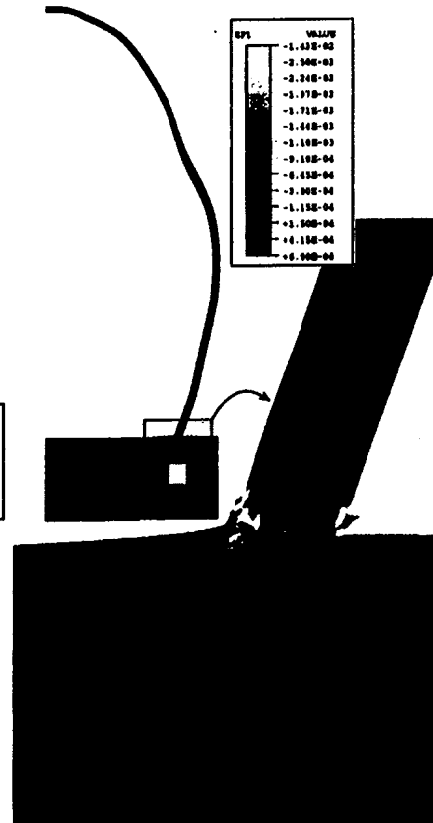


Figure 4-8. Axisymmetric Model, Minimum Principal Strain Contours (Displacements x 50) at P = 3.4 Pd

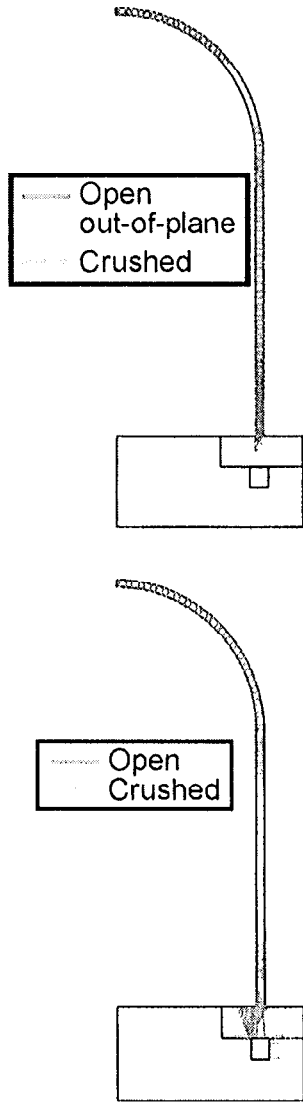


Figure 4-9a. Crack Pattern of Axisymmetric Model at 3.0 x Pd Pressure model14.inp

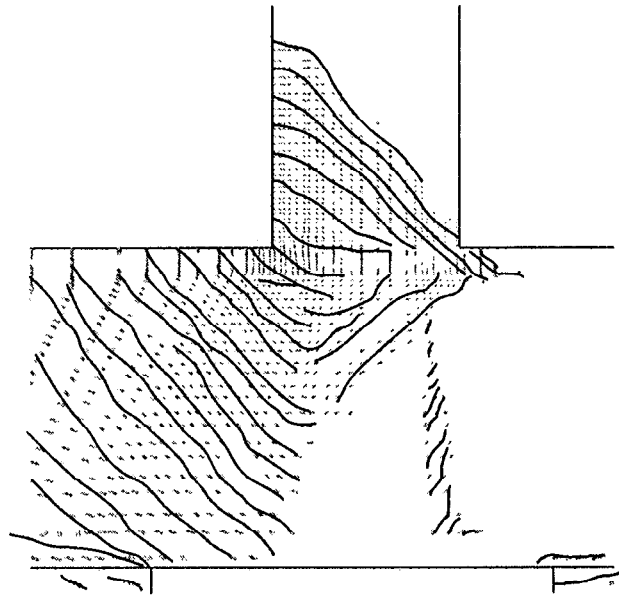


Figure 4-9b. Crack Patterns of Axisymmetric Model at 3.0 x Pd Pressure - Enlarged View

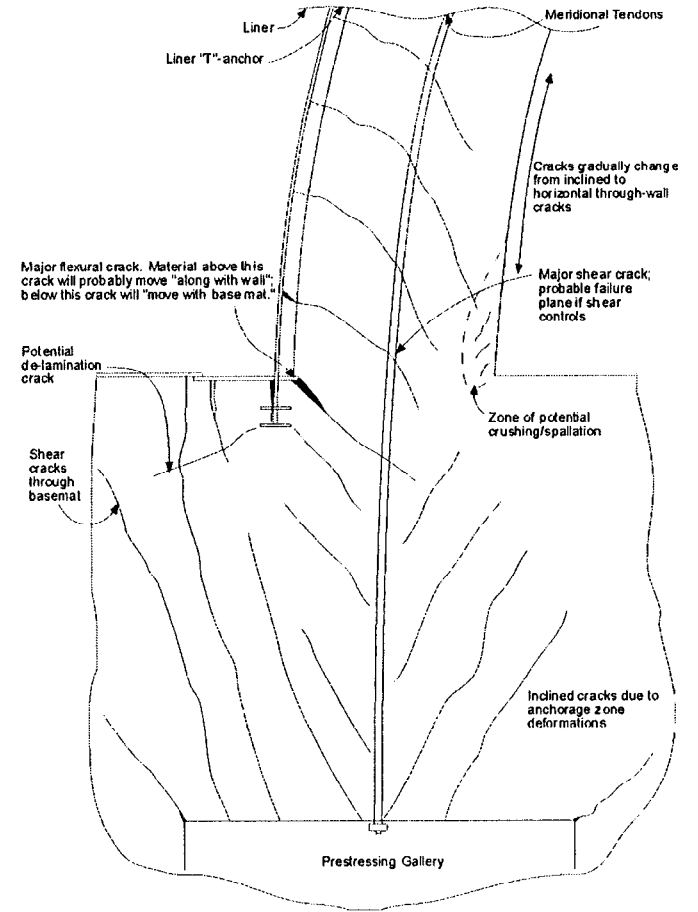


Figure 4-10. Deformed Shape and Crack Pattern of Wall-base Juncture Region

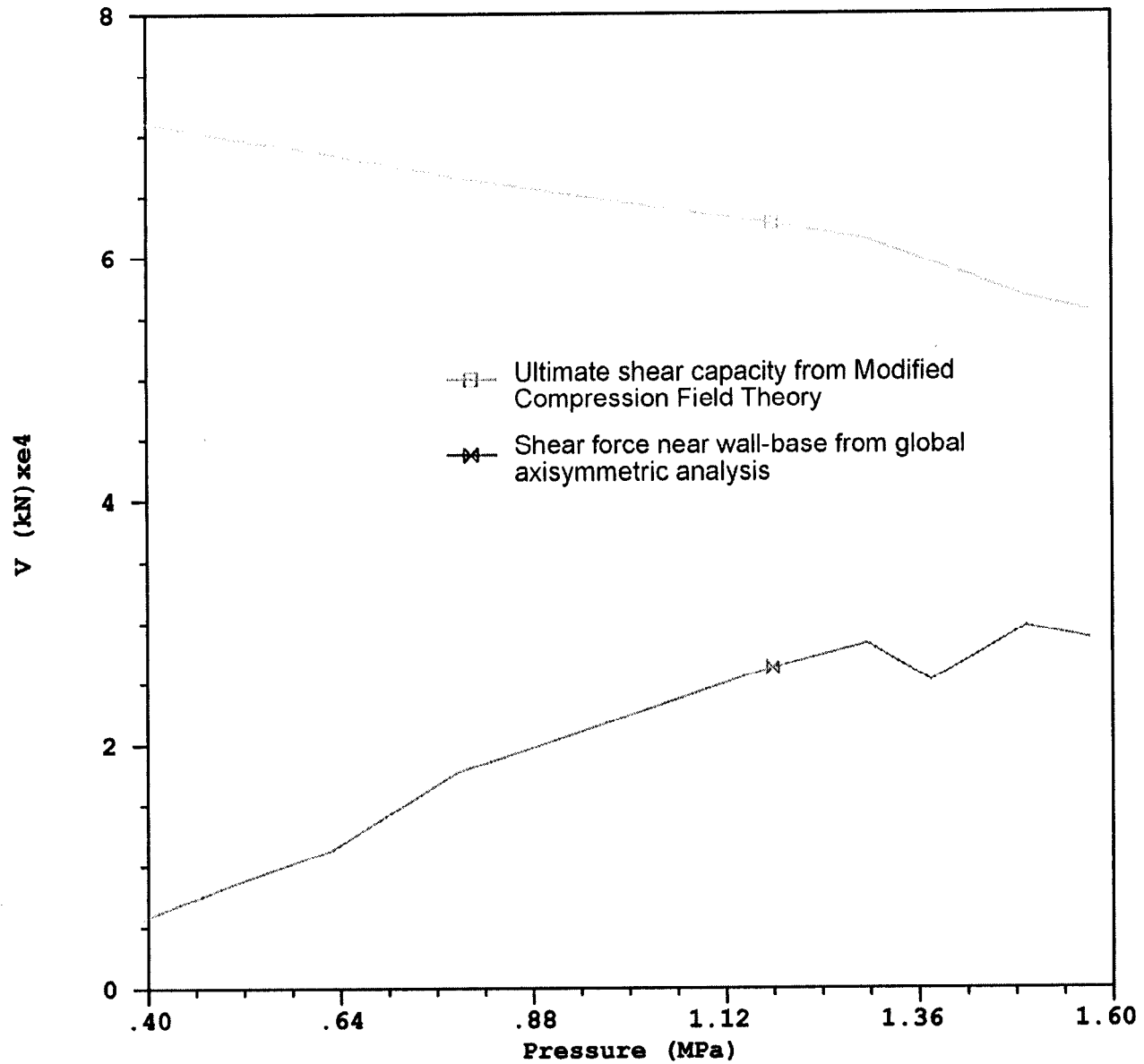


Figure 4-11. Comparison of PCCV Shear Strength from Modified Compression Field Theory to Shear Demand from the Global Analysis Model

## 5.0 3DCM MODEL ANALYSIS

### 5.1 Model Geometry

The three-dimensional cylinder midheight (3DCM) model is a 360 degree representation of a portion of the PCCV cylinder, that extends from Elev. 4.67m to Elev. 7.62m. For modeling convenience, the centerline elevations of the Equipment Hatch (E/H) and the Personnel Airlock (A/L) were assumed to be the same (this only required a few centimeters upward and downward adjustment of these centerlines from their true location). The E/H and A/L, therefore, were modeled in vertical half symmetry. The Mainsteam Group also was moved, though a little further (28 cm) so that it, too, could be represented in half symmetry. Both buttresses were modeled. The liner was explicitly modeled with shell elements, and liner anchors were modeled with beam elements. Rebar was modeled one-for-one with the rebar subelement modeling strategy described in earlier chapters. The liner grid density was not as fine as for the individual local models, so the 3DCM model was not used to predict "peak" local liner strains. The grid was considered fine enough to represent the stiffness and yielding behavior of the liner in order to predict reliable displacement versus pressure histories at the boundaries of local models.

The primary objectives of the 3DCM model were to provide:

- (1) a 3-D prediction of the radial displacement at the midheight of the cylinder;
- (2) prediction of complete tendon stress profiles for critical hoop tendons throughout the test pressure history;
- (3) accurate displacement and "far-field" strain versus pressure prediction for applying boundary conditions to and ranking the peak liner strains of local penetration studies.

The 3DCM model allowed correlation of the response of the local models to the pressure on the basis of the deformations experienced at the boundaries of the local models. The region represented by the 3DCM model is shown in Figure 5-1. The finite element model is shown in Figure 5-2. The model consists of 8-node brick elements, four through the wall thickness, 4-node shell elements for the liner, truss elements for tendons and friction ties, subelements for rebar, and 4-node shell elements for the hatch covers. The material properties used are the same as for the global axisymmetric analysis.

The prestressing tendons in the 3DCM model use the same friction modeling strategy as in the local penetration models and as in the dome of the axisymmetric analysis (Chapter 4). The tendon layout is illustrated in Figure 5-2. The hoop tendons are modeled "two-for-one" due to reduce grid size, but the meridional tendons are modeled "one-for-one". Chapter 4 covers the tendon friction modeling.

The reinforcement in the model is represented with ABAQUS subelements. These are generated in space using the ANAGEN program and plotted as shown, for example, in Figure 5-3. The actual rebar represented in the model is the rebar found by the model generator that intersects the concrete brick element boundaries. Thus rebar shown on Figures 5-3 that falls outside of the concrete boundaries does not become part of the finite element mesh. In addition to the bars shown, all through-thickness wall ties are included in all portions of the wall. The added stiffness provided by the "tendon sheath support frame" was also represented by adding rebar of area equivalent to the support frame at the locations of the support frame members. In the hoop direction the frame adds 3 hoops of area  $2.8 \text{ cm}^2$  each to the model, and in the meridional direction it adds 35 verticals of area  $4.61 \text{ cm}^2$  each to the model.

## 5.2 Boundary Conditions

For any partial model of a pressure vessel, application of the boundary conditions is difficult. The boundary condition assumptions applied to the 3DCM are shown in Figure 5-4. The philosophy used was to simulate the actual force conditions as closely as possible and apply the minimum of displacement constraints needed to prevent rigid body motion. The conditions applied are listed below.

- (1) Apply internal pressure on all interior surfaces (including hatch covers).
- (2) Apply vertical stress  $\sigma_z$  on the top "cut" surface.
- (3) Apply  $\theta_z = 0$  at the top surface (i.e. zero rotation about tangential axis.)
- (4) Constrain  $\Delta_z = 0$  at all nodes on the bottom surface.
- (5) At only 3 nodes, near the mid-height of the 3DCM model (Elev. 6.823 m) constrain  $\Delta_\theta$  (tangential displacement) = 0. Do not apply any radial constraints.

The  $\Delta_z = 0$  condition is a convenience that is needed to successfully execute the vertical prestressing step. This, of course, imposes  $\theta_\theta = 0$  around the bottom of the model.  $\theta_\theta = 0$  at the top and bottom is substantiated by behavior observed in the global axisymmetric analysis. At the top and bottom boundaries of the 3DCM model, the global analysis results show nearly zero slope. This is logical at the PCCV cylinder mid-height because of being equi-distant from the dome and the basemat. The top of the 3DCM model appears to also be a point of nearly zero slope before the wall deformation curves back inward toward the dome springline discontinuity. Though these zero-slope conditions are only approximate, they are numerically convenient and they help provide numerical stabilization of the edges of the 3DCM model. The displacements that are allowed to move freely are more important to the behavior prediction of interest, namely, radial displacement and, at the top boundary, vertical displacement. It should be noted that the top boundary is free to move vertically so the model will capture vertical extension or contraction variation with azimuth.

The horizontal displacement boundary conditions constrain only three degrees of freedom, the minimum possible to prevent rigid body motion of the model in the R- $\theta$  plane. The constraints are tangential only and the points are at the two buttresses and at the 180° azimuth. The buttresses are believed to provide tangential stiffness (beam action) so these points will probably have nearly zero tangential displacement in the actual structure. The 0° point also should move only radially due to the symmetry of this side of the wall centered around the M/S group. The 180° point, on the other hand, may move some tangentially, as the model deforms, due to the asymmetry of the E/H versus the P/A.

## 5.3 Tendon Prestressing

The methodology for prestressing is analogous to that described in Chapter 4 for the axisymmetric model meridional tendons. The target initial stresses, set by the designers, were shown in Figure 4-1. Also shown are comparisons to what these values would be estimated to be in a full scale prototype. The designers' primary goal in scaling the prestressing system was to match the overall level of prestress, but the figure shows some of the difficulties in scaling the effects of anchor set and other friction losses. The initial stresses applied to tendons were calculated with a similar procedure as described for the axisymmetric model. At hoop anchorages, the design stress after lock-off (xxx MPa) was applied uniformly. It should be noted, that because the model and tendons deform during prestress equilibration, the anchor stress application requires several trial iterations to achieve the desired anchor stress at all tendons at the end of the prestress loading step. The vertical tendon stresses were applied to the tendon element "tails" at the bottom of the model. The target stress for vertical tendons away from penetrations was the design stress (friction along straight tendon segments was ignored). The target stress for tendons with any path deviation caused by penetrations was reduced from the design stress by the angular friction

loss encountered between the base of the PCCV wall (Elev. 0) and the base of the 3DCM model. This theoretical loss along portions "outside" of the 3DCM model was calculated by hand.

#### 5.4 Tendon Anchor Set Loss Sensitivity Study

In the early stages of development of the 3DCM Model, the hoop tendon friction modeling was made uniform around the circumference of the cylinder. This leads to continuous angular friction losses extending from the buttress all around the circumference, but it ignores the anchor setting losses. After obtaining preliminary results without setting losses a modeling strategy was introduced to simulate the setting losses by reversing the orientation of the friction tie elements along the portion of the tendon path that friction theory would predict to be influenced by setting losses. This anchor set modeling strategy is illustrated in Figure 5-5. As illustrated later in this chapter, the introduction of these losses had a profound influence on the three-dimensional deformation behavior of the cylinder, particularly on the azimuthal distribution of radial displacement. To demonstrate why this might occur, the setting loss concepts are further illustrated in Figure 5-6. This figure shows that the zone of influence of setting losses is a full 45° from each tendon end. With 360° tendons jacked from both ends this is a total zone of influence of 180°, or half of the circumference! By comparison in Figure 4-1, this is about double the zone of influence that would be found in a full scale prototype, and the total amount of loss (in terms of stress) is more than 4 times that of the prototype! For the Scale Model this is due to the following:

- (1) Setting losses act over a certain length of tendon; since the 1:4 Scale PCCV tendons use similar jacking hardware to the full scale, the length over which setting losses act is similar, not scaled; in a 1:4 Scale model, this length covers a much larger azimuth.
- (2) Ancillary tests of the 1:4 Scale PCCV tendons demonstrate an angular friction coefficient of  $\mu=0.21$ , which is 30% to 50% larger than what commonly is found for full scale prototypes. This makes the total loss (in terms of stress) larger and exacerbates the influence of the setting losses on the model behavior.

Based on these observations and on the large influence observed from the first setting loss model, a parameter study was conducted to evaluate the sensitivity of the setting losses on behavior. The following cases with setting loss assumptions illustrated in Figure 5-6, were analyzed.

- Case 1: designer's calc for 1:4 Scale PCCV, 10° to tangency + 35°, total of 45° influence zone
- Case 2: prototypical setting loss, 10° to tangency +15°, total of 25° influence zone
- Case 3: small losses, 10° to tangency + 5°, total of 15° influence zone
- Case 4: No setting losses

It should be noted that the prestress loss calculations that correspond to the figure were shown in Figure 4-1. The results of the sensitivity study are best summarized by comparing the displacement patterns in the deformed shape plots of Figure 5-7. The plots support the following observations:

- At pressures higher than the tendon yield pressure, the cylinder response tends to be "bi-modal", because of the influence of the buttresses and/or the setting losses;
- The case with no losses and Case 3 show the largest displacements occurring at 0° and 180°, while Case 1 shows the largest displacements occurring at 90° and 270°;
- Case 2 shows the most uniform distribution of radial displacement;

- The "mode" of expansion of the cylinder has a major effect on the response and on the failure prediction.

These results were examined in great detail by ANATECH and Sandia and it was concluded that, given the large friction coefficient ( $\mu=0.21$ ), the setting loss assumption could produce the large variations in radial response demonstrated by the analysis. It was also observed, however, that the setting losses, usually expressed in length of slip (in mm), used by the designers was probably a conservative upper bound. The anchor slip assumed by the designers was 5mm. Most anchor slips measured in ancillary tests conducted by NUPEC were in the range of 3 to 3.5mm. It has also been noted from construction experience that slip can be further minimized during jacking by removing the jacking load slowly. In this fashion, it is believed that anchor slip could be reduced to as low as 1 to 2mm during construction. While NUPEC's official specification remains a not-to-exceed value of 5mm, since the anchor slip of Case 2 corresponds to the equivalent azimuth zone of influence of a full scale prototype, and since there is evidence that 2mm slip can be achieved in the model, it was decided to use Case 2 as the basis for the pretest prediction analysis. At a later date, perhaps just prior to pressure testing, an additional analysis may be run with an initial tendon stress distribution based on actual measurements after prestressing.

The stress contours in all of the tendons at the end of the prestressing step (for the "Case 2" assumption) are shown in Figure 5-8. After prestressing, pressure was applied to the model up to 3.8x the design pressure ( $3.8 P_d$ ). The deformed shapes at Prestress,  $2.0 P_d$ ,  $3.0 P_d$ , and  $3.5 P_d$  are shown in Figure 5-9. The radial displacements versus pressure are then shown in Figure 5-10. The most prominent observations of the displacement response are as follows:

- (1) At prestress, the  $0^\circ$  and  $180^\circ$  points move inward more than the buttresses;
- (2) By  $3.0 P_d$ , the  $0^\circ$  and  $180^\circ$  points deform outward much more than the buttresses;
- (3) The model deforms radially out more at 4.6752m (cylinder midheight) than at 8.9567m, which is the same trend as in the axisymmetric model;
- (4) The largest hoop expansion occurs at the Equipment Hatch, and the "free-field displacement" (displacement at  $0^\circ$  and  $180^\circ$ ) are slightly less and are approximately equal to each other;
- (5) At pressures greater than  $3.0 P_d$  the radial displacements at  $135^\circ$  (and elsewhere) become significantly larger in the 3DCM than in the axisymmetric analysis. Below  $3.0 P_d$ , the axisymmetric analysis agrees well with the  $135^\circ$  azimuth of the 3DCM.

The stress and strain in the hoop tendons of the 3DCM model is shown in Figure 5-11 for pressure =  $3.5 \times P_d$ . The plot shows how tendon yielding starts first at the lower most tendons near the equipment hatch. By  $3.5 P_d$ , strains exceed 5%, which causes a tendon rupture. In the actual test, propagation of a rupture might occur very quickly along the tendon's entire length; in the finite element analysis, however, convergence difficulties caused a much slower progression of the rupture.

Other response measures and indicators of damage are strain contours shown in deformed shape perspective views in Figure 5-12. These plots show the elevated strains associated with the following:

- (1) Local circumferential bending adjacent to each buttress;
- (2) Strain concentrations at terminations or step-downs in rebar patterns;
- (3) Strain concentrations near hatches or near the edges of wall embossments.

One of the key objectives of the 3DCM model was to predict the stress and strain behavior in cylinder hoop tendons. Three of the most critical tendons are instrumented: # H35, H53, and H68. Figure 5-13

shows the predicted stresses all along one of these tendons at 6 pressure milestones. This plot shows the effectiveness of the friction modeling strategy, the effects of reaching yield over a small portion of the tendon and the occurrence of a rupture. Tendon stress and force histories at specific standard output locations are not shown, but are included in Sandia's standard output location plots.

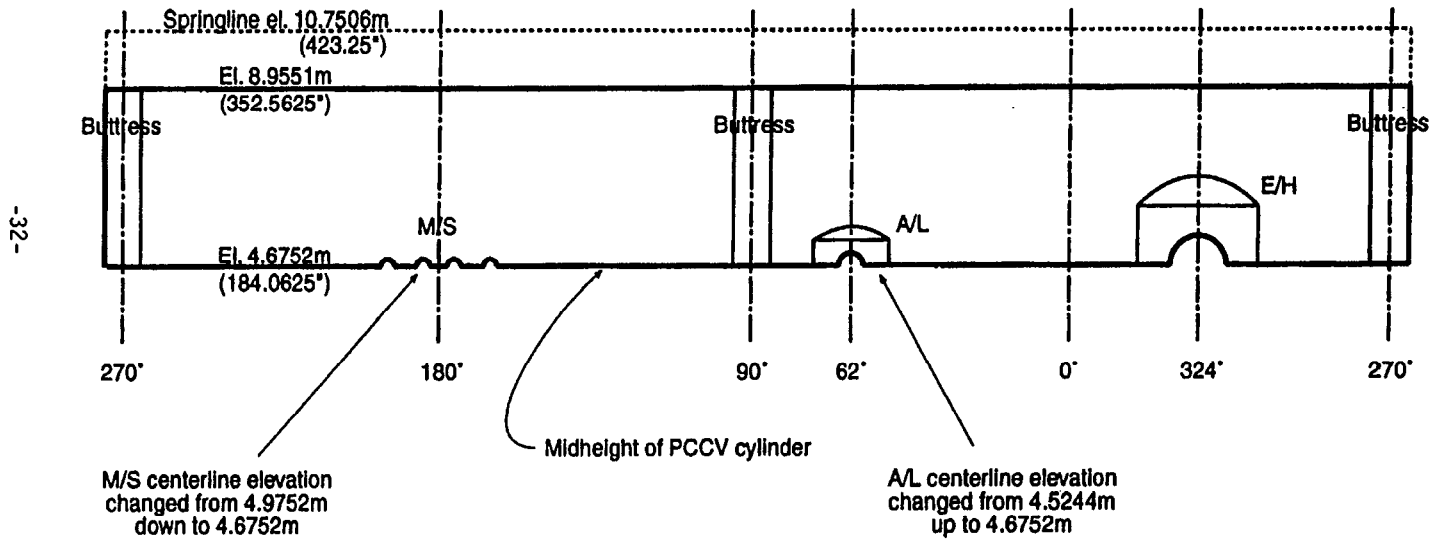


Figure 5-1. Inside "Stretchout" View of Portion of PCCV Modeled in 3DCM Model

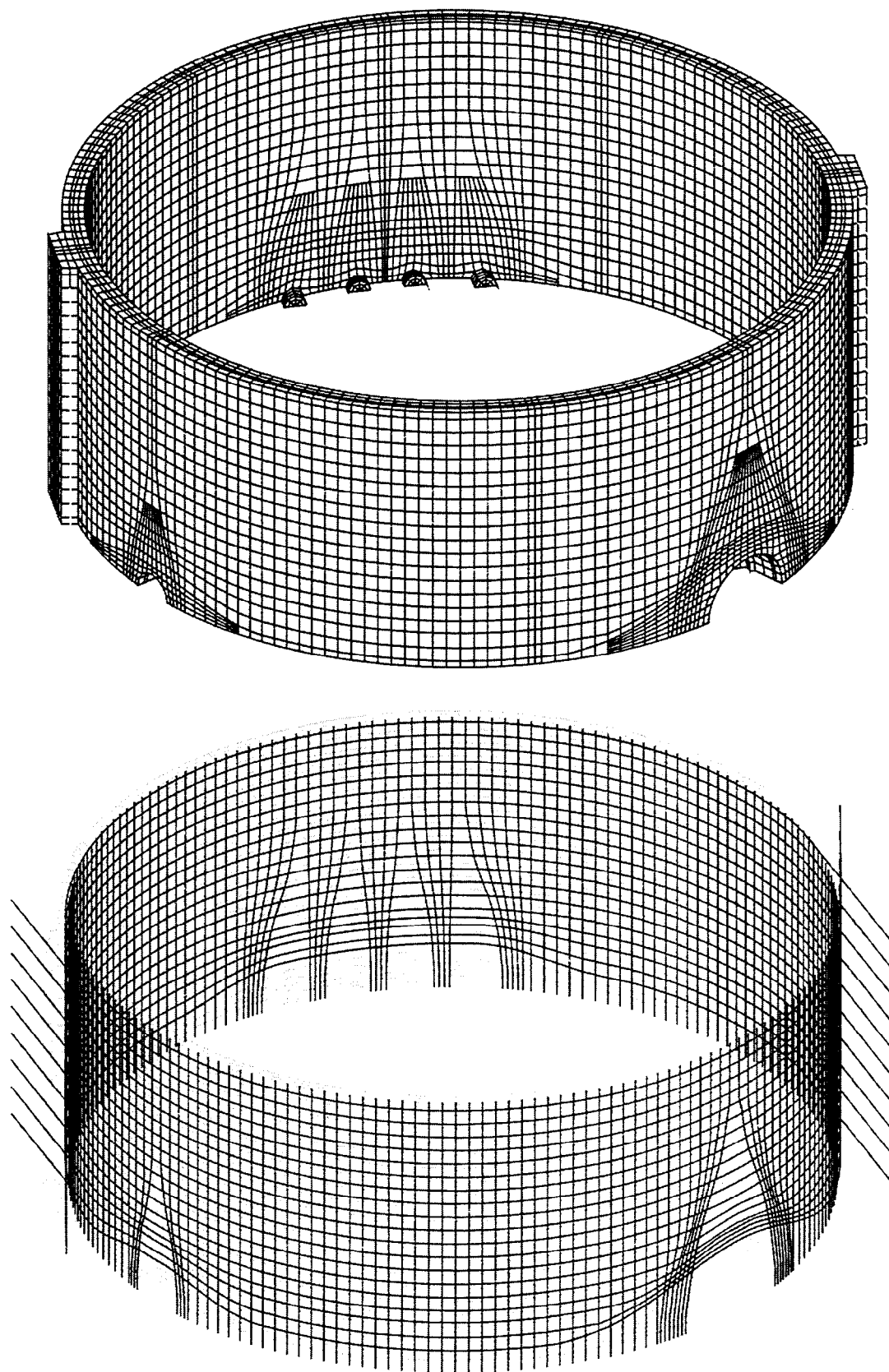
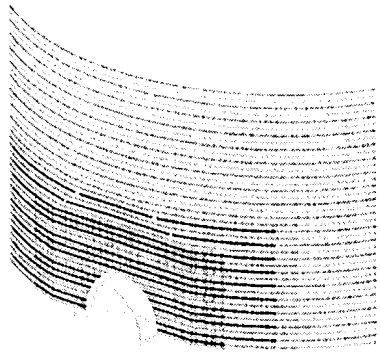
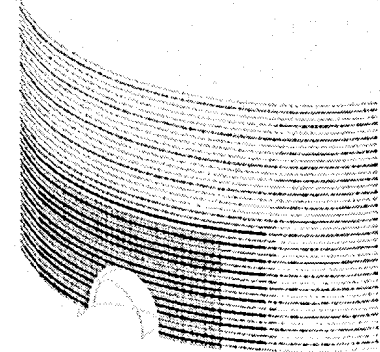


Figure 5-2. Isometric View of 3DCM Model and Tendon Modeling

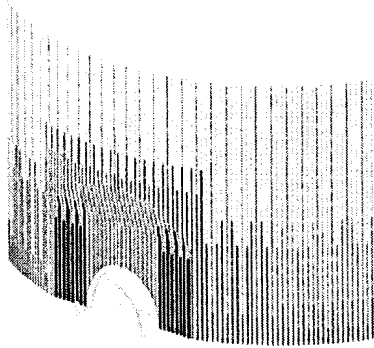


Inner Hoop Rebar

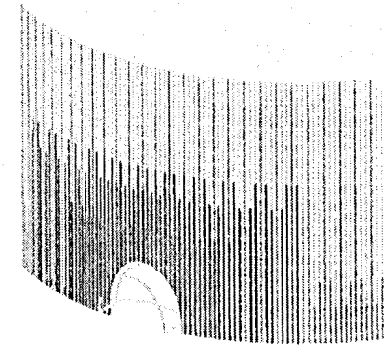


Outer Hoop Rebar

STRUCTURE	
	D10
	D13
	D16
	D19



Inner Vertical Rebar



Outer Vertical Rebar

Figure 5-3. 3DCM Rebar for 270° - 360° (E/H)

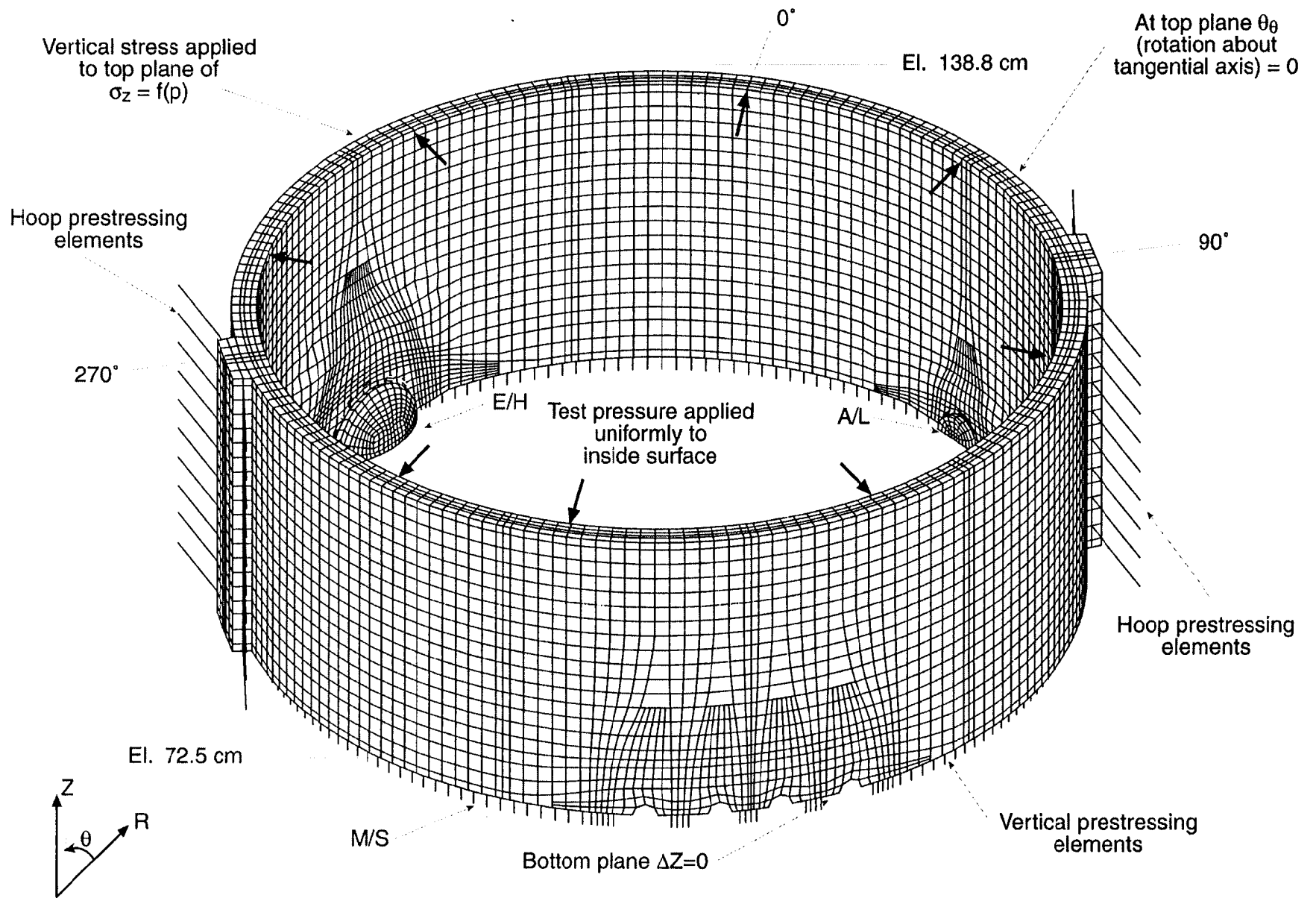
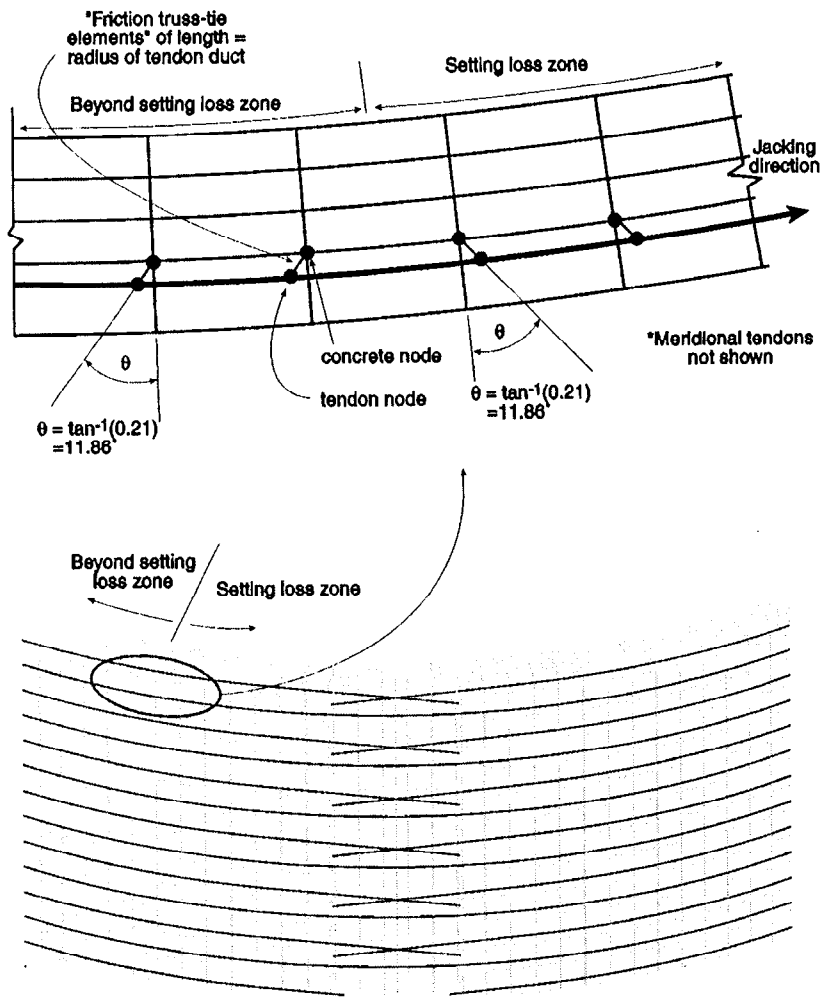


Figure 5-4. 3DCM Model Vertical Boundary Conditions



R-44

Figure 5-5. Changes to Tendon Friction Modeling to Include Setting Losses

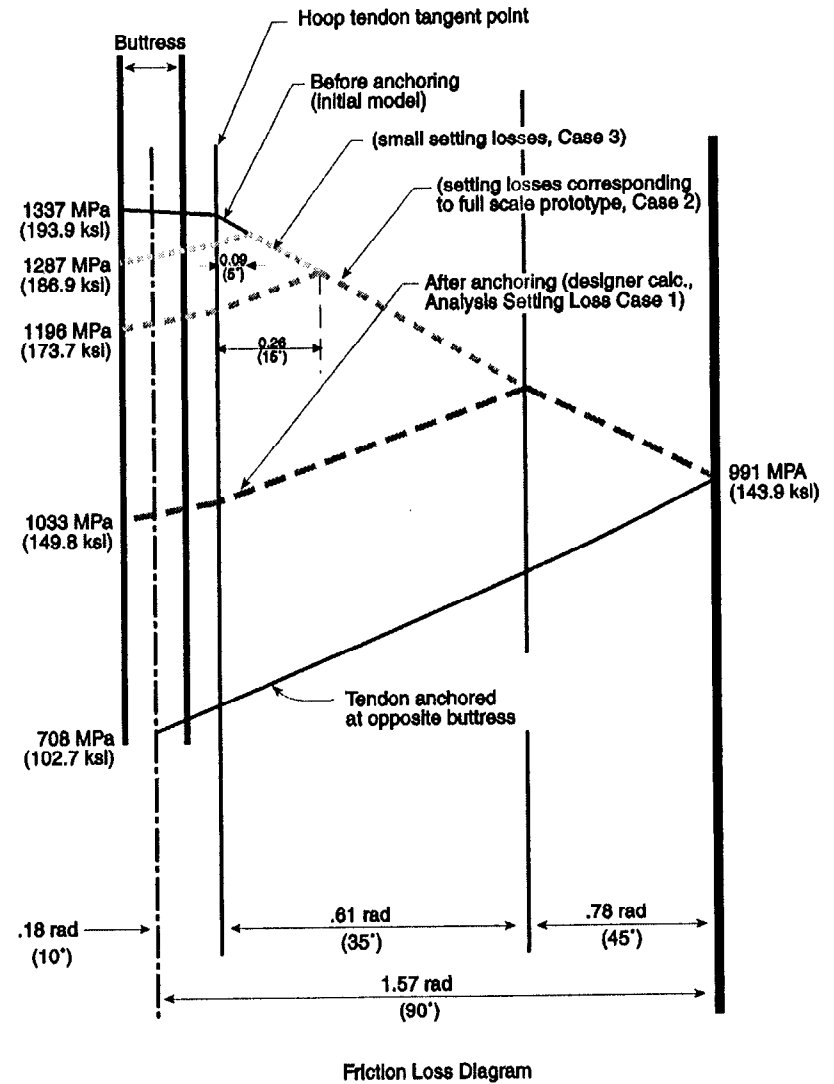


Figure 5-6. Other Setting Loss Cases for Parameter Study

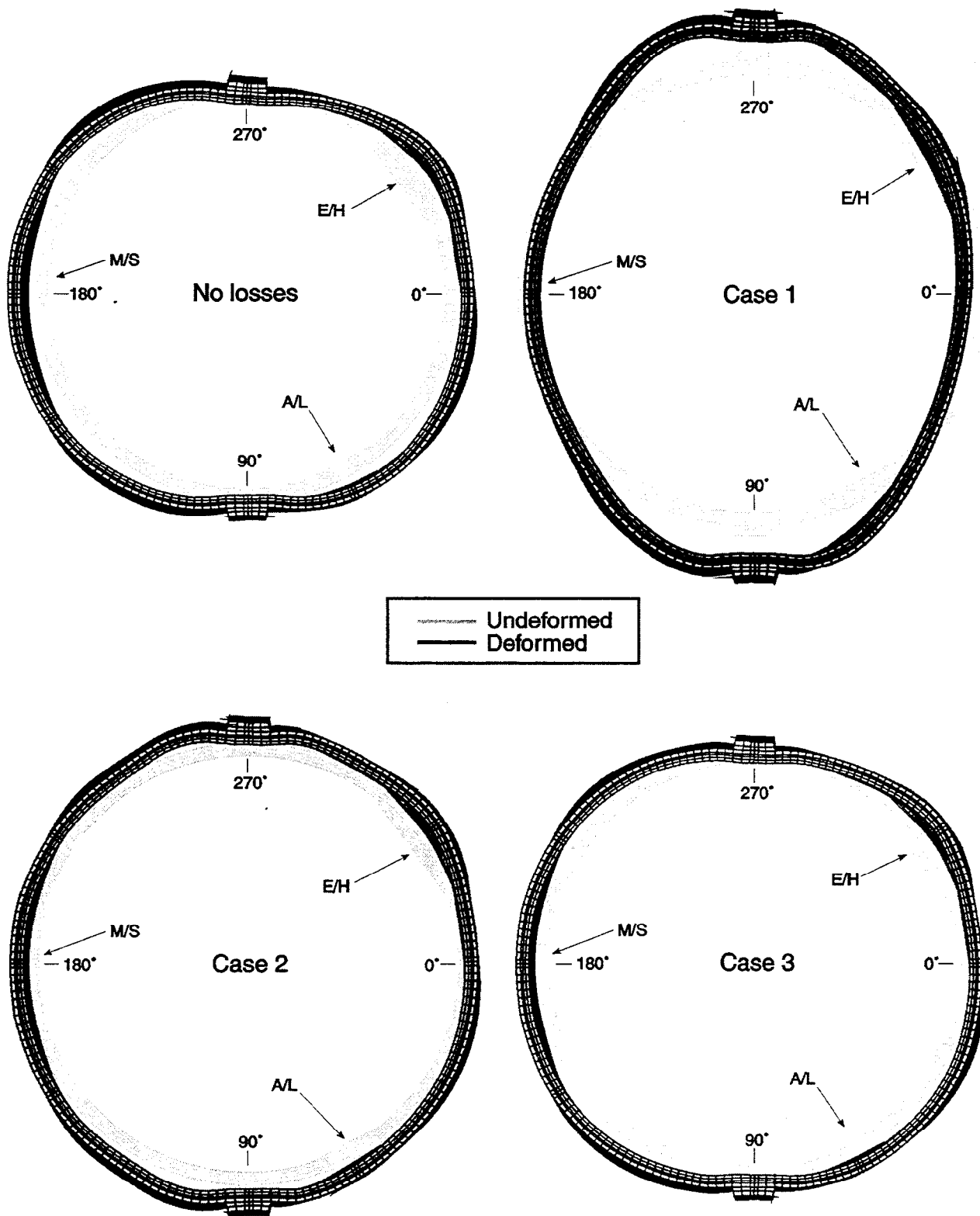
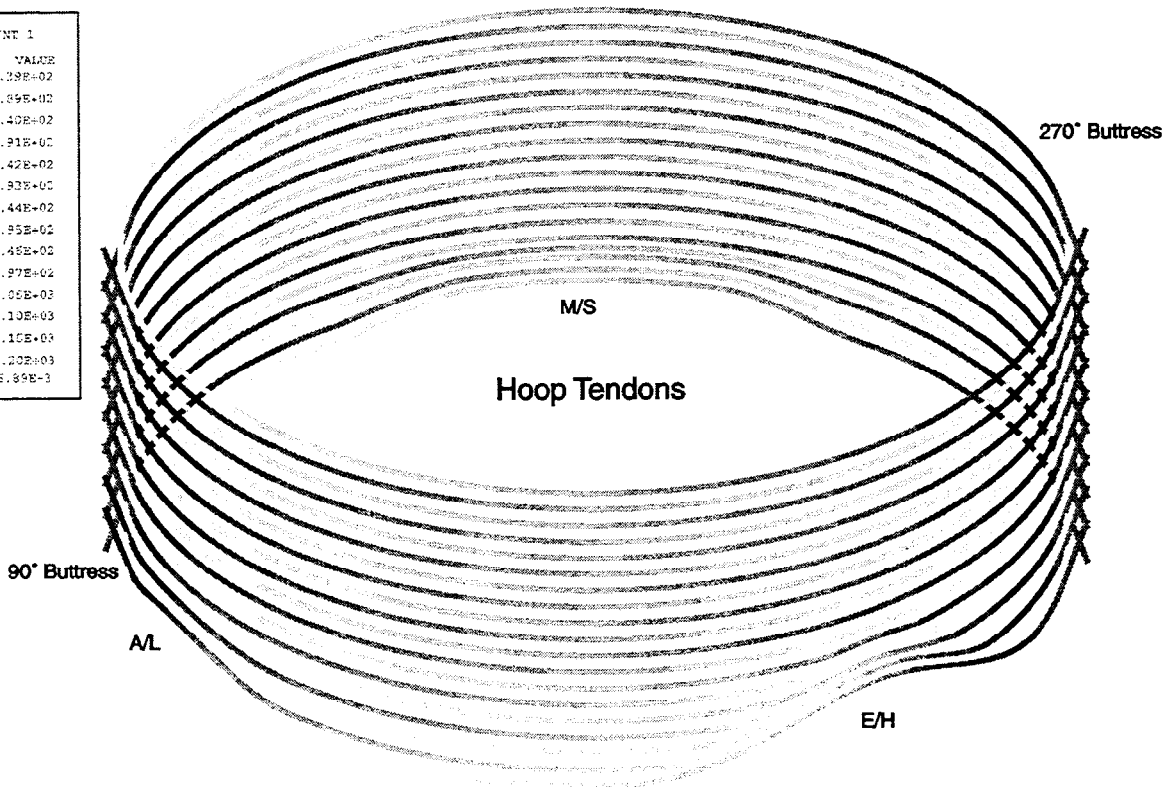
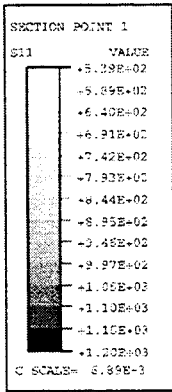
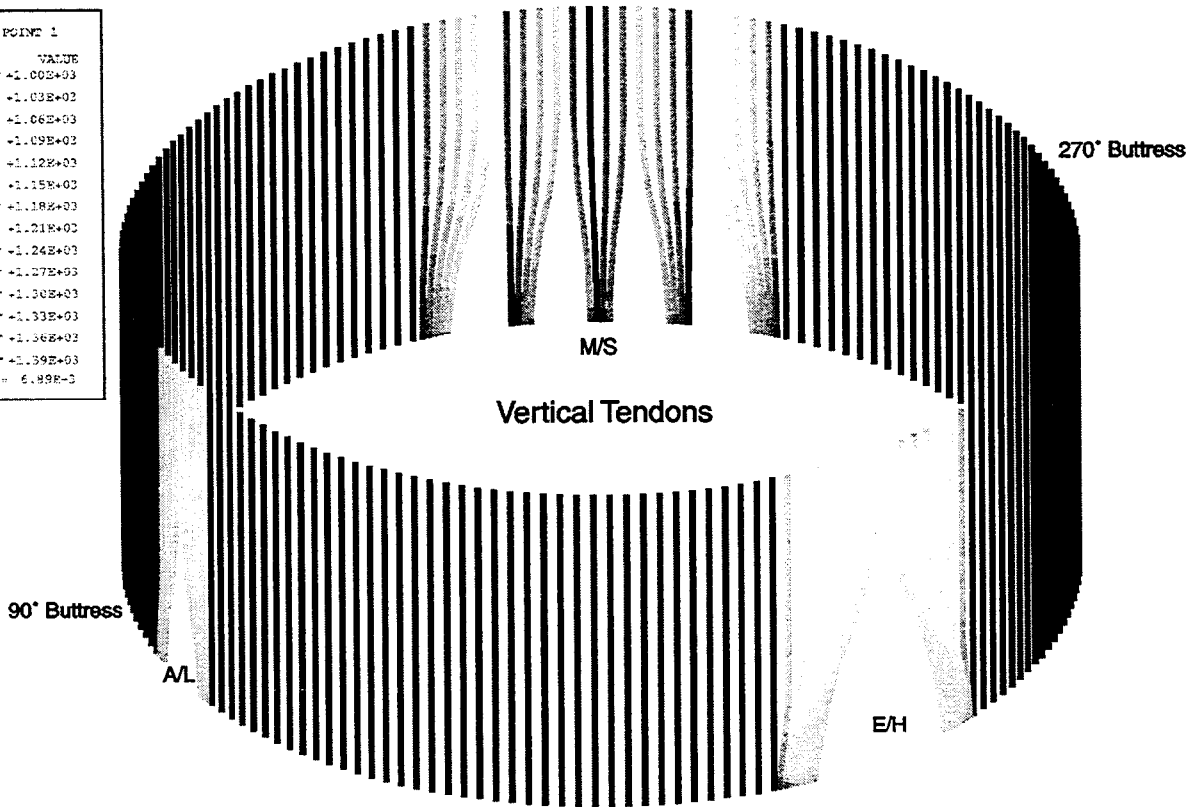
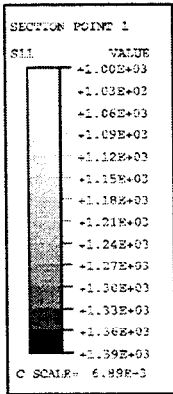
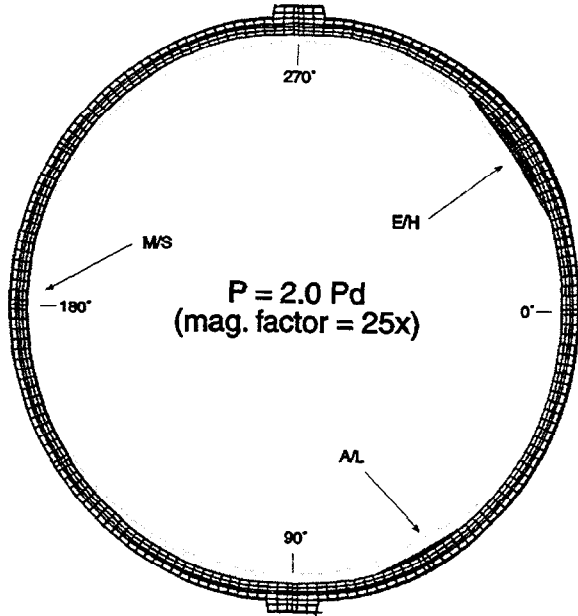
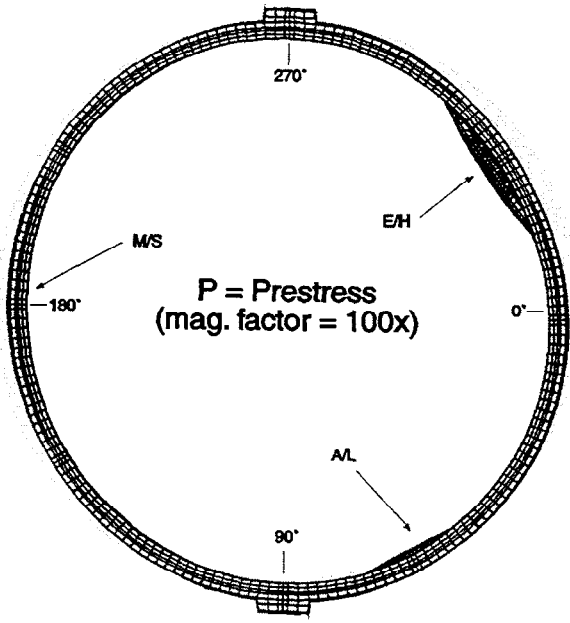


Figure 5-7. 3DCM Model Deformed Shape at Pressure = 3.5 Pd (mag. factor = 10x)  
 3dcm00.inp, 3dcm15.inp, 3dcm25.inp, 3dcm45.inp



3dcm.inp

Figure 5-8. Stress Contours in Tendons after Prestress



Undeformed  
— Deformed

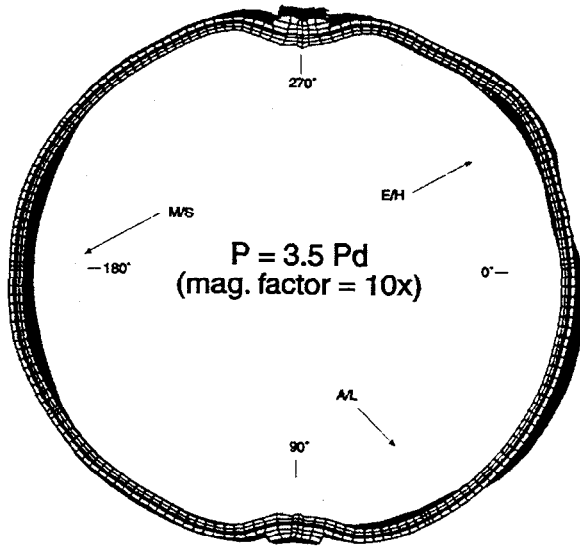
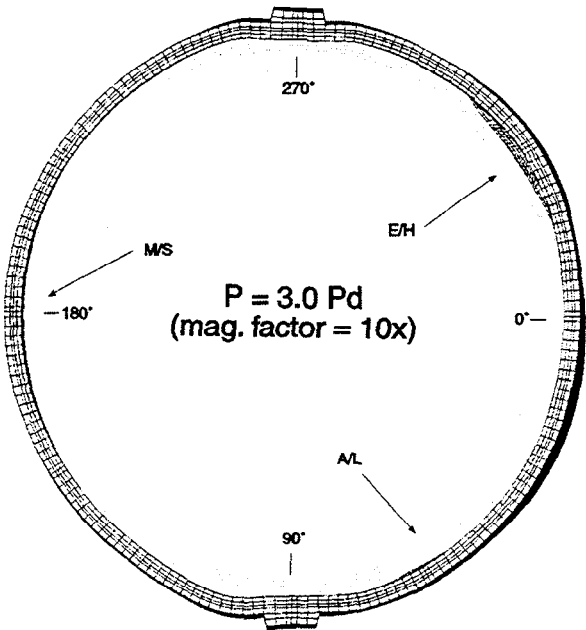
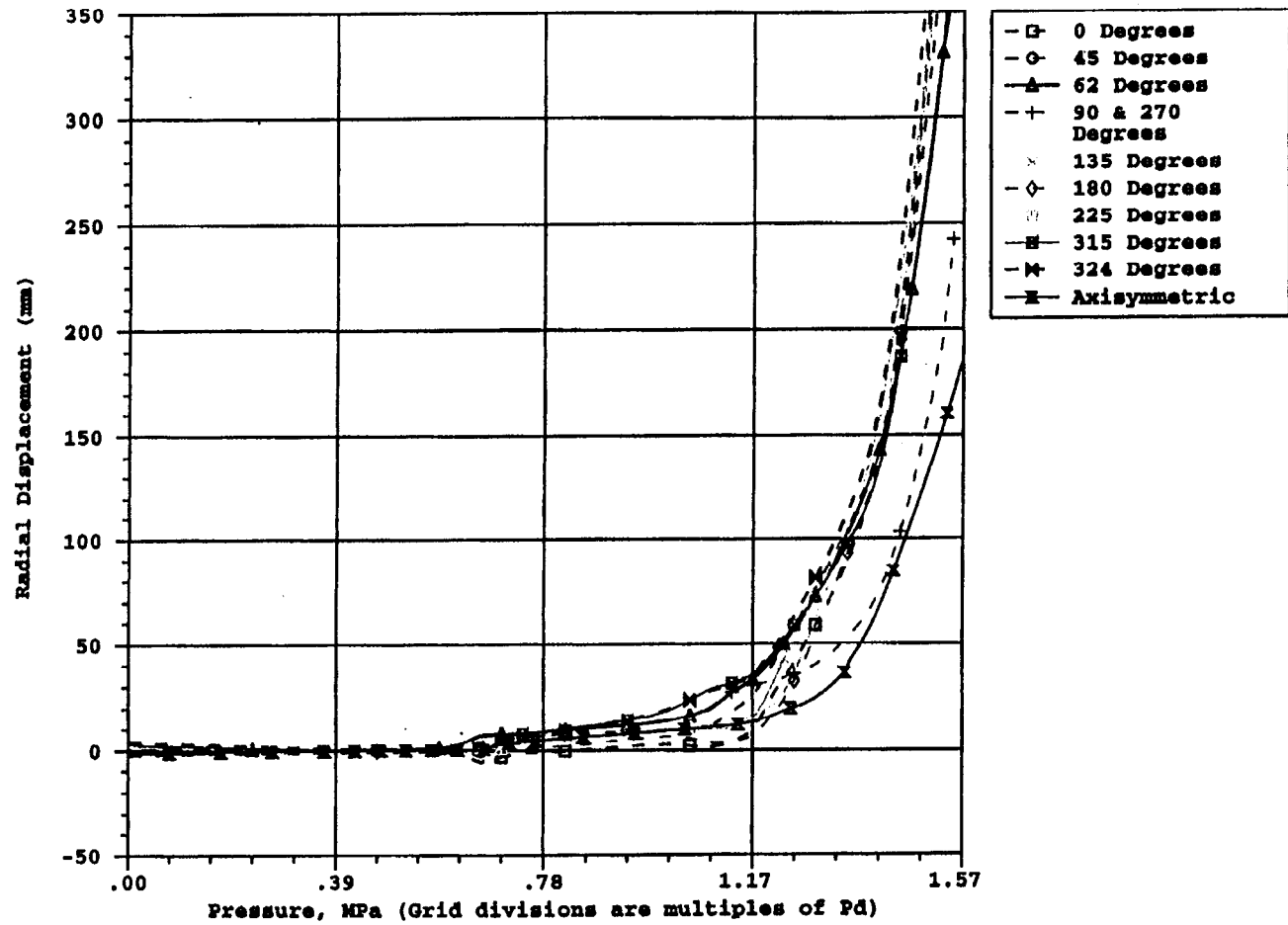


Figure 5-9. 3DCM Deformed Shapes at Various Pressures



3dcm.inp

Figure 5-10. 3DCM and Axisymmetric Radial Displacement Comparison vs. Pressure at Elevation 4.6752

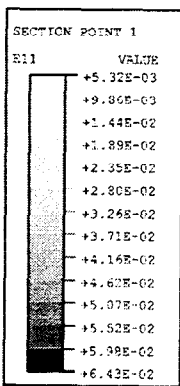
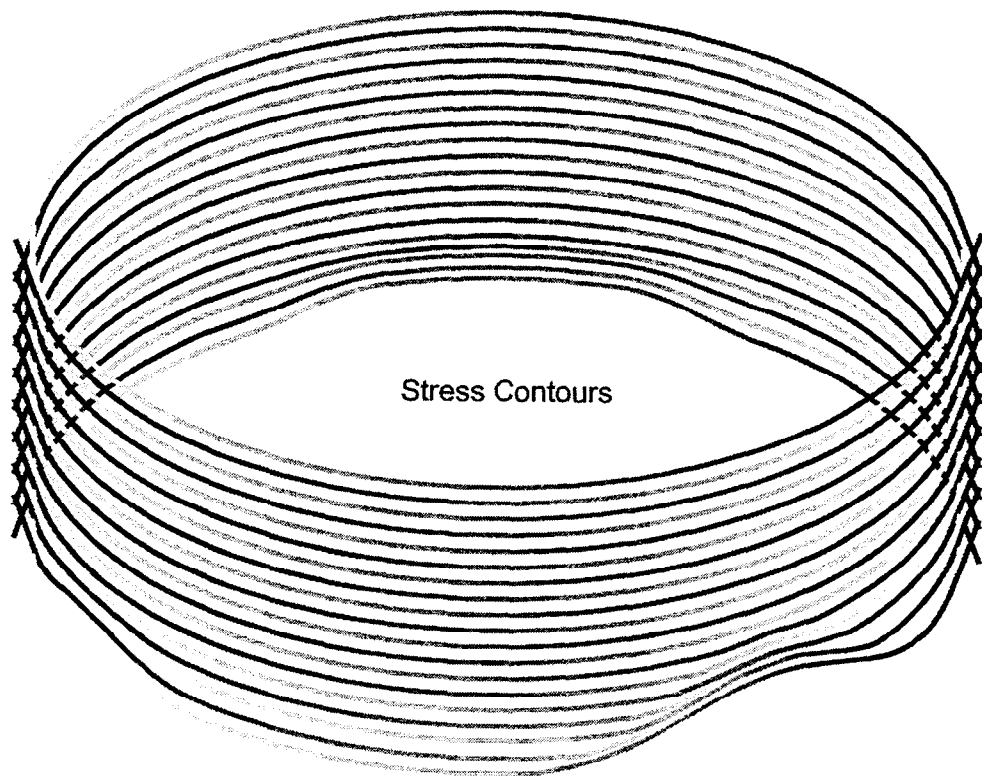
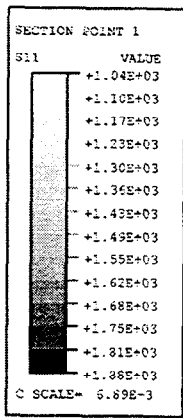


Figure 5-11. Stress and Strain Contour Plots of Hoop Tendons at P = 3.5 Pd

3dcm.inp

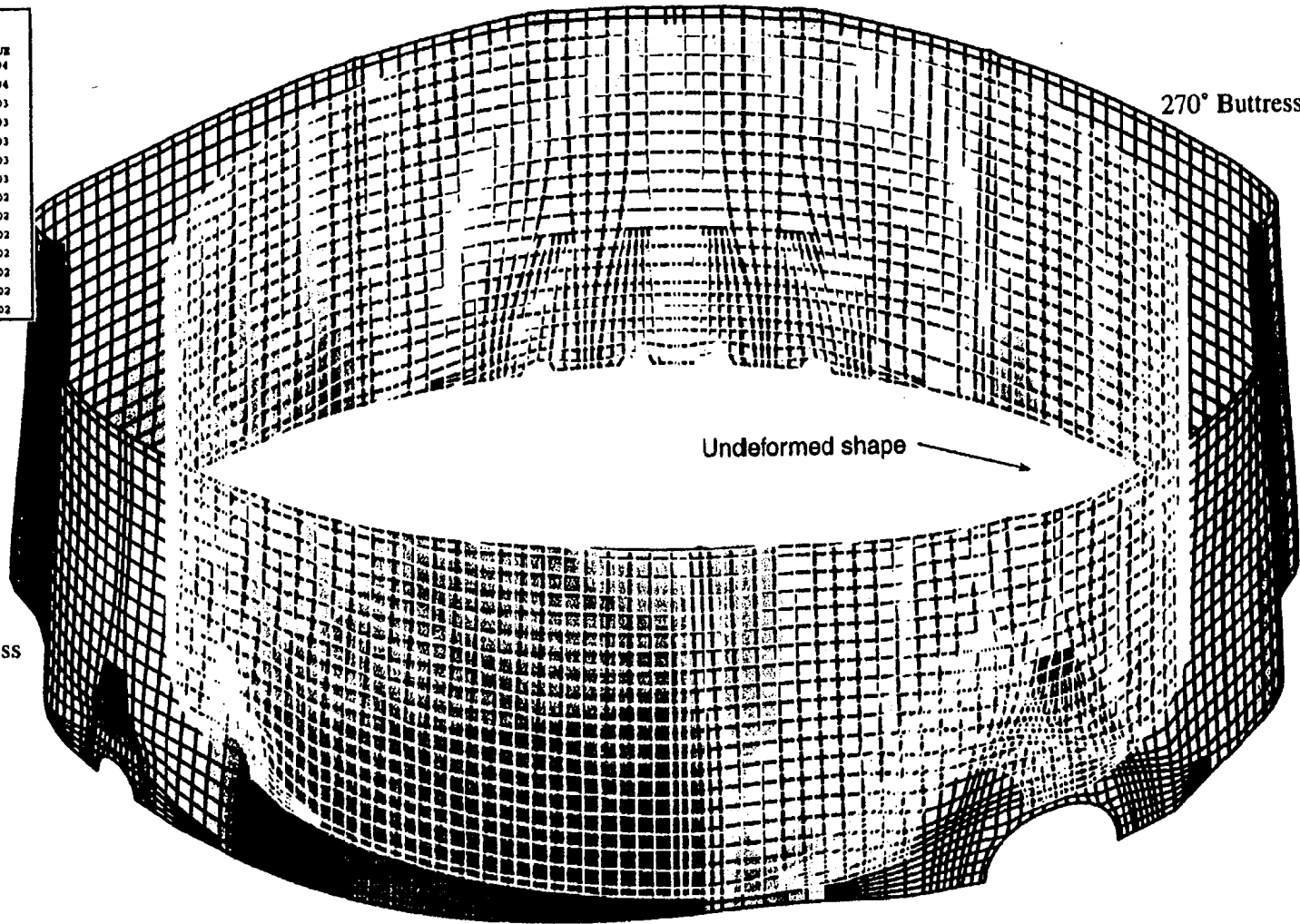
SECTION POINT 1	
E11	VALUE
	-6.37E-04
	+9.51E-04
	+2.54E-03
	+4.12E-03
	+5.71E-03
	+7.30E-03
	+8.89E-03
	+1.05E-02
	+1.21E-02
	+1.36E-02
	+1.52E-02
	+1.68E-02
	+1.84E-02
	+2.00E-02

-42-

R-50

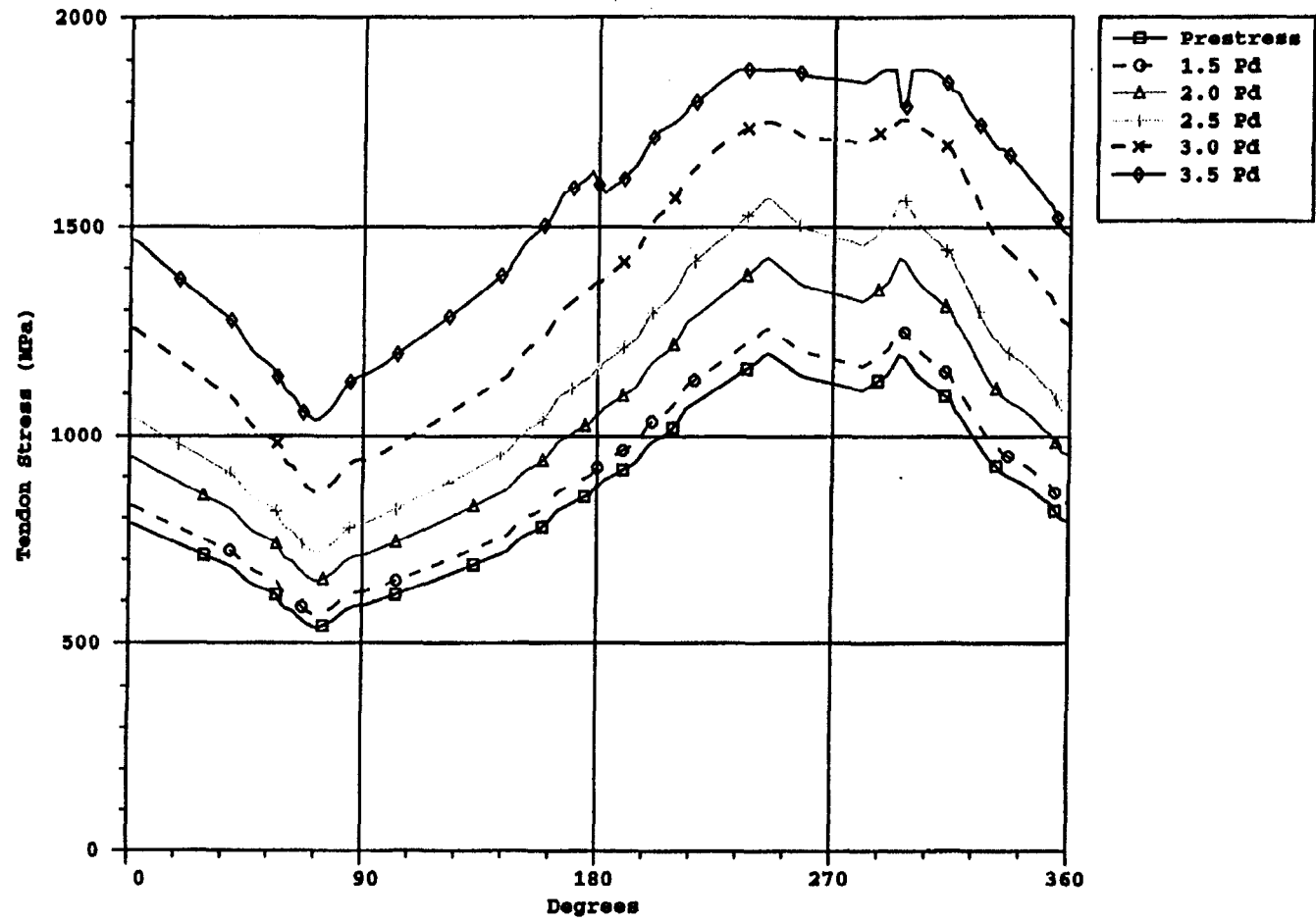
90° Buttruss

270° Buttruss



3dcm.inp

Figure 5-12. 3DCM Liner Hoop Strains at 3.0 Pd (Magnification factor = 35x)



3dcm.inp

Figure 5-13. Tendon Stress Profile for Instrumented Hoop Tendon #H35

## 6.0 LOCAL PENETRATION MODEL ANALYSIS

### 6.1 Characterization of Liner Anchor Behavior

Several 3D models were generated to analyze the penetration areas, including the Equipment Hatch, Personnel Airlock, and Main Steam regions. A detail common to each model is the interaction between the T-anchors and the surrounding concrete. The T-anchors and concrete move together in the radial direction during pressurization but the liner can "slide" along the liner concrete interaction surfaces in the tangential direction. This relative sliding is resisted by the T-anchors. Nonlinear behavior occurs in the vicinity of the anchors as the concrete is crushed and the liner and the T-anchors are strained plastically. A detailed model of a single Liner Anchor was used to analyze this relationship and its results were used to generate the nonlinear force-deflection characteristics for use in the 3D penetration models. The liner anchor behavior simulation was also calibrated to liner anchor pull tests conducted by NUPEC.

Modeling dimensions and boundary conditions of the Liner Anchor Model can be seen in Figure 6-1. Radial model length was determined from half of the wall thickness. Tangential distance was determined from mid-distance between T-anchors near penetrations (which were scaled one-for-one from the full scale prototype). The models were loaded as follows. The liner was strained tangentially according to the time history results from the axisymmetric analysis and in accordance with liner pressurization. Contact surfaces were applied at all interaction surfaces between the liner/anchor and concrete. A sensitivity study was done on the friction coefficient used on these surfaces using coefficients of  $\mu=0.2$  and  $\mu=0.5$ . The liner end opposite where displacement was applied was fixed from in-plane rotation. A sensitivity study was also done on this boundary condition between allowing this end to displace tangentially versus a fixed condition.

Figure 6-2 shows the radial and hoop strains in the liner and anchor at a liner hoop strain that is representative of global hoop strains in the cylinder near  $3.5 P_d$ . Strains reach 0.027 and -0.026. Figure 6-3 compares these test cases to a liner anchor pull test performed by NUPEC. The analytical model results show a somewhat larger force than the NUPEC test results, but the general force-deflection behavior is similar. The detailed analytical model of the anchors was, therefore, judged to provide reasonable simulation of the interaction phenomena.

All of the local models use a simplified method of modeling the anchors to simulate the behavior exhibited by the more detailed analysis (the Liner Anchor Model). Figure 6-4 shows the geometry of the anchor used in the local models. The anchor depth was reduced to 12 mm, and the "root" of this 12 mm high web is the point of fixity. An iterative process of modifying the thickness and shear stiffness of the anchors was used in order to match the results of the more detailed analysis. The results from the  $\mu = 0.2$  and "fixed" case were used as the most appropriate since their stiffness and ultimate capacity most closely matched NUPEC's test data. The thickness of the anchor web is 1.6 mm, whereas in the idealized representation in the local models of the penetrations, 6.6 mm was used. This method allowed close simulation of the T-anchor behavior using just the bending behavior of a shell element and not modeling the anchor/concrete interaction explicitly. Figure 6-5 shows the correlation between the one element simulation and the detailed Liner Anchor Model.

The hoop stiffeners were modeled with a similar technique in the local E/H and P/A models. It was determined that there were no regions of critical hoop stiffeners in the MS model so none were included. It is required that the depth of the anchor and the stiffener are equal for modeling purposes. The thickness to achieve the actual area for the stiffeners in the local models was calibrated to be 8.4mm as opposed to the actual 3.2mm.

## 6.2 Equipment Hatch Analysis

The 3D concrete and liner model of the Equipment Hatch region (E/H) is illustrated in Figures 6-6 through 6-8. The grid was developed by generating a concrete mesh based on the tendon layout and then joining the embedded edges of the T-anchor webs to the concrete mesh with the \*SURFACE attachment command in ABAQUS. The upper quadrant around the hatch was selected for modeling in order to have a local model completely encompassed by the 3DCM Model. Five layers of concrete elements through the wall thickness were used, and the liner was modeled with shell elements so that the liner bending and membrane behavior could be studied. Rebar in the concrete wall was modeled with ABAQUS rebar subelements, but tendons were modeled explicitly with truss elements and friction truss-tie elements as previously described for other models.

The loading and boundary conditions applied to the 3D E/H Model are shown in Figure 6-7. Only the stems of the anchors were modeled. The stem of the anchor elements to which the displacements were applied displace as if they are firmly embedded in the concrete. The shear force-deflection behavior of the stem in the hoop direction then distributes the deformations to the liner in a manner consistent with the liner anchor strength and deflection. Pressure was also applied to the inner liner surface. The displacement and pressure conditions were ramped up to those corresponding to 1.57 MPa, 228 psig (4 P<sub>d</sub>).

One of the most complex aspects of the 3D E/H model is the tendon modeling. As previously mentioned, significant effort was exercised in the tendon representation in order to:

- (1) Calculate the tendon stress distribution throughout the pressurization sequence including the effects of friction;
- (2) Calculate the displacements of the concrete wall correctly, since this drives the liner, and thereby refine the prediction of liner strain concentrations.

Each meridional tendon was modeled with a truss element and with friction truss-ties to adjacent concrete nodes as was described for the axisymmetric model dome (Chapter 4) and the 3DCM model (Chapter 5). The tie elements (also truss elements) have length equal to the half-diameter of the tendon ducts. When the tendon is curved, the truss ties are oriented at an angle of  $\tan^{-1}(0.21)$ . By assigning this system of tendon elements small displacement theory, the friction truss-ties always transmit the exact amount of theoretical angular friction force from the tendon to the concrete. When the tendon segment being tied is straight, the tie element is oriented perpendicular to the tendon (no friction). Thus, within the E/H model, wobble friction along straight runs of tendon is not considered. Wobble friction is considered, however, in the calculated estimates of tendon stresses at the boundaries of the models. These estimates of tendon stress at the boundaries are identified in Figure 6-8. The friction losses for segments of tendons outside the boundaries of the model were based on the formula

$$f_t = f_j e^{-(\mu_\alpha + k_s)}, \text{ where}$$

$f_t$  = tendon stress reduced due to friction

$f_j$  = tendon stress at the jack after setting losses

$$\mu = 0.21$$

$$k = 1.67 \text{ E-5 in}^{-1} \text{ (or } 6.575 \text{ E-6 cm}^{-1}\text{)}$$

The generation of the friction tie mesh required development of a special pre-processor. First each tendon was located in space by location of the design points of tangency from the PCCV drawings. (Generally there are 3 points that define the path of a tendon sweeping around the penetration.) Then the program used a least squares fit to compute the equation of each tendon path.

Next, the program located mathematical points of intersection of each of the tendon equations and placed a finite element node at each point. As shown, the vertical tendons were modeled individually (one-for-one), but for purposes of reducing the size of the preliminary analysis, the hoop tendons were modeled 2-for-1. Since the hoop tendons are laid out in pairs, this approximation is believed to result in negligible loss of accuracy. The program then located a friction tie node adjacent to each tendon node according to the following mathematical constraints.

- i. tie node lies in plane defined by tendon node<sub>i-1</sub>, node<sub>i</sub>, and node<sub>i+1</sub>;
- ii. vector from tendon node<sub>i</sub> to tie node has length equal to the radius of the duct;
- iii. vector from tendon node<sub>i</sub> to tie node makes angle of  $\tan^{-1}(0.21)$  with the chord subtended through node<sub>i-1</sub> and node<sub>i+1</sub>.

The remainder of the concrete nodes were then generated "around the tendon nodes" with ANAGEN, a mesh generator that serves as a pre-processor to ABAQUS.

The displacement results of the 3DCM model were used to drive the local E/H model with an algorithm whereby the local E/H model was subjected to the same average hoop strain history across the local model as was exhibited in the 3DCM. This provides the pressure versus "boundary condition" correlation. This average hoop strain in the 3DCM was computed as follows:

$$\varepsilon_{\theta_{\text{avg}}} = \frac{\Delta R_{270} + \Delta R_{324}}{2R} + \frac{\Delta \theta_{324}}{\frac{54^\circ}{180^\circ} \times \pi R}$$

The same average hoop strain versus pressure was then assumed for the local E/H model.

Deformation and strain results of the 3D analysis of the E/H are shown in Figures 6-9 through 6-12. The deformed shape plot (Figure 6-9) shows that the wall in the E/H region moves out fairly uniformly, except that the displacement at the hatch is less than at the buttress. This result contradicts the 3DCM model results, but in the authors judgment the overall displacement behavior of the 3DCM governs over that of the local model because of the limitations on the boundary conditions applied to the local E/H model.

The tendon stress and strain distributions in Figures 6-10 and 6-11 show the friction losses in the vicinity of the hatch and the build-up of tendon stresses and strains at high pressure.

The liner strain contours in Figure 6-12 show severely elevated strains near the ends of the vertical T-anchor and the hoop stiffener which terminate near the 3 o'clock position of the edge of the liner insert plate. Strains near the vertical stiffener reach 17% at 3.25 P<sub>d</sub>. This, as described in Chapter 7, was found to be the most likely liner failure location and failure pressure.

### 6.3 Personnel Airlock Analysis

The Personnel Airlock (A/L) is the second largest penetration in the PCCV model and it is located at the 62° azimuth, at Elevation 4.525 m. As with the Equipment Hatch, there are liner connection and anchorage details near the A/L that cause large strain concentrations; this makes the region near the A/L a candidate for a liner tearing failure mode.

As with the E/H, there are two specific kinds of large strain concentration locations associated with the A/L, namely, the zone near the end of a vertical T-anchor (at about the 2 o'clock position, using a clock face analogy to represent the penetration) and at the end of a horizontal stiffener, near the 3 o'clock position. Both of these details and the tendon and rebar geometries are similar to the Equipment Hatch, so much of the modeling discussion of the previous subsection is also relevant to the A/L. The A/L 3D local model is illustrated in Figure 6-13. The upper quadrant was modeled so that the model would be encompassed by the 3DCM and thereby have appropriate boundary conditions at all edges; and because the hoop stiffeners only occur in the upper quadrant.

Because the A/L is close to a buttress, the local model was extended over to the buttress centerline. This allows study of the local strain concentrations near the buttress in addition to those near the hatch. The modeling details for the local A/L model are similar to those developed for the Equipment Hatch model. The grid of the liner, anchors, and stiffeners, is shown in Figure 6-14. The liner-anchor interaction (shear force deflection behavior of the anchors) is modeled identically to the E/H, as is the method of attaching the liner/anchor mesh to the concrete mesh.

The hoop tendons are modeled 2 for 1 just as in the 3DCM and in the E/H local model and the meridional tendons are modeled one for one. The rebar generated for the local P/A model is identical to the 3DCM, so the reader is referred to Chapter 5 for this information.

A similar hoop strain versus pressure, boundary condition correlation was used for the A/L local model as was used for the E/H. Here the average hoop strain obtained from the 3DCM was the hoop strain at Elevation 4.525 m, occurring along the 28 degree arc between the A/L Centerline at 62 degrees and the 90-degree buttress. This provides the pressure correlation for all of the local A/L analysis results.

The 3D local model analysis results for the A/L are shown in Figures 6-15 through 6-17. Figure 6-15 shows deformed shape results, which show that the A/L deforms radially outward about the same amount as the buttress. (The A/L moves out more than the buttress in the 3DCM model analysis, and this deformation profile is deemed to be the more accurate prediction.)

Figure 6-16 shows tendon stress and strain contours at 3.75  $P_d$  pressure. Figure 6-17 shows liner strain and stress contours at 3.75  $P_d$  pressure, which shows that the most elevated liner strain concentration ("hot spot") is predicted to occur adjacent to the hoop stiffener and vertical T-anchor termination points (as in the E/H analysis).

### 6.4 Mainsteam Penetration Group Analysis

The Main Stream Penetration (M/S) is the third largest penetration in the PCCV. It consists of a group of four penetrations located at the 180° azimuth. As with the Equipment Hatch, there are liner connection and anchorage details near the M/S that cause strain concentrations; this makes the region near the M/S another candidate for a liner tearing failure mode.

There is only one specific kind of large strain concentration at the M/S location similar to that associated with the A/L and E/H, namely, the zone near the end of a vertical T-anchor (at about the 1:30 o'clock

position, using a clock-face analogy to represent the penetration). There are no terminations of hoop stiffeners on the 1.6 mm liner plate in this region, so this strain concentration does not exist for the M/S. Much of the modeling discussion in this chapter refers to the more detailed description of the similar modeling described earlier in this chapter for the E/H and the A/L.

The M/S 3D local model is illustrated in Figures 6-13 and 6-19. The choice of extent and modeling strategy for the local M/S model are itemized below.

- (1) Upper quadrant so the model would be encompassed by the 3DCM and thereby have appropriate boundary conditions at all edges;
- (2) Also upper quadrant because the critical liner anchor terminations only occurs in the upper quadrant; and
- (3) No tendons pass through this section so none were modeled, yet the edges of the model are still sufficiently far away to capture to strain concentration.

The modeling details for the local M/S model are similar to those developed for the Equipment Hatch model. The grid of the liner and anchors, is shown in Figure 6-19. The liner-anchor interaction (shear force deflection behavior of the anchors) is modeled identically to the E/H, as is the method of attaching the liner/anchor mesh to the concrete mesh. The rebar generated for the local M/S model is identical to the 3DCM, so the reader is referred to Chapter 5 for this information.

Unlike the E/H and A/L, which were given symmetry boundary conditions on both vertical boundary planes, the M/S was loaded directly with displacement versus pressure histories at each node along the boundaries of the model. These pressure histories (different at every node and in all three degrees of freedom) were obtained directly from the 3DCM. The end result of the average hoop strain correlation approach used for the E/H and A/L is believed to be the same as with the direct application of displacements to nodes used in the M/S model.

The 3D local model analysis results for the M/S are shown in Figures 6-20 and 6-21. Figure 6-15 shows deformed shape results, which show that the M/S model deforms radially outward fairly uniformly across the model.

Figure 6-21 shows liner strain contours, which shows that the elevated liner strain concentrations ("hot spots") are predicted to occur near the vertical T-anchor termination. Peak strains at  $3.8 P_d$  are only about 5%, which are generally lower than for the E/H or the A/L.

2 CASES:

1.  $\Delta\theta = 0$  (Fixed - simulates far-field case)
2.  $\Delta\theta = \text{Free}$  (Upper bound on shear applied to anchor)

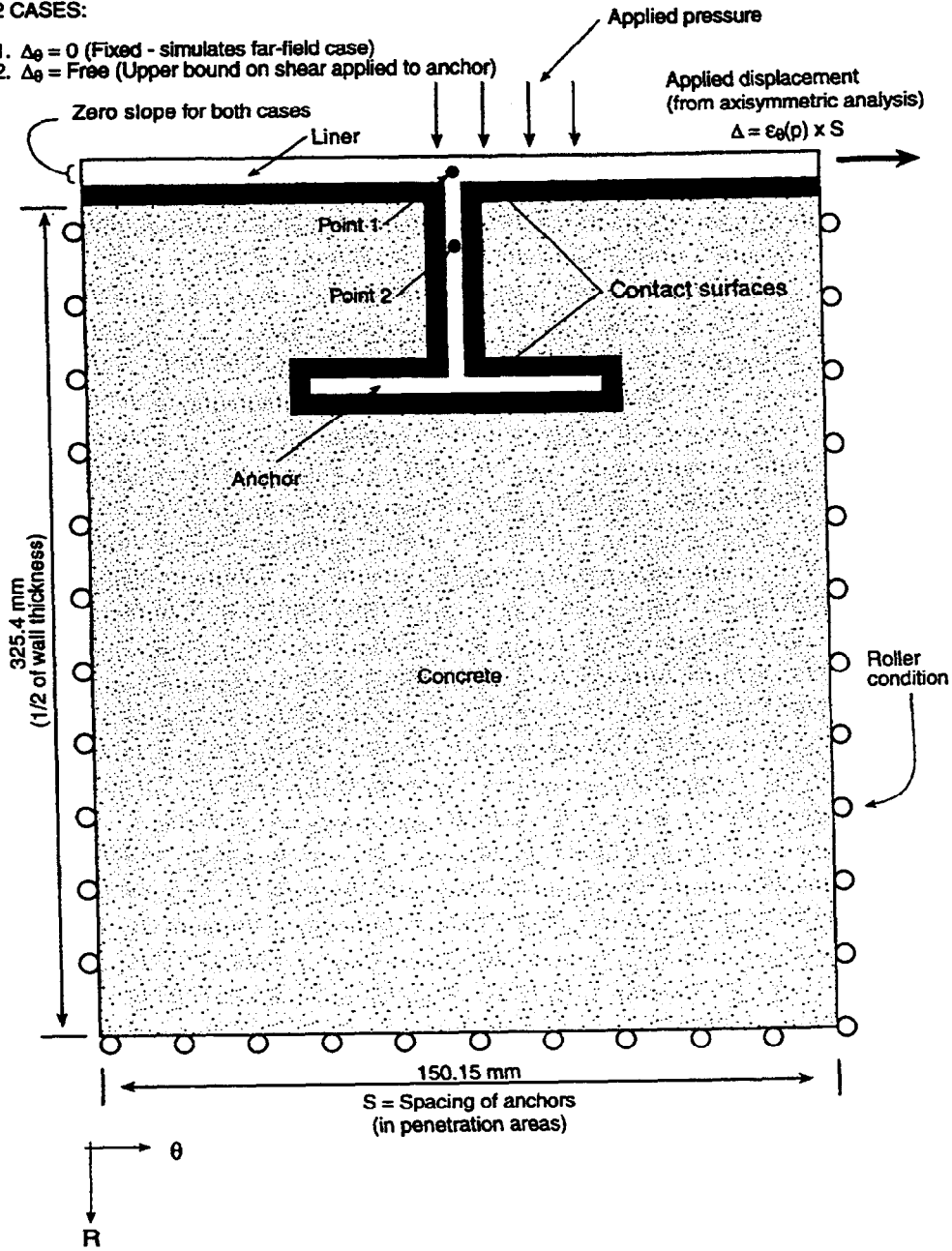


Figure 6-1. Schematic of Liner Anchor Model and Boundary Conditions

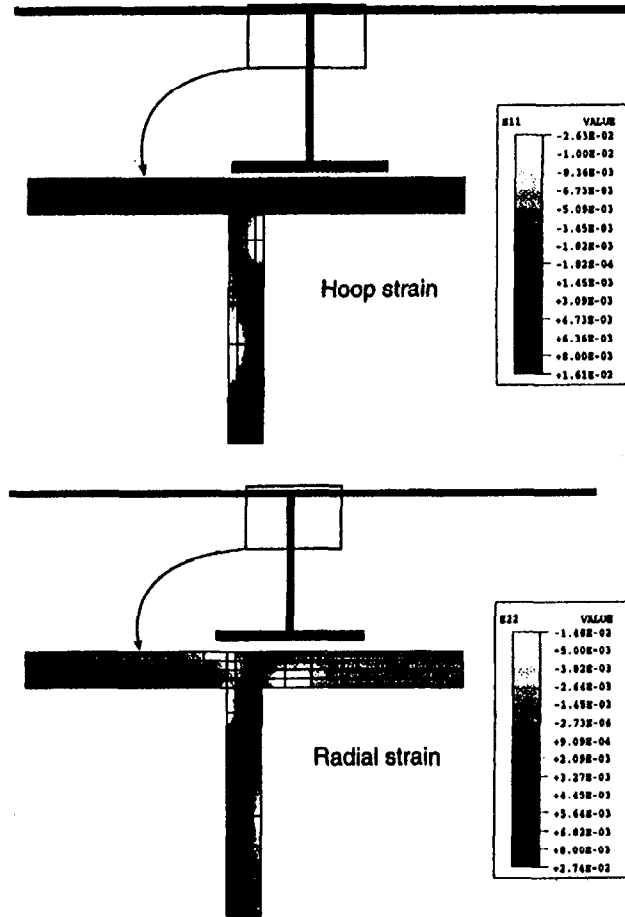


Figure 6-2. Strain Contours for Free Edge Case  
at Far-field Strain =  $8.4E-3$ ,  $\mu = 0.5$   
*free5.inp*

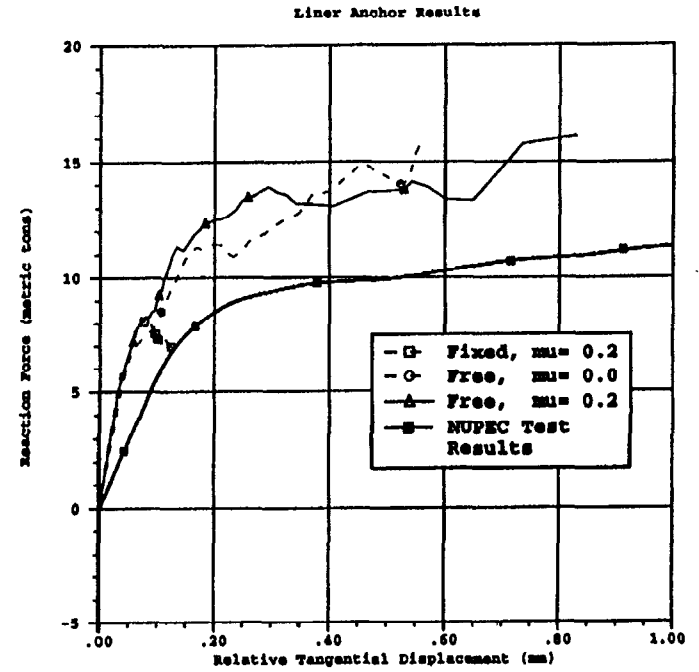


Figure 6-3. Force vs. Displacement Results  
for Liner Anchor Studies  
*fix2.inp, free0.inp, free2.inp*

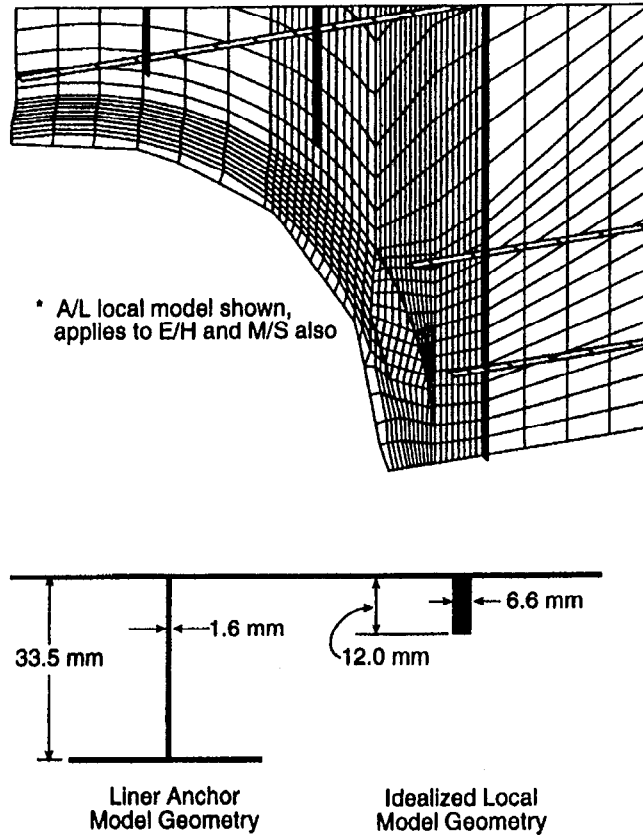


Figure 6-4. Idealized Modeling of Anchors and Stiffeners

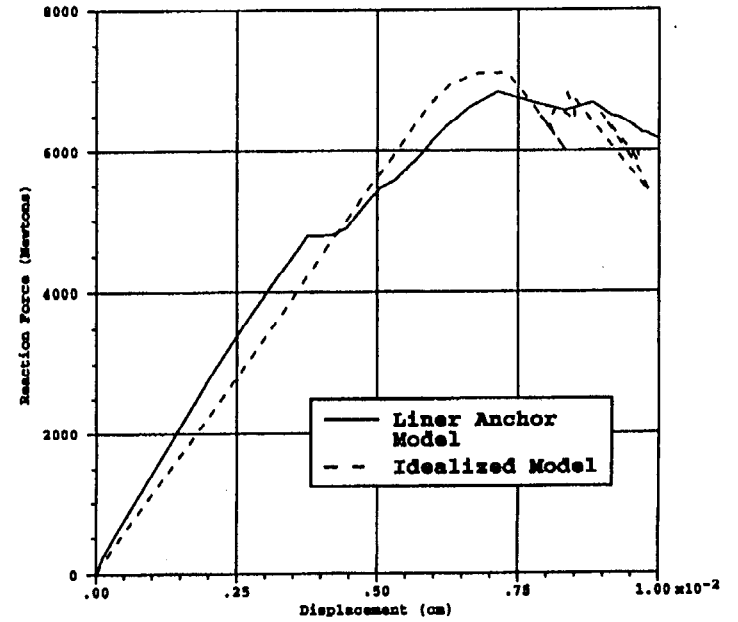
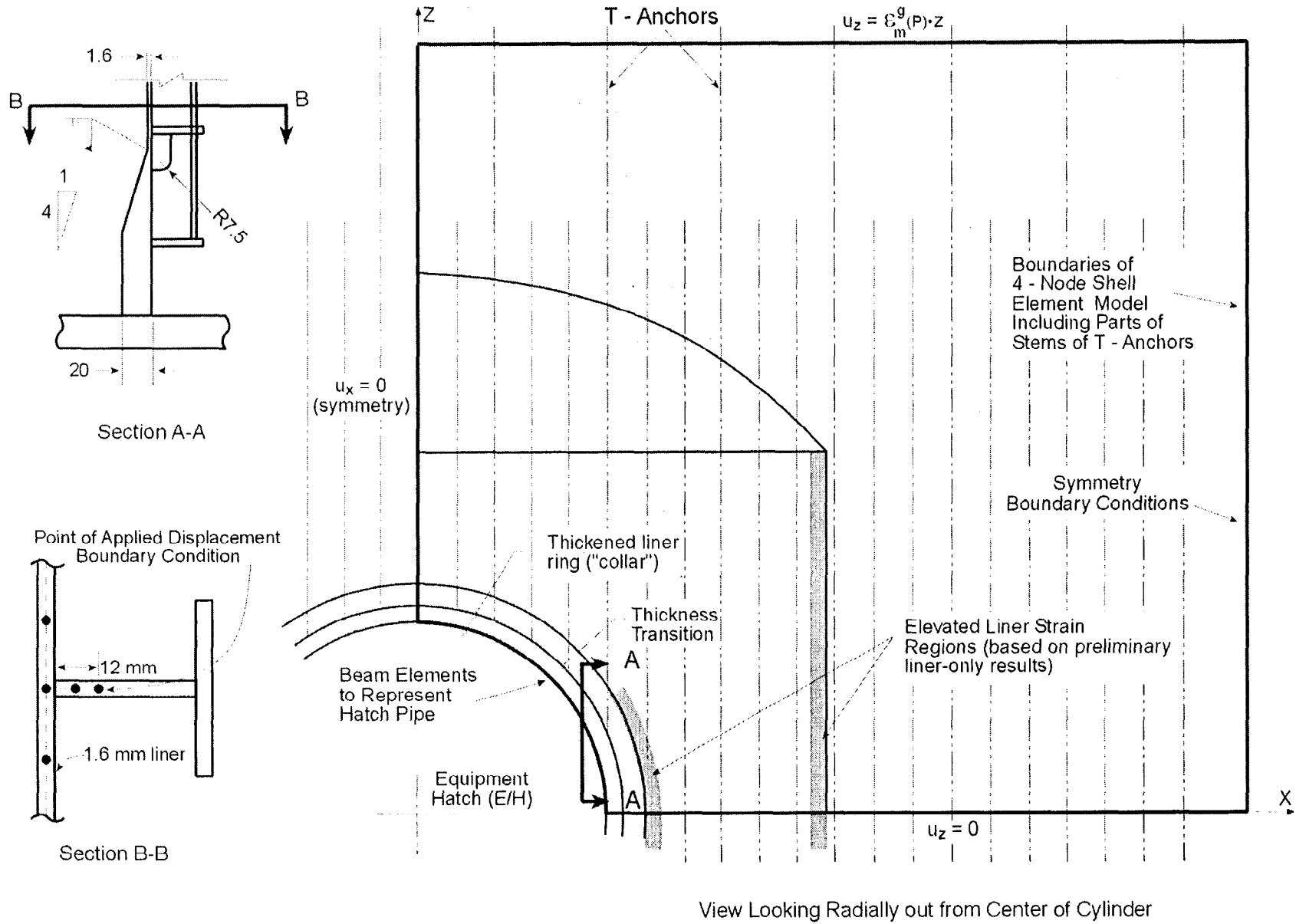


Figure 6-5. Force-Displacement Results of Liner Anchor Model vs. Idealized Model  
*fx2.inp, ideal.inp*



R-60

Figure 6-6. Detailed Liner Analysis Near E/H (View from Inside PCCV Looking Out Radially)

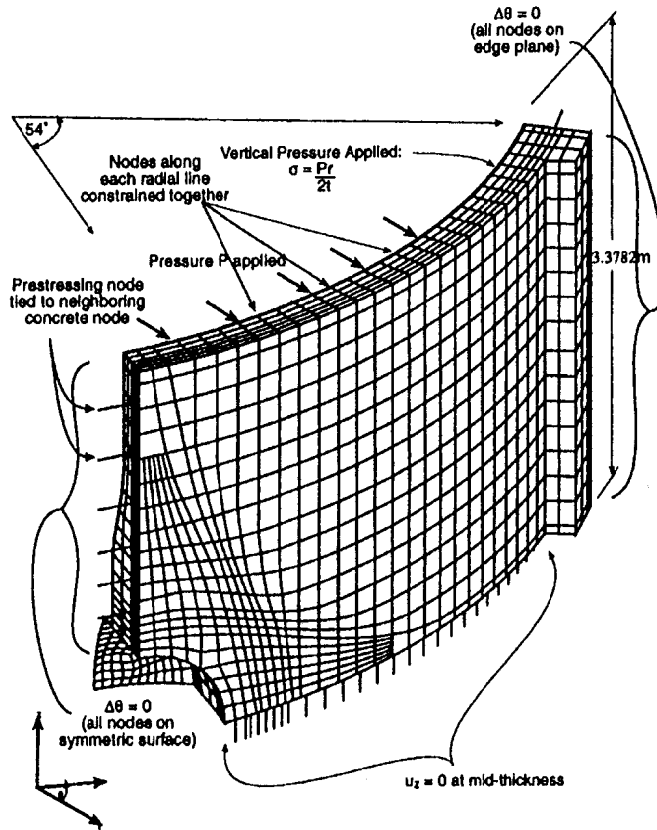


Figure 6-7. Boundary Conditions and Geometry for 3D Equipment Hatch Model

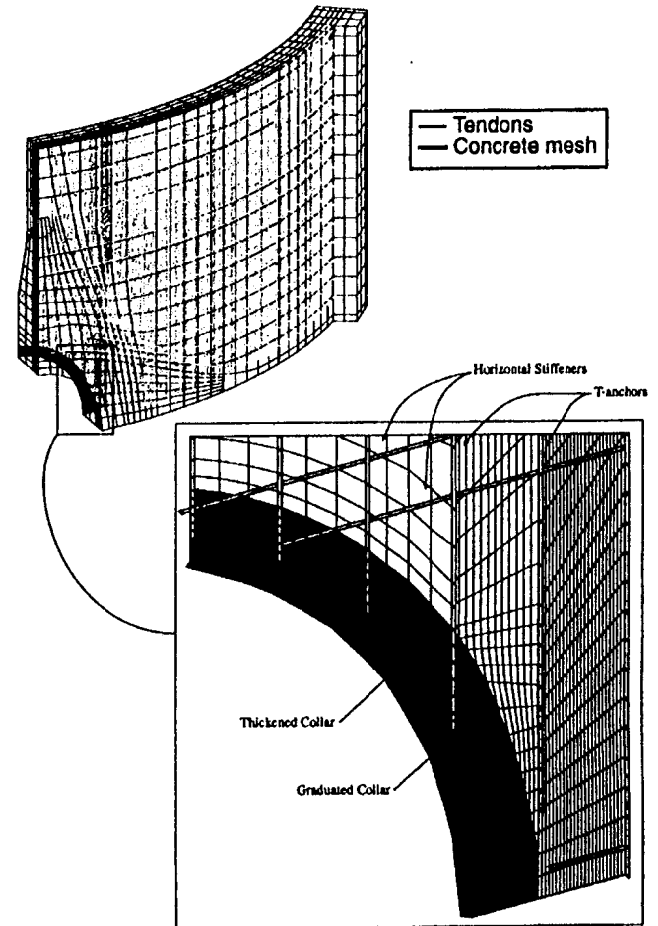
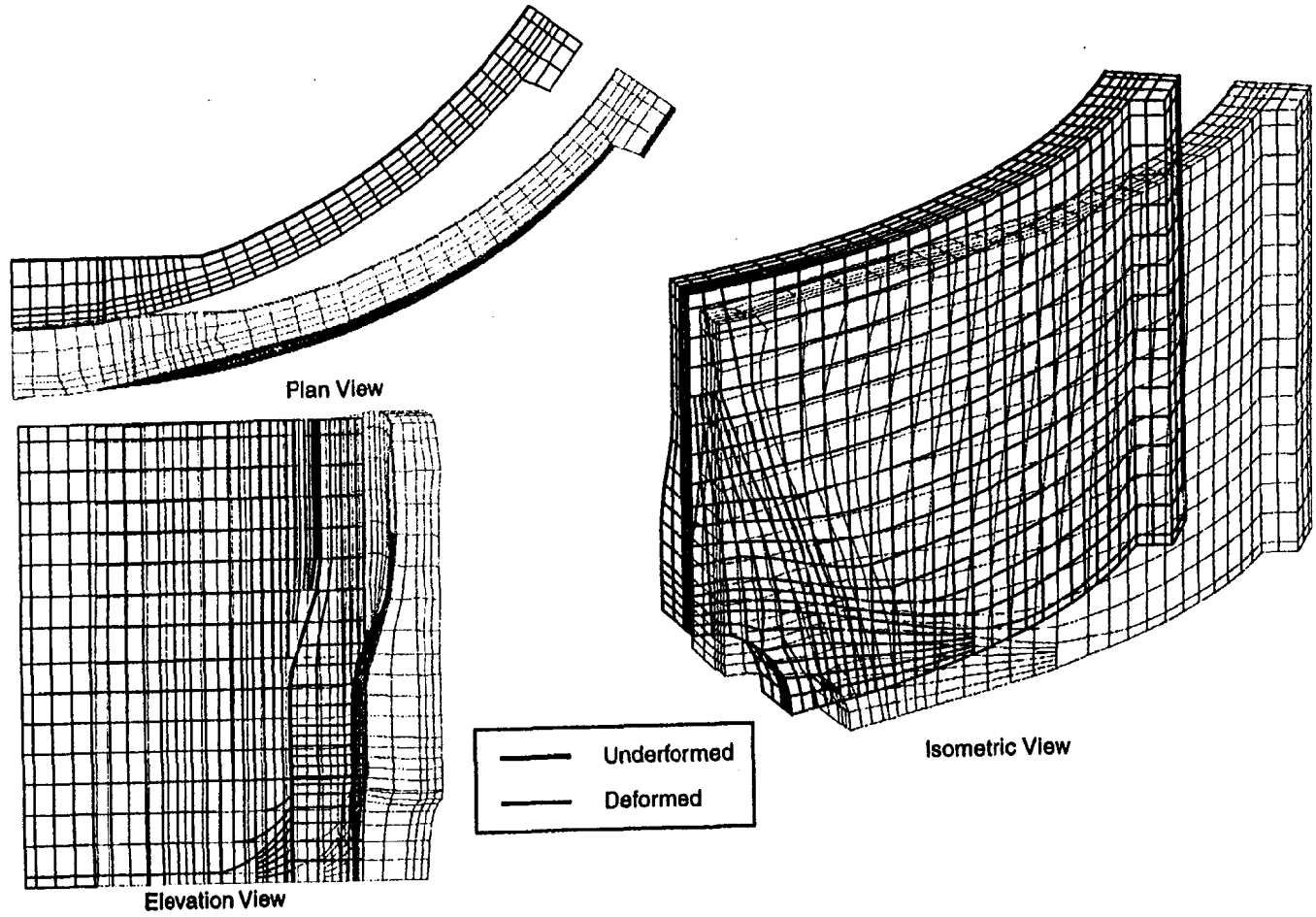


Figure 6-8. Finite Element Mesh including Tendons, Liner, Anchors, and Stiffeners



eh.inp

Figure 6-9. Deformed Shape of E/H Model at Pressure = 3.25 Pd (Magnification factor = 20x)

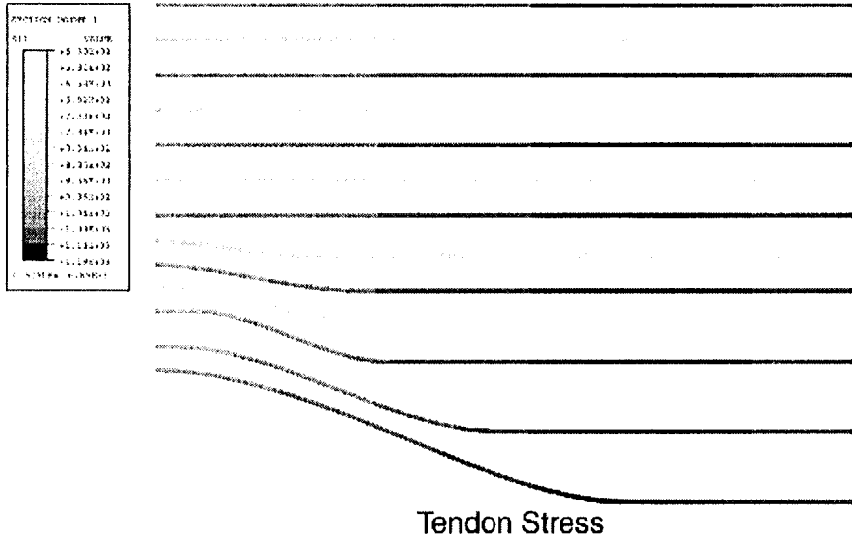


Figure 6-10. E/H Hoop Tendon Stress and Strain Contours at Prestress

eh.inp

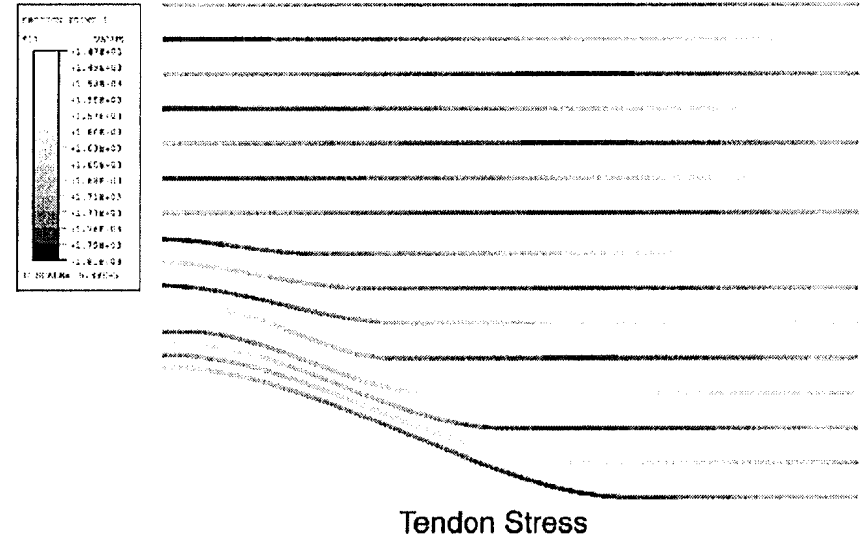
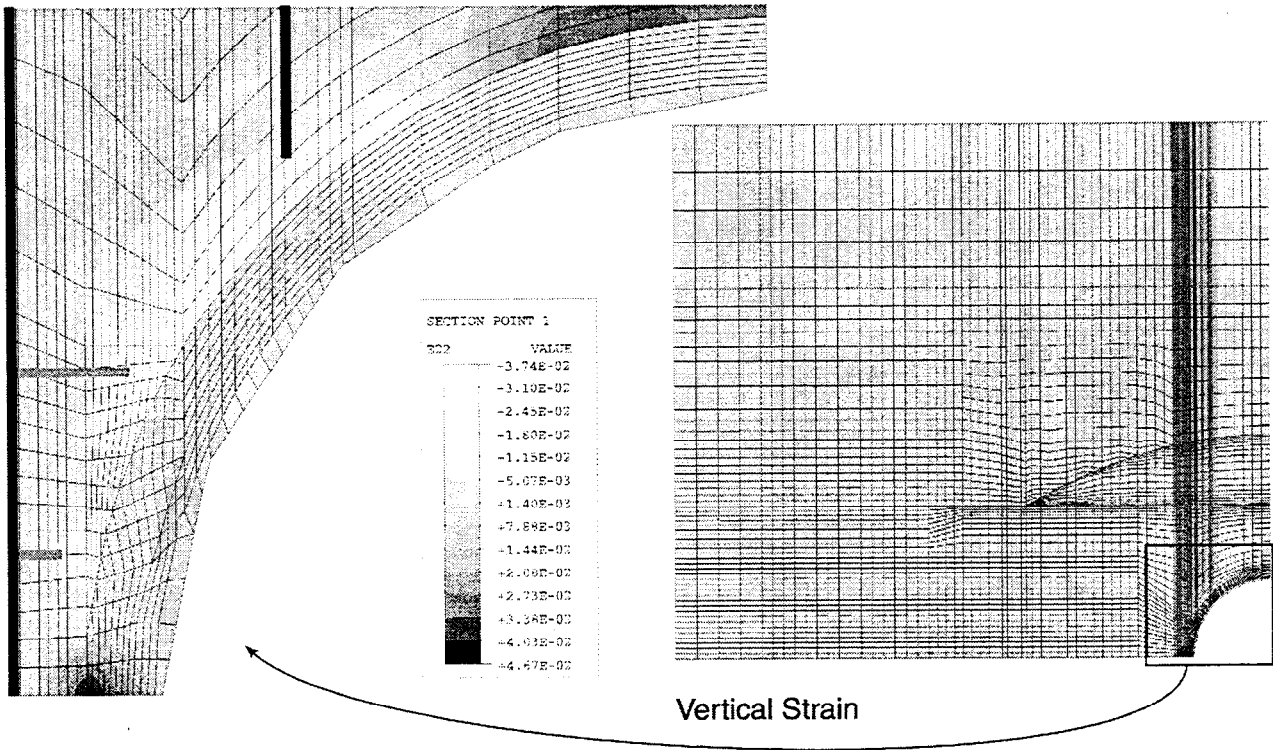
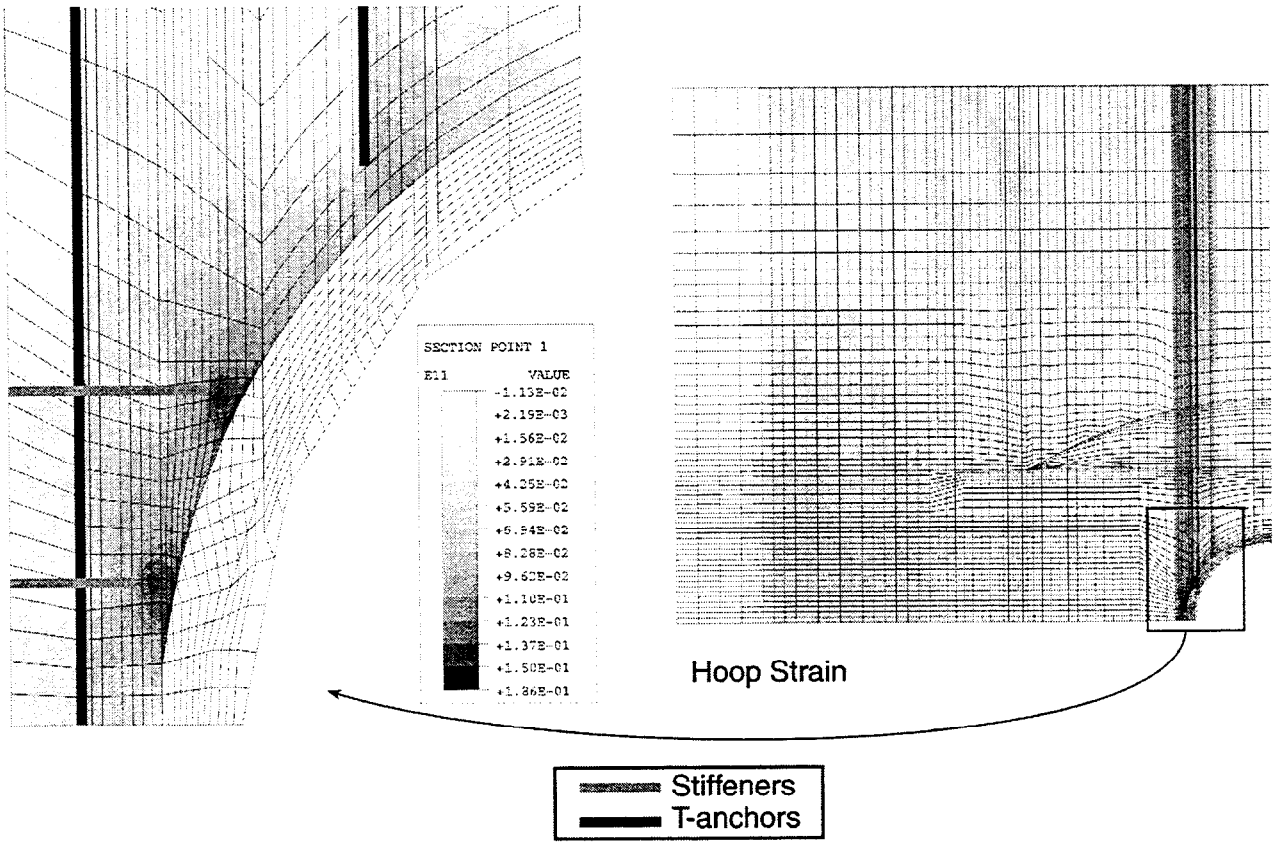


Figure 6-11. E/H Hoop Tendon Stress and Strain Contours at Pressure = 3.25 Pd



eh.inp

Figure 6-12. Liner Contour Strain Plots at P = 3.25 Pd

R-65

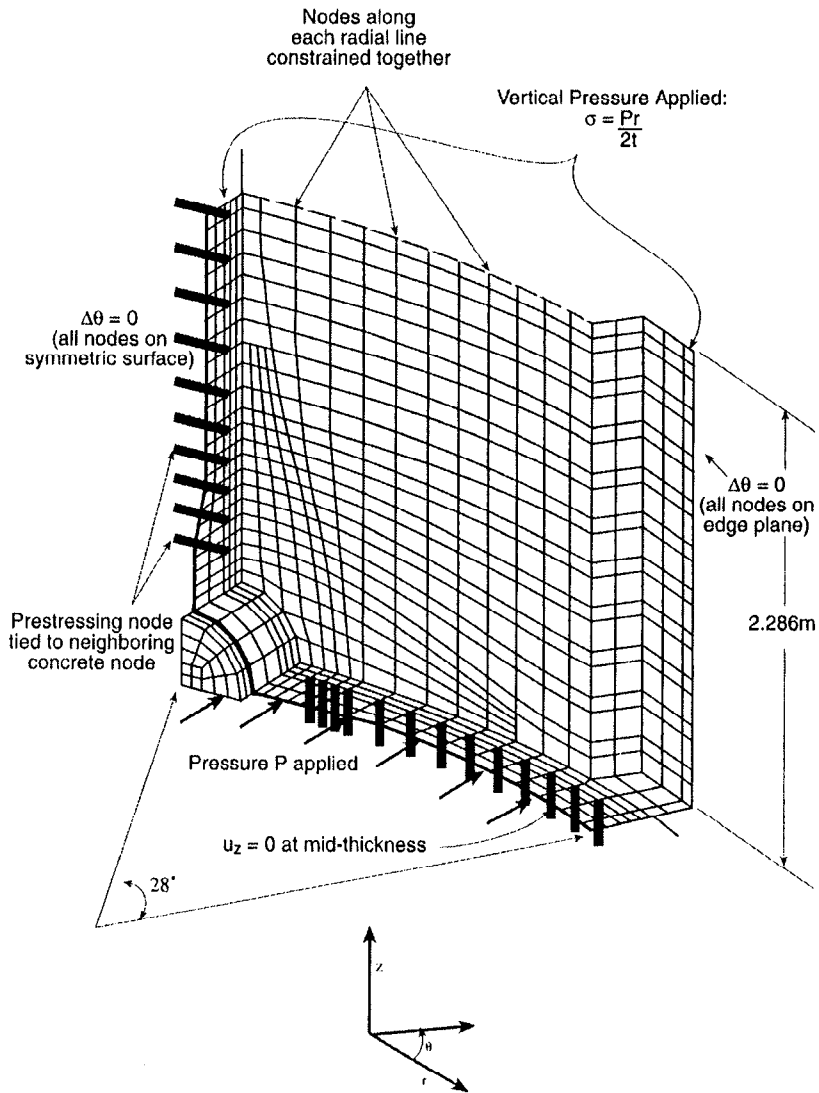


Figure 6-13. Boundary Conditions and Geometry for 3D Airlock Model

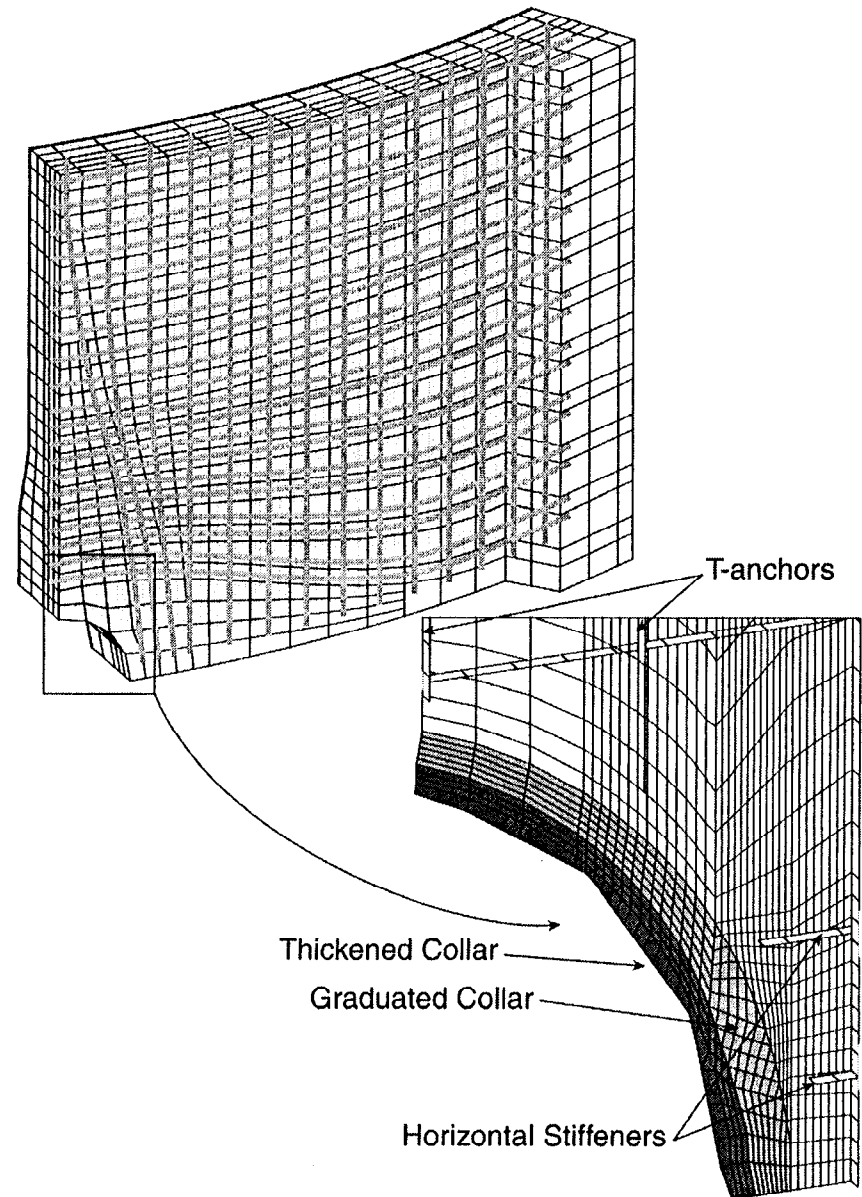
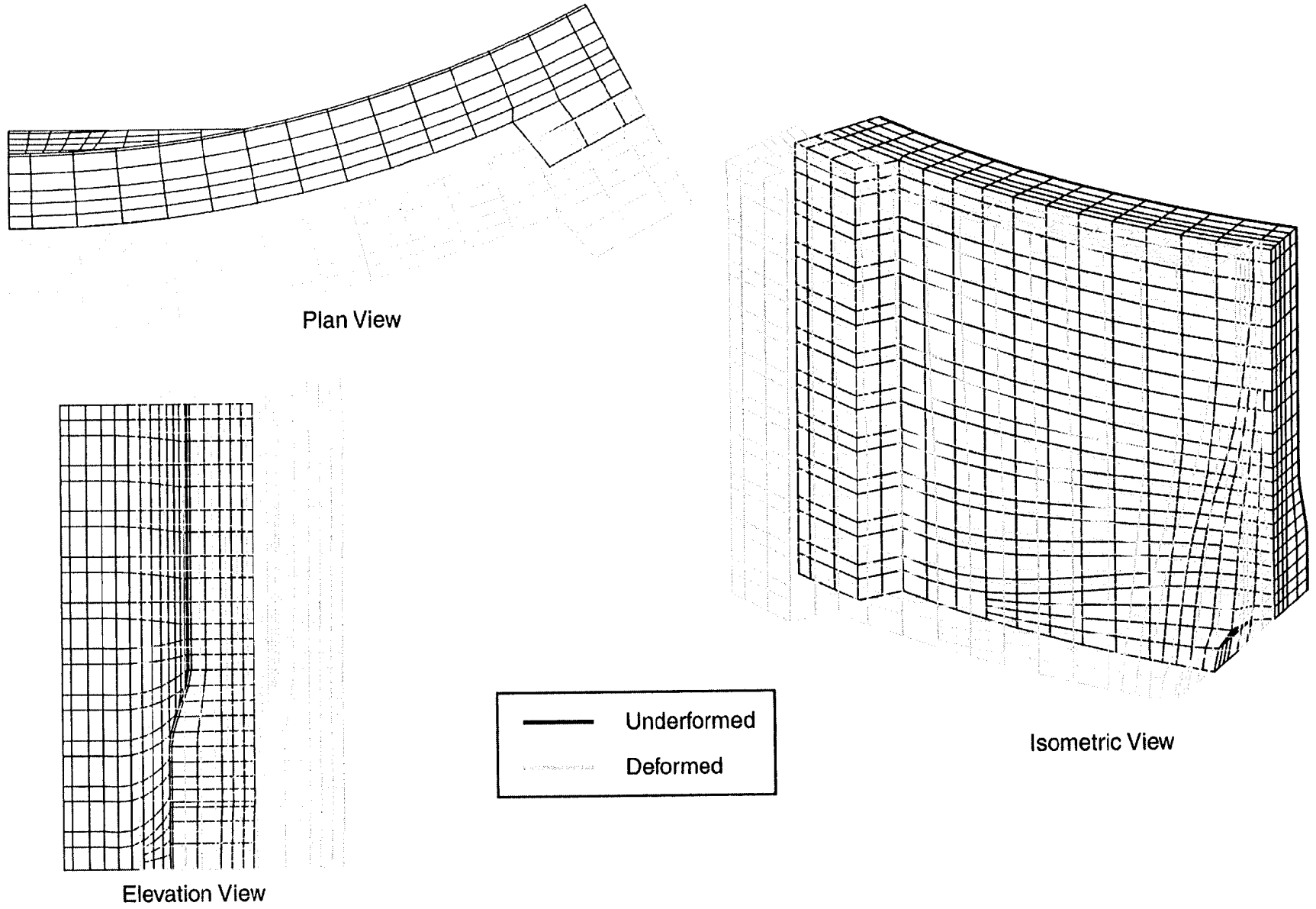
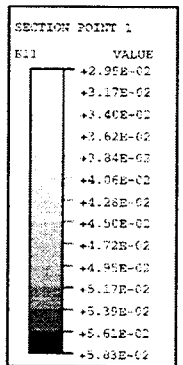
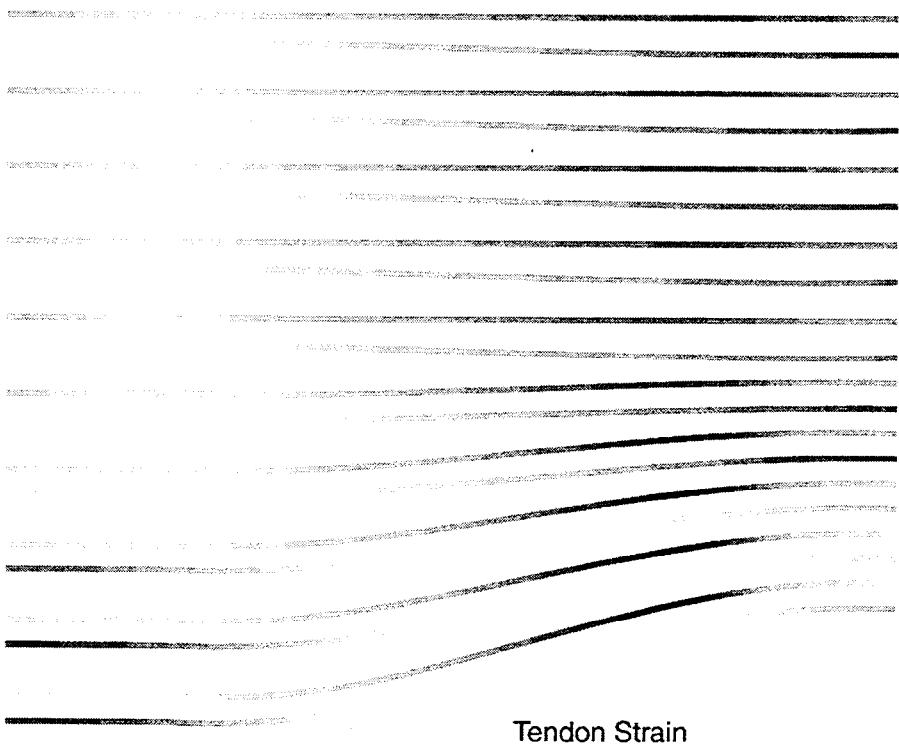
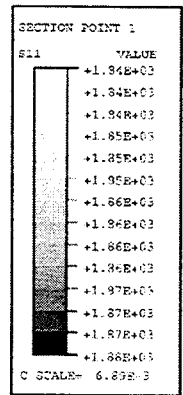
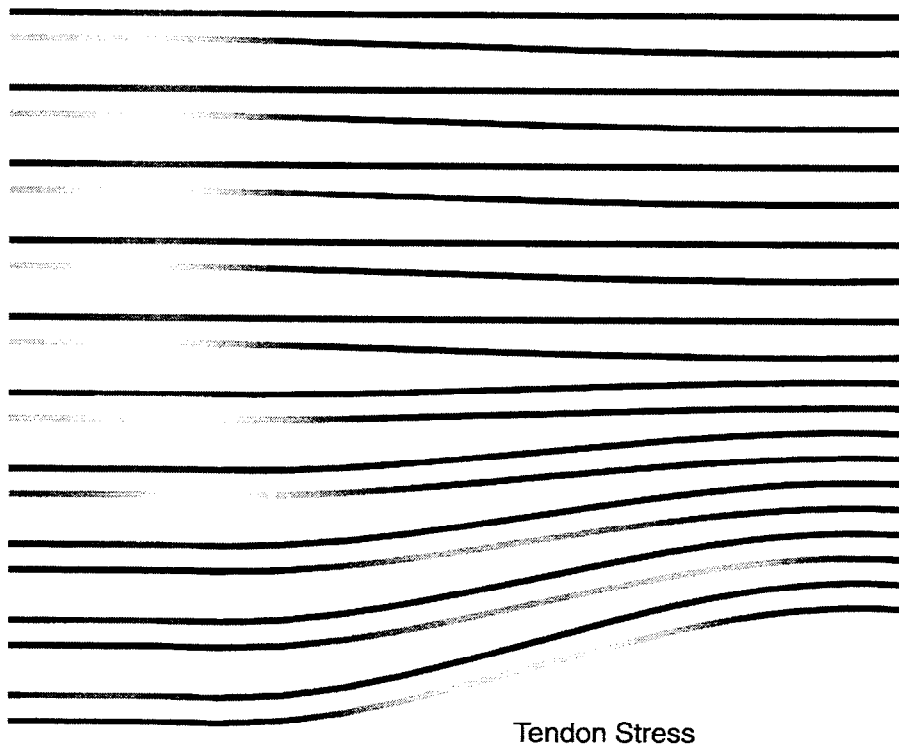


Figure 6-14. Finite Element Mesh including Tendons, Liner, Anchors, and Stiffeners

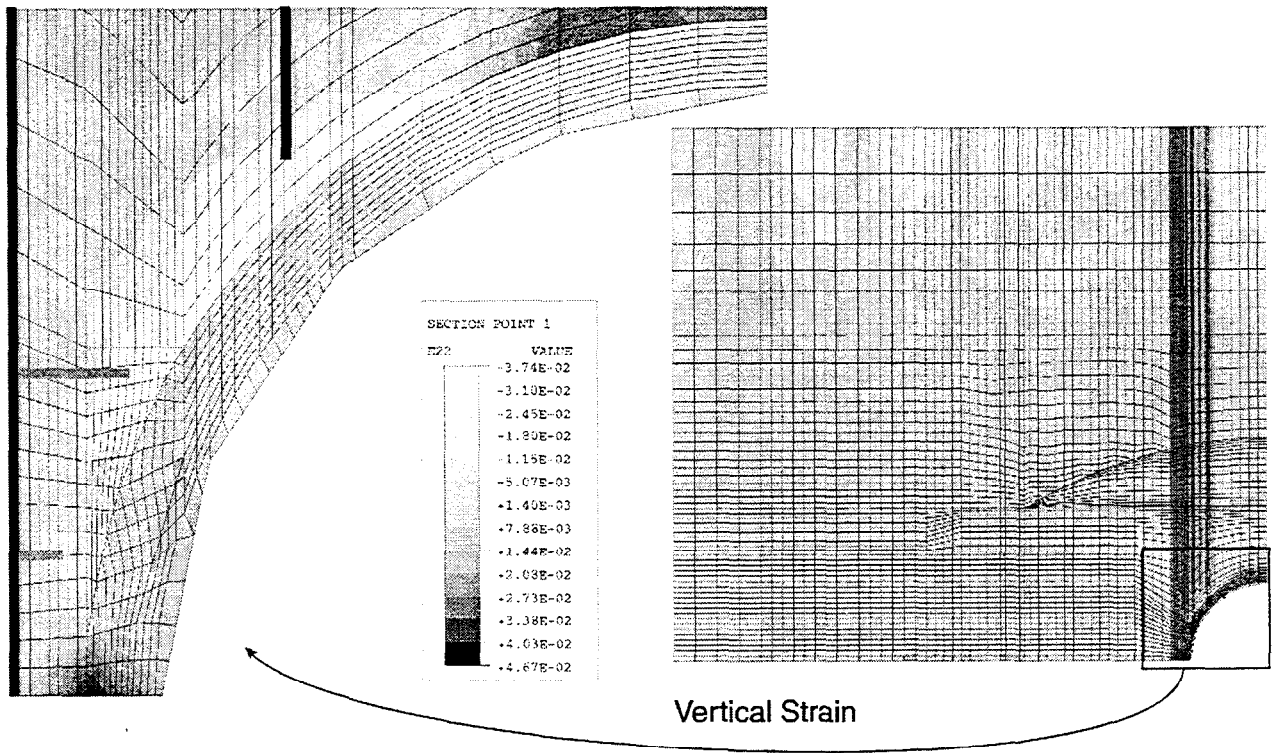
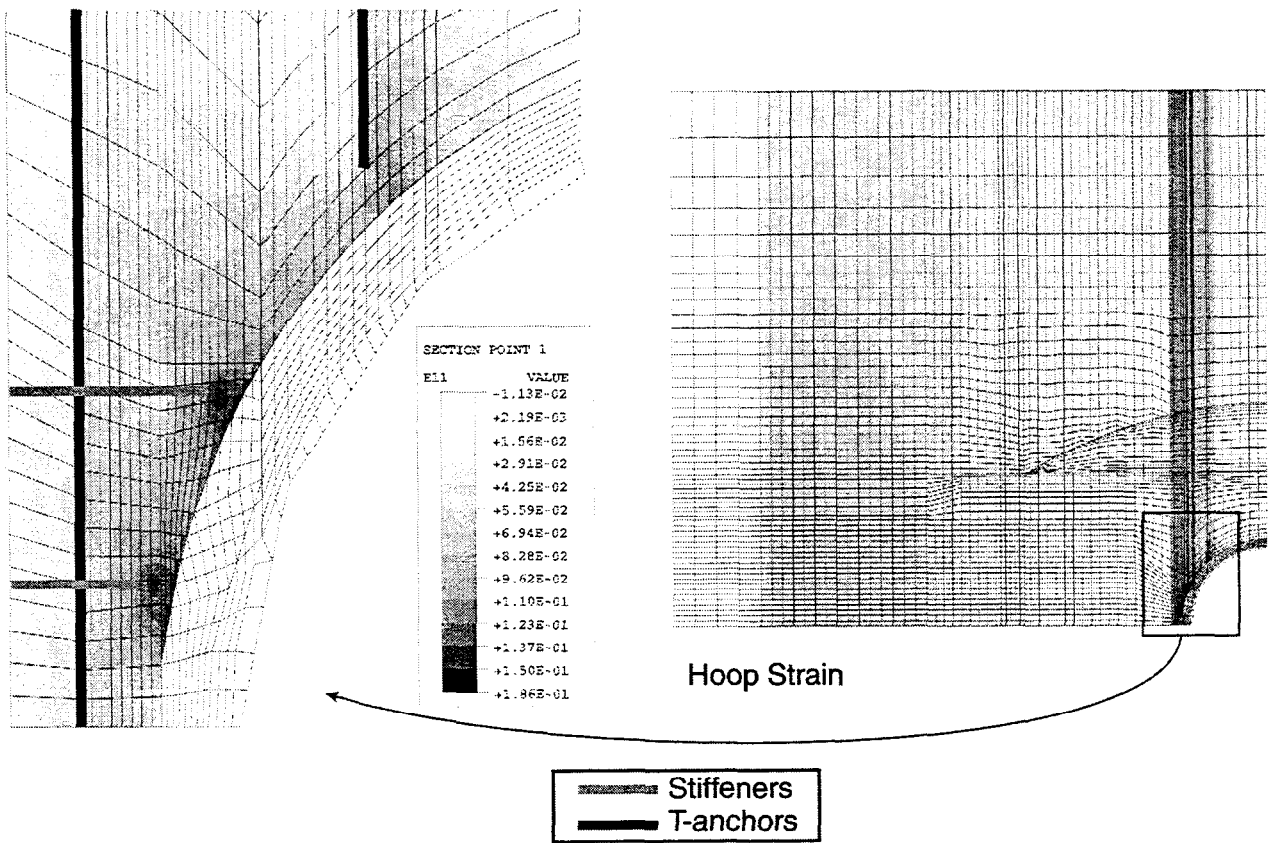


al.inp

Figure 6-15. Deformed Shape of A/L Model at Pressure = 3.75 Pd (Magnification factor = 2x)



*al.inp* Figure 6-16. A/L Hoop Tendon Stress and Strain Contours at Pressure = 3.75 Pd



al.inp

Figure 6-17. Liner Contour Strain Plots at  $P = 3.75 P_d$

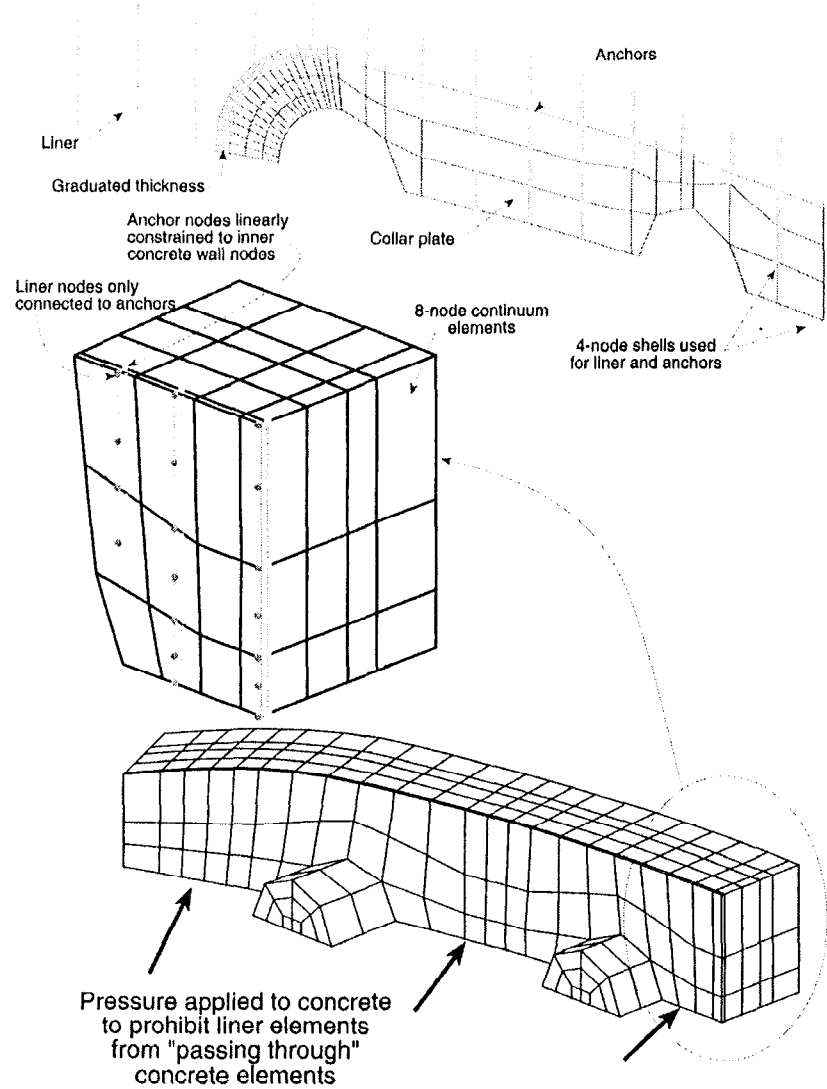


Figure 6-18. M/S Local Model Liner Details

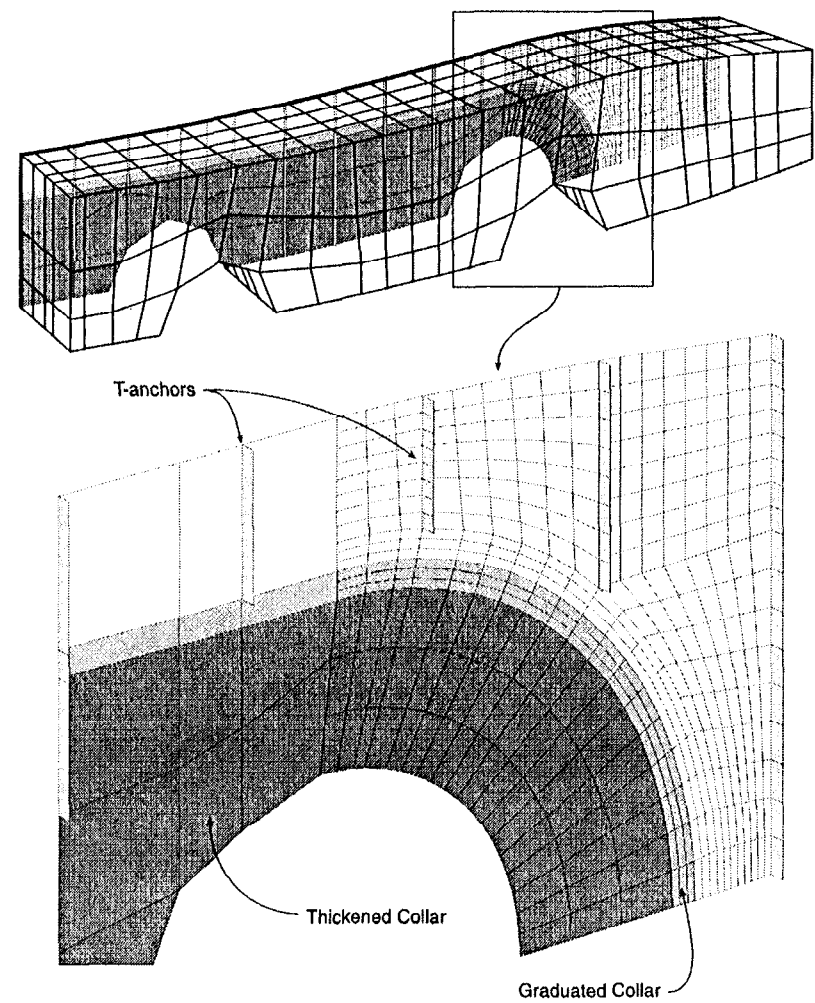
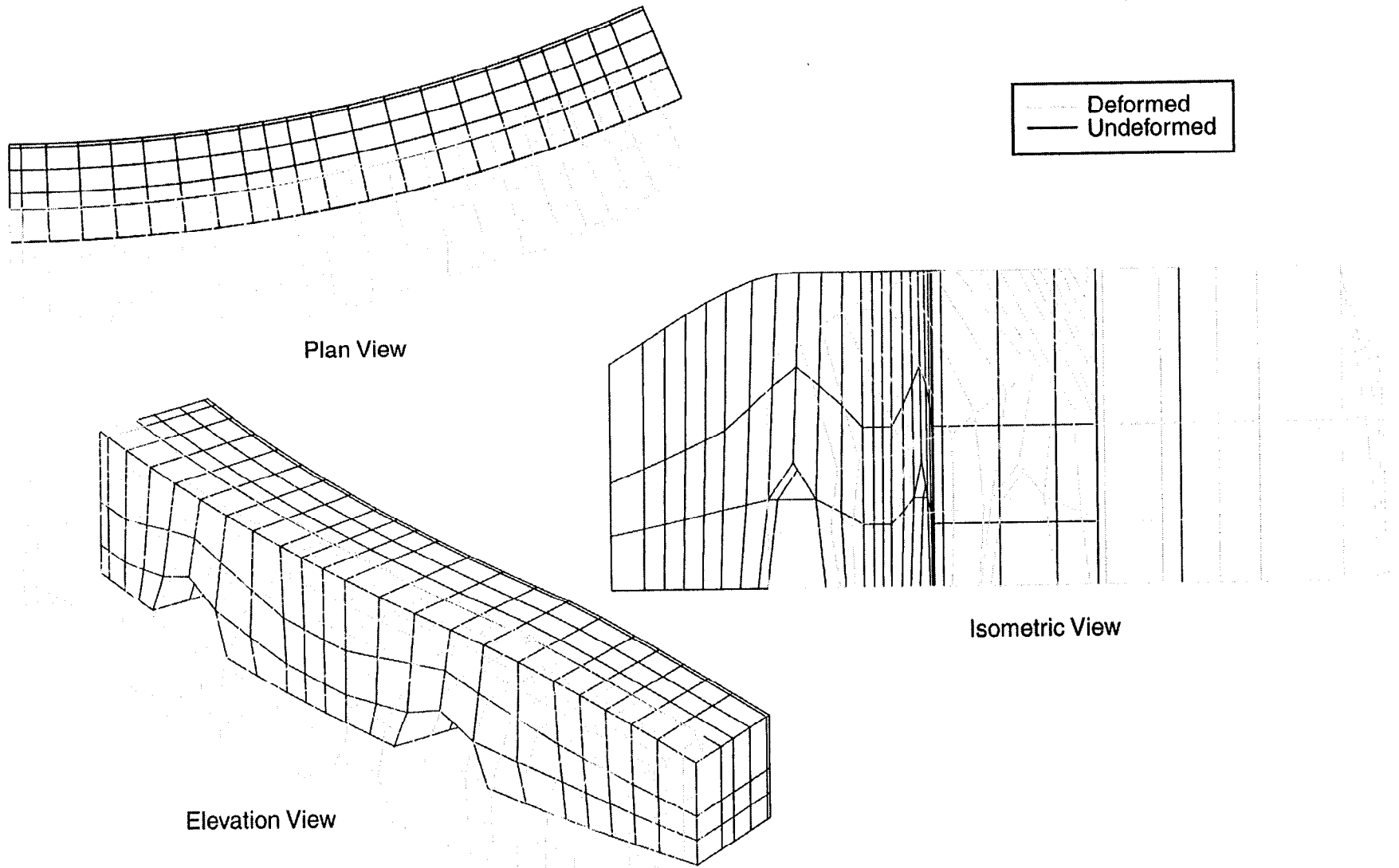


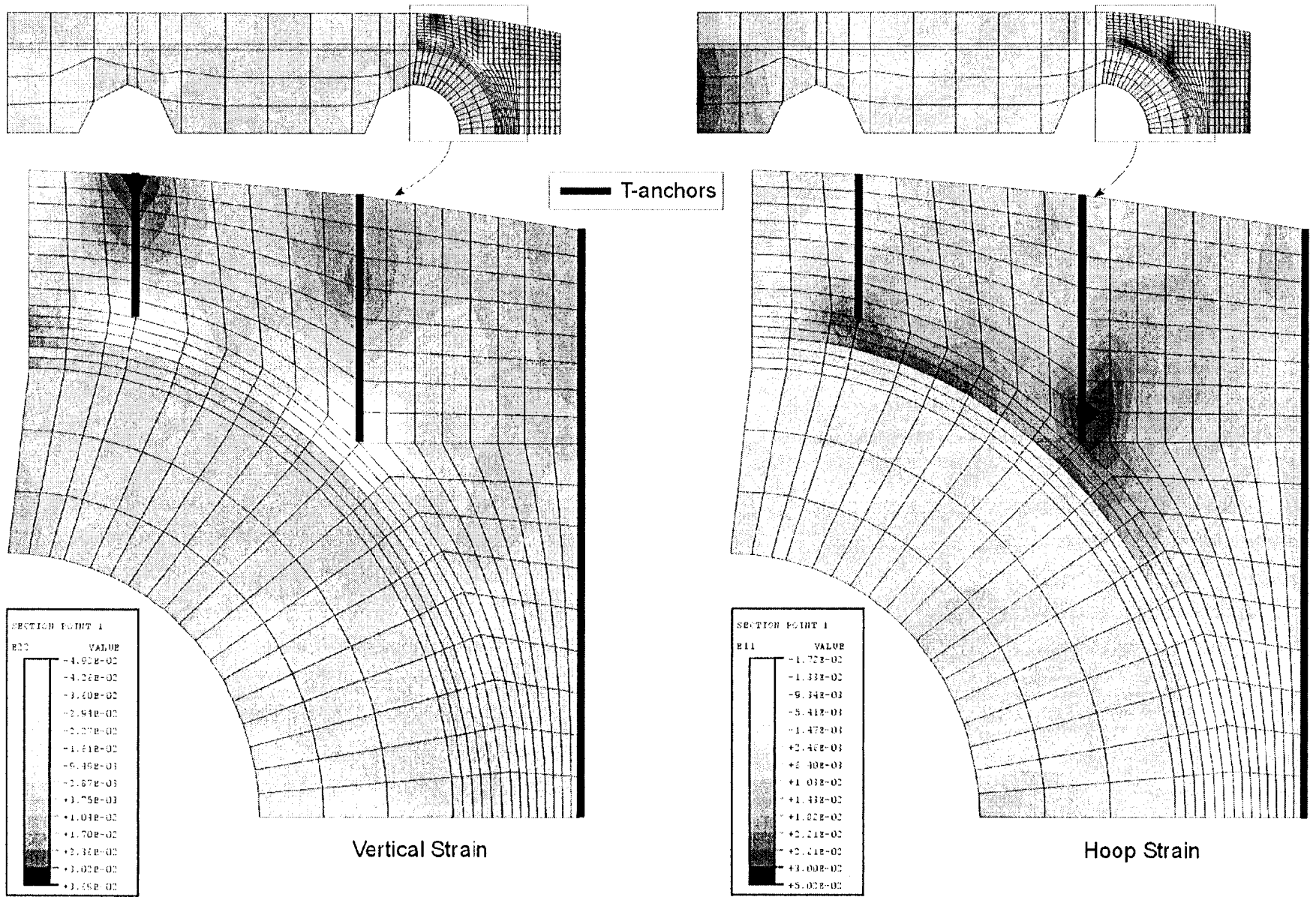
Figure 6-19. Finite Element Mesh including Liner and Anchors



ms.inp

Figure 6-20. Prestress Deformed Shape of M/S Model at Pressure = 3.8 Pd (Magnification factor = 2x)

R-71



ms mp

Figure 6-21. Liner Contour Strain Plots at P = 3.8 Pd

## 7.0 COMPARISONS AND CONCLUSIONS

### 7.1 Comparisons of Strains and Displacements in All Models

Each of Chapters 4, 5, and 6 discussed results of different models and drew conclusions on the failure modes for that region of the PCCV. This chapter merges these results into a response prediction for the whole structure. To do this requires comparison of the different model results and development of a failure sequence or ranking of the possible failure modes by pressure at which they can occur. Round Robin participation also required synopsis of particular pressure milestones as follows:

Table 7-1. 1:4 Scale PCCV Pretest Prediction Analysis Table of Response Events and Pressure Milestones

Event	How Derived	MPa	(psig)	$P_d$ Multiple
(1) First cracking of concrete in cylinder due to hoop stresses (occurs adjacent to buttresses)	3DCM Model	0.59	(86)	1.50
(2) First cracking of concrete in cylinder due to meridional stresses (occurs at wall-base juncture)	global axisym. model	0.57	(82)	1.4
(3) First yield of rebar in hoop direction of cylinder (occurs near buttresses)	3DCM	0.86	(125)	2.2
(4) First yield of rebar in meridional direction at wall-base juncture	global axisym.	1.10	(160)	2.8
(5) First cracking of concrete in dome above 45° dome angle	global axisym.	0.86	(125)	2.2
(6) First cracking of concrete in dome below 45° dome angle	global axisym.	0.94	(137)	2.4
(7) Hoop tendons reaching 1% strain (barrel mid-height)	3DCM	1.18	(171)	3.0
(8) " " " 2% strain " "	3DCM	1.27	(185)	3.2
(9) " " " 3% strain " "	3DCM	1.32	(192)	3.4

#### 7.1.1 Comparisons of Global Axisymmetric to 3DCM Results

The most fundamental response component which is likely to drive the failure of the PCCV model is the radial expansion of the cylinder. The radial displacement behavior of the 3DCM was compared with the radial displacement of the axisymmetric analysis in Figure 5-10. This comparison showed a similar trend and, up to a pressure of  $3x P_d$ , close agreement between the 135° azimuth of the 3DCM and the axisymmetric prediction. There are two important differences after  $3 x P_d$ , however, which directly influence the failure prediction:

- (1) By modeling the full 360° in three dimensions, the 3DCM model shows the variations in radial displacement with azimuth (large non-axisymmetry) and circumferential bending near the buttresses which are not represented by the axisymmetric model. This causes more local yielding and plastic deformation than the axisymmetric model predicts, and therefore, larger displacements at some azimuths.
- (2) Representing the complete tendon paths allows the 3DCM model to represent anchor set losses and the proper tendon stress distribution. This has allowed simulation of larger than average stress/strain in the tendon and earlier tendon yielding and earlier rupture than is predicted in the axisymmetric model.

Based on these comparisons, the axisymmetric analysis results are judged to provide an accurate representation of the PCCV model behavior up to about  $3 x P_d$ , and then prediction of the average response of the vessel when "averaged" around all azimuths. Therefore, for most of the Standard Output Location predictions (see the Appendix), the axisymmetric analysis is used. But, for predictions at

azimuths other than 135° and at elevations included within the 3DCM, the 3DCM results are used for the analysis standard output predictions.

### Qualitative Assessment of Failure Pressure

The ANATECH/Sandia Analysis and failure predictions are based on two distinct models and analysis: a global axisymmetric analysis and the 3DCM model. Because there are uncertainties with either analysis, but the 3DCM model reaches a limit-state at lower pressure than the axisymmetric model due to the inclusion of three dimensional effects, we believe the failure predictions based on the two distinct models make reasonable upper and lower bound confidence bands on failure pressure as follows:

- Minimum pressure reachable with 90% confidence: 1.18 MPa, 3.0  $P_d$  (based on 3DCM and local models)
- Maximum pressure reachable with 90% confidence: 1.42 MPa, 3.60  $P_d$  (based on the global axisymmetric analysis and a 2% global hoop strain criteria as an upper limit).

### *7.1.2 Comparisons of the Local Models*

To compare the high liner strain locations first requires comparisons of the driving strains of the local models. These comparisons are provided in Figure 7-1, which shows an estimate of the "driving strain" at the peak liner strain locations. The curves are constructed as follows:

- a. E/H: average hoop strain across the E/H local model, or the equivalent hoop strain driving the E/H region;
- b. A/L: average hoop strain across the A/L local model;
- c. M/S: radial displacement of the M/S,  $u_{ms}$  divided by R
- d. Meridional strain at the wall-base juncture (including bending effects)
- e. Hoop strain at the edge of the 90° buttress (including bending effects)

The formula for deriving the "average hoop strains" of the local models was described in Chapter 6. It can be noted that the buttress location is actually the largest of the "driving strains" in the model.

Figure 7-2 compares the peak strains at the same locations. For the A/L and E/H, there are two curves each because there are two kinds of strain concentration geometries at each location. (This is described in more detail in the next sub-section.) The peak strain at edges of buttresses is amplified by the presence of hoop stiffener splices at vertical weld seams in the liner. While this detail has not been specifically modeled, from experience with similar details in other structures, the strain concentration factor at such details is approximately equal to 3. Also, based on preliminary analysis work, a strain concentration exists at the wall-base juncture with a strain concentration factor of approximately 2. Thus, the peak strains near penetrations are pulled directly from local model analysis, and the curves for locations 1 and 5 are created by amplifying curves d and e of Figure 7-1 by concentration factors of 2 and 3, respectively. These important plots support the following observations.

- (1) At high pressures, the E/H has the largest strain concentrations and peak strain;
- (2) The concentrations near the ends of the hoop stiffeners are nearly equal to those near the ends of the T-anchors, but the concentration is largest near the T-anchor (Location 3);
- (3) At pressures greater than 3  $P_d$ , the A/L locations rank third and the M/S locations rank fourth. The A/L strain concentration is largest at the vertical T-anchor.

## 7.2 Comparisons and Ranking of Potential Failure Modes

With the analyses completed and results tabulated and plotted, final comparison and ranking of failure modes requires a return to the structural drawings and a review of observations of the as-built structural details. This review is summarized in the drawing excerpts in Figures 7-3 through 7-9. Figure 7-3 shows sample locations of the liner Strain Concentration Locations (SCL) that have been identified, and categorizes them as follows:

### Potential Liner Failure Locations

- | <u>SCL</u> | <u>Description</u>  |
|------------|---|
| 1.         | <u>Horizontal Stiffener Splice Straddling a Vertical Liner Seam</u> : These locations occur at dozens of locations in the model. They can be a straight connection or at a slight-angle re-entrant corner as shown in "D-D" of Figure 7-3. The sudden gap in the hoop stiffener at the "rat-hole" (needed for welding electrode access) tends to cause a strain riser near the liner seam weld zone, which is already somewhat less ductile than the virgin liner material. |
| 2.         | <u>Horizontal Stiffener Termination on the 1.6 mm Liner Near Thickened Insert Plate</u> . This is a "double" concentration caused by the hoop stiffener termination in a zone already subject to strain concentrations due to the adjacent material thickness change. These locations are always further exacerbated by the presence of the weld to the insert plate and the weld of the stiffener to the 1.6 mm liner.   |
| 3.         | <u>Vertical T-Anchor Termination on the 1.6 mm Liner Near Thickened Insert Plate</u> . Similar to SCL 2, except the vertical T-anchor is a stronger embedment (due to the T-flange) than that of the hoop stiffener. The T-anchor, however, does not carry hoop stress; the sudden transfer of hoop stress from stiffener to liner which is an additional source of strain concentration in SCL 2.  |
| 4.         | <u>Severe Acute Angle Weld Splices</u> . These occur at the confluence of normal splicing of liner segments with the edge of a penetration, such as is shown for the mainsteam penetrations in Figure 11-6 or as occurs at the corners of the embossed regions of the E/H and A/L.  |
| 5.         | <u>Wall-Base Juncture Liner Connection Detail</u> . Proximity to vertical T-anchor termination and to rigid basemat embedment cause strain concentration. The liner is not spliced here, however, so presumably, it retains its full ductility.   |

It should be noted that this is still an incomplete list; for example, strain concentrations are also known to occur at the crane rail attachment points and at the many horizontal welded seams coincident with vertical T-anchor splices. Locations such as these were eliminated from consideration early in the analysis work because of the relatively low "driving strains" that occur at these locations. Thus, to be placed on the list of competing failure locations requires occurrence of a strain concentration detail and a significant driving strain.

Figures 7-4 through 7-9 inventory the occurrences of these SCLs. Again, only locations with significant driving strains coincident with the SCL detail are identified. The locations shown in the figures are itemized below.

<u>Figure</u>	<u>Description</u>
7-4	Three Type 1 located at 95° azimuth (edge of buttress), and two (x2 for other side) Type 1 at edge of A/L embossment.

- 7-5 Six (x2 for symmetry) Type 1 at edge of E/H Embossment, and eight Type 1 at 275°/265° azimuth (edge of buttress).
- 7-6 Four Type 2 near 3 o'clock position of A/L; three Type 3 near 2 o'clock and 1:30 o'clock positions of A/L; four Type 4 at corners of embossment.
- 7-7 Four Type 2 near 3 o'clock position of A/L; four Type 3 near 2:30 o'clock positions of E/H; four Type 4 at corners of embossment.
- 7-8 Two Type 3 and two Type 4 near M/S Penetrations.
- 7-9 Two Type 3 and one of Types 1, 2 and 4 near F/W Penetrations.

### 7.3 Final Failure Predictions

This chapter has itemized the locations on the liner where high strains occur and has shown that Strain Concentration Type 3 (near the termination of the vertical stiffener) at the E/H develops the highest strain during the pressure range,  $3.0 P_d$  to  $3.4 P_d$ . In addition to this itemization, a thorough review of rebar strains, concrete strains and shear damage, and tendon stresses and strains has been conducted vis-a-vis each of the failure criteria described in Chapter 3. The result of this review did not reveal any failures in any structural components except in the liner. The liner failure pressure is calculated by comparing the strain versus pressure history in Figure 7-2 to the failure strain calculated from Equations 3-6 and 3-8. An additional factor of 0.6 is also applied to the Davis Triaxiality criteria because the peak liner strains are located in the vicinity of full penetration welds of the 1.6 mm liner to the thickened insert plate. (Development of this factor was also described in Chapter 3.) The final failure strain at the E/H location which coincides with the strain prediction is

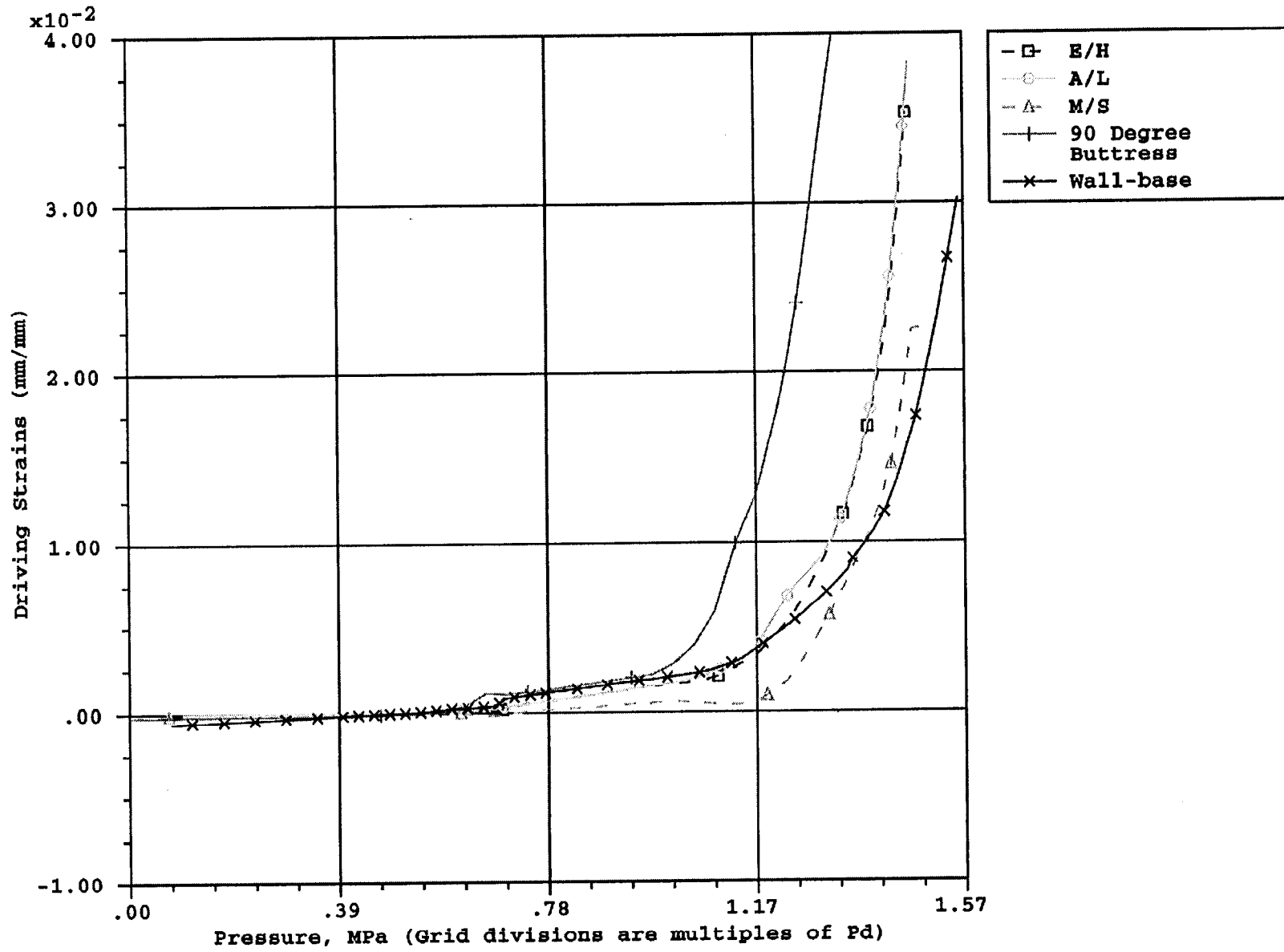
$$\text{Failure Strain} = \text{Calculated Strain} = 0.162$$

This strain is calculated to occur at Pressure =  $3.2 P_d$ , 1.25 MPa (185 psig).

This chapter has also presented a list of other candidate strain concentration locations. These are ranked in order of the pressure at which the analyses predict them to occur as follows:

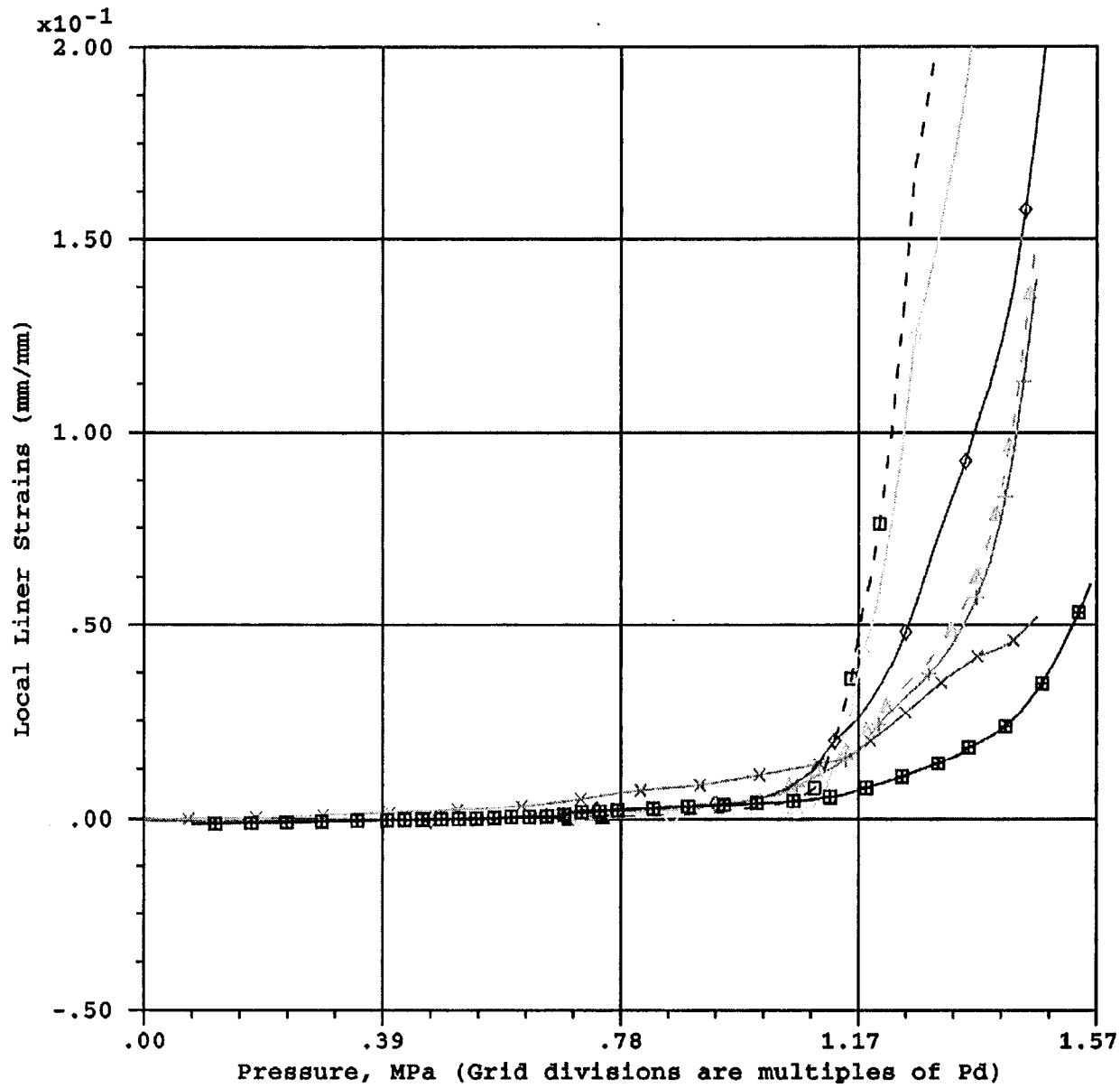
- (1) E/H near vertical T-anchor termination (as listed above -4 locations Type 3);
- (2) E/H near horizontal stiffener termination (4 locations, Type 2);
- (3) Near a weld seam with hoop stiffener rat-hole, 5 degrees from the centerline of 90 degree buttress (i.e. 95 degrees);
- (4&5) Similar to 1 and 2, but near the A/L (7 locations, Types 3 and 2);
- (6) Similar to 1, but near the M/S penetration (2 locations, Type 3);
- (7) Similar to 1 and 2, but near the F/W penetration (3 locations, Types 3 and 2);
- (8) Strain concentration Location Type 4 near F/W penetrations, M/S penetrations, and near E/H and A/L as shown in Figures 7-3 through 7-9.

The analysis then shows that a tendon rupture is likely at  $3.5 P_d$  for the tendon closest to the E/H, so this event/pressure milestone is predicted to be an upper bound on the failure pressure prediction. It should be noted, however, that a tendon rupture failure mode is predicted to be precluded by one or more of the liner tears which will lead to very large leakage rates and depressurization of the vessel.



eh.inp, al.inp, ms.inp,  
3dcm.inp, model14.inp

Figure 7-1. Driving Strains at Liner Strain Concentration Locations



eh.inp, al.inp, ms.inp,  
3dcm.inp, model14.inp

Figure 7-2. Peak Strains at Liner Strain Concentration Locations

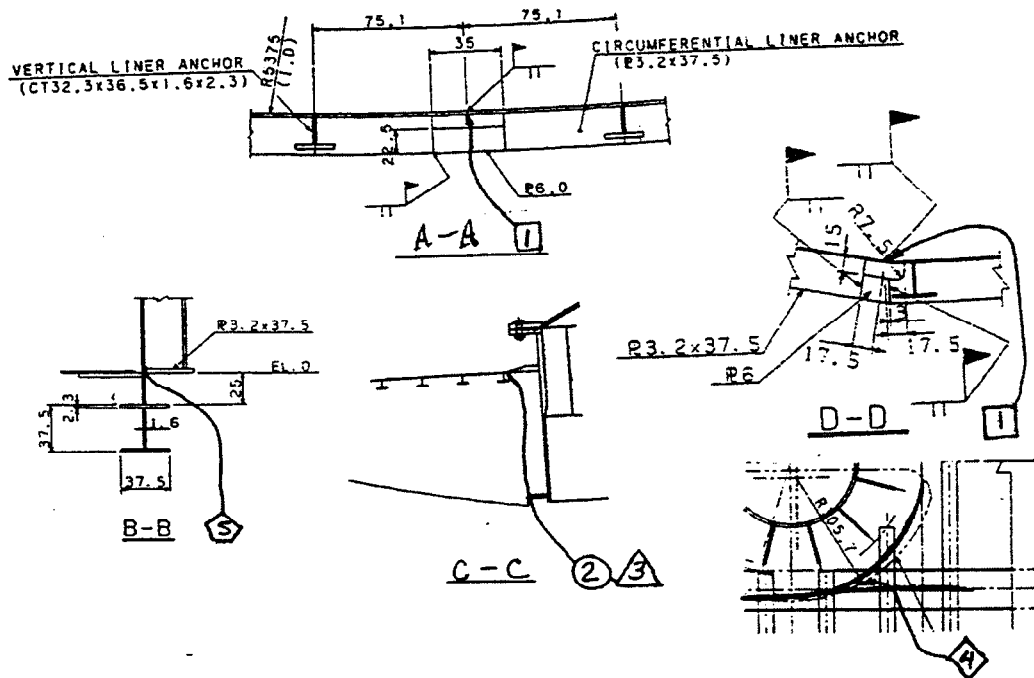
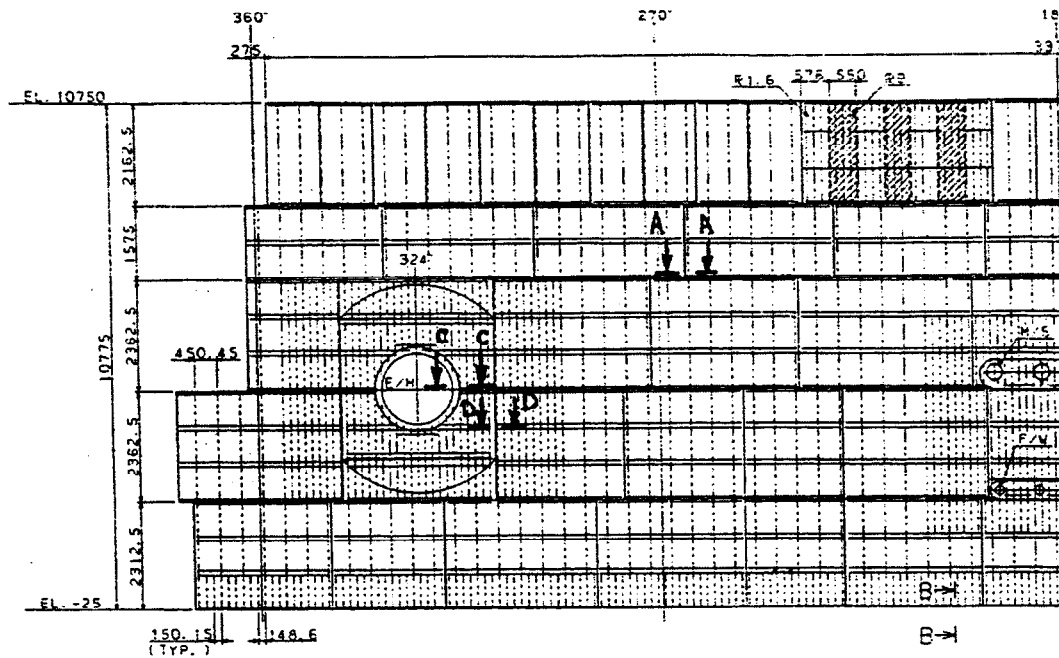


Figure 7-3. Categorization of Liner Strain Concentration Locations



R-80

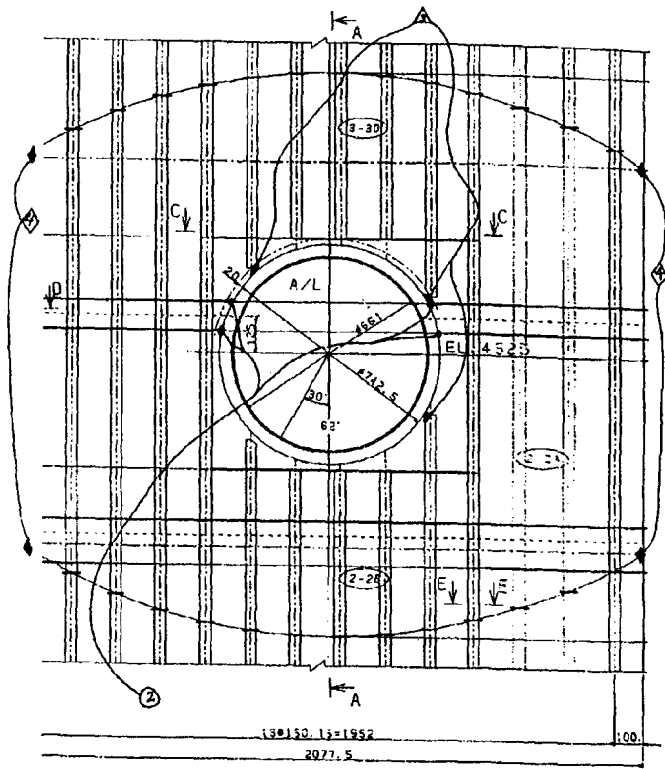


Figure 7-6. Strain Concentration Type 2,3,4 Near A/L

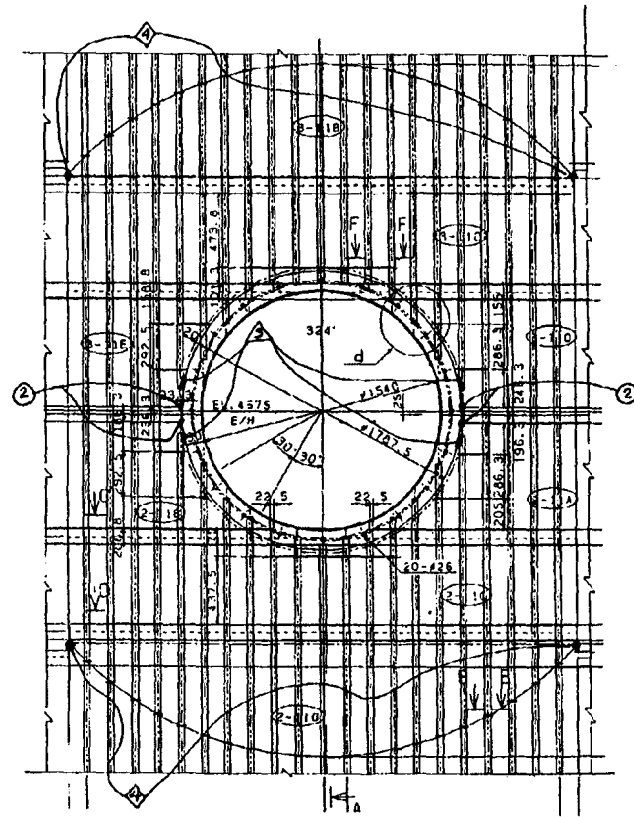


Figure 7-7. Strain Concentration Type 2,3,4 Near E/H

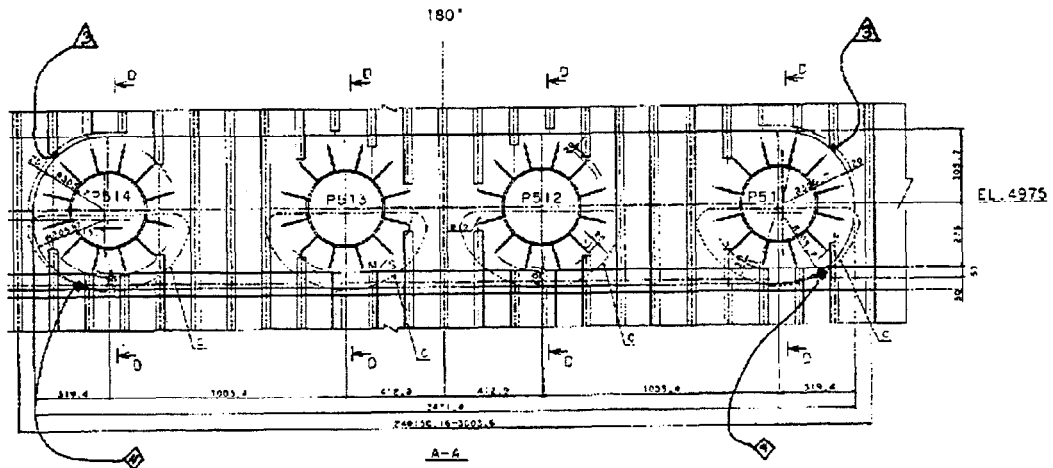


Figure 7-8. Strain Concentration Type 3,4 Near M/S Penetrations

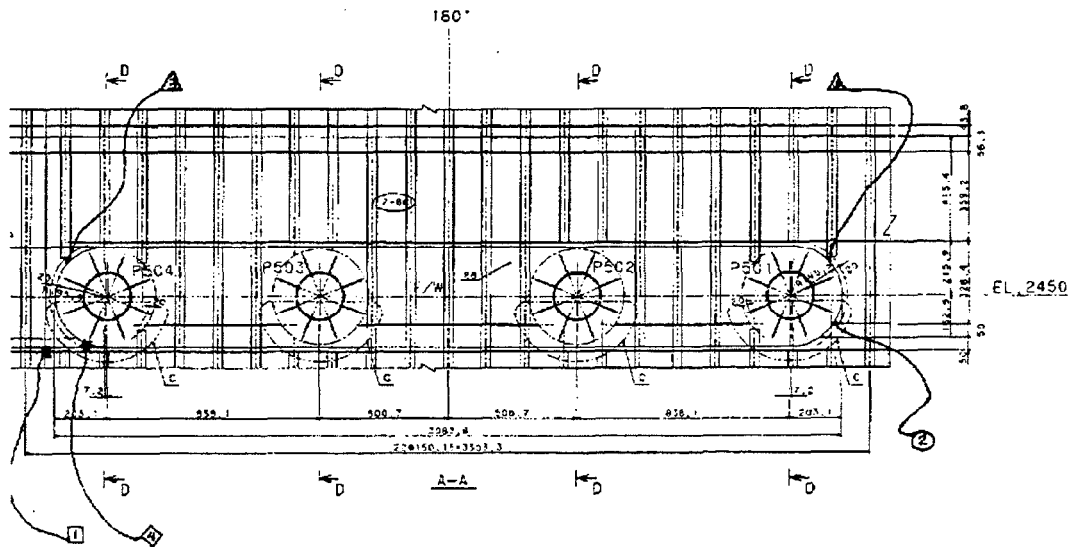


Figure 7-9. Strain Concentration Type 1,2,3,4 Near F/W Penetrations

## 8.0 REFERENCES

1. D. B. Clauss, Round-Robin Pretest Analyses of a 1:6 Scale Reinforced Concrete Containment Model Subject to Static Internal Pressurization, Sandia National Laboratories, SAND87-0891, NUREG/CR-4913, May 1987.
2. D. B. Clauss, Round-Robin Analysis of the Behavior of a 1:6 Scale Reinforced Concrete Containment Model Pressurized to Failure: Post-Test Evaluations, Sandia National Laboratories, SAND89-0349, NUREG/CR-5341, 1989.
3. M. F. Hesssheimer, R. A. Dameron, W. A. VonReisemann, "A Summary of Containment Integrity Research," Proceedings of the Seminar on Containment of Nuclear Reactors Weld in Conjunction with 14th SMiRT, August 25-26, 1997, Saclay, France.
4. R. A. Dameron, R. S. Dunham, Y. R. Rashid, Methods for Ultimate Load Analysis of Concrete Containments, Phase 2, ANATECH Report to EPRI, EPRI NP-4869M, March 1987.
5. R. A. Dameron, et al., Pretest Prediction of a 1:10 Scale Model Test of the Sizewell-B Containment Building, ANATECH Report to Sandia National Labs, Albuquerque, NM NUREG/CR-5671, 1990.
6. Y. R. Rashid, "Ultimate Strength Analysis of Prestressed Concrete Pressure Vessels," Nuclear Engineering and Design 7, 1968, pp. 334-344.
7. Y. R. Rashid, R. S. Dunham, R. J. James, R. A. Dameron, ANAMAT Concrete, Rebar, and Steel Material Models, ANACAP-U Theory Manual, ANATECH Report ANA-98-0243, April 1998.
8. H. D. Hibbitt, et al., ABAQUS User's Manual, Version 4.7, 1988.
9. Various, PCCV Drawing and Material Property Information (See Appendix A), documents provided by Sandia to ANATECH and to Round Robin Analysts for PCCV modeling, 1997-1998.
10. M. P. Collins, D. Mitchell, Prestressed Concrete Structures, 1997 by Response Publications.
11. M. J. Manjoine, "Elevated Temperature Mechanics of Metals," preprints of the 4th International Seminar on Inelastic Analysis and Life Prediction in High Temperature Environment, 7th SMiRT, August 1983.

**BIBLIOGRAPHIC DATA SHEET**

(See instructions on the reverse)

1. REPORT NUMBER  
(Assigned by NRC, Add Vol., Supp., Rev.,  
and Addendum Numbers, if any.)

NUREG/CR-6678  
SAND 00-1535

2. TITLE AND SUBTITLE

Pretest Round Robin Analysis of a Prestressed Concrete  
Containment Vessel Model

3. DATE REPORT PUBLISHED

MONTH	YEAR
August	2000

4. FIN OR GRANT NUMBER

Y6131

5. AUTHOR(S)

V.K. Luk

6. TYPE OF REPORT

Technical

7. PERIOD COVERED (Inclusive Dates)

8. PERFORMING ORGANIZATION - NAME AND ADDRESS (If NRC, provide Division, Office or Region, U.S. Nuclear Regulatory Commission, and mailing address; if contractor, provide name and mailing address.)

Sandia National Laboratories  
Albuquerque, NM 87185-0744

9. SPONSORING ORGANIZATION - NAME AND ADDRESS (If NRC, type "Same as above"; if contractor, provide NRC Division, Office or Region, U.S. Nuclear Regulatory Commission, and mailing address.)

Systems Safety Department  
Nuclear Power Engineering Corporation  
17-1, 3-Chome, Toranomon, Minato-Ku  
Tokyo 105, Japan

Division of Engineering Technology  
Office of Nuclear Regulatory Research  
U.S. Nuclear Regulatory Commission  
Washington, DC 20555-0001

10. SUPPLEMENTARY NOTES

S. Shibata, NUPEC Project Manager

J.F. Costello, NRC Project Manager

11. ABSTRACT (200 words or less)

The Nuclear Power Engineering Corporation of Japan and the U.S. Nuclear Regulatory Commission, Office of Nuclear Regulatory Research, are co-sponsoring and jointly funding a Cooperative Containment Research Program at Sandia National Laboratories in Albuquerque, New Mexico. As part of the program, a prestressed concrete containment vessel model will be tested to failure at Sandia in September 2000. The model, uniformly scaled at 1:4, is representative of the containment structure of an actual pressurized-water reactor plant (OHI-3) in Japan. The objectives of the internal pressurization test are to obtain data on the structural response of the model to pressure loading beyond design basis accident in order to validate analytical modeling, to find the model's pressure capacity, and to observe its response and failure mechanisms.

Seventeen organizations participated in a pretest Round Robin analysis to predict the structural response of the model under overpressurization. This report contains the analytical modeling procedures and the pretest predictions submitted by each organization. This report also includes composite plots of participants' analysis results at the 55 specified locations on the model.

12. KEY WORDS/DESCRIPTORS (List words or phrases that will assist researchers in locating the report.)

Prestressed Concrete Containment Vessel, Steel Containment Vessel, Failure Test,  
Model Analysis, International Participants, Failure Pressure and Mechanisms

13. AVAILABILITY STATEMENT

unlimited

14. SECURITY CLASSIFICATION

(This Page)

unclassified

(This Report)

unclassified

15. NUMBER OF PAGES

16. PRICE